

Mechanical, Thermal
and Environmental Testing
and Performance of

Ceramic Composites and Components

Michael G. Jenkins
Edgar Lara-Curzio
Stephen T. Gonczy

EDITORS

 STP 1392

STP 1392

***Mechanical, Thermal
and Environmental Testing
and Performance of
Ceramic Composites and
Components***

*Michael G. Jenkins, Edgar Lara-Curzio, and
Stephen T. Gonczy, editors*

ASTM Stock Number: STP1392



ASTM
100 Barr Harbor Drive
PO Box C700
West Conshohocken, PA 19428-2959

Printed in the U.S.A.

Library of Congress Cataloging-in-Publication Data

Mechanical, thermal, and environmental testing and performance of ceramic composites and components / Michael G. Jenkins, Edgar Lara-Curzio, and Stephen T. Gonczy, editors.

p. cm (STP; 1392)

"ASTM stock number: STP1392."

"Papers presented at the Symposium on Environmental, Mechanical, and Thermal Properties and Performance of Continuous Fiber Ceramic Composite (CFCC) Materials and Components held in Seattle, Washington on 18 May 1999"—Foreword.

Includes bibliographical references and indexes.

ISBN 0-8031-2872-X

1. Fiber-reinforced ceramics—Environmental testing. 2. Fiber-reinforced ceramics—Mechanical properties. 3. Fiber-reinforced ceramics—Thermal properties. I. Jenkins, Michael G., 1958- II. Lara-Curzio, Edgar, 1963- III. Gonczy, Stephen T., 1947- IV. Symposium on Environmental, Mechanical, and Thermal Properties and Performance of Continuous Fiber Ceramic Composite (CFCC) Materials and Components (1999: Seattle, Wash.)

TA455.C43 M45 2000

620.1'4—dc21

00-059405

Copyright © 2000 AMERICAN SOCIETY FOR TESTING AND MATERIALS, West Conshohocken, PA. All rights reserved. This material may not be reproduced or copied, in whole or in part, in any printed, mechanical, electronic, film, or other distribution and storage media, without the written consent of the publisher.

Photocopy Rights

Authorization to photocopy items for internal, personal, or educational classroom use, or the internal, personal, or educational classroom use of specific clients, is granted by the American Society for Testing and Materials (ASTM) provided that the appropriate fee is paid to the Copyright Clearance Center, 222 Rosewood Drive, Danvers, MA 01923; Tel: 978-750-8400; online: <http://www.copyright.com/>.

Peer Review Policy

Each paper published in this volume was evaluated by two peer reviewers and at least one editor. The authors addressed all of the reviewers' comments to the satisfaction of both the technical editor(s) and the ASTM Committee on Publications.

To make technical information available as quickly as possible, the peer-reviewed papers in this publication were prepared "camera-ready" as submitted by the authors.

The quality of the papers in this publication reflects not only the obvious efforts of the authors and the technical editor(s), but also the work of the peer reviewers. In keeping with long-standing publication practices, ASTM maintains the anonymity of the peer reviewers. The ASTM Committee on Publications acknowledges with appreciation their dedication and contribution of time and effort on behalf of ASTM.

Foreword

This publication, *Mechanical, Thermal and Environmental Testing and Performance of Ceramic Composites and Components*, contains papers presented at the Symposium on Environmental, Mechanical, and Thermal Properties and Performance of Continuous Fiber Ceramic Composite (CFCC) Materials and Components held in Seattle, Washington on 18 May 1999. ASTM Committee C28 on Advanced Ceramics sponsored the symposium in cooperation with Committees E08 on Fatigue and Fracture and D30 on Advanced Composites. Michael G. Jenkins, University of Washington, Edgar Lara-Curzio, Oak Ridge National Laboratory, and Stephen T. Gonczy, Gateway Materials Technology, presided as co-chairmen and are co-editors of the resulting publication.

Contents

Overview

vii

PLENARY

- Relationships of Test Methods and Standards Development to Emerging and Retrofit CFCC Markets**—T. R. BARNETT, G. C. OJARD, AND R. R. CAIRO 3

ROOM-TEMPERATURE TEST RESULTS/METHODS

- Multiple-Laboratory Round-Robin Study of the Flexural, Shear, and Tensile Behavior of a Two-Dimensionally Woven Nicalon™/Sylramic™ Ceramic Matrix Composite**—M. G. JENKINS, E. LARA-CURZIO, S. T. GONCZY, AND L. P. ZAWADA 15
- Test Procedures for Determining the Delamination Toughness of Ceramic Matrix Composites as a Function of Mode Ratio, Temperature, and Layup**—J. J. POLAHA AND B. D. DAVIDSON 31
- Detailed Study of the Tensile Behavior of a Two-Dimensionally Woven Nicalon™/Sylramic™ Ceramic Matrix Composite**—M. G. JENKINS AND L. P. ZAWADA 48
- Testing Methodology for Measuring Transthickness Tensile Strength for Ceramic Matrix Composites**—L. P. ZAWADA AND K. E. GOECKE 62
- Flexural and Tensile Properties of a Two-Dimensional Nicalon™-Reinforced Sylramic™ S-200 Ceramic Matrix Composite**—S. T. GONCZY AND M. G. JENKINS 86

TEST RESULTS/METHODS RELATED TO DESIGN IMPLICATIONS

- Stress-Rupture, Overstressing, and a New Methodology to Assess the High-Temperature Durability and Reliability of CFCCs**—E. LARA-CURZIO 107
- Use of Unload/Reload Methodologies to Investigate the Thermal Degradation of an Alumina Fiber-Reinforced Ceramic Matrix Composite**—C. X. CAMPBELL AND M. G. JENKINS 118
- Fiber Test Development for Ceramic Composite Thermomechanical Properties**—J. A. DICARLO AND H. M. YUN 134
- Effect of Fiber Waviness on the Tensile Response of 2D C(f)/SiC Ceramic Matrix Composites**—M. STEEN 148

Surface Finish and Notch Effect Model for Strength Predictions of Continuous Fiber Ceramic Composites (CFCCs)—M. RAMULU, M. G. JENKINS, AND S. KUNAPORN 160

Notch-Sensitivity of a Woven Oxide/Oxide Ceramic Matrix Composite—R. JOHN, D. J. BUCHANAN, AND L. P. ZAWADA 172

ENVIRONMENTAL EFFECTS AND CHARACTERIZATION

The Effects of Microstructural Damage on the Thermal Diffusivity of Continuous Fiber-Reinforced Ceramic Matrix Composites—S. GRAHAM, D. L. MCDOWELL, E. LARA-CURZIO, R. B. DINWIDDIE, AND H. WANG 185

Oxidation Behavior of Non-Oxide Ceramics in a High-Pressure, High-Temperature Steam Environment—M. K. FERBER, H. T. LIN, AND J. KEISER 201

The Time-Dependent Deformation of Carbon Fiber-Reinforced Melt-Infiltrated Silicon Carbide Ceramic Matrix Composites: Stress-Rupture and Stress-Relaxation Behavior in Air at 1000°C—E. LARA-CURZIO AND M. SINGH 216

The Relationship between Interphase Oxidation and Time-Dependent Failure in $\text{SiC}_f/\text{SiC}_m$ Composites—C. A. LEWINSOHN, C. H. HENAGER JR., E. P. SIMONEN, C. F. WINDISCH JR., AND R. H. JONES 229

DAMAGE ACCUMULATION AND MATERIAL DEVELOPMENT

Characterization of Damage Accumulation in a Carbon Fiber-Reinforced Silicon Carbide Ceramic Matrix Composite (C/SiC) Subjected to Mechanical Loadings at Intermediate Temperature—M. VERRILLI, P. KANTZOS, AND J. TELESMAN 245

Effect of Loading Mode on High-Temperature Tensile Deformation of a SiC/SiC Composite—Ö. ÜNAL 262

Effects of Temperature and Environment on the Mechanical Properties of Tyrano-Hex™ Composites—M. DRISSI-HABTI, N. TAKEDA, K. NAKANO, Y. KANNO, AND T. ISHIKAWA 276

Degradation of Continuous Fiber Ceramic Matrix Composites under Constant Load Conditions—M. C. HALBIG, D. N. BREWER, AND A. J. ECKEL 290

Damage Accumulation in 2-D Woven SiC/SiC Ceramic Matrix Composites—G. N. MORSCHER, J. Z. GYEKENYESI, AND R. T. BHATT 306

Summary 321

Author Index 327

Subject Index 329

Overview

In the nearly decade and a half since its establishment in 1986, ASTM Committee C28 has provided a major forum for promoting standardized terminology, guides, classifications, practices, and test methods for advanced (a.k.a. structural, fine, and technical) ceramics. In particular, since 1991 ASTM Subcommittee C28.07 on Ceramic Matrix ASTM Composites has actively and vigorously introduced and promoted standards and activities nationally (for example, through other ASTM committees, Military Handbook 17, ASME Boiler and Pressure Vessel Code, etc.) and internationally (for example, through ISO) for advanced ceramic matrix composites, specifically continuous fiber ceramic composites.

Continuing these efforts, this publication and the Symposium on Environmental, Mechanical, and Thermal Properties and Performance of Continuous Fiber Ceramic Composite (CFCC) Materials and Components which was held in Seattle, Washington, 18 May 1999 were sponsored by ASTM Committee C28. Twenty-two papers were presented at the symposium and this publication contains twenty-one peer-reviewed manuscripts on continuous fiber-reinforced advanced ceramic composites, related test methods (standards), materials characterization, and design applications.

The advancement of technology has often been limited by the availability of materials and understanding of their behavior. Reflecting this emphasis on materials, in the technology of today, the US government has supported programs such as the Continuous Fiber Ceramic Composites (CFCCs), High Speed Research, and Enabling Propulsion Materials Programs which target specific new materials such as CFCCs for a broad range of applications, from chemical processing, to stationary heat engines, to power generation, to aerospace vehicles. Such applications require that still-emerging materials such as CFCCs be refined, processed, characterized, and manufactured in sufficient volume for successful widespread use in aggressive thermal/mechanical/environmental operating conditions. Concurrently, as the materials are refined, designers must have access to material properties and performance databases in order to integrate the material systems into their advanced engineering concepts. Without extensive materials characterization, producers of materials cannot evaluate relative process improvements nor can designers have confidence in the performance of the material for a particular application.

Developing and verifying appropriate test methods as well as generating design data and design experience for advanced materials is expensive and time consuming. High-temperature ceramic composites are more expensive to process than monolithic ceramics, not just because of the extra cost of constituent materials but also because of labor-intensive fabrication steps. Equipment for testing at elevated temperatures is highly specialized and expensive. Unique and novel test methods must be developed to take into account thermal stresses, stress gradients, measurement capabilities, gripping methods, environmental effects, statistical considerations, and limited material quantities. It is therefore imperative that test methods be carefully developed, standardized, verified, and utilized so that accurate and statistically significant data are generated and duplication of efforts can be minimized in test programs. Similarly, design codes must be written to establish which information on material properties and performance are required for particular applications as well as which standard test methods are recommended to quantify this information.

The papers in this publication provide current results of research and development programs on continuous fiber ceramic composites. The papers are divided into four major categories:

1. Room-Temperature Test Results/Methods
2. Test Results/Methods Related to Design Implications
3. Environmental Effects and Characterization
4. Damage Accumulation and Material Development

The sections addressing these categories contain papers on various types of continuous fiber ceramic composites, including those with matrices synthesized by chemical vapor infiltration (CVI), polymer impregnation and pyrolysis (PIP), melt infiltration (MI), or viscous glass infiltration. The Room-Temperature Test Results/Methods section includes papers on results of a round-robin program that used several full-consensus standards, influence of various test parameters on the tensile, shear and flexural behavior, novel transthickness tensile strength method, and delamination "toughness" and its effects. The section on Test Results/Methods Related to Design Implications includes papers on stress rupture, stress-relaxation and overstressing effects on testing and design, unload/reload tensile tests, fiber testing, fiber waviness, surface finish notch effects and notch sensitivity. The papers in the Environmental Effects and Characterization section address the thermal diffusivity changes due to microstructural damage, oxidation behavior in aggressive environments, time dependent deformation, and the effects of interphase oxidation. In the section on Damage Accumulation and Material Development, papers address damage accumulation during mechanical loading, effect of loading mode, temperature and environmental degradation of a novel pre-commercial material, degradation under constant load, and process development of a novel material system.

With this symposium and the resulting special technical publication, ASTM has made another stride forward in standardization activities by providing a wealth of information on continuous fiber ceramic composites. This information will assist the research, processing, and design community in better understanding the behavior, characterization and design nuances of these materials. This information is also invaluable for standards and code development background as test methods continue to be introduced and verified for continuous fiber ceramic matrix composites.

Michael G. Jenkins
Department of Mechanical Engineering
University of Washington
Seattle, WA 98195-2600
Symposium co-chair and co-editor

Edgar Lara-Curzio
Mechanical Characterization and Analysis
Group
Oak Ridge National Laboratory
Oak Ridge, TN 37831-67064
Symposium co-chair and co-editor

Stephen T. Gonczy
Gateway Materials Technology
Mt. Prospect, IL 60056
Symposium co-chair and co-editor

Plenary

Terry R. Barnett,¹ Greg C. Ojard,² and Ronald R. Cairo²

Relationships of Test Methods and Standards Development to Emerging and Retrofit CFCC Markets

Reference: Barnett, T. R., Ojard, G. C., and Cairo, R. R. “**Relationships of Test Methods and Standards Development to Emerging and Retrofit CFCC Markets,**” *Mechanical, Thermal and Environmental Testing and Performance of Ceramic Composites and Components, ASTM STP 1392*, M. G. Jenkins, E. Lara-Curzio, and S. T. Gonczy, Eds., American Society for Testing and Materials, West Conshohocken, PA, 2000.

Abstract: The evolutionary path of ceramic matrix composites (CMCs) to viable candidate materials for current engineering designs of today and tomorrow has been littered with appropriate and inappropriate theoretical models, useful and useless test methods, and hopeful and hopeless materials systems. As continuous fiber ceramic composite (CFCC) material systems have been introduced, theoretical models and practical test methods have been proposed (and adopted) to characterize their behavior. Often these materials are targeted for specific applications intended to exploit the bulk CFCC as well as its constituent properties.

The unique position and expertise of the author’s employer, a private research laboratory, have enabled an up-close and detailed perspective on not only CFCCs and their characterization but also the targeted engineering applications. In this paper, a case study will be discussed regarding characterization of a CFCC for a particular application; a high temperature combustor liner in a gas turbine engine. The potential for standardized methods will be reviewed.

Keywords: ceramic, composite, continuous fiber ceramic composite, CFCC, ceramic matrix composite, ring burst, hoop testing

Background

The author’s employer is a private research laboratory with a well-established

¹Manager, Experimental Mechanics Section, Southern Research Institute, 757 Tom Martin Drive, Birmingham, AL 35211.

²Materials engineer and structures engineer, respectively, Pratt and Whitney, PO Box 109600, West Palm Beach, FL 33410.

test and measurement capability and is widely recognized as one of the top laboratories in the country for high temperature evaluation of advanced materials [1,2]. This position has enabled an up-close and detailed perspective on not only the ceramic matrix composites and their characterization but also the targeted engineering applications. In this paper, a case study will be discussed regarding hoop characterization of a CMC for a high temperature combustor liner in a gas turbine engine. The potential for standardized methods will be reviewed.

The pursuit of next generation supersonic transports to carry people around the world at twice the speed of sound has fostered the development of technology and materials to make the effort cost effective, reliable, and environmentally compatible. In order to meet these goals, companies have focused on advanced materials such as ceramic matrix composites [3,4]. CMCs have the potential to enable components to run hotter to improve thermodynamic efficiency and reduce noise and emissions. Innovative design and the judicious use of CMCs in hot section components of gas turbine engines and creative interfacing with metallic components are key to their successful implementation. The ability to run without surface cooling has made CMCs particularly attractive for combustor applications.

Case Study

Background

Material development on efforts like NASA's Enabling Propulsion Materials (EPM) program has shown that properties from flat panels fabricated out of a silicon carbide fiber/silicon carbide matrix (SiC/SiC) CMC can meet the design requirements for proposed combustor liners [3,4]. A key contributor to the success of fabrication was agreement and utilization of standard test methods that allowed testing to be done at a variety of independent test laboratories with results that were consistent from laboratory to laboratory. Testing was done in tensile, compressive, shear and flexural modes along with thermal property characterization on a variety of SiC/SiC CMCs.

Application of a CMC – Combustor Liners

A major concern with high-speed air transports is the addition of nitrogen oxides (NO_x) to the upper atmosphere [5]. To reduce NO_x emissions, new combustor configurations that improve thermodynamic efficiency are required - CMCs are viable candidate materials for such designs (Figure 1). Specific design parameters for the combustor require the material withstand temperatures up to 1200 °C depending on the engine cycle, and resist thermal gradients that produce bending in the axial direction and tensile stresses in the circumferential (hoop) direction (if bodies of revolution).

Not only does thermal loading induce mechanical stress but also a propensity for micro-structural degradation in oxidation prone CMCs [3,4,6,7]; thus, application is extremely challenging.

Application of Test Methodology – Hoop Tensile Evaluation

To assess the materials resistance to thermal stress induced by axial temperature gradients in combustor liners, one of the necessary properties is the hoop tensile strength. Data obtained from coupons of flat plates would be a starting point; however, it is generally known that as complexity of parts increase, properties tend to decrease because of the difficulty of replicating ideal processing conditions in curved or transitional regions or in the vicinity of unique out-of-plane features [8]. Consequently, a test methodology to characterize hoop properties is required.

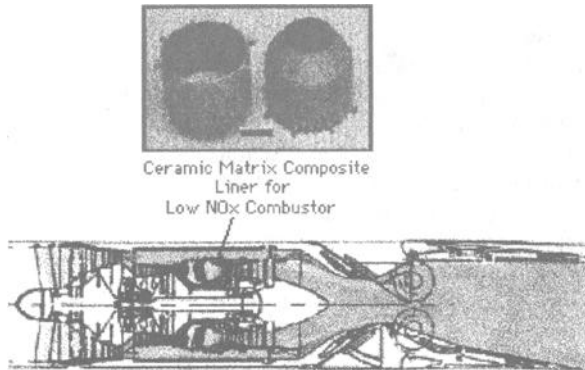


Figure 1 – CMC combustor liner [3]

In order to establish baseline room temperature hoop tensile properties, the hydrostatic ring test facility [9,10] shown in Figure 2 was used. The facility consists of a pressure vessel, a pump, and the ancillary equipment for measuring pressure and strain.

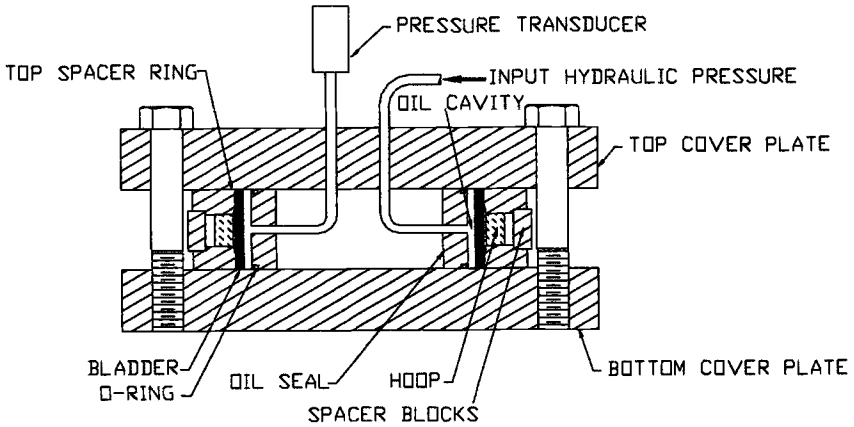


Figure 2 - Schematic of the room temperature hydrostatic ring test facility [9,10]

The pressure vessel is made in several pieces. The two cover plates are clamped together with a circle of bolts. The ring specimen is mounted between the upper and lower spacer rings. Spacer blocks, mounted between the spacer rings, maintain approximately 0.127 mm of clearance to allow for free radial movement. Application of pressure by hydraulic oil to a rubber bladder, which mates to the inner diameter (ID) of the ring, causes expansion of the specimen. (Note the facility is not size-limited and can accommodate rings ranging from ~1.6 cm to 76 cm ID by ~0.25 cm to 6.4 cm height.)

A string wrapped around the outside of the hoop and attached to spring-loaded linear variable differential transformers (LVDTs) mounted on a rigid frame (Figure 3) monitors the circumferential change in displacement with increasing pressure. The change in circumference can be transformed into the outer diameter (OD) circumferential strain. A pressure transducer is used to measure the pressure applied to the ring. The tensile hoop stress can be calculated using mechanics of materials relations for thin walled pressure vessels such that

$$\sigma = p \frac{r}{t} \tag{1}$$

where

- p = internal pressure
- r = inner radius, and
- t = wall thickness of hoop

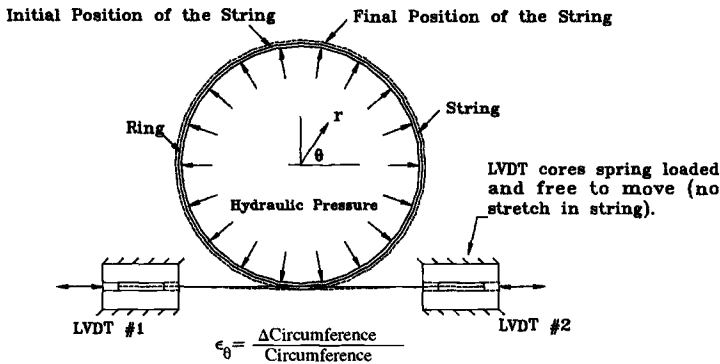


Figure 3 – LVDT/string arrangement for measuring hoop strain [9,10]

An X-Y plotter, or a data acquisition system, records the response of the ring under the applied pressure. The plot consists of internal pressure versus the deformation signal from the string. The data reported are ultimate hoop tensile strength, hoop elastic modulus, and hoop tensile strain-to-failure. Typical hoop stress-strain responses from ceramic matrix composites evaluated in this facility are shown in Figure 4.

Since the design of the combustor liner entails use at temperatures up to 1200 °C, hoop properties are required at these temperatures also. To obtain these properties, the elevated temperature hoop facility (Figure 5) was used [11].

As with the room temperature test, pressure is applied to a rubber bladder by hydraulic oil. However, in this case, the bladder mates to the ID of water-cooled wedges (18 total), which in turn mate to low thermal conductivity wedges, which then mate to the ID of the test ring. The wedge arrangement is required to reduce the radial temperature from 1200 °C at the ring to approximately room temperature at the bladder to prevent the bladder from melting. For this arrangement, it has been analytically and experimentally shown on an aluminum ring that the variation in circumferential stress as a result of the wedge loading is less than ± 5 percent [12]. (Further analysis is currently being conducted using finite elements to determine the pressure profile applied to the ID of the ring in both polar and axial directions and the true peak hoop stress in the CMC test ring.)

The ancillary equipment for the elevated temperature test is essentially as that for the room temperature test. Typical stress-strain responses at various temperatures from EPM SiC/SiC ceramic matrix composites evaluated in this facility are given below (Figure 6).

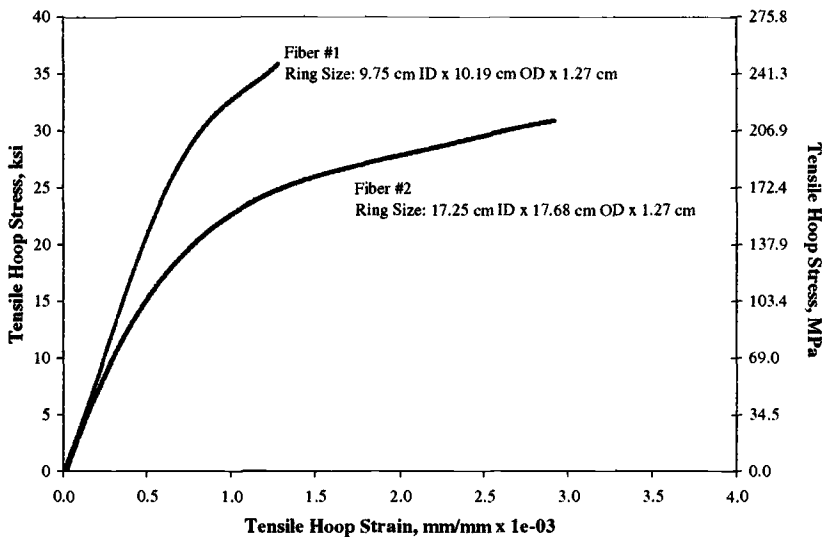


Figure 4 – Typical EPM SiC/SiC CMC circumferential stress-strain response at room temperature

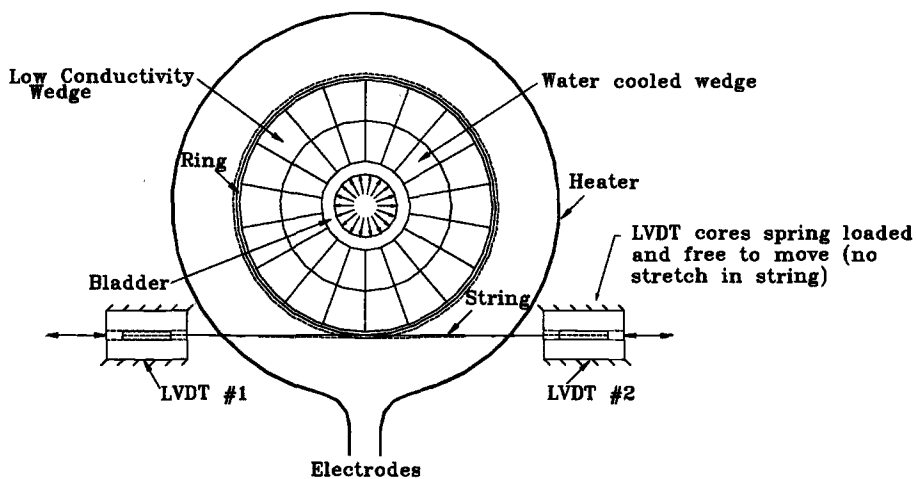


Figure 5 – Schematic of the elevated temperature hydrostatic ring test [11,12]

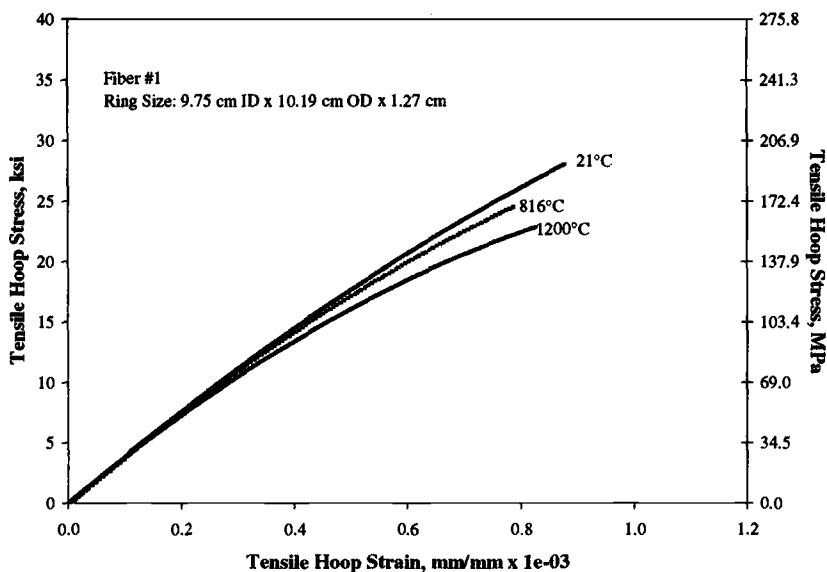


Figure 6 – Typical EPM SiC/SiC CMC circumferential stress-strain response at varying temperatures

Discussion

This case study demonstrates a good example of a test methodology developed “in-house” and its relationship to a specific CMC application - in this case, hoop testing of a CMC combustor liner. The test methodology is not limited to just combustor liners, i.e. the method is not a “single use” type and not application specific. Pressure vessels, exit cones, filters for hot gas filtration, and other body-of-revolution components are examples to which the methodology is directly applicable. If warranted, the current test methodology may be transferred to an existing nation, or international, standards writing body for formal normalization.

The American Society of Testing and Materials (ASTM), the European Committee for Standardization (CEN), NASA’s EPM program, the International Standards Organization (ISO), and others have developed, or are developing new standards for CMCs (Table 1), and monolithic advanced ceramics. It is important that test standards development continue because standards:

- provide guidelines and terms for transfer of consistent information between designers, manufacturers, and end users,
- provide consistent, meaningful data to users,
- provide consistent, meaningful data to material databases,
- permit confidence in data interchange and integration.

However, once introduced standards should not be used blindly. During development of standards, careful consideration should be given to ensure that the standard provides the proper guidelines for the data required and the technique is analogous (in terms of applied loading and boundary conditions) to the application, etc. Also, there are pitfalls to using only established standards, i.e., “on the books.” Pitfalls would include the test technique not being the best one available, or the technique being too generic and not addressing all technical issues that can, and eventually do come up, or the technique producing non-unique or multiple failure mechanisms.

An example is the tensile hoop strength of CMCs determined with an elastomeric insert. Although it is a viable technique of comparative testing for down-selecting materials, the hydrostatic methodology discussed previously has certain advantages such as better-defined boundary conditions and wider applicability. The hydrostatic approach might be the test of choice when developing and verifying analytical models. The boundary conditions are not affected by specimen size, diameter or height, or material. It is possible that the “calibrations” of the elastomeric insert might be affected by the changes in test specimen dimensions and material properties. Thus the choice of test method should be dictated by the information required.

Summary

In conclusion, test characterization of current and emerging materials should not be performed without challenging the prevailing test procedure and specimen configuration for relevance to the specific design application. There are many unique attributes such as high temperature, directional stress, anisotropy, or low strain-to-failure in these materials that require more precise understanding of the mechanics of deformable bodies.

Though not a replacement for rig or engine tests, judicious use of specialized laboratory test specimens and procedures can economically reduce component risk by highlighting unanticipated failure modes or damage accumulation mechanisms in a controlled environment.

Table 1 – *Examples of Test Standards Development for CMCs.*

Organization	Material	Method Reference Number
ASTM	Ceramic Matrix Composites	C1275 Tension Strength (Room Temp.)
		C1337 Creep, Creep Rupture
		C1292 Shear Strength
		C1341 CFCC Flexure Strength
		C1358 Compressive Strength
		C1359 Tensile Strength (Room Temp.)
		Cxxxx Trans-Thickness Tension
		Cxxxx Hoop Strength via Elastomeric Insert (Room Temp.)
		C1425 Interlaminar Shear

References

- [1] Air Force Materials Laboratory Technical Report AFML-TR-79-4002, "Test Methods for High Temperature Materials Characterization," February 1979.
- [2] Barnett, Terry R. and Starrett, H. Stuart, "Mechanical Behavior of High Temperature Composites," Southern Research Technical Report SRI-MME-94-290-6145-I-F, April 1994.
- [3] Enabling Propulsion Materials Program Annual Technical Progress Report, Period of Performance: 1 October 1996 – 30 September 1997, NASA Contract NAS3-23685.
- [4] Enabling Propulsion Materials Program Annual Technical Progress Report, Period of Performance: 1 October 1997 – 30 September 1998, NASA Contract NAS3-23685.
- [5] Tie, Xue Xi, et al, February 1994, "The Impact of High Altitude Aircraft on the Ozone Layer in the Stratosphere," *Journal of Atmospheric Chemistry*, Vol. 18, Issue 2, pp. 103-128.
- [6] Halbig, Michael C., Brewer, David N., Eckel, Andrew J., and Cawley, James D., "Stressed Oxidation of C/SiC Composites," NASA LeRC and U.S. ARL Technical Report E-10741, April 1997.
- [7] Prewo K., Johnson, B., and Starrett, S., "Silicon Carbide Fibre-Reinforced Glass-Ceramic Composite Tensile Behavior at Elevated Temperature," *Journal of Materials Science*, Volume 24, pp. 1373-9, 1989.
- [8] Ojard, G., Naik R., Cairo, R., Hornick J., Linsey, G., Brennan, J., and Amos, J., "Mechanical Characterization of Ceramic Matrix Composite Components", to be published in the Proceedings of the 1999 International Committee on Aeronautical Fatigue Symposium, Seattle, WA, July 12-16, 1999.
- [9] Barnett, Terry R., and Starrett, H. Stuart, "Hoop Evaluation of Flanged Ceramic Matrix Composite Subelements," Southern Research Technical Report SRI-ENG-94-915-8369-I-F, December 1994.
- [10] Barnett, Terry R., and Starrett, H. Stuart, "In-Plane and Hoop Tensile Evaluation of As-received and Burner-Rig Exposed Ceramic Matrix Composites for Turbine Engine Applications," Southern Research Institute Technical Report SRI-MME-94-055-7857.1-I-F, January 1994.

- [11] Bush, A. L., and Legg, J. K., "The Development of a High Temperature Ring Test Facility," Air Force Materials Laboratory Technical Report AFML-TR-74-275, January 1975.
- [12] Starrett, Stuart, Johnsen, Brian, and Gillis, Pam, "Analytical Study of the High Temperature Tensile and Compressive Ring Tests," Proceedings of the October 1982 JANNAF Meeting, Monterey, California.

Room-Temperature Test Results/Methods

Michael G. Jenkins,¹ Edgar Lara-Curzio,² Stephen T. Gonczy,³ and Larry P. Zawada⁴

Multiple-Laboratory Round-Robin Study of the Flexural, Shear, and Tensile Behavior of a Two-Dimensionally Woven Nicalon™/Sylramic™ Ceramic Matrix Composite

Reference: Jenkins, M. G., Lara-Curzio, E., Gonczy, S. T., and Zawada, L. P., “Multiple-Laboratory Round-Robin Study of the Flexural, Shear, and Tensile Behavior of a Two-Dimensionally Woven Nicalon™/ Sylramic™ Ceramic Matrix Composite,” *Mechanical, Thermal and Environmental Testing and Performance of Ceramic Composites and Components, ASTM STP 1392*, M. G. Jenkins, E. Lara-Curzio, and S.T. Gonczy, Eds., American Society for Testing and Materials, West Conshohocken, PA, 2000.

Abstract: A round-robin study was conducted on the flexural, shear, and tensile mechanical behavior of a Nicalon™ fiber-reinforced Sylramic™ matrix CFCC continuous fiber ceramic composite (CFCC) to: 1) determine the precision and bias of three ASTM test methods at room temperature for flexure, shear and tension [Test Method for Flexural Properties of Continuous Fiber-Reinforced Advanced Ceramics (C 1341), Test Method for Shear Strength of Continuous Fiber-Reinforced Advanced Ceramics at Ambient Temperatures (C 1292), and Test Method for Monotonic Tensile Strength Testing of Continuous Fiber-Reinforced Ceramic Composites with Solid Rectangular Cross-Sections at Ambient Temperatures (C 1275)]; 2) establish an expansive data base (e.g., Mil-Hdbk-17 CMC effort) for a single CFCC; and 3) evaluate a statistically-significant sample size of a single CFCC for processing and design purposes. The commercial CFCC was comprised of eight plies of ceramic grade Nicalon™ fiber fabric in a symmetric 0/90 lay-up, a proprietary boron-containing interphase, and a silicon nitrocarbide matrix (Sylramic™) derived from polysilazane. Ten each of flexure, in-plane tension, in-plane (Iosipescu) shear, and interlaminar (double notch compression) test specimens were tested by each of seven to ten different laboratories per the applicable ASTM test method for totals of sixty to one hundred replicate tests for each test type. With a few exceptions, coefficients of variation for repeatability and reproducibility ranged from 5 to 10%.

Keywords: ceramic composite, flexure, precision and bias, round-robin, shear, tension

¹ Associate professor, Department of Mechanical Engineering, University of Washington, Box 352600, Mechanical Engineering Building, Seattle, WA 98195-2600.

² Group leader, Mechanical Characterization and Analysis Group, Oak Ridge National Laboratory, P.O. Box 2008, MS 6069, Oak Ridge, TN 37831-6069.

³ President, Gateway Materials Technology, 221 S. Emerson, Mt. Prospect, IL 60056.

⁴ Research scientist, Air Force Research Laboratory, WL/MLLN, Wright-Patterson AFB, OH 45433.

Introduction and Background

“Reinforced” ceramic matrix composite (CMC) materials retain the desirable characteristics of monolithic advanced ceramics (e.g., high stiffness, low density, etc.) but exhibit increased “toughness” over their monolithic counterparts [1, 2]. Continuous fiber ceramic composites (CFCCs) are a special subset of the broader class of materials known as CMCs. CFCCs exhibit greatly increased “toughness” (i.e., energy absorption during deformation), thus providing the inherent damage tolerance and increased reliability that are critical in many engineering applications where the brittle nature of traditional ceramics renders the use of these materials unacceptable [1].

A variety of industrial applications have been targeted for CFCCs, including tubing, nozzles, vanes and supports in heat recovery equipment and heat engines [1, 2]. In the chemical industry, reformers, reactors and heat exchangers are other potential applications. In gas turbine power generation CFCC components allow increased temperatures resulting in substantial reductions in nitrous oxide (NO_x) emissions and savings in the cost of power generation [2].

Thermo-mechanical behavior (and its subsequent characterization) of CFCCs is currently the subject of extensive investigation worldwide [3-5]. In particular, determination of the properties and performance (mechanical, thermal, thermo-mechanical, physical, environmental, etc.) of CFCCs is required for: 1) basic characterization for purposes of materials development, quality control and comparative studies; 2) a research tool for revealing the underlying mechanisms of mechanical performance; and 3) engineering performance-prediction data for engineering applications and components design [3]. As CFCC prototype and trial products begin to reach the marketplace, the paucity of standards (i.e., test methods, classification systems, unified terminology, and reference materials) for these materials and the lack of CFCC design codes and their related data bases are limiting factors in commercial diffusion and industrial acceptance [4] of these advanced materials.

Standards

The term “standards” has many implications. To the researcher and the technical community it may be fundamental test methodologies and units of measure. To the manufacturer or end-product user it may be materials specifications and tests to meet performance requirements. Commercial standards equate to the rules and terms of information transfer among designers, manufacturers and product users [4]. There are even fundamental differences between levels of standards: company (internal use with only internal consensus); industry (trade/project use with limited organizational consensus); government (wide usage and varying levels of consensus); full-consensus (broadest usage and greatest consensus).

At present, there are few -- nationally or internationally -- full-consensus standards [5] for testing not only advanced ceramics and but especially CFCCs. However, of those standards that do exist, American Society for Testing and Materials (ASTM) standards are arguably considered the most technically rigorous and of the highest quality. Part of

this high regard is due to attention to such details as precision and bias (P&B) statements that provide the user with some insight as to the utility of the standard (e.g. inter and intralaboratory variability of the standard) Although ASTM requires P&B statements for all its standards, the current ASTM standards for CFCCs do not have such statements because of the newness of the subject materials.

Design Codes and Data Bases

The meaning of the term 'design code' is not generally well understood. As used here 'design code' is not a design manual (i.e., a "cookbook" design procedure resulting in a desired component or system). Instead, 'design codes' are widely-accepted, but general rules for the construction of components or systems with emphasis on safety [5]. A primary objective is the reasonably certain protection of life and property for a reasonably-long safe-life of the design. Although needs of the users, manufacturers and inspectors are recognized, the safety of the design can never be compromised.

A logical outcome of design codes is the incorporation of data bases of material properties and performance 'qualified' for inclusion in the code. 'Qualified' means that the data have been attained through testing per the statistical and test method requirements of the code. 'Qualified' data bases often require a minimum numbers of tests for 1) a particular batch of material and 2) multiple batches of material. Data bases may include primary summary data (e.g., mean, standard deviation, and numbers of tests) along with secondary data from the individual tests (e.g., numerical and graphical information such as stress-strain curves, temperature profiles, or test specimen geometry).

Design codes and their data bases may even be backed as legal requirements for implementing an engineering design (e.g., certification and compliance with the American Society of Mechanical Engineers (ASME) Boiler and Pressure Vessel Code is a legal requirement in forty-eight of the fifty United States). At present there are no national or international design codes allowing CFCCs in any type of code-controlled application. This situation may be hampering material utilization since designers cannot use a material directly in new designs, but instead must 1) show evidence that the material meets the requirements of the code and 2) obtain special permission to use the material in the code design. In addition material development is impaired since, without a demand for a new material, there is no incentive for further refinement.

Based on the needs of existing standards and the needs of evolving design codes/data bases for CFCCs several goals were set forth for this study: 1) to develop precision and bias statements for each of three national standards for CFCCs (required by ASTM), 2) to contribute to an expanded, reliable data base for CFCCs, 3) to provide statistical distributions of properties and performance of a single CFCC for a large statistical sample for design purposes, and 4) to provide statistical distributions of properties and performance of a single CFCC for a large statistical sample for production purposes.

For the purposes of this paper, the first goal of developing precision and bias statements is emphasized. The test material is first described followed by details of the experimental procedures. Intra- and interlaboratory test results are presented and compared. Finally, the results are discussed and summarized.

Test Material:

The test material was a commercially-available CFCC⁵ comprised of a ceramic grade Nicalon™ (Si-C-O) fiber-reinforced Sylramic™ (Si-C-N) matrix composite produced [6] in three stages: interphase deposition, fiber preform fabrication, and matrix formation.

Interphase formation took place via the chemical vapor infiltration (CVI) of a nominal 0.5 μm thick proprietary boron nitride (BN)-containing layer onto the ceramic-grade Nicalon™ fibers. Such a coating may act as a weak fiber/matrix interface to promote fiber debonding and pullout [6], thereby increasing the “toughness” of the bulk CFCC.

Fiber preforms were fabricated from two-dimensional eight harness satin weave cloths comprised of fiber bundles [6] stacked in alternating 0/90 lay-up to achieve “good nesting” of the weave and to provide a symmetric structure. The (0/90/0/90/90/0/90/0) stacking of eight cloth layers produced a preform thickness of ~2 to 3 mm and a nominal fiber volume fraction of 45%.

Matrix formation occurred by the multi-step polymer impregnation process (PIP) in which a polysilazane ceramic precursor polymer and silicon nitride powder were first used to infiltrate the fiber preform. After curing, the infiltrated preform was heated to approximately 1000°C in a controlled atmosphere to pyrolyze the cured polymer.

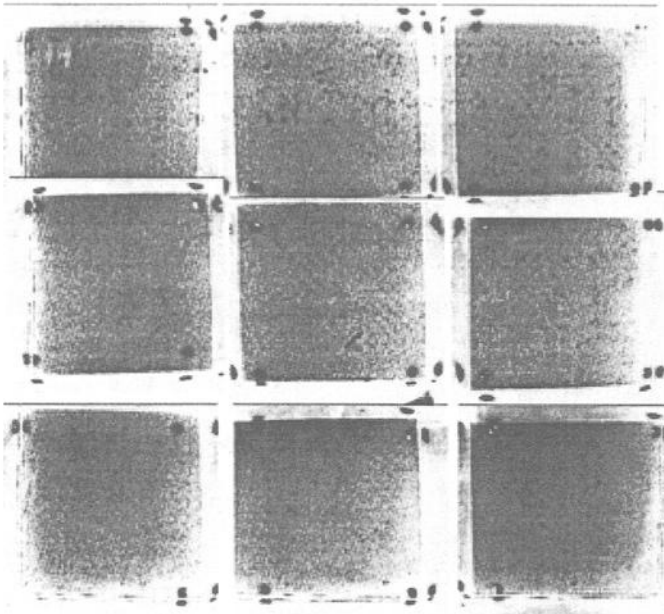


Figure 1 – Example of infrared imaging for one plate (nine separate images).

⁵ Sylramic S200, Dow Corning, Inc., Midland, MI in November 1997 (as of July 1999, Engineered Ceramics, Inc., San Diego, CA)

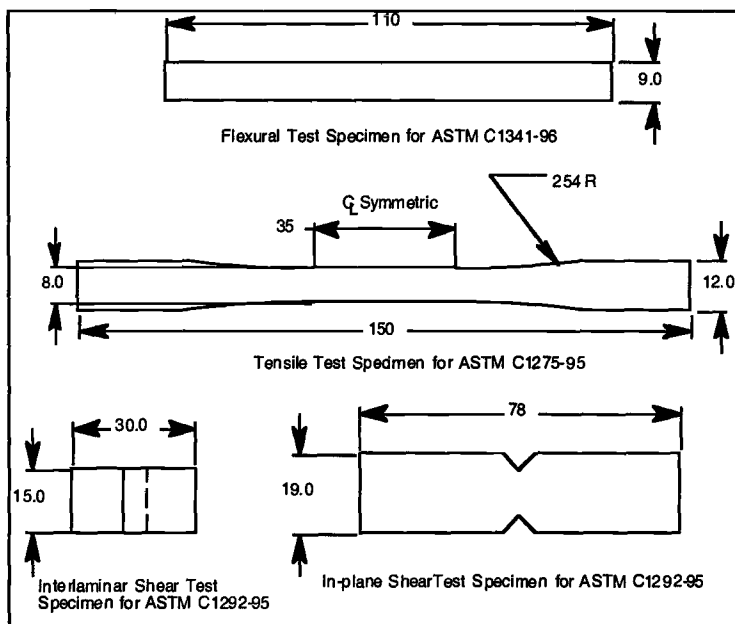


Figure 2 - Test specimens used as part of the round robin (dimensions in mm).

This cycle of impregnate, cure, pyrolyze was repeated five times on the whole plates at which time the basic test specimen blanks were cut from the plates. PIP cycles were continued from 17 to 19 times on the test specimen blanks to achieve less than 5% open porosity. Infrared nondestructive evaluation of all plates were conducted at the fifth infiltration step to identify any anomalies (Fig. 1).

Test specimen blanks were fabricated at the fifth PIP cycle using conventional machining and 40 to 100-grit electroplated diamond-grit router bits (1800 RPM) with no cutting fluids with 0.127 mm of material removed per pass [7]. For the flexural and tensile test specimens, the blanks were the final geometries (see Fig. 2). For the two shear test specimens (see Fig. 2), notches had to be cut in the blanks after the final PIP cycle using 220-grit diamond-grit wheel (3700 RPM) and a water-based cutting fluid.

Experimental Method

Pretest Procedures

Pertinent geometric dimensions on all four hundred test specimens were measured using digital calipers and micrometers as part of the pretest inspections [7]. The mass of each test specimens was determined and a geometric density was calculated for each test specimen using the measured mass and a volume calculated from the dimensions and geometry. Visual inspections were used to screen lower quality test specimens from those actual test specimens that were eventually shipped to round robin participants.

Ten tensile, five interlaminar shear, five in-plane shear and no flexural test specimens were screened out. All one hundred flexural test specimens, all one hundred tensile test specimens, and all one hundred in-plane shear test specimen blanks (i.e. prior to notching) were impulse resonance tested [7] for elastic modulus using ASTM Test Method Test Method for Dynamic Young's Modulus, Shear Modulus, and Poisson's Ratio for Advanced Ceramics by Impulse Excitation of Vibration (C 1259).

Test Procedures

Three ASTM standard test methods were employed to evaluate flexural [Test Method for Flexural Properties of Continuous Fiber-Reinforced Advanced Ceramics (C 1341)], in-plane and interlaminar shear [Test Method for Shear Strength of Continuous Fiber-Reinforced Advanced Ceramics at Ambient Temperatures (C 1292)], and tensile [Test Method for Monotonic Tensile Strength Testing of Continuous Fiber-Reinforced Ceramic Composites with Solid Rectangular Cross-Sections at Ambient Temperatures (C1275)] behavior of the subject material. Specifics regarding each of the protocols for the application of each test method are contained in the following sections.

Flexure - Ten laboratories (three governmental, six industrial and one academic) participated in the flexure tests [8] which were conducted per C 1341. Each laboratory conducted ten tests with all tests carried out in four-point, 1/4-point flexure (40 and 80-mm inner and outer spans, respectively) using roller supports and semi-articulating fixtures. Applied force and deflection (center point) were measured at a displacement rate of 0.1 mm/s under ambient conditions. A schematic illustration of the flexure test configuration and a photograph of the test setup at one of the laboratories are shown in Fig. 3. Some laboratories employed strain gages to measure longitudinal and/or transverse strain directly. Primary mechanical properties of interest included elastic modulus in flexure, flexural strength, and flexural strain at failure.

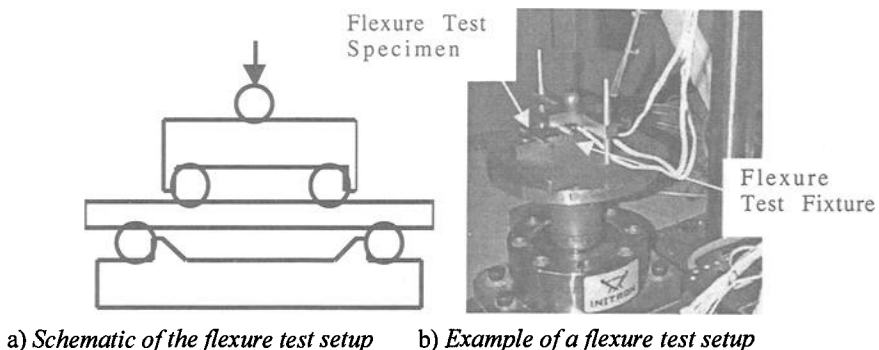


Figure 3 - Illustrations of flexure test setup per C 1341.

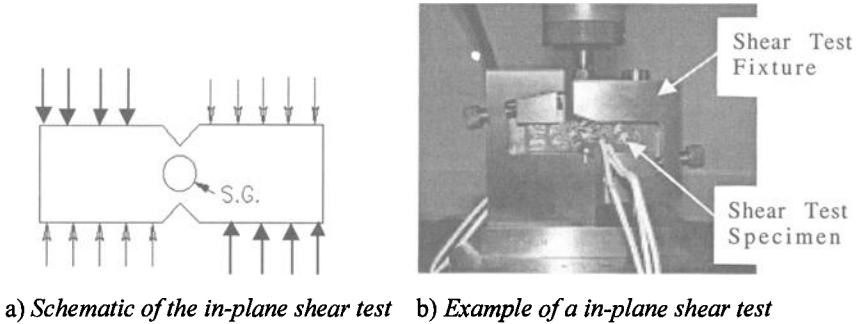


Figure 4 - Illustrations of in-plane shear test setup per C 1292.

Shear - Eight laboratories (three governmental, four industrial, and one academic) participated in the in-plane shear (Iosipescu, double V-notch) tests [9] which were conducted per C 1292. Each laboratory conducted ten tests with all tests carried out using Iosipescu-type shear test fixtures. Applied force and deflection were measured at a displacement rate of 0.05 mm/s under ambient conditions. A schematic illustration of the in-plane shear test configuration and a photograph of the test setup at one of the laboratories are shown in Fig. 4. Some laboratories employed 'shear' strain gages to determine in-plane shear modulus. Primary mechanical properties of interest included in-plane shear strength and in-plane shear modulus where appropriate.

Seven laboratories (three governmental, three industrial and one academic) participated in the interlaminar shear (double notch compression) tests [9] which were conducted per ASTM Test Method C 1292. Each laboratory conducted ten tests with all tests carried out using guided, anti-buckling shear test fixtures. Applied force and deflection were measured at a displacement rate of 0.05 mm/s under ambient conditions. A schematic illustration of interlaminar shear test configuration and a photograph of the test setup at one of the laboratories are shown in Fig. 5. The primary mechanical property of interest was the interlaminar shear strength.

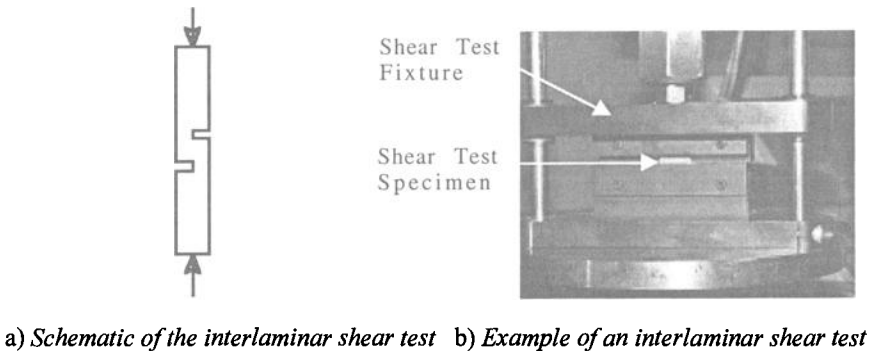
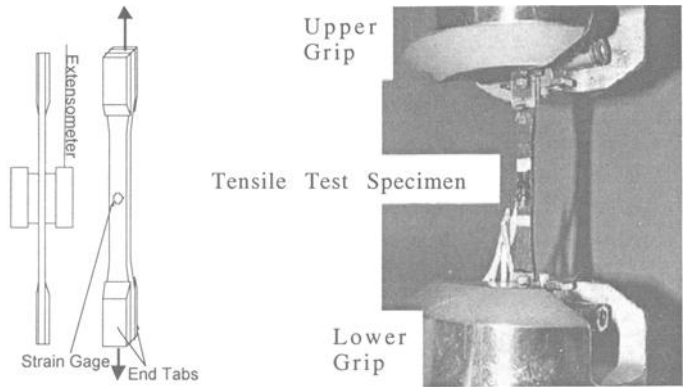


Figure 5 - Illustrations of interlaminar shear test setup per C 1292.



a) Schematic of the in-plane tensile test b) Example of an in-plane tensile test

Figure 6 - Illustrations of in-plane tensile test setup per C 1275.

Tension - Nine laboratories (two governmental, five industrial and two academic) participated in the tension (flat, “dog-bone” end-tabbed tensile test specimens) tests [10], which were conducted per C 1275. Each laboratory conducted ten tests with all tests carried out using hydraulically-loaded face-loading grips. Applied force and strain over extensometer gage lengths of 25 mm were measured at a displacement rate of 0.02 mm/s under ambient conditions. A schematic illustration of the tensile test configuration and a photograph of the test setup at one of the laboratories are shown in Fig. 6.

Some laboratories used strain gages to determine in-plane elastic modulus and Poisson’s ratio. Primary mechanical properties of interest included in-plane elastic modulus, proportional limit stress/strain, ultimate tensile strength/strain, and fracture strength/strain. Some laboratories determined modulus of resilience and modulus of toughness.

Results

Because of the nature of the round robin, confidentiality of the identities of the participating laboratories is preserved, except for the University of Washington, which coordinated the round robin. The results for the University of Washington are presented in all cases as an example of intralaboratory results. Other laboratories are identified in a code linked to the type of test (e.g., flexure: FLX-1, 2, 3...; tensile in plane: TIP-1, 2., 3...; shear in plane: SIP 1, 2, 3....; and shear interlaminar: SIL 1, 2, 3....)

Flexure

The intra- and interlaboratory comparison of two flexural properties (i.e., flexure elastic modulus and ultimate flexural strength) are presented in Figure 7. Note the relative lack of scatter both within and between laboratories for flexural elastic modulus (Fig. 7a), but the somewhat higher scatter for ultimate flexural strength. (Fig. 7b). The grand mean (i.e., statistical mean of all the results) with error bars of ± one standard deviation is to the far right of each figure.

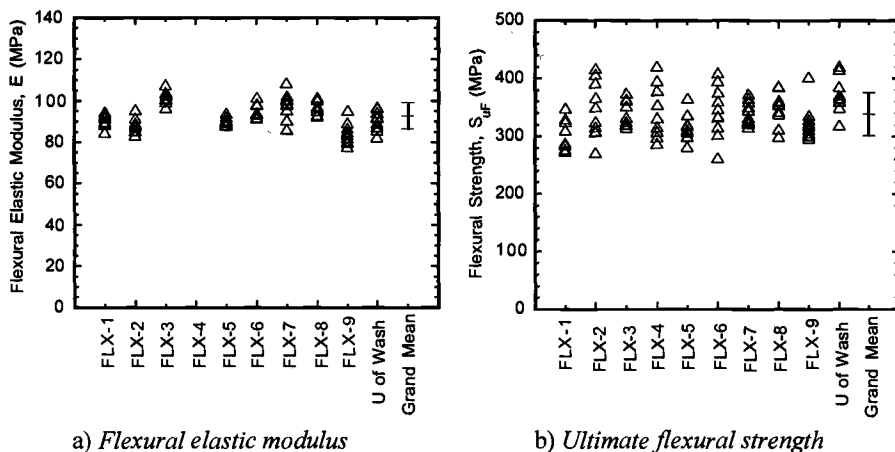


Figure 7 - Selected round-robin flexural test results.

Comparison of intra- and interlaboratory results are shown in Table 1 where the intra laboratory results are for the University of Washington. Sample size for the interlaboratory results is ten and for the interlaboratory results is one hundred.

Shear

The intra- and inter laboratory comparison of the two shear strengths (in-plane and interlaminar) are presented in Figure 8. Note the relative lack of scatter both within and between laboratories for in-plane shear strength (Fig. 8a), but the high degree of scatter for interlaminar shear strength. (Fig. 8b). The grand mean (i.e., statistical mean of all the results) with error bars of ± one standard deviation is to the far right of each figure.

Table 1 – Intra- and interlaboratory flexural test results.

Flexural Property	Intralaboratory		Interlaboratory	
	Mean ± 1 SD ^a	CV ^b	Grand Mean ± 1 SD	CV
Modulus of Elasticity (GPa)	91±5	5.2%	93±6	6.9%
Poisson's ratio	0.15±0.01	8.2%	NR ^c	NR
Proportional limit flexural stress (MPa)	138±12	9.1%	NR	NR
Strain at proportional limit flexural stress (m/m*10 ⁻⁶)	1280±160	12.2%	NR	NR
Ultimate flexural strength (MPa)	374±30	8.0%	339±37	10.9%
Strain at ultimate flexural strength (m/m*10 ⁻⁶)	4700±340	7.1%	4640±634	13.6%
Fracture flexural strength (MPa)	362±31	8.7%	NR	NR
Strain at fracture flexural strength (m/m*10 ⁻⁶)	4850±510	10.6%	NR	NR

^a SD = standard deviation.

^b CV = coefficient of variation.

^c NR = not required.

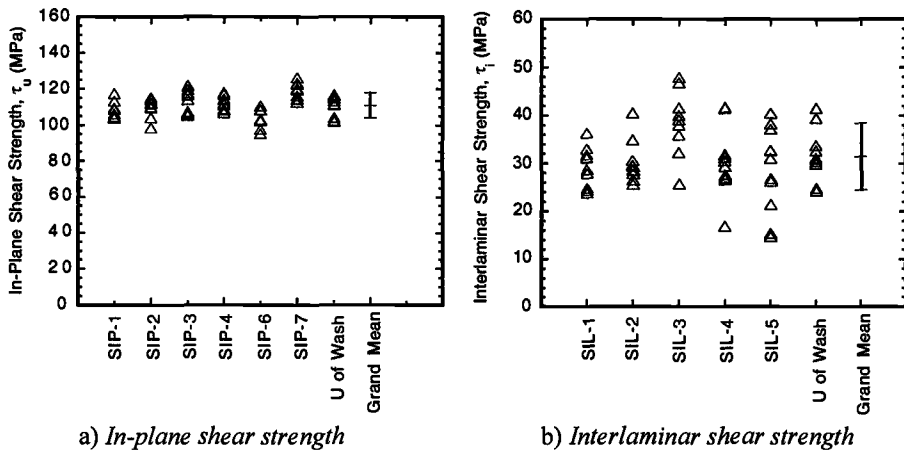


Figure 8 - Selected round-robin shear test results.

Comparison of intra- and interlaboratory results are shown in Table 2 where the intra laboratory results are for the University of Washington. Sample size for the interlaboratory results is ten for each shear test and for the interlaboratory results is eighty and seventy for the in-plane and interlaminar shear tests, respectively.

Tension

The intra- and interlaboratory comparison of two in-plane tensile parameters (elastic modulus and ultimate tensile strength) are shown in Fig. 9. Note the lack of relative scatter both within and between laboratories (Figs. 9a and 9b). The grand mean (i.e., statistical mean of all the results) with error bars of \pm one standard deviation is to the far right of each figure.

Table 2 – Intra- and interlaboratory shear test results.

Shear Property	Intralaboratory		Interlaboratory	
	Mean \pm 1 SD ^a	CV ^b	Grand Mean \pm 1 SD	CV
In-plane shear modulus (GPa)	33 \pm 1	4.5%	NR ^c	NR
In-plane proportional limit stress (MPa)	67 \pm 13	19.0%	NR	NR
Strain at in-plane proportional limit stress (m/m*10 ⁻⁶)	2280 \pm 432	18.9%	NR	NR
Ultimate in-plane shear strength (MPa)	111 \pm 6	5.3%	111 \pm 5	4.5%
Strain at ultimate in-plane shear strength (m/m*10 ⁻⁶)	2520 \pm 176	7.0%	NR	NR
Ultimate interlaminar shear strength (MPa)	32 \pm 6	17.3%	33 \pm 5	16.2%

^a SD = standard deviation.

^b CV = coefficient of variation.

^c NR = not required.

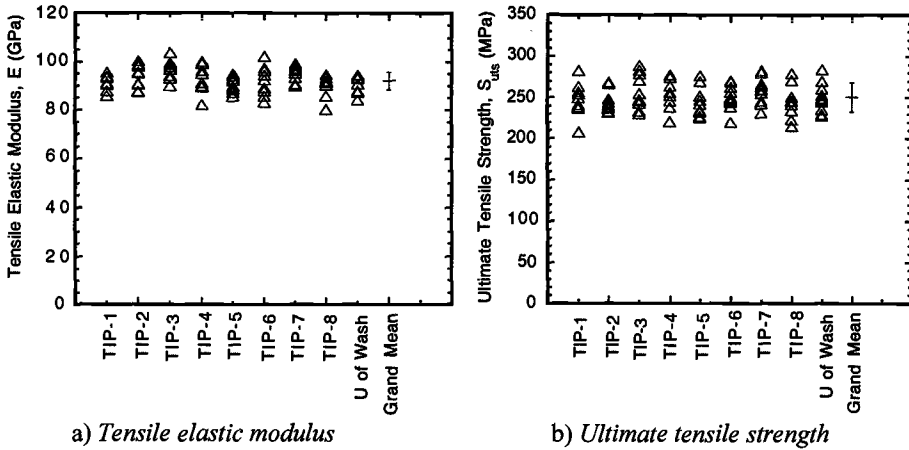


Figure 9 - Selected round-robin tensile test results.

Comparison of intra- and interlaboratory tensile results are shown in Table 3 where the intralaboratory results are for the University of Washington. Sample size for the interlaboratory results is ten and for the interlaboratory results is ninety.

Discussion and Summary

Flexure

All flexural test results were analyzed for the effect of test procedure and material on the repeatability and reproducibility of ultimate flexural strength, strain at fracture and elastic modulus in flexure [8]. In regard to test procedure, there was no statistical significance (Analysis of Variance (ANOVA) at 95% confidence) for test rate, drive

Table 3 – Intra- and interlaboratory tensile test results.

Tensile Property	Intralaboratory		Interlaboratory	
	Mean ± 1 SD ^a	CV ^b	Grand Mean ± 1 SD	CV
Modulus of Elasticity (GPa)	91±4	4.0%	92±6	6.7%
Poisson's ratio	0.12±0.01	7.3%	NR ^c	NR
Proportional limit stress (MPa)	83±3	3.1%	85±3	4.0%
Strain at proportional limit stress (m/m*10 ⁻⁶)	1000±0	0.0%	1000±0	0.0%
Ultimate tensile strength (MPa)	250±18	7.1%	251±18	7.2%
Strain at ultimate tensile strength (m/m*10 ⁻⁶)	4400±400	8.3%	4305±393	9.1%
Fracture strength (MPa)	250±18	7.1%	251±18	7.1%
Strain at fracture strength (m/m*10 ⁻⁶)	4400±400	8.3%	4310±393	9.1%
Modulus of Resilience (J/m ³)	41631±1282	3.1%	42266±1703	4.0%
Modulus of Toughness (J/m ³)	635502±100626	15.8%	623545±102405	16.42%

^a SD = standard deviation.

^b CV = coefficient of variation.

^c NR = not required.

Table 4 – Comparison of dimensional measurement procedure and results for flexure.

Lab	Measurement Tool	Thickness	Thickness	Width	Width
		Mean	CV ^a	Mean	CV
FLX-10	Knife Edge Caliper	2.64	2.2%	8.91	0.5%
FLX-7	Ball Micrometer	2.66	2.8%	9.01	1.1%
FLX-3	Knife Edge Caliper	2.72	3.4%	8.94	0.3%
FLX-4	Flat Anvil Micrometer	2.74	2.1%	9.02	0.3%
FLX-8	Knife Edge Caliper	2.76	2.9%	8.99	0.4%
FLX-1	Flat Anvil Micrometer	2.77	3.9%	9.01	0.3%
FLX-5	Flat Anvil Micrometer	2.77	2.9%	9.02	0.2%
FLX-9	Knife Edge Caliper	2.77	2.0%	9.00	0.2%
FLX-2	Flat Anvil Micrometer	2.78	4.5%	8.99	0.3%
FLX-6	Flat Anvil Micrometer	2.78	2.5%	8.99	0.3%
	Mean for All Test Specimens	2.74	2.9%	8.99	0.6%

^a CV = coefficient of variation.

mechanism on the test machine, type of articulation on the test fixture, method of determination of center point deflection, humidity, or level of preload. A procedural effect which was noted was the method of dimensional measurement as shown in Table 4.

C 1341 does not specify a particular method for dimensional measurement but does specify an accuracy of the dimensional measurement instrument. Some of the interlaboratory scatter in those properties dependent on dimensions raised to greater exponent powers (e.g., stress and/or strength) can be explained by variability in dimensional measurements. For example, an ultimate flexural strength of 374±27 MPa was calculated for Lab FLX-10 (University of Washington) in Table 4 using the thicknesses measured using a knife edge caliper (mean thickness of 2.64 mm). An ultimate flexural strength of 335±21 MPa was calculated using the thicknesses measured using a flat anvil micrometer (mean thickness of 2.77 mm). Material variability was also assessed. There were indications that plate to plate variations in properties existed because of differences in fiber strengths in each plate due to the effects of different interphase coating runs. These plate to plate differences are discussed in the tensile results subsection. From these round robin results, a precision and bias statement is suggested for C 1341 based on the results analysis using ASTM Practice for Conducting an Interlaboratory Study to Determine the Precision of a Test Method (E 691).

Precision: An interlaboratory test program* gave the following values for coefficients of variation for the most commonly measured flexural properties for a commercial CFCC (Sylramic S200) with a nominal fiber volume fraction of 45%, an average bulk density of 2200 kg/m³, and an average open porosity of 2.2% :

	Elastic Modulus, E	Flexural Strength, S _{flx}	Strain at Fracture, ε _f
CV% _r	4.4	9.9	14.1
CV% _R	7.1	11.1	13.6

r = repeatability (within laboratory) for 10 laboratories and 10 tests per laboratory

R= reproducibility (between laboratories) for 10 laboratories and 100 tests

Bias: No statement of bias can be made because no acceptable reference standard exists

* Supporting data can be found in the Appendix. Additional data are available from ASTM Headquarters.

Shear

All shear test results were analyzed for the effect of test procedure and material on the repeatability and reproducibility of in-plane and interlaminar shear strengths. In regard to test procedure, there was no statistical significance (ANOVA at 95% confidence) for test rate, drive mechanism on the test machine, type of test fixture, humidity, or level of preload. A possible procedural effect was noted regarding the notching of the interlaminar shear test specimens (notching was done in test specimen preparation). The relative depth of the notch can have an effect on the measured interlaminar shear strength as shown in Fig. 10. The unavoidable variability in machining these notches may have as much influence on the scatter in the interlaminar shear strength results as the porosity of the matrix in this matrix/interphase-dominated measurement. From these round robin results, the following precision and bias statement is suggested for C 1292 based on the analysis of the results using E 691.

Precision: An interlaboratory test program* gave the following values for coefficients of variation for the most commonly measured shear properties for a commercial CFCC (Sylramic S200) with a nominal fiber volume fraction of 45%, an average bulk density of 2200 kg/m³, and an average open porosity of 2.2%:

	In-plane Shear Strength, τ_u	Interlaminar Shear Strength, τ_i
CV% _r	2.0	7.6
CV% _R	4.9	17.7

r = repeatability (within laboratory) for 8 and 7 labs for in-plane and interlaminar respectively and 10 tests for each type of shear test per laboratory
 R=reproducibility (between laboratories) for 8 and 7 labs and 80 and 70 tests

Bias: No statement of bias can be made because no acceptable reference standard exists

* Supporting data can be found in the Appendix . Additional data are available from ASTM Headquarters.

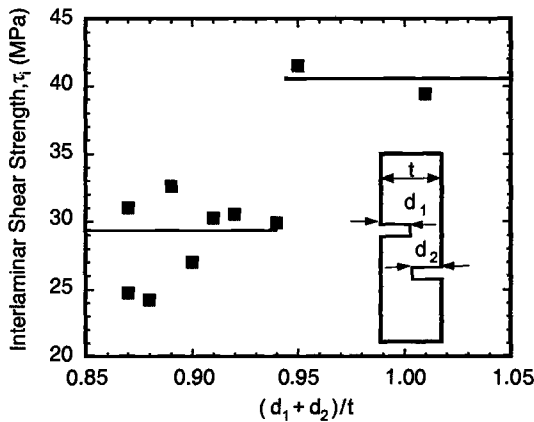


Figure 10 - Effect of variability in notch depth on interlaminar shear strength results.

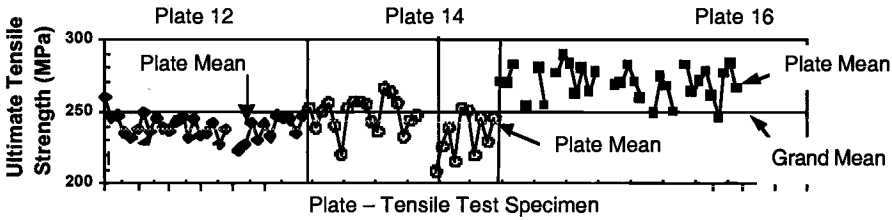


Figure 11 - Effect of plate of origin on ultimate tensile strength results

Tension

All tensile test results were analyzed for the effect of test procedure and material on the repeatability and reproducibility of various tensile properties [10]. In regard to test procedure, there was no statistical significance (ANOVA at 95% confidence) for drive mechanism on the test machine, grip pressure, strain gage measurement, temperature, humidity, pre/post test load train misalignment, and extensometer gage length. Two procedural issues were identified in reporting results: there is no single well-defined method for calculating elastic modulus in C 1275 (this did not cause variability in results as shown in Fig. 9 and Table 3) and there was no single method specified in the round robin for calculating proportional limit stress (this caused large variability until the stress-strain curves were reanalyzed using a specified proportional limit strain of 1000×10^{-6} m/m). The effect of material was evaluated for the effect of plate of origin, thickness, density, and porosity in elastic modulus, proportional limits stress, ultimate tensile strength, and strain at fracture. No effects of thickness, density or porosity were noted. Plate of origin did affect ultimate tensile strength and strain at fracture, both fiber-dominated properties (see Fig. 11). In these cases, plate 16 clearly showed greater ultimate tensile strengths and strains to fracture than did plates 12 and 14. Although a single lot of fiber was used to make all three plates, the fabric in each plate underwent different interphase coating runs which affected fiber strengths [10]. From these round robin results, the following precision and bias statement is suggested for C 1275 based on the analysis of the results using E 691.

Precision: An interlaboratory test program* gave the following values for coefficients of variation for the most commonly measured tensile properties for a commercial CFCC (Sylramic S200) with a nominal fiber volume fraction of 45%, an average bulk density of 2200 kg/m^3 , and an average open porosity of 2.2%:

	Elastic Modulus, E	Proportional Limit Stress, σ_0	Ultimate Tensile Strength, S_{UTS}	Strain at Fracture, ϵ_f
CV% _r	4.7	3.4	7.2	9.3
CV% _R	5.0	4.1	7.2	9.2

r = repeatability (within laboratory) for 9 laboratories and 10 tests for each laboratory
 R = reproducibility (between laboratories) for 9 laboratories and 90 tests

Bias: No statement of bias can be made because no acceptable reference standard exists

* Supporting data can be found in the Appendix. Additional data are available from ASTM Headquarters.

Acknowledgments

Research sponsored by the U.S. Department of Energy, Assistant Secretary for Energy Efficiency and Renewable Energy, Office of Industrial Technologies, Industrial Energy Efficiency Division and the Continuous Fiber Ceramic Composites Program under Contract DE-AC05-96OR22464 with Lockheed Martin Energy Research Corporation. The participating laboratories are acknowledged: AlliedSignal (Engines and Composites), Ames Laboratory, Army Research Laboratory, Cincinnati Testing Labs, Composite Testing and Analysis, Dow Corning, Gateway Materials Technology, NASA-Glenn Research Center, Northrup Grumman, Oak Ridge National Laboratory, Southern Research Institute, United Technology Research Center, University of Dayton Research Institute, University of Washington, Air Force Research Laboratory

References

1. Jenkins, M. G., Piccola, J.P., Jr., Mello, M. D., Lara-Curzio, E., Wereszczak, A. A., "Mechanical Behavior of a 3-D Braided, Continuous SiC Fiber-Reinforced / CVI SiC Matrix Composite at Ambient and Elevated Temperatures," *Ceramic Engineering and Science Proceedings*, Vol. 14, No. 9-10, 1993, pp. 991-997.
2. Karnitz, M. A., Craig, D. A., and Richlen, S. L., "Continuous Fiber Ceramic Composite Program," *Ceramic Bulletin*, Vol. 70, No. 3, 1991, pp. 430-435.
3. Phillips, D. C. and Davidge, R. W., "Test Techniques for the Mechanical Properties of Ceramic Matrix Fiber Composites," *Journal of British Ceramic Transactions*, Vol. 85, 1986, pp. 123-130.
4. Schneider, S. J. and Bradley, D. R., "The Standardization of Advanced Ceramics," *Advanced Ceramic Materials*, Vol. 3, No. 5, 1988, pp. 442-449.
5. Jenkins, M. G., "Standards and Codes for Ceramic Matrix Composites," *Advanced Composite Materials*, Vol. 8, No. 1, 1999, pp. 55-76.
6. French, J. E., "Ceramic Matrix Composite Fabrication: Polymer Processing," Chapter 7 in *Handbook on Continuous Fiber-Reinforced Ceramic Composites*, R.L. Lehman, S.K. El-Rahaiby, J.B. Wachtman, Jr., eds, Purdue Research Foundation, W. Lafayette, IN, 1995, pp. 269-299.
7. VanLandeghehn, P. L., "Intra- and Interlaboratory Round Robin Mechanical Test Evaluation of a Continuous Fiber Ceramic Composite (CFCC)" M.S. Thesis, University of Washington, Seattle, WA, 1999.
8. Gonczy, S.T. and Jenkins, M. G. "Multi-Laboratory Round Robin Study of the Flexural Behavior of a Continuous Fiber Reinforced Ceramic Matrix Composite (CMC)," *Ceramic Engineering and Science Proceedings*, Vol. 20, No. 3-4, 1999, pp. 615-624.
9. Lara-Curzio, E. and Jenkins, M. G., "Multi-Laboratory Round Robin Study of the Shear Behavior of a Continuous Fiber Reinforced Ceramic Matrix Composite (CFCC)," presented at the *23rd Annual Cocoa Beach Conference and Exposition*, (American Ceramic Society), Cocoa Beach, FL, 24-29 January 1999.

30 CERAMIC COMPOSITES AND COMPONENTS

10. Jenkins, M.G., and Zawada, L.P., "Detailed Study of the Tensile Behavior of a Two-Dimensionally Woven Nicalon™/Sylramic™ Ceramic Matrix Composite," *Mechanical, Thermal and Environmental Testing and Performance of Ceramic Composites and Components, ASTM STP 1392*, M.G. Jenkins, E. Lara-Curzio and S.T. Gonczy, Eds., American Society for Testing and Materials, West Conshohocken, PA, 2000.

Jonathan J. Polaha¹ and Barry D. Davidson²

Test Procedures for Determining the Delamination Toughness of Ceramic Matrix Composites as a Function of Mode Ratio, Temperature, and Layup

Reference: Polaha, J. J. and Davidson, B. D., “**Test Procedures for Determining the Delamination Toughness of Ceramic Matrix Composites as a Function of Mode Ratio, Temperature, and Layup,**” *Mechanical, Thermal and Environmental Testing and Performance of Ceramic Composites and Components, ASTM STP 1392*, M. G. Jenkins, E. Lara-Curzio, and S. T. Gonczy, Eds., American Society for Testing and Materials, West Conshohocken, PA, 2000.

Abstract: A study was conducted to improve upon currently used test procedures for determining the Mode I, Mode II and mixed-mode delamination toughness of ceramic matrix composite materials. Test methods and specimen geometries were chosen that may be used to test unidirectional or multidirectional layups. The test methods consisted of the Mode I double cantilever beam test, the Mode II end-notched flexure test and the mixed-mode single leg bending test. Procedures for these tests were developed that could be used at room or elevated temperature and for which a compliance calibration method of data reduction could be employed. These procedures were then used to perform a study on a Nicalon/MAS-5 fiber-reinforced ceramic to determine the effects of mode ratio, temperature and layup on delamination toughness. It was concluded that the three test methods combined can be used to provide sufficient information on the variation of toughness with mode mix for most design purposes.

Keywords: Ceramic matrix composite, delamination, Mode I, Mode II, mixed-mode, double cantilever beam, end-notched flexure, single leg bending

Introduction

Continuous fiber ceramic matrix composite (CMC) materials are increasingly being proposed for high temperature structural applications. However, laminated CMC materials with two-dimensional fiber architectures are susceptible to delamination failures. The determination of the delamination toughness of a given material, commonly

¹ Structural engineer, The Boeing Company, P.O. Box 3707, MC 67-FE, Seattle, WA, 98124-2207.

² Associate professor, Department of Mechanical, Aerospace and Manufacturing Engineering, Syracuse University, Syracuse, NY, 13244.

expressed through the critical energy release rate, G_c , is therefore important for purposes of design as well as for quantitative comparisons of various material systems.

Previous investigations into the toughness of CMC materials have shown that G_c is a function of mode ratio, layup and temperature [1,2]. The double cantilever beam (DCB) test is commonly used to determine the Mode I toughness, G_{Ic} [2,3], and the end-notched flexure (ENF) test may be used to determine the Mode II toughness, G_{IIc} [1,4,5]. The cracked four-point bend specimen is perhaps the most commonly used method for determining the mixed-mode toughness of CMCs [2,6]. Typically, beam theory-based methods of data reduction are used with all of these tests [1-6].

There are a number of difficulties with current delamination toughness testing procedures for CMC materials. For example, one must make certain assumptions about the material properties and the applicability of beam theory to reduce the data to obtain G_c ; these and other issues concerning the failure mode of these specimens [2,7] may affect the validity of the results. Another difficulty involves the way specimens are often obtained, where narrow test specimens are cut from unidirectional laminates and delaminations are simulated as an edge crack through the specimen's thickness [1,4,5]. These specimens have exceedingly large length-to-width and thickness-to-width ratios and may give different results than are found in practical structural geometries. Such methods are also limited to testing only unidirectional layups. Several techniques have also been used to assess the onset of crack advance, including nonlinearities in the load versus displacement response [4] or nonlinearities in the near-tip crack face displacements [5], but none of these has conclusively been shown to correspond to the onset of growth.

The goal of this investigation was to modify test procedures and/or data reduction techniques of currently existing test methods to provide the most accurate determination of the interlaminar fracture toughness of CMC materials as a function of mode ratio, temperature and layup. The DCB and ENF tests were used to determine the Mode I and Mode II toughnesses, respectively. A relatively new method, the single leg bending (SLB) test [8,9], was used to determine the mixed-mode toughness. This test produces a mixed-mode condition where $G_{II}/G \approx 0.4$; here, G_{II} is the Mode II energy release rate and G is the total energy release rate. These tests were chosen because the critical energy release rate for each may be obtained by the compliance calibration method of data reduction and the laminate properties need not be accurately known. A precracking procedure was developed such that starter cracks could be created along the plane of lamination. These test procedures were then used to study delamination in a Nicalon/MAS-5 fiber-reinforced ceramic. This material system was manufactured at the Corning Glass Works and is comprised of Nicalon silicon-carbide fibers and a magnesium aluminosilicate matrix [10]. The materials used in this study were reported to have a 45% fiber volume, a density of 2.6 g/cm³ and 0% porosity. Unidirectional [0]₁₆ specimens were tested in all three test configurations, and crossply [(90/0)₄]_S specimens were tested in the SLB configuration only. These test results provided data on the effects of mode ratio and layup on delamination toughness. In addition, all test configurations were run at both 21°C and 500°C to evaluate the effects of temperature. The elevated temperature condition was chosen to be somewhat below that temperature (650°C) where fiber oxidation has been observed [11] yet high enough that some mild effect of

temperature could be studied [12]. For all tests, nondestructive evaluation was used to determine the onset of delamination growth, and these results were correlated to more readily observable events.

Test Methods and Data Reduction

The DCB Test

The DCB test, as shown in Figure 1, was used to determine the Mode I fracture toughness, G_{Ic} , of the unidirectional specimens. The DCB fixture that was used in this study is illustrated in Figure 2. Load was applied to the specimen's cracked regions through a pair of mechanical loading tabs [13] that were machined from a nickel-based superalloy to provide the high temperature capability. The tabbed specimen was supported in the load frame with a pair of small superalloy clevises and water cooled grips.

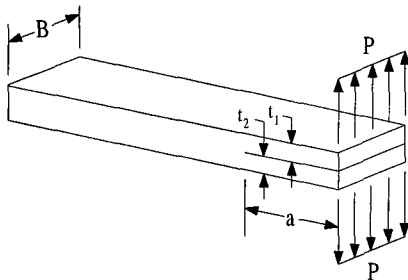


Figure 1 - *The DCB test.*

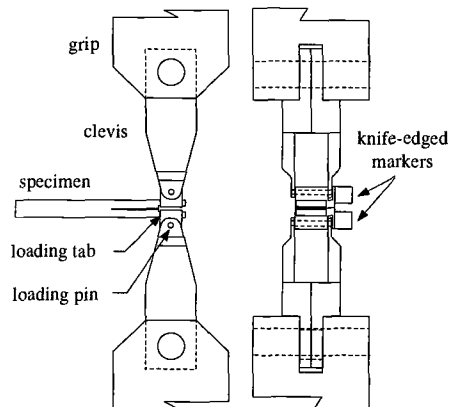


Figure 2 - *The DCB test fixture.*

It is generally accepted that a compliance calibration method is the most accurate method of data reduction for the DCB test, as one need not make assumptions about the material properties [14]. To this end, a procedure was developed for the compliance calibration of CMC DCB specimens at room and elevated temperatures. The crack opening displacement was determined using a laser micrometer to measure the gap between a pair of knife-edged markers which protruded from the loading tabs. The markers were integrally machined into the loading tabs such that their reference edges aligned with the specimen's cracked region centerlines at the load axis. The compliance of each specimen as a function of crack length was found from the slope of the load versus laser micrometer displacement data. However, it was later discovered that the clevis-grip linkages in the fixture permitted the specimen to rotate as the load was applied [13]. This affected the validity of the laser micrometer displacement measurements.

Thus, little confidence could be placed in our results by the compliance calibration method, since the displacement data from only a limited number of unaffected tests could be considered. It was therefore decided to utilize a classical beam theory (CBT) based method of data reduction for determining G_{Ic} . However, with the fixture problem remedied, the compliance method will still yield the best results, and it is recommended that it be used in future investigations.

By the CBT method, the specimen compliance, C , versus crack length, a , relation is defined as [13]

$$C = \frac{2a^3}{3D_{eff}} \quad (1)$$

This expression was fit to the slope of the deflection versus load data to determine the "effective" bending rigidity of the cracked region, D_{eff} . Use of D_{eff} accounts for the variations in thickness along the length of the cracked regions, the variation in fiber density through the laminate thickness, and the true three-dimensional constraint conditions (the test is generally not plane stress or plane strain). An average value of D_{eff} was determined from the limited number of fracture tests which were unaffected by the fixture problem reported earlier, and this average value was used for the reduction of all test data. Substituting Equation 1 into the fundamental equation for energy release rate [15]

$$G = \frac{P^2}{2B} \frac{\partial C}{\partial a} \quad (2)$$

yields the following expression for the mode I fracture toughness

$$G_{Ic} = \frac{P_c^2 a^2}{BD_{eff}} \quad (3)$$

In Equations 2 and 3, B is the specimen's width. This expression was used to obtain G_{Ic} for each specimen by using the critical load obtained for that specimen, P_c .

The ENF Test

The ENF test geometry, as shown in Figure 3, was used to determine the Mode II toughness, G_{IIc} , of the unidirectional specimens. All tests were performed in a three-point bend fixture that was fabricated from silicon-carbide to provide the high temperature capability. The test fixture had a half-span length, L , equal to 20 mm, and the support rollers had a diameter of 3.18 mm. Data reduction for all tests was performed by compliance calibration. To this end, a compliance versus crack length curve was developed for each specimen tested. Each specimen was loaded to approximately 50% of its predicted fracture load at five different crack lengths. These predictions were based on

preliminary tests that were performed to obtain an estimate of G_{IIc} . The crack lengths where the compliance tests were performed included the crack length at which the fracture test was to be run, a_c , as well as $a_c \pm 1.9 \text{ mm}$ and $a_c \pm 3.8 \text{ mm}$. To facilitate this process, the specimens were prepared with cracked and uncracked regions that were longer than required, and the crack length was adjusted by placing the specimen appropriately into the testing fixture. For each specimen, compliance tests were performed at each of the five crack lengths and the compliance at a given crack length, a , was obtained from the slope of a linear least-squares curve fit of the deflection versus load data. To minimize errors, each specimen was compliance tested at each crack length three different times, and at each crack length, the compliance used for data reduction was taken to be the average value obtained from the three tests. A compliance versus crack length curve was obtained, for each specimen, by fitting a polynomial of the form

$$C = C_0 + C_1a + C_2a^2 + C_3a^3 \tag{4}$$

to the compliance versus crack length data. We point out that other forms of this expression have been used for ENF data reduction; for instance, the second and first order terms of Equation 4 may be excluded. However, we have observed the full polynomial to provide the best fit of test data [7,14].

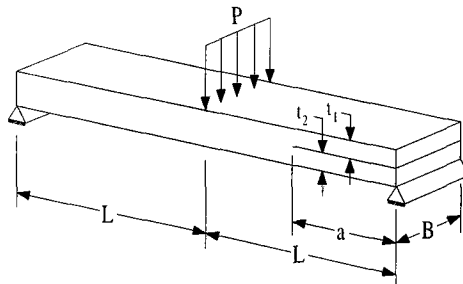


Figure 3 - The ENF test.

Once the compliance versus crack length relations were obtained for each specimen, all specimens were loaded to fracture. The fracture toughness for each specimen was obtained by substituting the appropriate compliance calibration curve, Equation 4, into Equation 2 to obtain

$$G_{IIc} = \frac{P_c^2}{2B} (C_1 + 2C_2a + 3C_3a^2) \tag{5}$$

where P_c is the load at the onset of delamination growth.

The SLB Test

The SLB test is shown in Figure 4. This test was used on both the unidirectional and crossply specimens to determine the fracture toughness at a mode ratio, G_{II} / G_I , of approximately 0.4. It is a simple test geometry and can be performed using the ENF fixture. SLB specimen preparation involves removing a portion of the lower cracked region from the specimen so that the three-point bending test of Figure 4 can be performed. The mode-mix for each individual SLB specimen was determined by a crack tip element analysis [16], and data reduction for the SLB tests was performed by compliance calibration. This was performed in an identical manner to that of the ENF test, with the exception that a polynomial of the form

$$C = C_0 + C_1 a + C_3 a^3 \tag{6}$$

was fit to the compliance versus crack length data for each SLB specimen. Exclusion of the second order term was necessary to eliminate inflection points which occurred in some of the curve fits [9]. Once the compliance versus crack length relations were obtained for each specimen, all specimens were loaded to fracture. The mixed-mode toughness for each specimen was obtained by substituting the appropriate compliance calibration curve, Equation 6, into Equation 2 to obtain

$$G_I = \frac{P_c^2}{2B} (C_1 + 3C_3 a^2) \tag{7}$$

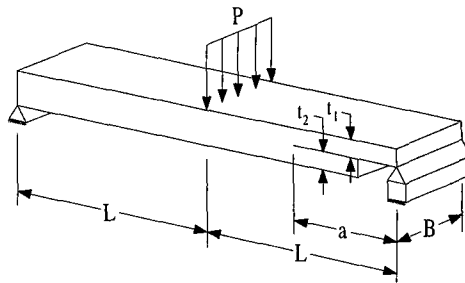


Figure 4 - *The SLB test.*

Specimen Preparation

Specimen Machining

One 155 mm x 155 mm, Nicalon/MAS-5 plate was supplied in a $[0]_{16}$ layup, and another was supplied in a $[(90/0)_4]_S$ layup. The average thicknesses were 3.0 mm for the unidirectional plate and 3.3 mm for the crossply plate. The plates were first cut into strips

that were 6.35 mm wide, using a 0.38 mm thick diamond blade and a standard cut-off saw, such that delamination growth would proceed in the 0° direction. The resulting strips were then scored with crack growth "guides" along their two cut sides at their mid-thickness centerline. This was done using a 0.18 mm thick diamond blade and a cut-off saw modified with a fixture that allowed the cut depth to be controlled with a micrometer head and the specimen to be traversed over the blade. The average depth of the cuts forming the crack growth guides was approximately 0.13 mm. The specimen width, B , used in the data reduction of all tests corresponded to the actual width less the depth of these two crack growth guiding grooves. Following the creation of the crack growth guides, a notch, approximately 2 mm long, was introduced at one end of the specimen, also along the centerline. This was performed using the cut-off saw with the 0.18 mm thick diamond blade and a separate fixture.

Specimen Precracking

Subsequent to the machining procedures described above, the strips were placed in the "precracking fixture" shown in Figure 5. In this fixture, a micrometer head is used to slowly drive a razor blade into the specimen notch and propagate a precrack from the notch tip by a prescribed amount [9,13]. The specimen precracking procedures were slightly different for the two layups and are therefore described separately below.

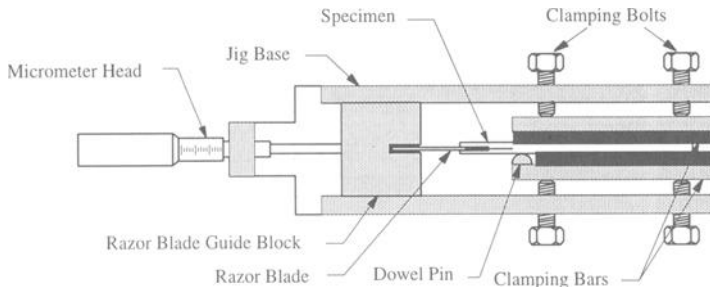


Figure 5 - *Specimen precracking fixture.*

For the unidirectional layups, the precracks were driven until they (1) reached a length of approximately 17 mm, or (2) deviated significantly from the midplane. When this latter case occurred, defined here as when $|t_1/t_2 - 1| > 0.17$, the specimen was trimmed off beyond the end of the precrack, the precracked portion was discarded, a new notch was introduced, and the process was repeated. When the former case occurred, the specimen was trimmed to a total length of approximately 55 mm. Here, t_1 and t_2 represent the thicknesses of the cracked regions as shown in Figures 1, 3 and 4. This process resulted in specimen and test geometries such that, when the ENF and SLB compliance calibration tests were performed, the right side loading fixture roller would only support the

specimen beneath the precracked surface. That is, for all tests, the notched portion of the specimen always remained outside of the lower fixture supports. This constraint kept the large finite thickness of the notch from affecting the specimen's compliance. In addition, the value of a_{min}/t_1 , where a_{min} is the shortest crack length used during compliance calibration, was sufficiently large that the specimen always behaved like a short beam and allowed Equations 4 and 6 to reasonably fit the compliance versus crack length data. Also, $(L - a_c)/t$ was sufficiently large so that transverse compression stresses in the vicinity of the center loading wedge would not affect the toughness [14]; here, t is used to denote the thickness of the uncracked region. Finally, those specimens for which several precrack attempts were required were typically tested in the DCB configuration. This was done when the remaining uncracked portion of the specimen was less than 55 mm but greater than 43 mm.

For the crossply layup, we were not able to precrack the specimens in a manner that would cause the crack to remain at the center 0/0 interface. After several different trial methods had been evaluated [9], we began introducing the notch within the 90° ply that was seven plies from the top of the specimen. The precrack was propagated from this point, for approximately 17 mm, and the specimen was not scored. For those cases where the delamination remained primarily within the 90° ply and the crack tip wholly within the 90° ply, the specimen was trimmed to a total length of 56 mm. This gave nearly the same a_{min}/t_1 as the unidirectional specimens, and a slightly larger $(L - a_c)/t$. The lower cracked region was then cut off at a distance of 2.5 mm from the crack tip and, similar to the case of the unidirectional SLB specimens, these resulting geometries were such that all compliance calibration tests could be performed with the loading fixture contacting only the precracked surface. For those specimens where the precrack reached almost 17 mm and the delamination moved out of the 90° ply, the specimen was trimmed off beyond the end of the precrack, a new notch was introduced, and the process repeated. The asymmetry of the crossply specimens was one of the reasons why these were tested in the SLB geometry only.

Test Procedures

Test Geometries and Mode Mixities

The initial crack lengths for the DCB specimens ranged from 9.2 mm to 18.8 mm and the average thickness ratio, t_1/t_2 , ranged from 0.89 to 1.07. For the ENF and unidirectional SLB test specimens, a_c ranged from 9.3 mm to 13.8 mm and for the crossply SLB specimens, $a_c = 9.6$ mm. For the ENF and unidirectional SLB specimens, t_1/t_2 ranged from 1.00 to 1.11 and for the crossply SLB specimens, from 0.61 to 0.66. Because the SLB test mode mix varies with the sublaminates thickness ratio, each SLB specimen was analyzed to determine its individual mode mix. The average mode mixity for the unidirectional SLB specimens was $G_{II}/G = 0.432$ and the range was 0.430 to 0.435. For the crossply SLB specimens, the average mode mixity was $G_{II}/G = 0.381$ and the range was 0.362 to 0.397. Additional details on the SLB mode mix calculations are presented in Ref 9.

Room Temperature Tests

The following general procedures apply for DCB, ENF and SLB testing, except where differences are described. All specimens were ultrasonically inspected (c-scanned) after precracking and prior to testing using a 25 MHz transducer and a system with a 200 MHz transient waveform digitizer. These results provided "baseline" delamination front profiles to which subsequent scans could be compared to assess whether delamination growth occurred. They were also used to accurately determine the location of the delamination front with respect to the tip of the notch. With this completed, the compliance tests were performed, followed by the fracture tests. All tests were performed in displacement control. The fracture tests for the DCB specimens were performed at a rate of 0.00063 mm/s which was chosen to provide slow and stable crack advance. The compliance and fracture tests for the ENF and SLB specimens were performed at a rate of 0.00127 mm/s. This was sufficiently slow to allow for real-time decisions to stop the test and check for crack advance.

To assist in determining the exact point of crack initiation, a laser interferometric displacement gage (LIDG), developed by Hartman and Nicholas [17], was used to monitor the real-time near-tip displacements during the fracture tests. The microhardness indents used by the LIDG [17] were placed on tiny platinum tabs bonded above and below the crack in the near tip region [13]. Similar to the procedure described in Ref 5, the load versus LVDT displacement and the load versus LIDG displacement curves were monitored in real-time during the fracture tests. When nonlinearities in either of these plots were observed, the test was stopped to assess whether crack advance occurred. This was accomplished by removing the specimen from the fixture and ultrasonically inspecting the region containing the delamination front. The limit of sensitivity of this system was approximately ± 0.25 mm; typically, there would be greater than approximately 0.75 mm of advance over all or some of the delamination front for us to be certain that delamination growth occurred. For those cases where the test was stopped and no discernible advance was evident from the ultrasonic images, the specimen was returned to the fixture and the test repeated in the same manner. In all cases, delamination advance was always observed well after the first nonlinearity in the load versus LIDG displacement, and the load versus LVDT displacement was found to be the more useful indicator of growth. Typically, delamination growth initiated shortly after a nonlinearity was observed in the load vs. LVDT plots. It was observed that, for all specimens, a compliance change of 0.5% to 2.5% coincided with the point at which growth was observed from the c-scan images.

When the c-scanned images indicated that the entire delamination front advanced, the peak load that occurred prior to stopping the test was taken as P_c . This critical load was used with the appropriate equation (3, 5 or 7) to determine the fracture toughness as obtained by that test method. If the entire delamination front had not advanced, the specimen was returned to the fixture and re-loaded until delamination growth occurred over the entire front. Once growth had occurred in a specimen, a second test was performed in an identical manner. Since our precracking fixture produced Mode I precracks, for the SLB and ENF tests, this second test was therefore made with a precrack created under the test mode-mix conditions.

Elevated Temperature Tests

The elevated temperature tests were performed identically to those at room temperature (RT), with the exception that they were run in a furnace with large ports for optical viewing and to accommodate the laser light paths. Figure 6 shows a schematic of the high temperature test configuration for the SLB tests, and also gives additional detail on the three-point bending fixture used for these tests and the ENF tests. The furnace was sufficiently large to accommodate either the fixture shown or that used for the DCB tests (Figure 2). The furnace was supported from brackets attached to the load frame support posts, and cooling attachments were utilized for both the actuator and load cell connections. Prior to any of the high temperature (HT) tests (compliance calibration or fracture), the specimen and fixture were allowed to "soak" in the furnace for a period of time sufficient for the system to reach uniform temperature conditions. The duration of the soak, approximately 10 minutes for DCB specimens and 45 minutes for ENF or SLB specimens, was primarily dependent upon the time required for the different test fixtures to reach thermal equilibrium. For the high temperature ENF and SLB compliance calibration tests, the position of the specimen was adjusted using alumina push rods. To account for thermal expansions, careful measurements of the fixture and specimens at 21°C and at 500°C were obtained using an optical microscope with a digital displacement readout. This allowed the room temperature c-scans to be used to position the specimen accurately when it was in the furnace, i.e., to obtain the desired crack length for the compliance and fracture tests.

Results and Discussion

The DCB Test

Values for the Mode I fracture toughness of the unidirectional specimens are presented in Table 1. The second column in this table presents G_{Ic} as determined for the first increment of delamination growth. The third, fourth and fifth columns present the toughness values determined from the second, third and fourth increments. As these latter columns reflect resistance (R) curve behavior, they have been denoted as G_{IR} . The sixth, seventh and eighth columns show the changes in crack length from the first to second, second to third, and third to fourth increments of crack growth, respectively. Referring to the G_{Ic} values from the first increment of growth, it is observed that the toughness decreases with temperature by approximately 24 percent. A lower elevated temperature toughness is also observed for the second, third and fourth increments of crack advance. It is also apparent that there is considerable R-curve behavior (increasing toughness with increasing crack advance) in these specimens, and that the amount of toughening is roughly proportional to the total amount of growth.

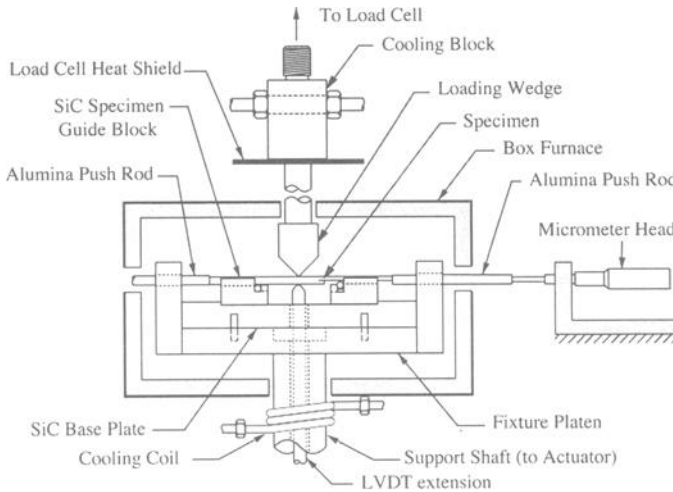


Figure 6 - High temperature test configuration.

The ENF test

Values of the Mode II fracture toughness for the unidirectional RT and HT specimens are presented in Table 2. The superscript in the second column heading indicates that these results were obtained from a Mode I precrack (from the first increment of growth from a given specimen), and the superscript in the third column heading indicates that these results were obtained from a Mode II precrack (from the second increment of growth from a given specimen). The fourth column in either table (RT or HT) presents the change in crack length from the test with a Mode I precrack to the test with a Mode II precrack, and the fifth column gives the increase in toughness for the Mode II precracked test as compared to the test with a Mode I precrack. Comparing first the RT and HT G_{IIc} values, it is observed that the toughness obtained from both Mode I and Mode II precracks decreases with temperature and, at either temperature, a significantly lower toughness is obtained with a Mode I than with a Mode II precrack. It is interesting to note that the magnitude of ΔG_{IIc} is the same for both the RT and HT tests. It is likely that this increase in G_{IIc} is due to R-curve effects as well as the difference between a Mode I and a Mode II precrack. That is, in the absence of R-curve effects, a specimen with a Mode I precrack will produce a lower toughness than a Mode II precrack [18]. However, the precrack type may not account for all of the toughness increase between the Mode I and Mode II precracked results. Note that, in terms of percentage of G_{IIc} , the greater increase is observed in the HT tests. These tests also exhibited larger average Δa values, indicating that toughness likely increases with increasing amounts of crack advance.

Table 1- DCB test results.

RT Specimens							
Spec.	G_{Ic}^1 (J/m^2)	G_{IR}^2 (J/m^2)	G_{IR}^3 (J/m^2)	G_{IR}^4 (J/m^2)	Δa_{1-2} (mm)	Δa_{2-3} (mm)	Δa_{3-4} (mm)
17a	51.0	49.7	59.5	79.4	0.53	0.15	0.38
22a	61.1	53.3	62.3	62.4	0.23	0.46	0.23
16a	62.4	81.0	78.5	90.0	1.60	0.38	0.99
15a	73.3	77.7	80.4	76.6	0.38	0.61	0.61
18c	45.8	59.3	74.0	67.9	0.91	1.52	0.15
AVG.	58.7	64.2	70.9	75.3	0.73	0.63	0.47
S. D.	10.7	14.3	9.5	10.7	0.55	0.53	0.34
HT Specimens							
21a	47.4	54.8	52.1	50.7	0.84	0.38	0.46
19a	41.2	54.2	50.4	59.2	2.97	1.52	0.15
22b	36.5	44.8	48.2	57.7	0.69	0.61	0.38
4a	43.0	47.5	57.3	53.6	2.13	1.45	0.08
18a	56.3	61.9	62.9	66.3	1.14	0.69	0.53
AVG.	44.9	52.6	54.2	57.5	1.55	0.93	0.32
S. D.	7.5	6.7	5.9	6.0	0.97	0.52	0.20

The SLB test

The G_c values obtained from all SLB specimens are presented in Table 3. The second and third column headings are similar to those of Table 2, except that the second increment of crack advance in these tests occurred from a mixed-mode precrack. The fourth column in the table presents the change in crack length from the test with a Mode I precrack to the test with a mixed-mode precrack, and the fifth column gives the increase in toughness for the mixed-mode vs. Mode I precracked test. We point out that some of these values differ from those presented for the same specimens in Ref 9 due to refinements made to the crack length measurements taken from the c-scan images. Referring first to the G_c^{MI} values, it is observed that there is no effect of temperature, and that the $[(90/0)_4]_S$ layup is the tougher of the two. For the unidirectional tests from the mixed-mode precracks, it is observed that the amount of toughening is roughly scaled by the amount of crack advance. There is once again no significant effect of temperature, and the higher ΔG_c values obtained in the HT tests are primarily a result of the larger Δa values that occurred. Interestingly, the proportional increase in the average Δa from the RT to the HT tests, roughly 1.5 times, essentially matches the proportional increase in the average ΔG_c . For the crossply specimens tested with the mixed-mode precracks, a similar toughening that is roughly scaled by Δa is observed. Here, the proportional difference in Δa for the RT as compared to the HT tests, approximately two times, essentially matches the proportional difference in ΔG_c between the two test groups. This indicates that the toughening in these specimens may be primarily an R-curve effect, rather than the result of the different type of precrack. Finally, since toughness generally increases with

increasing $G_{II}/G [I]$, the greater toughness evidenced by the crossply specimens cannot be attributed to their different mode mix.

Table 2 - ENF test results.

RT Specimens					HT Specimens				
Spec.	G_{IIc}^{MI} (J/m^2)	G_{IIc}^{MII} (J/m^2)	Δa (mm)	ΔG_{IIc} (J/m^2)	Spec.	G_{IIc}^{MI} (J/m^2)	G_{IIc}^{MII} (J/m^2)	Δa (mm)	ΔG_{IIc} (J/m^2)
21b	210.5	367.4	0.56	156.9	14c	104.1	406.2	1.75	302.0
3b	203.9	308.5	0.91	104.6	16c	132.7	170.4	1.14	37.7
21c	221.8	355.1	0.86	133.2	6b	109.3	213.2	0.54	103.9
3a	275.5	427.3	0.31	151.8	12c	82.2	249.0	1.14	166.9
1b	170.8	248.9	0.81	78.1	17c	148.5	191.3	0.90	42.7
AVG.	216.5	341.4	0.69	124.9	AVG.	115.4	246.0	1.09	130.6
S. D.	38.0	66.7	0.26	33.3	S. D.	25.8	94.1	0.44	109.3

Table 3 - SLB test results.

[0] ₁₆ RT Specimens					[0] ₁₆ HT Specimens				
Spec.	G_c^{MI} (J/m^2)	G_c^{MM} (J/m^2)	Δa (mm)	ΔG_c (J/m^2)	Spec.	G_c^{MI} (J/m^2)	G_c^{MM} (J/m^2)	Δa (mm)	ΔG_c (J/m^2)
10b	61.1	70.6	0.76	9.6	19b	51.4	70.7	1.52	19.3
19c	43.3	52.7	0.30	9.4	7b	60.1	80.4	1.15	20.2
20b	48.7	57.2	1.22	8.6	1a	80.5	132.0	2.67	51.4
13b	51.3	56.9	0.13	5.6	13c	39.7	61.5	1.21	21.8
9a	48.9	98.3	2.50	49.4	20c	40.4	62.7	0.99	22.2
AVG.	50.7	67.1	0.98	16.5	AVG.	54.5	81.4	1.51	27.0
S. D.	6.5	18.7	0.95	18.5	S. D.	16.8	29.2	0.68	13.7

[(90/0) ₄] _s RT Specimens					[(90/0) ₄] _s HT Specimens				
Spec.	G_c^{MI} (J/m^2)	G_c^{MM} (J/m^2)	Δa (mm)	ΔG_c (J/m^2)	Spec.	G_c^{MI} (J/m^2)	G_c^{MM} (J/m^2)	Δa (mm)	ΔG_c (J/m^2)
8a	112.0	137.5	3.12	25.5	12a	74.3	95.3	0.76	21.0
11b	34.7	101.4	2.51	66.7	13a	67.9	82.0	0.99	14.1
22a	69.9	107.0	0.76	37.1	11a	66.0	116.2	0.76	50.2
7a	72.3	137.5	1.60	65.2	9b	58.7	66.9	1.07	8.2
13b	59.2	85.5	1.91	26.3	10b	62.0	84.3	1.22	22.3
AVG.	69.6	113.8	1.98	44.2	AVG.	65.8	88.9	0.96	23.2
S. D.	28.0	23.0	0.90	20.4	S. D.	5.9	18.3	0.20	16.1

Post Failure Examination

Following the tests, the delaminated surfaces of many of the specimens were propped open and examined from their edges to look for fiber bridging. Next, the specimens were split along their entire length and the delaminated surfaces of the cracked regions were

examined. Both of these examinations were done with an optical microscope at various magnifications and viewing angles.

All three unidirectional specimen types exhibited fiber bridging in both the region of the Mode I precrack and in the region of crack growth during the tests. Examination of the fractured surfaces showed relatively few broken fibers in the region of the Mode I precrack for all specimen types. Thus, the bridged fibers in this region, which were at a relatively shallow angle, were presumed to have nestled back into the precrack surface. For the DCB specimens, these same fracture surface characteristics were also observed in the region of crack growth during the tests. For the ENF and SLB specimens, however, there was a dramatic increase in surface roughness in the region of crack growth. The transition began at the location where the first fracture test was conducted and was characterized by large numbers of broken fibers. The majority of these fibers were pulled up from the plane of the crack at a relatively steep angle and, on the crack surface of the upper cracked region, their broken ends were pointing in the direction of crack advance. Optical measurements indicated that this was accompanied by a trend of decreasing t_I with increasing Δa for both specimen types. This trend was somewhat more pronounced for the SLB specimens where the crack had generally moved sufficiently to be just out of the scored crack growth guides by the end of the test from the mixed-mode precrack. In general, crack advance for the DCB and the ENF tests was relatively interlaminar while crack advance for the SLB specimens was *intralaminar*. It is therefore possible that, similar to the DCB and ENF test results, a decrease in toughness with increasing temperature exists for the mixed-mode condition. However, it is overshadowed by the toughening associated with intralaminar crack advance.

For the crossply SLB specimens, fiber bridging was also observed. In many specimens, this was in both the precrack and test regions. Upon examination of the fractured surfaces, it was found that the delaminated region in the center of the specimen had often moved into the 0° ply by the end of the Mode I precrack, although it was still within the 90° ply at the specimen's edges. For those specimens or those regions of various specimens where delamination growth remained within the 90° ply, crack branching generally occurred, with the crack advancing at two or three different planes within the ply. When the primary delamination left the 90° ply, it always did so into the upper 0° ply. In these cases, bridged fibers from the Mode I precracked region and from the test region generally stayed intact until the end of the test from the mixed-mode precrack. Thus, it appears that the two primary toughening mechanisms in the crossply layup are crack branching within the 90° ply and the extensive length and number of bridged fibers when the primary crack enters a 0° ply. Toughening in the unidirectional layup was also due to fiber bridging, but the length and number of fibers bridging the crack at any one time was less. In both layups, the numbers of bridged fibers are due to the crack rapidly changing planes as it grows under the mixed-mode conditions. Similar to the unidirectional layup, the crossply specimens showed a general trend of decreasing t_I with increasing Δa . By the end of the test from the mixed-mode precrack, the delamination had moved a sufficient amount from its original plane that the data reduction procedure was deemed to no longer be accurate, and further R-curve behavior could therefore not be examined.

Application to Design

The data of Tables 1 to 3 indicates that, regardless of mode-mix, the minimum toughness will be obtained from a Mode I precrack. Thus, the fracture interaction diagram presented in Figure 7 shows the Mode I precracked toughnesses from the various tests plotted versus their respective mode ratios. Each point in the figure represents the mean value from a test type and the "error bars" indicate ± 1 standard deviations. From this figure it is readily apparent that G_{Ic} from the DCB test is roughly equivalent to G_c from the SLB test. This indicates that there is little dependence of fracture toughness upon the mode mix from G_{II}/G of 0.0 to 0.4 for this material and, when considering delamination growth in this regime for design purposes, one may need only to test DCB specimens. Also, note that the higher toughness from the crossply, mixed-mode specimens, as compared to the unidirectional results, is accompanied by a greater amount of experimental scatter. Thus, in view of the decreased design values that come from test data with a disperse distribution, as well as the difficulty in testing the crossply specimens, it may be most appropriate to base design values on unidirectional test results. However, further study is needed on this issue.

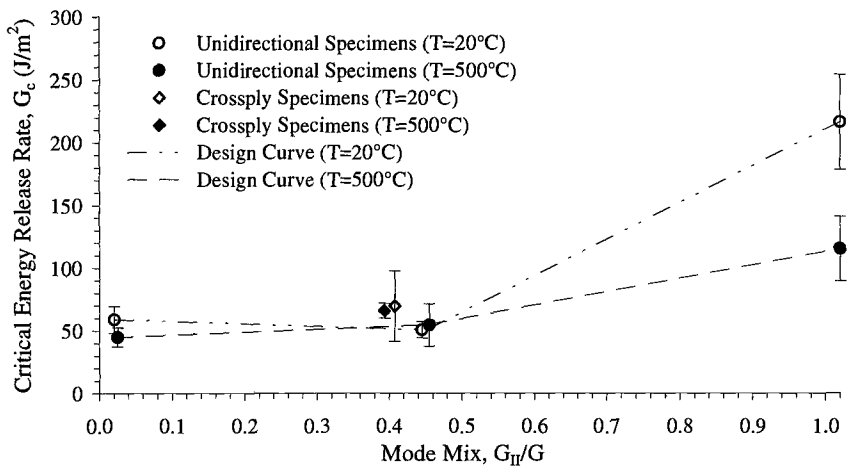


Figure 7 - Fracture interaction diagram.

Conclusions

This study has demonstrated test procedures for assessing the toughness of CMC materials that are believed to be better than those previously used for this purpose [1-6]. The precracking procedure developed as part of this work produces delamination growth along the plane of lamination similar to that which will be observed in practice. Further, this produces test specimens that may be compliance calibrated to obtain the most accurate toughness values at either room or elevated temperatures. For these test

methods, the onset of crack advance may also be correlated to readily observable events which do not require monitoring near-tip displacements. In view of our results, a 0.5% offset value taken from the load vs. deflection data may provide a conservative criterion for defining a critical load. This is similar to the approach described in the Standard Test Method for Mode I Interlaminar Fracture Toughness of Unidirectional Reinforced Polymer Matrix Composites (ASTM Standard D5228-94).

The data generated as part of this study illustrates the fracture behaviors that may occur in CMC materials as a function of temperature, layup, mode ratio and precrack type. For a given layup, it may be most appropriate to use that value of toughness obtained from a Mode I precrack for prediction of delamination initiation, as this will give the most conservative result. However, any observed R-curve effects may be used to investigate the propensity of the delamination to continue to grow, provided that the R-curve is obtained during the test without the delamination moving a significant amount from its original plane. When this latter event occurs, as was observed herein, the accuracy of the compliance calibration (or any other) method of data reduction becomes questionable. Finally, it has been shown that, for many materials, the combination of unidirectional DCB, SLB and ENF tests will provide sufficient information on the variation in toughness with mode mix for most design applications.

Acknowledgments

This work was primarily supported through the NASA/Syracuse University Center for Hypersonics, NASA Headquarters Grant NAGW-3713, Isaiah Blankson, monitor. Additional support was provided by the Materials Behavior Branch of Wright Laboratory (WL), where the majority of this work was performed. The authors gratefully acknowledge the help of a great number of the personnel at WL and at the University of Dayton Research Institute, and in particular Dr. Theodore Nicholas for his assistance on all phases of this project, Dr. Andrew Rosenberger for assistance in developing the experimental set-up, and Mr. Larry Zawada for providing the materials used.

References

- [1] Mall, S. and Hoobler, M. A., "Fracture Toughness of a Fiber-Reinforced Ceramic Composite Under Mode I and Mode II Loadings," *Achievement in Composites in Japan and the United States, Proceedings of the Fifth Japan-U.S. Conference on Composite Materials (CCM-V)*, A. Kobayashi, Ed., 1990, pp. 211-218.
- [2] Shercliff, H. R., Vekinis, G. and Beaumont, P. W. R., "Direct Observation of the Fracture of CAS-Glass/SiC Composites; Part I - Delamination," *Journal of Materials Science*, Vol. 29, 1994, pp. 3643-3652.
- [3] Kaute, D. A. W., Shercliff, H.R., and Ashby, M.F., "Delamination, Fibre Bridging and Toughness of Ceramic Matrix Composites," *Acta Metallurgica et Materialia*, Vol. 41, No. 7, 1993, pp. 1959-1970.
- [4] Mall, S. and Mol, J. H., "Mode II Fracture Toughness Testing of a Fiber-Reinforced

- Ceramic Composite," *Engineering Fracture Mechanics*, Vol. 38, No. 1, 1991, pp. 55-69.
- [5] Mall, S. and Truskowski, J. W., "Characterization of Mode II Fracture Behavior in a Fiber-Reinforced Ceramic Composite Utilizing Laser Interferometry," *Experimental Mechanics*, Vol. 32, No. 3, September 1992, pp. 234-239.
- [6] Charalambides, P. G., Lund, J., Evans, A. G. and McMeeking, R. M., "A Test Specimen for Determining the Fracture Resistance of Bimaterial Interfaces," *Journal of Applied Mechanics*, Vol. 56, 1989, pp. 77-82.
- [7] Davidson, B. D., Altonen, C. S. and Polaha, J. J., "Effect of Stacking Sequence on Delamination Toughness and Delamination Growth Behavior in Composite End-Notched Flexure Specimens," *Composite Materials: Testing and Design (Twelfth Volume)*, ASTM STP 1274, C.R. Saff and R.B. Deo, Eds., American Society for Testing and Materials, 1996, pp. 393-413.
- [8] Davidson, B. D. and Sundararaman, V., "A Single Leg Bending Test for Interfacial Fracture Toughness Determination," *International Journal of Fracture*, Vol. 78, No. 2, 1996, pp. 193-210.
- [9] Polaha, J. J., Sherwood, T. W. and Davidson, B. D., "Effects of Temperature and Layup on the Mixed-Mode Delamination Toughness of a Ceramic Matrix Composite Material," Proceedings of *The Eleventh International Conference on Composite Materials*, (ICCM-11), Paper No. 2518/0319, 1997.
- [10] Larsen, D. C., "Thermally Durable Glass-Ceramic Matrix Composites," *Corning Incorporated R&D Status Report No. 11 for May 1 - June 30, 1992*, Contract F33615-90-C-5909, 1992.
- [11] Huger, M., Souchard, S., Gault, C., "Oxidation of Nicalon SiC Fibres," *Journal of Materials Science Letters*, Vol. 12, 1993, pp. 414-416.
- [12] Sutherland, S., Plucknett, K. P., and Lewis, M. H., "High Temperature Mechanical and Thermal Stability of Silicate Matrix Composites," *Composites Engineering*, Vol. 5, No. 10-11, 1995, pp. 1367-1378.
- [13] Polaha, J. J., "Effects of Temperature and Mode Ratio on the Delamination Toughness of a Ceramic Matrix Composite Material," M.S. Thesis, Syracuse University, Syracuse, N.Y., 1997.
- [14] Polaha, J. J., Davidson, B. D., Hudson, R. C. and Pieracci, A. "Effects of Mode Ratio, Ply Orientation and Precracking on the Delamination Toughness of a Laminated Composite," *Journal of Reinforced Plastics and Composites*, Vol. 15, No. 2, February 1996, pp. 141-173.
- [15] Broek, D., "Elementary Engineering Fracture Mechanics," *Martinus Nijhoff*, 1982, p. 124.
- [16] Davidson, B. D., Hu, H. and Schapery, R. A., "An Analytical Crack Tip Element for Layered Elastic Structures," *Journal of Applied Mechanics*, Vol. 62, No. 6, June 1995, pp. 294-305.
- [17] Hartman, G. and Nicholas, T., "An Enhanced Laser Interferometer for Precise Displacement Measurements," *Experimental Mechanics*, 1992, pp. 234-239.
- [18] Davidson, B. D. and Koudela, K. L., "Influences of the Mode Mix of Precracking on the Delamination Toughness of Laminated Composites," *Journal of Reinforced Plastics and Composites*, Vol. 18, No. 15, 1999, pp. 1408-1414.

Michael G. Jenkins¹ and Larry P. Zawada²

Detailed Study of the Tensile Behavior of a Two-Dimensionally Woven Nicalon™/Sylramic™ Ceramic Matrix Composite

Reference: Jenkins, M. G. and Zawada, L. P., “Detailed Study of the Tensile Behavior of a Two-Dimensionally Woven Nicalon™/Sylramic™ Ceramic Matrix Composite,” *Mechanical, Thermal and Environmental Testing and Performance of Ceramic Composites and Components, ASTM STP 1392*, M. G. Jenkins, E. Lara-Curzio, and S. T. Gonczy, Eds., American Society for Testing and Materials, West Conshohocken, PA, 2000.

Abstract: A round-robin study was conducted on the tensile behavior of a Nicalon™ fiber reinforced Sylramic™ ceramic matrix composite (CMC). The goals of the US federal government-funded study were: 1) to determine the precision and bias of ASTM Test Method for Monotonic Tensile Strength Testing of Continuous Fiber-Reinforced Ceramic Composites with Solid Rectangular Cross-Sections at Ambient Temperatures (C 1275), 2) to establish an expansive data base for a single CMC, and 3) to evaluate a statistically-significant sample size of a single CMC for processing and design purposes. The CMC was comprised of eight plies of ceramic grade Nicalon™ fabric in a symmetric 0/90 lay-up, a proprietary boron nitride-containing interphase, and a silicon nitrocarbide matrix derived from polysilazane. Tabbed in-plane, reduced gage-section tensile test specimens (3 x 12 x 150-mm overall, 3 x 8 x 35-mm gage section) were monotonically tested in displacement control (0.02 mm/s) at room temperature in face-loaded grips. Five industrial, two governmental, and two academic laboratories participated, each testing ten tensile test specimens for a total of ninety tests. Results were analyzed for variations in test procedures between laboratories, material density/porosity/panel of origin, elastic constants, and nondestructive evaluation characteristics. Repeatability and reproducibility were assessed from coefficients of variation that ranged from 4 to 10%.

Keywords: ceramic matrix composite, precision and bias, round-robin, tension

Introduction and Background

Continuous fiber ceramic composites (CFCCs) are a special subset of the broader class of materials known as ceramic matrix composites (CMCs). In general, CMC materials retain the desirable characteristics of monolithic advanced ceramics (e.g., high

¹ Associate professor, Department of Mechanical Engineering, University of Washington, Box 352600, Mechanical Engineering Building, Seattle, WA 98195-2600.

² Research scientist, Air Force Research Laboratory, WL/MLLN, Wright-Patterson AFB, OH 45433.

stiffness, low density, etc.) while exhibiting increased "toughness" over monoliths [1, 2]. Because of their continuous fiber "reinforcements," CFCCs exhibit greatly increased "toughness" (i.e., energy absorption during deformation). This "toughness" provides the inherent damage tolerance and increased reliability that are critical in many engineering applications where the catastrophic (i.e., damage intolerant), brittle behavior of most monolithic advanced ceramics makes them unacceptable to designers [1].

The myriad of industrial applications envisioned for CFCCs includes reformers, reactors and heat exchangers in the chemical industry as well as tubes, nozzles, vanes and supports in heat engines and heat recovery equipment [1, 2]. Power generation applications of CFCC components in gas turbines would lead to increased operating temperatures, reductions in emissions and cost savings during power production [2].

However, before designers can exploit the thermal, mechanical, and environmental advantages of CFCCs, the materials must be unequivocally and unambiguously characterized. In particular, the mechanical properties and performance must be systematically measured and cataloged, first, in ambient conditions and, then, under progressively greater temperatures and more aggressive environments to assess any "weakness" in the material at the end-use conditions.

The tensile test is the most common and fundamental mechanical test of any engineering material [3]. For isotropic, homogenous materials, the applied uniaxial stress state and corresponding strain response in the gage section of a properly designed tensile test specimen is unequivocal and unambiguous. Analysis of the resulting stress-strain curves provides a plethora of information on both the elastic behavior and the inelastic behavior of the material. The subsequent veritable cornucopia of information on elastic constants, strengths, and plasticity/ductility makes the tensile test the most valuable mechanical properties test possible for a design engineer [3].

It is interesting to note that of all the increasing number of "standard" test methods developed for CFCCs to date [4, 5], the tensile test at room temperature is the most common such test standard. These test methods range from full-consensus national/international standards to limited-consensus trade/industry "standards." Full-consensus standards include Comité Européen de Normalisation (CEN) ENV 658-1 [6] introduced in 1991, ASTM Test Method for Monotonic Tensile Strength Testing of Continuous Fiber-Reinforced Ceramic Composites with Solid Rectangular Cross-Sections at Ambient Temperatures (C 1275) introduced in 1995 and International Organization for Standardization (ISO) DIS 15733 [7] approved in 1999. Limited-consensus trade/industry "standards" include High Speed Research/Enabling Propulsion Materials (HSR/EPM) HSR/EPM-D-001-93 [8] introduced in 1993 and Petroleum Energy Center (PEC) PEC-TS CMC01 [9] introduced in 1997.

Of the various world-wide tensile test standards, ASTM standards are arguably considered the most technically rigorous and of the highest quality. Part of this high regard is because of the attention to such details as precision and bias (P&B) statements which provide the user with some insight as to the utility of the standard (e.g. intra- and interlaboratory variability of the standard). Although ASTM requires P&B statements for all its standards, the current ASTM standard for tensile testing CFCCs at room temperature (C 1275) does not have such a statement because of the "newness" of the subject materials (i.e., CFCCs) at the time of the development/approval of the standard.

Partly based on the needs of existing standards and the needs of evolving design codes/data bases for CFCCs, several goals were set forth for a federally-funded round

robin program [10] for mechanical testing of CFCCs: 1) to develop precision and bias statements for the US national standard for tensile testing CFCCs (required by ASTM), 2) to contribute to an expanded, reliable data base for CFCCs, 3) to provide statistical distributions of properties and performance of a single CFCC for a large statistical sample for design and processing purposes.

In this paper, the test material is first described followed by details of the experimental procedures. Intra- and interlaboratory test results are presented and compared. Finally, the results are interpreted, discussed and summarized.

Test Material

The commercially-available CFCC³ consisted of ceramic grade Nicalon™ (Si-C-O) fiber reinforcing a Sylramic™ (Si-C-N) matrix. The CFCC was produced [11] in three stages: interphase deposition, fiber preform fabrication, and matrix formation.

Deposition of the interphase was accomplished via the chemical vapor infiltration (CVI) of proprietary boron nitride (BN)-containing layers on the of ceramic-grade Nicalon™ fibers to a nominal thickness of 0.5 μm. This coating may act as a weak fiber/matrix interface to promote fiber debonding and pullout [11], thereby increasing the “toughness” of the bulk CFCC.

Fabrication of fiber preforms took place using two-dimensional eight harness satin weave cloths comprised of the coated fiber bundles [11] arranged in an alternating 0/90 layup to give both a symmetric structure and "good nesting" of the weave. Eight cloth layers were stacked (0/90/0/90/0/90/0) to produce a nominal preform thickness of 3 mm and nominal fiber volume fraction of 45% in a panel measuring 305 mm x 305 mm.

Formation of the matrix occurred by the multi-step polymer impregnation process (PIP). During PIP a polysilazane ceramic precursor polymer and silicon nitride powder were infiltrated into the fiber preform. After curing, pyrolysis of the cured polymer occurred by heating the infiltrated/cured preform to ~1000°C in a controlled atmosphere

One hundred tensile test specimen shapes (Fig. 1) were fabricated from three panels (numbered 12, 14 and 16) out of a total of nine panels at the fifth PIP cycle using conventional machining and 40 to 100-grit electroplated diamond-grit router bits (1800 RPM) with no cutting fluids and 0.127 mm of material removed per pass [12]. PIP cycles then continued on individual tensile test specimens until less than 5% average open porosity and average density of 2200 kg/m³ were achieved (total of 17 to 19 cycles).

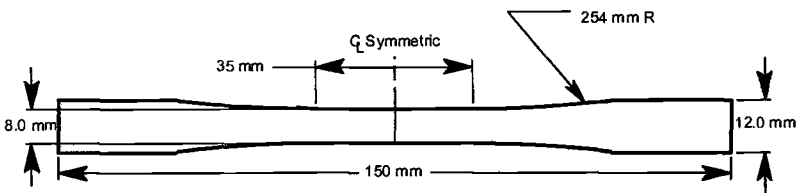


Figure 1 - Tensile test specimen geometry used in the round robin.

Sylramic S200, Dow Corning, Corp., Midland, MI in November 1997 (as of July 1999, Engineered Ceramics, Inc., San Diego, CA).

Experimental Method

Pretest Procedures

Pertinent geometric dimensions (e.g., width and thickness of gage and grip section as well as overall length) of all one hundred tensile test specimens were measured using digital calipers and micrometers as part of the pre-test inspections [12]. The mass of each tensile test specimen was determined and a geometric density was calculated for each tensile test specimen using the measured mass and a volume calculated from the dimensions and geometry. Visual inspections were used to screen lower quality tensile test specimens from those tensile test specimens that were eventually shipped to round robin participants. Ten tensile test specimens were screened, with “defects” ranging from surface and edge “gouges” to double transition radii to non-symmetry about the longitudinal axis (i.e. transition radii out of tolerance). All one hundred tensile test specimens were impulse resonance tested [12] for signature analysis (because the tensile test specimen geometry was a non “standard” shape for the impulse excitation test method) using ASTM Test Method Test Method for Dynamic Young’s Modulus, Shear Modulus, and Poisson’s Ratio for Advanced Ceramics by Impulse Excitation of Vibration (C 1259). Resonant frequencies were within 1% of the mean for all tests indicating no anomalous or obviously “defective” test specimens.

After these pretest measurements and inspections, each tensile test specimen was indelibly marked with a unique identification number linking it to its panel of origin. Each tensile test specimen was then placed in its own individual marked and sealed rigid container (clear polymer shipping tube). Tensile test specimens were then semi-randomly divided into nine groups of ten tensile test specimens, insuring that each group contained equal numbers of tensile test specimens from each panel of origin.

Test Procedures

C 1275 was employed to evaluate the tensile behavior of the subject material. Nine laboratories (two governmental, five industrial and two academic) participated in the tension tests. Specifics regarding the tensile testing protocol are as follows.

Each laboratory conducted ten tests with all tests carried out using face-loading grips. E-glass/epoxy end tabs (Fig. 2) and a commercial two-part epoxy adhesive were supplied along with tabbing instructions. These tabs were applied by each participant prior to tensile testing. Prior to, and immediately upon completion of the tensile tests, load train alignment was verified to be less than 5% bending.

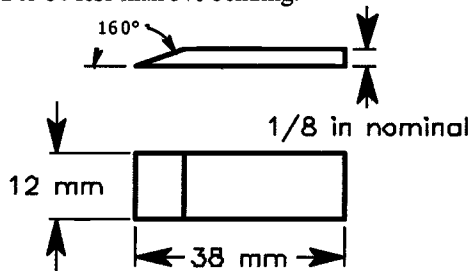
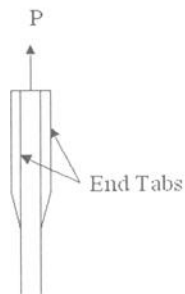


Figure 2 – End tabs for tensile test specimens.



a) Schematic of the in-plane tensile test b) Example of an in-plane tensile test

Figure 3 - Illustrations of in-plane tensile test setup per C 1275.

Per C 1275, force and strain transducers were verified and/or calibrated. Applied force and strain over extensometer gage lengths of 25 mm were measured at a displacement rate of 0.02 mm/s under ambient conditions. A schematic illustration of the tensile test configuration and a photograph of the test setup at one of the laboratories is shown in Fig. 3.

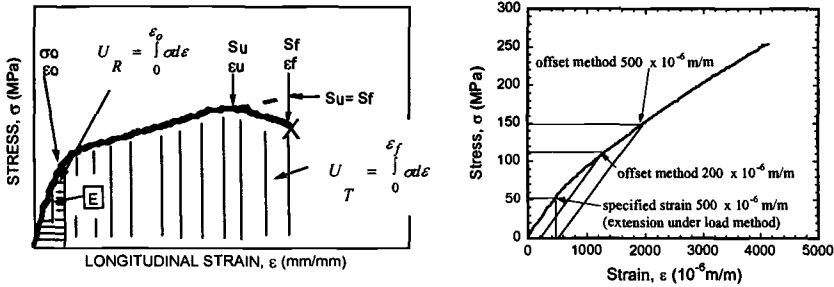
Some participants employed strain gages (in addition to the required extensometry) to determine in-plane elastic modulus and Poisson's ratio. Primary mechanical properties per C 1275 of interest included in-plane elastic modulus, proportional limit stress/strain, ultimate tensile strength/strain, fracture strength/strain. Some participants also determined modulus of resilience and modulus of toughness. All participants supplied both electronic ("raw" data) and hard copies of the stress-strain curves.

Results

Because of the nature of the round robin, confidentiality of the identities of the participating laboratories is preserved. Participating laboratories are identified as consistently reported numbers (e.g., 1, 2, 3...).

C 1275 requires reporting of nine individual mechanical properties (in-plane elastic modulus, proportional limit stress/strain, ultimate tensile strength/strain, fracture strength/strain), modulus of resilience and modulus of toughness as well as stress-strain curves for each test (see Fig. 4). Summary statistics (mean, standard deviation, and coefficient of variation) are also required for each test set. Participants were asked to submit this information in both digital and hard copy forms. Despite the reporting requirements of C 1275, some participants did not report all nine properties, and their stress-strain curves were evaluated by the round robin coordinators to extract the necessary information.

Table 1 shows summary comparisons of one set of intralaboratory results and the interlaboratory results. Figures 5, 6, and 7 show graphical comparisons of intra- and interlaboratory results for elastic modulus, ultimate tensile strength and strain at fracture, respectively.



a) Schematic stress-strain curve b) Methods for proportional limit [12]

Figure 4 - Schematics of tensile mechanical properties (per C 1275).

Note the proportional limits in Table 1. C 1275 lists two methods for determining the proportional limit stress: offset at a specified strain and extension under load at a specified strain. No single method or specified strain was dictated in the round robin protocol. Three combinations of methods and specified strains were used by participants to determine the proportional limit stress, σ_0 , (see Fig. 4b) resulting in an interlaboratory mean, standard deviation, and coefficient of variation of 93 MPa, 40 MPa and 43.5%, respectively. However, when the digital stress-strain curves were reanalyzed using the extension under load method at a specified offset strain of 1000 x 10⁻⁶ m/m, the interlaboratory proportional limit stress had a mean, standard deviation, and coefficient of variation of 85 MPa, 3 MPa and 4.0%, respectively. Comparison of intra- and interlaboratory results for proportional limits are shown in Fig. 8. Note that the specified strain of 1000 x 10⁻⁶ m/m for the extension under load method was determined using a method involving a 10% deviation of stress from linearity [13] which is currently not included in C 1275.

Table 1 – Intra- and interlaboratory tensile test results.

Tensile Property	Intralaboratory (UW)		Interlaboratory	
	Mean ± 1 SD ^a	CV ^b	Grand Mean ± 1 SD	CV
Modulus of Elasticity (GPa)	91±3.7	4.0%	93±5	5.0%
Poisson's ratio	0.12±0.01	7.30%	NR ^c	NR
Proportional limit stress (MPa)	83±3	3.1%	85±3	4.0%
Strain at proportional limit stress (m/m*10 ⁻⁶)	1000±0	0.0%	1000±0	0.0%
Ultimate tensile strength (MPa)	250±18	7.1%	251±17.7	7.1%
Strain at ultimate tensile strength (m/m*10 ⁻⁶)	4400±400	8.3%	4305±393	9.1%
Fracture strength (MPa)	250±18	7.1%	251±17.7	7.1%
Strain at fracture strength (m/m*10 ⁻⁶)	4400±400	8.3%	4305±393	9.1%
Modulus of Resilience (J/m ³)	41631±1282	3.1%	42266±1703	4.0%
Modulus of Toughness (J/m ³)	635502±100626	15.8%	623545±102405	16.4%

^a SD = standard deviation.
^b CV = coefficient of variation.
^c NR = not required.

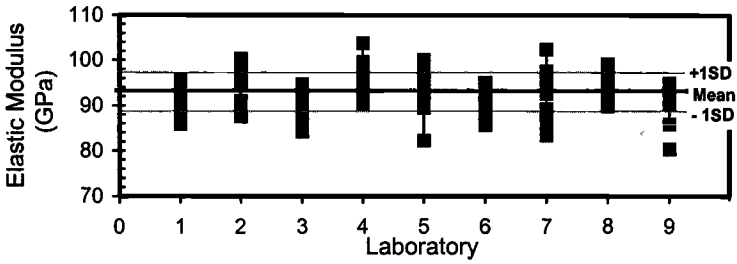


Figure 5 – Intra- and interlaboratory results for elastic modulus.

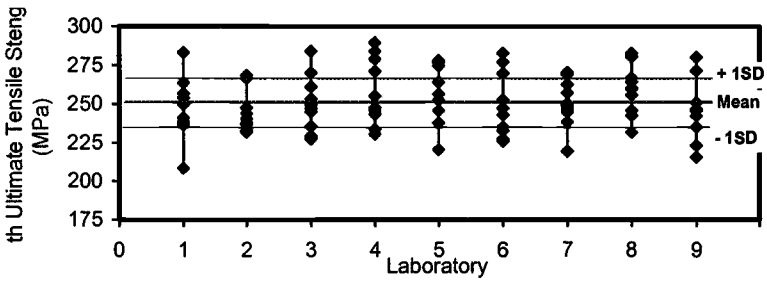


Figure 6 – Intra- and interlaboratory results for ultimate tensile strength.

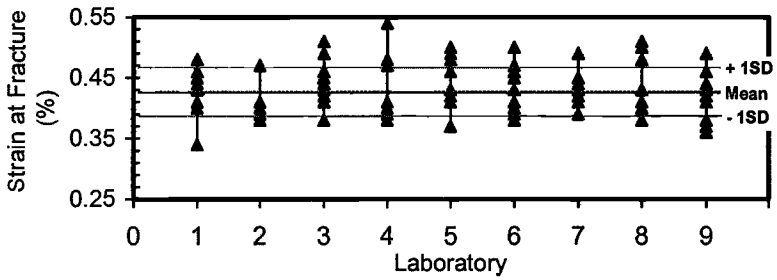


Figure 7 – Intra- and interlaboratory results for strain at fracture.

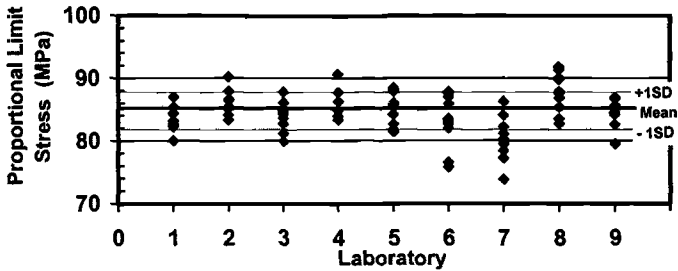


Figure 8 – Intra- and interlaboratory results for proportional limit stress.

Another area not explicitly mandated in C 1275 is detailed aspects of the dimensional measurement equipment. C 1275 suggests several possible metrology methods, although the required minimum accuracy, regardless of method, is 0.01 mm. Table 2 lists a variety of metrology instruments for dimensional measurements used by the participating laboratory, along with the resulting measurement statistics for two dimensions (gage section thickness and width). Generally, statistics for width (measured between the machined edges) are consistent within and but not necessarily between laboratories. Thickness (measured between as processed, woven surfaces) shows large variability within and between laboratories. Although there is not an apparent correlation between variability in measurement of thickness and variability in measurement of width within the same laboratory, the consistent results between laboratories for measurement of thickness suggests that for as-processed woven surfaces, flat anvil micrometers might provide a better measurement of "average" local dimensions.

Table 2 – Comparison of dimensional measurement instruments and results.

Laboratory Number	Measurement Tool	Thickness	Thickness	Width	Width
		Mean (mm)	Coefficient of Variation	Mean (mm)	Coefficient of Variation
8	Ball Micrometer	2.70	2.90%	8.04	0.30%
2	Flat Anvil Micrometer	2.76	2.70%	8.00	0.50%
4	Flat Anvil Micrometer	2.77	2.90%	7.84	1.50%
6	Flat Anvil Micrometer	2.77	1.30%	8.02	0.20%
7	Calipers	2.77	2.10%	8.06	0.70%
5	Flat Anvil Micrometer	2.78	2.30%	8.05	0.40%
1	Ball Micrometer	2.80	2.70%	7.97	0.40%
3	Flat Anvil Micrometer	2.80	2.80%	8.06	0.30%
9	Calipers	2.81	1.50%	8.02	0.70%
	For All Test Specimens	2.77	2.50%	8.01	1.00%

Table 3 – Test procedure differences between participating laboratories.

	Laboratory Number								
	1	2	3	4	5	6	7	8	9
Loading Mechanism - Screw_(S) or Servo-Hydraulic (H)	S	H	S	H	H	S	S	H	H
Grip Pressure (MPa)	0.21	0.14	7.5	5	NA	8	0.65	0.04	0.7
Strain Measurement - Strain Gage (S) Extensometer (X)	X	X	2X, S	X	X	X, S	X	X	X
Temperature (°C)	28	20	21	24	24	20	23	22	22
Humidity (% RH)	34	38	59	39	62	54	50	50	52
Pre-Test % Bending	3.4	2.3	3.6	0.2	3.9	<5	1.8	1.9	.5
Post-Test % Bending	4.2	2.6	4.0	1.5	4.8	<5	NA	2.2	1.1
Extensometer Gage Length (mm)	25.4	33	25	12.7	25.4	25	25	25.4	25.3

Effects of Variations in Test Procedure

Between the various participating laboratories certain differences were noted in test procedure as summarized in Table 3. These differences occurred in areas that are neither specifically mandated in C 1275 nor were they addressed explicitly in the round robin protocol. The effects of these differences were analyzed using an analysis of variance (ANOVA) at the 95% confidence level for each participating laboratory’s set of results. The ANOVA results for three representative mechanical properties (elastic modulus, ultimate tensile strength, and strain at fracture) are shown in Table 4. Note that except for an apparent effect of loading mechanism for elastic modulus and possible effects of extensometer gage length for elastic modulus and strain at fracture, none of the differences in test procedure affected the test results in a statistically significant way. For the apparent effect on elastic modulus it should be noted that only one participant’s statistics (mean and standard deviation) for elastic modulus (97±4 GPa) were much greater than the grand mean and standard deviation (93±5 GPa). However, this same participant also used an extensometer gage length of 12.7 mm which is less than the 25-mm gage length used by the other eight participants as mandated in C 1275. Thus, the effect of loading mechanism may be confused with the effect of extensometer gage length.

Effects of Variations in Material

Two different types of effects of material variations were identified: those linked to the panels of origin (i.e., panel thickness and constituents/processing of individual panels) and those linked to individual tensile test specimens (i.e. density and porosity). Four mechanical properties (elastic modulus, proportional limit stress, ultimate tensile strength, and strain at fracture) were correlated to panel of origin as shown in Figures 9, 10, 11, and 12. It is obvious that there is no effect of panel of origin on elastic modulus and proportional limit stress while there is a strong apparent effect of panel of origin on ultimate tensile strength and strain at fracture.

Table 4 – *Effects of differences in test procedure on three mechanical properties from ANOVA (95% Confidence).*

	Elastic Modulus	Ultimate Tensile Strength	Strain at Fracture
Loading Mechanism	Yes	No	No
Load Train Coupler	No	No	No
Grip Pressure	No	No	No
Strain Measurement	No	No	No
Temperature	No	No	No
Humidity	No	No	No
Pre-Test % Bending	No	No	No
Post-Test % Bending	No	No	No
Extensometer Gage Length	Possible	No	Possible

An ANOVA confirms that, at the 95% confidence level, there are statistically significant differences of ultimate tensile strength and strain at fracture (both fiber-strength dominated mechanical properties) for tensile test specimens taken from Panels 12, 14 and 16. Further investigation revealed that while the fiber lot comprising these panels was the same, the fabrics for each panel were coated in different “runs” resulting in reductions of mean fiber strengths of up to 20% and increased ‘scatter’ in fiber strengths. Analysis of differences in panel thickness did not show strong correlations of the mechanical properties to panel thickness.

Although ANOVA did indicate statistically significant difference of density ($2190 \pm 10 \text{ kg/m}^3$, $2200 \pm 10 \text{ kg/m}^3$, and $2210 \pm 10 \text{ kg/m}^3$ for Panels 12, 14, and 16, respectively) and open porosity ($2.36 \pm 0.77\%$, $2.83 \pm 0.96\%$, and $2.91 \pm 1.12\%$ for Panels 12, 14, and 16, respectively), no correlations were found between mechanical properties and density and open porosity. Lack of correlation may have been due to the small scatter and close means of these parameters from panel to panel which were masked by the stochastic nature of the material itself. These results are summarized in Table 5.

Table 5 - *Summary of the effects of some material variations on mechanical properties from ANOVA (95% confidence).*

	Elastic Modulus	Proportional Limit Stress	Ultimate Tensile Strength	Strain at Fracture
Panel – (Number 12, 14 or 16)	No	No	Yes	Yes
Panel Thickness (2.6 to 2.95 mm)	No	No	No	No
Density (2180 to 2330 kg/m ³)	No	No	No	No
Open Porosity (1.03% to 4.94%)	No	No	No	No
Surface Area of Gage Section	No	No	No	No
Volume of Gage Section	No	No	No	No

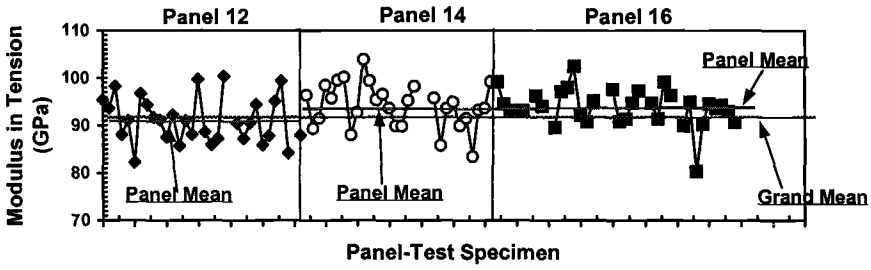


Figure 9 - Effect of panel of origin on elastic modulus results.

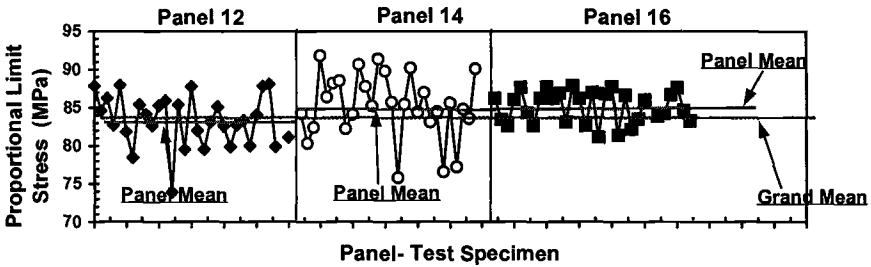


Figure 10 - Effect of panel of origin on proportional limit stress results.

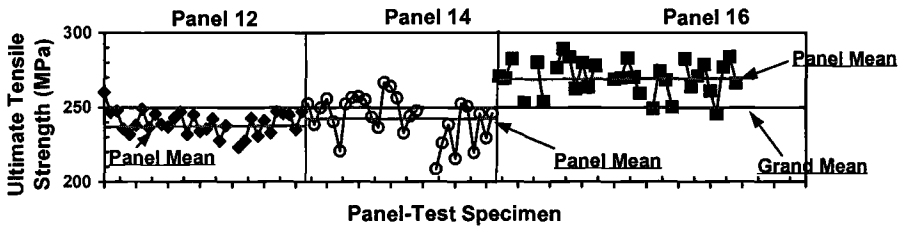


Figure 11 - Effect of panel of origin on ultimate tensile strength results.

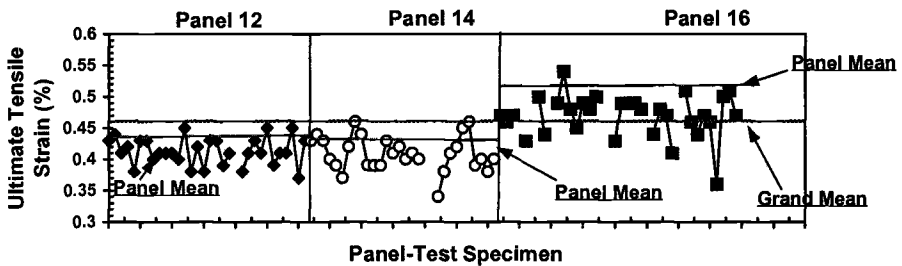


Figure 12 - Effect of panel of origin on strain at fracture results.

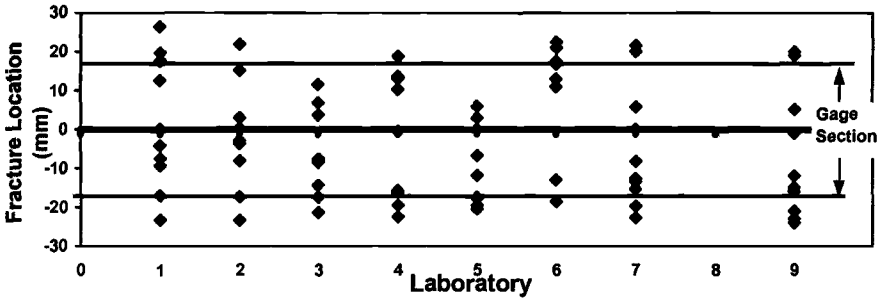


Figure 13 – Fracture locations for each participating laboratory (gage section is +17.5 and -17.5 mm about the longitudinal midpoint of the tensile test specimen (0 mm)).

Effects of Tensile Test Specimen Geometry

C 1275 does not mandate any single tensile test specimen geometry, but instead gives guidelines on how to choose a particular geometry for a particular material system. The tensile test specimen geometry shown in Fig. 1 was chosen to produce a smooth transition of stress from the face-loaded grip section into the uniformly stressed gage section. One measure of the success of this tensile test specimen geometry is to assess the number of fracture locations in the 35-mm long, uniformly-stressed gage section. Figure 13 shows comparisons of intralaboratory fracture locations where the gage section is defined as +17.5 and -17.5 mm about the longitudinal midpoint (0 mm). Note that despite the requirement in C 1275 to report fracture location, one laboratory did not. Note also that a number of test specimens from each laboratory fractured outside or nearly outside the gage section. Although, C 1275 suggests that tests with fracture locations outside the gage section be treated as invalid tests, Fig. 14 suggests that there is no correlation between ultimate tensile strength and fracture location.

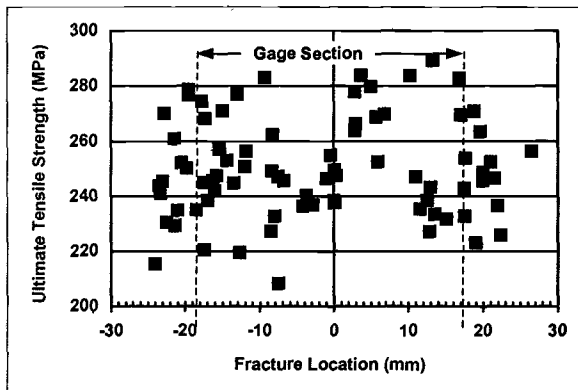


Figure 14 – Lack of correlation between ultimate tensile strength and fracture location.

Repeatability and Reproducibility

ASTM Practice for Conducting an Interlaboratory Study to Determine the Precision of a Test Method (E 691) was used to evaluate the intra- and interlaboratory results for validity and for repeatability and reproducibility. As part of E 691, a one-way ANOVA was conducted at the 99.5% confidence level to screen for outliers. At this level of confidence for h and k statistics, no outliers were identified either within or between laboratories for elastic modulus, ultimate tensile strength or strain at fracture. Finally, E 691 was applied to the round robin results to produce the following suggested precision and bias statement for C 1275.

Precision: An interlaboratory test program* gave the following values for coefficients of variation for the four of the more commonly measured tensile properties for a commercial CFCC (Sylramic S200) with a nominal fiber volume fraction of 45%, an average bulk density of 2200 kg/m³, and an average open porosity of 2.2%:

	Elastic Modulus, E	Proportional Limit Stress, σ_o	Ultimate Tensile Strength, S_{uts}	Strain at Fracture, ϵ_f
CV%r	4.7	3.4	7.2	9.3
CV%R	5.0	4.1	7.2	9.3

r = repeatability (within laboratory) for 9 laboratories and 10 tests for each laboratory
 R = reproducibility (between laboratories) for 9 laboratories and 90 tests

Bias: No statement of bias can be made because no acceptable reference standard exists

* Supporting data can be found in the Appendix. Additional data are available from ASTM Headquarters.

Acknowledgments

Research sponsored by the U.S. Department of Energy, Assistant Secretary for Energy Efficiency and Renewable Energy, Office of Industrial Technologies, Industrial Energy Efficiency Division and the Continuous Fiber Ceramic Composites Program under Contract DE-AC05-96OR22464 with Lockheed Martin Energy Research Corporation. The participating laboratories are acknowledged: AlliedSignal Engines, Cincinnati Testing Labs, Composites Testing and Analysis, Dow Corning, Gateway Materials Technology, Oak Ridge National Laboratory, Southern Research Institute, University of Dayton Research Institute, University of Washington, Air Force Research Laboratory.

References

- Jenkins, M. G., Piccola, J. P., Jr., Mello, M. D., Lara-Curzio, E. and Wereszczak, A. A., "Mechanical Behavior of a 3-D Braided, Continuous SiC Fiber-Reinforced / CVI SiC Matrix Composite at Ambient and Elevated Temperatures," *Ceramic Engineering and Science Proceedings*, Vol. 14, No. 9-10. 1993, pp. 991-997.
- Karnitz, M. A., Craig, D. A. and Richlen, S. L., "Continuous Fiber Ceramic Composite Program," *Ceramic Bulletin*, Vol. 70, No. 3, 1991, pp. 430-435.

3. Han, P., *Tensile Testing*, ASM International, Materials Park, OH, 1992
4. Phillips, D. C. and Davidge, R. W., "Test Techniques for the Mechanical Properties of Ceramic Matrix Fiber Composites," *Journal of British Ceramic Transactions*, Vol. 85, 1986, pp. 123-130.
5. Jenkins, M. G., "Standards and Codes for Ceramic Matrix Composites," *Advanced Composite Materials*, Vol. 8, No. 1, 1999, pp. 55-76.
6. ENV 658-1 "Tensile Strength of Continuous Fiber Reinforced Ceramic Composites," Comité Européen de Normalisation, Brussels, Belgium, 1991.
7. DIS 15733 "Fine ceramics (Advanced ceramics, Advanced technical ceramics)- Test method for tensile stress-strain behavior of continuous fiber-reinforced composites at room temperature," International Organization for Standards, Geneva, Switzerland, 1999.
8. HSR/EPM-D-001-93 "Monotonic Tensile Testing of Ceramic Matrix, Intermetallic Matrix and Metal Matrix Composite Materials," NASA-Glenn Research Center, Cleveland, OH, 1993.
9. PEC-TS-CMC01 "Test Method for Tensile Stress-Strain Behavior of Continuous Fiber Reinforced Ceramic Matrix Composites at Room and Elevated Temperatures," Petroleum Energy Center, c/o Japan Fine Ceramics Center, Nagoya, Japan, 1997.
10. Jenkins, M. G., Lara-Curzio, E., Gonczy, S. T., Zawada, L. P., "Multiple Laboratory Round Robin Study of Flexural, Shear, and Tensile Behavior of a Two-Dimensionally Woven Nicalon™/Sylramic™ Ceramic Matrix Composite," *Mechanical, Thermal and Environmental Testing and Performance of Ceramic Composites and Components*, ASTM STP 1392, M. G. Jenkins, E. Lara-Curzio and S. T. Gonczy, Eds., American Society for Testing and Materials, West Conshohocken, PA, 2000.
11. French, J. E., "Ceramic Matrix Composite Fabrication: Polymer Processing," Chapter 7 in *Handbook on Continuous Fiber-Reinforced Ceramic Composites*, R.L. Lehman, S.K. El-Rahaiby, J.B. Wachtman, Jr., eds, Purdue Research Foundation, W. Lafayette, IN, 1995, pp.269-299.
12. VanLandeghe, P. L., "Intra- and Interlaboratory Round Robin Mechanical Test Evaluation of a Continuous Fiber Ceramic Composite (CFCC)," Master of Science Thesis, University of Washington, Seattle, WA, 1999.
13. Piccola, J. P., Jr., "Effects of Test Parameters on Tensile Mechanical Behavior of a Continuous Fiber Ceramic Composite (CFCC)," Master of Science Thesis, University of Washington, Seattle, WA, 1993.

Larry P. Zawada¹ and Kenneth E. Goecke²

Testing Methodology for Measuring Transthickness Tensile Strength for Ceramic Matrix Composites

Reference: Zawada, L. P. and Goecke, K. E., "Testing Methodology for Measuring Transthickness Tensile Strength for Ceramic Matrix Composites," *Mechanical, Thermal and Environmental Testing and Performance of Ceramic Composites and Components*, ASTM STP 1392, M. G. Jenkins, E. Lara-Curzio, and S. T. Gonczy, Eds., American Society for Testing and Materials, West Conshohocken, PA, 2000.

Abstract: This paper discusses experimental methods and test results from a program established to evaluate the transthickness tensile strength of ceramic matrix composites (CMC). Experimental techniques discussed include adhesives, test specimen design, gripping, and fixturing. Testing apparatus and testing protocol are addressed. In addition to addressing experimental techniques, two studies were conducted. The first study investigated the effect of test specimen geometry using circular and square cross section test specimens. The circular button type test specimens were 19 mm in diameter, while the square test specimens were 16.8 mm on a side. Analysis of the test results revealed no statistically significant difference between the two test specimen geometries. The second study involved a mini-round-robin test program undertaken to evaluate a draft test standard and to evaluate the accuracy of the test method. In addition, transthickness tensile strength results from several different CMCs are presented. An attempt is made to correlate between the measured transthickness tensile strength and the varying CMC microstructures investigated.

Keywords: adhesive, ceramic matrix composite, fixtures, methodology, transthickness tension, oxide/oxide

In recent years there been significant gains in the processing, manufacturing, and evaluation of advanced, high temperature ceramic matrix composites (CMCs). Because of their light weight and high temperature capability, they are now being used to manufacture and validate demonstration components for advanced aerospace turbine engines. Applications currently being manufactured include combustor liners, turbine seals, shrouds, vanes, and

¹Materials research engineer, Ceramics Development & Materials Behavior Branch, Metals, Ceramics & NDE Division, Materials and Manufacturing Directorate, Air Force Research Laboratory, Wright-Patterson AFB, OH 45433-7817.

²Chief mechanical technician, Structural Integrity Division, 300 College Park, University of Dayton Research Institute, Dayton, OH, 45469-0128

exhaust nozzle divergent flaps and seals. Design teams for these components have had a particularly challenging time dealing with the attachments. The attachment schemes are constrained by the limited transthickness tensile strength exhibited by many CMC systems. In addition, almost all of these applications have thermal stresses through the thickness, resulting in stresses that can produce delaminations or cracking [1]. Shown in Fig. 1 is a photograph of a CMC component for the F110 turbofan engine that powers the F-16C Fighting Falcon. The component is an exhaust nozzle divergent flap, and consists of a CMC insert and a metal backing structure. The attachment scheme was limited to a picture frame type arrangement because of the poor transthickness strength. In addition, this component experiences significant thermal stresses both axially and through-the-thickness. A component such as this flap highlights the importance of transthickness strength. It is an important property that needs to be well documented for CMCs to be fully utilized.

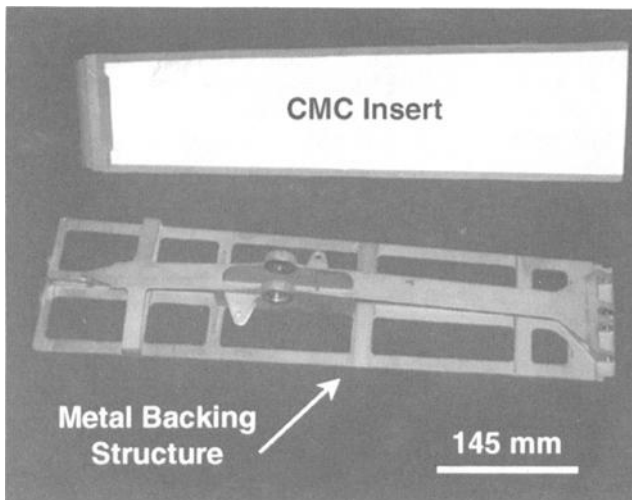


Figure 1. Photograph of a CMC divergent flap for a F110 turbofan exhaust nozzle. The CMC flap is shown mounted in the backing structure. The CMC is exposed to the hot gas flow path, while the metal backing structure provides structural support.

The most common methods used to evaluate off-axis properties of CMCs are the shear tests [2-6]. Although shear test methods are used to evaluate shear interlaminar strength (τ_{31} , τ_{32}) in advanced ceramics, there is significant difficulty in test specimen machining and testing. Improperly prepared notches can produce non-uniform stress distribution in the shear test specimens, and can lead to ambiguity of interpretation of strength results. Such difficulties are identified in an American Society for Testing and Materials (ASTM) test standard titled, "Standard Test Methods for Shear Strength of Continuous Fiber-Reinforced Advanced Ceramics at Ambient Temperatures," and identified as C1292-95. Shear test specimens also rarely produce a gage section that is in a

state of pure shear. Uniaxially-loaded transthickness tensile strength tests measure the tensile interlaminar strength (σ_U^T), avoid the complications listed above, and provide information on mechanical behavior and strength for a uniformly stressed material. It is important to note that the ultimate strength value measured is not a direct measure of the matrix strength, but a combination of the strength of the matrix and the level of bonding between the fiber, fiber/matrix interphase, and the matrix.

Very little information exists in the literature concerning transthickness tensile strength of composites. Lara-Curzio [7] determined the transthickness tensile strength of a unidirectional carbon-carbon composite, and found the room temperature strength to be 2.53 ± 0.23 MPa for six test specimens. Failure occurred primarily by decohesion at the fiber-matrix interfaces. Such a low average value highlighted the poor off-axis mechanical properties exhibited by unidirectional carbon-carbon. A carbon-carbon composite was also tested by Roy [8]. The composite consisted of a woven eight-harness-satin-weave (8HSW) balanced fabric assembled using three different stacking sequences. Transthickness tensile strength was measured to range from 3.5 MPa to 5.5 MPa. These values are also low and clearly identify the weak nature of the carbon matrix. Barnett [9] measured the transthickness tensile strength of a silicon carbide fiber-reinforced calcium-aluminosilicate CMC. The composite was made by hot pressing unidirectional plies together to form a tile using a stacking sequence of (0/90)4s. Five test specimens provided an average transthickness tensile strength of 5.6 MPa and a standard deviation of 0.97 MPa. Barnett only provided a limited description of the test technique, and there was no discussion of the results.

The limited data reported above identifies that composites do indeed exhibit low transthickness tensile strength. In light of the importance of transthickness tensile strength for applications utilizing CMCs, a program was undertaken to develop a test method for the determination of transthickness tensile strength (σ_U^T) for continuous fiber-reinforced CMCs at ambient temperature. For this investigation, transthickness is defined as the direction parallel to the thickness (i.e., out-of-plane dimension), and is normal to the plies for laminates and woven cloth. For a Cartesian coordinate system, the x-axis and the y-axis are in the plane of the test specimen. The transthickness direction is normal to the plane and is labeled the z-axis. For CMCs, the plane of the test specimen contains the larger of the three dimensions and is parallel to the fiber layers for uni-directional (1-D), bi-directional (2-D), and woven composites. For tri-directional (3-D) laminates this direction is taken to be parallel to the thickness and associated with the "z" direction. However, a CMC with a 3-D architecture with even a small volume fraction of fibers in the "z" direction will be hard to test successfully. A schematic of a CMC tile identifying the x, y, and z directions is provided in Fig. 2.

To date, several different CMCs have been studied using the test method described below. This paper describes the intricacies of the test equipment and the testing procedure. Results are presented in three sections. The first investigated test specimen geometry. The second presents results from a mini-round-robin that evaluated a draft ASTM test standard titled, "Transthickness Tensile Strength of Continuous Fiber-Reinforced Advanced Ceramics at Ambient Temperature." This is a new test standard and does not presently

have a number designation. The third section presents transthickness tensile strengths for several distinctly different CMC systems.

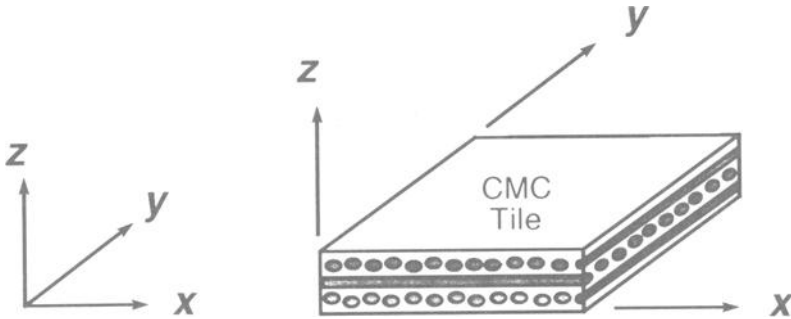


Figure 2. Schematic of a cross-ply CMC tile showing the x , y , and z directions. Directions x and y are in the plane of the tile that contains the larger of the three dimensions, while the z direction is normal to this plane.

Test Method Development

The philosophy used in developing the test method was that it should utilize simple fixturing, provide for excellent repeatability, and provide a reasonable level of through-put. Generally, five technical areas were addressed in designing the test equipment and developing the test method. These were: (1) adhesives, (2) test specimen, (3) fixturing, (4) load train couplers, and (5) gripping. For this test method, fixturing is referred to as the device(s) bonded to the test specimen. It is this device(s) that is actually gripped, screwed, or pinned to the load train. The fixturing transmits the applied load to the test specimen. The following sections describe the important features of the test equipment and several of the technical issues that were addressed in developing the draft full consensus ASTM test method.

Adhesives

In conducting a transthickness tensile test, an adhesive is required to bond the test specimen to the fixturing, as it is not normally possible to directly grip the test specimen. Adhesives come in many forms. Single-part adhesives that air cure at room temperature are the easiest to use, but generally exhibit low strength. Two-part adhesives require a bulk resin along with a catalyst to activate curing. These adhesives demonstrate moderate strength, and often require glass beads of a specific size to produce a bond line of specific thickness for optimum bonding. To obtain the correct bond thickness, a compressive load must be applied during the cure cycle. Compressive loads can range up to 0.28 MPa. One of the limitations of this technique is that extra care is required to measure out the same amount of adhesive for each test. Often excess adhesive is used to ensure a complete bond line. This can pose a problem, as adhesive

should not flow up or down the edges of the test specimen.

Single-part adhesives that cure at an elevated temperature generally produce very high-strength bonds. Several of these elevated temperature curing adhesives are produced in sheets that are easily cut to the desired shape using scissors or cutting blades. A tack agent is often used to keep the film in place on the fixturing. Excess film extending beyond the test specimen can easily be trimmed off before the cure cycle. Use of film adhesives resulted in the same amount of adhesive being used during each test and minimized the influence of the adhesive on measured transthickness strength.

Adhesives that cure at an elevated temperature are usually very sensitive to the maximum temperature. If the maximum temperature is not reached, the cure will not occur. If the temperature is too high, the adhesive will be weak. In using elevated temperature cure cycles, it was found that not reaching the maximum temperature or not soaking at the maximum temperature for the required time frequently resulted in bond line failure. The reason for this is that the mass of the fixturing may not heat up at the same rate as the furnace, and that box furnaces are not completely isothermal. To solve this problem, thermocouples were attached to the fixturing to ensure that the cure temperature was reached and maintained, and the overall cure cycle was followed.

Porous CMCs may allow the adhesive to penetrate the face of the test specimen into the interior. For porous CMC systems, a spare test specimen should be bonded to a small block of material similar to the fixturing using the standard procedure. The assembly should then be sectioned metallographically to determine the depth of penetration of the adhesive into the test specimen. The adhesive should not penetrate more than one fiber ply, or less than 10 % of the thickness from each face. Roy [8] studied penetration of adhesive into a carbon/carbon composite containing approximately 10% porosity and found that the adhesive penetrated only into the surface ply.

There are many types of adhesives available, and it is important to select an adhesive strong enough to fail the test specimen. Strength of the adhesive can be easily evaluated by bonding the fixturing together without the test specimen and performing the transthickness tension test on just the adhesive. This provides a good check to verify that the adhesive possesses sufficient strength. During the development of this test method, several common adhesives were investigated. After a thorough investigation, a commercially available film adhesive³ was selected because of its ease of use and strong reproducible bond strength. This film adhesive was used for all experiments unless otherwise stated.

Test Specimen

Test Specimen Design - The geometry of transthickness tensile test specimens is primarily dependent on the dimensions of the available material. For example, if the strength of an as-fabricated component is required, then the dimensions of the resulting test specimen may reflect the thickness and width of

³ FM-1000 Adhesive Film, Product Brochure Number BPT 234A, American Cyanamid Company, Polymer Products Division, Engineered Materials Department, Wayne, New Jersey 07470

the component, up to limits of the testing machine and test fixturing available. If it is desired to evaluate the effects of mechanical loading of previously conditioned test specimens, then the size of the transthickness test specimen will be limited by the size of the conditioned test specimen. Size should not be determined without the consideration of the size of the fiber and the fiber preform architecture. Woven 8HSW cloth, produced with either silicon carbide or oxide fiber tows containing fibers approximately 10-15 μm in diameter, typically have a unit cell of 7-9 mm. It is recommended that the test specimen width or diameter should be maintained, as a minimum, at a value equal to the repeating distance of the fiber architecture, or 10 mm, whichever is greater. Any larger size is acceptable if the required loads meet the machine limitations.

Conventional test specimens for advanced ceramics have circular cross-sections for uniaxially loaded samples, as described in the ASTM test standard titled, "Standard Test Method for Tensile Strength of Monolithic Advanced Ceramics at Ambient Temperatures," designation C1273-95a. Test specimens with circular cross sections are easier to align in the test machine and generally have less machining-induced defects. Test specimens with square or rectangular cross sections are more difficult to place in the test machine so as to maintain concentricity with the load train. Machined edges of rectangular test specimens are easily damaged, both during machining and in handling. Therefore, a circular cross section test specimen with a diameter of 19 mm was selected as the preferred geometry for the transthickness tensile test method. It incorporates more than two unit cells of typical fiber weaves, such as 8HSW, and avoids the corners found on square or rectangular cross section test specimens.

There may be instances when square or rectangular cross section test specimens may be desirable, especially when testing sections cut out of other larger test specimens that have been conditioned or tested using other test methods. Several test specimens described in the results section were machined from untested tensile specimens. It is important to note that as the test specimen cross-sectional area is decreased, defects at machined edges may have more of an influence on the measured strength. As stated above, larger test specimens are preferred whenever possible.

Factors such as porosity will have a strong influence on measured strength. Therefore, the volume of material subjected to a uniform tensile stress for a single uniaxially-loaded transthickness tensile test may be a significant factor in determining the ultimate strength of CMCs. Studies to determine the exact influence of test specimen volume on strength distributions for CMCs have not been completed. It should be noted that strengths obtained using other recommended test specimens with different volumes and areas may vary due to these volume differences.

Test Specimen Preparation - The transthickness tensile test specimen should simulate the surface/edge conditions and processing route of the intended application. Many processing routes require no machining, such as sintered, as-cast, hot pressed, or injection molded parts. As-processed test specimens might possess rough surface textures and non-parallel edges and may be prone to premature failure if there are stress concentrations at the edges of the test specimen. In addition, non-machined edges can have an apparent beneficial effect, because as-processed test specimens may have all the porosity at the

edges filled in. This can have a beneficial effect on measured strength, as porosity at machined edges can act as stress concentration sites and reduce measured strength.

It is customary to machine only the edges of the transthickness tensile test specimen. However, the faces can be machined to make them parallel, to reduce the surface roughness, or to remove high spots. Machining of the faces will facilitate the process of bonding the test specimen to the fixturing by improving parallelism, but some surface roughness actually helps bonding. During this investigation it was found that extensive roughness associated with some 8HSW fiber architectures prohibited complete bonding by trapping air pockets. For extensive surface roughness, some machining of the surfaces may be required.

The cutting and grinding should be performed in an initial and final grinding operation using resin bonded diamond tooling. Commercial machining companies were contacted for identification of appropriate machining practices for CMCs. A synopsis of these practices is as follows. Initial rough grinding used a material removal rate of 0.03 mm per pass and a 180-240 grit diamond grinding wheel for the entire initial rough grinding process. Initial rough grinding stopped when 0.3 mm of material remained to be removed. Final grinding was performed using a material removal rate of 0.015 mm per pass and a 320-400 grit diamond wheel. This machining procedure was used for all test specimens unless otherwise stated.

Transthickness tensile test specimens using the circular cross-section were core drilled to an oversized diameter and diamond ground to the final dimensions using the final grinding procedure listed earlier. Final grinding was performed in a direction normal to the test specimen edges with the grinding wheel rotating in the plane containing the x and y-directions to avoid fraying the reinforcing ceramic fibers.

Some CMCs have a protective seal coat applied to the outer surface of the composite. In these instances, the coating was removed prior to testing to determine the transthickness tensile strength of the substrate CMC. Sometimes the seal coatings are an integral part of the CMC, and the determination of the tensile strength between the seal coating and the substrate may be of interest. An example of evaluating a coating on a CMC is given in the results section.

Fixturing

Test Specimen Fixtures - It is difficult to grip a test specimen directly to conduct a transthickness tensile test. Thus, fixturing must be bonded to the test specimens. It is the fixturing that is then gripped or connected to the load train by pins and couplers.

Alignment Fixtures For Bonding - Non-fixed load trains require that an alignment jig be used when bonding the test specimen to the fixturing. The fixturing and test specimens are assembled in the alignment jig, and the adhesive is allowed to cure. For elevated temperature cures the whole assembly is placed in a furnace and cured at temperature.

Adhesive may flow past the edges of the test specimen, and this should be avoided. The adhesive can be restricted from bonding to the alignment

device by placing Teflon sheet between the alignment device and the fixturing. However, the adhesive may tend to flow along the edges of the test specimen when Teflon is used. Therefore, if Teflon is used, a thorough check of the bonded test specimen will need to be made to ensure that excessive adhesive is not present on the sides of the test specimen. Spacers can be used between the alignment device and the fixturing. These spacers allow for gaps between the adhesive and the alignment device to prevent them from bonding together while at the same time keeping the test specimen in proper alignment. A schematic showing a side view of a test specimen, fixturing, and alignment spacer is given in Fig 3a. A photograph showing one possible combination of alignment fixture, spacer, test fixtures, and test specimen is shown in Fig 3b. An alternative alignment device is shown in Fig 4, and it has a screw at the top that can be tightened to produce a compressive load.

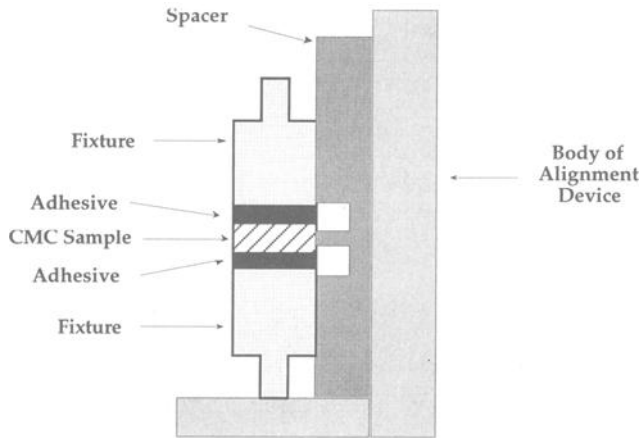


Figure 3a. Schematic showing a side view assembly of an alignment fixture, spacer, test fixture, and test specimen assembled in preparation for curing the adhesive before conducting a transthickness tension test.

Adhesive may flow past and around the edges of the test specimen during the cure cycle. Other researchers [9] have shown that excessive adhesive can be removed by machining the entire assembly after the adhesive has cured. The machining should maintain a concentricity of ± 0.0127 mm and utilize the machining practices listed earlier. Machining of the test fixturing will be easier when it is made out of graphite [9]. If the test specimen strength is so great that the graphite pull rods fail, the assembly can be machined to produce a smaller gage section area in the test specimen.

Load Train Couplers

Various types of devices (load train couplers) were evaluated for attaching the assemblies to the testing machine [7-12]. The load train couplers in conjunction with the type of gripping device play a major role in the alignment

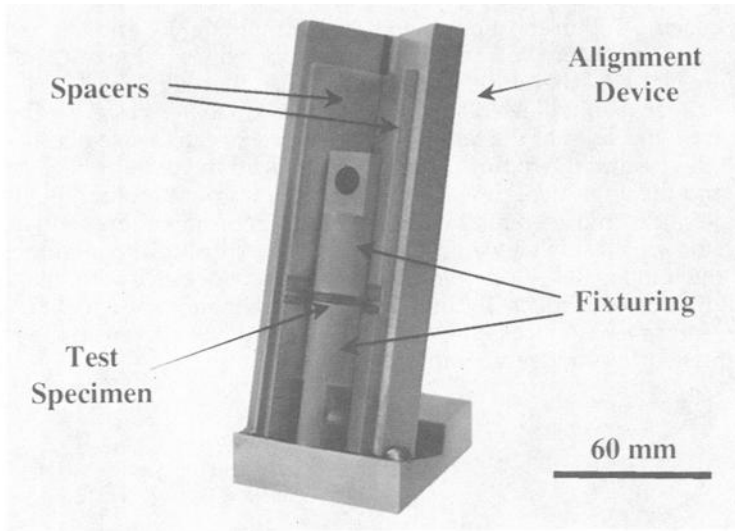


Figure 3b. Photograph of alignment device, fixturing, spacers, and test specimen showing how all of the components are assembled for the adhesive cure cycle.

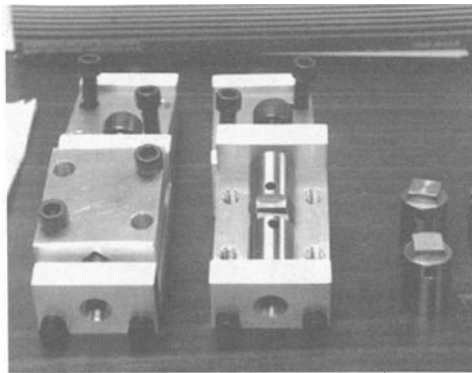


Figure 4. Photograph of alignment device and fixturing showing how all the components are assemble for the adhesive cure cycle

of the load train and thus, subsequent bending imposed in the test specimen. Both fixed and non-fixed load train couplers were investigated.

Fixed couplers incorporate devices that require either a one-time, pre-test alignment adjustment of the load train which remains constant for all subsequent tests or an in-situ, pre-test alignment of the load train which is conducted separately for each test specimen and each test. Such devices [10,13]

usually employ angularity and concentricity adjusters to accommodate inherent load train misalignments, and have two translational degrees of freedom and three rotational degrees of freedom fixed. A schematic diagram of a fixed load train that was investigated first is shown in Fig. 5.

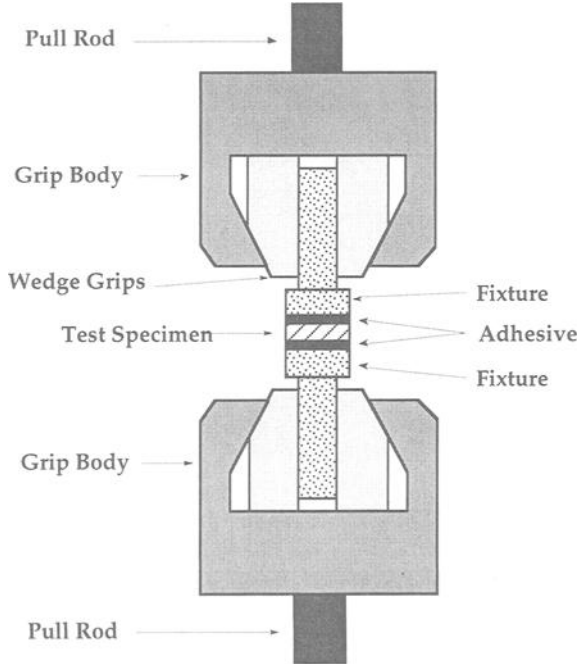


Figure 5. Schematic of one possible arrangement for a fixed load train that uses an active grip interface.

The use of fixed load train couplers requires that the test specimens be bonded to the fixturing after the fixturing has been mounted in the test frame. One drawback resulting from this requirement was that productivity was greatly reduced. For each sample ample time had to be allowed for the adhesive to cure, resulting in only two tests being conducted each day. This slow rate of throughput convinced the authors to consider other techniques to make the test technique more productive.

Non-fixed load train couplers typically incorporate devices which promote self-alignment of the load train during the movement of the crosshead or actuator. Such devices rely upon freely moving linkages to eliminate applied moments during loading. Knife edges, universal joints or ball joint rod ends, hydraulic couplers, or air bearings are examples [9,12,14-16] of such devices. A schematic diagram of one possible arrangement for a non-fixed load train is shown in Fig. 6, and includes the use of universal rod ends (sometimes called ball joint rod ends) threaded into both ends of the fixtured test specimen. The universal rods allow for a full range of angular motion. A photograph of the fixturing and universal rod ends is shown in Fig. 7. Several iterations have yielded the

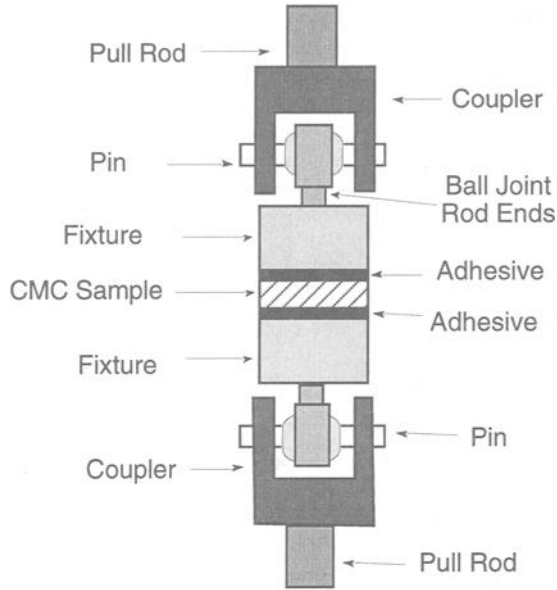


Figure 6. Schematic of one possible arrangement for a non-fixed load train that uses a passive grip interface.

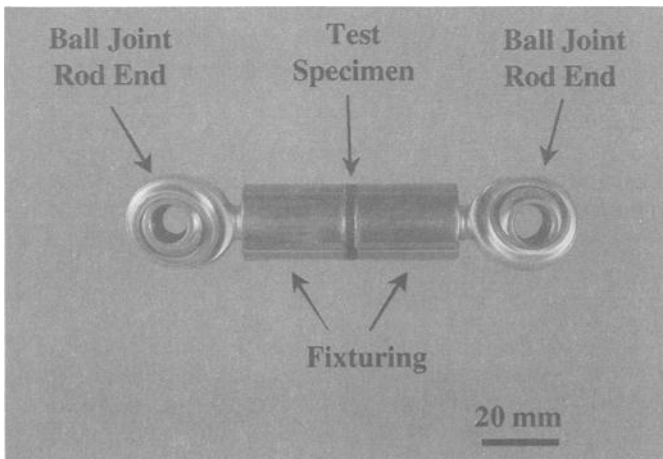


Figure 7. Photograph of a transthickness tensile test specimen bonded to fixturing. Fixturing is assembled with universal rod ends (ball joint rod ends) for improved alignment.

following testing configuration. Threaded pull rods are aligned for concentricity and angularity. These pull rods are mounted with pin loaded couplers. The fixturing is mounted with ball joint rod ends as shown in Fig 7. This combination is now the preferred test configuration for conducting transthickness tension tests.

Non-fixed load train couplers allowed for many test specimens to be prepared ahead of time using the alignment device described above. Once the test specimens were bonded to the fixturing, they were all tested in a very short period of time. This greatly increased throughput and minimized machine time.

Gripping

Various types of gripping devices were investigated for transmitting the load applied by the testing machine to the test fixtures and into the test specimens. Active grip interfaces that use a continuous application of a mechanical, hydraulic, or pneumatic force to transmit the load applied by the test machine to the test fixtures were investigated first. They worked well, but the requirement for performing bonding within the load train resulted in only two tests per day.

Passive grip interfaces transmit the load applied by the test machine through a direct mechanical link and avoid the need for grips. Passive grip interfaces may act through pin loading via pins in the fixturing. Generally, close tolerances of linear dimensions are required to promote uniform contact as well as to provide for non-eccentric loading.

Test Procedure

All testing, unless otherwise stated, was performed on a servo-hydraulic machine using a passive grip interface. Couplers were mounted to threaded pull rods. The pull rods were fixed and were aligned for angularity and concentricity. A schematic of the load train is detailed in Fig. 6. Several load cells were used depending on the expected maximum load. These load cells ranged from 1.0 kN for the lowest strength CMC to 25 kN for the strongest CMC.

After each test, the fractured test specimen was removed from the fixturing by using a 400°C heat treatment for 15-30 minutes. The heat treatment turns most adhesives into fine residual powder. After removing the adhesive, the bonding faces of the fixturing were lightly sand blasted. Care had to be taken not to damage the fixturing during sand blasting by excessive erosion. The final step involved a thorough cleaning of the bonding faces of the fixturing using appropriate solvents. Test specimens were stored in a desiccator until ready for assembly.

The test specimen and fixturing were bonded together using the alignment device shown in Fig 3b. Once bonded, the assembly was carefully placed in the load train. A preload was applied to remove the 'slack' from the load train and to keep the load train "tight." The preload was selected to be less than 1% of the expected failure load, or less than 20 N, whichever was lower.

Test modes and rates can have distinct and strong influences on fracture behavior of advanced ceramics, even at ambient temperatures, depending on

test environment or condition of the test specimen [17]. Test modes may involve load or displacement (commonly called stroke) control. The preferred method for a servo-hydraulic machine is load control. Load control provides for higher accuracy than does displacement control, because of the very small displacements that occur during transthickness tension testing.

Recommended rates of testing are intended to be sufficiently rapid to obtain the maximum possible tensile strength at fracture of the material, and produce final fracture in 5-10 s. Stress rates of 2-5 MPa/s were used in this study. The authors did explore displacement control tests, and found rates of 0.01-0.05 mm/s sufficient.

Data acquisition rates are very important in capturing the failure load and depended on the loading rates used to conduct the test. A data acquisition rate was selected to capture the maximum load within 1%. For all tests, the data acquisition rate was set using both load increments and time increments.

It is very important to identify if the failure occurred in any part of the adhesive. If failure occurs at the adhesive or part of the adhesive the test data cannot be used in the direct calculation of a mean transthickness tensile strength.

Results

Test results are described in the following three sub-sections. The first deals with the effect of test specimen geometry. The second section addresses the results of a mini-round-robin program, while the third presents test results from several CMC systems. A wide range of CMC types have been investigated, and observations between CMC type and resulting transthickness tensile strength are discussed.

Test Specimen Geometry

For this investigation, test specimen geometries consisting of both circular and square cross sections were evaluated. Finite element calculations were performed for the square cross section test specimen for the loading conditions and test specimen thickness investigated within this study. Stress levels along the four corner edges were found to be lower than the interior, except for right at the bonded edge. Stress levels along the sides and interior of the test specimen were all uniform.

The commercially available CMC selected to study the effect of specimen geometry consisted of unidirectional plies of Nicalon™ silicon carbide fibers⁴ in a magnesium aluminosilicate matrix. The matrix of the composite contained five weight percent borosilicate glass. The CMC will be referred to as SiC/MAS-5⁵. The CMC was manufactured by hot pressing 16 plies of unidirectional tape in a [(0/90)₄]_s stacking sequence into a 150 mm x 150 mm tile that was approximately 2.75 mm thick. Fiber volume fraction was measured to be approximately 35-40%.

Test specimens were machined from the CMC tile into square and circular cross section test specimens. The square test specimens were selected to be 16.8 mm wide (282.2 mm²), while the circular test specimens were machined

⁴ Nicalon™, registered trademark of Nippon Carbon co., Ltd.

⁵ SiC/MAS-5, Corning Glass Works, Sullivan park, Corning, New York 14831.

to a final diameter of 19 mm (283.5 mm²). These dimensions produce cross-sectional areas that are nearly identical, allowing for the same volume of material to be investigated. The test specimens were machined and then bonded to fixturing using adhesive film. Testing was performed as described in the Test Procedure section and detailed in the draft ASTM test standard for measuring transthickness tensile strength. A total of 36 test specimens were tested.

A schematic showing the location of the test specimens as machined from the tile is shown in Fig. 8a. The first 12 test specimens were machined and tested. Several months later the remaining test specimens were machined in the same manor as the first 12, and tested in the same manor. No test specimens were machined within 20 mm of the tile edge to avoid possible edge effects. The square and circular cross section test specimen geometry was alternated throughout the tile to minimize possible location effect or variations in the tile from one side to the other. Measured transthickness tensile strength values are shown for each test specimen in Fig. 8b. Three test specimens had failures that

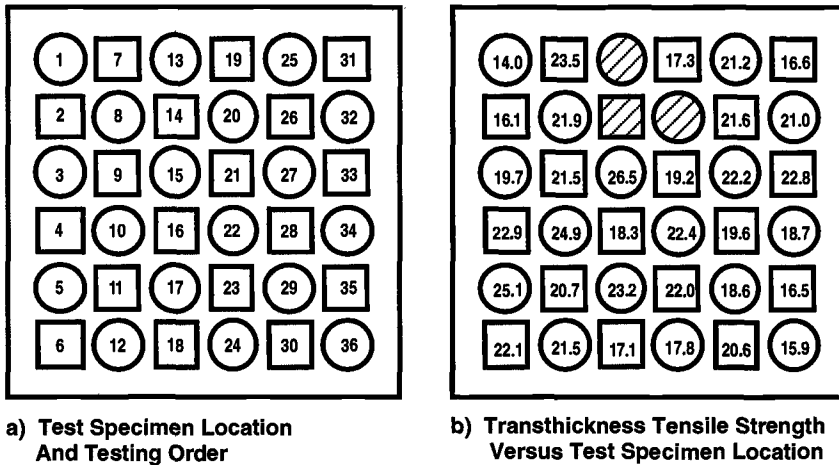


Figure 8. Schematic for the Nicalon/MAS-5 CMC tile showing: A) Location for each test specimen and the order they were tested, and B) Corresponding transthickness tensile strength (hatch marks indicate invalid tests) for each test specimen.

occurred at the CMC/adhesive bond line because of insufficient cure and highlights the need for tight control of temperature during the cure cycle. They are identified as the cross hatched test specimens in Fig. 8b, and their results were deleted from the analysis. Strength values ranged from a low of 14 MPa to a high of 26.5 MPa. The test results were plotted in chronological order, as shown in Fig. 9 in a plot of ultimate transthickness tensile strength versus test specimen number. There is not a dramatic trend in the data, but some subtleties do exist. The mean strength value for the first 12 test specimens is higher than the mean strength value for the remaining 21 test specimens. In addition, a best fit line to the test data produced a negative slope and a difference of approximately 2 MPa from one side of the tile to the other side. Such behavior

may reflect a slight inhomogeneity across the tile. However, given the pattern for machining the test specimens out of the tile, this observation may be misleading. A much more thorough analysis would have to be performed.

To study the effects of test specimen geometry, a statistical box plot of the data is shown in Fig 10. The boxes shown in the plot are bounded top and bottom by the upper and lower quartiles, respectively. Each box encloses roughly 50% of the variable population. The lines running through the interior of the boxes are median values while the darkened symbols are the mean values. The lines extending from the top and bottom of each box mark the minimum and maximum values that fall within an acceptable range. Any value outside of this range, called an outlier, is displayed as an individual point using an open circular symbol. Outliers above the box are those points whose value is greater than the sum of the upper quartile plus 1.5 times the interquartile distance. Outliers below the box are those points whose value is less than the sum of the lower quartile plus 1.5 times the interquartile distance. The number of points within each population are shown in parenthesis under each box. Actual values for the mean, median, and standard deviation are shown above the plot in table format.

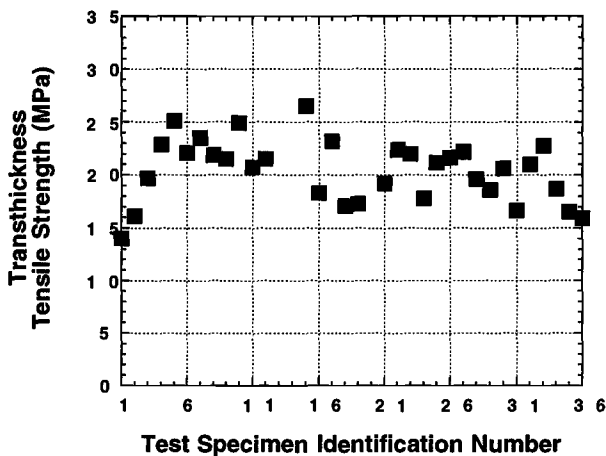


Figure 9. Ultimate Transthickness tensile strength versus the order in which each test specimen was tested. Material was Nicalon/MAS-5.

The circular cross section test specimens had an average strength value of 20.9 MPa, while the square cross section test specimens had an average strength value of 19.9 MPa. These values are quite close and suggest there is no significant effect of specimen geometry. The standard deviation value for all the test specimens is rather small, only ± 3 MPa, indicating this CMC tile exhibited consistent properties. The standard deviation of the square cross section samples (± 2.5 MPa) is slightly less than the circular cross section test specimens (± 3.4 MPa), and the median and means are also slightly less. It is speculated that

the square cross section test specimens might have had slightly lower values because of the machined corners and/or 13% increase in length of machined edges. Any microstructural abnormalities or machining defects at corners (or edges) would act as stress concentration sites and limit ultimate strength. In contrast, the higher standard deviation and higher strength of the circular test specimens may have been influenced less by edge effects, and therefore gives a more realistic picture of the variability of the microstructure. It would take many more tests to determine if these speculations are accurate.

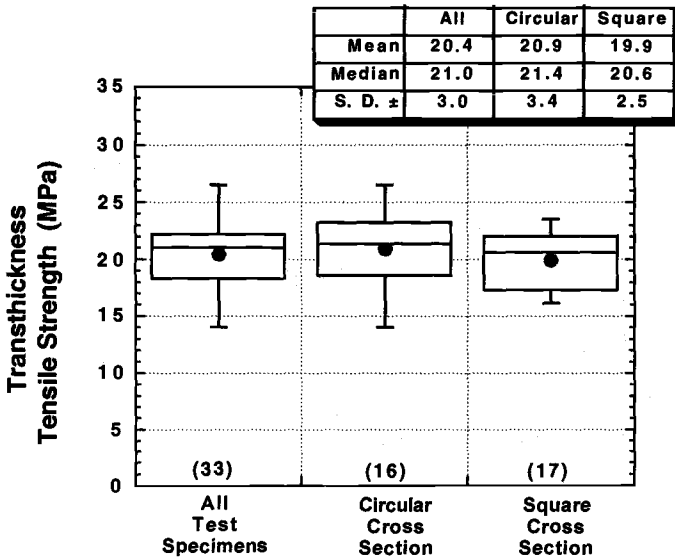


Figure 10. A statistical plot showing the upper and lower quartiles of transthickness tensile strength for Nicalon/MAS-5 tested using both circular cross section (19 mm) and square cross section (16.8 mm) test specimens.

A statistical analysis of the results was performed. Hypothesis testing was performed on the means of the two populations, and made use of the T-distribution. For the analysis a 95% significance level was used. Results of the analysis found that there was no statistically significant difference between the means of the circular and square cross section test specimens. A similar hypotheses test for comparison of variances for two normal populations was also performed using a F-distribution. Again no statistical significant difference was observed.

The standard deviation in transthickness tensile strength for all tested specimens was only approximately 15%. The relatively small standard deviation value may be a result of the hot pressing method used to manufacture the CMC. This family of glass-ceramic CMCs are hot pressed in an initial glassy phase, and then heat treated to promote crystallization. By hot pressing in the glassy phase, high density can be achieved. Density measurements show these CMCs to be near theoretical density. Porosity measurements made using a helium pycnometer technique identified a pore surface area of only 0.3 m²/g,

and verified that the CMC was fully dense. Fully dense CMCs are absent of large pores that may influence the transthickness strength measurements.

Mini-Round-Robin

To evaluate the effectiveness of the test method, a mini-round-robin was conducted. Four laboratories used the procedure described in the draft ASTM test standard for measuring transthickness tensile strength. The commercial CMC was Nicalon™ silicon carbide fiber-reinforced silicon-nitro-carbide⁶, referred to here as SiC/SiNC. Eight plies of 8HSW were used to manufacture the CMC, and the fiber volume fraction was approximately 45%. This material was selected for the mini-round-robin because it was the same material used for three large round robin testing programs performed to measure the precision and bias for three ASTM standards [18].

In this case the test specimens were machined from existing untested dogbone tensile test specimens. Three 10 mm x 10 mm test specimens were machined from each tab area of the tensile test specimens. A total of 40 test specimens were machined, with ten being supplied to each laboratory. Each group of ten test specimens were evenly distributed from the tensile test specimens. Three of the participating laboratories utilized the film adhesive described previously, while the fourth used a two-part liquid adhesive.

Results of the tests from the four laboratories are shown in Fig. 11 as a statistical plot similar to Fig 10. Note that three of the laboratories had at least one failure in the adhesive. The average strength value of 23.5 MPa for all tested specimens represents good strength for this CMC. In fact, the average strength value is higher than that of the denser hot-pressed SiC/MAS-5. One observation that stands out is the mean strength value for the University of Washington. This value of 29.9 MPa appeared to be significantly higher than the other three laboratories.

An analysis of variance technique was used to compare the means recorded by each of the four participating laboratories. For a significance level of 5%, the method did suggest a significant difference in the means. This suggests there was a difference between the results from the University of Washington and the other three laboratories, while there was not a difference between the other three laboratories. However, this difference disappeared when the confidence level (significance level of 2.5%) was raised to 97.5%. Therefore, the conclusion really depends upon which level of confidence one desires. Conclusions identical to the contrast results on the means with a 5% significance level were reached using Duncan's multiple range test, which is a popular test for comparing all pairs of means.

One value worth further discussion is the standard deviation of ± 6.2 MPa for all tested specimens. This value is nearly identical to the standard deviation of ± 6.3 MPa measured for the as-received Nextel 312/BlackGlas discussed in the following section. These two values are approximately twice the reported standard deviation for SiC/MAS-5. A more accurate way to assess the scatter is in terms of percentages. The SiC/SiNC CMC exhibited a standard deviation that was 25% of the mean, while the SiC/MAS-5 CMC had a standard deviation

⁶ SiC/SiNC, Nicalon-Sylramic S-200, Dow Corning, 3901 Saginaw Road, Midland, Michigan 48686.

that was only 14.7% of the mean. It is suggested that the larger values of standard deviation might be the result of the microstructure of the CMC. The SiC/SiNC was manufactured by a polymer infiltration and pyrolysis (PIP) process. During processing, the composite was infiltrated with an organic resin and then given a heat treatment to transform the resin into the ceramic matrix and in effect densify the matrix. Processing of this composite consisted of multiple infiltration's to produce a CMC with a measured open porosity of approximately 2.7%, as measured by the Archimedes method. The porosity measurements had a standard deviation of 0.99%, with a maximum of 4.96% and a minimum of 1.03%. This porosity commonly consists of large and sometimes long pores in the matrix, as clearly shown by Lee et al. [19]. The material Lee investigated had 11% porosity. If one of these stringer type pores appears at the test specimen edges or corner, it will act as a large stress concentration site and reduce strength. Results here and below for this type of CMC suggest that the shape and size of the porosity may have contributed to the larger standard deviation.

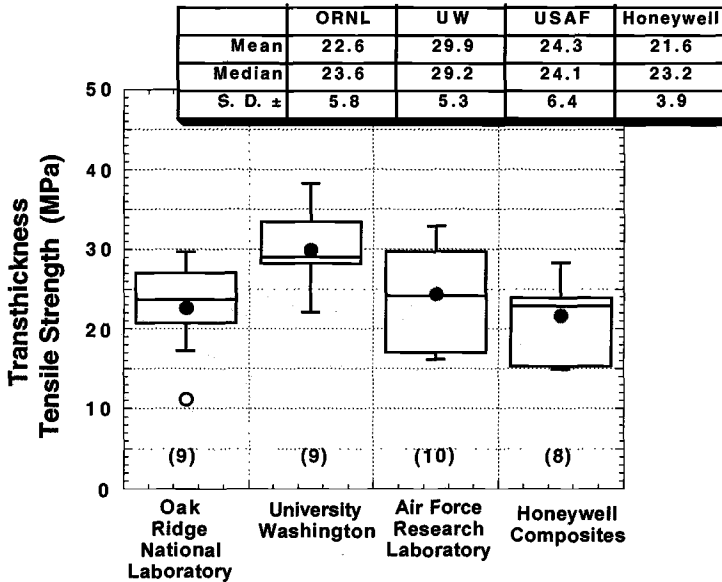


Figure 11. A statistical plot showing the upper and lower quartiles of transthickness tensile strength for Nicalon/SiNC tested by four laboratories. Test specimens had a square cross section (10 mm).

Other CMCs

The test method has been used to measure transthickness tensile strength of several CMCs. Some of the test specimens were in the as-processed condition, while others were machined from existing test specimens. Listed in Table 1 are the type of CMC tested, manufacturer, number of tests, and average

strength values with standard deviation for all as-received test specimens.

Tensile test specimens of Nicalon™ silicon carbide fiber-reinforced amorphous silicon-oxy-carbide⁷ matrix were sectioned into 10 mm x 10 mm test specimens. The composite was manufactured using eight plies of 8HSW cloth and had a fiber volume fraction of approximately 35-40 %. The amorphous silicon oxycarbide matrix material is called Blackglas™ ceramic⁸. Testing was performed as described in the Test Procedure section. Transthickness tests conducted on four test specimens produced an average strength of 10.0 MPa and a standard deviation of 2.9 MPa. This CMC was manufactured using a procedure similar to the SiC/SiNC CMC listed above. However, the transthickness tensile strength is significantly less. Optical studies of polished cross sections showed that the composite had extensive porosity. Image analysis indicated that the total volume fraction of porosity was approximately 10%, and the average transthickness tensile strength correlates with that observation. The proprietary fiber coating was also known to be of poor quality and most likely influenced strength.

Table 1 – *Transthickness tensile strengths of several as-received CMCs.*

CMC	COMPANY	TESTS	STRENGTH
Nextel 610/AS (1)	GEAE (6)	6	7.1 ± 1.0 MPa
Nextel 720/AS (1)	GEAE	6	2.8 ± 1.3 MPa
Nextel 610/AS (1)	3M	5	2.9 ± 0.7 MPa
Nextel 720/AS (1)	ECI (7)	6	2.7 ± 1.6 MPa
Nicalon/BlackGlas (1)	NG (8)	4	10.0 ± 2.9 MPa
Nextel 312/BlackGlas (2)	NG (8)	3	29.1 ± 6.3 MPa
SCS-6/Si3N4 (3)	TSM (9)	3	33.5 ± 3.1 MPa
SCS-6/Si3N4 (4)	TSM (9)	4	36.7 ± 5.0 MPa
SiC/MAS-5 (2)	CGW (10)	16	20.9 ± 3.4 MPa
SiC/MAS-5 (5)	CGW (10)	17	19.9 ± 2.5 MPa
SiC/SiNC (1)	DC	36	24.7 ± 6.2 MPa

(1) Square Specimen, 10 mm x 10 mm	(6) General Electric Aircraft Engines
(2) Circular Specimen, D = 19 mm	(7) Engineered Ceramic, Inc.
(3) Circular Specimen, D = 25 mm	(8) Northrop Grumman
(4) Rectangular Specimen, 14.5 mm x 15 mm	(9) Textron Specialty Materials
(5) Square Specimen, 16.8 mm x 16.8 mm	(10) Corning Glass Works, Inc
	(10) Dow Corning

A second CMC system with a Blackglas matrix was also evaluated. Testing was performed as described in the Test Procedure section. This CMC was made with Nextel™ 312 oxide fibers⁹ that were woven into a 5HSW fiber form. Circular cross section test specimens 19 mm in diameter were used. Test results in Table 1 show that the as-processed material demonstrated an average transthickness tensile strength of 29.1 MPa and a standard deviation of ±6.3

⁷ SiC/Blackglas, Northrop Grumman Corporation, Pico Rivera, California, 90660

⁸ Blackglas™ is a trademark of AlliedSignal Inc.

⁹ Nextel™ is a trademark of 3M

MPa. Several test specimens were heat treated for 50, 100, 500 h at 600°C to determine the stability of the CMC, and the results are shown in Table 2. With increasing time at temperature, the strength decreased rapidly. After the 500 hours, the strength had dropped to only 5.7 MPa. Such a large decrease in strength indicates that extensive oxidation had occurred within the CMC. The oxidative attack occurred at the interphase between the fiber and matrix as well as in the matrix itself.

Table 2 – Effect of heat treatment on the transthickness tensile strength of Nextel 312/Blackglas.

HEAT TREATMENT	TESTS	STRENGTH
As-Received	3	29.1 ± 6.3 MPa
600°C / 50 Hours	3	12.7 ± 2.0 MPa
600°C / 100 Hours	3	8.4 ± 0.7 MPa
600°C / 500 Hours	3	5.7 ± 0.6 MPa

NOTE: Circular Cross-Section Test Specimen, D = 19 mm
Material: Nextel312/Blackglas

Four different oxide/oxide CMCs were studied using 10 mm x 10 mm test specimens machined from straight sided tensile test specimens. The four CMCs were designated as follows: 1) GEAE Nextel™610/AS¹⁰, 2) 3M Nextel™610/AS¹¹, 3) GEAE Nextel™720/AS¹², and 4) ECI Nextel™720/AS¹³. All of these CMCs were manufactured with no interphase between the fibers and matrix, and relied on a very porous aluminosilicate matrix for toughness. A more complete description of these CMCs and the testing procedure is given by Zawada [20]. Testing was performed as described in the Test Procedure section. Results from the tests are shown in Fig. 12 as a statistical plot similar to Fig. 10. The GEAE Nextel™610/AS CMC was substantially stronger than the other three CMCs. At this time there is no information as to why this difference was observed. What stands out is that the transthickness tensile strength of these CMCs is low. The requirement of no interphase and a low energy matrix with porosity may limit this class of CMC to 10-15 MPa. Such low strength values will pose a significant challenge to the design community.

The final CMC investigated was designated SCS-6/Si₃N₄¹⁴. This CMC utilized the large, 150 micron diameter silicon carbide monofilaments identified as SCS-6. Samples were manufactured using unidirectional plies stacked up symmetrical in a [(0/90)₁₂]_s orientation, for a total of 24 plies. Tiles were hot pressed, and then circular test specimens were machined from the tile. After machining, the test specimens were given a protective exterior seal coating. Porosity was approximately 1% as measured by the Archimedes method.

These tests were some of the first transthickness tension tests conducted by the authors, and the load train for these initial tests was of a fixed

¹⁰ General Electric Aircraft Engines, Evendale, Ohio 45215

¹¹ 3M, St. Paul, Minnesota 55144

¹² General Electric Aircraft Engines, Evendale, Ohio 45215

¹³ Engineered Ceramic Incorporated, San Diego, California 92121

¹⁴ Textron Specialty Materials

configuration as shown in Fig. 5. The fixturing was placed into the load train and aligned. The test specimens were then mounted to the fixturing using a two part adhesive¹⁵ and a compressive load. Each test took approximately half a day to complete because of the cure cycle for the adhesive. On the first two tests the failure occurred between the exterior seal coating and the substrate CMC. The strength of the coating was found to be approximately 15 MPa. For subsequent testing, the coating was carefully ground off using a 70 grit diamond polishing wheel followed by a 400 grit diamond wheel. Several test specimens were machined into rectangular test specimens and tested to see if there was an effect of test specimen geometry. This particular CMC was being evaluated for a high temperature application, and it was important to determine if long term exposures would reduce the transthickness tensile strength. A dogbone test specimen was given a heat treatment of 1309°C for 185 hours, and then rectangular test specimens were machined from the tab area.

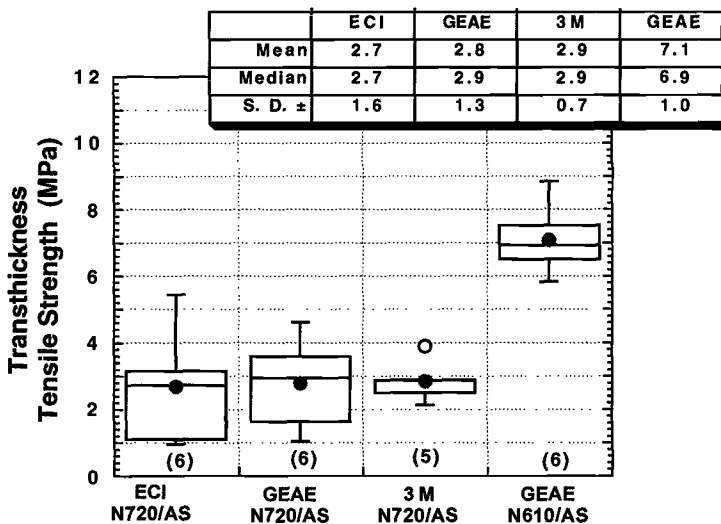


Figure 12. A statistical plot showing the upper and lower quartiles of transthickness tensile strength for four different oxide/oxide CMCs. Test specimens had a square cross section (10 mm).

Results of the as-received material are shown in Table 1 for both the circular and rectangular cross section test specimens. Results of the heat treated test specimens are presented in Table 3, along with the average strength for four rectangular test specimens similar to those cut from the heat treated dogbone test specimen. Average strength values were 33.5 MPa for the circular test specimens, 36.7 MPa for the rectangular test specimens, and 25.3 MPa for the heat treated material. There was little difference in test specimen geometry,

¹⁵ EA-9394

but there was a significant decrease in strength as a result of the thermal aging. However, the decrease was not as significant as for the Nextel™312/Blackglas, even though the exposure temperature was over 700°C greater. The thermally aged test specimens were sectioned, mounted, and polished to study the microstructure. Optical micrographs clearly showed that the carbon coating around the SCS-6 fibers was severely oxidized, and that several of the fibers actually had cracks running along their length. Cracks along the length of SCS-6 fibers are not common, and suggest that the heat treatment produced a difference in the bonding between the fiber and matrix, and a change in the residual stress state of the CMC. It is suggested that these damage mechanisms are the most likely cause of the reduction in strength. No changes were observed (optically) to have occurred in the Si₃N₄, beyond some slight reactions located at the surface of the composite.

Table 3 – Effect of heat treatment on the transthickness tensile strength of SCS-6/Si₃N₄.

HEAT TREATMENT	TESTS	STRENGTH
As-Received	4	36.7 ± 5.0 MPa
1309°C / 185 Hours	4	25.3 ± 6.9 MPa

NOTE: Rectangular Cross-Section Test Specimen, 14.5 mm x 15 mm
 Material: SCS-6/Si₃N₄

Conclusions

A viable test method for evaluating the transthickness tensile strength of CMCs has been successfully developed and utilized. Combined use of film adhesives, alignment devices, and flexible load trains allow for fast, repeatable, and accurate bonding of the test specimen to the fixturing. Procedures for test specimen mounting and for conducting the transthickness tension test have been identified and documented.

For any test method the design of the test specimen is vital for obtaining valid results. In this study two different CMCs were investigated using circular, square, and rectangular test specimens. It was found that for Nicalon/MAS-5, square test specimens and circular test specimens having a cross-sectional area of approximately 282 mm² exhibited no geometry effect on measured strength. The same was found for the SCS-6/Si₃N₄ CMC investigated.

Test specimen geometry has been addressed. However, very little is known about test specimen size effects. In addition, the actual volume of material tested versus the total surface area of the machined edges needs to be studied.

Issues about the effects of microstructure have clearly been identified. Fully dense CMCs such as the hot pressed Nicalon/MAS-5 have a relatively small standard deviation for transthickness strength. A mini-round-robin on Nicalon/SiNC identified this material as having a wide range in strength values. It is suggested that this larger scatter may be the result of the large pores in the matrix that are characteristic of this class of material. Another important

observation was that extended time at temperature can result in changes in the CMC, both by oxidation as well as stability of the constituents. Changes such as these can have a pronounced effect on the transthickness tensile strength.

Depending on the manufacturing route selected and the fiber coating, the resulting CMC can possess a wide range of transthickness tensile strength values. In this investigation, values have ranged from less than 1 MPa to as high as 45 MPa. Clearly transthickness tensile strength values need to be measured and addressed for each design project considering CMCs.

References

- [1] John, R., Zawada, L. P., and Kroupa, J.L., "Stresses Due to Temperature Gradients in Ceramic-Matrix-Composite Aerospace Components," *Journal of the American Ceramic Society*, Vol. 82, No. 1, 1999, pp. 161-168.
- [2] Fang, N. J. J. and Chou, T.-W., "Characterization of Interlaminar Shear Strength of Ceramic Matrix Composites," *Journal of the American Ceramic Society*, Vol. 76, No. 10, 1993, pp. 2539-2548.
- [3] Brondsted, P., Heredia, F. E., and Evans, A. G., "In-plane Shear Properties of 2-D Ceramic Matrix Composites," *Journal of the American Ceramic Society*, Vol. 77, No. 10, 1994, pp. 2569-2574.
- [4] Cady, C., Heredia, F. E., and Evans, A. G., "The In-Plane Mechanical Properties of Several Ceramic Matrix Composites," *Journal of the American Ceramic Society*, Vol. 78, No. 8, 1995, pp. 2065-2078.
- [5] Keith, W. and Kedward, K., "Shear Damage Mechanisms in a woven, Nicalon-Reinforced Ceramic-Matrix Composite," *Journal of the American Ceramic Society*, Vol. 80, No. 2, 1997, pp. 357-364.
- [6] Effinger, M. R., Tucker, D. S., and Barnett, T. R., "Tensile and Interlaminar shear Evaluation of Du Pont Lanxide CMCs," *Ceramic Engineering and Science Proceedings*, Vol. 17, No. 4, 1996, pp. 316-323.
- [7] Lara-Curzio, E., Bowers, D., and Ferber, M. K., "The Interlaminar Tensile and Shear Behavior of a Unidirectional C-C Composite," *Journal of Nuclear Materials*, 230, 1996, pp. 226-232.
- [8] Roy, A. K., "A Self-Aligned Test Fixture for Interlaminar Tensile Testing of Two-Dimensional Carbon-Carbon Composites," *Journal of Composite Materials*, Vol. 28, No. 4, 1994, pp. 367-379.
- [9] Barnett, T. R. and Starrett, H.S., "Room and Elevated Temperature Mechanical and Thermal Properties of Corning Nicalon/CAS" WRDC-TR-90-4131, Wright Research and Development Center, Wright Patterson Air Force Base, Ohio, 1992.
- [10] Hartman, G. A., Zawada, L. P., and Russ, S. M., "Techniques for Elevated Temperature Testing of Advanced Ceramic Composite Materials," *Proceedings of the Fifth Annual Hostile Environment and High Temperature Measurement Conference*, Society for Experimental Mechanics, Bethel, Connecticut, 1988, pp. 31-38.
- [11] Lewis, D., III "Tensile Testing of Ceramics and Ceramic-Matrix Composites," *Tensile Testing*, ASM International, Materials Park, Ohio, 1992, pp. 147-181.
- [12] Holmes, J. W., "A Technique for Elevated Temperature Creep and Tensile

- Fatigue Testing of Fiber-Reinforced Ceramics," *Journal of Composite Materials*, Vol. 26, No. 6, 1992, pp. 915-932.
- [13] Amaral, J.E. and Pollock, C.N., "Machine Design Requirements for Uniaxial Testing of Ceramics Materials," *Mechanical Testing of Engineering Ceramics at High Temperatures*, B.F. Dyson, R. D. Lohr, and R. Morrell, Eds., 1989, pp. 51-68.
- [14] Liu, K. C. and Brinkman, C. R., "Tensile Cyclic Fatigue of Structural Ceramics," Proceedings of the 23rd Automotive Technology Development Contractors' Coordination Meeting, P-165, Society of Automotive Engineers, Warrendale, Penn., 1986, pp. 279-284.
- [15] Mejia, L. C., "High Temperature Tensile Testing of Advanced Ceramics," *Ceramic Engineering and Science Proceedings*, Vol. 10, No. 7-8, 1989, pp. 668-681.
- [16] Jenkins, M. G., Ferber, M. K., Martin, R. L., and Tennery, V. T., "Study and Analysis of the Stress State in a Ceramic, Button-Head, Tensile Specimen," Oak Ridge National Laboratory Technical Memorandum, ORNL/TM 11767, September (1991).
- [17] Shuler S. F. and Holmes, J. W., "Influence of Loading Rate on the Monotonic Tensile Behavior of Fiber Reinforced Ceramics." Available through: Ceramic Composites Research Laboratory, Dept. of Mechanical Engineering and Applied Mechanics, 1065 GGBL, The University of Michigan, Ann Arbor, MI 48109-2125, Research Memorandum No. 102, September, 1990.
- [18] Gonczy, S. T. and Jenkins, M., "Tensile Testing of Nicalon™ 2-D Fiber-Reinforce Sylramic™ S-200 Ceramic Composites – A Multi-laboratory Round-Robin Test," Gateway Materials Technology Report # TR 99-1, April, 1999.
- [19] Lee, S. S., Zawada, L. P., Staehler, J. M., and Folsom, C. A., "Mechanical Behavior and High-Temperature Performance of a Woven Nicalon™/Si-N-C Ceramic Matrix Composite," *Journal of the American Ceramic Society*, Vol. 81, No. 7, 1998, pp. 1797-1811.
- [20] Zawada, L. P., "Longitudinal and Transthickness Tensile Behavior of Several Oxide/Oxide Composites," *Ceramic Engineering and Science Proceedings*, Vol. 19, No. 3, 1998, pp. 327-340.

Stephen T. Gonczy¹ and Michael G. Jenkins²

Flexural and Tensile Properties of a Two-Dimensional Nicalon™ -Reinforced Sylramic™ S-200 Ceramic Matrix Composite

Reference: Gonczy, S. T. and Jenkins, M. G., “**Flexural and Tensile Properties of a Two-Dimensional Nicalon™-Reinforced Sylramic™ S-200 Ceramic Matrix Composite,**” *Mechanical, Thermal and Environmental Testing and Performance of Ceramic Composites and Components, ASTM STP 1392*, M. G. Jenkins, E. Lara-Curzio, and S. T. Gonczy, Eds., American Society for Testing and Materials, West Conshohocken, PA, 2000.

Abstract: A round robin study of mechanical test methods provided an opportunity for direct comparison of flexural and tensile test methods and results for one hundred ninety test specimens (one hundred flexure and ninety tension) of a commercial ceramic fiber-reinforced ceramic matrix composite (Sylramic™ S-200) consisting of eight plies of ceramic grade (CG)-Nicalon™ eight harness satin weave (8HSW) fabric in a silicon-carbonitride matrix (Sylramic™) with a boron-nitride-containing interphase coating. Flexural test specimens (110 x 9 x 3 mm) were tested in four-point quarter-point loading per ASTM Test Method for Flexural Properties of Continuous Fiber-Reinforced Advanced Ceramic Composites (C 1341). Grand means for the ultimate “flexural strength,” flexural strain at ultimate “flexural strength,” and elastic modulus in flexure for the ten laboratories, were 339 MPa, 4640 $\mu\text{m}/\text{m}$ and 93 GPa, respectively. The dog-bone tensile test specimens (150 x 12 x 3 mm) were tested per ASTM Test Method for Monotonic Tensile Strength Testing of Continuous Fiber-Reinforced Advanced Ceramics with Solid Rectangular Cross-section Specimens at Ambient Temperatures (C 1275). Grand means for ultimate tensile strength, strain at ultimate tensile strength, and elastic modulus for the nine laboratories were 251 MPa, 4310 $\mu\text{m}/\text{m}$ and 93 GPa, respectively. A key finding was that the ultimate flexural strength values calculated from the conventional beam bending equations are not representative of the measured ultimate tensile strength. The key material variable was the tensile strength of the coated ceramic fibers, rather than fiber volume fraction, bulk density, or open porosity. Dimensional measurements was a key experimental variable.

Keywords: continuous-fiber reinforced ceramic composite, advanced ceramic, tension testing, flexure testing, Nicalon,™ Sylramic™

¹ Research director, Gateway Materials Technology, 221 S. Emerson, Mt. Prospect, IL 60056

² Associate professor, Department of Mechanical Engineering, University of Washington, Box 352600, Mechanical Engineering Building, Seattle, WA 98195-2600

Introduction

Continuous fiber-reinforced ceramic composites (CFCCs) are being developed as replacement materials for metallic alloys for high temperature applications. CFCCs offer the potential of higher temperature operation, lower weight, and improved damage tolerance [1,2]. Near-term aerospace applications include exhaust components and hot-gas ducting for turbine engines, where the weight savings would improve fuel efficiency and the low signature properties would have military applications. CFCCs have industrial applications [3] as heat exchangers, combustors, and filters to improve durability and increase operating temperatures.

Because CFCCs are complex composites, often with high-strength fibers in low-strength, brittle matrices, the question arises as to how CFCC systems can be reliably and reproducibly tested. The ideal mechanical test for CFCCs provides definitive test results, uses low-cost test fixtures and employs simple, easily-machined test specimen geometries [4]. In regard to mechanical property characterization of CFCCs, flexural testing has the advantages of low-cost test specimen fabrication with simple test fixturing. However, the relationship between the experimentally-measured loads and the state of stress in a CFCC test specimen subjected to bending is complicated. Conventional beam bending equations cannot be used to analyze the state of stress and strain in CFCC test specimens subjected to flexure, because these materials are not homogeneous. In addition, for stresses greater than the proportional limit tensile stress, the stress-strain relation is not only nonlinear but is also non-symmetric in tension and compression. In contrast, uniaxial tensile tests produce an unequivocal test result, based on uniform stress/strain conditions in the test specimen. However, this advantage is contrasted with more costly tensile test specimen preparation and tensile test fixtures that are expensive and complex.

American Society for Testing Materials (ASTM) Subcommittee C28.07 on Ceramic Matrix Composites has developed test methods for flexure and tension testing CFCCs: ASTM Test Method for Flexural Properties of Continuous Fiber-Reinforced Advanced Ceramic Composites (C 1341) and ASTM Test Method for Monotonic Tensile Strength Testing of Continuous Fiber-Reinforced Advanced Ceramics with Solid Rectangular Cross-section Specimens at Ambient Temperatures (C 1275).

Federal³ funding supported a round-robin evaluation in 1998 of the two ASTM flexural and tensile testing standards for CFCCs. The round robin evaluations were organized with the objectives of determining the precision of the ASTM test methods for CFCCs and of assessing the statistical distribution of mechanical properties for a single CFCC. The round robin study also provided the opportunity for a direct comparison of flexural and tensile test results for a single CFCC.

³ Continuous Fiber-Reinforced Ceramic Composite Program (U. S. Department of Energy) and the Air Force Research Laboratory.

Experimental Materials And Procedures

Material

Ten panels of a commercial CFCC⁴ (Sylramic™ S-200) were fabricated, using eight plies of ceramic grade (CG) Nicalon™⁴ fabric [eight-harness satin weave (8HSW)] in a silicon-carbonitride matrix [based on a preceramic polymer impregnation process (PIP)] with a silicon nitride powder filler. The ply architecture was a symmetric 0/90 fabric lay-up (0/90/0/90/90/ 0/90/0). The Nicalon™ tows had been precoated with a proprietary boron nitride interphase via chemical vapor deposition (CVD). The test specimens were diamond-grit cut and ground through the thickness to the required shapes after the fifth PIP cycle (i.e., impregnation, cure, pyrolysis). Fabric faces were not machined. PIP cycles were then continued until the target density had been achieved (as measured by less than 5% open porosity). The finished test specimens had a average bulk density of 2.2 g/cm³, an estimated nominal fiber volume fraction of 45 %, an average porosity of 2.7 %, and a nominal thickness of 3 mm.

Experimental Procedures

The flexural test specimens (110 mm x 9 mm x ~3 mm) were cut from four panels. The flexural test specimens were randomly divided into groups of ten for distribution to the ten laboratories for ambient temperature testing per C 1341. In addition to the requirements of C 1341, the round robin protocol imposed the following flexural testing parameters:

- Four-point quarter-point flexural testing geometry (steel or ceramic articulating or semi-articulating fixtures) with an 80-mm outer span and a 40-mm inner span
- Displacement control at a rate of 0.10 mm/s
- Strain calculated from the measured center-point deflection

The tensile test specimens (150 mm x 12 mm x ~3 mm) had a contoured geometry (dog-bone shape) with a reduced width gage section (35 mm x 8 mm) and transition radii of 254 mm, were cut from three panels. The tensile test specimens were randomly divided into groups of ten for distribution to the nine laboratories, who were required to

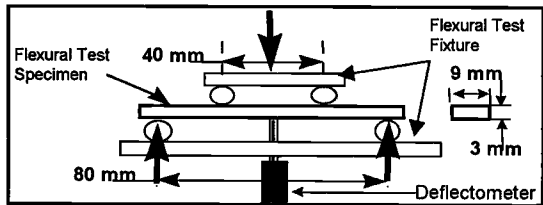


Figure 1 – Flexural test specimen and four-point quarter-point flexural testing geometry.

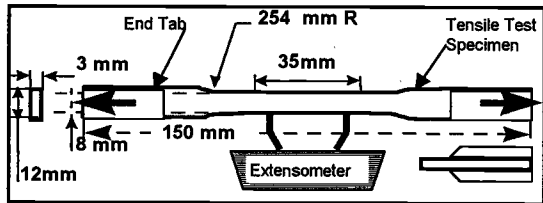


Figure 2 – Tensile test specimen geometry.

⁴ Sylramic™ S-200, Dow Corning Corporation, Midland, MI in November 1997 (as of July 1999, Engineered Ceramics, Inc., San Diego, CA).

test the tensile test specimens at ambient conditions per C 1275. In addition to the requirements of C 1275, the round robin protocol imposed the following tensile testing parameters:

- Displacement control at a rate of 0.02 mm/s
- Face-grip loading with E-glass epoxy end tabs adhered to the test specimens
- Strain measured by a 25 mm gage length extensometer

The stress and strain along with elastic constants, strengths and elongation parameters in flexure and tension were calculated using the equations contained in C 1341 and C 1275, respectively. The flexural equations in C 1341 are based on the assumptions of isotropic, homogeneous material with linear elastic stress-strain relation and symmetric behavior in tension and compression. These assumptions are not fully valid for CFCC materials, particularly at strain levels greater than the proportional limit.

Round-Robin Organization

The round robin testing program in flexure and tension was conducted with a total of thirteen different laboratories.⁵ Some laboratories conducted both flexure and tension tests, some just flexure and some just tension. The flexure and tension tests were conducted between January and September 1998.

Experimental Results

Summary

Figure 3 shows the summary of three selected flexural and tensile properties of the Sylramic™ S-200 at ambient conditions. The figure shows the results normalized to the tensile values, with the normalized grand mean values noted by the bars along with arrows showing \pm one standard deviation.

There were one hundred flexural test specimens tested with only one anomalous test. The flexural breaking loads were on the order of 375 N with center point deflections on the order of 2.5 mm.

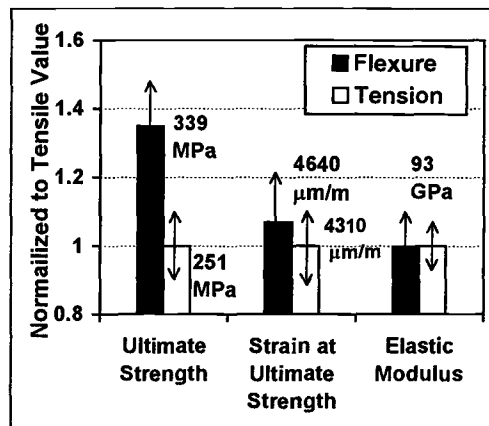


Figure 3 -- Comparison of selected ambient flexural and tensile test results (Sylramic™ S-200)

⁵ Air Force Research Laboratory, WPAFB, OH; AlliedSignal Engines, Phoenix, AZ; Cincinnati Testing Labs, Cincinnati, OH; Composite Testing and Analysis, Ann Arbor, MI; Dow Corning Corporation, Midland, MI; NASA-Lewis Research Center, Cleveland, OH; Northrop Grumman, Pico Rivera, CA; Oak Ridge National Laboratory, Oak Ridge, TN; Southern Research Institute, Birmingham, AL; U.S. Army Research Laboratory, Aberdeen PG, MD; United Technology Research Center, East Hartford, CT; University of Dayton Research Institute, Dayton, OH; University of Washington, Seattle, WA.

Table 1 – Selected ambient flexural and tensile properties (Sylramic™S-200)

Property	-----Flexural-----		-----Tensile-----	
	Mean	Coef.Variation	Mean	Coef.Variation
Ultimate Strength	339 MPa	10.9%	251 MPa	7.2%
Strain at Ultimate Strength	4640 μm/m	13.6%	4310 μm/m	9.1%
Elastic Modulus	93 GPa	6.9%	93 GPa	5.0%
Test Specimen Count	100		90	

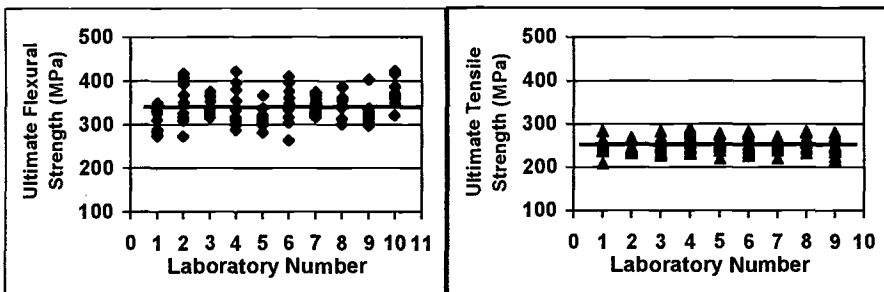
All the flexural test specimens fractured on the tensile surface with no compression or shear fractures noted. The ninety tensile test specimens were tested with fifty-eight fracture locations in the gage-section and thirty-two fracture locations just outside the gage section. Tensile fracture loads were on the order of 5600 N. There was no statistical difference in the ultimate tensile strengths calculated for tensile test specimens that fractured in or out of the gage section. The mean and coefficient of variations for the ultimate strength, strain at ultimate strength and elastic modulus values in flexure and tension are given in Table 1.

Ultimate Strength

Figure 4 shows the distribution of ultimate strengths in flexure and tension for the different laboratories in the round robin study, with a horizontal line indicating the grand mean for the entire population. (Note that the identification numbers are not the same for the different laboratories conducting the flexure tests and the tension tests.) The grand mean for the ultimate flexural strength is 35% greater than the grand mean for the ultimate tensile strength. In addition, the flexural test results have much more variation both within and between laboratory results.

Strain at Ultimate Strength

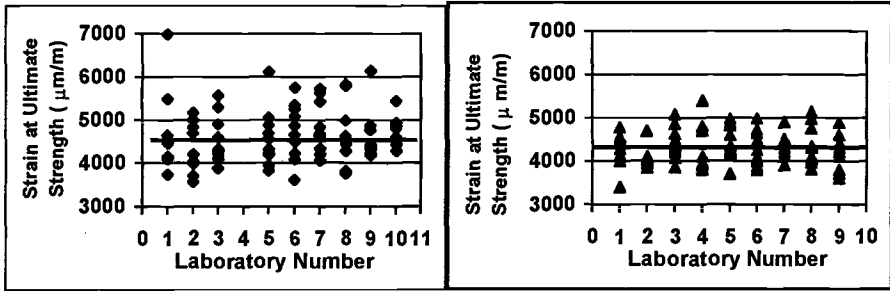
The results for the strain at ultimate strength in flexure and tension are shown by laboratory in Figure 5, again using a horizontal line to indicate the grand mean for the entire population. For the strain at ultimate strength, there is much less difference



a) Ultimate flexural strength

b) Ultimate tensile strength

Figure 4 – Ambient ultimate strength in flexure and tension (Sylramic™ S-200).



a) Strain at ultimate flexural strength b) Strain at ultimate tensile strength

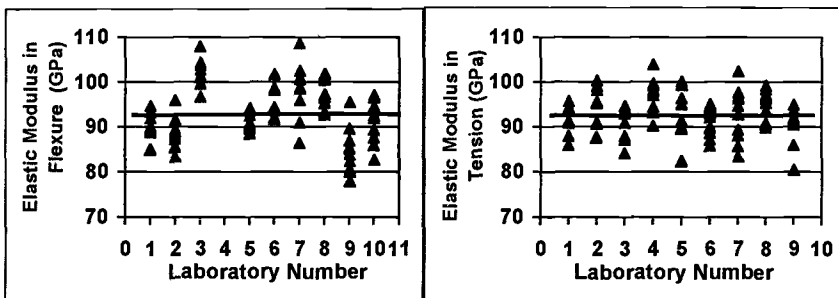
Figure 5 – Strain at ultimate strength in flexure and tension (Sylramic™ S-200).

between flexural and tensile results (flexural mean value is only 7% greater than the tensile mean value), as compared to the difference in ultimate strength mean values (flexural mean value is 35% greater than the tensile mean value). The results for strain at ultimate flexural strength again show much greater variation, as compared to the tensile results.

Elastic Modulus

Figure 6 shows the elastic modulus results determined in for flexure and tension by laboratory, again with the horizontal line showing the grand mean for the entire population. In contrast to the results for ultimate strength and strain at ultimate strength, the elastic modulus values determined in flexure and tension are essentially equivalent. However, the flexural results again show greater variation between laboratories.

The distinct differences between the flexural and tensile strength and strain results in terms of both the grand mean values and the observed inter-laboratory variations are the result of fundamental differences in test methods, experimental procedure differences between laboratories, and material variation.



a) Elastic modulus in flexure b) Elastic modulus in tension

Figure 6 – Elastic modulus values in flexure and tension (Sylramic™ S-200).

Tensile Test Fracture Location

The nine laboratories in the tensile test study were asked to report the location of the tensile test fracture using the center point of the tensile test specimen as the zero point and measuring fracture locations in millimeters from the center point. Laboratory Number 8 did not report failure locations. Figure 7 maps the ultimate tensile strengths against fracture locations with the uniform gage section indicated at +/- 17.5 mm.

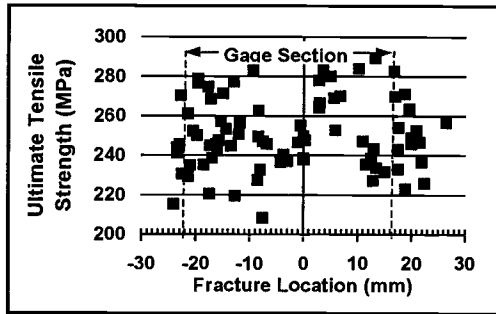


Figure 7 – Ultimate tensile strength results mapped against fracture location (Sylramic™ S-200).

Discussion and Analysis

Differences in Flexural and Tensile Stress Calculation Methods

The first discussion point is as to why the ultimate flexural strength values are greater than the ultimate tensile strength values. The tensile results are unequivocal, because the stress-strain condition is uniaxial and uniform. Figure 8 shows representative stress-strain curves for the flexure and tension tests. Figure 8 illustrates that the stress-strain curves in flexure and tension are similar in the linear-elastic region (i.e., equivalent slopes and proportional limits), but deviate in the nonlinear region, with the flexure tests showing greater strength, but roughly equivalent failure strain. This is consistent with the effect of nonlinear tensile stress-strain behavior and laminar architecture in ceramic composites, as described by Buesking [5] in his analysis of flexural behavior in laminated CFCCs.

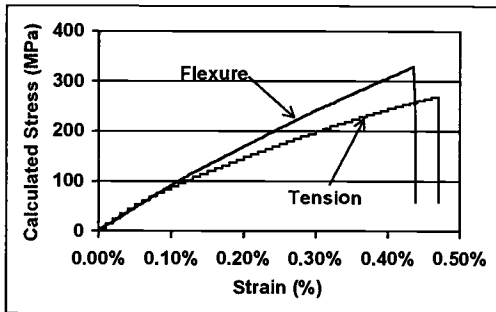


Figure 8 – Representative stress-strain curves in flexure and tension (Sylramic™ S-200).

Conventional beam bending equations assume linear elastic stress-strain response and do not account for nonlinear and non-symmetrical tensile/compressive stress-strain behavior. Nonlinear, non-symmetrical behavior causes the neutral axis to shift to the compressive face in order to maintain force equilibrium. This shift produces a much different stress distribution than that assumed by the conventional beam bending relations. Buesking’s study [5] showed that CFCC flexural strengths calculated with the conventional beam bending relations are 38% to 60% greater than the measured tensile strengths of the CFCC. Those calculated differences are similar to the difference (~35%) observed between the grand means of the ultimate flexural strengths and the ultimate tensile strengths observed in this study. The results of this study on a commercial CFCC confirm the conclusion from Buesking [5] that “a computed modulus of rupture, which is based on assumptions of a linear, homogeneous material, is an incorrect measure of the composite strength.”

Table 2- Flexural results (ambient) by laboratory (Sylramic™ S-200).

Flexural Results – Sorted Mean Values											F-Value	F-Crit 95%	
Strength (MPa)	302	315	325	341	342	342	345	347	350	374	339	3.41	1.99
Coef. Variation %	9.1	7.3	9.2	13.3	6.5	5.9	12.8	14.0	8.0	8.0	10.9		
Lab Number	# 1	# 5	# 9	# 4	# 3	# 7	# 6	# 2	# 8	# 10	All		
Strain (µm/m)	4421	4530	4582	4596	4633	4741	4732	4697	4840		4640	0.32	2.07
Coef. Variation %	13.3	12.4	14.6	12.8	15.5	13.8	20.6	7.1	12.9		13.6		
Lab Number	# 2	# 3	# 9	# 5	# 8	# 6	# 1	# 10	# 7		All		
Modulus (GPa)	84.7	88.5	89.8	90.9	91.2	95.7	97.0	98.1	101.4		93.0	16.82	2.05
Coef. Variation %	6.0	4.0	3.7	2.3	5.2	3.5	3.2	6.6	3.5		6.9		
Lab Number	# 9	# 2	# 1	# 5	# 10	# 6	# 8	# 7	# 3		All		
Thickness (mm)	2.78	2.78	2.77	2.77	2.77	2.76	2.74	2.72	2.66	2.64	2.74	2.94	2.00
Coef. Variation %	2.5	4.5	2.0	2.9	3.9	2.9	2.1	3.4	2.8	2.2	2.9%		
Lab Number	#6	#2	#9	#5	#1	#8	#4	#3	#7	#10	All		
Width (mm)	9.02	9.02	9.01	9.01	9.00	8.99	8.99	8.99	8.94	8.91	8.99	8.06	1.99
Coef. Variation %	0.2	0.3	0.3	1.1	0.2	0.3	0.3	0.4	0.3	0.5	0.6%		
Lab Number	#5	#4	#1	#7	#9	#6	#2	#8	#3	#10	All		

Variations in Procedures for Flexure Tests

Table 2 lists the means for the flexural results for the laboratories in increasing order. Means for dimensions are listed in decreasing order. There is a 23% difference between the greatest and least mean values for ultimate flexural strength. An analysis of variation (ANOVA) at the 95% confidence level shows that there is a statistically significant difference in mean ultimate flexural strength among the ten sets of results. If a second ANOVA is conducted, excluding the low and high value data from Laboratory Numbers 1 and 10, the F-value and F-Crit (95%) are 1.18 and 2.13, respectively. This shows that, with the exclusion of the least and greatest strength result sets, the mean strength values for the remaining eight laboratories are equivalent, based on a 95% null hypothesis.

The range for the means for the strain at ultimate flexural strength is less with a 10% difference between the maximum and minimum values. The ANOVA shows that the means for the ten sets of results for strain at ultimate flexural strength are statistically equivalent.

For the elastic modulus values, the range for the means of the elastic modulus in flexure is 20% between maximum and minimum values. The ANOVA of the elastic modulus results shows that the mean values for elastic modulus are not equivalent across the ten sets of results.

It was determined that different laboratories used different tools for measuring the thickness: knife edge calipers, flat anvil micrometers, and ball micrometers. These different methods gave different average thicknesses for the flexure test specimens in each laboratory. The equations for ultimate flexural strength in C 1341 use the thickness value to the inverse second power. The equations for elastic modulus for flexure in C 1341 uses the thickness value to the inverse third power. Any significant variations in thickness

Table 3 – Variations between laboratories in flexure test procedures.

Statistical Effect (t-test at 95% Confidence)	Ultimate Flexural Strength	Strain at Ultimate Flexural Strength	Elastic Modulus in Flexure
<u>Cross-Head Rate</u> -- 1 laboratory tested at 0.004 mm/s versus 0.10 mm/s for the 9 other laboratories	None	None	9% effect
<u>Drive Mechanism</u> -- 8 laboratories used screw drive machines; 2 laboratories used hydraulic systems.	None	None	3% effect
<u>Articulated Test Fixtures</u> -- 2 laboratories used fully articulated fixtures; 8 used semi-articulated.	None	None	None
<u>Fixed rollers</u> --1 laboratory used fixed, non-rolling rollers.	None	None	None
<u>Center Point Deflection (CPD) Measurement</u> --5 laboratories measured CPD directly. 4 laboratories calculated CPD from cross-head deflection, using deflection equations.	None	None	5% effect
<u>Measured humidity</u> -- From 21% RH to 62% RH.	None	None	None
<u>Preload</u> -- 4 laboratories preloaded the test specimens, using loads of 5, 20, and 30 N (Breaking loads = 300 N)	None	None	None

would have a magnified effect on the calculations of ultimate flexural strength and elastic modulus in flexure. The fact that Laboratory Number 10 has the greatest ultimate flexural strength values and also reported the smallest thickness value illustrates this thickness measurement effect. The thickness measurement factor has a strong effect in calculations for any of the flexural properties. This factor has to be carefully considered, especially for dimensional measurements between woven surfaces.

Differences in flexure testing methods between laboratories may also produce variations in ultimate flexural strength and elastic modulus values. Among the ten laboratories, there were minor variations in test procedures in the displacement rates, the drive mechanisms, the fixturing, center-point deflection measurement, humidity, and preloading.

The statistical analysis of the effect of those differences on the measured flexural properties is summarized in the Table 3. None of the experimental variables had an effect on the observed/calculated flexural stress or strain. There was a small, but statistically significant effect, on elastic modulus from the drive mechanism and the deflection measurement method. However, the greater variation in elastic modulus values in flexure between laboratories could also depend on other experimental differences: determination of the strain values and calculation of the slope of the linear section of the load-deflection curve.

Variations in Procedures for Tensile Tests

Table 4 lists the means for tensile test results in increasing order by laboratory. Means for dimensions are listed in decreasing order. An ANOVA at the 95% confidence level was conducted on the three selected tensile properties with the F-statistics also given in Table 4. For ultimate tensile strength and strain at ultimate tensile strength, the

Table 4- Tensile results (ambient) by laboratory (Sylramic™ S-200).

Ambient Tensile Data – Ranked Mean Values											F-Value	F-Crit 95%
Strength (MPa)	244	246	247	249	250	251	256	258	259	251	0.94	2.14
<i>Coef. Variation %</i>	5.4	7.9	8.0	8.3	7.1	6.1	7.2	8.3	6.2	7.2		
<i>Lab Number</i>	#2	#9	#1	#6	#3	#7	#5	#4	#8	<i>All</i>		
Strain (µm/m)	4130	4200	4240	4290	4335	4350	4372	4416	4410	4305	0.60	2.06
<i>Coef. Variation %</i>	8.2	9.8	9.4	8.3	12.2	6.2	10.2	9.0	8.3	9.1		
<i>Lab Number</i>	#2	#9	#1	#6	#4	#7	#8	#5	#3	<i>All</i>		
Modulus (GPa)	90.5	90.7	91.0	91.6	92.7	93.8	94.1	94.8	97.3	93.0	2.72	2.06
<i>Coef. Variation %</i>	5.0	3.0	3.6	3.3	6.4	6.0	4.9	3.6	3.9	5.0		
<i>Lab Number</i>	#9	#3	#6	#1	#7	#5	#2	#8	#4	<i>All</i>		
Thickness (mm)	2.81	2.80	2.80	2.78	2.77	2.77	2.77	2.76	2.70	2.70	2.22	2.06
<i>C o/ Variation %</i>	1.5	2.7	2.8	2.3	2.9	1.3	2.1	2.7	2.9	2.5		
<i>Lab Number</i>	#9	#1	#3	#5	#6	#4	#7	#2	#8	<i>All</i>		
Width (mm)	8.06	8.06	8.05	8.04	8.02	8.02	8.00	7.97	7.84	8.01	16.4	2.06
<i>C o/ Variation %</i>	0.7	0.3	0.4	0.3	0.2	0.7	0.5	0.4	1.5	1.0		
<i>Lab Number</i>	#3	#7	#5	#8	#9	#6	#2	#1	#4	<i>All</i>		

F-values were all less than the F-crit, showing that the means among the nine laboratories were equivalent. However, for the elastic modulus results, the F-value was greater than the F-crit at the 95% confidence level. A review of the results shows that the elastic modulus results for Laboratory Number 4 are outside the 95% confidence range, compared to the other sets of results.

The ANOVA shows that the means for thickness and width, measured by each laboratory, are not equivalent. For thickness, Laboratory Number 8 is outside the 95% confidence range and for width Laboratory Number 4 is outside the 95% confidence range. The out-of-range thickness and width measurements for those two laboratories correlate with the greater values for ultimate tensile strength and elastic modulus.

The observed dimensional variations show that a key experimental parameter in the tensile tests is the accurate and precise measurement of the gage section dimensions. Any experimental variation in the dimension measurements (especially for the thinner dimension, where the percentage effect is accentuated) will have a direct effect on the calculated values for ultimate tensile strength and elastic modulus.

A second issue is whether differences in testing methods between the laboratories produce variations in tensile property measurements. Among the ten laboratories, there were minor variations in tensile test procedures in the drive mechanism, pre- and post-test bending the grip pressure, load-train coupler, extensometer gage length, and humidity.

Table 5 shows the results of statistical analyses of the effects of different test procedures on the tensile results. No significant effects were noted, except for elastic modulus measurements. The 3% difference was statistically significant, but small in magnitude.

Table 5 -- Variations between laboratories in tensile test procedures.

Statistical Effect (t-test at 95% Confidence)	Ultimate Tensile Strength	Strain at Ultimate Tensile Strength	Elastic Modulus in Tension
<u>Drive Mechanism</u> -- 4 laboratories used screw drive machines; 5 laboratories used hydraulic systems.	None	None	3% effect
<u>Pre- and Post-Test Bending</u> -- Measured values were all less than 5%, with a low of 0.2% and a high of 4.9%	None	None	None
<u>Grip Pressure</u> -- Grip pressures ranged from 0.2 MPa to 8 MPa	None	None	None
<u>Load Train Couplers</u> -- 2 laboratories used self-aligning fixtures; 7 used rigid	None	None	None
<u>Measured humidity</u> -- From 34% RH to 62% RH.	None	None	None
<u>Extensometer Gage</u> -- 1 lab used a 12.5 mm gage length; 7 used 25-33 mm gage lengths	None	NA	NA

Variations of Material in the Flexural Test Specimens

The one hundred flexural test specimens were cut from four panels (Panel Numbers 14, 17, 18, 19). The material variations between test specimens and within sets of test specimens consisted of differences in thickness, fiber volume fraction and different lots of coated Nicalon™ fabric. The flexural test results (by panel number) are given in Table 6, along with the F-statistics from the ANOVA.

The ANOVA at the 95% confidence level of the ultimate flexural strength results indicates that for the panels, the means of ultimate flexural strength and of elastic modulus in flexure for the four panels are equivalent. The ANOVA shows that there is a statistically significant difference in the means of the strain at ultimate flexural strength for the four panels, with Panel Number 18 having a greater strain at ultimate flexural strength.

The material and geometry factors that could affect the flexural results for the test specimens and explain the variation within and between sets include: 1) variation in the fiber volume fraction between test specimens (as measured by thickness variations between panels; 2) variations in the tensile strength of the coated Nicalon™ fiber in the different panels; 3) variations in the density and residual porosity between test specimens.

Table 6 -- Flexural test results by panel (Sylramic™ S-200).

	Panel Number 14	Panel Number 17	Panel Number 18	Panel Number 19	All	F-Value	F-Crit (95%)
<i>Test Specimen Count by Panel</i>	10	20	42	27	99		
<i>Mean of Strength (MPa)</i>	334	329	350	331	339	2.48	2.70
<i>Coef. Variation Strength %</i>	9.5	10.2	11.5	9.8	10.9		
<i>Mean of Strain (µm/m)</i>	4590	4360	5000	4320	4640	9.49	2.71
<i>Coef. Variation Strain %</i>	6.4	11.6	14.3	7.3	13.6		
<i>Mean of Elastic Modulus(GPa)</i>	88	94	94	92	93	2.64	2.71
<i>Coef. Var. Elastic Modulus %</i>	3.6	6.7	7.1	6.7	6.9		

Table 7 – Tensile strength of coated Nicalon™ fibers and ultimate flexural strengths.

Coating Lot Number	8-97-4-4	8-97-4-5	8-97-5-2	
Coated Fiber Tensile Strength (Mean - Maximum, Minimum) (GPa)	1.83 -- 2.78, 1.00	2.11 -- 2.83, 1.36	1.99 -- 2.83, 1.33	
Mean of Ultimate Flexural Strength by Panel (MPa)	Panel Number 14 - 334	Panel Number 17 - 328.7	Panel Number 18 - 350.4	Panel Number 19 330.6

The manufacturer of the test material reported that although all the panels for the flexural test specimen had been fabricated from the same lot of Nicalon™ fabric, the fabric had been coated in three different processing runs giving different fiber strengths, as shown in Table 7. The large variation in fiber tensile strength is an obvious explanation for the observed variation in flexural test results. Unfortunately, there are no fiber tensile strength results that can be related to the ultimate flexural strengths of individual flexural test specimen to establish an experimental correlation.

An average thickness was determined for each flexural test specimen based on the measurement of thickness at three points. The mean thickness for each set of flexural test specimens is given in Table 8, along with the coefficient of variation.

Flexural test specimens from Panel Number 17 were somewhat thicker (4.3%) than the grand mean of all the test specimens, while flexural test specimens from Panel Number 18 were somewhat (2.2%) thinner. Two comparisons of the thickness results did show that the differences in thickness for Panel Numbers 17 and 18 were statistically significant.

Figure 9 shows a plot of the ultimate flexural strength versus the mean thickness of each panel for that set of flexural test specimens. The plot includes a least squares linear regression trend line through the entire data with the correlation factor squared (R^2) shown.

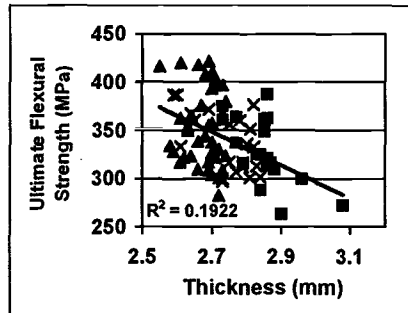


Figure 9 --Ultimate flexural strength vs. thickness (Sylramic™ S-200).

For the ultimate flexural strength in Figure 9, there appears to be decrease in strength with increasing thickness, which is logical, because an increase in thickness decreases the fiber volume fraction.

However, the correlation factor squared (R^2) has a value of 0.1922 between the ultimate flexural strength and the test specimen thickness which indicates a much greater portion of (>80%) of the correlation line is due to unaccountable events and only about 20% of this correlation is described by this line.

Table 8 -- Thickness results summary for flexural test specimens (Sylramic™ S-200).

	Panel Number 14	Panel Number 17	Panel Number 18	Panel Number 19	All
Test Specimen Count	9	19	38	24	90
Mean Thickness (mm)	2.74	2.85	2.67	2.74	2.73
Coef. of Variation	1.7%	2.8%	1.8%	2.9%	3.4%

Analysis of results for strain at ultimate flexural strength and elastic modulus in flexure as functions of the mean measured thickness shows the same low correlation factors squared with no strong effect of thickness on the observed results. The main conclusion is that fiber volume fraction (as determined by a fixed number of plies in various thickness flexural test specimen) does not correlate closely with the observed variability in flexural test results.

Variations in Material for Tensile Test Specimens

The ninety tensile test specimens were cut from three panels, designated as Panel Numbers 12, 14, and 16. The manufacturer used the same materials and procedures to lay up, laminate, and densify the three panels, as described in the materials section. Ideally, all the tensile test specimens should have the same architecture, thickness, and orientation. The tensile test results (by panel number) are given in Table 9. By inspection of Table 9, it is obvious that the panels do not have equivalent values for ultimate tensile strength, strain at ultimate tensile strength or elastic modulus in tension. Panel Number 16 has significantly greater ultimate tensile strength and strain at ultimate tensile strength than Panel Numbers 12 and 14. There is much less difference in results by panel for the elastic modulus.

However, statistically there is a slight difference with Panel Number 12 having a slightly less mean elastic modulus (91 GPa) compared to the mean values for the other two panels. The possible sources for the observed differences in tensile test results for the panels are:

- Variation in the tensile strength of the coated Nicalon™ fiber in the different panels.
- Variation in the fiber volume fraction between tensile test specimens (as measured by thickness variations between panels.).
- Variations in the bulk density and porosity between tensile test specimens.

The manufacturer of the test material reported that although all the panels had been fabricated from the same lot of Nicalon™ fabric, the fabric had been coated in three separate coating runs. Single fiber tensile tests had been conducted on the coated fibers and the calculated fiber tensile strengths for the three sets of coated fibers are given in Table 10.

Table 9 -- Tensile test results by panel (Sylramic™ S-200).

Data	Panel Number 12	Panel Number 14	Panel Number 16	All	F-Value	F-Crit (95%)
<i>Test Specimen Count from Panel</i>	31	28	31	90		
<i>Mean Tensile Strength (MPa)</i>	239	243	270	250	55.56	3.10
<i>Coef. Variation %</i>	3.3	6.1	4.3			
<i>Mean Strain (µm/m)</i>	4120	4080	4690	4300	41.81	3.10
<i>Coef. Variation %</i>	5.2	6.7	7.4			
<i>Mean Elastic Modulus(GPa)</i>	91	94	94	93	4.27	3.10
<i>Coef. Variation %</i>	5.3	4.9	4.2			

Table 10 -- *Tensile strength of coated Nicalon™ fibers and ultimate tensile strengths*

<i>Fiber Properties</i>	<i>Panel Number 12</i>	<i>Panel Number 14</i>	<i>Panel Number 16</i>
Coating Run Number --	8-97-4-4	8-97-4-5	8-97-5-2
Original Fiber Tensile Strength (Mean – Max , Min) (GPa)	2.38 -- 2.83,1.74	2.50 -- 3.22,1.98	2.43 -- 3.05,1.54
Coated Fiber Tensile Strength (Mean -- Max , Min) (GPa)	1.83 -- 2.78,1.00	2.11 -- 2.83,1.36	1.99 -- 2.83,1.33
<i>Composite Properties</i>			
Mean - Ultimate Tensile Strength (MPa)	239	243	270
Mean - Strain at Ultimate Tensile Strength ($\mu\text{m/m}$)	4120	4080	4690
Mean - Elastic Modulus in Tension (GPa)	91	94	94

The results show that, after the proprietary coating process, there is about a 20% decrease in the mean tensile strength of the Nicalon™ fibers, from approximately 2.5 GPa before coating to approximately 2.0 GPa after coating. There also appears to be greater variability in the tensile strength of the coated Nicalon™.

If the means of the ultimate tensile strength, strain at ultimate tensile strength, and elastic modulus for the three panels are cross-compared to the mean tensile strength of the coated lots of Nicalon™ fibers in the different panels, there does not appear to be a strong correlation between the mean fiber tensile strength and the tensile test results. However, with the large amount of scatter in the results and the limited statistical information on the fiber tensile strengths, it is not valid to draw absolute conclusions about the effect of fiber tensile strength from this limited set of information.

The mean thickness values for the tensile test specimens from each panel are shown in Table 11. It is obvious that test specimens from Panel 12 are significantly thicker (4.4%) than the test specimens from the other two panel sets, as confirmed by the ANOVA F-statistics. The question then become whether the differences in thickness can be related to differences between panels in ultimate tensile strength, strain at ultimate tensile strength, and elastic modulus.

Figure 10 plots the ultimate tensile strength results versus the thickness for the three panels and includes a least squares linear regression trend line for each set of results. It is apparent that the tensile test specimens from Panel Number 16 have the greatest ultimate tensile strength. However, ultimate tensile strengths do not vary with increasing thickness (which would decrease the fiber volume fraction).

Table 11 -- *Thickness results summary for tensile test specimens (Sylramic™ S-200)..*

	Panel Number 12	Panel Number 14	Panel Number 16	All	F-Value	F-Crit(95%)
Test Specimen Count	31	28	31	90		
Mean Thickness (mm)	2.85	2.73	2.74	2.77	55.9	3.10
Coef. of Variation for Mean	1.8%	1.9%	1.4%	2.5%		

Tensile test specimens from Panel Number 14 have distinctly less ultimate tensile strengths compared to those from Panel Number 16, even though thickness values are similar. Ultimate tensile strengths from Panel Number 14 are equivalent to the strengths from the Panel Number 12, which are thicker and have a lower fiber volume fraction. Least squares, linear regression trend lines for Panel Numbers 12 and 14 have negative slopes, but the correlation factor squared (R^2) is low enough that a strong correlation cannot be confirmed. It appears that the fiber volume fraction is not a dominant factor for these three sets of tensile test specimens from the three panels.

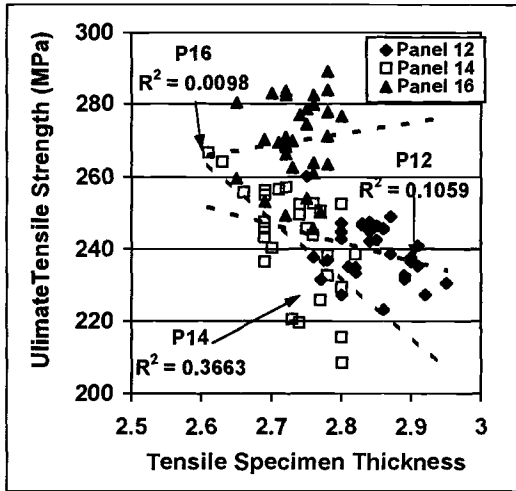


Figure 10 – Ultimate Tensile strength vs. thickness (Sylramic™ S-200).

Similar analyses of the effect of thickness on the strain at ultimate tensile strength and the elastic modulus show no significant effect of the thickness and/or fiber volume fraction (within the range of this study and this material on the strain at ultimate tensile strength and the elastic modulus).

The densities of all the finished the tensile test specimens were measured by the manufacturer of the material by Archimedes method, producing a bulk density and a percentage open porosity for each test specimen. The mean, standard deviation, and maximum and minimum values for the bulk density by Archimedes method are given in Table 12. The coefficients of variation for the three sets of results are very “tight,” less than 0.3%.

If the ultimate tensile strength values are plotted (Figure 11) against the bulk density, there is a flat trend for all three set of results for the three panels: the ultimate tensile strength has no significant dependence on the measured bulk density. The tensile test specimens from Panel Number 16 have a greater ultimate tensile strength, although there is no significant effect of bulk density. Correlation coefficients squared are all less than 0.05. Similar analyses of bulk density effects on strain at ultimate tensile strength and elastic modulus also show no significant effect.

Table 12 – Archimedes method for density on tensile test specimens(Sylramic™ S-200)

	Bulk Density (g/cm ³)				Percent Open Porosity			
	Panel 12	Panel 14	Panel 16	All	Panel 12	Panel 14	Panel 16	All
Mean	2.19	2.20	2.21	2.20	2.36	2.83	2.91	2.71
CoV	0.2%	0.3%	0.3%	0.5%	33%	34%	39%	37%
Max	2.19	2.21	2.22	2.22	4.94	4.86	4.96	4.96
Min	2.18	2.19	2.19	2.18	1.28	1.18	1.03	1.03

In the final analysis of these results, bulk density has no observable effect on the selected tensile test properties, such as ultimate tensile strength as shown in Figure 11.

The next material variable considered was open porosity. The mean measured open porosity for all the tensile test specimens was 2.7%, as shown in Table 12. The coefficients of variation for these porosity sets are much greater (30-40%) than the variation in densities. An ANOVA of the open porosity results shows a statistical difference among the means for the three sets of results from the three panels. Tensile test specimens from Panel Number 12 have less open porosity than the tensile test specimens from Panel Numbers 14 and 16.

The ultimate tensile strength results for the three sets of results from the three panels are plotted against the measured open porosity in Figure 12. As was observed in the plots for thickness and density (Figures 10 and 11), the correlation coefficients squared are less than 0.15 for all three data sets. It is apparent that open porosity is not a major controlling factor for the ultimate tensile strength. The strain at ultimate tensile strength and elastic modulus follow similar patterns with little correlation to porosity.

Conclusions

1. Based on the results from the two round-robin studies, the mean and coefficient of variation for the ultimate strength, strain at ultimate strength and elastic modulus for flexure and tension tests of Sylramic™ S-200 under ambient conditions are given in Table 13.
2. In the linear elastic region of the stress-strain curve, the flexural response of the Sylramic™ S-200 follows the conventional beam bending

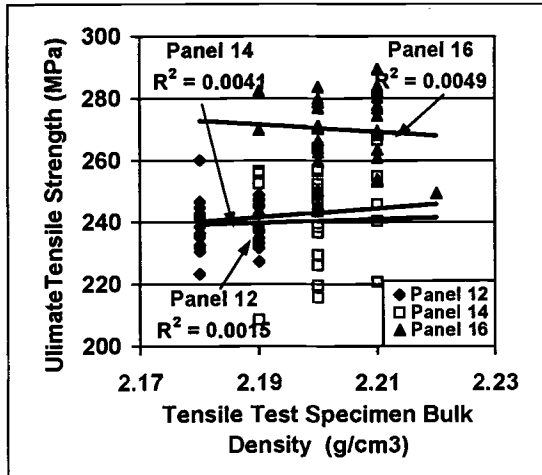


Figure 11 – Ultimate tensile strength vs. bulk density (Sylramic™ S-200).

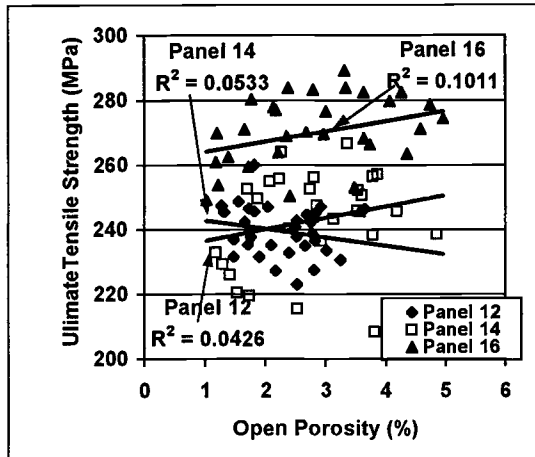


Figure 12 – Ultimate tensile strength vs. bulk density (Sylramic™ S-200)..

Table 13 – Flexural and tensile mechanical properties at ambient conditions (Sylramic™ S-200).

Property	-----Flexure-----		-----Tension-----	
	Mean	Coef.Variation	Mean	Coef.Variation
Ultimate Strength	339 MPa	10.0%	251 MPa	7.2%
Strain at Ultimate Strength	4640 μm/m	13.69.1%	4310 μm/m	13.6%
Elastic Modulus	93.0 GPa	6.9%	93.0 GPa	5.0%

relations for stress and strain, as shown by the equivalence of the stress-strain curves in tension and flexure and the equal values of elastic moduli. However, once the tensile stress-strain behavior of the composite becomes non-linear, the stress in the flexural test specimen **cannot** be calculated from the experimentally-measured load using conventional beam bending relations

3. The differences in the ultimate flexural strength and strain at ultimate flexural strength results from the ten labs did not correlate with variations in minor test variables (test rate, drive mechanism, articulation, roller freedom of motion, deflection measurement method, humidity, preload).
4. There were no statistically significant differences in the results for ultimate tensile strength and strain at ultimate tensile strength for the nine laboratories. For the elastic modulus in tension there was a statistically-confirmed difference, which may have been resulted from variability in the dimensional measurements between laboratories. Variations in tensile test equipment and procedures had no observable effect on the tensile properties.
5. There were distinct differences in flexural and tensile properties between test specimens cut from different panels. These differences may have resulted from variations in the tensile strength of the reinforcing fibers introduced during the coating process. However, the statistical information on fiber strengths was not available to conduct a direct correlation with the mechanical properties of the Sylramic™ S-200 test specimens.
6. Variations in fiber volume fraction, bulk density, and open porosity had little effect on the measured flexural and tensile mechanical properties. All the correlation coefficients squared were less than 0.20 for the comparisons of material characteristics to mechanical properties of the Sylramic™ S-200.

Acknowledgments

The authors thank all of the principal investigators at the participating round-robin laboratories for their generous donation of time and effort in conducting the flexure and tension tests.

References

- [1] Sheppard, L. M., "Enhancing Performance of Ceramic Composites," *American Ceramic Society Bulletin*, Vol. 70, No. 4, 1992, pp. 617-631.
- [2] Lewis, D., "Continuous Fiber Reinforced Ceramic Matrix Composites: A Historical Overview," *Handbook on Continuous Fiber-Reinforced Ceramic Matrix Composites*, Edited by R. L. Lehman, S. K. El-Rahaiby, J. B. Wachtman Jr., Purdue Research Foundation, West Lafayette, IN, 1995, pp. 1-34.
- [3] Richlen, S. "Applications of Fiber-Reinforced Ceramic Matrix Composites," *Handbook on Continuous Fiber-Reinforced Ceramic Matrix Composites*, Edited by R. L. Lehman, S. K. El-Rahaiby, J. B. Wachtman Jr., Purdue Research Foundation, West Lafayette, IN, 1995, pp. 495-526.
- [4] Cranmer, D. "Test Methods for Ceramic Matrix Composites," in *Handbook on Continuous Fiber-Reinforced Ceramic Matrix Composites*, Edited by R. L. Lehman, S. K. El-Rahaiby, J. B. Wachtman Jr., Purdue Research Foundation, West Lafayette, IN, 1995, pp. 325-354.
- [5] Buesking, K. and Barnett, T. "Nonlinear Flexure Behavior of High Temperature Composites," *High Performance Composites for the 1990's*, Edited by S. K. Das, C. P. Ballard, and F. Mariker, The TMS Society, Warrendale, PA, 1991, pp. 283-293.

Test Results/Methods Related to Design Implications

Edgar Lara-Curzio¹

Stress-Rupture, Overstressing, and a New Methodology to Assess the High-Temperature Durability and Reliability of CFCCs

Reference: Lara-Curzio, E., “Stress-Rupture, Overstressing, and a New Methodology to Assess the High-Temperature Durability and Reliability of CFCCs,” *Mechanical, Thermal and Environmental Testing and Performance of Ceramic Composites and Components, ASTM STP 1392*, M. G. Jenkins, E. Lara-Curzio, and S. T. Gonczy, Eds., American Society for Testing and Materials, West Conshohocken, PA, 2000.

Abstract: A testing methodology is proposed to assess the durability and reliability of non-oxide continuous fiber-reinforced ceramic composites for high temperature applications. The strategy is based on determining the reliability of these materials when subjected to random loading schedules consisting of mechanical load and temperature spikes that are superimposed upon otherwise constant stress and temperature values. The frequency and magnitude of the mechanical load and temperature spikes would be representative of the number and characteristics of the transients that are associated with a particular industrial application and that are expected to occur over the life of the component. The effect of overstressing on the stress-rupture behavior of a ceramic grade (CG) Nicalon™ fiber-reinforced silicon carbide (SiC) matrix composite was investigated and results are presented from tests conducted in ambient air at 950°C.

Keywords: ceramic-matrix composites, durability, reliability, high temperature, stress-rupture, overstressing, testing.

Introduction

The development of continuous fiber-reinforced ceramic-matrix composites (CFCCs) has been driven by the expectation of substantial economic and environmental benefits if these materials are used in aerospace and energy-related industrial applications [1]. Many of the potential applications for CFCC components are characterized by long service lives that are measured in tens of thousands of hours, and service conditions that involve elevated temperatures and aggressive environments. Some of these applications include filters and heat-exchangers for coal-fired power plants and combustor liners for gas turbine engines [1].

As the development of non-oxide CFCCs nears maturation, a need has risen for databases containing information on their long-term thermomechanical behavior and methodologies for design and life prediction. The distinct behavior of these materials

¹ Group leader, Mechanical Characterization and Analysis Group, Oak Ridge National Laboratory, P. O. Box 2008, Oak Ridge, TN, 37831-6069.

when stressed beyond the so-called matrix cracking stress poses challenging questions as to the best way of evaluating these materials for purposes of generating long-term thermomechanical data bases and validation of life-prediction methodologies. Figure 1 is a typical tensile stress-strain curve for a two-dimensional (2-D) CFCC obtained by monotonically loading/unloading the test specimen to/from increasingly larger stress levels after each cycle. The proportional limit stress (σ_{pl}) is associated with the onset of nonlinear stress-strain behavior and with the formation of hysteresis loops that result from matrix cracking and frictional sliding of the fibers bridging those matrix cracks. In the absence of fibers and fiber coatings that are environmentally stable in oxidizing environments, the proportional limit stress has long been considered the maximum allowable design stress for non-oxide CFCCs in applications involving oxidizing environments at elevated temperatures.

Traditionally, the durability and long-term reliability of candidate materials for elevated temperature applications for which service stresses and temperatures are more or less constant, is determined through stress-rupture tests. These tests are often carried out at temperatures and stresses that bracket the expected service conditions. In general terms, stress-rupture testing consists in determining the time necessary for a test specimen to fail when subjected to a constant mechanical load. However, experience demonstrates that even in applications in which the design stresses and temperatures are supposed to be constant, components invariably will be subjected to thermal and mechanical excursions outside the design conditions. In the case of non-oxide CFCCs, even if the constant service/design stress is less than the proportional limit stress, thermal and mechanical excursions could result in overstressing the material beyond the proportional limit stress, even if for short periods of time. Such occurrences would result in the formation of matrix cracks that could serve as avenues for the ingress of the environment to the interior of the composite.

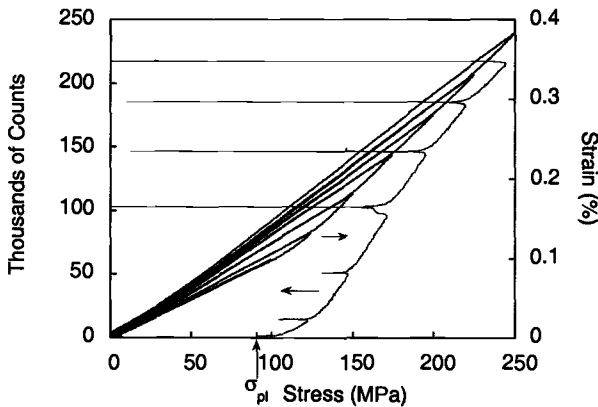


Figure 1 - Stress-strain-acoustic emission count plot obtained during the tensile loading/unloading evaluation of a 2-D CFCC. Each loading/unloading cycle was obtained at an increasingly larger stress level. Note that the proportional limit stress coincides with the onset of nonlinear behavior, acoustic emission activity and formation of hysteresis loops [2].

Depending on the nature of the environment, the temperature, the magnitude of overstressing and the ability of the matrix (or lack of) to heal cracks, overstressing could lead to the failure of the composite. Figure 2 shows a plot of stress versus time obtained from the stress-rupture evaluation of CG-Nicalon™/SiC 2-D CFCC in air at temperatures between 600°C and 1000°C. In the absence of substantial creep deformation this composite exhibits endurance at stresses less than the matrix cracking stress [3], while at stresses greater than the matrix cracking stress the strength of this material decreases with time as

$$\sigma \approx t^{-0.25} \tag{1}$$

where σ is the strength and t is time.

Based on these results it appears that for non-oxide CFCCs the application of test methodologies based on traditional stress-rupture testing at stresses greater than the proportional limit stress will result in conservative life data, whereas stress-rupture testing at stresses less than this stress level will yield overly unrealistic results. To overcome these limitations a new methodology based on random overstressing is proposed. The principle of this methodology is to simulate and assess the effects of transients that are characteristic of a specific application and that may subject CFCCs to stresses beyond the proportional limit stress, on their durability and reliability. In the next sections this testing methodology is described and a prelude of its demonstration is presented by evaluating the effect of systematic overstressing on the stress-rupture behavior of a CG-Nicalon™ fiber-reinforced SiC CFCC in ambient air at 950°C.

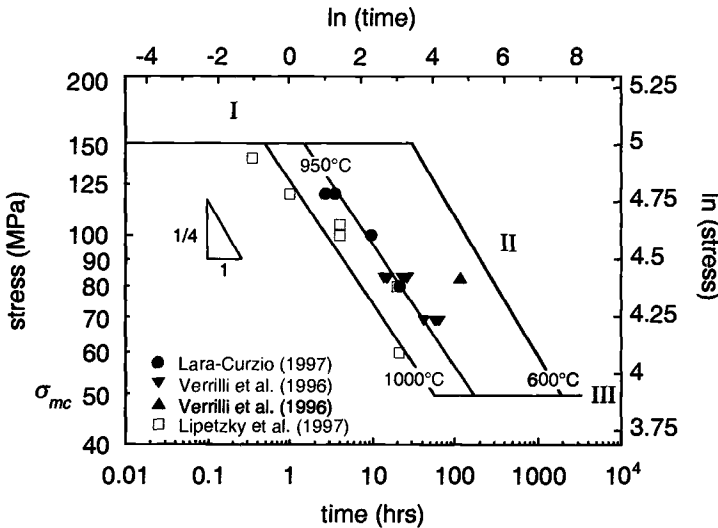


Figure 2 - Stress-rupture behavior of CG-Nicalon™/SiC in air at various temperatures. □ (1000°C). ●, ▼ (950°C). ▲ (600°C). Lines correspond to model predictions [4].

Methodology

The main idea behind the methodology described in this paper is to generate reliability data for a CFCC when it is subjected to a loading schedule that is representative of the industrial application for which it is being considered. Figure 3 is a schematic representation of such a schedule. The schematic in Figure 3 shows the thermal and mechanical histories of a hypothetical application. Both histories include overstressing conditions which are simulated by the application of mechanical load and temperature "spikes". These spikes are superimposed onto otherwise flat profiles of stress and temperature (design stress and temperature). The magnitude and occurrence of these spikes would be representative of the transients associated with that particular application, but in this methodology these "spikes" would be applied randomly. For example, in reference to Figure 3, in the case of a component in a gas turbine engine, stress and temperature spikes would be representative of the deviations from the design stress and temperature during (a) start ups, (b) shut downs and flame outs, (c) foreign object impact, etc. The magnitude of the spikes would be estimated from thermal and stress calculations associated with these events, whereas their occurrence would be random but related to the total number of these incidents that occur over the life of the component. Knowledge about the nature, characteristics and frequency of occurrence of these events should be readily available from operating histories of the specific components and application. Also in Figure 3 there is an example of the stress and thermal histories associated with the operation of a filter in coal-combustion or coal-gasification power plants. In this case, in addition to the steady state operating conditions of stress and temperature, the filters are also subjected to transients associated with the operation of the plant that include periodic backpulse cleaning which is represented by the cyclic changes (d) in stress and temperature in Figure 3.

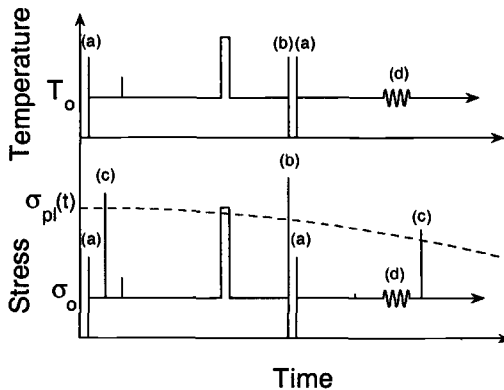


Figure 3 - Schematic representation of conceptual thermal and mechanical random loading schedules for conducting modified stress-rupture tests. The proportional limit stress σ_{pl} (depicted by the dashed line) can decrease with time because of environmental effects or redistribution of internal stresses.

Another consideration when using certain non-oxide CFCCs in these applications is the fact that the proportional limit stress may change with time as a result of environmental degradation or from redistribution of internal stresses in the composite [5-6]. This has been represented in Figure 3 as a decreasing proportional limit stress with time.

As a prelude to the evaluation of this proposed new methodology, the effect of the systematic application of mechanical spikes superimposed on a constant stress, on the life of a non-oxide CFCC was investigated. The objective of this investigation was to validate the premise that the application of spikes would shorten the life of a composite but that the obtained life would be longer than that of a test specimen subjected to a constant stress of magnitude similar to that of the spikes. In the next sections a preliminary evaluation of the proposed methodology is presented.

Experimental

The material used in this study consisted of CG-Nicalon™ [0/90] plain weave fabric, coated with a 0.1 μm -thick layer of pyrocarbon prior to matrix densification. The SiC matrix was densified by chemical vapor infiltration (CVI) and contained an enhancement of proprietary composition². The total volume fraction of fibers was 40%. The tensile test specimens had a reduced gauge section and an outer seal coating of SiC that was applied by chemical vapor deposition (CVD) after the test specimens had been machined. The width of the gauge section contained 3 wavelengths of the fabric weave pattern. Figure 4 shows a schematic of the tensile specimen.

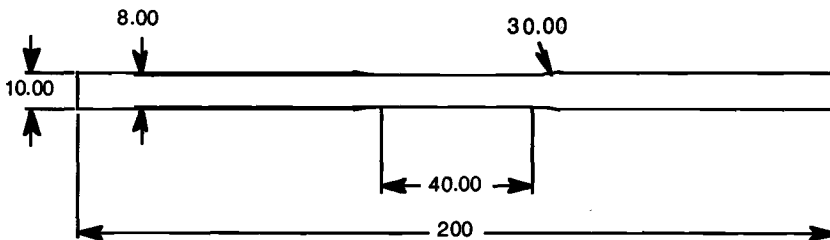


Figure 4 - Schematic of tensile specimen used in study. Dimensions in mm.

Tensile stress-rupture tests were conducted per ASTM Test Method for Creep and Creep Rupture of Continuous Fiber-Reinforced Ceramic Composites Under Tensile Loading at Elevated Temperatures, C 1337, in ambient air (24 to 40 % relative humidity) using an electromechanical testing machine equipped with hydraulically-actuated grips. The test specimen deformation was monitored over a uniformly-heated 25-mm long gauge length using a low-contact force capacitance extensometer. The alignment of the load train was verified prior to each test using a strain gauged metallic test specimen per

² Honeywell Composites Inc., Newark, DE 19740

ASTM Test Method for Monotonic Tensile Strength Testing of Continuous Fiber-Reinforced Advanced Ceramics with Solid Rectangular Cross-Sections at Ambient Temperatures, C1275. The grip wedges were water-cooled to preserve the adhesively bonded aluminum end-tabs that were used to minimize damage of the test specimen during gripping. The test specimens were heated at a constant rate of 20°C per minute from ambient temperature to the test temperature of 950°C using a compact resistance-heated furnace. This was followed by a 20 minute "soaking" period at which point the test specimens were mechanically stressed at a constant rate of 5 MPa per second up to the test stress of 80 MPa. Then stress spikes were applied, superimposed to the constant stress level of 80 MPa, at a rate of 10 MPa per second. The tests were complete when the specimens failed. The results were compared with existing stress-rupture data for the same material at stresses of 80, 100 and 120 MPa.

Results and Discussion

Figure 5 shows the strain histories of stress-rupture tests conducted at constant stress levels of 80, 100 and 120 MPa. The resulting strain vs. time curves indicate that the material became increasingly compliant with time, and that it exhibited accelerated deformation prior to failure. Both the increasing compliance and accelerated deformation prior to failure result from the progressive breakdown of the fiber bundles in the composite as detailed elsewhere [4, 7-8].

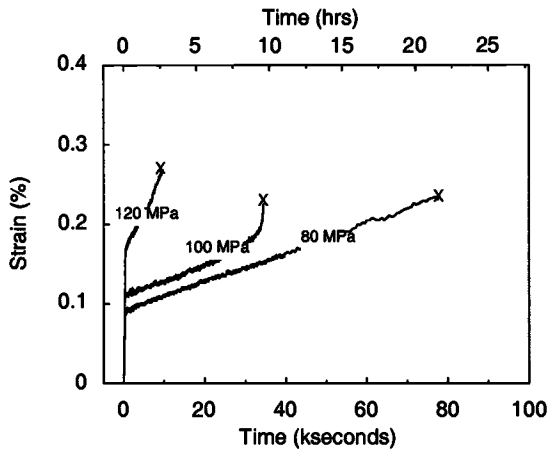


Figure 5 - Strain histories of stress-rupture tests of CG-Nicalon™/SiC conducted in ambient air at 950°C at constant stress levels of 80, 100 and 120 MPa.

In the three cases the applied stress was greater than the proportional limit stress of the material [σ] as indicated by the tensile stress vs. strain curves in Figure 6. The stress-rupture results summarized in Figures 5 and 6 were used as a base-line to evaluate the effect of overstressing on the stress-rupture behavior of the material. Evidently, when applying the proposed methodology to an actual case, it would be necessary to conduct stress-rupture tests at the design stresses (i.e. less than the matrix cracking stress at a

level at which the specimen is expected to survive for periods of time greater than the required life of the component) in order to define the baseline behavior of the material.

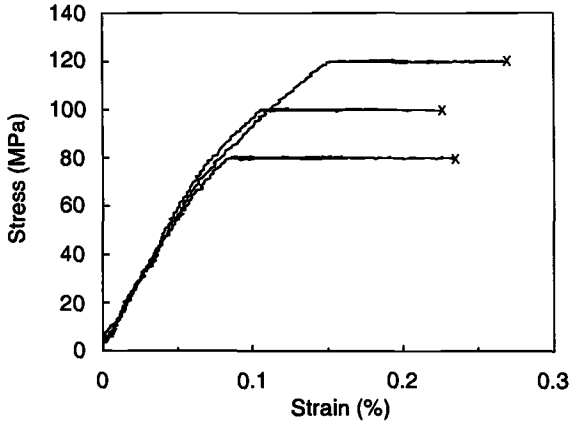


Figure 6 – Stress-strain curves associated with stress-rupture tests of CG-Nicalon™/SiC conducted in ambient air at 950°C and stress levels of 80, 100 and 120 MPa.

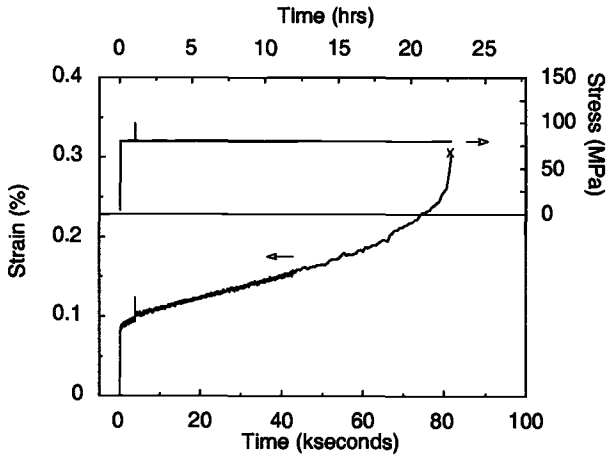


Figure 7 - Stress and strain histories for stress-rupture test at 80 MPa and one stress-spike of 20 MPa applied the first hour of the test.

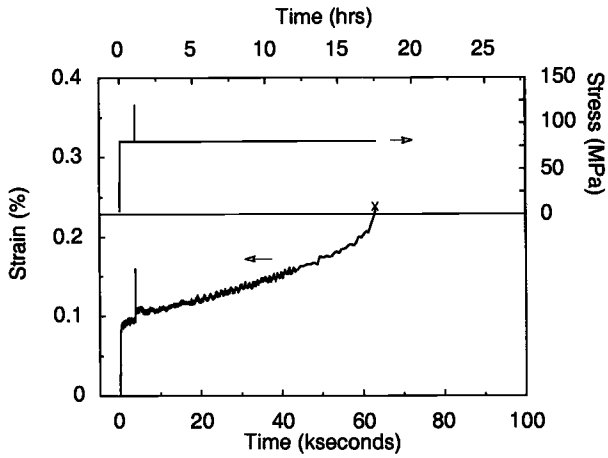


Figure 8 - Stress and strain histories for stress-rupture test at 80 MPa and one stress-spike of 40 MPa applied the first hour of the test.

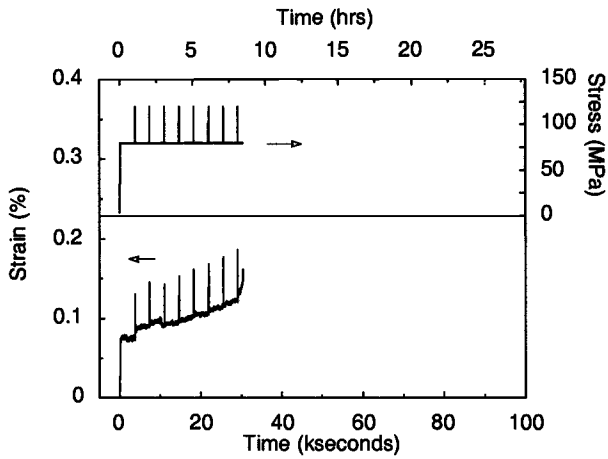


Figure 9 - Stress and strain histories for stress-rupture test at 80 MPa and several stress-spike of 40 MPa applied every hour after the first hour of the test.

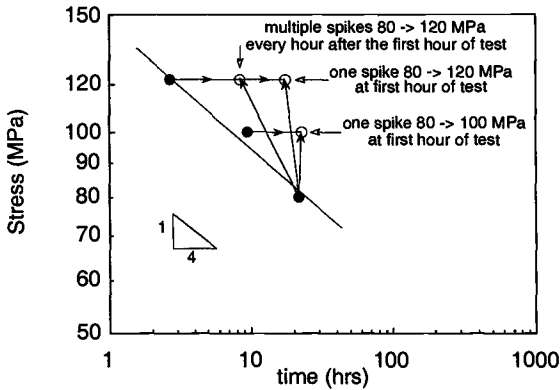


Figure 10 - Stress versus time-to-failure for stress-rupture tests at 950°C. Solid circles [7] are from regular stress-rupture tests in ambient air at 950°C. Open circles are from stress-rupture tests that included overstressing conditions.

Figure 7 shows the stress and strain histories of a stress-rupture test at 80 MPa with one spike of 20 MPa applied at the first hour of the test. The stress spike is clearly visible in the stress and strain histories. Note that qualitatively the resulting strain history is similar to those shown in Figure 5, which were obtained from regular stress-rupture tests, and that the application of a single spike of 20 MPa has little effect on the life of the material (22.7 hours vs. 21.6 hours) when not subjected to any spikes. However the application of a single stress spike of 40 MPa has a significant effect on the life of the composite. Figure 8 shows the stress and strain histories associated with a test at a constant stress of 80 MPa and one stress spike of 40 MPa applied after the first hour of the test. In this case the life of the material was reduced from 21.6 hours to 17.6 hours. Note that the resulting strain history also is similar to those obtained from regular stress-rupture tests. The effect of overstressing is even more significant when applying multiple stress spikes. Figure 9 shows the stress and strain histories of a test where stress spikes were applied every hour after the first hour of the test for the duration of the test. In this case, the specimen failed shortly after the application of the eighth stress spike and the life of the composite (8.45 hours) was less than one half of the life of the specimen subjected to a constant stress of 80 MPa. However, at the same time, it was three times longer than the life of a specimen subjected to a constant stress of 120 MPa.

The results from these tests are summarized in Figure 10 in a plot of stress versus time-to-failure. In this plot the closed circles represent the results of regular stress-rupture tests at stresses of 80, 100 and 120 MPa and correspond to the tests summarized in Figures 5 and 6. The open circles in Figure 10 correspond to stress-rupture tests that included the application of stress spikes. Note that the results of the latter tests are bound by the results of regular stress-rupture tests at 80 and 120 MPa. This observation validates the premise that this test methodology, i.e., the superposition of stress spikes onto otherwise constant stresses, provides a more realistic approach for determining the life of a non-oxide CFCC than would a series of regular stress-rupture tests. In this

exercise either one or multiple stress spikes were applied at the first hour of the test and regularly every hour afterwards. In the application of this methodology to a real case it will be necessary to evaluate test specimens subjected to random temperature and stress spikes, where the number, the characteristics and the occurrence of the transients would be specific to the industrial application of interest. The results from these tests would provide probability of failure and failure rate data necessary for the validation of life prediction and design schemes and models.

Summary

A methodology was described to assess the effect of overstressing on the reliability of CFCCs. The rationale for this methodology is based on the fact that non-oxide CFCCs exhibit distinct behavior at stresses greater than and less than the proportional limit stress, so that regular stress-rupture tests at stresses above and below the proportional limit stress yield either very conservative, or utterly unrealistic results, respectively. The methodology is based on the generation of reliability data when specimens are subjected to random thermomechanical loading histories that would be representative of the transients associated with a given application and that include overstressing events. In this paper the effect of the systematic application of overstressing events on the durability of a CG-Nicalon™/SiC CFCC was investigated. It was found that overstressing reduces the life of the material and that the amount of reduction is proportional to the magnitude and frequency of the overstressing events. It was also found that when overstressed, the life of the material is bound by the failure times when subjected to traditional stress-rupture tests at the lowest and largest stresses in the stress history. These results suggest that this methodology appears to be a realistic approach for assessing the reliability of non-oxide CFCCs at elevated temperatures.

Acknowledgments

This work was sponsored by the U.S. Department of Energy, Assistant Secretary for Energy Efficiency and Renewable Energy, Office of Industrial Technologies, Industrial Energy Efficiency Division and Continuous Fiber Ceramic Composites Program, under contract DE-AC05-00OR22725 with UT-Battelle, LLC. The author is indebted to Mr. Phil Craig of Honeywell Composites, Inc. for supplying the test specimens used in this study.

References

- [1] Karnitz, M. A., Craig, D. F. and Richlen, S. L., "Continuous Fiber Ceramic Composite Program," *Ceramic Bulletin*, Vol. 70, 1991, pp. 430-435.
- [2] Lara-Curzio, E., Ferber, M. K., Boisvert, R., and Szweda, A., "The High Temperature Tensile Fatigue Behavior of Polymer-derived Ceramic Composites," *Ceramic Engineering and Science Proceedings*, Vol. 16, No. 4, 1995, pp. 341-349.
- [3] Verrilli, M. J., Calomino, A. M., and Brewer, D. N., "Creep-Rupture Behavior of

a Nicalon™/C/SiC Composite,” in **Thermal and Mechanical Test Methods and Behavior of Continuous Fiber Ceramic Composites**, ASTM STP 1309, M. G. Jenkins, S. T. Gonczy, E. Lara-Curzio, N. E. Ashbaugh and L. P. Zawada Eds., American Society for Testing and Materials, Philadelphia, PA 1996

- [4] Lara-Curzio, E., “Analysis of Oxidation-Assisted Stress-Rupture of Continuous Fiber-Reinforced Ceramic Matrix Composites at Intermediate Temperatures,” *Composites Part A*, Vol. 30, No. 4, 1999, pp. 549-554.
- [5] Lara-Curzio, E., and Russ, C. M., “On the Matrix Cracking Stress and the Redistribution of Internal Stresses in Brittle-Matrix Composites,” *Materials Science and Engineering*, Vol. A250, 1998, pp. 270-278.
- [6] Widjaja, S., Jakus, K., Ritter, J. E., Lara-Curzio, E, Sun, E. Y., Watkins, T. R., and Brennan, J., J., “Creep-Induced Residual Stress Strengthening in Nicalon™ Fiber- Reinforced BMA Glass-Ceramic Matrix Composites,” *Journal of the American Ceramic Society*, Vol. 82, No. 3, 1999, pp. 200-210.
- [7] Lara-Curzio, E., “Stress-Rupture of Nicalon™/SiC Continuous Fiber Ceramic Composites in Air at 950°C,” *Journal of the American Ceramic Society*, Vol. 80, No. 12, 1997, pp. 3268-72.
- [8] Lara-Curzio, E., “Oxidation-Induced Stress-Rupture of Fiber Bundles,” *Journal of Engineering Materials and Technology* , vol. 120, April 1998, pp. 105-10.
- [9] Lipetzky, P., Stoloff, N. S., and Dvorak, G. J., “Atmospheric Effects on High Temperature Lifetime of Ceramic Composites,” *Ceramic Engineering and Science*, Vol. 18, No. 4, 1997, pp. 335-362.

Christian X. Campbell¹ and Michael G. Jenkins²

Use of Unload/Reload Methodologies to Investigate the Thermal Degradation of an Alumina Fiber-Reinforced Ceramic Matrix Composite

Reference: Campbell, C. X. and Jenkins, M. G., "Use of Unload/Reload Methodologies to Investigate the Thermal Degradation of an Alumina Fiber-Reinforced Ceramic Matrix Composite," *Mechanical, Thermal and Environmental Testing and Performance of Ceramic Composites and Components, ASTM STP 1392*, M. G. Jenkins, E. Lara-Curzio, and S. T. Gonczy, Eds., American Society for Testing and Materials, West Conshohocken, PA, 2000.

Abstract: Oxide fiber-reinforced/oxide matrix continuous fiber-reinforced ceramic composites (CFCCs) have the potential of resisting high-temperature degradation in the increasingly aggressive environments of the emerging applications of this still-evolving class of materials. However, a major design and processing limitation of CFCCs is the lack of information on the *in situ* properties and performance of the composite constituents (i.e., fibers, interphase, and matrix). Monotonic and unload/reload tensile tests were conducted in ambient air on CFCC test specimens in the unexposed condition and after 10- and 100-h exposures at 600, 800, 1000 and 1200°C. Two methodologies were used for the evaluation of the unload/reload tensile test results to extract constitutive property data on the residual stress state, interfacial shear stress, interfacial debond resistance, and damage state of the composite. The phenomenological approach is based on the stiffness degradation of the composite with incremental load steps. The analytical approach is based on the shape of the unload/reload hysteresis loops.

Keywords: continuous fiber ceramic composite, tension test, unload/reload, thermal exposure, hysteresis, residual stress, interfacial shear stress, fiber/matrix interphase

Introduction

A typical continuous fiber ceramic composite (CFCC) with a weak fiber/matrix interphase exhibits two independent mechanical responses that can be used to probe constitutive material properties when subjected to intermittent unload/reload cycles. One of the responses involves the evolution of damage in the composite caused by increasing the maximum loading stress of each unload/reload cycle. This incremental damage results in a decrease in the load-bearing cross-sectional area of the composite and manifests as a decrease in the elastic modulus of the composite [1]. Hysteresis loops in the tensile stress-strain curve is another response that is commonly observed in CFCCs subjected to tensile unload/reload cycles [1]. This hysteresis behavior is indicative of energy-dissipating mechanisms that are characteristic of CFCCs and evolve from fiber/matrix sliding mechanisms [1].

Two methodologies have been developed to extract constituent material properties from an unload/reload tensile test using these two material responses. The first methodology, labeled a phenomenological approach, is based on the stiffness degradation of the composite with

¹ Engineer, Siemens Westinghouse Power Corporation, 4400 Alafaya Trail, Orlando, FL 32826-2399

² Professor, University of Washington, Department of Mechanical Engineering, Box 352600, Stevens Way, Seattle, WA 98195-2600

incremental load steps [1-3]. The phenomenological approach can be applied when the damage evolution is dominated by matrix damage (i.e., there is little fiber damage) and crack closure occurs upon unloading. The phenomenological approach can be used to deduce the residual stress state and the damage state of the composite, and is unaffected by fiber/matrix interfacial properties. The second methodology, labeled an analytical approach, has been developed to relate the hysteresis behavior, thus the energy dissipation characteristics, of the CFCC to constituent material properties. Using this approach, constituent properties such as the residual stress state, interfacial shear stress, interfacial debond resistance, and compliance can be calculated by extracting secondary parameters and relationships from the shape of the hysteresis loops [4-7].

Both the phenomenological and analytical methodologies can be used to probe the effect of environmental exposure on the constituent properties of a CFCC. For example, unload/reload testing could characterize changes due to thermal exposure that arise from changes in the fiber/matrix interfacial properties, creep of the fibers, and/or damage of the matrix. Since the phenomenological and analytical methodologies are independent, each can be used as a check for the other.

Unload/reload tensile testing is a promising technique to maximize the amount of information that can be obtained from a single test. This is important for developmental materials such as CFCCs, for which it is particularly costly to create a mechanical properties database. Monotonic tensile testing is a favored test technique because it is reproducible and information rich, i.e., data such as elastic modulus, proportional limit stress, modulus of toughness, percent elongation, ultimate and fracture strengths are contained in monotonic tensile data. Unload/reload tensile testing can be performed instead of monotonic tensile testing if the tensile data obtained from an unload/reload tensile test is directly comparable to the existing database of monotonic tensile properties.

In this study, a comparison of monotonic and unload/reload tensile test data is presented for a limited number of samples of the same test material. The phenomenological and analytical methodologies for analysis of unload/reload tensile test data are presented and used to characterize the residual stress state and interfacial shear stress of the test material. A discussion ensues on the insights provided by unload/reload analysis into the effects of thermal exposure of the test material.

Test Material

The test material was a Nextel™ 610 alumina fiber-reinforced alumina composite commercially produced³ [8] in three stages: fiber preform fabrication, interphase deposition and matrix formation.

Fiber preforms were fabricated from plain-woven cloths with an eight-harness satin weave. The fiber preforms were placed in a chemical vapor infiltration (CVI) reactor to deposit a 0.2 to 0.5 μm thick boron nitride (BN) layer. A BN coating may act as a weak fiber/matrix interphase to promote fiber debonding and pullout, thereby increasing the "toughness" of the CFCC. A final 3 to 4 μm thick coating of silicon carbide (SiC) was deposited by CVI to protect the debonding layer from degradation during matrix processing.

Matrix formation occurred by the controlled growth of alumina through the fiber preform via the directed metal oxidation (DIMOX™) of a molten aluminum alloy. After matrix processing, a metal removal step was performed on the CFCC plate to reduce the residual metal content to 1-2 wt% [9]. The CFCC plates were machined into "dogbone" test specimens by diamond-grit cutting into blanks, followed by abrasive water jet (AWJ) cutting into test specimens [10].

³ Vintage 1994 DuPont Lanxide Composites, Newark, DE.

Test Procedures

The effects of elevated temperature on material properties and performance were evaluated through tensile tests at room temperature following 10-h and 100-h exposures to 600, 800, 1000 or 1200°C ambient air (i.e., exposure tests). Room temperature monotonic tensile tests were performed under displacement control at 0.003 mm/s in accordance with Standard Test Method for Monotonic Tensile Strength Testing of Continuous Fiber-Reinforced Ceramic Composites with Solid Rectangular Cross-Sections at Ambient Temperatures (ASTM C1275). No standard test method exists for unload/reload tensile tests, although a methodology has been proposed [4] and subsequently applied to various CFCCs [1,6]. Figure 1 illustrates the difference between the displacement (control) profiles and the corresponding stress-strain profiles of a monotonic and unload/reload tensile test. In the unload/reload tests of this study, displacement control at 0.003 mm/s was used for both the unload and reload sequences with force related to stress as the control limit for each sequence. Maximum stress in each sequence was increased by 8-10 MPa from the previous maximum. Minimum stress was always 0 MPa. Further details on the testing procedures are presented elsewhere [10].

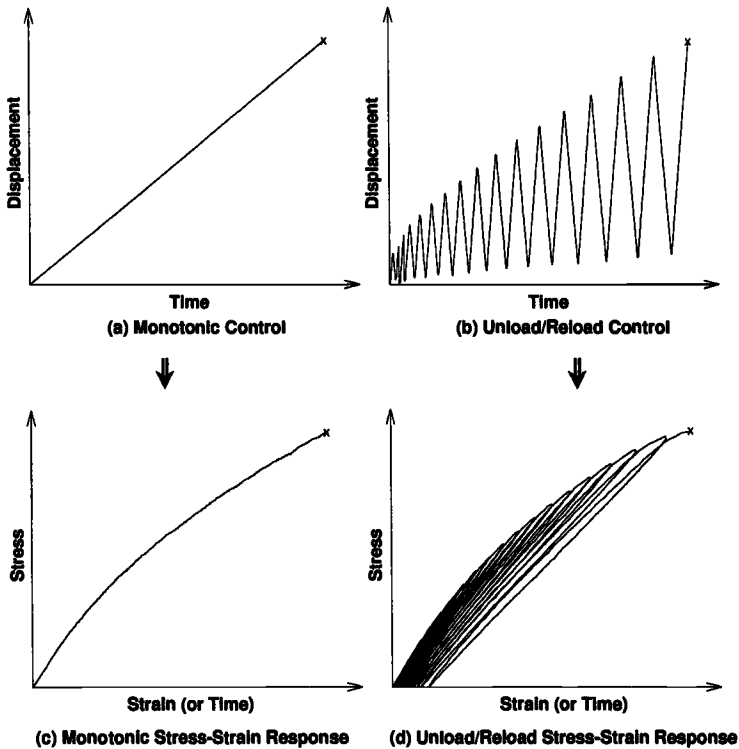


Figure 1: Illustration of the displacement vs. time profiles (control profiles) for (a) monotonic and (b) unload/reload tensile tests, and the corresponding load vs. strain (or time) profiles for (c) monotonic and (d) unload/reload tensile tests. Strain and time are nearly equivalent since the test is performed using constant displacement rate.

Monotonic and Unload/Reload Tensile Test Results

Unload/reload tensile testing is a promising test technique because of the abundance of information that can be extracted from the data, especially for composite materials such as CFCCs. To gain maximum utility from the results, material property data extracted from unload/reload tensile testing must be comparable to the existing database of material properties (i.e., from monotonic tensile testing). Thus, this study compared monotonic tensile test results with unload/reload tensile test results.

A comparison of monotonic and unload/reload stress-strain responses for unexposed test specimens is shown in Figure 2. Note that the monotonic stress-strain curve nearly follows the peaks of the hysteresis loops of the unload/reload stress strain curve. It was hypothesized that stress strain curves useful for extracting monotonic test data according to test method ASTM C1275 could be constructed from a curve fit of the peaks of the hysteresis loops. The similarity of the monotonic and unload/reload tensile data suggested that unload/reload cycling did not adversely affect the measured material properties and performance (i.e., no additional cumulative damage or stress redistribution). However, a limited number of test specimens were tested in this study, a larger study could provide a more statistically significant basis for comparing monotonic and unload/reload tensile test results.

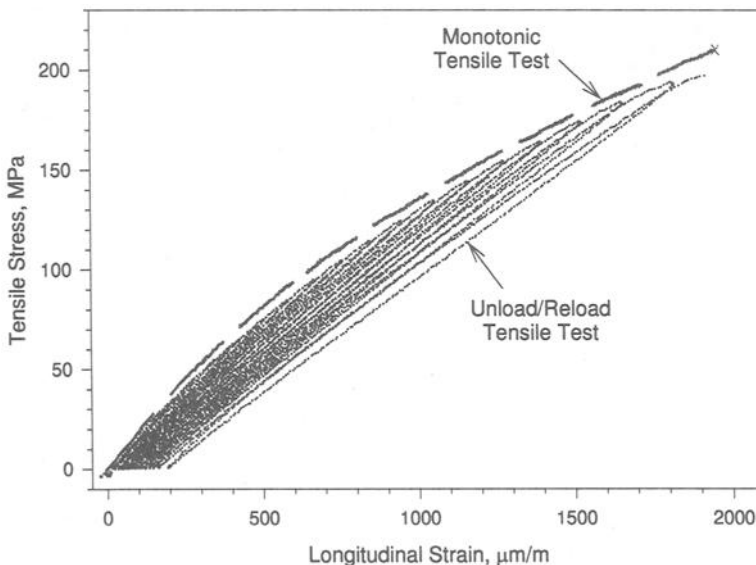


Figure 2: Comparison of monotonic and unload/reload tensile stress-strain response for unexposed test specimens.

Figure 3 shows the ultimate tensile strength and modulus of toughness plotted as functions of exposure temperature. At an exposure temperature of 600°C, the ultimate tensile strength and modulus of toughness *increased* after the 10-h exposure and *decreased* after the 100-h exposure. Likewise, the proportional limit stress remained relatively unchanged at around 55 MPa after the 10-h exposure, but nearly doubled to 105 MPa after the 100-h exposure. Analysis of the retained property data after exposure at 600°C showed that the good composite behavior was either retained or actually improved after the 10-h exposure, but that the composite was embrittled after the 100-h exposure. This indicated strongly time-dependent thermal degradation at 600°C.

In comparison, the thermal degradation mechanisms at exposure temperatures of 800 and 1000°C appear to be weakly time dependent, as observed by the proximity of the 10-h and 100-h exposure data. Figure 4 shows a Larson-Miller parameter plot of the retained ultimate tensile strength data, albeit based on a limited number of test specimens, that suggests different thermal degradation mechanisms may be at work in the different temperature regimes. The 600°C exposure data appears to be set apart from the other temperature data, and its trendline shows a large negative slope that indicates strongly time-dependent thermal degradation. The 800 and 1000°C data appears to fall on a trendline with a much smaller slope than the 600°C data, thus indicating less time-dependent thermal degradation. Thermal degradation appears to become more strongly time dependent again at 1200°C, suggesting a different degradation mechanism.

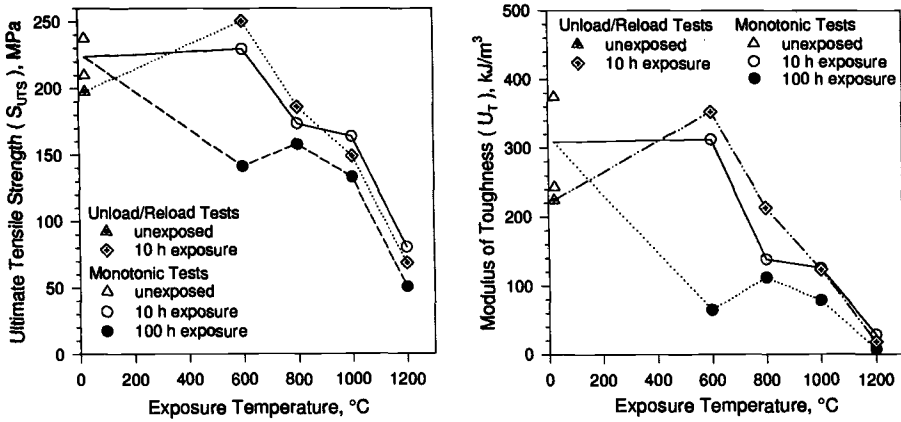


Figure 3: Measured material properties from monotonic and unload/reload tensile tests. Lines connect data points. Each data point represents a single test.

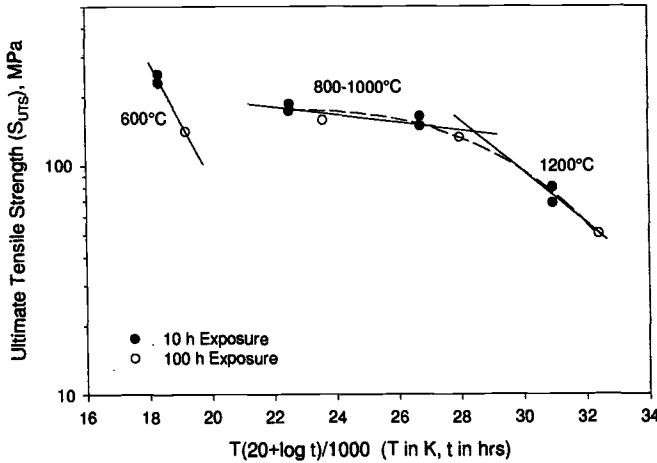


Figure 4: Larson-Miller parameter plot of the retained ultimate tensile strength data.

Phenomenological Interpretation of Unload/Reload Tensile Tests

The phenomenological approach is based upon progressive matrix damage during incremental unload/reload tensile testing, which can be related to the residual stress state of the CFCC if an inflection point does not occur upon unloading. Figure 5 shows two forms of an unload/reload hysteresis loop for a CFCC, (a) without an inflection point, and (b) with an inflection point. As described by Steen *et al.* [1,3], an inflection point can be attributed to incomplete crack closure (which is commonly caused by the presence of debris in the crack wake). If there is no inflection point and there is limited fiber failure, then the first order linear regression lines, E_a , of the *whole* hysteresis loop for individual unload/reload cycles will meet at a common intersection point [1]. Upon visual inspection of the unload/reload stress strain curves (for example, see Figure 2), it did not appear that the unload portions of the hysteresis loops contained an inflection point, thus linear fits were applied to the entire curves. Figure 6 shows that the first order linear regressions fit to selected unload/reload cycles for the test specimen exposed for 10 h at 600°C did intersect at a distinct point. Intersection points were also observed for the other unload/reload test specimens. The existence of an intersection point is evidence that cumulative damage in the CFCC during the tensile test is limited to the matrix, and that there is little fiber damage prior to final fracture [1].

For the results shown in Figure 6, the visually-determined intersection point for stress was -49.0 MPa, and the numerically-determined intersection point for stress was -49.8 ± 24.8 MPa (mean \pm standard deviation for intersections of all regression lines with each other). While the values of the intersection points from the two techniques are comparable, the scatter is large because of the near parallelism of the regression lines [1].

The magnitude of the residual stress in the composite is related to the stress coordinate of the intersection point, $\sigma_{intersect}$. The fiber residual stress is given by [1]

$$\bar{\sigma}_f^T = \sigma_{intersect} / V_{longitudinal\ fibers} \tag{1}$$

and the matrix residual stress is given by [1]

$$\bar{\sigma}_m^T = -\sigma_{intersect} / (V_{matrix} + V_{transverse\ fibers}) \tag{2}$$

where $\bar{\sigma}_f^T$ and $\bar{\sigma}_m^T$ are the residual stresses on the fibers and matrix, respectively. $V_{longitudinal\ fibers}$, $V_{transverse\ fibers}$, and V_{matrix} , are the volume fractions of the longitudinal fibers, transverse fibers, and matrix, respectively. A value of $\frac{1}{2}V_f$ was used for both $V_{longitudinal\ fibers}$ and $V_{transverse\ fibers}$ in the present analysis.

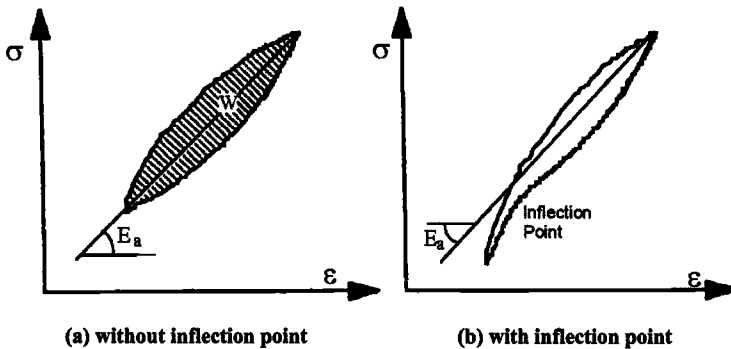


Figure 5: Schematic of a single hysteresis loop (a) without and (b) with an inflection point upon unloading [1].

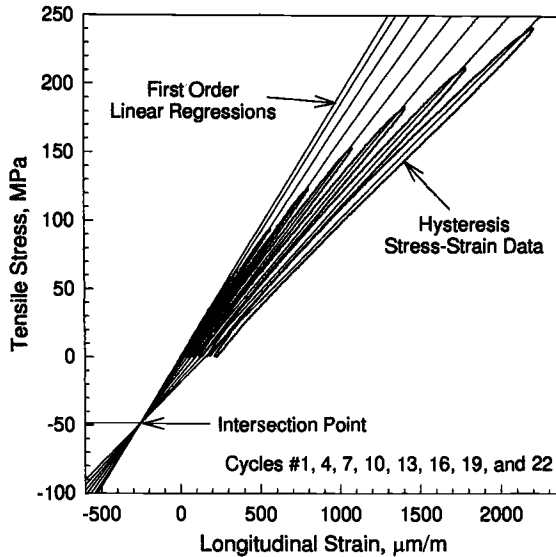


Figure 6: Application of the phenomenological approach (intersection point methodology) for the specimen exposed at 600°C for 10 h.

The basis of the phenomenological approach to unload/reload analysis was explored by Figure 7, which shows early stage and late stage hysteresis loops with their corresponding linear curve fits for one of the unload/reload tensile tests. This figure describes how the progression of matrix damage leads to a common intersection point and why this point is related to the residual stress state of the CFCC.

The state of a CFCC on the hysteresis stress-strain curve can be defined by the combination of matrix damage state and stress state. At States A and B (the zero matrix stress state), a force is placed on the composite of equal magnitude and opposite sign to the residual stress of the matrix, resulting in a net stress on the matrix of zero. Assumptions are made that the residual stress state has not changed, and there has been insignificant fiber damage between States A and B. The difference is that the matrix is undamaged at State A, but is severely cracked at State B. If this is the case, the same fibers are supporting the same compressive stress; since there is no stress on the matrix in either case, the condition of the matrix has no effect on the location of this intersection point.

States C and D represent the “resting” state of the composite (zero composite stress point). Since the composite has yet to be stressed beyond its elastic limit stress, State C represents the undamaged resting state of the composite. Note that this point is at the origin. At State D, the matrix has been damaged, thus has a reduced elastic modulus and is unable to fully support the residual stress of the fibers. The composite has a permanent strain, ϵ_0 , due to the relaxation of the residual fiber stress that is no longer supported by the matrix.

The early stage hysteresis loop (C-E) is linear elastic up to the peak stress at State E and shows very little hysteresis. The late stage hysteresis loop (D-F) shows significant hysteresis up to the peak stress at State F. Hysteresis is related to frictional sliding of the fiber/matrix interface. Since frictional sliding is reversible, a first order linear regression of the hysteresis loops remove the effect of frictional sliding. The slope that remains is indicative of the state of the matrix, and the intersection point is not dependent on the state of the fiber/matrix interface.

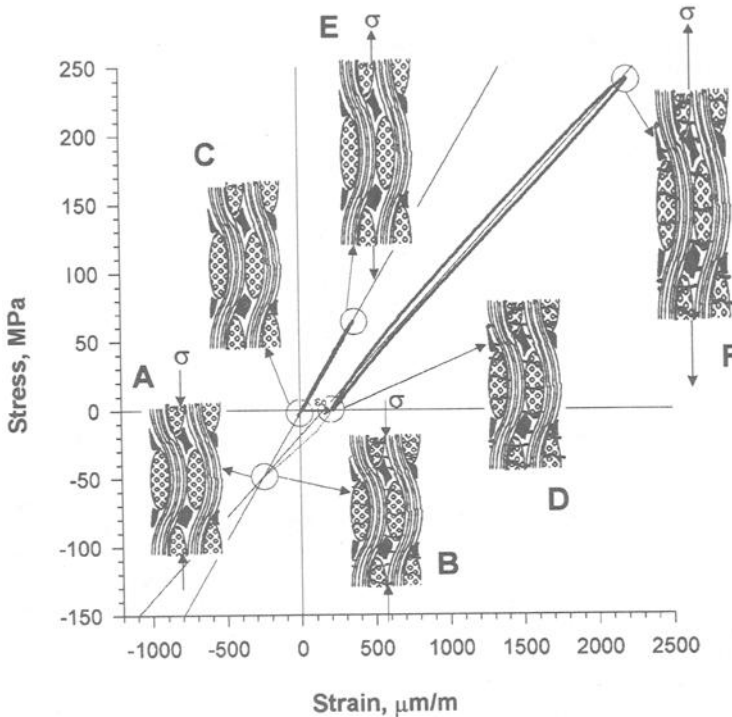


Figure 7: Relation of the intersection point to the progressive matrix damage in an unload/reload tensile test.

Analytical Interpretation of Unload/Reload Tensile Tests

While not used in the phenomenological approach described previously, the shape of a hysteresis loop contains a great deal of information about the state of a CFCC [5]. The analytical approach derives relationships between a CFCC's constitutive properties and material parameters with the shape of the unload/reload hysteresis loops.

Domergue *et al.* [7] applied the analytical method to two representative two-directionally (2D) reinforced material systems. One system was characterized as having a small debond energy (SDE), and the other was characterized as having a relatively large debond energy (LDE). The test material of the present study was considered an LDE material based on its similarity to that of the LDE material (a 2D woven Nicalon fiber-reinforced CVI silicon carbide (SiC_f/SiC)) from reference [7]. Thus, the analysis methodology developed for LDE materials was used for the present analysis, and assumptions were made using the SiC_f/SiC composite as a guideline.

The description of the analytical approach begins with a description of hysteresis loop development. Cracking usually initiates in the 90° plies along the fiber direction [7]. As the uniaxial stress increases, multiple parallel cracks form in the 90° ply and the cracks begin to penetrate the 0° ply normal to the fiber direction. Hysteresis strains develop as the matrix cracks enter the 0° ply, caused by interactions of the cracks with the fibers and the interface. Interface sliding and debonding control these interactions, which are manifested in the shape of the hysteresis loop [7]. Conversely, cracking in the 90° ply does not lead to hysteresis strains because there are no interactions between the cracks and the fiber reinforcement.

A schematic illustration showing the features of a hysteresis loop along with applicable nomenclature used in the large debond energy (LDE) methodology is presented in Figure 8. Important aspects of the analysis are summarized as follows (see Figure 8)

- The applied stress at the onset of matrix cracking in the 0° plies, thus the onset of hysteresis strain, is designated as the matrix microcracking stress (σ_{mc}).
- ϵ_0 is the permanent strain upon unloading.
- σ_p is the peak stress of the unload/reload cycle.
- The residual stiffness of the composite is E^* , and the residual compliance of the composite is $1/E^*$.
- $\delta\epsilon_{max}$ is the maximum strain (or width) of the hysteresis loop. The transition stress, σ_r , is the point where the reload (or unload) section of the stress-strain curve transitions from a parabolic to a linear curve.
- The matrix crack saturation point is denoted as σ_s .

The model shown in Figure 8 was developed for unidirectionally (UD) reinforced CFCCs, but was extended to 2D reinforced CFCCs (including woven) [4,7]. Subsequent nomenclature for non-UD CFCCs uses a bar notation⁴ (e.g., $\bar{\sigma}$ and \bar{E}).

Many of the features of an unload/reload hysteresis loop can be evaluated using a model based on the inverse tangent modulus (ITM). The ITM is the inverse of the instantaneous slope of the stress-strain curve [7]. The model was developed using relations derived by Hutchinson and Jensen [12] and Marshall [13] for fiber debonding and sliding in a model composite system. Based upon this model, the expected form of an ITM curve for the reloading portion of the hysteresis cycle is shown in Figure 9 [7].

ITM curves exhibit three principal features [7]:

1. The initial value of the ITM is a measure of the elastic compliance of the composite, $1/\bar{E}^*$ (i.e., matrix damage modulus), which is indicative of the state of matrix cracking.
2. The slope of the ITM plotted as a function of stress and designated as the interface friction index ($\bar{\xi}$), is a measure of sliding at the fiber/matrix interfaces.
3. The transition between the linear region and the plateau is indicative of an inherent resistance to interface debonding. This transition stress is the same as the parabolic to linear transition observed on the hysteresis loop.

The debond stress, $\bar{\sigma}_i$, is related to the transition stress as follows [7].

$$\bar{\sigma}_i = \bar{\sigma}_p - \frac{\bar{\sigma}_r}{2} \tag{3}$$

Four independent parameters determine the shape of a hysteresis loop. Three of the four can be obtained from experimental unload/reload data using ITM analysis. They are the compliance (\bar{E}^*), the interface friction index ($\bar{\xi}$), and the interface debond resistance ($\bar{\sigma}_i$). The fourth parameter, the residual stress ($\bar{\sigma}^T$), can be calculated from the other three using Eq 4 such that

$$\bar{\sigma}^T = \frac{-2 \cdot \bar{\sigma}_p^{-2} \cdot \bar{\xi} \cdot \left(\frac{\bar{\sigma}_i}{\bar{\sigma}_p} - 1 \right)^2 + \epsilon_0}{\left(4 \cdot \bar{\sigma}_p \cdot \bar{\xi} \cdot \left(1 - \frac{\bar{\sigma}_i}{\bar{\sigma}_p} \right) + \left(\frac{1}{\bar{E}} - \frac{1}{E} \right) \right)} \tag{4}$$

⁴ To remain consistent with the notation used by Domergue *et. al.* [7], the bar superscript is used to refer to values measured on a 2D composite without the use of load partitioning.

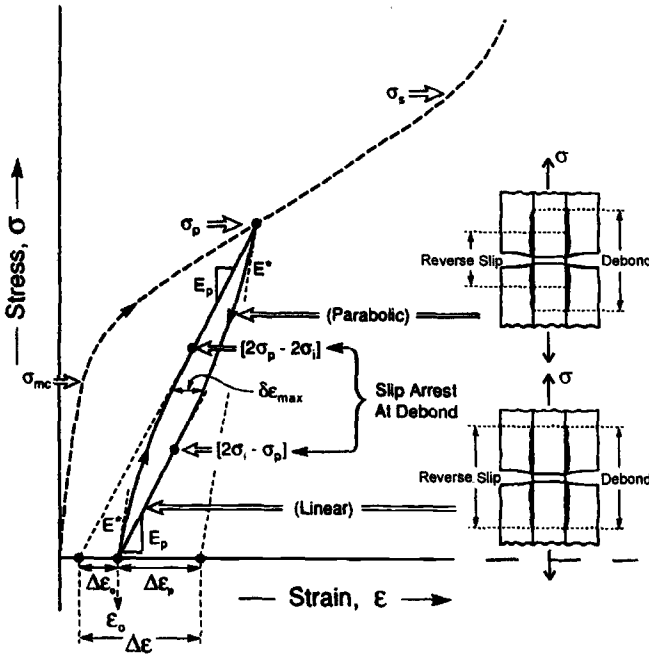


Figure 8: Features of a hysteresis loop for a material with large debond energy [5].

Two techniques were used to obtain ITM plots from the experimental unload/reload tensile data. The segment fitting technique is illustrated in Figure 10a for the test specimen exposed at 600°C for 10 h. In this technique, strain data is separated into small groups (in this case 22 data points in each group) and a linear fit is made through each group to obtain its ITM. The ITM data were then plotted against peak applied stress and the resulting ITM curves were visually inspected.

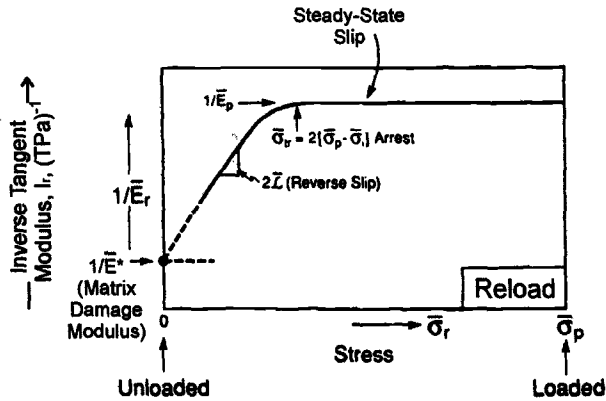


Figure 9: Schematic of the expected inverse tangent modulus upon reloading for a LDE composite [7].

The transition stress and the interface friction index were found by a trial-and-error technique of separating the data into two segments and using linear curve fits, until a close match between the two curve fits was found at the transition stress. This technique worked best for the later stages of the unload/reload tensile test, when the hysteresis loops were more fully developed. Early in the unload/reload tensile test (e.g., reload cycles #5 and #8 in Figure 10a), the ITM curve did not take the form of the expected ITM curve shown in Figure 9. Therefore, it was not possible to obtain all the parameters (e.g., transition stress and interface friction index) required for ITM analysis for the early unload/reload cycles.

The polynomial fitting technique is demonstrated in Figure 10b for the same data. In this case, a polynomial was fit to the loading portion of the hysteresis stress-strain curve, and the ITM data were obtained by taking derivatives of the polynomial curve fit. The slope of the linear portion of the curve gave the interface friction index. The transition stress was found by drawing lines along the data, as shown, and finding the intersection point. The composite compliance ($1/\bar{E}^*$) was found by the ITM value at zero stress.

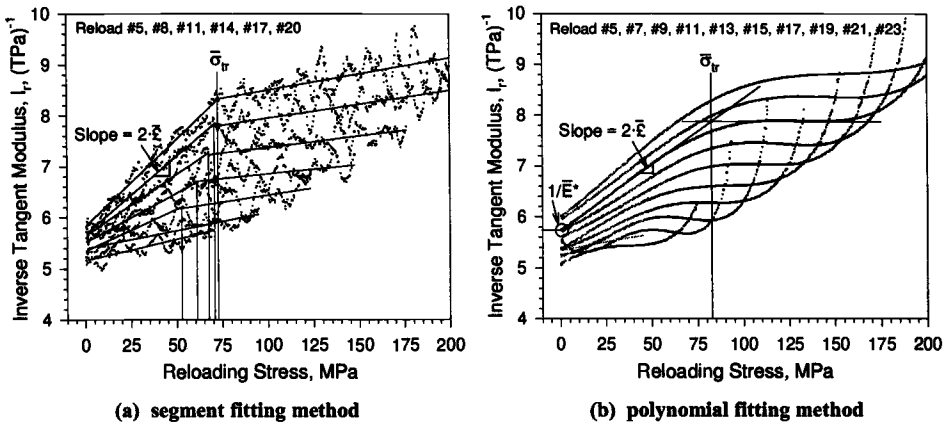


Figure 10: Examples of the two methods for determining $\bar{\sigma}_t$, $1/\bar{E}^*$, and \bar{E} using the same data from the specimen exposed at 600°C for 10 h.

Once the transition stress, $\bar{\sigma}_t$, is determined from ITM analysis, the debond stress, $\bar{\sigma}_i$, can be calculated using Eq 3. The ratio of the debond stress over the peak applied stress, $\bar{\sigma}_i/\bar{\sigma}_p$, occurs in both the numerator and the denominator of Eq 4, and is a constant for each unload/reload tensile test. This ratio was determined by finding the slope of the linear regression relating the debond stress, $\bar{\sigma}_i$, and the peak applied stress, $\bar{\sigma}_p$, while forcing the

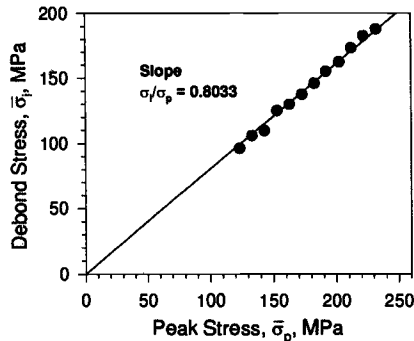


Figure 11: Relation of the debond stress, $\bar{\sigma}_i$, with applied stress, $\bar{\sigma}_p$ for specimen exposed at 600°C for 10 h.

curve-fit through the origin, as shown in Figure 11. Using this ratio, the composite compliance, $1/\bar{E}^*$, the interfacial friction index, \bar{f} , and the permanent strain, ϵ_p , from the individual hysteresis loops, the residual stress of the matrix can be calculated by Eq 4 for each unload/reload cycle. A mean and standard deviation can be calculated from this set of unload/reload cycles to determine the residual stress state of the test specimen.

Residual Stress State

The residual stress state was calculated from the same unload/reload tensile test data using the two independent methods. Figure 12 shows the residual matrix stress of each test specimen as determined by the two methods. There is reasonable agreement, although the phenomenological approach produced values that were 10-25 MPa greater than the analytical approach. Both methods showed an increase in residual stress with increasing exposure temperature.

The subjectivity of the phenomenological approach appears to be less than that of the analytical approach since a single intersection point can be clearly seen from the hysteresis stress-strain curves (see Figure 6). The analytical approach, on the other hand, relies on data derived from ITM analysis, which may involve visual trial-and-error fitting of scattered data to determine such material parameters as the transition stress and the interfacial friction index (see Figure 10). For this reason, the results from the phenomenological approach are considered to be the better estimates of the residual stress state of the CFCC. Nevertheless, the similarity of the results from the two approaches is encouraging. This similarity is especially important for the analytical approach, which is a powerful and versatile technique that can be used to probe the constitutive properties and parameters of a CFCC and can be used for predictive purposes.

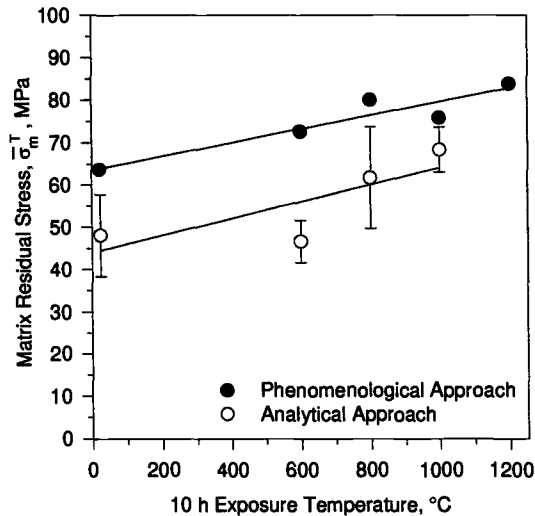


Figure 12: Residual matrix stresses as a function of exposure temperature. Lines represent linear regressions.

Interfacial Shear Stress

The interfacial shear stress, τ , is an important constituent property of a CFCC. If matrix crack saturation occurs, then the interfacial shear stress can be estimated from the average debond length, ℓ , at matrix crack saturation or at specimen failure by [7]

$$\tau \cong \frac{r \cdot (\sigma - \sigma_i) \cdot (1 - V_{f0}) E_m}{2 \cdot \ell \cdot E_L \cdot V_{f0}} \tag{5}$$

where V_{f0} is the volume fraction of the longitudinal fibers within the 0° ply, E_L is the elastic modulus of the 0° ply, E_m is the elastic modulus of the matrix in the 0° ply, σ_i is the partitioned debond stress, σ is the partitioned stress at saturation or at specimen failure, and r is the fiber radius [7].

Matrix crack saturation is observed by plotting the hysteresis loop maximum width, $\delta\epsilon_{max}$, (or area of hysteresis loop, W) vs. peak stress, see Figure 13. Crack saturation would be indicated by an inflection of these curves [7]. It appeared that the test specimen exposed at 600°C for 10 h was nearing matrix crack saturation when fracture occurred. Figure 13 shows a hypothetical continuation of the curve after fracture for this test specimen to demonstrate the condition of matrix crack saturation. All other test specimens failed before reaching matrix crack saturation.

Crack spacing measurements were not performed in this study, so the interfacial shear stress could not be estimated by Eq 5 for the test specimen that neared crack saturation. However, since the interface friction index, \bar{f} , is a measure of sliding at the interface, the relative magnitudes of the interfacial shear stress can be determined for a set of unload/reload tensile tests. For instance, changes in the interfacial friction index can be used to qualitatively assess changes in the interface with exposure time and temperature [7]. For unload/reload tensile tests, the interface friction index was found to increase linearly with increasing peak applied stress, as shown in Figure 14 for the test specimen exposed at 600°C for 10 h. The slope of the linear fit shown in Figure 14 provided insight into of the interfacial shear stress of the test specimen.

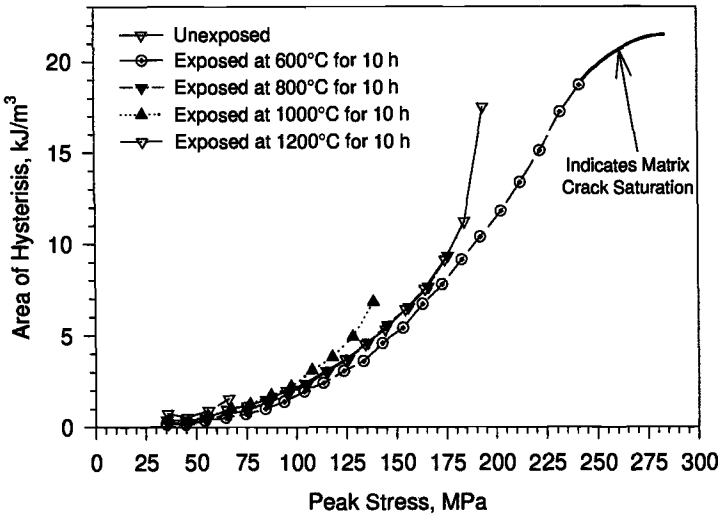


Figure 13: Area of the hysteresis loops plotted against peak applied stress.

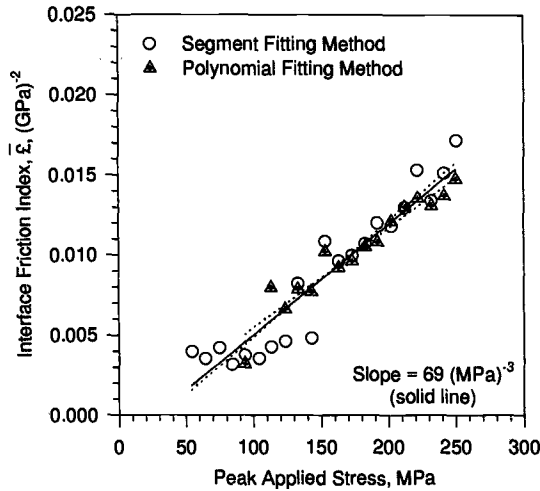


Figure 14: Interface friction index ($\bar{\epsilon}$) vs. peak applied stress for the specimen exposed at 600°C for 10 h. The solid line represents a linear regression of all data on the plot. The dotted lines represent linear regressions of data from each fitting technique.

Figure 15 shows the magnitude of the slope for each unload/reload test specimen plotted against 10-h exposure temperature. A decrease in the magnitude of this slope indicates an increase in the interfacial shear stress. The data shows that the test specimen exposed at 600°C, which was the unload/reload tensile test specimen with the greatest ultimate tensile strength and modulus of toughness, also possessed the greatest interfacial shear strength. The unexposed test specimen possessed the lowest interfacial shear stress (i.e., the slope with the smallest magnitude).

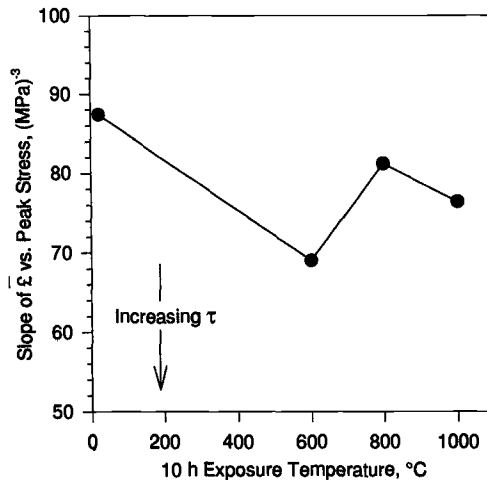


Figure 15: Slope of $\bar{\epsilon}$ vs. peak stress showing changes in the interfacial sliding stress, τ , with exposure temperature. Lines connect data points.

Discussion

The monotonic tensile test results showed strongly time-dependent thermal degradation at an intermediate exposure temperature of 600°C, and weakly time-dependent thermal degradation at the higher exposure temperatures of 800 and 1000°C. Unload/reload tensile testing provided some important insights into the thermal degradation mechanisms, particularly during the 600°C exposure. Figure 12 shows that the increase in interfacial shear stress (compared to the unexposed test specimen) due to the 10-h thermal exposure was greater at 600°C than at 800 and 1000°C. The 10-h exposure at 600°C actually caused an improvement in mechanical properties (i.e., the ultimate tensile strength and modulus of toughness) due to the increased interfacial shear stress. However, the 100-h exposure at 600°C caused severe embrittlement of the composite, which was evidenced by its high proportional limit stress, low modulus of toughness, and the lack of fiber pullout observed on the fracture surface. Because the fibers and the matrix were expected to be stable at this relatively low exposure temperature, it was likely that the cause of this embrittlement was greatly increased fiber/matrix shear stress. This provided evidence that the same mechanisms that caused the increase in fiber/matrix shear stress after the 10-h exposure at 600°C continued during the 100-h exposure. Test specimens exposed for 100 h at 800 and 1000°C, on the other hand, showed greater "toughness" and greater fiber pullout at the fracture surface than the test specimen exposed for 100 h at 600°C. Thermal exposure at 1200°C caused severe degradation of the composite.

Both the phenomenological and analytical approaches showed increasing residual stress with increasing 10-h thermal exposure temperature. This can be attributed to the increase in the fiber/matrix shear stress due to thermal exposure. As the composite was cooled from the initial fabrication temperatures (~1000°C), thermal expansion mismatch stress was able to partially relax by fiber/matrix sliding. The magnitude of the residual stress was inversely proportional to the fiber slip length that occurred upon cooling. During thermal exposure, the composite attained a new stress state. The increase in the fiber/matrix shear stress that occurred during thermal exposure resulted in a decrease in the fiber slip length that occurred upon cooling, thus diminishing the composite's capability to relax thermal expansion mismatch stress. Since increasing the thermal exposure temperature increased the magnitude of the residual stress that arose upon cooling, and since increasing fiber/matrix shear stress diminished the capability to relax this stress, the residual stress increased due to increasing thermal exposure temperature.

Conclusions

Salient conclusive aspects of this investigation may be enumerated as follows.

1. Monotonically-loaded stress-strain response was similar to peak unload/reload stress-strain response regardless of material condition (i.e., as-received or exposed).
2. Strongly time-dependent thermal degradation, caused by rapidly increasing fiber/matrix shear stress, was observed at 600°C. Less time-dependent thermal degradation was observed at 800 and 1000°C; this suggested that the interphase was more stable at 800 and 1000°C than at 600°C. Severe thermal degradation was observed at 1200°C.
3. Analysis of the unload/reload stress-strain response using the two analysis methodologies indicated that the tensile residual stress in the matrix increased with increasing exposure temperature. This was attributed to increasing fiber/matrix shear stress due to thermal exposure.

Acknowledgments

Research sponsored by the U.S. Department of Energy, Assistant Secretary for Energy Efficiency and Renewable Energy, Office of Industrial Technologies, Industrial Energy Efficiency Division and the Continuous Fiber Ceramic Composites Program under Contract DE-AC05-96OR22464 with Lockheed Martin Energy Research Corporation.

References

- [1] Steen, M. and Valles, J. L., "Unloading-Reloading Sequences and the Analysis of Mechanical Test Results for Continuous Fiber Ceramic Composites," *Thermal and Mechanical Test Methods and Behavior of Continuous Fiber Ceramic Composites* ASTM STP 1309, M. G. Jenkins, E. Lara-Curzio, S. T. Gonczy, N. E. Ashbaugh, L. P. Zawada, Eds., ASTM, West Conshohocken, PA, 1996, pp. 49-65.
- [2] Steen, M., "Residual Stress State and Damage Mechanisms in Ceramic Matrix Composites Inferred From Uniaxial Tests Incorporating Unloading and Reloading Sequences," Fourth Euro Ceramics, S. Meriani and V. Sergo, Eds., Vol. 3, 1995, pp. 61-70.
- [3] Steen, M., "Effect of Residual Stresses on the Mechanical Response of Continuous Fibre Reinforced Ceramic Matrix Composites," *Advanced Multilayered and Fibre-Reinforced Composites*, Y. M. Haddad, Ed., NATO ASI Series Vol. 43, Kluwer Academic Publishers, 1998, pp. 297-305.
- [4] Evans, A. G., Domergue, J.-M., and Vagaggini, E., "Methodology for Relating the Tensile Constitutive Behavior of Ceramic-Matrix Composites to Constituent Properties," *Journal of the American Ceramic Society*, Vol. 77, No. 6, 1994, pp. 1425-55.
- [5] Vagaggini, E., Domergue, J.-M., and Evans, A. G., "Relationships between Hysteresis Measurements and the Constitutive Properties of Ceramic Matrix Composites: I, Theory" *Journal of the American Ceramic Society*, Vol. 78, No. 10, 1995, pp. 2709-20.
- [6] Domergue, J.-M., Vagaggini, E., and Evans, A. G., "Relationships Between Hysteresis Measurements and the Constitutive Properties of Ceramic Matrix Composites: II, Experimental Studies on Unidirectional Materials," *Journal of the American Ceramic Society*, Vol. 78, No. 10, 1995, pp. 2721-31.
- [7] Domergue, J.-M., Heredia, F. E., and Evans, A. G., "Hysteresis Loops and the Inelastic Deformation of 0/90 Ceramic Matrix Composites," *Journal of the American Ceramic Society*, Vol. 79, No. 1, 1996, pp. 161-70.
- [8] Fareed, A. S., Schiroky, G. H., and Kennedy, C. R., "Development of BN/SiC Duplex Fiber Coatings For Fiber-Reinforced Alumina Matrix Composites Fabricated by Directed Metal Oxidation," *Ceramic Engineering and Science Proceedings*, Vol. 14, No. 9-10, 1993, pp. 794-801.
- [9] Fareed, A. S., et. al., *Ceramic Engineering and Science Proceedings*, Vol. 11, No. 7-8, 1990, pp. 782-94.
- [10] Campbell, C. X., Jenkins, M. G., "In Situ Determination of Constituent Properties and Performance in an Oxide-Oxide CFCC," *Ceramic Engineering and Science Proceedings*, Vol. 20, No. 3, 1999, pp. 545-554
- [11] Campbell, C. X., "Thermomechanical Response of a Continuous Fiber Ceramic Composite (CFCC) Affected by Thermal Degradation and Residual Stress State," MS Thesis, University of Washington, Seattle, WA, 1998.
- [12] Hutchinson, J. W., Jensen, H., "Models of Fiber Debonding and Pull-Out in Brittle Composites with Friction," *Mechanics of Materials*, Vol. 9, 1990, pp. 139-63.
- [13] Marshall, D. B., "Analysis of Fiber Debonding and Sliding Experiments in Brittle Matrix Composites," *Acta Metallurgica et Materialia*, Vol. 40, 1992, pp. 427-41.

James A. DiCarlo¹ and Hee Mann Yun²

Fiber Test Development for Ceramic Composite Thermomechanical Properties

Reference: DiCarlo, J. A. and Yun, H. M., “Fiber Test Development for Ceramic Composite Thermomechanical Properties,” *Mechanical, Thermal and Environmental Testing and Performance of Ceramic Composites and Components, ASTM STP 1392*, M. G. Jenkins, E. Lara-Curzio, and S. T. Gonczy, Eds., American Society for Testing and Materials, West Conshohocken, PA, 2000.

Abstract: Many of the key thermomechanical tensile properties of continuous-fiber ceramic composites (CFCC), such as ultimate fast-fracture strength and long-term rupture strength, are controlled by the deformation and fracture properties of the reinforcing fibers. For this reason, research efforts are ongoing at NASA to develop fiber test procedures and composite property models that will allow use of the fiber data to accurately predict these CFCC strength properties for a variety of potential application conditions. Because of the current interest in two-dimensional woven composites, emphasis is being placed on the testing of single small-diameter fibers and single-ply fabrics. The primary objective of this paper is to review the status of these efforts. It is shown that the fabric tests and procedures need further development in order to use bundle strength theory to predict the fast-fracture strength of as-fabricated CFCC. On the other hand, the single-fiber tests using simple composite rupture models yield predictions in good agreement with available data for CFCC rupture strength at high temperatures.

Keywords: Fiber testing, fabric testing, creep-rupture, Larson-Miller, Monkman-Grant, CFCC rupture modeling, matrix cracking, environmental effects

Introduction

For many years, NASA has been testing commercial and developmental ceramic fibers in order to determine two key thermomechanical properties: (1) fiber tensile strength as a function of time, temperature, environment, and gauge length, and (2) fiber creep strength as a function of time, temperature, environment, and creep strain. General test methods and fiber property goals have been discussed in the literature [1] as well as property data for almost all fiber types of current and past interest as reinforcement of continuous-fiber ceramic composites (CFCC) [2-4]. Initial studies were focused on

¹ Senior scientist, Ceramics Branch, NASA Glenn Research Center, MS 106-5, 21000 Brookpark Road, Cleveland, OH, 44135.

² Resident research associate from Cleveland State University, NASA Glenn Research Center, MS 106-5, 21000 Brookpark Road, Cleveland, OH 44135.

ranking fiber behavior on a relative basis using test conditions representative of those expected during CFCC fabrication and service. These data have been and continue to be used to select the best fiber types for fabricating developmental CFCC and also to guide fiber vendors for achieving improved performance.

More recent studies have focused on using the fiber data on an absolute basis to analyze and predict CFCC thermomechanical performance under simple test conditions [5,6]. Particular emphasis is being placed on developing fiber test procedures and composite property models that will allow accurate predictions of the fiber-controlled CFCC structural properties across wide ranges of time, temperature, and service environments. This information can be very useful to materials engineers to decide, for example, whether a given CFCC system with certain fibers and fiber architectures will have sufficient structural capability to compete with other available structural materials under a particular set of application conditions. This information will also be useful as a basis for composite failure mode analysis since ultimate tensile failure of the CFCC is typically controlled by the deformation and fracture behavior of the reinforcing fibers.

The objectives of this paper are (1) to briefly review the status of fiber test and composite modeling methods currently being employed at NASA and (2) to demonstrate how these methods can be used to understand and predict key fiber-controlled strength properties of CFCC. Focus is placed on test methods currently being used for measuring the room-temperature tensile strength of single plies of woven fabric and the high-temperature stress-rupture behavior of single fibers in order to predict, respectively, the ultimate strength of as-fabricated CFCC under fast-fracture conditions and the long-term rupture strength of CFCC under high-temperature constant load conditions. The rationale for the test approaches and modeling methods are discussed, and the accuracy of each property model is evaluated by comparing predictions with available CFCC strength data. Relevant results are presented for ceramic fibers of current technical interest for CFCC reinforcement, including oxide-based fibers, such as Nextel 610 and Nextel 720, and SiC-based fibers, such as Nicalon, Hi-Nicalon, and Sylramic.

Results and Discussion

Ultimate Fast-Fracture Strength of CFCC after Fabrication

For predicting the ultimate tensile fast-fracture strength of as-fabricated composites in general, one approach that has been used is to measure the tensile strength characteristics of the reinforcing fibers in their as-produced condition [7]. This is typically done by selecting a certain number of single-fiber specimens (~10 to 100) and then measuring the fracture load and cross-sectional area (or diameter) for each fiber specimen. With this data set of individual fiber strengths measured at a convenient gauge length (typically 25 mm), one can then apply statistical theory, such as Weibull theory, to characterize the fracture probability of the fibers and the ultimate strength capability of a multifilament bundle composed of these same fibers. For example, Corten [8] has shown that if the individual fibers can fracture independently within the bundle, the bundle strength σ_B at a gauge length L can be predicted by

$$\sigma_B(L) = \sigma_f(L_0) \cdot R \cdot G \quad (1)$$

Here, σ_f is the average tensile strength of the individual fibers as measured at gauge length L_o ; and R and G are statistical factors that account, respectively, for the ratio between bundle and average fiber strength at L_o and for gauge length differences between L and L_o . Using two-parameter Weibull theory with a Weibull modulus m as a measure of strength variation, one can show that

$$\mathbf{R} = (me)^{-1/m} / \Gamma(1 + m^{-1}) \quad \text{and} \quad \mathbf{G} = (L_o / L)^{1/m} \quad (2)$$

where e is the natural logarithm base and Γ is the gamma function. This bundle strength theory can then be used to predict σ_{cu} , the ultimate tensile strength of an as-fabricated composite, by the following relation:

$$\sigma_{cu} = V_f^* \cdot \sigma_B(L_e) = V_f^* \cdot \sigma_f(L_o) \cdot \mathbf{R} \cdot \mathbf{G} \quad (3)$$

Here, V_f^* is the effective volume fraction of multifilament fibers aligned along the applied stress direction and $L = L_e$ is the effective gauge length at which this bundle ultimately fractures within the composite. This length, which is determined by the nature of the fiber-matrix interface, is crudely equivalent to twice the average fiber pullout length observed on the composite fracture surface.

For ceramic matrix composites, which are typically reinforced by fibers with small diameter ($\sim 10 \mu\text{m}$), there are many possible issues regarding the ability of the single-fiber approach of Equation 3 to yield accurate predictions of CFCC ultimate strength. For example, the measured single-fiber strength statistics may not be the same as those for the fibers in the as-fabricated CFCC. This could be due, for instance, to spool-to-spool variations in fiber fracture characteristics and diameters. Thus errors can arise due to the small number of tested fibers in relation to the total number of reinforcing fibers in the CFCC test specimen ($\sim 10\,000$ to $100\,000$). Also, for handling purposes the small-diameter fibers are usually provided by the fiber manufacturer in the form of tows or multifilament bundles containing ~ 400 to 800 fibers per tow. There then exists the possibility of error in the fiber fracture statistics due to handling damage or to strength bias in the process of removal of single fibers from the tows. In addition, the strength characteristics of the as-produced fibers can be altered or degraded by the CFCC fabrication processes (such as, weaving, interphase coating, and matrix formation). Another potential issue is that it is usually inconvenient to measure cross-sectional area (or diameter) for each fiber specimen. In this case, an average diameter is often assumed, which, depending on the diameter distribution, can also introduce errors in the fiber strength statistics [9].

A further concern with single fiber testing is that even if fiber spools could be fabricated with reproducible strength statistics (highly unlikely), a high degree of statistical accuracy is still required in order to make the two extrapolations typically needed to predict CFCC ultimate strength. The first extrapolation is a prediction of the strength of a multifilament fiber bundle at the single-fiber test gauge length (R factor of Equation 2). The second extrapolation (G factor of Equation 2) is a prediction of the strength of this bundle at the effective gauge length of the bundle within the CFCC. This length can be very short (typically $\ll 25 \text{ mm}$), due primarily to the small fiber diameter and relatively high fiber-matrix interfacial strength [7]. Thus errors can arise not only in

assuming the extrapolations are valid outside the single-fiber data set, but also in the estimation of the effective bundle gauge length within the CFCC.

In lieu of the potential accuracy issues with single fiber testing for predicting ultimate strength of as-fabricated CFCC, NASA has been attempting to develop alternate fiber test methods which (1) eliminate and/or minimize many of the single-fiber problems and (2) are simple enough to be performed by CFCC manufacturers as possible quality-control tests. As such, NASA has recently focused on the strength testing of single-ply woven fabrics, which are the basic fiber structures used in most commercial CFCC today [10]. These fabrics are typically formed by the cross weaving (warp and fill directions) of multifilament fiber tows. In general, the average spacing between tows is selected so that when fabric plies are stacked in a three-dimensional architecture, the final CFCC contains ~20% fiber volume fraction aligned in each of two orthogonal directions (0° and 90°). The number of stacked plies, N , typically ranges from 4 to 12. Since CFCC strength properties are generally measured along one of these directions, it follows that strength testing of one fabric ply will allow a large fraction ($\sim 1/N$) of the number of fibers contributing to CFCC tensile properties. In addition, errors due to estimation of load-bearing fiber area are minimized because fabrics of the same fiber type show little variation in weight per planar area, implying the same cross-sectional area per tow in both the fabric and CFCC tests (see Appendix). Thus the single-ply fabric test minimizes errors due to at least three issues associated with single-fiber testing: (1) insufficient number of tested fiber samples in relation to the in-situ CFCC situation, (2) subsequent fiber degradation due to a key CFCC fabrication step (weaving), and (3) single fiber to bundle strength extrapolation.

For initial development of a single-ply fabric test, 0/90 fabrics were employed consisting of various types of SiC fibers in a five-harness satin weave architecture with weight per area of $\sim 300 \text{ g/m}^2$. Test specimens were prepared by cutting each fabric so that exactly ten tows were pulled in either the warp or fill direction with a gauge length of either 25 or 100 mm. Plastic grips of 25 mm length were attached by epoxy on the specimen ends so that typical fabric specimen dimensions before mounting were ~ 8 to 12 mm in width and either 75 or 150 mm in length. The fiber tows within as-produced fabric were usually coated by the fiber manufacturer with a polymer-based sizing in order to improve handling and minimize fiber damage due to abrasion during weaving. The sizing compositions (typically polyvinyl alcohol or polyethylene oxide) were chosen to leave little or no carbon char during high-temperature composite fabrication. When strength tested, the fabrics with sizing often displayed higher fracture loads than similar fabrics that were thermally treated under inert conditions to remove the sizing. This strength difference between sized and unsized fabrics (also observed for tows [11]) was especially evident for those SiC fiber types with rougher surfaces and coarser-grained microstructures. Thus it was concluded that during the tensile testing of fabrics (or tows) at room temperature, the fiber bundles must be coated with compliant coatings, such as sizing, in order to prevent strength loss due to detrimental mechanical interactions between the individual fibers. This conclusion was supported by the fact that when unsized fabrics were re-coated with typical compliant interfacial coatings used for CFCC, such as carbon or boron nitride (BN), the fabric strengths returned to their original values with sizing.

Another observation during initial development of the fabric test was that fabric strengths with sized fibers generally decreased with increasing gauge length. This behavior is expected for fibers that fractured independently within the tows and within the gauge section, as was confirmed by optical observations of the fractured fiber ends. However, when the fabrics were impregnated with a polymer-based resin for improved fabric handling (polyvinylpyrrolidone, ~30% weight gain), fracture strengths were observed to be effectively independent of fabric gauge length between 25 and 100 mm. For this particular resin, the 100 mm long specimens were observed to fracture in approximately four confined zones of ~20 mm in length with individual fiber pullout lengths ranging from 5 to 20 mm as measured from a resin-containing fracture surface. This observation of multiple matrix cracking explains the relatively high strengths of the impregnated fabrics with gauge lengths greater than 25 mm in that they behaved like one-layer polymer matrix composites with an effective bundle gauge length or load transfer length of ~20 mm [12].

Because of the ease of specimen preparation for the impregnated-fabric test and its composite-like fracture behavior, efforts were initiated to validate this test for predicting ultimate fast-fracture strength of as-fabricated CFCC. To accomplish this, the impregnated-fabric test was performed on five different lots of 0/90 fabric containing three different SiC fiber types: Hi-Nicalon (one lot), Sylramic (three lots), and a low-strength developmental Sylramic (one lot). Two-dimensional SiC/SiC composites containing eight plies from the same fabric lots were then fabricated and their ultimate strengths measured in the 0° direction. The fiber-matrix interphase coating for these CFCC was BN formed by chemical vapor infiltration (CVI); whereas the matrix was highly dense siliconized-SiC formed first by CVI SiC followed by SiC slurry and silicon

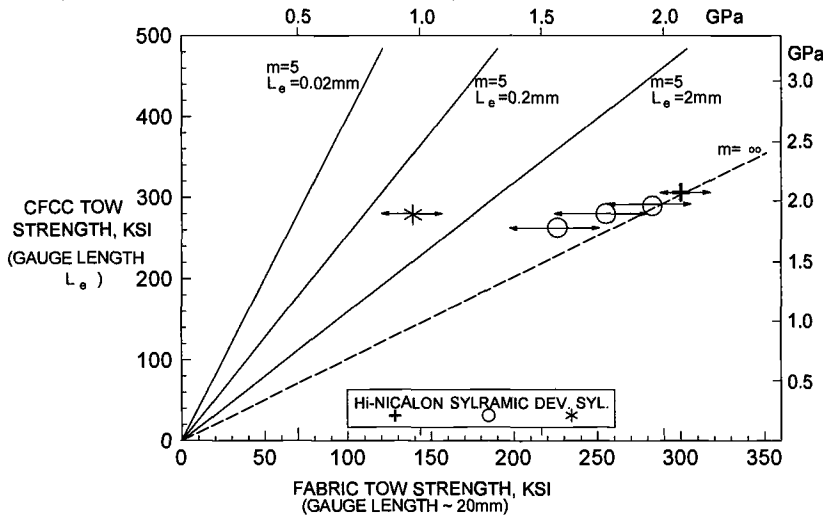


Figure 1. Comparison of measured tow strengths for as-fabricated SiC/SiC composites and resin-impregnated single-ply as-woven pieces from same fabric used in CFCC. Dashed line assumes a one-to-one empirical correlation; solid lines are based on theoretical G factor of Eq. 2.

melt infiltration. Figure 1 compares the average strength per tow (see Appendix) for the impregnated fabrics and for CFCC fabricated from these fabrics. About four to ten tests were performed on each fabric lot (~20 mm gauge length); but only one CFCC strength measurement was made per fabric lot. As might be expected based on bundle theory, scatter in the fabric strengths were small (standard deviations of ~10%). Also on an absolute scale, the fabric strengths were ~70% of the average strengths of single fibers at ~20 mm. By bundle strength theory, this R factor of ~0.7 implies fiber m values ranging from ~4 to 6 (see Equation 2), a result in good agreement with the m values measured from single-fiber strength data [11].

In terms of the ability to use fabric strength to predict CFCC strength, the dashed line in Figure 1 with a slope of unity ($m = \infty$) shows that the impregnated-fabric strengths could in most cases be empirically correlated with those of the as-fabricated CFCC. However, on a theoretical basis, this one-to-one relationship is not to be expected since the fabric tow strengths were measured at ~20 mm and the CFCC tow strengths at a much smaller effective gauge length, L_e . Actual measurements of average fiber pullout lengths on the CFCC fracture surfaces indicated L_e values ranging from 0.02 to 2 mm. Assuming these L_e values and an average Weibull modulus of $m = 5$ for these fiber types [11], one can calculate the solid lines of Figure 1 to show the theoretical strength relationships that should be expected. Except possibly for the developmental Sylramic fiber, these lines indicate that the tow strengths within as-fabricated CFCC are much less than those that would be expected from the as-produced fabric strength data, which at least for the three different Sylramic lots woven from different spools at different times are fairly consistent. Although other mechanisms may be operating, these results suggest that the as-produced Sylramic and Hi-Nicalon fabric strengths may have been degraded by one or more of the CFCC fabrication processes and that if these processes were identified and eliminated, higher CFCC ultimate fast-fracture strengths may be possible.

These preliminary results indicate that the impregnated-fabric test has potential for understanding and predicting in a convenient manner the ultimate strength capability of CFCC. Clearly, as indicated by the Figure 1 results, more developmental efforts are required. For example, it would be desirable to fracture the fabric bundles at the short gauge lengths representative of those in cracked CFCC. This approach should yield m measurements more representative of fiber strength distributions at these short lengths. One method for achieving this could be to impregnate the fabric with a more brittle resin either by increasing the resin content, changing the resin composition, and/or by performing the tests below room temperature where the resin may act more like a ceramic. In addition, it would be desirable to use the fabric test to understand whether fiber strengths can indeed be degraded during certain CFCC fabrication processes. This is another clear benefit of fabric specimens over single fibers because the fabrics can be more easily subjected to some of the complicated processes currently being used by CFCC commercial vendors. Studies to develop the fabric test further in this area are currently underway. Indeed, initial results suggest that SiC fiber strengths can degrade when their fabrics are coated with CVI BN interphases at low temperature and then subsequently exposed to matrix infiltration processes at high temperature [13].

Rupture Strength of CFCC at High Temperatures

For predicting CFCC rupture strength or CFCC fracture time under constant load conditions at high temperatures, it would be desirable at first glance to utilize the same fabric test approaches developed at room temperature. However, at temperatures greater than $\sim 400^\circ\text{C}$, environment-related fiber-fiber interactions in multifilament specimens can be more severe and more uncontrollable than at room temperature. This is the case both for inert and oxidizing test environments. For example, in an argon environment, polymer-derived sizings and resins decompose and allow detrimental fiber-fiber surface interactions to occur. Even if carbon or boron-nitride interfacial coatings were to be used, there may be sufficient pressure of oxygen in the test environment that these coatings could also degrade or disappear. Also, under oxidizing conditions such as ambient air, the high oxygen pressure not only removes all of these fiber coatings, but also allows SiC-based fibers to bond to each other. This bonding in turn allows the fracture of the weakest fibers in multifilament bundles to cause premature fracture of the stronger fibers. Although this can be a potential CFCC failure mode, it is certainly not one desired by the general CFCC community in which achieving maximum strength capability from the reinforcing fibers is a primary objective.

Because of these multifilament test issues and because the primary goal is to predict maximum rupture strength capability of CFCC in which fibers can fracture independently, NASA is currently pursuing test methods that measure the rupture behavior of single fibers as a function of time, temperature, environment, and gauge length. This approach was also selected because some of the single-fiber test issues previously discussed for predicting CFCC fast-fracture strength from simple bundle theory are somewhat minimized. For example, under rupture conditions, the strength-controlling flaws created in ceramic fibers are typically larger than as-produced flaws or flaws introduced by fiber handling or CFCC fabrication conditions. Thus fiber rupture is often controlled by flaw-growth mechanisms that are not related to those controlling fast-fracture behavior. In addition, in the creep-rupture regime, the sizes of these new high-temperature flaws are generally narrower in distribution so that fiber rupture strengths are more deterministic ($m \rightarrow \infty$) and less statistical in nature than fiber tensile strengths at room temperature. From a testing point of view, this implies that although the rupture strengths of ceramic fibers are less than their fast-fracture strengths, they are less dependent on gauge length [14], on handling, on tow-to-tow process variations, or on any other factors that can change the distribution of strength-controlling flaws at room temperature, such as strength reduction effects due to CFCC process conditions. Thus, as will be demonstrated, one can work in most cases directly with single as-produced fiber rupture data and bundle theory in order to predict maximum CFCC rupture strength at intermediate and high temperatures without significant error.

The test procedures that are being employed at NASA for measuring both the creep and rupture behavior of single fibers are described in detail elsewhere [1,14]. In general, these measurements are made using cold grips; that is, the ends of each fiber specimen are epoxied to paper grips and then the specimens are hung vertically with their center sections placed in the hot zone of a vertical furnace. Typical hot zone lengths are 25 and 100 mm; while typical grip to grip lengths are ~ 200 mm. The application of a constant load and measurement of creep deformation are achieved, respectively, by hanging a deadweight and attaching a LVDT (linear variable differential transformer) extensometer from the bottom grip. Generally two types of tests are employed: stress rupture (constant

load and constant temperature) and slow warm-up (constant load, constant rate of temperature change). These tests are primarily conducted from 1000 to 1400°C under oxidizing (air) and inert (argon) conditions. The creep and rupture measurements are typically made across a time range from ~0.01 to over 100 hours.

For simplifying analysis of the single-fiber fracture data, it was determined that by using simple thermal-activation theory [5, 15], one can combine the results of the two rupture tests with fiber fast-fracture strength data as a function of temperature to yield a single master curve or Larson-Miller (LM) plot [16] for each fiber type. This curve describes the applied stress at fracture (or fiber rupture strength) versus the time-temperature dependent parameter q given by

$$q \equiv Q_r / 2.3R = T (\log t_r + 22) \tag{4}$$

Here Q_r is the effective activation energy for fiber rupture; R is the universal gas constant (8.314 J/mol-K); T (Kelvin) is the absolute temperature for the rupture test; t_r (hours) is the fiber rupture time, and the LM constant (22) was determined by best fitting Eq. 4 to the fiber rupture data [15]. Thus, Larson-Miller theory assumes that rupture activation energy Q_r is not constant, but increases with time and temperature. Complete LM curves covering a wide range of temperatures and stresses are shown in Figure 2 for two types of oxide-based fibers: Nextel 610 and Nextel 720, and for three types of SiC-based fibers: Nicalon, Hi-Nicalon and Sylramic. These best-fit LM curves were measured in air for a ~25 mm gauge length (i.e., furnace hot zone length). Key microstructural properties for the five different fiber types are described elsewhere [2]. The many important basic and practical implications of the Figure 2 rupture curves are also discussed elsewhere [6].

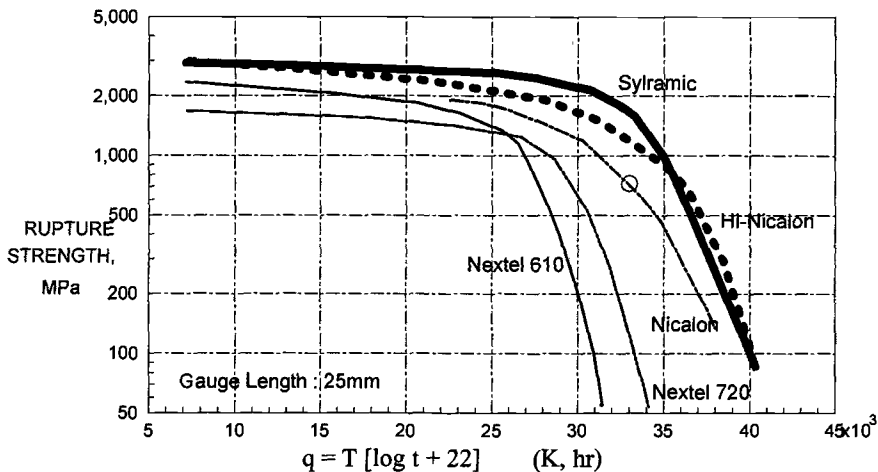


Figure 2. Best-fit Larson-Miller curves for average rupture strength of single as-produced fibers in air. Open data point for Nicalon fiber was calculated using CFCC rupture results in literature [17].

For modeling CFCC rupture strength, it is important to consider two simple but practical cases: cracked and uncracked matrices. For the first case, it can be assumed that the composite contains through-thickness matrix cracks that are bridged by one large fiber bundle that contains many fibers. These cracks could have developed during CMC fabrication due to a thermal expansion mismatch between the fibers and matrix, or during CMC service due to some random overstress or the need for a high application stress. To develop a composite rupture model in relation to the typical test methods employed to measure CFCC rupture strength, it is assumed that the cracked CFCC is being subjected to a relatively constant uniaxial stress σ_c at a constant temperature T in a particular gaseous environment g . As described by Equation 3, ultimate fracture or rupture of the CFCC should then occur at time t_r when the following stress condition is satisfied:

$$\sigma_c = \sigma_{cr} = V_f^* \cdot \sigma_{Br}(t_r, T, g, L_e) \quad (5)$$

Here σ_{cr} is the CFCC rupture strength, V_f^* is the effective fiber volume fraction bridging the through-thickness cracks in the stress direction, σ_{Br} is the rupture strength of the fiber bundle within the cracks, and L_e is the effective gauge length within the cracks.

For determining σ_{Br} in Equation 5, Curtin [7] has shown that for fast-fracture tests on single fibers and as-fabricated composites, the product $[R \cdot G]$ in Equation 1 is found to be approximately equal to unity both by experiment and by theory when one takes into account bundle effects ($R < 1$) and interfacial conditions ($G > 1$). Thus, for those composite systems where individual fibers retain their strengths and can fracture independently, a good approximation for the room-temperature fast-fracture strength of fiber bundles at L_e is the average strength of single fibers measured at ~ 25 mm gauge length. As discussed above, this approximation is not strictly valid for the as-fabricated SiC/SiC CFCC of this study, possibly due to new flaws introduced in the fibers by the composite processing conditions. However, single-fiber rupture strengths at elevated and high temperatures are typically lower than their as-produced fast-fracture strengths and often independent of CFCC processing conditions. Thus, for composite rupture at these temperatures, one might assume the rough approximation that $R \cdot G \approx 1$ so that

$$\sigma_{Br}(t_r, T, g, L_e) \approx \sigma_{fr}(t_r, T, g, 25 \text{ mm}) \quad (6)$$

where σ_{fr} is the average rupture strength of single fibers measured at ~ 25 mm gauge length. It follows then from Equations 5 and 6 that the maximum rupture strength of cracked CFCC should be approximately predictable from the following relation:

$$\sigma_{cr} \approx V_f^* \cdot \sigma_{fr}(q, g, 25 \text{ mm}) \quad (7)$$

Here, it is assumed that the fibers will fracture independently so that $\sigma_{fr}(q, g, 25 \text{ mm})$ can be directly determined from the single-fiber LM curves measured under the appropriate environmental conditions, such as the air curves of Figure 2. It should be noted that Equation 7 is essentially a rule-of-mixtures (ROM) approach to the strength of cracked CFCC. However, as discussed above, fiber strengths in the high-temperature creep-rupture regime tend to become deterministic ($m \rightarrow \infty$) so that bundle theory would indeed predict ROM strength behavior under these conditions (that is, $R = G = 1$).

Although the physical assumptions used for the cracked-CFCC model of Equation 7 are very simple (and perhaps unrealistic for many actual CFCC applications), they do closely simulate typical test conditions that have been used to evaluate the rupture properties of CFCC [18]. For example, Morscher [19] has evaluated the effects of pre-cracked matrices on the stress rupture behavior of SiC/SiC minicomposites containing Hi-Nicalon multifilament tows, BN interphases, and SiC matrices that were produced by chemical vapor infiltration. Under ambient air conditions at elevated and high temperatures, he found that the Figure 2 curve for the Hi-Nicalon fiber gave very good predictions of the CFCC rupture times as long as the BN interphases were retained on the fibers. That is, maximum CFCC strength versus q behavior was observed as long as the fibers were able to fracture independently and did not become bonded to the matrix or each other by silica growth on the exposed fiber surfaces. Attack of the BN interphases by the ambient air occurred primarily at intermediate temperatures from ~600 to 1000°C (q values from ~22000 to 30000). At higher temperatures and q values, the BN interphases retained their functionality, presumably due to the fact that the applied stresses were low enough to allow the small crack openings in the SiC matrix to be sealed by silica growth. These minicomposite results not only show the usefulness of the Figure 2 single-fiber results for CFCC with through-thickness matrix cracks, but also indicate the important strength degradation effects that can occur when SiC-based fibers and current interphases are exposed to oxidizing conditions. Thus single-fiber LM data plus Equation 7 can give a fairly accurate estimation of the effects of time, temperature, and environment on the maximum rupture strength behavior of cracked CFCC as long as the fibers fracture independently within the matrix cracks and bridging fiber bundles.

Besides minicomposites, high-temperature stress rupture data also exist in the literature for woven two-dimensional SiC/SiC CFCC with cracked matrices. For example, Zhu et al. [17] recently performed creep and rupture studies at 1300°C in air on CFCC with Nicalon fibers and SiC matrices. For applied stresses that were high enough to crack the SiC matrices, one can use Equation 7 with the reported V_f^* value of 20% to convert the SiC/SiC rupture results into rupture strength versus q data for the Nicalon fiber bundles bridging the cracks. The open data point in Figure 2 shows one converted example. The good agreement with the LM curve for single Nicalon fibers again supports the assumptions of the cracked-CFCC rupture model.

At some low applied stress, it is to be expected that the matrix of a well-constructed CFCC will not develop through-thickness cracks. For this case of an uncracked matrix, the structural load on the CFCC at high temperature will be shared in a time-dependent manner by the fibers and the matrix. Since the fibers are not fully stressed, one cannot use Equation 7 or the LM curves of Figure 2 to predict fiber and CFCC rupture time. To cover this situation, the following model has been proposed to predict CFCC rupture [6]. For an uncracked CFCC, the fiber and matrix will experience the same axial strain (isostrain conditions). Thus under creep-rupture conditions, the CFCC, matrix, and fiber experience the same creep-rate. It can then be assumed that the average rupture time of the reinforcing fibers within the CFCC can be predicted from creep-rate versus rupture time data for the reinforcing fiber. Such data can be obtained directly from Monkman-Grant (MG) plots for the fibers [20], which in turn can be determined by making both creep and rupture time measurements during the single fiber tests. The solid lines of Figure 3 show, for example, best-fit MG lines that have been measured for Nextel 610

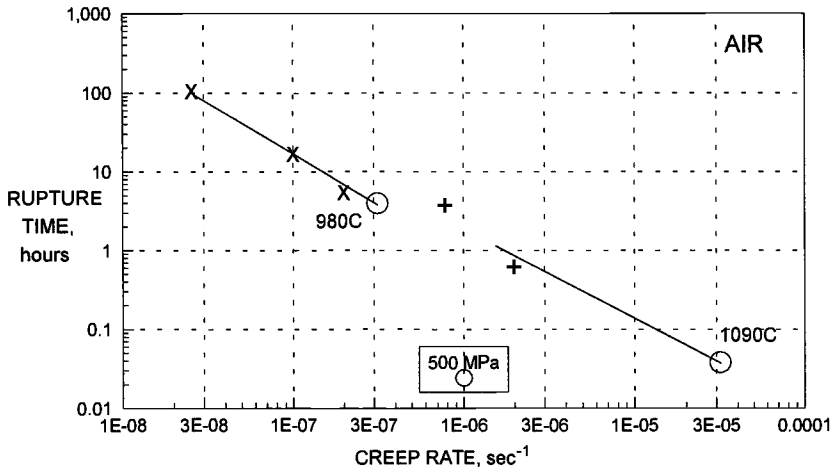


Figure 3. Best-fit Monkman-Grant lines for the rupture time in air for as-produced Nextel 610 single fibers at 980 and 1090°C at stresses of 500 MPa and below. Data points are CFCC rupture results at 1000°C (X) and 1100°C (+) [22].

fibers at 980 and 1090°C in air [21]. Thus, this model for the rupture of uncracked CFCC is based on understanding the CFCC creep rate at different stress levels and then using fiber MG plots such as those shown in Figure 3 to predict fiber and presumably CFCC rupture times. This model therefore allows prediction of CFCC ultimate rupture strength versus CFCC rupture time from knowledge of CFCC creep rate versus applied stress.

Currently, very little data exist in the literature to confirm the accuracy of this rupture model for uncracked CFCC. It would appear that this is the case because researchers tend to study CFCC creep-rupture at stress levels high enough to crack the matrices. As developmental efforts are successful in raising this cracking stress level, more data in the uncracked CFCC region should be available for model verification. Nevertheless, in support of this model, Zuiker [22] has recently analyzed the creep and rupture behavior of an oxide/oxide CFCC reinforced by Nextel 610 fibers. At 1000 and 1100°C in air, after a very rapid transient stage, these CFCC showed a long steady-state creep stage prior to rupture. The author calculates that during this stage both the fiber and matrix are carrying significant fractions of the CFCC load, so that conditions for the uncracked model should apply. If one plots the rupture times for the oxide-oxide CFCC at different values for the CFCC creep rate, one obtains the data points (X = 1000°C; + = 1100°C) shown in Figure 3. It can be seen that these points are in excellent agreement with the MG solid lines measured for the Nextel 610 single fibers at approximately the same temperatures. Thus the rupture times of these CFCC could have been predicted from the CFCC steady-state creep rates and the fiber MG lines. Clearly more work is needed in this area because research efforts are increasing matrix cracking strengths and because more and more CFCC applications are being identified where stresses are low enough to avoid matrix cracking but high enough to cause composite creep and rupture.

Summary and Conclusions

This paper has reviewed the status of fiber test procedures, fiber specimen selection, and composite theories currently being employed at NASA to understand and predict CFCC ultimate tensile strength at room temperature and CFCC rupture strength at elevated and high temperatures. For the room-temperature ultimate tensile strength of as-fabricated CFCC, strength tests on resin-impregnated single-ply fabrics were shown to be a viable approach for understanding factors affecting final CFCC strengths. For example, instances of CFCC strengths lower than predicted from as-woven fabric tests and bundle theory suggest fiber and fabric degradation due to CFCC fabrication processes. For the rupture strength of cracked CFCC, rupture tests on single fibers at ~25 mm gauge length were shown to yield Larson-Miller master curves, which were then used with simple composite theory to predict CFCC rupture strengths in good agreement with limited CFCC data in literature. Instances of lower than predicted CFCC rupture strengths at intermediate temperatures suggest loss of fiber fracture independence due to environmentally induced interphase degradation and fiber bonding. For the rupture strength of uncracked CFCC, creep-rupture tests on single fibers yielded Monkman-Grant master lines that offer a new and interesting approach for predicting the rupture time of in-situ fiber bundles based on the creep rate of the uncracked CFCC.

In evaluating the current state of fiber test development at NASA, it would appear that thermomechanical tests on fibers in the proper specimen forms and under the proper CFCC fabrication and service conditions can be useful not only for identifying types with the best properties, but also for predicting with reasonable accuracy the maximum strength performance that can be expected for CFCC reinforced by the fibers. As such, the fiber test data offer a basis not only for CFCC life modeling, but also for CFCC failure mode analysis. At the present time, resin-impregnated fabric tests on specimens that have been exposed to the various CFCC fabrication processes appear to be the most useful for understanding CFCC strength behavior at room temperature. On the other hand, single fiber tests either on as-produced specimens or on specimens pre-treated under CFCC processes appear best for CFCC rupture behavior at high temperatures. Clearly more CFCC thermomechanical property data are required in order to validate current fiber and fabric test methods and predictive CFCC property models. This in turn should result in improved fiber test methods both for CFCC quality control and for CFCC thermostructural property design.

Appendix

Procedure for Determining Average Tow Strengths for CFCC and Single-Ply Fabrics

For a two-dimensional CFCC specimen with 0° tows aligned in the applied stress direction, the average tensile strength per tow, σ_t , can be determined from

$$\sigma_t = P_c / (x w_c N A_t) = \sigma_c h_c / (x N A_t) \quad (1A)$$

Here P_c = CFCC ultimate tensile fracture load,
 σ_c = CFCC ultimate tensile strength,

h_c = average thickness of CFCC specimen used to determine σ_c ,
 x = number of tows per unit dimension along the specimen width,
 w_c = average width of CFCC specimen,
 N = number of plies, and
 A_t = average cross-sectional area of tows.

For a single-ply fabric specimen with ten tows aligned along the applied stress direction, σ_t can be simply determined from the fabric ultimate tensile fracture load, P_F , that is

$$\sigma_t = P_F / (10 A_t) \quad (2A)$$

In both cases, A_t , the average cross-sectional area of tows, can be determined by measuring the weight, W , and planar area, A , of the fabric pieces used in the tests; that is,

$$A_t = W / [A (x + y) \rho] \quad (3A)$$

Here, y = number of tows per unit dimension along the specimen length and
 ρ = average fiber density.

For different fiber types, very little scatter has been observed in A_t for pieces from large fabric lots of each type. Thus in using fabric strength to predict CFCC strength, the possibility for errors related to cross-sectional area are small (compare Equations 1A and 2A). However, errors could arise if partially cut 0° tows at the machined edges of CFCC lose all of their load-carrying ability instead of a fraction as assumed by the equations above. At worse, for a typical CFCC tensile specimen width of ~ 1 cm, this effect could degrade CFCC ultimate strength by about 10%.

References

- [1] DiCarlo, J. A., "Property Goals and Test Methods for High Temperature Ceramic Fibre Reinforcement," *Ceramics International*, Vol. 23, 1997, p. 283.
- [2] DiCarlo, J. A. and Dutta, S., "Continuous Ceramic Fibers for Ceramic Composites", *Handbook On Continuous Fiber Reinforced Ceramic Matrix Composites*, R. Lehman, S. El-Rahaiby, and J. Wachtman, Jr., Eds., CIAC, Purdue University, West Lafayette, Indiana, 1995, pp. 137-183.
- [3] Tressler, R. E. and DiCarlo, J. A., "High Temperature Mechanical Properties of Advanced Ceramic Fibers," *Proceedings for HTCMC-1*, R. Naslain, J. Lamon, and D. Doumeingts, Eds., Woodland Publishing Ltd., Cambridge, England, 1993, p.33.
- [4] Tressler, R. E. and DiCarlo, J. A., "Creep and Rupture of Advanced Ceramic Fiber Reinforcements," *Proceedings for HTCMC-2*, Vol. 1, A. G. Evans and R. Naslain, Eds., *Ceramic Transactions*, Vol. 57, 1995, p. 141.
- [5] DiCarlo, J. A. and Yun, H. M., "Thermostructural Performance Maps for Ceramic Fibers," *Proceedings of CIMTEC '98*, Florence, Italy, 1998.
- [6] DiCarlo, J. A. and Yun, H. M., "Factors Controlling Stress-Rupture of Fiber-Reinforced Ceramic Composites," *Proceedings of ICCM-12*, Paris, France, 1999.

- [7] Curtin, W. A., "Ultimate Strengths of Fibre-Reinforced Ceramics and Metals," *Composites*, Vol. 24, 1993, pp. 98-102.
- [8] Corten, H. T., "Micromechanics and Fracture Behavior of Composites," *Modern Composite Materials*, L. J. Broutman and R. H. Krock, Eds., Addison-Wesley, Reading, MA, 1967, pp. 27-105.
- [9] Lara-Curzio, E., "On the Relationship Between the Parameters of the Distributions of Fiber Diameters, Breaking Loads and Fiber Strengths," submitted for publication in the *Journal of Materials Science Letters*, 1999.
- [10] DiCarlo, J. A. and Bansal, N. P., "Fabrication Routes for Continuous Fiber-Reinforced Ceramic Composites (CFCC)," NASA/TM – 1998 –208819.
- [11] Yun, H. M. and DiCarlo, J. A., "Thermomechanical Characterization of SiC Fiber Tows and Implications for CMC," *Proceedings of ICCM-12*, Paris, France, 1999.
- [12] Rosen, B. W., "Thermomechanical Properties of Fibrous Composites," *Proceedings Royal Society of London*, Vol. A.319, 1970, pp. 79-94.
- [13] Yun, H. M. and DiCarlo, J. A., "Thermostructural Behavior of SiC Fiber Fabrics and Implications for CMC," submitted for publication in *Ceramic Engineering and Science Proceedings*, 2000.
- [14] Yun, H. M., Goldsby, J. C., and DiCarlo, J. A., "Tensile Creep and Stress-Rupture Behavior of Polymer Derived SiC Fibers," *Ceramic Transactions*, Vol. 46, 1994, pp. 17-28.
- [15] Yun, H. M. and DiCarlo, J. A., "Time/Temperature Dependent Tensile Strength of SiC and Al₂O₃-Based Fibers," *Ceramic Transactions*, Vol. 74, 1996, pp. 17-26.
- [16] Larson, F. R. and Miller, J., "A Time-Temperature Relationship for Rupture and Creep Stresses," *Transactions ASME*, Vol. 74, 1952, pp. 765-775.
- [17] Zhu, S., Mizuno, M., Nagano, Y., Cao, J., Kagawa, Y., and Kaya, H., "Creep and Fatigue Behavior in an Enhanced SiC/SiC Composite at High Temperature," *Journal of American Ceramic Society*, Vol. 81, No. 9, 1998, pp. 2269-2277.
- [18] Holmes, J. W. and Wu, X., "Elevated Temperature Creep Behavior of Continuous Fiber-Reinforced Ceramics," *High Temperature Mechanical Behavior of Ceramic Composites*, S. Nair, and K. Jakus, Eds., Butterworth-Heinemann, Newton, MA, 1995, pp.193-259.
- [19] Morscher, G. N., "Tensile Stress Rupture of SiC/SiC Minicomposites with Carbon and Boron Nitride Interphases at Elevated Temperatures in Air," *Journal of American Ceramic Society*, Vol. 80, No. 8, 1997, pp. 2029-2042.
- [20] Monkman, F. C. and Grant, N. J., "An Empirical Relationship between Rupture Life and Minimum Creep Rate," *Proceedings ASTM*, Vol. 56, 1956, pp. 593-620.
- [21] Yun, H. M., Goldsby, J. C., and DiCarlo, J. A., "Time-Temperature Effects on the Rupture and Creep Strength of Oxide Fibers," to be published.
- [22] Zuiker, J. R. "A Model for the Creep Response of Oxide-Oxide Ceramic Matrix Composites", *Thermal and Mechanical Test Methods and Behavior of Continuous-Fiber Ceramic Composites*, ASTM STP 1309, M. Jenkins, S. Gonczy, E. Lara-Curzio, N. Ashbaugh, and L. Zawada, Eds., American Society for Testing and Materials, West Conshohocken, PA, 1997, pp. 250-263.

Marc Steen¹

Effect of Fiber Waviness on the Tensile Response of 2D C(f)/SiC Ceramic Matrix Composites

Reference: Steen, M. “Effect of Fiber Waviness on the Tensile Response of 2D C(f)/SiC Ceramic Matrix Composites,” *Mechanical, Thermal and Environmental Testing and Performance of Ceramic Composites and Components, ASTM STP 1392*, M. G. Jenkins, E. Lara-Curzio, and S. T. Gonczy, Eds., American Society for Testing and Materials, West Conshohocken, PA, 2000.

Abstract: The mastercurve approach was employed to analyze the response of a satin weave and a plain weave reinforced C(f)/SiC ceramic matrix composite under tensile loading at both room and elevated temperatures. For each test specimen, the mastercurve was used to determine the magnitude of the axial residual stresses and to derive the “actual” values of the constituent properties, namely the first additional matrix cracking stress and the fiber fracture stress. It is shown that the waviness of the fiber reinforcement affects the matrix cracking stress but that the type of weave does not influence the in-situ fiber strength properties.

Keywords: ceramic matrix composites, plain weave, satin weave, tensile behavior

Introduction

Among continuous fiber reinforced ceramic matrix composites (CFCCs), woven CFCCs are expected to show a different mechanical response from those that are obtained by simply stacking unidirectional plies. Indeed, the undulation that goes hand in hand with the woven bundle reinforcement used to increase interlaminar and through-thickness strength, gives rise to a different stress state. The effect of undulation or of waviness cannot usually be investigated separately because, when designing experiments, it is not possible to control this parameter independently when designing experiments by modifying the reinforcement geometry. In the present investigation, the effect of reinforcement geometry on the material’s mechanical response is studied for carbon (C) fiber reinforced silicon

¹ Research officer, Institute for Advanced Materials, Joint Research Centre, P.O.Box 2, NL-1755 ZG Petten, the Netherlands.

carbide (SiC) matrix composites manufactured by chemical vapor infiltration (CVI). Two reinforcement geometries were studied: a plain weave with equal volume fraction of reinforcement in the warp and weft direction, and an eight-harness satin weave (8HSW). Test specimens from these two composites were subjected to tensile tests at room and elevated temperatures, with the loading direction coinciding with one of the reinforcement directions.

Materials and Experimental Procedure

Both CFCCs (designated C(f)/SiC) were manufactured by CVI. The fibers for the plain and satin weave are produced by different manufacturers but have the same physical and mechanical properties which are summarized in Table 1. The fiber carbon cloths were first coated with a pyrocarbon coating layer by chemical vapor deposition. Subsequently the SiC matrix was deposited in a number of runs. Details of the fiber coating and matrix infiltration are proprietary, but for both weave types processing parameters were identical in as far as possible. The resulting porosity is about 10 percent.

Table 1 – Room Temperature As-Received Fiber Properties.

Reinforcement Geometry	Plain Weave	Satin Weave
type	Torayca T300*	Besfight HTA**
density [g/cm ³]	1.76	1.77
nominal diameter [μm]	7	7
average tensile strength for 50 mm [MPa]	3400	3400
elastic modulus [GPa]	238	235

* Torayca data sheet No. TY-111A, June 1983

** Toho carbon fiber Besfight, data No-3

The tensile tests were performed under stress control in a closed loop controlled testing machine using waisted rectangular cross section test specimens according to EN 658-1. The test specimens were clamped in water-cooled hydraulic grips. During some of the tests, unloading-reloading cycles were performed in order to determine the average axial residual stress in the fibers and in the matrix according to the procedure outlined in [1]. Tests at room temperature were carried out in ambient air, whereas those at high temperatures are performed under a vacuum better than 10^{-4} Pa in order to avoid any environmental effect. High temperature tests were also carried out at sufficiently high stress rates (> 5 MPa/s) to suppress any time-dependent response. Heating was done by an inductively heated susceptor that surrounds the parallel length of the test specimen. Details of the test set-up and procedures are given in [2].

The following parameters characterizing the time-independent mechanical response were investigated: shape of the stress-strain curve, irreversible strain

accumulation, stiffness evolution, residual stress state, and in-situ matrix and fiber strength properties.

Stress-Strain Curves

C(f)/SiC composites have a large thermal expansion mismatch between the C-fiber and the SiC matrix. Upon cooling from the processing temperature high tensile axial residual stresses develop in the matrix. The magnitude of these residual stresses can exceed the strength of the matrix, thus causing matrix cracking which partially relieves the residual stresses. At room temperature the as-processed composites typically exhibit an extensively micro-cracked matrix. The presence of these cracks causes non-linear behavior upon loading, and hence it is very difficult, if not impossible, to determine the initial elastic modulus and the matrix cracking stress [3, 4]. This is clearly evident from the stress-strain curves at room temperature presented in Figure 1. However, the stress-strain curves for the two weave types look quite different: for the plain weave an inflection point occurs in the envelope of the loading parts and the irreversible strain accumulation at zero load is much larger. Both factors indicate that fiber-dominated behavior is reached for the plain weave C(f)/SiC at high stresses.

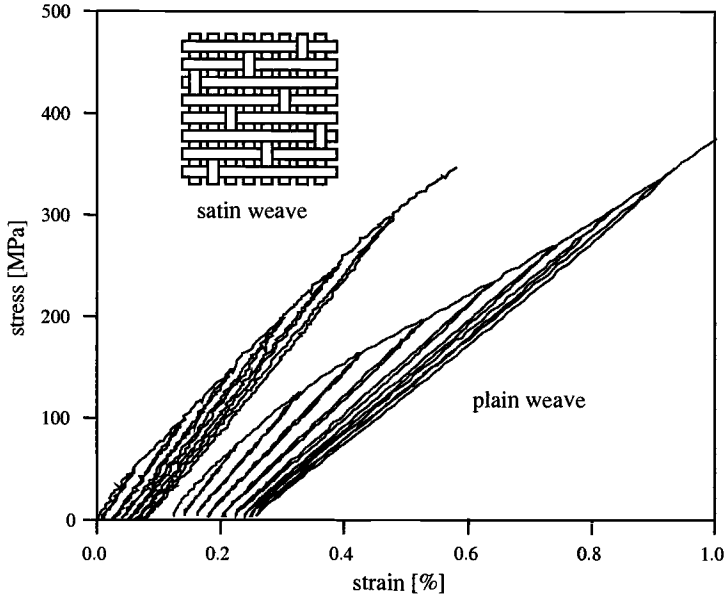


Figure 1 – Stress-strain curves for plain and satin weave C(f)/SiC at room temperature. The curve for the plain weave has been offset horizontally to enhance clarity.

As expected from the expansion mismatch the linear elastic part of the tensile stress-strain curve is more pronounced at 1200°C than at room temperature and the axial stiffness is greater because the matrix is under residual axial compression and the matrix cracks are closed (see Figure 2). Also, an inflection point occurs upon unloading at 1200°C, whereas it is absent at room temperature. In the absence of matrix debris opposing matrix crack closure, the relief of the compressive residual matrix stresses upon progressive interfacial debonding causes this inflection point.

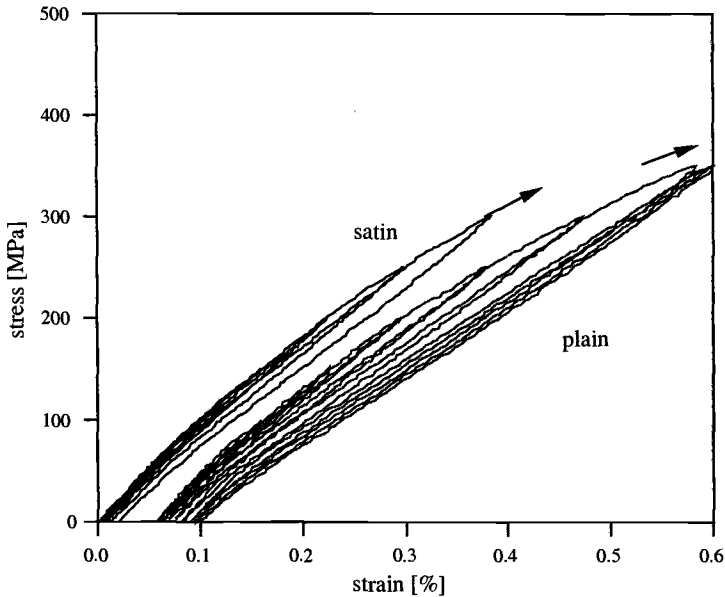


Figure 2 – Stress-strain curves for plain and satin weave C(f)/SiC at 1200°C. The curve for the plain weave has been offset horizontally to enhance clarity. (The arrows indicate that failure did not occur at the maximum applied stress in the test).

Evolution of Axial Stiffness

From the unloading-reloading cycles it is possible to determine the average elastic modulus as a function of the previously attained maximum stress. Typical examples are shown in Figure 3 for tests performed at room temperature and 1200°C for both weave types. In all cases the axial stiffness decreases. However, for the plain weave at room temperature the decrease levels off to a “saturation” level. This indicates again that fiber-dominated behavior (complete interfacial debonding) is reached at high stresses. From the saturation modulus of

approximately 50 GPa the fiber volume fraction oriented in the loading direction can be calculated as 0.22. For the satin weave at room temperature and for both weave types at 1200°C a saturation modulus is not observed, consistent with the absence of an inflection point in the loading part of the stress-strain curve.

Irreversible Strain Accumulation

The irreversible strain accumulation is shown versus the maximum previous stress in Figure 4. For both weave types the same temperature dependence is observed. Irreversible strain accumulation at 1200°C is much less than at room temperature, suggesting that the composite is less damaged at high temperatures. Similarly as for the stiffness reduction, a saturation in the irreversible strain accumulation is observed for the plain weave at room temperature, again

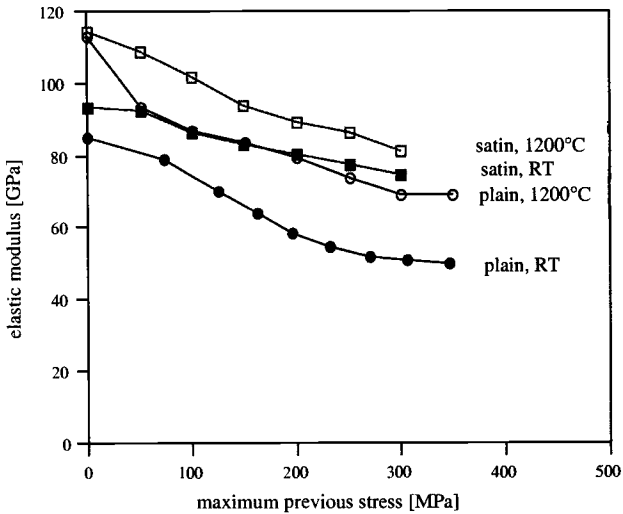


Figure 3 – Axial stiffness versus maximum applied previous stress.

manifesting fiber-dominated behavior. In all other cases a monotonic increase with stress is observed, which implies that interfacial debonding is not complete. As will be demonstrated later, however, the presentation of Figure 4 gives false qualitative, and hence also incorrect quantitative information.

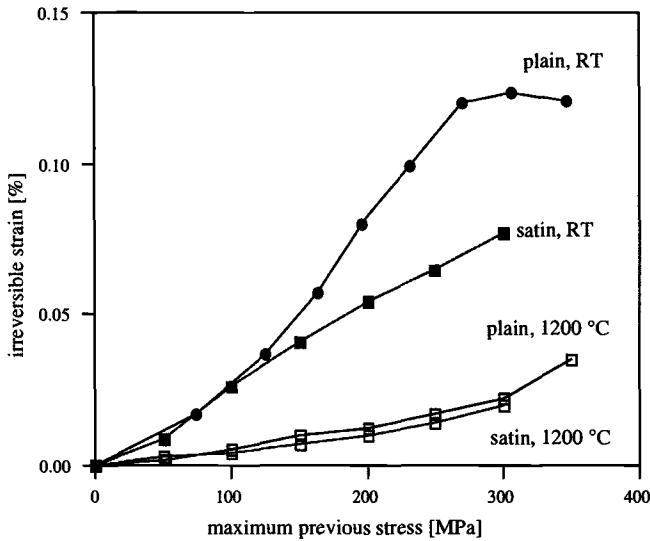


Figure 4 – Permanent strain versus maximum applied previous stress.

Axial Residual Stresses and Mastercurve

As explained in [1], it is possible to determine the average axial residual fiber stress and strain from the common intersection point of the regression lines to consecutive unloading-reloading loops as long as fiber failure has not occurred. This intersection point represents the true or actual origin of the stress-strain curve of the composite corrected for the existence of axial residual stresses. When stress-strain curves obtained on individual test specimens are translated so that their respective common intersection points coincide, they all superimpose. The resulting curve in the (actual strain, actual stress)-plane is called “mastercurve” and uniquely represents the time-independent tensile response of the investigated composite. The result of this translation for tests on the plain and satin weave C(f)/SiC is shown in Figure 5. As can be observed, for both weave types, the data at 1200°C fall close to the true origin, whereas those at room temperature lie in their extension and correspond to high values of the actual stress and strain.

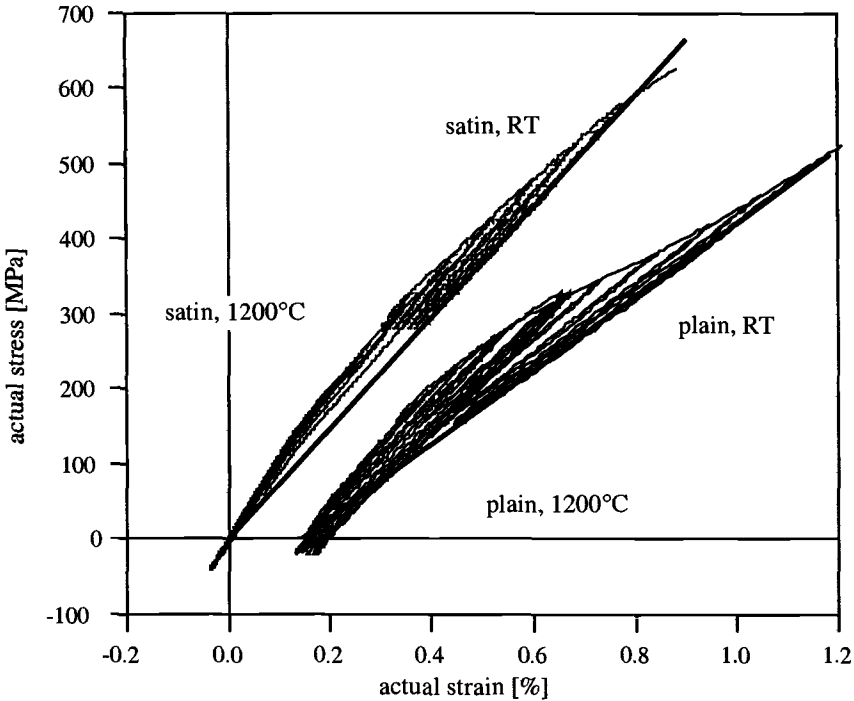


Figure 5 – Mastercurve for the plain and satin weave C(f)/SiC. The curve for the plain weave has been offset horizontally to enhance clarity.

The fiber-dominated behavior for the plain weave composite at room temperature manifests itself in the mastercurve by coinciding with a straight line through the origin with a slope of $E_f V_f$, where E_f stands for the fiber modulus and V_f for the fiber volume fraction in the direction of loading. A straight line fitting the room temperature data has a slope 52 GPa, from where $V_f=0.22$ is obtained using the value of E_f listed in Table 1. It can be observed from Figure 5 that the $E_f V_f$ line for the plain weave intersects the unloading traces of the stress-strain curves at 1200°C, and that the intersection point coincides with the inflection point in the unloading phase. The extension of the unloading trace below the $E_f V_f$ line hence represents the occurrence of matrix crack closure. This closure does not occur at room temperature because the actual stress is too high in this case.

The slope of the $E_f V_f$ line fitting the results on the satin weave C(f)/SiC is 74 GPa, corresponding to $V_f=0.315$. Unlike for the plain weave, the room temperature stress-strain curve descends below the $E_f V_f$ line at high actual stresses. This indicates that fiber failure occurred at these high stress levels, which resulted in a decrease in V_f . Again at 1200°C the inflection point upon unloading coincides with the intersection of the $E_f V_f$ line.

A very important observation from Figure 5 is that in none of the considered cases does irreversible strain accumulation occur in reality. Indeed, the actual irreversible strain accumulation is defined as the strain accumulation at zero actual stress. For both weave types at room temperature the intersection of the unloading traces with the actual horizontal axis always coincides with the actual origin itself, *i.e.* zero permanent strain. At 1200°C, it appears from Figure 5 that some small actual strain accumulation occurs for both weaves. This accumulation is however only apparent because the intersection with the actual horizontal axis occurs in the range of closed matrix cracks (below the respective $E_f V_f$ -line). The irreversible strain accumulation at *nominal* zero load represented in Figure 4 is hence only apparent, and cannot be attributed any physical meaning in terms of a damage parameter.

A similar argument can be applied for the *nominal* stiffness reduction shown in Figure 3. Figure 6 shows the axial stiffness determined from the unloading-reloading loops plotted versus the actual maximum previously reached stress. Whereas four different curves were observed in Figure 3, the stiffness evolution for each weave type in Figure 6 can be presented by a single curve independent of temperature. Stiffness reduction can hence be used as a damage parameter provided that its stress dependence is expressed versus actual stress. From Figure 6 it also appears that the composites reinforced with satin weave are more damage-resistant than those reinforced with plain weave.

The value of the elastic modulus corresponding to the undamaged state, *i.e.* with closed matrix cracks, can be determined from the slope of the loading line through the origin in the masterplot. This modulus equals 148 GPa for the plain weave and 163 GPa for the satin weave. The former agrees well with the values quoted in [4], which range from 135 GPa at room temperature to 152 GPa at 1200 °C.

In-Situ Strength Properties

From the respective mastercurves presented in Figure 5 it is possible to determine the “actual” values of the stresses corresponding to particular events in the loading history for the two types of C(f)/SiC composite. At high nominal applied stresses, fiber failure is observed, as evidenced by non-closed unloading-reloading loops in the satin weave or by composite failure in the plain weave. Because the matrix is already micro-cracked after processing, the nonlinearity at lower stresses represents a measurable effect of *additional* matrix cracking [4]. This is confirmed by the sudden increase of the irreversible strain upon exceeding this applied stress. Table 2 lists the average values and standard deviations of the actual stresses corresponding to the onset of nonlinearity and to fiber failure, as well as of the intersection point stresses from the unloading-reloading loops.

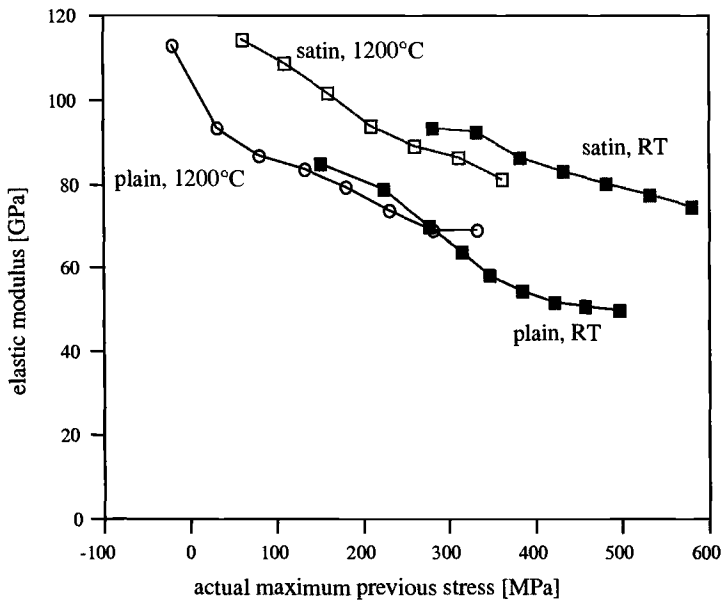


Figure 6 – Axial stiffness evolution versus maximum actual stress.

Table 2 - Actual Stresses for Matrix Cracking and Fiber Failure in C(f)/SiC, as well as Intersection Point Stresses.

	Actual Additional Matrix Cracking Stress [MPa]	Actual Fiber Failure Stress [MPa]	Intersection Stress [MPa]
plain weave RT	211 ± 15	568 ± 4	- 160 ± 12
plain weave 1200°C	208 ± 13	560	- 66 ± 117
plain weave, all	210 ± 14	565 ± 5	
satin weave RT	322 ± 18	583 ± 42	-270 ± 66
satin weave, 1200°C	293 ± 13	-	12 ± 82
satin, all	303 ± 20	583 ± 42	

Matrix Strength

It appears from Table 2 that the scatter in the value of the actual stress for additional matrix cracking is very small for all the conditions considered and that it does not depend on temperature. This indicates that additional matrix cracking during tensile loading is deterministic in nature. For all test specimens tested, the

actual additional matrix cracking stress is greater than the absolute value of the intersection point stress. This means that the additional matrix cracking stress is greater than the residual axial tensile stress in the matrix, as it should be.

The difference in actual additional matrix cracking stress between the two types of reinforcement for C(f)/SiC is caused by a geometry effect. Indeed, the effect of size on strength gives rise to lower values of the additional matrix cracking stress for larger matrix block lengths. In the plain weave composite larger block lengths are expected because of the uniformity of the stress state induced by the symmetry of the reinforcement. For the satin weave, on the other hand, the unbalanced reinforcement geometry results in a less homogeneous stress state that has its highest magnitude near the cross-overs of the longitudinal and transverse bundles, and matrix cracking has indeed been observed to be concentrated there. The confinement of high stresses to small regions can thus explain the higher value of the actual stress corresponding to additional matrix cracking for the satin weave.

In-Situ Fiber Strength

Table 2 also shows that the actual stress corresponding to fiber failure does not depend on temperature, nor on reinforcement geometry. However, this stress (average 575 MPa) applies at the level of the composite. To arrive at the actual stresses acting on the fibers it has to be corrected by the fiber volume fraction oriented in the direction of loading. This results in stresses of 1825 and 2614 MPa for the satin and plain weave composite, respectively. Using the Weibull strength distribution parameters of T300 fibers, namely $m = 6.0$ and $\sigma_0 = 882$ MPa for a reference volume of 1 mm^3 , together with an average value $s = 36.3 \text{ } \mu\text{m}^2$ for the cross section s of a fiber [5], the characteristic fiber strength for a 10 mm gauge length is calculated as 3307 MPa. This length is chosen because it corresponds to the extensometer gauge length, the readings of which are used to detect fiber failure. Using this value, the failure probability at the stress corresponding to fiber and composite failure can be determined from the Weibull failure probability expression as 22% for the plain weave. This value is greater than the critical fraction $\alpha_c = 15\%$ of broken fibers in a T300 fiber bundle given by [5]

$$\alpha_c = 1 - \exp(-l/m) \quad (1)$$

which indicates that the plain weave composite behaves as a set of loose fiber bundles prior to composite failure. In this case, the composite strength should coincide with the average bundle strength given by [5]

$$S_r = \sigma_0(m.e.l)^{-1/m} \quad (2)$$

With $\sigma_0 = 3307$ MPa the characteristic fiber strength for $l = 10$ mm, an average bundle strength $S_r = 3$ GPa is obtained, which agrees nicely with the average composite failure stress of $622/V_f = 2830$ MPa.

The failure probability of the fibers in the satin weave composite at the onset of fiber failure (1825 MPa) is 3%, which is much less than the critical bundle failure ratio. In this composite, progressive fiber failure can thus take place after the first fibers have failed, and the instantaneous V_f decreases until composite fracture. From the average actual composite failure stress of 610 MPa and failure strain of 0.87 % taken from the master curve, $E_f V_f$ at failure is calculated as 70 GPa. Compared to the original value of 74 GPa, a decrease in V_f of 5% is obtained. This agrees very well with the failure probability of 6% corresponding to the instantaneous fiber stress of $(610/0.315)/0.95 = 2038$ MPa.

This discussion confirms that the strength properties of the fibers in the two types of composite are not affected by the thermo-mechanical treatment during composite processing. The difference in failure behavior between the two reinforcement types is caused by the different amounts of interfacial debonding at the onset of first fiber failure which causes the plain weave composite to behave as a set of fiber bundles, whereas in the satin weave load transfer across the interface is still possible after the first fibers have failed.

Conclusions

It has been shown that the tensile behavior at room and high temperatures of a C(f)/SiC CFCC can be unified by the mastercurve approach. The mastercurve is unique for a given reinforcement geometry. Comparing the mastercurves for plain and satin woven C(f)/SiC it appears that the actual stress for additional matrix cracking is affected by the weave type of the reinforcement, whereas the in-situ fibre strength properties are independent of it. The difference in failure behavior is caused by different amounts of interfacial debonding in both types of reinforcement.

Acknowledgments

This work has been performed under the Research and Development program of the European Commission. The author thanks SEP Division de la Snecma for supplying the test specimens.

References

- [1] Steen, M., "Tensile Mastercurve of Ceramic Matrix Composites: Significance and Implications for Modelling," *Materials Science and Engineering*, Vol. A250, 1998, pp. 241-248.

- [2] Steen, M. and Bressers, J., "A Facility for Uniaxial Testing of CMCs at High Temperatures," *High Temp. Chem. Processes*, Vol. 3, 1994, pp. 263-371.
- [3] Wang, M. and Laird, C., "Characterisation of Microstructure and Tensile Behaviour of a Cross-Woven C-SiC Composite," *Acta Materialia*, Vol. 44, No. 4, 1996, pp. 1371-1387.
- [4] Camus, G., El Bouazzaoui, R., Baste, S., and Abbé, F., "Mechanical and Ultrasonic Characterisation of Damage of a 2D Woven C/SiC Composite," *Third Euro-Ceramics*, P. Duran, J. F. Fernandez, Eds., Vol. 3, Spain, 1993, pp. 779-784.
- [5] Lebrun, G., "Comportement Thermomécanique et Durée de Vie de Composites à Matrice Céramique: Théorie et Expérience," Thèse de l'Université de Bordeaux, 1996.

Mamidala Ramulu,¹ Michael G. Jenkins,² and Sawalee Kunaporn³

Surface Finish and Notch Effect Model for Strength Predictions of Continuous Fiber Ceramic Composites (CFCCs)

Reference: Ramulu, M., Jenkins, M. G., and Kunaporn, S., “Surface Finish and Notch Effect Model for Strength Predictions of Continuous Fiber Ceramic Composites (CFCCs)” *Mechanical, Thermal and Environmental Testing and Performance of Ceramic Composites and Components, ASTM STP 1392*, M. G. Jenkins, E. Lara-Curzio, and S. T. Gonczy, Eds., American Society for Testing and Materials, West Conshohocken, PA, 2000.

Abstract: Surface texture and process defects resulting from net-shape machining of continuous fiber ceramic composites (CFCCs) are often ignored in the design and analysis of component parts. Recently a mathematical model was proposed which defines the effects of surface texture and notch effects on the strength of engineering components in terms of an effective stress concentration factor (k_t). This model was experimentally verified using flexural strength resulting for a graphite/bismaleimide laminate. A further verification of the model applied to CFCC materials is presented in here using tensile test results. It was found that the model successfully predicts the retained strength of CFCCs resulting from net-shape machining over a large range in surface quality.

Keywords: ceramic composite, surface roughness, notch effect, stress concentration

Nomenclature

- k_t stress concentration
- R_a arithmetic average roughness; the arithmetic deviation of the surface profile from the centerline
- R_q root-mean-square height; the RMS height distribution of the surface profile within the sampling length
- R_y maximum peak-to-valley height; distance from the highest peak to the deepest valley within the sampling length of the surface profile
- R_z ten-point height; average distance between the five highest peaks and the five deepest valleys within the sampling length of the surface profile

¹ Professor, University of Washington, Department of Mechanical Engineering, Box 352600, Seattle, WA, 98195-2600

² Associate professor, University of Washington, Department of Mechanical Engineering, Box 352600, Seattle, WA, 98195-2600

³ Graduate student, University of Washington, Department of Mechanical Engineering, Box 352600, Seattle, WA, 98195-2600

- PSDF $G(\omega)$, power spectral density function; description of the general frequency composition of the waveform in terms of the mean square value of each component
- ACF $\rho(\tau)$, autocorrelation function; a measure of similarity between two identical but laterally shifted waveforms (profiles)
- ω radial frequency $2\pi/L$, where L is the wavelength
- τ lag or delay of the autocorrelation function

Introduction

Fiber-reinforced ceramic composites retain many of the desirable characteristics of traditional monolithic ceramics such as high stiffness, low density, corrosion resistance and excellent high temperature characteristics, but exhibit a greatly increased "toughness" over their monolithic counterparts [1]. Continuous fiber ceramics composites (CFCCs) are of particular interest because of their greatly increased "toughness," which serves to improve their inherent damage tolerance and increase reliability.

However, more information about the behavior and characteristics of CFCCs in general is required before these materials can be fully incorporated into industrial applications and their full potential realized [1,2]. While fairly extensive research has been conducted to characterize the properties of various CFCCs, to date limited research has focused on the surface characteristics generated by secondary processing techniques (i.e., material removal processes) and its influence on material properties. Since surface roughness and dimensional tolerance are closely related, and it is generally necessary to specify a smooth finish to maintain a close tolerance in the finishing process [3,4]. For many practical design applications, it is the dimensional tolerance that imposes a limit on the maximum allowable roughness. The reliability of machined components in high strength applications, is often critically dependent upon the quality of surfaces produced by machining. Thus, it is necessary to investigate the material removal process in machining of CFCCs and to understand the resulting surface finish. This paper studies the surface roughness characteristics of machined test specimens and analyzes the surface texture-generated notch effects on the mechanical properties of CFCCs. Notch influence was evaluated by using an effective stress concentration model [5]. Model predictions were compared to experimental tensile test results for a precommercial CFCC.

Effective Stress Concentration Model

The surface integrity resulting from net shape machining of fiber reinforced composites is composed of the surface texture and constituent disruption. Both these features contribute to the surface geometry and are defined quantitatively in terms of standard surface roughness parameters. In general, the effects of geometric discontinuities on the strength of engineering components are approached using a stress concentration factor (k_t). For example, the stress concentration resulting from a single semi-elliptical notch under a state of uniaxial tension shown schematically in Figure 1 can be approximated in terms of the notch depth (t) and root radius (ρ) as [6]

$$k_t = 1 + 2\sqrt{\frac{t}{\rho}} \quad (1)$$

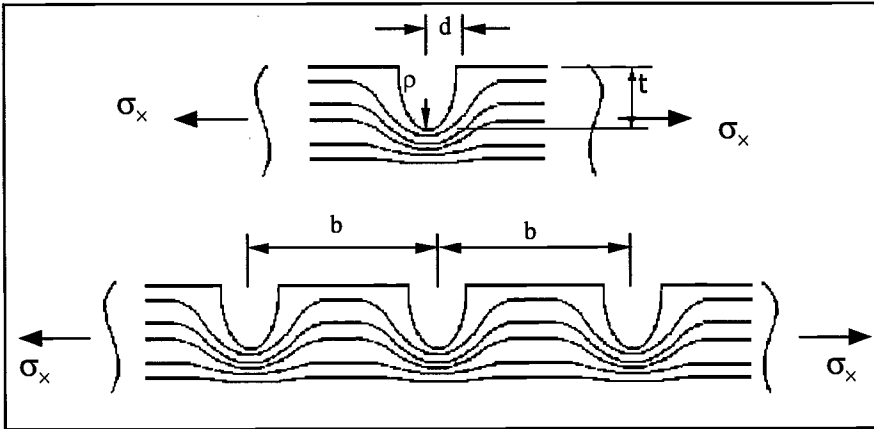


Figure 1- Schematic diagram of single and multiple surface notches.

A simple model was recently proposed [5] to describe the influence of machined surface texture on the mechanical performance of engineering materials in terms of an effective stress concentration factor (\bar{k}_t). The model was developed considering an ideal sinusoidal surface contour described by $z = a \cos(x/l)$ with vertical amplitude (a), spatial wavelength (l) and wavelength of ($2\pi l$), where x is the x -direction distance and l is spatial wavelength, as shown in Figure 2. The apparent stress concentration for this notch geometry is considered in terms of the "effective" major and minor axis lengths as

$$\bar{k}_t = 1 + 2 \frac{\bar{t}}{\bar{d}} \tag{2}$$

Note that the only modification of Equation 2 from Equation 1 is the use of the notch half-width (\bar{d}) rather than the root radius ($\bar{\rho}$) which is used to describe the root radius for an elliptical notch. The major and minor axis half-lengths \bar{t} and \bar{d} , and the root radius ($\bar{\rho}$) are related by $\bar{\rho} = \frac{\bar{d}^2}{\bar{t}}$. Because of an unknown degree of stress relief posed by adjacent notches, the effective notch height (\bar{t}) of the ideal sinusoidal surface may be considered simply as the quantity (na), where n is the factor which refers to the stress state ($n=1$ for shear and $n=2$ for tension) [5]. The notch half-width (\bar{d}) for this special case is not necessarily coupled with the selection of notch height and can be found from inscribing the notch with a semi-circle of constant radius ($\bar{\rho}$) as shown for a single wavelength in Figure 2. Accounting for these geometric features, the effective stress concentration factor takes the form

$$\bar{k}_t = 1 + n \frac{2a}{\bar{\rho}\pi} \tag{3}$$

The theoretical definition for the average surface roughness (R_a) of a machined surface is

$$R_a = \frac{1}{L} \int_0^L |z| dx \tag{4}$$

where L is the profile length in the x -direction.

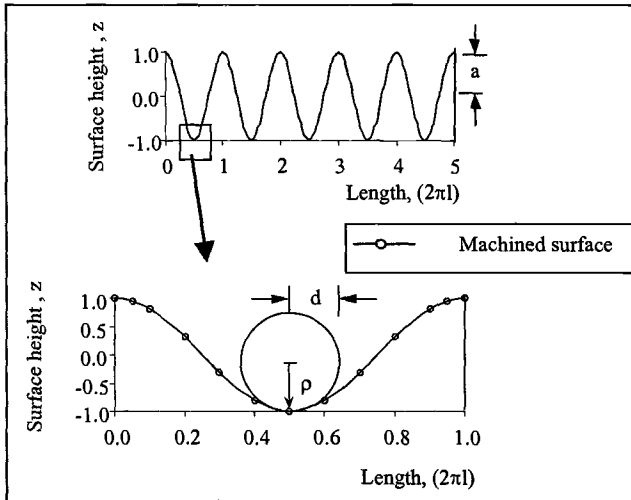


Figure 2- Definitions of the effective notch geometry for an ideal sinusoidal surface.

For a sinusoidal surface height distribution in the form $z = a \cos(x/l)$ as shown in Figure 2, the average roughness can be found using Equation 4 and is given by $(2a/\pi)$. Hence, Equation 3 reduces to

$$\bar{k}_t = 1 + n \frac{R_a}{\rho} \tag{5}$$

Equation 5 describes a sinusoidal waveform where the macroscopic surface plane is parallel with the surface mean line over the measurement cutoff length. For conditions in which the surface contains superimposed waviness and roughness, the ratio of peak to valley height (R_y) to ten-point roughness (R_z) can be used for rectification of the corresponding effective notch factor. For any sinusoidal waveform the ratio of (R_y/R_z) is unity. Similarly, this ratio for any other periodic waveform (triangular, square etc.) is also unity, provided that there is no apparent (i.e., local) curvature over the measurement cutoff length. However, for waviness in which the wavelength exceeds the measurement cutoff length, R_y and R_z begin to deviate. The ratio (R_y/R_z) undoubtedly forecasts these changes on the notch geometry. Therefore, the final expression for the \bar{k}_t from a machined surface in terms of the standard roughness parameters is given by

$$\bar{k}_t = 1 + n \left(\frac{R_a}{\rho} \right) \left(\frac{R_y}{R_z} \right) \tag{6}$$

Material dependencies including microstructure, anisotropy, heterogeneity etc. are all accounted for within the empirical constant (n). To account for processing induced surface texture using Equation 6, the standard roughness parameters including R_a , R_y and R_z are needed. In addition to these parameters, the effective notch root radius ($\bar{\rho}$) must be obtained from an assessment of the surface profile using a graphical radius gage.

Experimental Procedures

An experimental investigation was performed to evaluate the surface characteristics and to determine the effects of surface texture resulting from net shape machining on the strength of CFCCs. The following description represents a summary of the experimental methods and procedures.

Test Material

Test material used in this study was a commercially-produced⁴, ceramic grade Nicalon™ (Si-C-O) fiber-reinforced alumina (Al_2O_3). The composite was produced in three stages: fiber preform fabrication, interphase deposition (chemical vapor deposition of boron nitride) and matrix formation [proprietary directed metal oxidation (DIMOX™) process]. The two-dimensional reinforced composite contained 35-38% volume fraction of fibers and an estimated ~20% volume fraction of porosity [7].

Equipment and Procedures

An equal number of “dog-bone” test specimens were prepared from rectangular blanks using diamond-grit grinding and abrasive waterjet (AWJ) cutting after first diamond-grit cutting the blanks using a 179 mm diameter, 1.5 mm thick metal bonded 60-80 grit diamond wheel at a rotational speed of ~1650 RPM with a 25-127 mm/min traverse rate. The test specimen geometries were then either diamond grit ground with a 203 mm diameter, 12.7 mm thick plate and bonded 60-80 grit diamond-grit wheel at a rotational speed of ~1430 RPM and 25-127 mm traverse rate; or AWJ cut with a 380 MPa supply pressure, 80 mesh garnet abrasive, 0.33 mm sapphire orifice, 0.76 mm diameter nozzle and 50 mm/min traverse feed rate. The process conditions chosen in this series of experiments were based on the preliminary trial experiments. Ten test specimens each were obtained using the two aforementioned methods of machining for a total of 20 test specimens. All of the test specimen dimensions conformed to the geometry specified for tensile tests. Specifics of the material tensile tested per Test Method for Monotonic Tensile Strength Testing of Continuous Fiber-Reinforced Ceramic Composites with Solid Rectangular Cross-Sections at Ambient Temperatures (C1275)] can be found in Reference [7].

Machined surfaces were then examined to study the amount of microgeometric variations, and to investigate the roughness characteristics of the profiles. A stylus instrument was used for profile and roughness. Surface profiles were obtained by using a surface profilometer that had a probe radius of 2.54 μm . Surface roughness characteristics were evaluated based on a cutoff length of 0.8 mm. Several surface

⁴ Dupont-Lanxide Composites, Inc, Newark, DE – 1995 Vintage

profiles were taken in both the longitudinal (parallel to the cutting direction) and transverse directions (perpendicular to the cutting direction). The measurement length (or traverse length) of the surface profile was approximately 3 to 8 mm for both the longitudinal and transverse directions. For all profiles the standard surface roughness parameters were calculated according to ANSI B46.1-1986 [8] including the average surface roughness (R_a), root mean square roughness (R_q), peak to valley height (R_y), and ten-point roughness (R_z). In addition, the apparent profile valley radius (ρ) was determined for the surface profiles using a graphical radius gage. For both the longitudinal and transverse measurements, the roughness measurement length met the 2.4 to 8 mm traverse length requirement for a cutoff of 0.8 mm.

Results and Discussion

Surface Quality

Figure 3 shows typical surface roughness profiles in the transverse direction for each of the two machining processes under rough or preliminary trial cutting conditions. Comparison of the mean average surface roughness, R_a , of diamond-grit cut/ground and AWJ-cut test specimens showed that the R_a of 6.04 μm for AWJ cut surfaces was over six times as rough as the R_a of 0.91 μm for diamond-grit cut/ground surfaces. This greater roughness indicates that AWJ cutting generated considerably more damage and led to a much rougher cut. However, the surface roughness was reduced by a factor of two, when the AWJ process conditions were changed to near optimal. (i.e., industrial)

Summary of the average surface roughness parameters evaluated in all test specimens for both longitudinal and transverse direction measurements were given in Table 1 for the two fabrication techniques used in this investigation. Note that the average surface roughness parameters obtained in longitudinal direction are smaller than the transverse direction measurements regardless of the machining process. The ratio of average peak-to-valley height (R_y) to the average surface roughness, (R_a) is, approximately, $R_y/R_a = 6$ and for both machining processes. Therefore, R_a is not a representative surface roughness parameter in composite materials. These results clearly

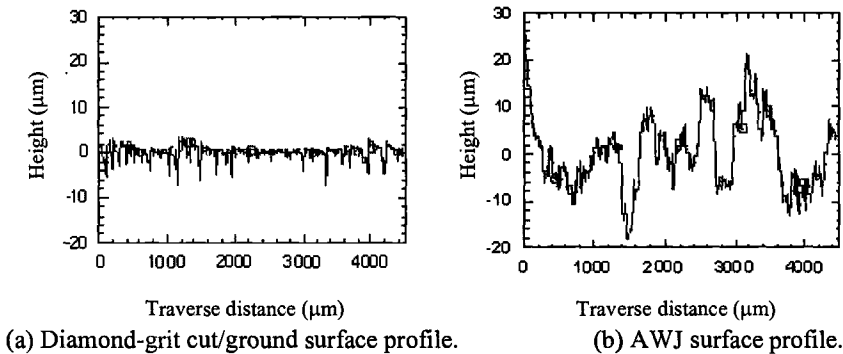


Figure 3-Representative surface profiles of cut surfaces.

demonstrate that the surface roughness parameters are direction dependent and are consistent with results for polymer matrix composites [4].

In order to study the surface statistics and randomness, the typical longitudinal surface profiles were evaluated with height distribution, cumulative height distribution, auto-correlation and power spectra as shown in Figure 4 for both diamond cut and AWJ machining processes respectively. Figure 4a shows the surface profile that consists of short wavelength fine irregularities superimposed on long wavelength coarse irregularities.

Figure 4b show the height distribution, and it was observed that the surface profile of AWJ skewed positively. An auto-correlation function (ACF) corresponding to Figure 4a is shown in Figure 4c, with correlation lengths of approximately 40 μm and 110 μm for diamond and AWJ machined surfaces respectively. The power spectrum density function (PSDF) graph, in Figure 4d, shows that the dominant wavelengths correspond to a peak in the PSDF curve for $\omega/2\pi$ of 0.005 to 0.0143. Similar observations were made for surface roughness measurements in the transverse direction and hence were not presented here.

Table 1-Summary of the surface roughness parameters.

Test Specimen	Direction	No.	Ra (μm)	Ry (μm)	Rz (μm)	$\rho(\mu\text{m})$	k_t
Diamond-grit cut-ground	Parallel	B1	0.87	6.71	4.53	74	1.03
		L1	1.34	7.62	5.78	87	1.04
		L2	0.44	4.36	3.13	5.2	1.24
		L3	1.27	8.19	5.84	63	1.06
		L4	0.75	5.67	4.15	33	1.06
		L5	1.29	6.53	4.93	45	1.08
		Mean	0.93	6.51	4.69	52	1.09
		Std.	0.36	1.37	1.03	28	0.07
	Perpendicular	B1	0.99	7.24	4.98	28	1.10
		L1	1.34	8.20	5.16	85	1.05
		L2	1.44	9.97	7.02	40	1.10
		L3	1.41	8.50	5.90	22	1.18
		L4	1.43	9.93	6.36	37	1.12
		L5	1.39	9.69	6.15	32	1.14
	Mean	1.32	8.77	5.88	42	1.11	
	Std.	0.05	0.78	0.61	22	0.04	
AWJ	Parallel	B2	1.22	7.55	5.93	105	1.03
		L6	2.84	13.83	10.32	117	1.07
		L7	3.01	13.08	9.99	105	1.08
		L8	2.90	12.94	9.71	63	1.12
		L9	2.86	13.82	11.28	96	1.07
		L10	3.12	14.43	12.27	112	1.07
		Mean	2.57	12.24	9.45	97	1.07
		Std.	0.19	0.78	1.07	19	0.02
	Perpendicular	B2	1.38	8.53	5.84	20	1.20
		L6	2.46	17.65	14.61	115	1.05
		L7	2.01	13.29	10.49	72	1.07
		L8	1.70	11.49	9.01	53	1.08
		L9	1.68	11.36	9.43	72	1.06
		L10	2.71	17.86	13.17	110	1.07
	Mean	1.85	12.46	9.88	66	1.09	
	Std.	0.43	2.98	2.26	25	0.02	

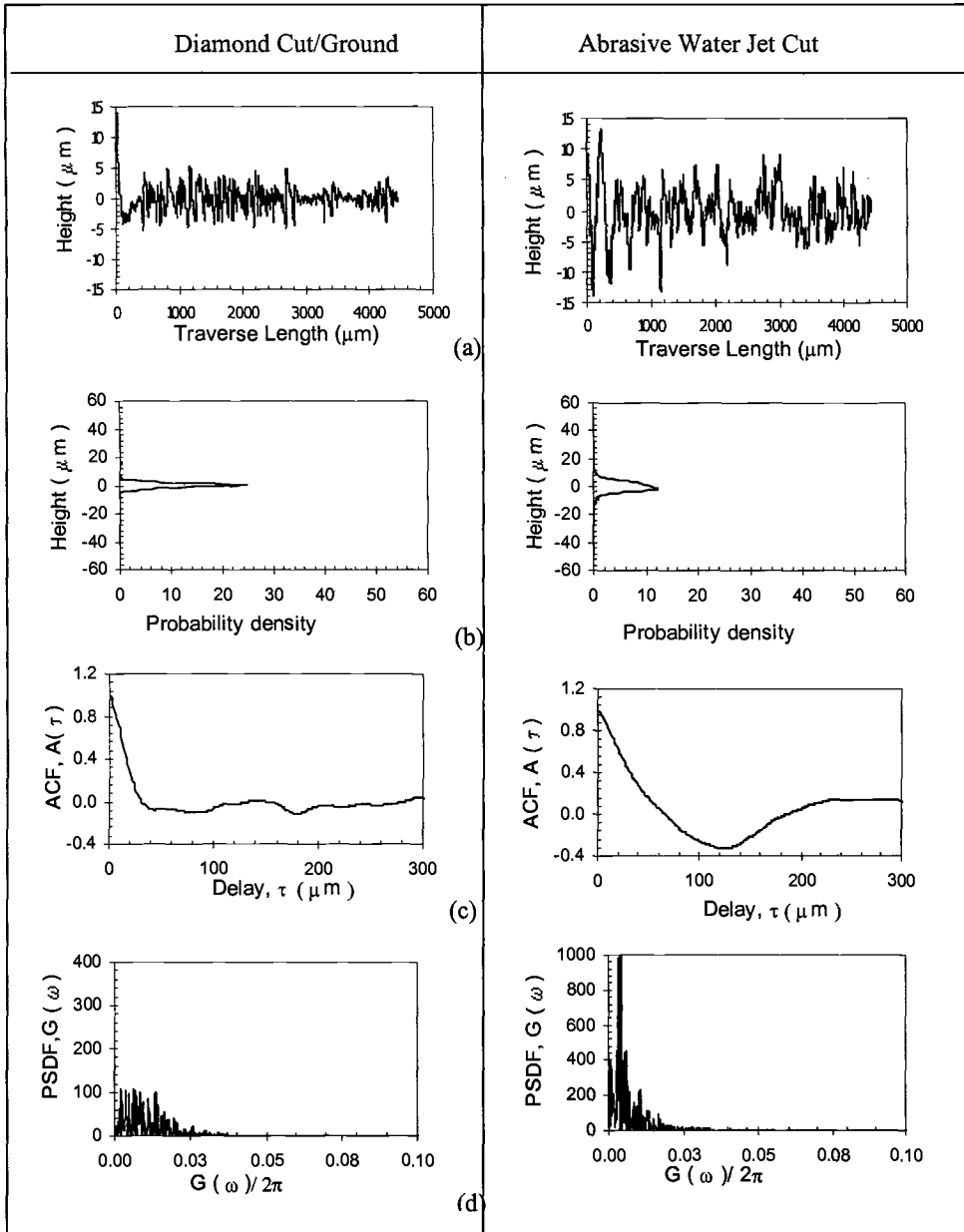


Figure 4- (a) Typical surface roughness profiles, (b) height distribution, (c) auto-correlation function, and (d) the power spectral density.

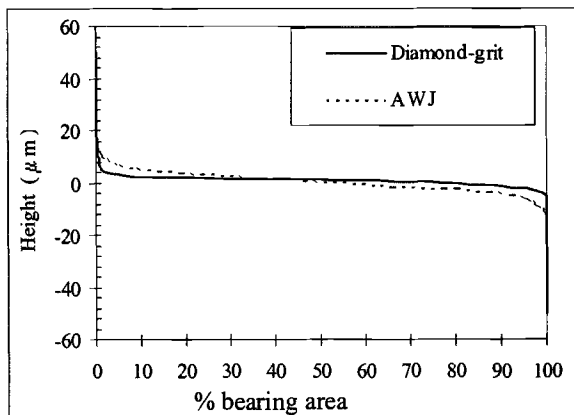


Figure 5 - Typical Abbott-Firestone curve.

Figure 5 shows the Abbott-Firestone curve or bearing ratio, correspond to the surface profile shown in Figure 1 for both machined processes. Abbott-Firestone curve or bearing ratio is the terminology commonly used to describe the percentage ratio of material to air of the surface profile at any contact surface level [5]. Note that the diamond-grit machined surface is flatter than AWJ-generated surface. It was also observed that the profiles for diamond-grit machined and AWJ-cut surfaces were periodic, symmetrical, and nearly Gaussian, as over 90% of the cumulative height distribution for both surfaces are in a straight line. Figure 6 shows the plot of profile statistical parameters, skewness versus kurtosis for all the test specimens. Essentially the skewness shows the degree of symmetry of the profile while the kurtosis shows the degree of pointedness or bluntness of the waveform. It is interesting to note that the longitudinal surface measurements skewed positively and the transverse measurement on the other hand skewed negatively regardless of the cutting method used for CFCCs.

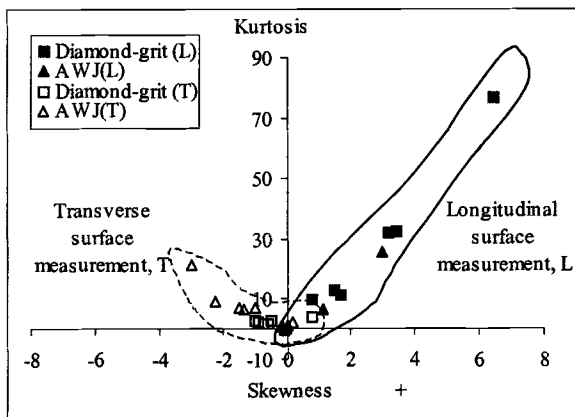


Figure 6 - Skewness vs. Kurtosis.

(Note that the "envelopes" are drawn as guides to the eye to show the range of the data)

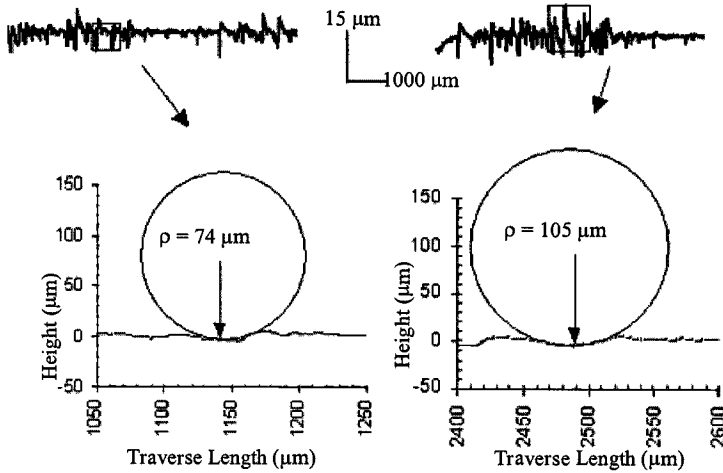


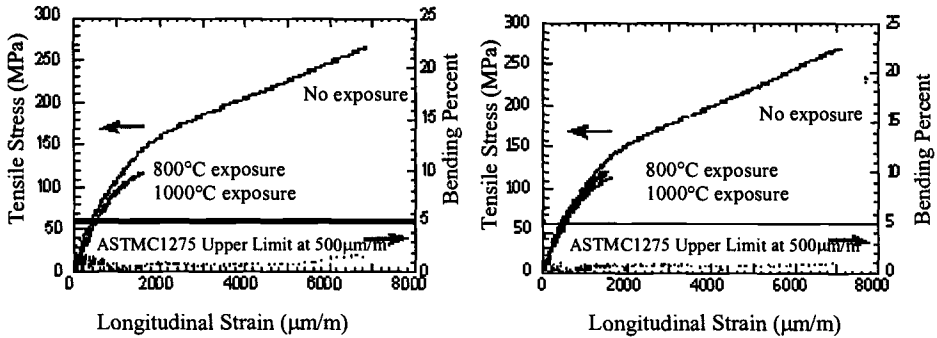
Figure 7-A typical profile valley resulting from diamond-grit and AWJ machining.

Notch Effects

The surface quality of a component is generally inferred by the average surface roughness (R_a). However, rarely does the R_a provide a reliable estimate for the reduction in component performance. Since the average roughness is not considerably influenced by spatial differences in surface height and therefore could not distinguish process dependent textural variations other than the difference in average surface height.

The effects of net-shape machining and surface texture on the strength of CFCCs were also examined using the effective stress concentration factor (\bar{k}_t). The average root radii were determined graphically as shown in Figure 7; surface roughness parameters required for the model and the calculated \bar{k}_t were also listed for the CFCC in Table 1. The material constant of 2.0 was used. Note that the effective stress concentration factor (\bar{k}_t) generated by the diamond-grit and AWJ machining processes gave almost the same value, inferring that the load at failure in these test specimens must be same, if failure was controlled by notch or sensitive surface mechanisms.

Figure 8 shows the stress-strain response of the CFCC test specimens fabricated using both the processes at room temperature and high temperature environment. Indeed no difference was observed between the stress-strain behaviors under tensile loading diamond-grit ground and AWJ cut of CFCC test specimen's, possibly because the \bar{k}_t 's were equal. The ratio of ultimate tensile strengths measured at failure in diamond-grit ground test specimens and AWJ-cut test specimens is about 0.95. The predicted strength ratio using the effective stress concentration model is 0.98 which is a difference of 3%. Although the proposed relation provides a simple way to estimate the performance of the composites, it correlates well with trends between ultimate load to failure and surface texture.



(a) Diamond-grit cut/ground test specimens (b) AWJ-cut test specimens

Figure 8-Post exposure tensile test stress (σ)-strain (ϵ)-strain response (0.003 mm/sec R.T. in ambient air) [7]

Previous investigations concerning the notch sensitivity of FRP materials have suggested that only the maximum notch depth is important [3]. However, notch shape was found to be an important component of the machined surface texture influencing the tensile strength in this study. Therefore, the profile valley radius is an important aspect of surface texture resulting from net-shape machining of CFCCs and should be considered in the selection of a method of machining.

Conclusions

The influence of surface texture resulting from net-shape machining on the strength of CFCCs was examined in this study. A new model that treats the effects of machined surface texture in terms of an effective stress concentration factor (\bar{k}_t) was verified using results from an experimental analysis. It was found that the average surface roughness (R_a) does not provide a reliable measure that can be used to infer the strength of CFCC components. However, the ten point roughness (R_z) provided a consistent measure of surface quality which could be used to estimate the strength, regardless of the method of machining. The reduction in tensile strength resulting from the machined surface texture was successfully predicted using the effective stress concentration factor (\bar{k}_t).

Acknowledgements

Research sponsored by the U.S. Department of Energy, Assistant Secretary for Energy Efficiency and Renewable Energy, Office of Industrial Technologies, as part of the CFCC Program under Contract DE-AC05-96OR22464 with Lockheed Martin Energy Systems, Inc.

References

- [1] Jenkins, M. G., Piccola, J. P., Mello, Jr., M. D, Lara-Curzio, E., Wereszczak, A. A., "Mechanical Behavior of a 3-D Braided, Continuous SiC Fibre-Reinforced / CVI SiC Matrix Composite at Ambient and Elevated Temperatures," *Ceramic Engineering and Science Proceedings*, Vol. 14, No. 9-10, 1993, pp.991-997.
- [2] Karnitz, M. A., Craig, D. A., and Richlen, S. L., "Continuous Fiber Ceramic Composite Program," *Ceramic Bulletin*, Vol. 70, No. 3, 1991, pp. 430-435.
- [3] Arola, D., and Ramulu, M., "Net Shape Manufacturing and the Performance of Polymer Composites Under Dynamic Loads," *Experimental Mechanics*, Vol. 37, No.4, 1997, pp. 379-385.
- [4] Ramulu, M., Wern, C. W., and Garbini, J. L., "Effect of Fiber Direction on Surface Roughness Measurements of Machined Graphite/Epoxy Composite," *Composites Manufacturing*, Vol.4, No. 1, 1993, pp. 39-51.
- [5] Arola, D., and Ramulu, M., "An Examination of the Effects from Surface Texture on the Strength of Fiber Reinforced Plastics" *Journal of Composite Materials*, Vol. 33, No.2, 1999, pp. 102-123.
- [6] Neuber, H., *Kerbspannungslehre*, Springer-Verlag, 1958, pp. 159-163.
- [7] Fehlmann, K. R., "Effects of Material Removal Processes and Elevated Temperature Exposure on Properties and p\Performance of Continuous Fibre Ceramic Composites," Master of Science Thesis, University of Washington, 1996, Seattle, WA
- [8] ANSI Standard B46.1, "Surface Texture (Surface Roughness, Waviness & Lay)", American National Standards Institute, Washington, D.C., 1986.

Reji John,¹ Dennis J. Buchanan,² and Larry P. Zawada¹

Notch-Sensitivity of a Woven Oxide/Oxide Ceramic Matrix Composite

Reference: John, R., Buchanan, D. J., and Zawada, L. P., “Notch-Sensitivity of a Woven Oxide/Oxide Ceramic Matrix Composite,” *Mechanical, Thermal and Environmental Testing and Performance of Ceramic Composites and Components, ASTM STP 1392*, M. G. Jenkins, E. Lara-Curzio, and S. T. Gonczy, Eds., American Society for Testing and Materials, West Conshohocken, PA, 2000.

Abstract: Oxide/oxide ceramic matrix composites (CMC) are currently being demonstrated in high-temperature aerospace applications. An oxide/oxide CMC under consideration by the U.S. Air Force is Nextel720/AS, which consists of an alumina-silica matrix (AS) reinforced with a woven Nextel720 fiber mat. The fracture behavior of notched Nextel720/AS at room and expected service temperatures is discussed in this paper. Specimens with semi-circular and narrow double-edge notches were tested under monotonic loading in laboratory air at 23 to 1200°C, and under sustained (creep) loading at 1100°C. The results show that Nextel720/AS is notch-insensitive at low temperatures ($\leq 1000^\circ\text{C}$) and $\approx 22\%$ notch-sensitive at higher temperatures ($\geq 1100^\circ\text{C}$) under tensile loading. At 1100°C, the notch-sensitivity increased significantly under sustained loading.

Keywords: ceramic matrix composite, creep, fracture, notch-sensitivity, notch strength, oxide/oxide, sustained loading

Introduction

Ceramic matrix composites (CMC) consisting of an oxide matrix and oxide fibers with no engineered fiber-matrix interphase are currently being demonstrated for high-

¹ Materials research engineers, Materials & Manufacturing Directorate (AFRL/MLLN), Air Force Research Laboratory, Wright-Patterson AFB, OH, 45433-7817.

² Associate research engineer, Structural Integrity Division, University of Dayton Research Institute, 300 College Park, Dayton, OH, 45469-0128.

temperature aerospace applications due to their inherent resistance to oxidation. Many investigations [1-11] have shown that oxide/oxide CMC exhibit excellent tensile and fatigue properties at room and elevated temperatures. For example, tensile and fatigue strength of Nextel610/alumina-silica (Nextel610/AS) decreased by only 15-20% when tested at elevated temperatures of $\approx 1000^{\circ}\text{C}$ [1-3,7,8]. Nextel610 fibers and Nextel610/AS are susceptible to excessive creep deformation at temperatures $\geq 1000^{\circ}\text{C}$ [7,8,12,13]. In contrast, Nextel720 fibers exhibit significant creep resistance up to 1200°C [12,13]. Hence, oxide/oxide CMC with Nextel720 fibers are under consideration by the US Air Force for some applications with temperature requirements in the range of $1000\text{-}1200^{\circ}\text{C}$. Current targeted aerospace turbine engine components, such as combustors, combustor liners, divergent flaps and seals, contain bolted attachment points and cooling holes. Local stresses in these regions often exceed the proportional limit of the composite resulting in damage and crack initiation. Hence, component design using oxide/oxide CMC will therefore require knowledge of the notched fracture behavior and damage progression under service thermomechanical loading conditions.

Recently, the notched fracture behavior of oxide/oxide CMC systems with Nextel610 and Nextel720 fibers have been studied [10,11,14]. Levi et al. [10] and Heathcote et al. [11] reported room temperature fracture results of Nextel610/Mullite-Alumina and Nextel720/Mullite-Alumina, while Kramb et al. [14] reported the fracture behavior of Nextel610/AS at room temperature and 950°C . Kramb et al. [14] concluded that the apparent fracture toughness decreased by $\approx 50\%$ when the temperature was increased from 23 to 950°C . This sharp decrease in fracture toughness is in contrast to the slight decrease in unnotched tensile strength [7,8]. The temperature effects on the fracture behavior of notched Nextel720/AS are unavailable. This paper discusses the results of a study of the notched fracture behavior of Nextel720/AS under tensile and creep loading at temperatures from 23 to 1200°C .

Material

The Nextel720/AS CMC used in this investigation was produced by Engineered Ceramics, Inc. (subsidiary of Composite Optics, Inc.). The Nextel720 fibers, produced by the 3M Company [15], consist of fine grained ($<0.5\ \mu\text{m}$) polycrystalline alpha alumina plus mullite. The composition of the fibers includes 85% Al_2O_3 and 15% SiO_2 and the average fiber diameter $\approx 10\text{-}12\ \mu\text{m}$. These fibers were woven into a balanced eight harness satin weave (8HSW) cloth. The plies were warp aligned during lay-up, however alternating plies were rotated about the warp direction so that fill fibers were matched with fill fibers, warp fibers matched with warp fibers. This lay-up provides better nesting of the plies and minimizes panel warpage. The composite panel used in this study contained 12 plies. Sections of the Nextel720 cloth were prepregged with alumina powder and a silica forming polymer before stacking. No coating was applied to the fibers before prepregging. The laminate was then warm molded to produce the green state ceramic tile. Sintering the green tile in air at $\approx 1000^{\circ}\text{C}$ removed the organic binders and produced a porous alumina-silica matrix. The resulting composite matrix is weakly bonded to the fibers without a naturally occurring or engineered interphase. The matrix

contains approximately 87 wt.% single crystal submicron alumina suspended in 13 wt.% silica. Image analysis of polished cross sections (see Fig. 1) showed that the fiber volume fraction was 45%. Figure 2 shows extensive microcracking present throughout the matrix as a result of the shrinkage, which occurred during the pyrolysis processing. These microcracks are distributed throughout the composite with spacing ranging from 50 to 200 μm prior to machining and testing. The specimens were machined out of 150 x 150 mm plates and tested as discussed in the next section.

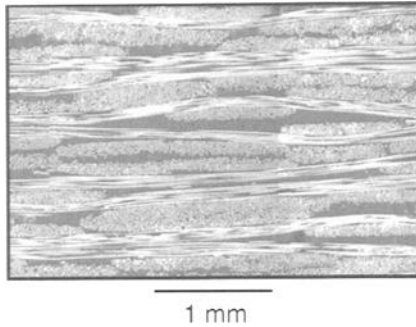


Figure 1. *Microstructure of (0/90) woven Nextel720/AS.*

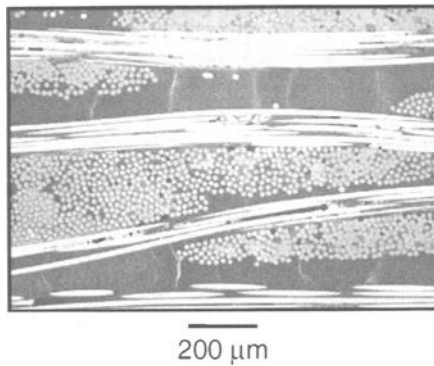


Figure 2. *Close-up view of microstructure highlighting the matrix cracks due to processing.*

Experimental Procedure

Test Procedure

The double-edge notched specimen geometry shown in Fig. 3, was used for all the notched fracture and creep tests. The specimen ends were rigidly clamped resulting in

rotationally constrained end conditions. The overall dimensions of the specimens were: width (W) = 15.0 mm, thickness (B) \approx 2.5 mm and height (between clamped ends) \approx 100 mm. The semicircular notches were made using a diamond coated grinding bit and the narrow notches were cut using diamond saws. Diamond saws with different thicknesses were used to achieve a wide range of stress concentrations at the notch tip.

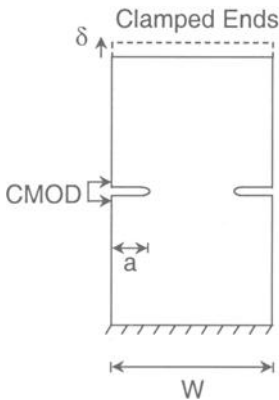


Figure 3. Schematic of the double edge notched geometry.

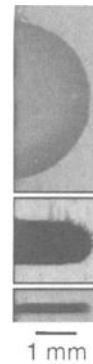


Figure 4. Photographs of notch geometries used during this study.

Typical notch geometries are shown in Fig. 4. The narrowest notch had a notch root radius of 0.11 mm. Most of the data were generated using specimens with a notch length to width ratio of $2a/W \approx 0.25$. Some specimens with deeper notches were also tested at room temperature and 1100°C. During the fracture and creep tests, crack mouth opening displacement (CMOD) was measured using a high temperature extensometer with alumina rods. The fracture tests were conducted under load-line displacement control at a rate ($\dot{\delta}$) of 0.005 mm/s. This loading rate corresponded to time to peak load of \approx 35 - 40 s. The loading portion during the creep tests was achieved under load control using a rate of 20 MPa/s. Unnotched creep rupture tests were conducted using dogbone specimens. All the tests were conducted in laboratory air using an automated, servo-controlled, hydraulic, horizontal test system [16].

Elevated Temperature Testing

Heating of the test specimen was achieved using a closed-loop controlled, 2 zone oven. Uniform heating ($\pm 1.2\%$ of average) was achieved across 15 mm in length centered on the specimen notch. Various methods of thermocouple attachment were investigated. Platinum-10%Rhodium, S-type, beaded thermocouples were first wire tied

to the specimen with the thermocouple bead in contact with the specimen surface. A small drop of Zircar® (Zircar Products, Inc., 110 North Main Street, NY 10921) ceramic adhesive was then placed over the thermocouple bead and spread to cover the bead surface. The adhesive was cured for 15 minutes at room temperature plus 15 minutes at 100°C resulting in a hard, adhesive, insulating cover for the thermocouple bead while assuring contact with the specimen surface during testing. The adhesive was white in color, matching the color of the Nextel720/AS specimen, which eliminated temperature errors due to differential radiant heat absorption. The Zircar® was also easily removed from the specimen surface after testing. The wire ties were removed prior to testing. The specimen temperature during the creep rupture tests on unnotched specimens was controlled using instrumented companion specimens.

Finite Element Analysis

The results from various notch geometries were compared on the basis of the initial stress concentration factor, $K_{t,net}$ as discussed in the next section. $K_{t,net}$ is defined as the ratio of the stress at the notch tip to the net-section stress. During this study, the finite element (FE) code, FRANC2D/L [17] was used to calculate $K_{t,net}$ assuming orthotropic properties for Nextel720/AS. The orthotropic properties of (0/90) woven Nextel720/AS are unavailable (measurements are in progress at AFRL/MLLN). Kramb et al. [18] and Heathcote et al. [11] have reported the orthotropic properties of Nextel610/AS and Nextel610/Mullite-Alumina, respectively. Using the stress-strain data from Ref. 9 to obtain the modulus, Poisson's ratio (ν) reported by Heathcote et al. [11], and shear modulus, G_{12} reported by Kramb et al. [18], we assumed the following properties for Nextel720/AS: $E_{11} = 75$ GPa, $E_{22} = 75$ GPa, $G_{12} = 18$ GPa, and $\nu_{12} = \nu_{13} = \nu_{23} = 0.05$. Note that $G_{12} \approx 0.5 \times G_{iso}$, where G_{iso} is given by $E/[2(1+\nu)]$. Similar difference between G_{12} and G_{iso} were also reported for Nextel610/AS [18] and Nextel610/Mullite-Alumina [11]. $K_{t,net}$ calculated using orthotropic FE analysis was ≈ 15 and 18% higher than that calculated using isotropic FE analysis for the semicircular hole and the narrowest notch, respectively.

Results and Discussion

The unnotched tensile [9] and creep behaviors of Nextel720/AS are shown in Figs. 5 and 6, respectively. Young's modulus (E) and the ultimate tensile strength (UTS) are relatively stable from 23 to 1200°C. UTS ranged from 170 to 186 MPa while E ranged from 75 GPa at 23°C to 57 GPa at 1200°C. At 1100°C, under sustained (creep) loading, the applied stress versus rupture time shows the familiar negative slope. The creep limit ≈ 145 MPa ($\approx 80\%$ of UTS) after 100 hr loading at 1100°C. The high creep limit after 100 hrs of exposure at 1100°C highlights the thermal stability of the oxide/oxide composite.

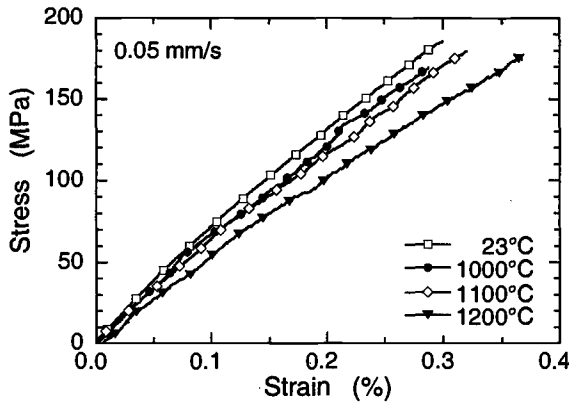


Figure 5. Tensile behavior of unnotched Nextel720/AS. [9]

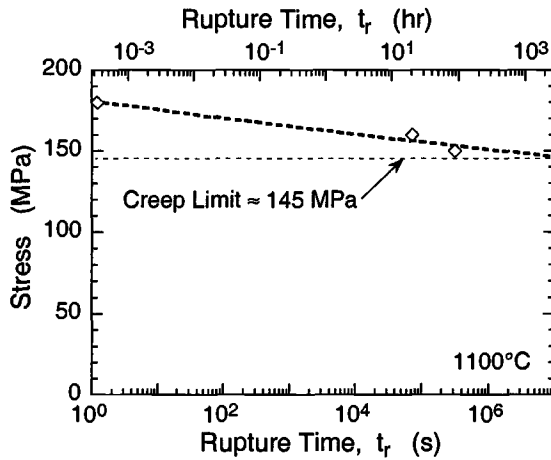


Figure 6. Creep rupture behavior of unnotched Nextel720/AS at 1100°C.

The results of the notched tensile strength tests at 23, 1000, 1100 and 1200°C are shown in Fig. 7. Figure 7 shows the net-section strength, $\sigma_{net,u}$ as a function of the initial stress concentration factor, $K_{t,net}$ for the same notch length to width ratio, i.e., $2a/W \approx 0.25$. $\sigma_{net,u}$ is insensitive to K_t for temperatures up to 1000°C and decreases $\approx 22\%$ at higher K_t for temperatures $\geq 1100^\circ\text{C}$. Additional data are required to confirm the trend at temperatures $\geq 1100^\circ\text{C}$. Figure 8 shows the effect of notch length on the net-section strength at 23 and 1100°C. At $2a/W \approx 0.25$, $\sigma_{net,u}$ decrease $\approx 17\%$ and $\approx 20\%$ at room temperature and 1100°C, respectively.

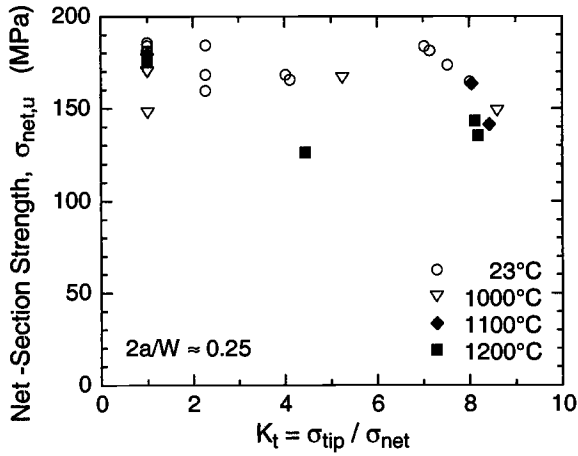


Figure 7. Effect of initial stress concentration on the net-section strength. ($2a/W \approx 0.25$)

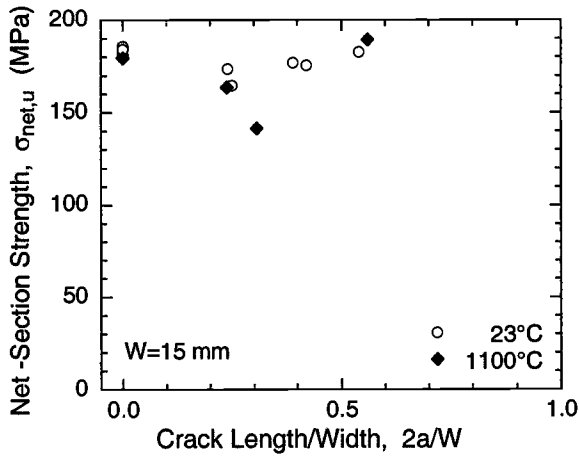


Figure 8. Notch length effect on the net-section strength ($W=15$ mm, $K_t \approx 7-9$).

The creep rupture behavior of the notched Nextel720/AS at 1100°C is compared with the unnotched behavior in Fig. 9. The notched data was obtained using specimens with the narrowest notch ($K_{t,net} \approx 7-9$). The tensile data are also shown in the figure corresponding to rupture time, $t_r \approx 1.2$ s. As discussed earlier, Nextel720/AS exhibited a slight notch-sensitivity under tensile loading at 1100°C, i.e. the notched strength is $\approx 15\%$

lower than the unnotched strength corresponding to $t_r = 1.2$ s. At stress levels lower than the notched tensile strength, Nextel720/AS exhibited substantial deformation leading to failure under sustained (creep) loading.

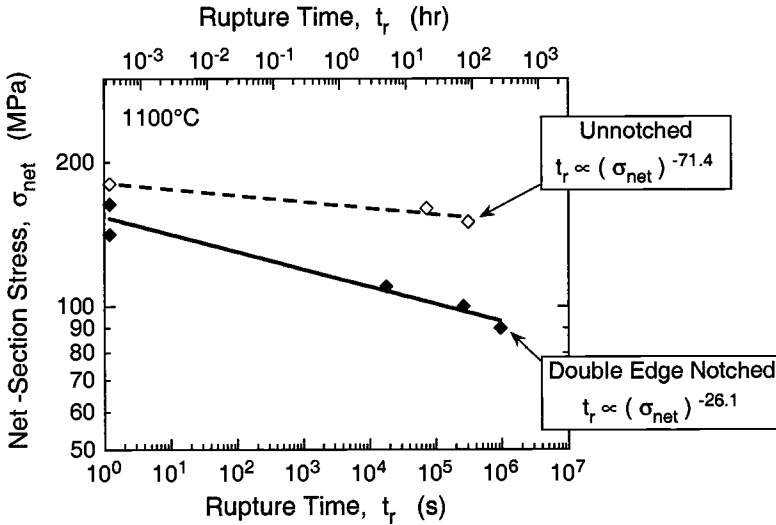


Figure 9. Notch effects on creep rupture behavior of Nextel720/AS. $K_{t,net}$ of double edge notched specimens ranges from 7 to 9.

Figure 9 shows that for the same net-section stress, the rupture times for the notched specimens were significantly lower than that for the unnotched specimens. The stress exponent for the notched specimens (≈ 25.3) is substantially lower than that for the unnotched specimens (≈ 71.4). Hence, the notch-sensitivity of Nextel720/AS at 1100°C increases significantly with increase in exposure time. These results are based on specimens with sharp notches. Tests are in progress to assess the influence of the initial K_t (hole vs. sharp notch) on the creep behavior. Fractographic studies are also in progress to understand the damage mechanisms leading to the increased notch-sensitivity under creep loading.

Summary

The fracture behavior of notched oxide/oxide CMC Nextel720/AS was investigated at 23-1200°C. Specimens with semicircular and narrow (saw-cut) double-edge notches were tested under monotonic loading in laboratory air at 23 to 1200°C, and under sustained (creep) loading at 1100°C. The results show that Nextel720/AS is notch-

insensitive at low temperatures ($\leq 1000^{\circ}\text{C}$) and $\approx 22\%$ notch-sensitive at higher temperatures ($\geq 1100^{\circ}\text{C}$) under tensile loading. At 1100°C , the notch-sensitivity increased significantly under sustained (creep) loading. For ≈ 300 hr duration of loading at 1100°C , the net-section strength decreased from 150 MPa for the unnotched specimens to 90 MPa for the notched specimen. Consequently, the stress exponent in the creep rupture time relationship decreased from ≈ 71 to ≈ 25 , when $K_{t,\text{net}}$ increased from 1.0 to $\approx 7-9$.

Acknowledgments

This research was conducted at the Materials and Manufacturing Directorate, Air Force Research Laboratory (AFRL/MLLN), Wright-Patterson Air Force Base, OH 45433-7817. Dennis Buchanan was supported under an onsite contract number F33615-98-C-5214. The authors gratefully acknowledge the assistance of Ms. Debbie Garner in conducting the experiments.

References

- [1] Zawada, L.P. and Lee, S.S., "Mechanical Behavior of CMCs For Flaps and Seals," *Proceedings of Advanced Research Projects Agency (ARPA) Advanced Ceramics Technology Insertion Program (ACTIP) Annual Review*, W.S. Coblenz, Ed., Washington, DC, August 1994.
- [2] Zawada, L.P. and Lee, S.S., "Mechanical Behavior of CMCs For Flaps and Seals," *Proceedings of Advanced Research Projects Agency (ARPA) Advanced Ceramics Technology Insertion Program (ACTIP) Annual Review*, W.S. Coblenz, Ed., Washington, DC, August 1995.
- [3] Zawada, L.P. and Lee, S.S., "Evaluation of Four CMCs For Aerospace Turbine Engine Divergent Flaps and Seals," *Ceramic Engineering and Science Proceedings*, Vol. 16, No. 4, 1995, pp. 337-339.
- [4] Lundberg, R. and Eckerbom, L., "Design and Processing of All-Oxide Composites," *Ceramic Transactions*, Vol. 58, 1995, pp. 95-104.
- [5] Mouchon, E. and Colombari, Ph., "Oxide Ceramic Matrix/Oxide Fiber Woven Fabric Composites Exhibiting Dissipative Fracture Behavior," *Composites*, Vol. 26, 1995, pp. 175-182.
- [6] Lange, F.F., Tu, W.C., and Evans, A.G., "Processing of Damage-Tolerant, Oxidation-Resistant Ceramic Matrix Composites by a Precursor Infiltration and Pyrolysis Method," *Materials Science and Engineering*, Vol. A195, 1995, pp. 145-150.
- [7] Zawada, L.P. and Lee, S.S., "The Effect of Hold Times on the Fatigue Behavior of an Oxide/Oxide Ceramic Matrix Composite," *Thermal and Mechanical Test Methods and Behavior of Continuous-Fiber Ceramic Matrix Composites*, ASTM STP 1309, M.G. Jenkins, S.T. Gonczy, E. Lara-Curzio, N.E. Ashbaugh, and L.P. Zawada, Eds., American Society for Testing and Materials, Philadelphia, PA, 1996.

- [8] Lee, S. S., Zawada, L. P., Hay, R. S. and Staehler, J., "High Temperature Mechanical Behavior and Characterization of an Oxide/Oxide Composite," *Journal of the American Ceramic Society*, Submitted for publication, October 1998.
- [9] Zawada, L.P., "Longitudinal and Transverse Tensile Behavior of Several Oxide/Oxide Composites," *Ceramic Engineering and Science Proceedings*, Vol. 19, No. 3, 1998, pp. 327-340.
- [10] Levi, C.G., Yang, J.Y., Dalgleish, B.J., Zok, F. W. and Evans, A.G., "Processing and Performance of an All-Oxide Ceramic Composite," *Journal of the American Ceramic Society*, Vol. 81, No. 8, 1998, pp. 2077-2086.
- [11] Heathcote, J.A, Gong, X.-Y, Yang, J., Ramamurty, U., and Zok, F.W., "In-Plane Mechanical Properties of an All-Oxide Ceramic Composite," *Journal of the American Ceramic Society*, Vol. 82, No. 10, 1999, pp. 2721-2730.
- [12] Wilson, D.M., Lieder, S.L., and Lueneburg, D.C., "Microstructure and High Temperature Properties of Nextel 720 Fibers," *Ceramic Engineering Science Proceedings*, Vol. 16, No. 5, 1995, pp. 1005-1014.
- [13] Yun, H.M. and DiCarlo, J.A., "Time/Temperature Dependent Tensile Strength of SiC and Al₂O₃-Based Fibers," *NASA Technical Memorandum 107370*, NASA Glenn Research Center, Cleveland, OH, USA, 1996.
- [14] Kramb, V.A., John, R., and Zawada, L.P., "Notched Fracture Behavior of an Oxide/Oxide Ceramic Matrix Composite," *Journal of the American Ceramic Society*, Vol. 82, No. 11, 1999, pp. 3087-3096.
- [15] 3M Company Product Data Sheet, 3M Ceramic Fiber Products, 3M Center-Building 207-1W-11, St. Paul, MN 55144-1000.
- [16] Hartman, G.A. and Russ, S.M., "Techniques for Mechanical and Thermal Testing of Ti3Al/SCS-6 Metal Matrix Composites," *Metal Matrix Composites: Testing, Analysis, and Failure Modes*, ASTM STP 1032, W. S. Johnson, Ed., American Society for Testing and Materials, West Conshohocken, PA, 1989, pp. 43-53.
- [17] James, M. and Swenson, D., "FRANC2D/L: A Crack Propagation Simulator for Plane Layered Structures," Kansas State University, Manhattan, KS, U.S.A., Available through the Internet at <http://www.mne.ksu.edu/~franc2d/>, 1997.
- [18] Kramb, V.A. and John, R., "Deformation Behavior Around Notches in Oxide/Oxide Ceramic Matrix Composites," To be submitted for publication, 1999.

Environmental Effects and Characterization

Samuel Graham,¹ David L. McDowell,² Edgar Lara-Curzio,³ Ralph B. Dinwiddie,³ and Hsin Wang³

The Effects of Microstructural Damage on the Thermal Diffusivity of Continuous Fiber-Reinforced Ceramic Matrix Composites

Reference: Graham S., McDowell, D. L., Lara-Curzio, E., Dinwiddie, R. B., and Wang, H., "The Effects of Microstructural Damage on the Thermal Diffusivity of Continuous Fiber-Reinforced Ceramic Matrix Composites," *Mechanical, Thermal and Environmental Testing and Performance of Ceramic Composites and Components, ASTM STP 1392*, M. G. Jenkins, E. Lara-Curzio, and S. T. Gonczy, Eds., American Society for Testing and Materials, West Conshohocken, PA, 2000.

Abstract: The relationship between microstructural damage and the thermal diffusivity of unidirectional reinforced Nicalon™-LAS II was investigated. Damage in the form of matrix-microcracking and fiber-matrix debonding was induced in the composites through monotonic and cyclic mechanical loading. The thermal diffusivity of the composites was measured in directions transverse and parallel to the fiber axis by the standard flash diffusivity method. The results showed that damage induced by mechanical loading only affected the thermal diffusivity parallel to the fiber direction. Mechanical loading followed by oxidation of the carbonaceous interface resulted in significant changes in the longitudinal and transverse thermal diffusivity of the mechanically-damaged samples. These experiments showed the important role of the interfacial conductance on both the longitudinal and transverse thermal diffusivity. The experimental data, along with finite element calculations, were used to assess the use of micromechanics-based models in predicting an effective thermal conductivity of damaged composites.

Keywords: thermal conductivity, thermal diffusivity, flash diffusivity, damage, micromechanics

Introduction

Ceramic matrix composites (CMCs) which possess weak fiber-matrix interfacial bonding are often capable of withstanding substantial amounts of load-induced microstructural damage. The weak interfacial bonding facilitates debonding and sliding of the fiber and matrix

¹ Graduate student, Woodruff School of Mechanical Engineering, Georgia Institute of Technology, Atlanta, GA, 30332-0405

² Professor, Woodruff School of Mechanical Engineering, Georgia Institute of Technology, Atlanta, GA, 30332-0405

³ Research staff, Oak Ridge National Laboratory, Oak Ridge, TN, 37831-6064.

in the presence of high local stresses. This deformation allows the reinforcement to bridge microcracks and reduce local driving forces. Ceramic composites are characterized by a distribution of damage entities rather than a single, dominant flaw. Therefore, continuum level models incorporating interaction between damage entities are necessary to describe material behavior. The development and interaction between damage entities often results in permanent changes in the integrity and performance of the ceramic composites. Such changes may limit the applicability of ceramic composites in situations where load-induced damage may occur. In general, much research attention has been placed on studying the changes in mechanical properties, mechanical behavior, and the prediction of damage evolution under mechanical loading. However, most intended applications for ceramic matrix composites involve high temperatures and rapidly changing thermal boundary conditions. In such cases, the temperature and thermal stress distributions may augment any mechanical or residual stress fields in assisting the propagation of existing flaws. Therefore, it is desirable to understand how changes in microstructural damage affect the thermal performance of these materials, in particular the thermal conductivity. A reduction in thermal conductivity may lead to higher temperatures and temperature gradients for CMCs subjected to thermal loading environments. An increase in temperature and temperature gradients may lead to a fully-coupled thermomechanical failure process and thus limit the use of these materials. Therefore, understanding the relationship between damage and thermal conductivity is important in evaluating the overall performance of the composite, as well as for predicting the behavior of thermally driven field variables (e.g., thermal stresses, displacements, heat fluxes, and temperature gradients).

The characterization of the behavior of damaged materials is a fundamental problem in damage mechanics. One of the most widely used approaches in assessing the effects of damage on material behavior is through the modeling of effective properties. For the case of thermal conductivity, effective medium theories idealize the damaged material as a homogeneous medium possessing an unknown effective thermal conductivity. Under the same boundary conditions as the damaged sample, the new homogenized material will conduct the same amount of heat for the same average temperature gradient. Based on this definition, the effective thermal conductivity is often defined as [1]

$$K_{eff} = \frac{q^*}{\Delta T / d} \quad (1)$$

where q^* is the average heat flux and $\Delta T/d$ is the applied temperature gradient.

Micromechanics models that specifically include properties of damage entities may be used to estimate contributions from the damage entities through effective thermal conductivity measurements [cf. 1-3]. This information may then be used in a numerical analysis to predict the local behavior of the composite containing damage in the presence of heat flow. However, the accuracy of estimating the properties of damage entities will depend on the validity of the models used to correlate the material behavior. Although many research studies have reported the degradation of thermal conductivity with the introduction of cracking in ceramic composites [cf. 4], little or no information is given about the damage state

found in the material. Such information is invaluable in assessing the capabilities of current models in predicting the effect of damage on effective thermal conductivity.

The purpose of this research study is to evaluate the use of micromechanics models in determining the effective thermal conductivity of composites. These models are compared to experimental data which details the degradation in thermal conductivity with a measurable damage parameter (i.e., crack density).

Experimental Approach

Unidirectional CG-Nicalon™ reinforced lithium alumino silicate glass ceramic composites (CG-Nicalon™-LAS II) were used in this study. The composites had a 36 percent fiber volume fraction and the fibers had an average radius of 7.5 μm. The samples were manufactured at the United Technologies Research Center by standard hot pressing techniques. Straight-sided tensile samples (15.24 cm long, 0.846 cm wide, and 0.254 cm thick) were cut using a diamond blade. Glass-epoxy tabs 3.81 cm long were bonded to the grip section to prevent damage during gripping. One of the surfaces of the specimen was polished in various steps up to a final step using 1-μm diamond grit in order to observe any matrix cracking on the surface. All mechanical tests were conducted in a 100 KN servohydraulic test frame equipped with a high resolution, low-contact force capacitance extensometer with a 25 mm gage length.

Mechanical loading parameters were determined by subjecting a specimen to loading and unloading to increasingly larger loads (incremental loading test). Baseline material behavior was studied by increasing the tensile load on a sample by small amounts while measuring the stress-strain response, acoustic emission, and crack density. Crack density values were obtained by averaging the number of parallel matrix cracks over a 1 cm region of the gage section measured by cellulose acetate replication. Based on the crack density evolution data obtained from this experiment (Fig. 1), monotonic loading tests were performed to stresses between 300 and 450 MPa in 50 MPa increments at a loading rate of 50 N/sec to induce various levels of transverse matrix cracking and fiber-matrix debonding. This provided a testing range which included from low to saturated crack density, while avoiding significant fiber fracture. Fatigue tests were also performed at 350 MPa and a stress ratio of $R=0.1$ up to 1×10^5 cycles to induce wear of the fiber-matrix interface. Since the majority of matrix microcracking forms during the first few cycles, most cyclic fatigue tests were limited to approximately 1×10^4 cycles. This limit allowed a finite amount of interfacial wear to occur while avoiding fatigue failures. Fatigue tests were performed at frequencies of 1 Hz and 30 Hz to investigate the effect of loading frequency on the thermal conductivity of the material.

The thermal conductivity of the samples were indirectly measured through flash diffusivity experiments. The thermal diffusivity obtained from these measurements is linearly related to the thermal conductivity by the heat capacity of the material. Thus, thermal conductivity may be calculated in a straight forward manner. Room temperature thermal diffusivity measurements were made using the flash diffusivity method [5] with heat loss correction by the method of Clark and Taylor [6]. Samples were mounted in front of a 4800 W·s⁻¹ xenon flash lamp and the rear surface was monitored by a single point liquid nitrogen cooled InSb infrared detector. The incident flash pulse was on the order of 5 ms while the scan times were on the order of 4 seconds, so finite pulse time corrections were not required. Measurements were conducted both transverse and parallel to the fiber direction. For measurements

transverse to the fiber direction, tests were performed directly on the tensile samples. For measurements parallel to the fiber axis (transverse to matrix cracks), small (2.7 mm long, 8.46 mm wide, and 2.54 mm thick) were cut from the gage section of the tensile specimens using a low speed diamond saw. Approximately 100-200 μm were removed from each end using diamond grinding disk in order to provide a uniform thickness and to remove any damage caused by cutting with the diamond saw. To further study the importance of the integrity of the fiber-matrix interface on the thermal diffusivity, samples were oxidized at 500°C for 48 hours after mechanical loading. This procedure was used to remove the carbonaceous interface which forms during the processing of the material. The coating acts as a thermal coupling of the fiber and matrix and may affect the conductivity of the material once removed.

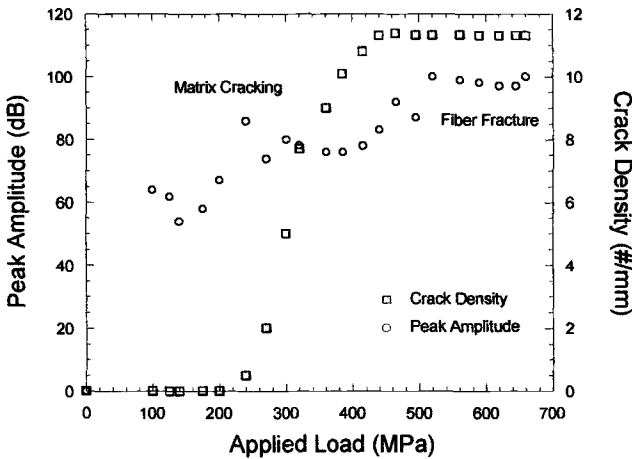


Figure 1- *Transverse matrix crack density and peak acoustic emission activity versus applied tensile stress. Matrix cracking begins above 215 MPa and saturates at about 430 MPa. Fiber fractures begin to occur above 500 MPa.*

Results

Mechanical Testing

The room temperature tensile behavior of the material studied is shown in Figure 2. The stress-strain curve exhibits non-linear behavior and hysteresis when loaded above 350 MPa. The proportional limit stress is approximately 300 MPa, although matrix cracking initiates well before this point (around 215 MPa) as shown in Figure 1. It was found that the modulus of the material with increasing stress reached a maximum decrease of 14% at 450 MPa. This behavior is attributed to a significant accumulation of transverse matrix microcracks and frictional sliding along debonded fiber-matrix interfaces. Analysis of the acetate film replicas from the tested samples showed that the linear crack density ranged from 4.1 cracks/mm at 300 MPa to 9.8 cracks/mm at 450 MPa as listed in Table 1.

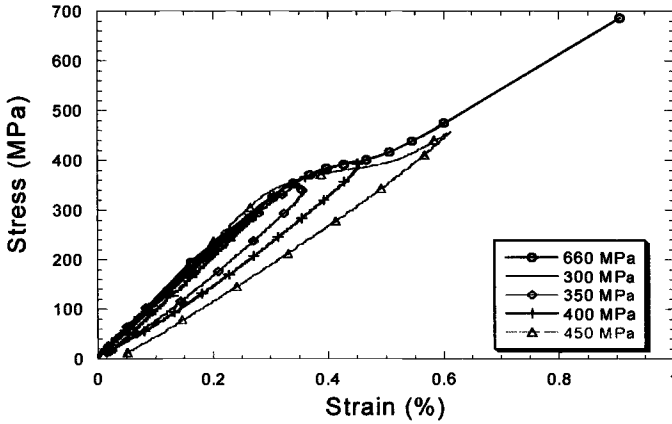


Figure 2- Stress-strain behavior of CG-Nicalon™-LAS II subjected to loading/unloading to stresses of 300 MPa, 350 MPa, 400 MPa, 450 MPa, and then to failure.

Table 1- Crack densities for monotonic and fatigue tests.

Monotonic	Maximum Load	Crack Density (cracks/mm)
	300 MPa	4.1
	350	7.5
	400	8.6
	450	9.8
<i>Fatigue (R=0.1)</i>		
1 Hz / 10,000 cycles	350	7.3
1 Hz / 100,000 cycles	350	8.1
30 Hz / 10,000 cycles	350	7.5
30 Hz / 20,000 cycles	350	7.8

The stress-strain response of CG-Nicalon™-LAS II subjected to fatigue loading at 350 MPa at 30 Hz is shown in Figure 3. A reduction in the modulus on the order of 24% resulted between the first and 10,000th cycle. In addition, a permanent hysteresis loop developed in the stress-strain response which stabilized after several loading cycles. The increase in compliance is due to a decrease in frictional shear stress caused by wear at the fiber matrix interface. The large changes in compliance between the initial and final loading cycles were approximately the same for all fatigue tests irrespective of the loading frequencies in this study. Due to the frictional heating of the samples during fatigue, the temperature response of a sample cycled at 30 Hz was monitored using a 256 by 256 focal plane array InSb infrared camera. Figure 4 shows the change in surface temperature of a sample fatigued at 350 MPa

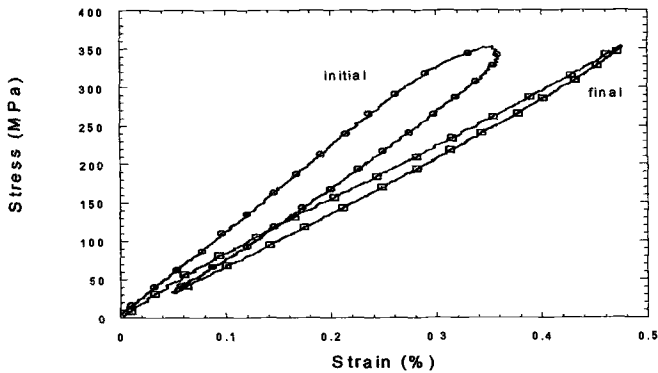


Figure 3- Stress-strain response of a sample cyclically loaded to 350 MPa at 30 Hz for 10,000 cycles. Plot shows data for the initial and final cycle.

and 30 Hz for 20,000 cycles. It is clear from these data that significant frictional dissipation occurred within the sample from the 20°C increase in temperature. This heating occurred along debonded interfacial slip zones and was an indication that irreversible internal damage had occurred in the material. Similar temperature increases have also been reported for fatigue-tested Nicalon-CAS [7]. Acetate film replication showed that the crack density of the fatigue tests were on the order of 7.6 cracks/mm for all specimens tested to $\approx 1 \times 10^4$ cycles, regardless of the loading frequency. The sample tested to 1×10^5 cycles showed a slightly higher crack density of 8.1 cracks/mm. A summary of the crack densities is listed in Table 1.

Thermal Diffusivity Tests

The room temperature thermal diffusivity of as-processed samples was found to be 0.0085 cm²/s and 0.008 cm²/s parallel and transverse to the fibers, respectively. Thermal diffusivity measurements were repeated after monotonic and fatigue loading to determine the relationship between changes in thermal diffusivity with quantified crack density changes. Thermal diffusivity values were determined by taking the average of at least 10 measurements from each condition.

Measurements transverse to the fiber axis resulted in no measurable change in thermal diffusivity in spite of irreversible changes in mechanical behavior and interfacial wear as evidenced by the specimen heating. The absence of any measurable change in thermal diffusivity may be explained by processes which occur during the fabrication of the composite. For LAS composites reinforced with Nicalon, the matrix possess a much smaller coefficient of thermal expansion than the fiber, being $10^{-6}/^{\circ}\text{C}$ and $4 \times 10^{-6}/^{\circ}\text{C}$, respectively. Previous studies on this material system [8, 9] have revealed that tensile residual stresses may develop during cool down from processing which are large enough to debond the fiber and matrix. This thermal residual stress is enhanced in regions of clustered fibers. Nonuniform distribution of fibers is typical in this composite (Figure 5) and is attributed to the manufacturing process. TEM results have also shown the existence of circumferential cracks

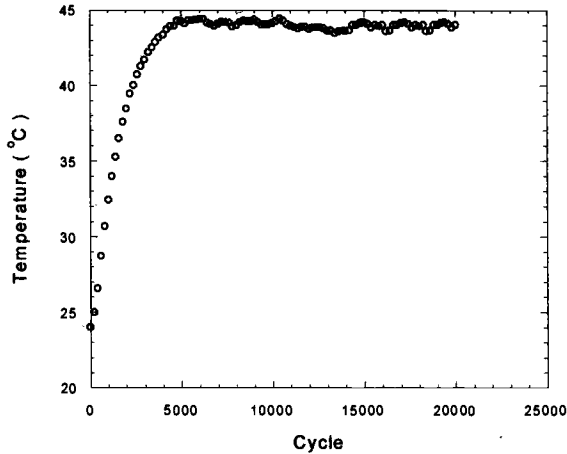


Figure 4- Change in specimen surface temperature during fatigue at 350 MPa and 30 Hz for 20,000 cycles.

between the fiber and matrix in this composite system [9]. These cracks were shown to be more prevalent in areas of clustered fibers. Therefore, it is likely that significant amounts of fiber-matrix debonding was present in the composite prior to any mechanical testing.

During the hot pressing of the material, a carbon-rich layer develops at the fiber-matrix interface. The thermal conductivity of the carbon interface is typically much higher than those of the fiber and matrix which are approximately 1.4 W/m·K and 1.6 W/m·K, respectively [10, 11]. This high thermal conductivity coating acts to thermally couple the behavior of the constituents regardless of debonding of the fiber-matrix interface. Any contacting points which exist along the interface will provide sufficient interfacial contact conductance and a negligible change in transverse thermal diffusivity after tensile loading. Thus, mechanical loading does not induce significant changes in the thermal resistance of the fiber-matrix interface above that which exists from processing.

Changes of thermal diffusivity parallel to the fiber direction (transverse to matrix cracks) are shown in Figure 6 for both monotonically and fatigue loaded specimens. Since thermal diffusivity sample dimensions were on the order of 2.5 mm, samples contained between 10-25 cracks, depending on the crack density. Thermal diffusivity results showed that small, yet measurable changes occurred in the longitudinal thermal diffusivity. With the maximum crack density being 9.8 cracks/mm, the maximum decrease in measured thermal diffusivity was on the order of 3.5%. The largest variation in thermal diffusivity changes were exhibited by samples which were monotonically loaded to large crack densities. At similar crack densities, the monotonically loaded and fatigue loaded specimens exhibited a similar degradation in thermal diffusivity. Thus, the increase in crack density dominates any other effects caused by fatigue loading to the longitudinal thermal diffusivity degradation. A much smaller variation of thermal diffusivity degradation is seen in the fatigued samples where crack densities were virtually the same. The limited changes in longitudinal thermal diffusivity may also be attributed to the thermal coupling between the fiber and matrix through the carbonaceous

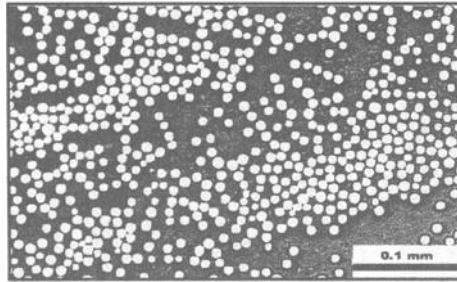


Figure 5- Optical micrograph of nonuniform fiber distribution in CG-Nicalon™-LAS II.

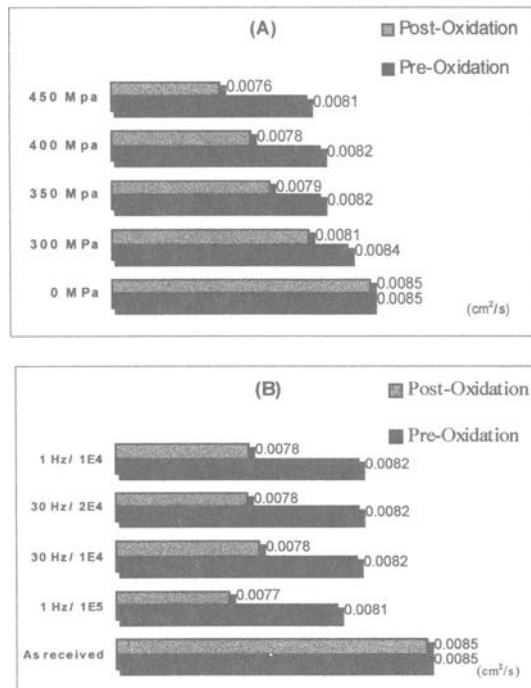


Figure 6- Changes in longitudinal thermal diffusivity for A) monotonically loaded specimen and B) specimens fatigued at 350 MPa and varying frequencies before and after oxidation.

coating. To examine this possibility, the thermal diffusivity samples were oxidized in laboratory air at 500°C for 48 hours to remove the carbon interface. The thermal diffusivity transverse to the fiber direction decreased by 26% to 0.0059 cm²/s.

Figure 6 also shows the change in longitudinal thermal diffusivity after the oxidation exposure. The decrease in thermal diffusivity was much greater after oxidation, with the

maximum change being on the order of 10%. By removing the interface, conduction paths for heat flow from the cracked matrix to the more conducting fiber are broken. This process reduces the amount of heat that the fibers carry and thus the overall thermal conductivity of the composite. Therefore, the coupling of the fiber and the matrix by a high thermal conductivity interface is shown to be a very important factor in controlling both the longitudinal as well as transverse thermal diffusivity of the composites.

Modeling

The data obtained from the mechanical loading, oxidation, and thermal diffusivity experiments were used to evaluate two micromechanics models in correlating thermal conductivity degradation. A thermal conductivity model Lu and Hutchinson derived based on shear-lag analysis was used to predict the changes in longitudinal thermal conductivity with increasing crack density [3]. In this model, the effective thermal conductivity is given by

$$K_{eff}^L = K_o \left(1 + \frac{(1 - V_f) K_m \tanh(\eta l / 2r_f) / (\eta l / 2r_f)}{V_f K_f (1 + (2K_o B_c / \eta V_f K_m) \tanh(\eta l / 2r_f))} \right)^{-1} \tag{2}$$

In Equation 2, K_o is the initial effective conductivity, K_m and K_f are the conductivities of the matrix and fiber, V_f is the fiber volume fraction, B_c is the Biot number for the matrix cracks, r_f is the fiber radius, l is the spacing between matrix cracks, and η is a function of the fiber-matrix interface conductance. Here, the Biot number is defined by $H_c r_f / K_f$ where H_c is the thermal conductance of the matrix cracks. A condition of total debonding was assumed in this model to avoid the case of a varying thermal resistance along the fiber-matrix interface. This assumption was a first approximation since the experimentally determined properties for the interfacial conductance are an average over all fibers and a distribution of debonding. The fiber-matrix interface conductance values required by this model were estimated by correlating the change in transverse thermal conductivity using the model of Hasselman and Johnson [2]

$$K_{eff}^t = K_m \left[\frac{\left(\frac{K_f}{K_m} - 1 - \frac{K_f}{r_f H_i} \right) V_f + \left(1 + \frac{K_f}{r_f H_i} + \frac{K_f}{K_m} \right)}{\left(1 + \frac{K_f}{r_f H_i} - \frac{K_f}{K_m} \right) V_f + \left(1 + \frac{K_f}{r_f H_i} + \frac{K_f}{K_m} \right)} \right] \tag{3}$$

In Equation 3, H_i is the thermal conductance of the fiber-matrix interface and is used to determine the value of η in Equation 2. In order to determine H_i and H_c , transverse thermal diffusivity data were converted to thermal conductivity by multiplying by the heat capacity of the material which was measured to be 1.68 J/cm³·K. These effective thermal conductivity values were correlated by Equation 3 by adjusting H_i . After determining H_i , H_c was estimated by Equation 2 through a single point correlation of the change in thermal diffusivity of the

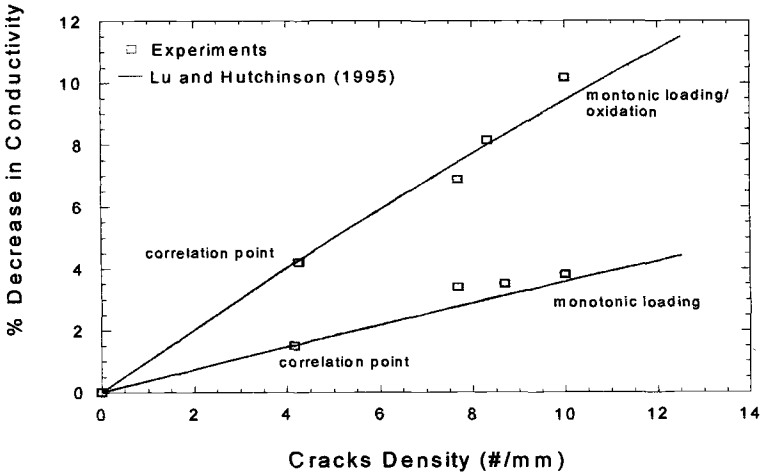


Figure 7- Correlation of thermal conductivity degradation with samples loaded to 300 MPa and prediction for higher load levels with Equation 2. Data show the degradation in thermal diffusivity of monotonically loaded samples before and after oxidation.

sample loaded to 300 MPa. These two conductance parameters were then held fixed while varying the crack density in order to correlate the change in conductivity for the remaining data. It was assumed that the damage induced in the material would have no effect on volumetric heat capacity and that it remained constant. Thus, relative changes in damage were linearly related to relative changes in thermal diffusivity. Conversion of thermal diffusivity data to thermal conductivity for predicting these relative changes is not necessary, based on this approximation.

Figure 7 shows the predicted degradation of the longitudinal thermal conductivity degradation for samples loaded above 300 MPa. The interfacial thermal conductance values were found to be $4.0 \times 10^5 \text{ W/m}^2\cdot\text{K}$ before oxidation and $4.88 \times 10^4 \text{ W/m}^2\cdot\text{K}$ after oxidation. These values of interfacial thermal conductance are consistent with values reported for other ceramic composites reported the literature [12]. The thermal conductance of the cracks was found to be $1.6 \times 10^4 \text{ W/m}^2\cdot\text{K}$ and were assumed to remain the same for both oxidized and nonoxidized samples. Based on these data, it can be seen that the combination of Equations 2 and 3 can be used to predict the change in thermal conductivity of the samples very well.

As seen in Figure 7, there is little difference in the thermal diffusivity of the samples which were tested between 350-450 MPa. However, larger differences were seen between these same samples after oxidizing the samples. The larger change in thermal diffusivity of the oxidized samples was more easily detected by the measurement technique. The small changes in thermal diffusivity observed for the unoxidized specimens were much harder to detect and may contain more error. For the unoxidized specimens, 15 - 20 measurements were made in order to verify the consistency in results.

By performing a parametric study using Equation 2, it was found that the decrease in thermal conductivity with high values of interfacial conductance varied almost linearly with crack density. However, this behavior became nonlinear once the interfacial conductance is

significantly degraded. By removing the thermal resistance of the cracks entirely, the longitudinal thermal conductivity did not change irrespective of the interfacial conductance. Thus, a complex relationship exists between the crack density and the conductance characteristics along crack and debond interfaces in controlling thermal conductivity degradation. A reduction in longitudinal conductivity is not seen in the undamaged material, which is expected. This is due to the fact that a rule of mixtures relationship holds for the longitudinal thermal conductivity of a crack-free composite even in the presence of an interfacial thermal resistance [3]. However, once matrix cracking occurs, the thermal resistance causes the most efficient path of heat conduction to be a transfer of thermal energy from the matrix to the undamaged fiber. Therefore, the coupling of the fiber and matrix plays an increasingly important role in controlling the thermal diffusivity of the material as the level of matrix cracking increases. Such behavior has been predicted analytically and numerically, and is verified by the experimental data presented here.

Discussion

The experimental data presented show a clear indication that the thermal resistance between the fiber and matrix plays an important role in controlling the longitudinal and transverse thermal diffusivity, once damage is present in the matrix. Since the model is based on shear-lag type analysis, the results presented here are limited to a simple unidirectional reinforcement geometry. Extensions to more complex geometries may be accomplished by applying this method to individual ply levels and using an averaging method similar to classical lamination theory to obtain global properties. However, this will be valid only for composite damage consisting of cracks which lie perpendicular to the fiber axis and debonding of the fiber and matrix. For more generalized damage and fiber orientations, a phenomenological continuum level model based on internal state variable theory may be necessary. Such models use tensorial characterization of the damage state and provide a general formulation for the effect of such variables on the macroscopic response [13]. Therefore, expressions for effective thermal conductivity do not have to be derived each time the fiber orientation and/or crack orientations are rearranged. However, such models require the determination of model parameters (constants) which may be difficult to determine experimentally.

Contact Resistance of a Crack with Surface Roughness

The reduction of thermal diffusivity in ceramic composites will decrease the ability of the material to transport heat under minimal temperature gradients. In the areas of localized damage, this reduction of conductivity may cause a localized temperature increase. In the event that severely nonuniform temperatures are established, local stress gradients will develop due to the local hot spots being surrounded by cooler material. Since the thermal resistance of the crack interfaces are pressure dependent, these thermal stresses will affect the value of the interfacial thermal conductance of matrix cracks. A reduction in crack resistance will lower local temperature gradients and compressive thermal stresses. Therefore, a nonlinear coupling between internal damage, temperature, and stress fields will exist in the presence of heat flow.

The effect of compressive stresses on the thermal conductivity of a material containing matrix cracks was estimated with Equation 2. A pressure dependent contact conductance model based on the contact of elastic asperities was used to predict the interfacial conductance of compressively loaded cracks [14], i.e.

$$H_c = 1.54 \frac{K_s m}{\sigma} \left(\frac{P}{H_e} \right)^{0.94} + H_o \quad (4)$$

where H_c is the thermal conductance of the crack, K_s is the harmonic mean conductivity of the two surfaces in contact, m is the contact angle, P the contact pressure, H_e is the elastic hardness, H_o is the conductance at zero pressure, and σ is the surface roughness. Values of crack thermal conductance predicted by Equation 4 were used in the model of Lu and Hutchinson. The values of H_i and H_o , in this case, were assumed to be 1×10^4 W/m·K. Crack interfacial pressures were varied between 0 and 450 MPa to illustrate a range of low to very high interface crack pressures. As an example, Figure 8 displays the decrease in thermal conductivity for the cracked composites as a function of crack density under a compressive stress of 100 MPa. The plots show the variation of the effect of an applied load across the crack faces with decreasing surface roughness. For decreasing surface roughness, the compressive stress has an increasing affect on the thermal conductance of the matrix cracks. For the case of $\sigma = 10$ nm and a load of 100 MPa, the contribution of the cracks to the degradation of conductivity is drastically reduced. The conductivity remains almost constant with increasing crack density.

For LAS composites, microcracks propagate through the matrix by cutting through grains or propagating around them. A surface roughness on the order of a fraction of the grain size is expected since the surfaces were once mated together and are constrained from large translations by the reinforcing fibers. Grain sizes for LAS typically range from 200 - 1,000 nm [15]. Therefore, the behavior of LAS composites under compressive loading is expected to fall in-between the plots for $\sigma = 100$ nm and $\sigma = 10$ nm in Figure 8. In general, a fully-coupled thermomechanical approach is needed to solve the problem of pressure dependent thermal conductivity degradation in composites.

Nonuniform Distribution

Based on the experimental data presented, it has been shown that the thermal conductance between the fiber and the matrix plays a critical role in determining the effective conductivity of ceramic composites. The accuracy of determining interfacial conductance values through the correlation of transverse thermal conductivity values relies upon the validity of the analytical model used. The majority of micromechanics models used often account for fiber distribution and interaction in a limited manner. However, fiber distribution effects on the transverse thermal conductivity of composites containing a thermal barrier resistance are not well-documented. In order to assess the applicability of Equation 3 to composites possessing various distributions of fibers, a finite element study was performed using ABAQUS.

The composite behavior was modeled using a random distribution of 24 fibers (Figure 9). A total of 6420 eight-noded quadrilateral elements were used while 683 interface

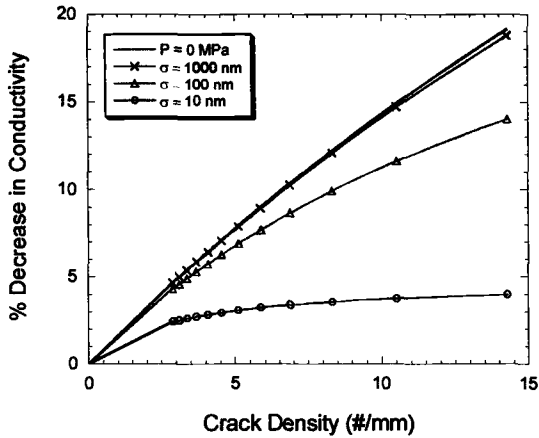


Figure 8- The effect of pressure dependent thermal resistance on the longitudinal thermal conductivity as predicted by Eqs. (1) and (4). Data shows unloaded sample versus samples with a crack pressure of 100 MPa. In this study, $B_i = 0.075$.

elements were employed to introduce a thermal resistance at the fiber-matrix interface. To approximate a representative volume element, random periodic boundary conditions were employed [cf. 16]. The fiber volume fraction was taken as 39% and the fiber matrix conductivity ratio, K_f/K_m as 10. This K_f/K_m ratio was taken higher than the ratio for CG-Nicalon-LAS material to examine a larger contrast between the fiber and matrix properties. A comparison of the Equation 3 with the finite element results is shown in Figure 10. In this case, small fiber distribution effects were observed at high and low interfacial thermal conductance values. This was manifested by a very small under prediction of the thermal conductivity at high conductance values and a slight over prediction at low conductance values. However, the values predicted by Equation 2 were within 6-10 % of the finite element solutions. The increased complexity of including fiber distribution effects into an analytical model to correct for the deficiencies of the Hasselman and Johnson approach may not be warranted for the fiber volume fractions and fiber-matrix properties studied.

Distribution effects are expected to become more prevalent as the percolation threshold is approached. At high volume fractions, greater deviations between the Hasselman and Johnson model and the actual thermal conductivity values will result. At lower volume fractions fiber distribution effects are negligible due to the averaging procedure used to define effective thermal conductivity. In relating the average heat flux to the temperature gradient applied at the boundaries, the perturbation of local field variables around fibers are smeared out. At low volume fractions, these perturbations are small and average values of local responses may be estimated by simple micromechanics approaches as used to derive Equation 3. As the percolation threshold is approached and exceeded, these fluctuations will become large enough that they affect the global average properties of the material. Therefore, it is conceivable to use a micromechanics based approach such as Equation 3, to determine an average fiber-matrix interfacial conductance value at low to moderate fiber volume fractions.

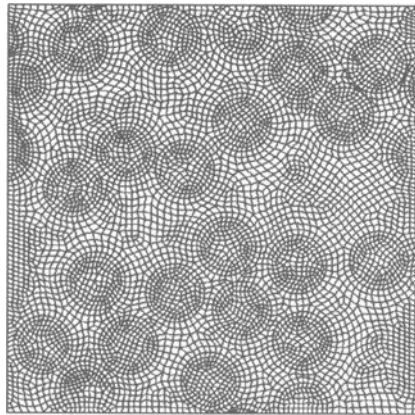


Figure 9- Random-periodic distribution of fibers for finite element study.

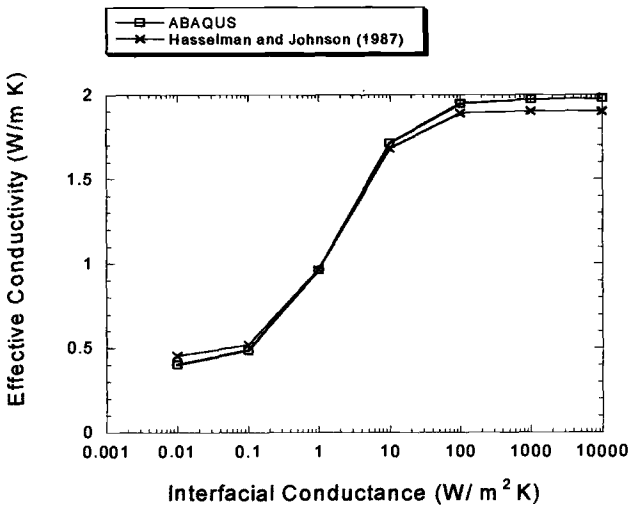


Figure 10- Comparison of finite element results for effective transverse thermal conductivity with Equation 3. Here, $K_f/K_m = 10$.

This value may then be used in a numerical scheme (i.e., finite elements) in order to study the effect of microstructural damage on the local responses through the microstructure.

Conclusions

The experimental data presented has shown that load-induced damage only affects the longitudinal thermal conductivity of CG-Nicalon™-LAS II. In the longitudinal direction, the

thermal diffusivity is controlled by a complex relationship between fiber-matrix conductivity, matrix cracking density, and the thermal conductance characteristics of the damage interfaces. The change in longitudinal thermal diffusivity is minimal due to the thermal coupling between the fiber and matrix. However, once the fiber and matrix are decoupled, much larger changes in thermal diffusivity are manifested both parallel and transverse to the fiber direction. Because of the carbonaceous interface that is generally found in Nicalon™-glass-ceramic composites, this result is expected to extend to similar material systems.

For the material system in this study, the thermal conductivity of the fiber and matrix were almost identical. In cases where the fiber conductivity is much higher than the matrix, negligible degradation in longitudinal thermal conductivity is expected for crack densities most commonly encountered. This is due to the fact that the fibers carry the majority of the heat flux and “short-circuit” the cracks. This result is in contrast to toughened monolithic ceramics where microcracking has a more detrimental effect on thermal diffusivity.

The use of the shear-lag model for modeling the degradation of longitudinal thermal conductivity showed very good results for the experimental data presented. However, this model is only applicable to composites containing unidirectional reinforcement and transverse matrix cracks. The micromechanics models of Hasselman and Johnson[2] also showed excellent prediction capabilities of transverse thermal conductivity. Although classified as a dilute concentration model, relatively reliable results for fiber volume fractions up to 40% and fiber/matrix conductivity ratios up to 10. For fiber volume fractions approaching or exceeding the percolation threshold, the actual thermal conductivity will deviate from the model since significant interaction effects will exist. By combining the shear-lag and transverse conductivity models, it is possible to estimate average conductance values for matrix cracks and the fiber-matrix interface from effective conductivity measurements. Such information will be invaluable as input into finite element solutions to study the distribution of local field variables of damaged composites subjected to heat flow. These studies may give some insight into the interaction and propagation of damage in thermally-loaded composites system.

Acknowledgment

Research sponsored by the Southeast University Research Association and the Assistant Secretary for Energy Efficiency and Renewable Energy, Office of Transportation Technologies, as part of the High Temperature Materials Laboratory User Program, Oak Ridge National Laboratory, managed by Lockheed Martin Energy Research Corp. for the U.S. Department of Energy under contract number DE-AC05-96OR22464.

References

- [1] Benveniste, Y. and Miloh, T., “The Effective Conductivity of Composites with Imperfect Thermal Contact at Constituent Interfaces,” *International Journal of Engineering Science*, Vol. 24, No. 9, 1986, pp. 1537-1552.
- [2] Hasselman, D. P. H. and Johnson, L., “Effective Thermal Conductivity of Composites With Interfacial Thermal Barrier Resistance,” *Journal of Composite Materials*, Vol. 21, 1987, pp. 508-515.
- [3] Lu, T. J. and Hutchinson, J. W., “Effect of Matrix Cracking on the Overall Thermal Conductivity of Fibre-Reinforced Composites,” *Philosophical Transactions of the*

Royal Society of London A, Vol. 351, 1995, pp. 595-610.

- [4] Hasselman, D. P. H., Venkateswaran, A., Yu, M., and Tawil, H., "Role of Interfacial Debonding and Matrix Cracking in the Effective Thermal Diffusivity of SiC Fibre-Reinforced Chemical Vapour Deposited SiC Matrix Composites," *Journal of Materials Science Letters*, Vol. 10, 1991, pp. 1037-1042.
- [5] Parker, W. J., Jenkins, R. J., Butler, C. P., and Abbott, G. L., "Flash Method of Determining Thermal Diffusivity, Heat Capacity, and Thermal Conductivity," *Journal of Applied Physics*, Vol. 32, No. 9, 1961, pp.1679-1684.
- [6] Clark, L. M. and Taylor, R. E., "Radiation Loss in the Flash Method for Thermal Diffusivity," *Journal of Applied Physics*, Vol. 46, No. 2, 1975, pp.714-719.
- [7] Holmes, J. W., Wu, X., and Sørensen, B. F., "Frequency Dependence of Fatigue Life and Internal Heating of a Fiber-Reinforced/Ceramic-Matrix Composite," *Journal of the American Ceramic Society*, Vol. 77, No. 12, 1994, pp. 3284-3286.
- [8] Sørensen, B. F., Sørensen, O. T. and Talreja, R., "Thermomechanical Fatigue of Ceramic Matrix Composites: Analysis of Mechanisms at a Microscale," *Failure Mechanisms in High Temperature Composite Materials*, ASME-AMD, Vol. 22, 1991, pp. 7-13.
- [9] Bischoff, E., Rühle, M., Sbaizero, O., and Evans, A. G., "Microstructural Studies of the Interfacial Zone of a SiC-Fiber-Reinforced Lithium Aluminum Silicate Glass Ceramic," *Journal of the American Ceramic Society*, Vol. 72, No. 5, 1994, pp. 741-745.
- [10] Hasselman, D.P.H., Johnson, L.F., Syed, R., Taylor, M. P., and Chyung, K., "Heat Conduction Characteristics of a Carbon-Fibre-Reinforced Lithia-Alumino-Silicate Glass-Ceramic," *Journal of Materials Science*, Vol. 22, 1987, pp. 701-709.
- [11] Brennan, J. J., Bentsen, L. D. and Hasselman, D. P. H., "Determination of the Thermal Conductivity and Diffusivity of Thin Fibers by the Composite Method," *Journal of Materials Science*, Vol. 17, 1982, pp. 2337-2342.
- [12] Bhatt, H., Donaldson, K. Y., Hasselman, D. P. H., and Bhatt, R. T., "Role of the Interfacial Thermal Barrier in the Effective Thermal Diffusivity/Conductivity of SiC-Fiber-Reinforced Reaction-Bonded Silicon Nitride," *Journal of the American Ceramic Society*, Vol. 73, No. 2, 1990, pp. 312-316.
- [13] Weitsman, Y., "Damage Coupled with Heat Conduction in Uni-Axially Reinforced Composites," *Constitutive Modelling For Nontraditional Materials*, ASME-AMD, Vol. 85, 1988, pp. 161-174.
- [14] Mikic, B. B., "Thermal Contact Conductance: Theoretical Considerations," *International Journal of Heat and Mass Transfer*, Vol. 17, 1974, pp. 205-214.
- [15] Bereznoi, Anatolii, *Glass-Ceramics and Photo-Sitalls*, Plenum Press, New York, 1970, pp. 282.
- [16] Ostoja-Starzewski, M., Sheng, P. Y., and Jasiuk, I., "Influence of Random Geometry on Effective Properties and Damage Formation in Composite Materials," *Journal of Engineering Materials and Technology*, Vol. 116, 1994, pp. 384-391.

M. K. Ferber,¹ H. T. Lin,¹ and J. Keiser¹

Oxidation Behavior of Non-Oxide Ceramics in a High-Pressure, High-Temperature Steam Environment

Reference: Ferber, M. K., Lin, H. T., and Keiser, J., "Oxidation Behavior of Non-Oxide Ceramics in a High-Pressure, High-Temperature Steam Environment," *Mechanical, Thermal and Environmental Testing and Performance of Ceramic Composites and Components*, ASTM STP 1392, M. G. Jenkins, E. Lara-Curzio, and S. T. Gonczy, Eds., American Society for Testing and Materials, West Conshohocken, PA, 2000.

Abstract: This paper provides a review of two recent studies undertaken to examine the oxidation behavior of monolithic SiC and SiC-SiC composites in simulated and actual gas turbine environments. In the first study, a high-pressure and high-temperature test facility was used to expose a variety of structural ceramics and ceramic matrix composites to 15% water vapor carried in an air environment at 10 atm of total pressure and 1204°C. The second study involved the exposure of a SiC-SiC combustor liner in an industrial gas turbine for approximately 2300 h at a total pressure of 10 atm and peak liner temperature of 1150°C.

In the two studies microstructural analyses were used to measure the rates of both silica scale formation and SiC recession. These experimentally determined rates were then compared with values predicted from established oxidation/volatilization models. The estimates of the temperature and pressure sensitivities of the oxidation and volatilization rate constants, required for this comparison, were obtained from the literature. For the case of the combustor liner, the recession rate of SiC was well described by the model. However, the predicted rates of scale formation in both studies were significantly lower than the corresponding experimental values. Possible reasons for this discrepancy are addressed.

Keywords: silicon carbide, silicon nitride, ceramic, composite, CFCC, parilinear oxidation, microstructural analysis

Introduction

Monolithic silicon nitride and silicon carbide ceramics as well as continuous fiber reinforced ceramics are leading candidates for use as high-temperature, structural components in advanced gas turbines [1-5]. These materials offer the following advantages over their metallic counterparts: (1) low density, (2) refractoriness, (3) adequate short-term strength, (4) good corrosion and oxidation resistance at intermediate to high oxygen partial pressures, and (5) their shape fabrication technology is mature.

The gas turbine components, where ceramics could be inserted, include

¹ Research Staff, Oak Ridge National Laboratory, P. O. Box 2008, MS 6069, Oak Ridge, TN, 37831-6069.

combustors, transition sections, hot gas ducts, vanes, and turbine blades. All but turbine blades are classified as stationary components. The materials for the stationary component require moderate hot strength, good thermal shock resistance, and shape stability. The rotating turbine blades call for higher strength materials and tolerance to impact. These components must also operate reliably for extended periods (>30000 h for industrial gas turbines).

Because the aforementioned materials are typically fabricated from SiC or Si₃N₄, their long-term reliability depends upon the formation of a passive oxide layer. This situation arises when the diffusion of the oxidant controls the oxidation and the rate of scale growth decreases with time in accordance with parabolic rate kinetics. Unfortunately, the gas turbine environment includes water vapor at pressures well in excess of 1 atmosphere. For a given temperature, oxidation of both silicon nitride and silicon carbide is increased by (1) the replacement of oxygen by water vapor and (2) an increase in the pressure of the oxidant [6-8]. In addition, the high velocities and presence of water in the environment can lead to the volatilization of the normally protective silica layer. The modeling of this behavior is discussed in the next section.

Paralinear Model

The competing processes of scale formation and scale volatilization ultimately lead to the linear recession of the ceramic substrate (paralinear kinetics).² For the case of SiC, the total change in weight is the sum of two components, Δw_1 , the increase in weight arising from the oxidation of SiC, and Δw_2 , the loss in weight arising from volatilization of the silica scale. The resulting paralinear kinetics are described by the two equations

$$t = (\alpha^2 k_p / (2k_1^2)) [-2k_1 \Delta w_1 / (\alpha k_p) - \ln(1 - 2k_1 \Delta w_1 / (\alpha k_p))] \quad (1a)$$

and

$$\Delta w_2 = -\beta k_1 t \quad (1b)$$

where t is the time, k_p is the parabolic oxidation rate constant, and k_1 is the linear rate constant for silica scale volatilization. The values of the constants, α and β , depend upon the molecular weights (MW) of the oxidation species. In the case of SiC, these constants are calculated from the following expressions

$$\alpha = MW(\text{SiO}_2) / [MW(\text{O}_2) - MW(\text{C})] \quad (2a)$$

and

$$\beta = MW(\text{SiC}) / MW(\text{SiO}_2) \quad (2b)$$

To apply these expressions to the experimental data described in this paper, the temperature and pressure sensitivities of k_1 and k_p must first be known. As discussed in Ref 8, volatilization of silica in the presence of water vapor occurs primarily by the formation of a gaseous Si(OH)₄ species. For lean burn conditions examined in Ref 8, k_1 for a number of SiC based materials was found to be well described by the expression,

² The discussion that follows including the derivations of Eqs 1 through 9 is based upon the work in Ref 6.

$$\beta k_p \text{ (mg/cm}^2 \text{ h)} = 2.04 \exp(-108 \text{ kJ/mole/RT}) v^{1/2} P_{\text{total}}^{3/2}, \quad (3)$$

where v is the gas velocity in m/sec, T is the absolute temperature (K), and P_{total} is the total pressure in atmospheres. The β term must be included in Eq 3 in order to convert the silica recession rate, represented by k_p , to the SiC recession rate.

The pressure and temperature sensitivities of k_p were recently measured in Ref 7. The data are reproduced in Figure 1. For temperatures above 1100°C, the pressure dependency is to a first approximation independent of T . Therefore, k_p can be represented by the expression

$$k_p = A \exp(-Q/RT) P_{\text{H}_2\text{O}}^N \quad (4)$$

where Q is the activation energy and N is a constant. A multi-linear regression analysis was used to simultaneously estimate A , Q , and N . The k_p data at 1100°C were not used in this fitting procedure due to a possible change in oxidation mechanism at this temperature [7]. The lines in Figure 1, which illustrate the best fit to the data, are described the equation

$$k_p \text{ (mg}^2\text{/cm}^4 \text{ h)} = 0.22 \exp(-56.7 \text{ kJ/mole /RT}) P_{\text{H}_2\text{O}}^{0.8} \quad (5)$$

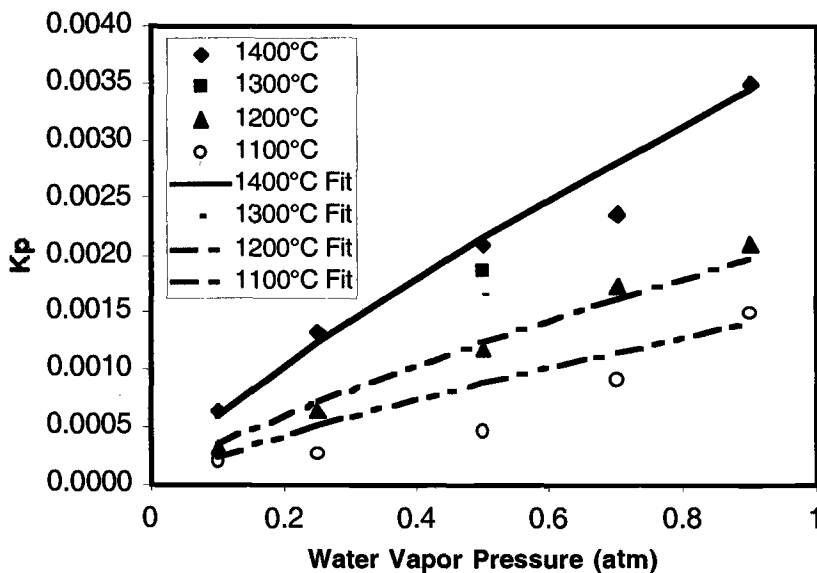


Figure 1 Pressure and temperature sensitivities of K_p generated from data found in [7]. The units for K_p are $(\text{mg}^2/\text{cm}^4 \text{ h})$. The lines represent the multi-linear regression fit of the data to the model described in the text.

Equations 1 through 5 describe parabolic kinetics in terms of the specific weight changes. The thickness of the silica scale, X_{SiO_2} , can be related to Δw_1 via the expression

$$X_{\text{SiO}_2} = \Delta w_1 \alpha / \rho_{\text{SiO}_2} \quad (6)$$

where ρ_{SiO_2} is the density of the scale. Likewise, the thickness of the scale that has volatilized, $X_{\text{SiO}_2(\text{v})}$, is given by

$$X_{\text{SiO}_2(\text{v})} = -\Delta w_2 / \beta / \rho_{\text{SiO}_2} \quad (\Delta w_2 < 0) \quad (7)$$

Finally, the thickness of the SiC recession zone is related to the total thickness of the silica scale through the expression

$$X_{\text{SiC}} = (X_{\text{SiO}_2} + X_{\text{SiO}_2(\text{v})}) \beta \rho_{\text{SiO}_2} / \rho_{\text{SiC}} \quad (8a)$$

or using Eqs 6 and 7

$$X_{\text{SiC}} = (\Delta w_1 \alpha \beta - \Delta w_2) / \rho_{\text{SiC}} \quad (8b)$$

where ρ_{SiC} is the density of the SiC. Using these equations, the relationship between silica scale thickness and time is

$$t = (k_p / (2k_1^2)) [-2k_1 X_{\text{SiO}_2} / (k_p) - \ln(1 - 2k_1 X_{\text{SiO}_2} / (k_p))] \quad (9)$$

where k_p and k_1 are the parabolic and volatilization rate constants, respectively, expressed in terms of thickness rather than specific weight.

In accordance with the parabolic model, Δw_1 and X_{SiC} increase to constant values at which time the generation of the silica scale by oxidation is balanced exactly by the loss of the scale due to volatilization. The steady-state thickness of the scale, X_{SiO_2} (ss), is given by $(k_p / (2k_1))$. The total weight of the system, $\Delta w_1 + \Delta w_2$, continues to decrease due to the linear dependence of Δw_2 upon time. The recession of the SiC also continues in accordance with Eq 8.

A major objective of this research was to compare the SiC recession and oxidation rates predicted from the parabolic model described above with available experimental data. In this case the experimental data were obtained from two recent studies [9, 10] undertaken to examine oxidation behavior of SiC based materials in simulated and actual gas turbine environments. In the first study [9], a high-pressure and temperature test facility (HPTTF) was used to expose a variety of structural ceramics and ceramic matrix composites to steam. The second study involved the exposure of SiC-SiC combustor liners (Figure 2) in field tests of a Centaur 50S natural gas turbine.³

Experimental Procedure

The materials investigated in this paper are summarized in Table 1. The composite materials were exposed as coupons in the HPTTF and as combustor liners in the field test of an industrial gas turbine. In most cases, a dense chemical vapor deposited (CVD) SiC seal coat was applied to surfaces of the SiC-SiC specimens. The monolithic sintered-alpha silicon carbide was exposed only in the HPTTF.

³ Solar Turbines, Dan Diego, CA.

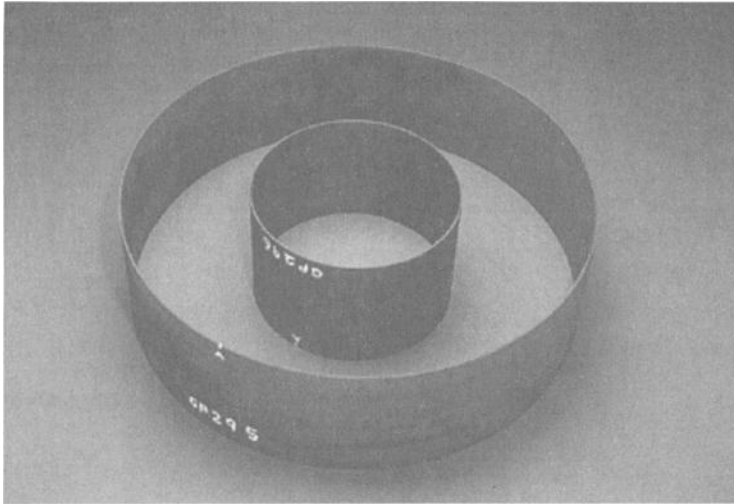


Figure 2 SiC-SiC combustor liner utilized in a field test of Solar Turbine’s Centaur 50S Natural Gas Turbine. The diameters of the inner and outer liners are 330 mm (13 in) and 762 mm (30 in), respectively.

Table 1-Summary of materials examined in this program.

Material	Supplier	Comments
SA SiC	Carborundum Company Niagara Falls, NY 14302-0832	Exposed in the HPTTF
Enhanced SiC/SiC-PyC-CG-Nicalon	AlliedSignal Composites, Inc. P.O. Box 9559 Newark, DE 19714-9559	Exposed in the HPTTF Liner field-tested for 1000 h
Enhanced SiC/SiC-PyC-Hi-Nicalon	AlliedSignal Composites, Inc. P.O. Box 9559 Newark, DE 19714-9559	Exposed in the HPTTF Liner field-tested for 2250 h
Enhanced SiC/SiC-BN-Hi-Nicalon	AlliedSignal Composites, Inc. P.O. Box 9559 Newark, DE 19714-9559	Exposed in the HPTTF Liner field-tested for 2250 h

An overview of the high-temperature, high-pressure test facility is shown in Figure 3. The primary components of the test system were the furnace, ceramic containment tubes, and gas supply system. The top-loading furnace was capable of 1550°C operation and had external dimensions of about 1.2 m on each side with a hot zone that was approximately 25 cm wide by 41 cm deep by 66 cm high. The top cover of the furnace had six holes. As shown in Figure 3a, each hole accommodated a 8.9 cm OD containment tube (SA SiC). These tubes, which were 1.2 m long, contained the test atmosphere. Approximately 28 cm of the tube extended above the top of the furnace. The

tubes were closed at the end that extends into the furnace and the open end had an expanded section to provide a sealing surface and a means to hold the tube. This expanded section accommodated a stainless steel flange that contained fittings so that a pressurized gas mixture could be fed to and removed from the tubes at pressures up to 20.4 atm (300 psia).

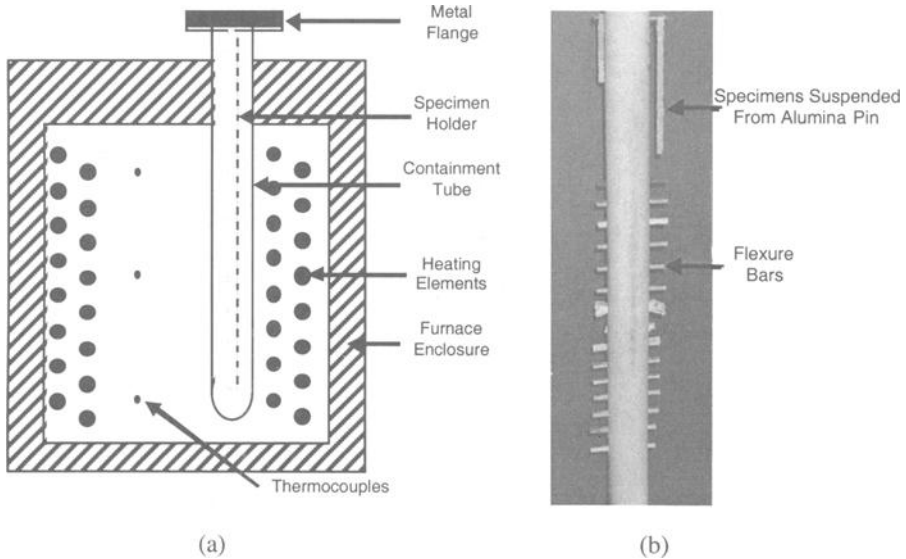


Figure 3 Key elements of the High-Pressure and Temperature Test Facility (HPTTF) including (a) schematic drawing of pressure containment tube and (b) Aluminum Oxide Specimen Holder.

An aluminum oxide hollow-tube specimen holder (Figure 3b) was suspended within each ceramic containment tube. This tube was approximately 0.9 m in length and 4.5 cm in diameter with a 0.635 cm wall thickness. In order to accommodate the specimens to be exposed, regularly spaced slots were machined into the holder. These slots could accept standard flexure bars 3 by 4 by 50 mm in size. As shown in Figure 3b, larger sized specimens were hung from aluminum oxide pins placed through the machined slots.

The gas supply system permitted a measured amount of bottled gas to be combined with a controlled amount of steam to simulate the atmosphere. For these studies, the flow of air, which was used as the carrier gas, was regulated with a mass flow controller. A pneumatically driven metering pump controlled the supply of high-purity distilled water to the evaporator. The amounts of air and distilled water supplied to the system were manually adjusted to the desired proportions (typically to maintain 15% steam). The gas mixture was fed to each of two SA SiC ceramic containment tubes used in this study.

The effluent gas from the ceramic tubes was conducted to a pneumatically driven back-pressure control valve which was controlled through a feedback loop that incorporated a pressure transducer. Water in the effluent was condensed in an air-cooled coil, collected and the volume measured. The volume of the remaining effluent gas was

determined using a calibrated flow meter.

Table 2 lists the environmental test conditions for the HPTTF. Because the gas velocity was low, volatility effects were expected to be negligible in accordance with Eq 3. Specimens in the form of either flexure bars or tensile coupons were exposed for repeated periods of 500 h. In a few instances selected specimens were exposed for a single 100 h test. After a 500 h exposure, each specimen was weighed and measured. Following removal of small sections for microstructural analysis, the specimens were weighed again and then loaded into the specimen hold for the subsequent exposure.

Table 2 Summary of exposure environments considered in this work.

Environment	Pressure (atm) Total/Water Vapor	Test Duration (h)	Velocity (m/s)	T (°C)
HPTTF	10/1.5	100	0.0005	1204
H ₂ O in Air [9]		500		
Combustor Liner [10]	10/1.5	2250	61	1150

In the case of the combustor liner field tests, the nominal gas pressure and velocity in the combustor were 10 atm (with 15% water vapor) and 61 m/sec, respectively (Table 2). The peak liner temperature was 1150°C [10]. To date, liners with an accumulated exposure time of 2250 h have been characterized.

In both of the aforementioned studies, the measurement of weight changes associated with oxidation and volatilization of the silica scale proved either unreliable in the case of the HPTTF exposure (due to spallation of the scale upon cooling) or impractical in the case of the combustor liner. In order to overcome this problem, scale thickness and SiC recession for the specimens exposed in the HPTTF were measured from polished cross sections using an optical microscope equipped with calibrated x-y stages. The resolution of these measurements was better than 1 μm . In the case of the combustor liners, the rate of recession of the CVD SiC seal coat, which was always present on the as-fabricated liners, was determined by noting the approximate time required for the first breach of the seal coat. The complete penetration of the seal coat was identified during periodic boroscope inspections by the appearance of a white scale. In the present study, the times to breach the seal coats were determined for three liners each having different initial seal coat thicknesses. Consequently a plot of initial thickness versus penetration time was used to estimate the rate of seal coat recession.

Results

HPTTF Data

Scanning electron micrographs of polished cross sections of SA SiC and CVI SiC-SiC materials are shown in Figures 4 and 5, respectively. The scales on both materials consisted of a thick defective (cracked and porous) silica layer, which was identified by x-ray diffraction as cristobalite. In the case of the SiC-SiC composite, a thin amorphous silica layer was present at the surface of the CVD SiC seal coat (Figure 6). The thickness of the amorphous layer stayed constant at 4-6 μm throughout the exposure. Two mechanisms may have been responsible for the extensive vertical cracking observed in the silica layer. The first, which occurred at temperature, involved the transformation of the amorphous scale (density = 2.21 g/cm^3) to the crystalline silica (density = 2.37 g/cm^3).

The second mechanism, which occurred upon cooling, was the conversion of β cristobalite to α cristobalite. The volume decrease associated with both processes would lead to the generation of in-plane tensile stresses.

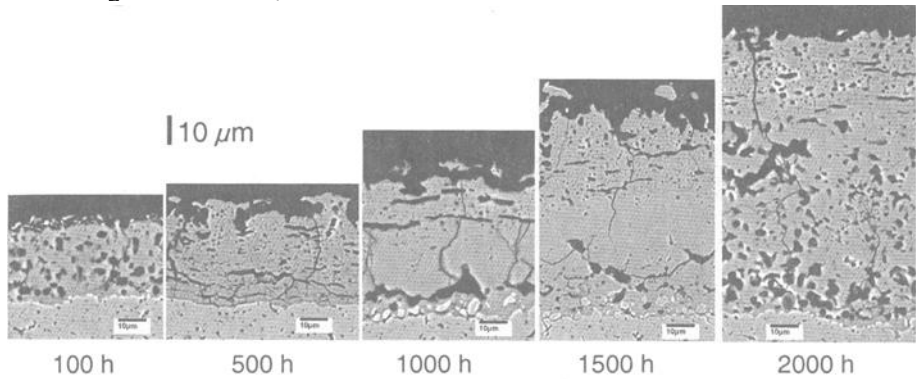


Figure 4 Scanning electron micrographs of a SA SiC specimen exposed in the HPTTF.

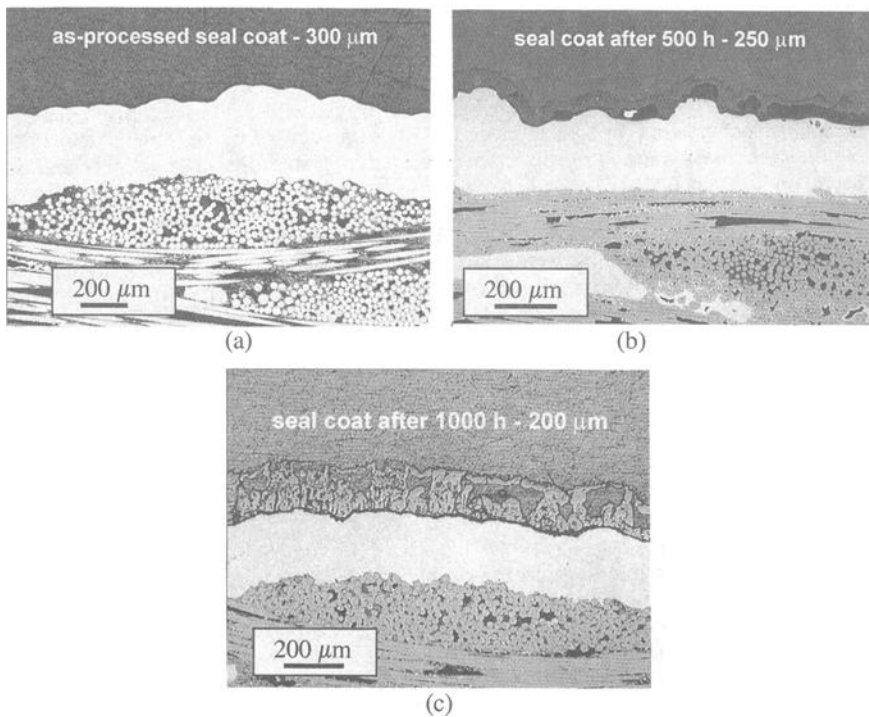


Figure 5. Scanning electron micrographs of a SiC-SiC specimen exposed in the HPTTF for (a) 0, (b) 500, and (c) 1000 h.

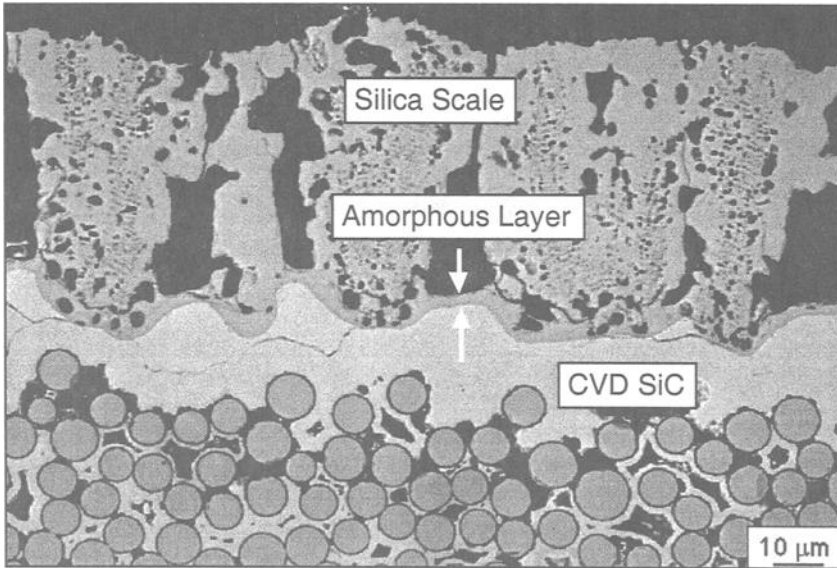


Figure 6 Thin amorphous silica layer.

In addition to the cracks, extensive porosity was also observed. The most likely source of this porosity was the evolution of gas during the oxidation of the SiC. Image analysis of the scale microstructures (excluding the cracks) further revealed that the area fraction of pores increased with time. Given the extensive damage present in the outer silica scale, its effectiveness as a barrier to oxygen (or water vapor) diffusion may have been limited. As discussed below this observation is consistent with the fact that parabolic oxidation rate constant required to fit the experimental oxidation data was much larger than the value predicted from Eq 5.

The recession and oxidation data obtained for the dense SA SiC in the HPTTF exposure are shown in Figure 7 (symbols). Because the gas velocities in the HPTTF are relatively low, volatilization of the silica scale is negligible. As a result, the scale thickness does not reach a steady-state value but continues to increase with time. Using the HPTTF environmental data in Table 2, the values of k_i and k_p were estimated from Eqs. 3 and 5, respectively (see Table 3). These numbers were then used to calculate the silica thickness and SiC recession as a function time in accordance with Eqs 1, 6, 7, and 8. The predicted trends (solid lines in Figure 7) significantly underestimate the experimental data.

It must be emphasized that the extrapolation of the oxidation data in Ref 7 to the conditions in the HPTTF is based upon the assumption that silica scale morphology is independent of environment. Because the scales formed in the HPTTF were heavily damaged, their effectiveness as an oxidation barrier was reduced significantly over that in Ref 7. This difference may be accounted for by increasing the value of the oxidation rate constant. Although a much better fit is obtained if k_p is increased by a factor of 10 (Figure 8), the predicted curves are parabolic while the actual data exhibit more of a linear

dependence upon time. There are number of possible mechanisms that could give rise to linear oxidation (and recession). The first concerns the effectiveness of the silica scale as a diffusion barrier. In particular, image analysis of the SA SiC micrographs showed that the area fraction of pores increased with time. Assuming that the porosity reduces the effectiveness of the silica as a diffusion barrier, this behavior would counter the tendency for parabolic scale formation. A similar role of porosity has been discussed in Ref [7].

Table 3 Summary of rate parameters for the two environments.

Environment	k_p (mg ² /cm ⁴ h) Eq. 5	k_1 (mg/cm ² h) Eq. 3
HPTTF H ₂ O in Air	3.0×10^{-3}	3.28×10^{-4}
Gas Turbine Combustor	2.5×10^{-3}	8.2×10^{-2}

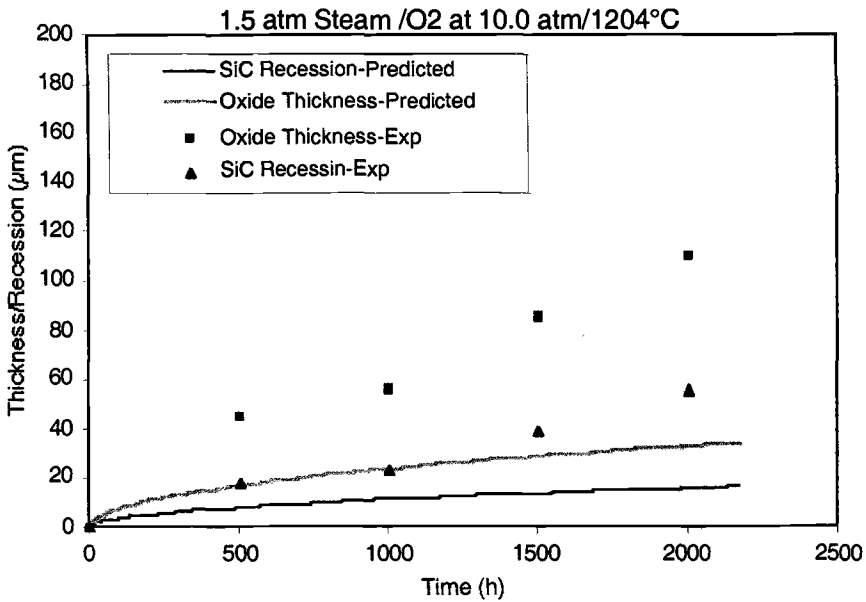


Figure 7 Comparison of SiC recession and oxidation data obtained in the HPTTF with model predictions.

The second mechanism for the linear time dependencies of SiC oxidation and recession in the HPTTF concerns the rate controlling process. As discussed in Ref 11, oxidation of SiC involves three sequential steps: (1) diffusion of the oxidant to the silica-ceramic interface, (2) oxidation reaction at the interface, and (3) diffusion of the gaseous reaction products from the interface to the free surface. Parabolic oxidation kinetics will

only prevail if either Steps 1 or 3 are rate limiting. At ambient pressures the diffusion of the oxidant through the scale is generally assumed to be the slow step. An increase in the oxidant pressure increases the transport rate through the scale and thus k_p in accordance with Eq 4. If the oxidation reaction (Step 2) is somewhat insensitive to pressure as suggested by limited data in Ref 7, an increase in oxidant pressure may cause Step 2 to become rate limiting.

Combustor Liner Data

The SiC-SiC combustor liners utilized in the field tests of Solar Turbine’s Centaur 50S natural gas turbine had protective CVD SiC seal coats. The combined effects of high water vapor pressure and high gas velocity led to relatively high SiC recession rates. Once the seal coat was breached, a white scale formed quickly due to the extensive oxidation of the underlying composite (Figure 9). The subsequent microstructural analysis of the liner showed that the oxide scale that formed along the surface exposed directly to the combustion environment reached a steady-state thickness of approximately 5 μm (Figure 10). In order to estimate the rate of seal coat recession, the time at which the seal coat was first breached was determined from periodic boroscope inspections of the turbine. It was assumed that the initial breach of the seal coat occurred in the highest temperature region of the liner (taken as 1150°C). Data for three liners having different initial seal coat thicknesses are shown in Figure 11.

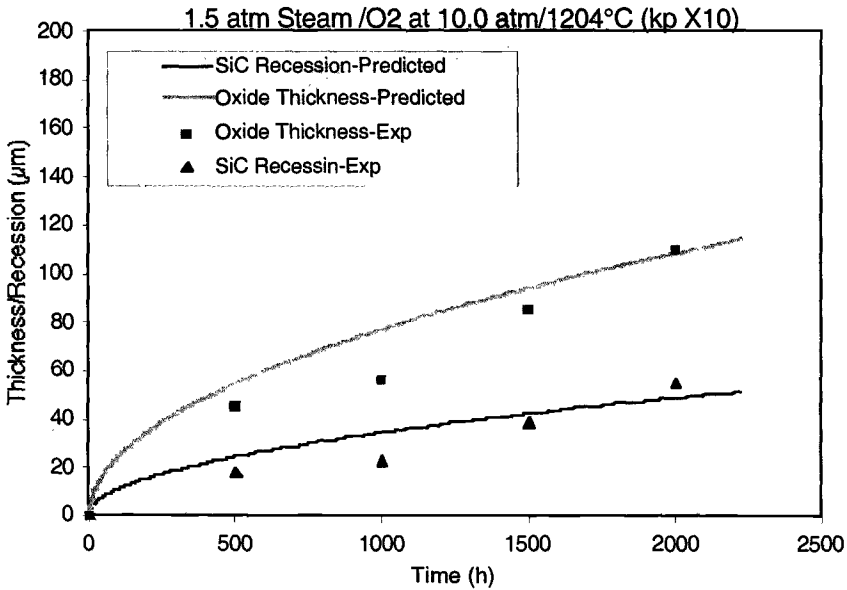


Figure 8 Effect of increasing k_p upon model predictions.

Using the environmental data in Table 2, the values of k_i and k_p were estimated from Eqs 3 and 5, respectively (see Table 3). The predicted SiC recession curve (see Figure 11) slightly over-predicts the experiment recession data. The most likely reason for this discrepancy is that the combustor liner was not continually operated at the peak conditions given in Table 1. Therefore, the estimated value of k_i , which controls the recession rate in the case of the combustion environment, represents the maximum value rather than an effective average. The steady-state thickness of the silica scale, which was also estimated from the model, was $0.66 \mu\text{m}$ (Figure 11), which is well below the value measured experimentally. As in the case of the HPTTF results, much better agreement was obtained by increasing k_p by a factor of 10. In this case, the predicted steady-state thickness was $5.5 \mu\text{m}$. Because SiC recession is controlled by the k_i value, the predicted recession curve was not affected by increasing k_p .

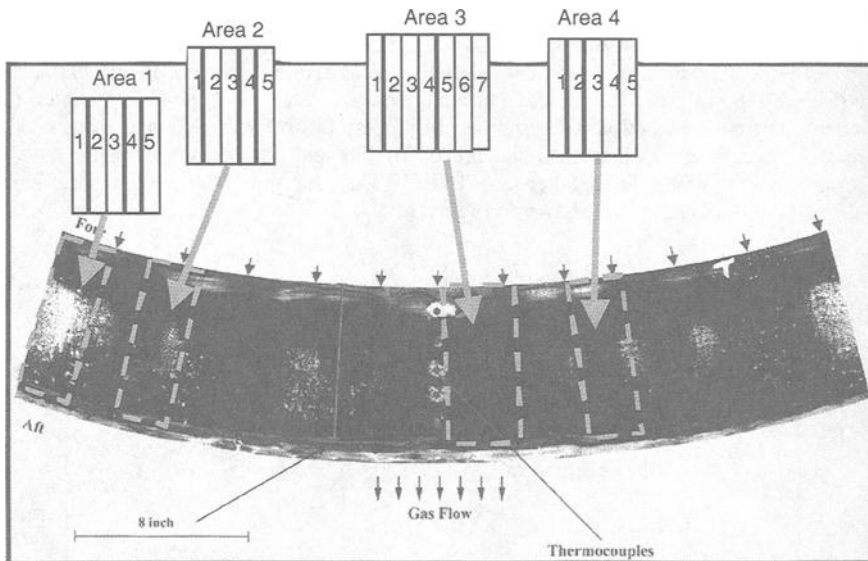


Figure 9 Panoramic view of surface of inner liner exposed for 2250 h. The white patches represent regions in which the seal coat was breached. Strips from 4 areas (designated 1-4) were sectioned for microstructural and mechanical property measurements.

The model may be tested further by predicting the thickness of the oxide scale formed along the internal SiC coated surfaces of the composite. Because these surfaces were isolated from the high gas velocities, volatilization effects were negligible ($k_i \ll 0$). As shown in Figure 12, the thickness after 2250 h was approximately $75 \mu\text{m}$, which is in fair agreement with the value of $100 \mu\text{m}$ predicted assuming that k_p is a factor of 10 higher than the value given in Table 3.

Surface Exposed to
Combustion Environment
Oxide Thickness = 5 μm

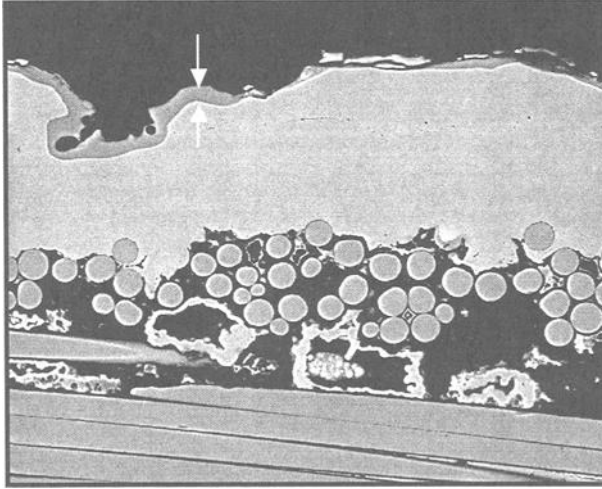


Figure 10 Cross-section of inner liner showing oxide scale on the CVD seal coat.

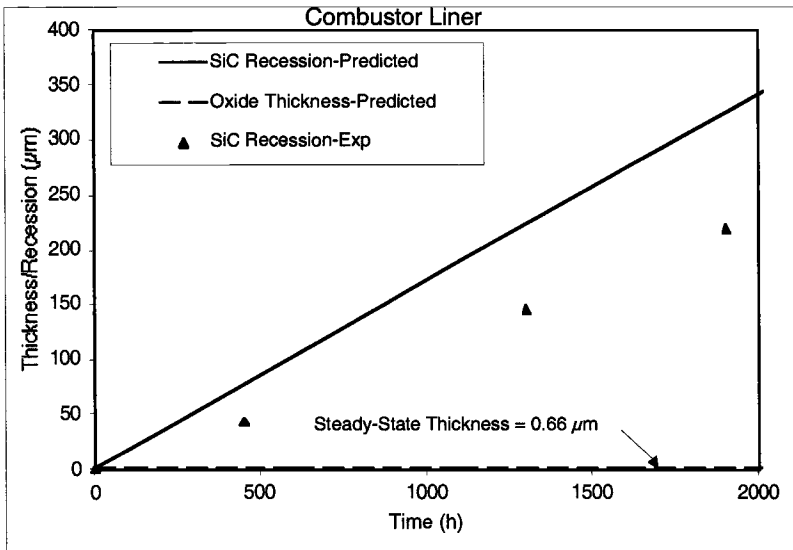


Figure 11 Comparison of CVD SiC recession and oxidation data obtained in the combustion environment with model predictions.

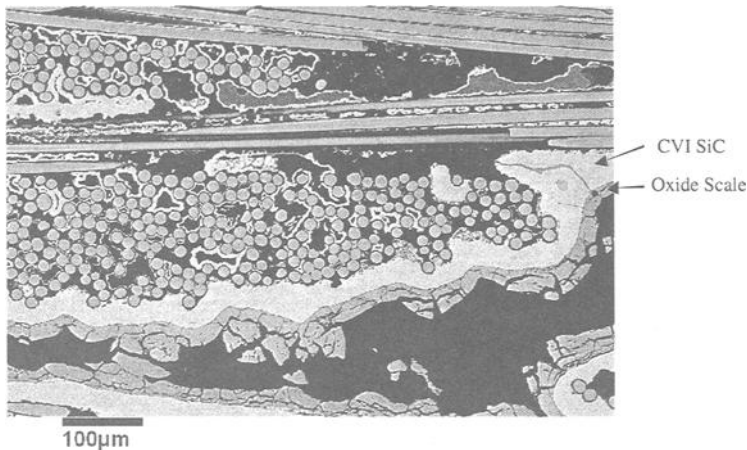


Figure 12 Cross-section of inner liner showing oxide scale on the internal SiC surfaces.

Conclusions

The exposure of SiC based ceramics in the HPTTF led to rapid oxidation. The silica scales were extensively damaged as reflected by the presence of cracks and pores. In terms of the porosity, the extent of this damage increased as the scale grew. In the case of the combustion environment, the high gas velocities lead to the volatilization of the silica scale.

For the case of the HPTTF tests, volatility effects could be neglected. The rate of oxidation was much higher than that predicted by extrapolating the data generated in Figure 1. This difference could in part be attributed to the ineffectiveness of the damaged silica scale as a diffusion barrier. Much better agreement was obtained by increasing the extrapolated value of the parabolic rate constant by a factor of 10.

The application of the paralinear oxidation model to experimental combustor liner results provided a good estimate of the SiC recession rate. However, the predicted value of the steady-state silica scale thickness, which depends upon the rate constants for both parabolic oxidation and linear volatilization, was significantly lower than the experimental value. Once again better agreement was obtained by increasing parabolic rate constant by a factor of 10. These results suggest that the silica scale volatility is fairly well described by Eq 3 while the oxidation data (Figure 1) tend to underestimate the parabolic rate constant when extrapolated to higher pressures.

Acknowledgements

This research was sponsored by the U. S. Department of Energy's Office of Industrial Technologies for the Advanced Turbine Systems Program, under contract DE-AC05-96OR22464 with Lockheed Martin Energy Research Corporation.

References

- [1] Anson, D., Ramesh, K. S., and DeCorso, M., "Application of Ceramics To Industrial Gas Turbines"; Volume 1 Technology Background; Volume 2 Economics, Market

Analysis, and R&D Plan DOE/CE/40878-1&2; Battelle Columbus March 1991.

[2] Helms, H. E., Johnson, R. A., and Groseclose, L. E., "AGT 100-Advanced Gas Turbine Technology Development Project," pp. 137-55 in Proceedings of the Twenty-Third Automotive Technology Development Contractors' Coordination Meeting P-165, Society of Automotive Engineers, Warrendale, PA, March 1986.

[3] van Roode, M., "Ceramic Retrofit Program," pp. 77-93 in Proceedings of the Joint Contractors Meeting: FE/EE Advanced Turbine Systems Conference FE Fuel Cells and Coal-Fired Heat Engines Conference, DOE/METC-93/6132, August 1993.

[4] Carruthers, D. and Lindberg, L., "Critical Issues for Ceramics for Gas Turbines," pp. 1258-1272 in Third International Symposium on Ceramic Components and Materials for Engines, edited by V. J. Tennery, American Ceramic Society, Westerville, Ohio, 1988.

[5] Haley, P. J., Holtman, R. L., Groseclose, L. E., Hilpisch, S. J., and Bell III, A. H., "Advanced Turbine Technology Applications Project [ATTAP]," pp. 19-29 in Proceedings of the Twenty-Ninth Automotive Technology Development Contractors' Coordination Meeting, Society of Automotive Engineers, Warrendale, Penn., June 1992.

[6] Opila, E. J. and Hann, Jr., R. E., "Paralinear Oxidation of SiC in Water Vapor," *Journal American Ceramic Society*, Vol. 80, No. 1, pp. 197-205, (1997).

[7] Opila, E. J., "Variation of the Oxidation Rate of Silicon Carbide with Vapor Pressure," *Journal American Ceramic Society*, Vol. 82, No. 3, pp. 625-36, (1999).

[8] Smialek, J. L., Robinson, R. C., Opila, E. J., Fox, D. S., and Jacobson, N., "SiC and Si₃N₄ Recession due to SiO₂ Scale Volatility Under Combustor Conditions," *Advanced Composite Materials*, Vol. 8, No. 1, pp. 33-45, (1999).

[9] Keiser, J. R., Howell, M., and Pint, B. A., "Long-Term Corrosion of Ceramics in High Temperature Steam Environments," unpublished data, Oak Ridge National Laboratory, June 1998.

[10] More, K. L., Tortorelli, P. F., Ferber, M. K., Walker, L. R., Keiser, J. R., Brentnall, W. D., Miriyala, N., and Price, J. R., "Exposure of Ceramics and Ceramic Matrix Composites in Simulated and Actual Combustor Environments," to be presented at ASME TURBO EXPO '99, June 7-10, 1999, Indianapolis, Indiana.

[11] Luthra, K. L. "Some New Perspectives on Oxidation of Silicon Nitride and Silicon Nitride," *Journal American Ceramic Society*, Vol. 74, No. 5, pp. 1095-1103, (1991).

Edgar Lara-Curzio¹ and M. Singh²

The Time-Dependent Deformation of Carbon Fiber-Reinforced Melt-Infiltrated Silicon Carbide Ceramic Matrix Composites: Stress-Rupture and Stress-Relaxation Behavior in Air at 1000°C

Reference: Lara-Curzio, E. and Singh, M., "The Time-Dependent Deformation of Carbon Fiber-Reinforced Melt-Infiltrated Silicon Carbide Ceramic Matrix Composites: Stress-Rupture and Stress-Relaxation Behavior in Air at 1000°C," *Mechanical, Thermal and Environmental Testing and Performance of Ceramic Composites and Components, ASTM STP 1392*, M. G. Jenkins, E. Lara-Curzio, and S. T. Gonczy, Eds., American Society for Testing and Materials, West Conshohocken, PA, 2000.

Abstract: The stress-rupture and stress-relaxation behavior of carbon fiber-reinforced melt-infiltrated silicon carbide composites was investigated in ambient air at 1000°C. It was found that the compliance of the material increases continuously with time when subjected either to a constant composite stress or strain in air at 1000°C. The changes in compliance are explained based on the oxidation of the fiber coating, and on the oxidation, loss of cross-sectional area and rupture of the reinforcing fibers. In the case of stress-rupture, the load previously carried by failed fibers is redistributed to their surviving neighboring fibers inducing further fiber failure. During stress-relaxation, fiber failure is reflected directly on the reduction of the load carried by the composite.

By monitoring the expansion of the specimens during heating, prior to the application of the stress or strain, it was possible to determine the liner coefficients of thermal expansion of the material between 200°C and 1000°C.

Keywords: ceramic-matrix composites, stress-rupture, stress-relaxation, oxidation, thermal expansion, melt infiltration, silicon carbide, carbon

Introduction

Carbon/carbon composites have found widespread use in the aerospace industry in such applications as aircraft disk brakes, atmospheric reentry vehicles, and rocket nozzles, to mention just a few. However, despite their outstanding thermal and mechanical properties, carbon/carbon composites have two major disadvantages: their cost and their lack of oxidation resistance in air at temperatures above 300°C.

For example, to achieve adequate densification with the two most widely used routes for the synthesis of carbon/carbon composites, namely chemical vapor infiltration (CVI) and polymer impregnation and pyrolysis (PIP), long infiltration times and multiple

¹ Group leader, Mechanical Characterization and Analysis Group, Oak Ridge National Laboratory, P. O. Box 2008, Oak Ridge, TN, 37831-6069.

² Senior scientist, Dynacs Engineering Co., NASA Glenn-Research Center, Cleveland, OH 99999

impregnation and pyrolysis cycles are required, respectively. These in turn represent the major source of high production costs.

Because of its excellent oxidation resistance silicon carbide has long been considered a good candidate to replace carbon as the matrix in carbon/carbon composites. Recently techniques have been developed to densify silicon carbide bodies using the melt-infiltration approach [1]. In this case, the silicon carbide matrix is synthesized by the infiltration of molten silicon or silicon alloys into a fiber preform that previously had been impregnated with carbon-based resins. The reaction between silicon and carbon results in the formation of silicon carbide and controllable amounts of silicon species, while capillary forces in the liquid phase are responsible for the complete infiltration of the fibrous preform. The main advantages of this route to the synthesis of silicon carbide over conventional approaches (i.e., chemical vapor infiltration) are low cost, short processing times and the possibility of achieving full densification.

One of the objectives of this paper is to compare the performance of carbon fiber-reinforced melt-infiltrated silicon carbide composites (C/SiC-MI) with that of carbon fiber-reinforced chemical vapor infiltrated silicon carbide composites (C/SiC-CVI). In particular, their durability will be compared in air at elevated temperatures as determined by stress-rupture testing.

Effinger et al. determined that a C/SiC-CVI composite (pyrolytic graphite-coated T-300 carbon fibers) maintains its tensile strength of 550 MPa up to 800°C in air and that its strength decreases at higher temperatures to a value of 375 MPa at 1400°C [2]. The loss of strength was attributed to fiber oxidation as a result of diffusion of oxygen through matrix microcracks. At the same time, the tensile elastic modulus of the material was found to increase with temperature reaching a maximum value of 140 GPa at 1300°C from 100 GPa at room temperature.

Halbig et al. investigated the stress-rupture behavior of C/SiC-CVI composite (pyrolytic graphite-coated T-300 carbon fibers) in air at temperatures between 350°C to 1500°C and at stresses of 69 MPa and 172 MPa [3]. Halbig and co-workers found that the life of specimens tested at temperatures of 750°C and above was less than 2 hours and that specimens tested at lower temperatures did not fail, but lost more than one half of their original strength after 25 hour-long tests. Records of the strain histories of these tests showed that the compliance of the specimens increased continuously with time and that there was accelerated deformation prior to failure.

Lamouroux and Camus studied the oxidation behavior of C/SiC-CVI composites (pyrolytic graphite-coated PAN-derived graphite fibers) [4]. They found that oxygen reaches the interior of the composite by diffusion through matrix cracks and that these cracks can form both by the application of stress and from processing as a result of the mismatch in the thermoelastic properties of the constituents. They also found that the reaction of the environment with the fibers results in fiber oxidation and in an effective loss of material. These authors also studied the effect of thermal treatments in air between 700°C and 1400°C, on the room temperature tensile properties of the same composite material [5]. They found that morphological changes in the material could be related to the observed changes in the mechanical properties. After treatments at temperatures below 800°C it was found that the fibers that were located near the matrix cracks exhibited notches that translated into drastic loss of tensile strength of the composite. The notching oxidation of the fibers was less extended in air when compared to exposures in dry oxygen. It was also found that the carbon interface is preferentially consumed near the microcrack tips where free surfaces are present and that locally uncoated fibers get oxidized rapidly in these regions in which the carbon coating has been removed. Exposures to air at temperatures above 1000°C also resulted in a loss of strength but less dramatic than the effect of exposure at intermediate temperatures, although there was evidence of damage of the fibers located at the outer layers of the composite. Degradation of the mechanical properties after exposure at low temperatures was controlled by reaction kinetics between carbon and oxygen whereas during exposure at intermediate temperatures the process was controlled

by the diffusion of the gaseous species through the cracked SiC coating. In the latter case degradation was not uniform, decreasing gradually from the surface inwards into the specimen. At higher temperatures oxidation of the SiC outer coating and the formation of SiO₂ resulted in the sealing of the interior of the composite [6].

Recently Lebrun et al. developed a model to predict the life of carbon fiber-reinforced CVI-SiC matrix composites when subjected to stress-rupture at elevated temperatures [7]. It was determined that the life of this material is controlled by the oxidation kinetics of the constituents and by the fraction of fiber breaks. Model predictions were in good agreement with experimental data obtained from the evaluation of minicomposites.

Another purpose of this paper is to characterize the time-dependent behavior of C/SiC-MI composites when subjected to stress-relaxation conditions in air at elevated temperatures. Although stress-rupture tests are typically used to assess the durability and reliability of materials, often stresses arise as a result of thermal gradients and hence are driven by imposed strains. Therefore, it was decided to evaluate the durability of C/SiC-MI when subjected to constant applied strains and determine the relationship between these two modes of testing. In the next sections the experimental procedures are described in detail, followed by results and discussion of stress-rupture and stress-relaxation tests.

Experimental

Material

The material investigated consisted of sixteen layers of T-300 carbon fiber plain weave. The fibers were coated -via chemical vapor deposition- with a thin layer of pyrolytic carbon, followed by an overcoat of silicon carbide to prevent reaction of the fibers during matrix densification. The matrix was densified by infiltrating the coated fiber preform with a molten silicon alloy that reacted with a carbonaceous resin mixture that had been applied to the fabric. The final fiber volume fraction was 36-38%. Figure 1 shows the cross-sectional area of one specimen.

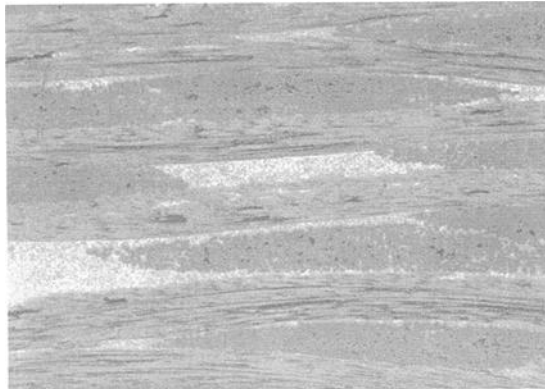


Figure 1 - *Optical micrograph of C/SiC-MI composite (100X).*

Procedure

The test specimens were machined into shoulder-loaded coupons using conventional diamond grinding techniques. A set of in-house water-cooled grips were used to transfer the load to the specimens and the grips were connected to the load train using two self-aligning couplers to minimize unwanted bending strains.

The tests were performed in ambient air (45-55%RH) and 1000°C in accordance with ASTM Test Method for Creep and Creep Rupture of Continuous Fiber-Reinforced Ceramic Composites Under Tensile Loading at Elevated Temperatures (C1337) using an electromechanical universal testing machine equipped with a resistance-heated furnace with MoSi₂ heating elements. Specimen deformation was monitored using a low-contact force capacitance extensometer over a gauge length of 25 mm.

The specimens were heated to the test temperature in 15 minutes and then were allowed to reach thermal equilibrium which was determined by the constancy of the strain with time. To allow for the thermal expansion of the specimen during heating, a constant load of 100 N was maintained in the load train. After achieving thermal equilibrium, the specimens were mechanically loaded at a constant rate of 1 MPa/s to the test stress. For stress-rupture tests, the load was maintained at a constant level thereafter for the duration of the test, while for stress-relaxation tests, once the test stress was reached, the control of the machine was changed from load-controlled to strain-controlled using the extensometer as the feedback signal. The strain at that point was maintained at a constant level for the duration of the test and the load was monitored with time. The tests were concluded when the specimens failed, at which point the furnace was turned off and the specimens allowed to cool down with the furnace.

Results

Stress-Rupture

Figure 2 shows the stress and strain histories of a stress-rupture test carried out at 1000°C and at a test stress of 69.5 MPa. The plot is divided into three stages. Stage I corresponds to the heating stage in which the specimen was heated with the furnace working at 100% power until reaching the set-point of 1000°C. During this stage a load of 100 N, which translates into approximately 5 MPa, was maintained at a constant level to activate the self-aligning couplers and to allow for the free expansion of the specimen. At the end of the heating segment the specimen was allowed to equilibrate thermally, which typically was achieved within 15 minutes. By cross-plotting the strain versus temperature data (see Figure 3) it was possible to determine the thermal expansion of the material which could be best described by a second-order polynomial of the form

$$\epsilon_{thermal} (\%) = -0.0047 + 2.069 \times 10^{-4} T + 6.919 \times 10^{-8} T^2 \quad (1)$$

which yields values for the linear coefficient of thermal expansion as follows

$$\alpha_{20-600} = 2.53 \text{ ppmK}^{-1}$$

$$\alpha_{400-800} = 2.8 \text{ ppmK}^{-1}$$

$$\alpha_{600-1000} = 3.2 \text{ ppmK}^{-1}$$

Although the expansion of the extensometer arms contributed to the total measured displacement and was not accounted for in the values given above, it is expected that this contribution introduces a very small error.

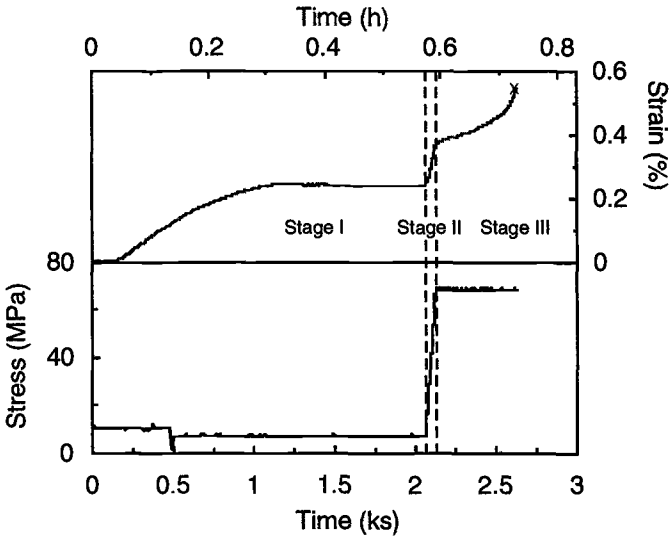


Figure 2- Strain and stress histories of a stress-rupture test conducted at 1000°C and a stress of 69 MPa. Stage I corresponds to the heating stage. Stage II corresponds to mechanical loading, and in Stage III the composite stress is maintained constant while the strain increases continuously until failure.

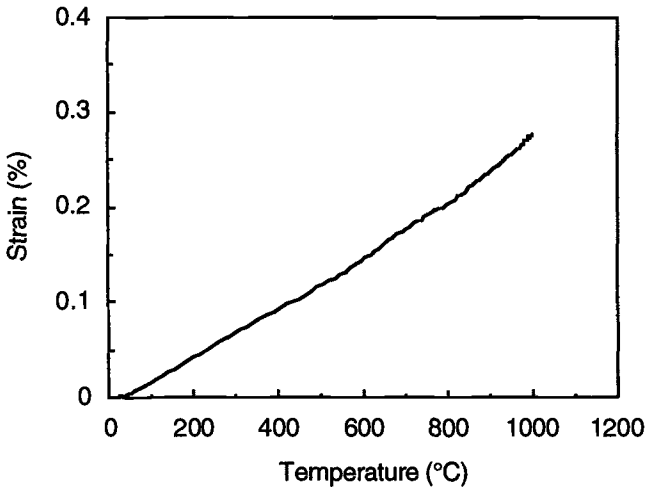


Figure 3 - Thermal expansion of C/SiC-MI composite between ambient temperature and 1000°C.

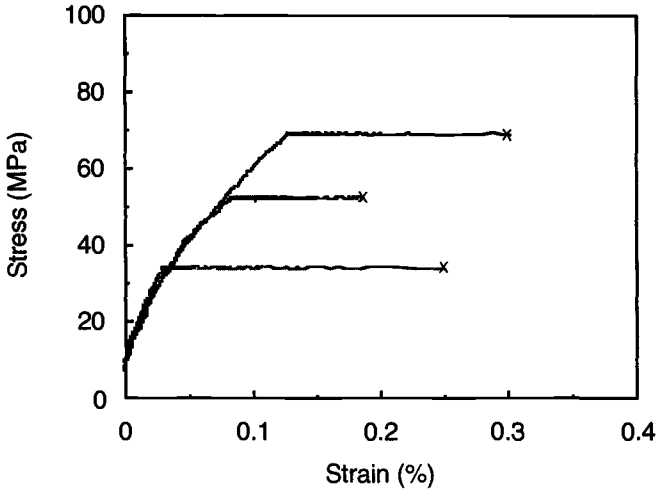


Figure 4 - Stress versus strain curves obtained during stress-rupture testing of C/SiC-MI in air at 1000°C and stresses of 35, 52.5 and 69 MPa.

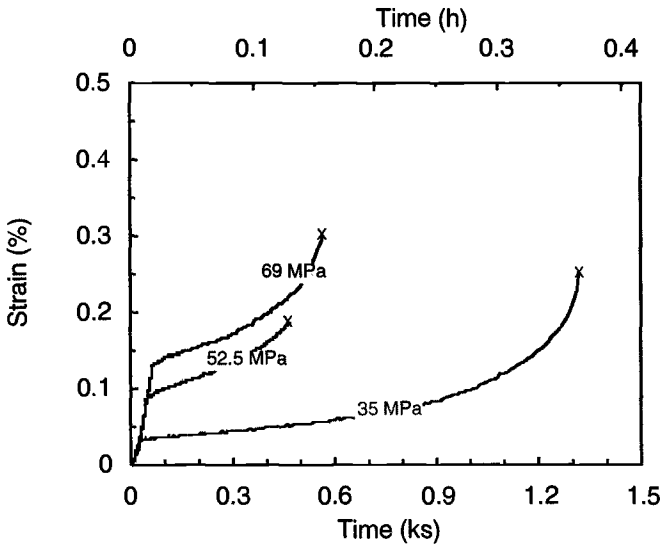


Figure 5 - Strain versus time curves obtained during the stress-rupture testing of C/SiC-MI in air at 1000°C and stresses of 35, 52.5 and 69 MPa.

At the end of the soaking period the specimen was mechanically loaded at a rate of 1 MPa/s to the test stress (Stage II) and then the load was maintained at a constant level thereafter (Stage III). The tests were completed when the specimens failed. During Stage III the compliance of the specimens increased continuously and the rate of deformation accelerated just prior to failure.

By cross-plotting the strain versus stress data during Stages II and III it was found that the stress-strain curves were non-linear. Figure 4 shows three stress versus strain curves obtained during stress-rupture tests conducted at stresses of 35, 52.5 and 69 MPa. The slope of the stress versus strain curves at the start of the curve was approximately 76 GPa. Note that the tests start at a stress level of 5 MPa because it was necessary to maintain the specimens under slight tension in order to allow for the operation of the two self-aligning joints incorporated to the load train

The strain versus time curves, which are shown in Figure 5, indicate that the compliance of the specimens increased continuously, first at a decreasing rate and then, prior to failure at an accelerated rate. Strain versus time curves of similar shape have been observed when SiC/SiC CFCCs are subjected to stress-rupture testing at elevated temperatures. The shape of these curves has been explained on the basis of the cumulative failure of the reinforcing fibers aligned in the loading direction [8-9]. In the case of carbon fibers, and based on the morphological analysis of these fibers after oxidation [5], it is concluded that oxidation is responsible for the reduction in the effective cross-sectional area of the fibers and eventually for their failure. The sections of the fibers that are bridging the transverse matrix cracks will oxidize fastest and fail, redistributing the load that they were previously carrying among the surviving fibers. Eventually the failure of a critical number of fibers at the plane of a given transverse matrix crack results in the failure of the composite.

After the specimens failed, they were allowed to cool down at the natural cooling rate of the furnace. Figure 6 is a scanning electron micrograph of the fracture surface of a specimen after stress-rupture testing. Note that the fibers have completely disappeared leaving behind "holes" in the matrix that were previously filled by the fibers. In this case, the fibers were consumed by oxidation both during testing and later on during cooling.

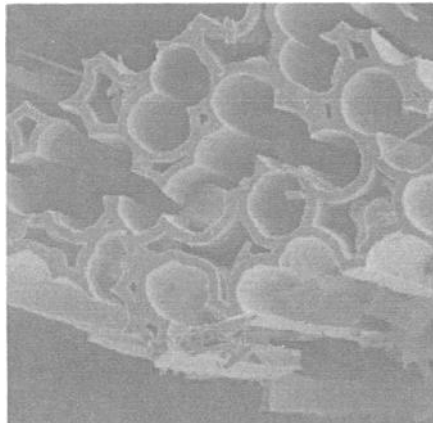


Figure 6 - Scanning electron micrograph of C/SiC-MI after stress-rupture testing in air at 1000°C. Note that the fibers have disappeared leaving behind holes in the matrix. Average fiber diameter is 8 μm .

Comparison of the times to failure between this material and C/SiC-CVI under similar conditions indicates that although the rate of loss of composite strength is the same for both, the latter exhibits longer endurance (Figure 7). This suggests that the mechanism responsible for the loss of strength in both composites is the same (i.e.- fiber oxidation) but the lack of a protective coating on the C/MI-SiC matrix composites used in this study allowed for faster ingress of the environment to the interior of the composite, particularly through the machined edges, resulting in shorter life times.

Stress-Relaxation

The procedure of stress-relaxation testing is similar to that described above for stress-rupture testing. The only difference is that when the stress reached the test stress, the control of the test machine was changed from load-controlled to strain-controlled and that extension of the specimen was maintained constant for the duration of the test. Figure 8 shows the stress and strain histories of a relaxation test at 1000°C at an initial stress of 35 MPa.

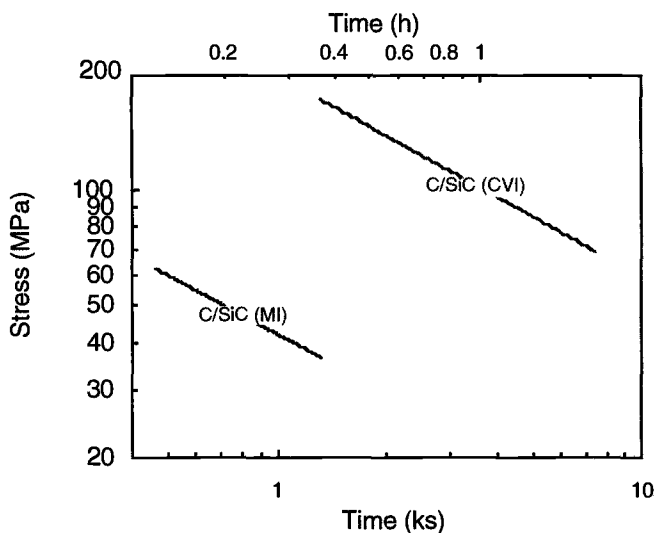


Figure 7 - Comparison of stress-rupture behavior between C/SiC(CVI) and C/SiC(MI) at 1000°C in air. Data for C/SiC-CVI from [3].

Stage I corresponds to the heating segment of the test, followed by Stage II where similarly to the stress-rupture tests, the specimen was allowed to reach thermal equilibrium. Just like during the conduction of stress-rupture tests, the specimen was heated with the furnace operating at 100% output power until reaching the test temperature. It can be observed that after reaching the test temperature, the specimen reached thermal equilibrium within 15 minutes. In Stage II the specimen was loaded at a constant loading rate of 1 MPa/s to the test stress of 35 MPa. At the end of the loading segment the control of the machine was changed from load-controlled to strain-controlled using the extensometer as

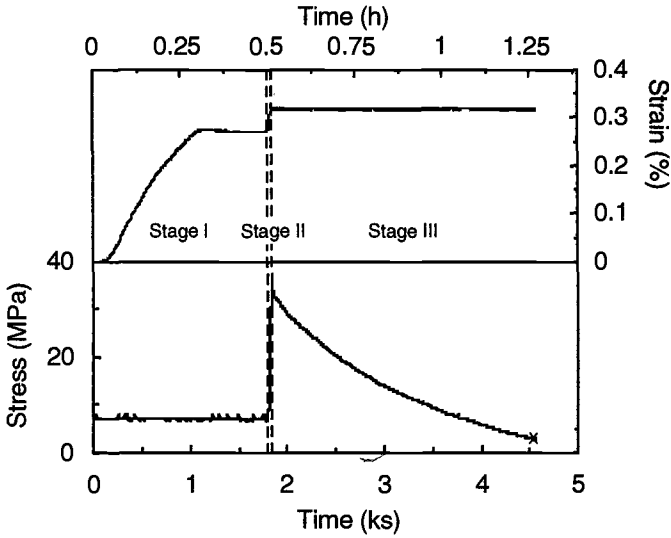


Figure 8- Strain and stress histories of a stress-relaxation test conducted at 1000°C and an initial stress of 35 MPa. Stage I corresponds to the heating stage, Stage II corresponds to mechanical loading, and in Stage III the composite strain is maintained constant while the stress decreases continuously until failure.

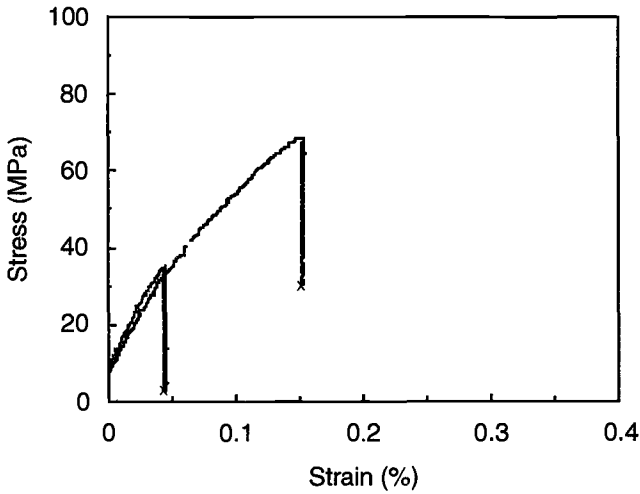


Figure 9- Stress histories of stress-relaxation tests conducted at 1000°C and initial stresses of 35 MPa and 69 MPa.

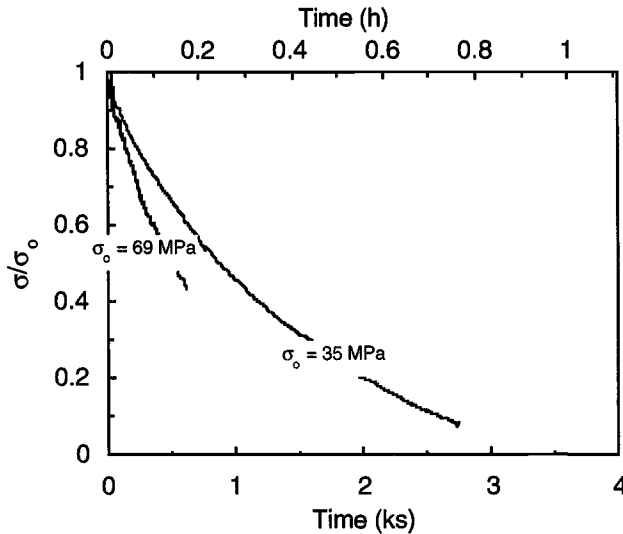


Figure 10- Normalized evolution of stress during stress-relaxation. Note that the rate of stress-relaxation is faster for higher initial stress.

the feedback signal, and the extension of the specimen was maintained constant thereafter until failure. Figure 9 shows the stress-strain curves from two stress-relaxation tests conducted at initial stresses of 35 and 69 MPa and indicates that as during the stress-rupture tests, the loading portion of the stress-strain curve is non-linear. By normalizing the stress to the initial stress the results of two stress-relaxation tests are summarized in Figure 10. Note that the rate of stress-relaxation is different for the two tests, but that in both cases it could be fitted by an exponential expression according to Equation 2.

$$\frac{\sigma(t)}{\sigma(0)} = e^{-bt} \quad (2)$$

Discussion

The time-dependent changes in compliance observed during the stress-rupture and stress-relaxation testing of the material investigated result from the operation of various micromechanical and thermochemical mechanisms. For example, during stress-rupture testing, the elongation of the specimen results from elastic and inelastic deformation upon the application of stress, from the opening and growth of cracks in the CVI-SiC coating and MI-SiC matrix, and from the failure of the reinforcing fibers. Cracks in the matrix are formed during cooling from the processing temperature as a result of the mismatch in thermoelastic properties of the constituents. Once the cracks are open and the specimen is exposed to air at 1000°C the fiber coating surrounding the fibers will oxidize. This will result in a change in the stress profile along the length of the fibers, in the decohesion

between the fibers and matrix and in turn, in time-dependent elongation of the composite. The time-dependent changes in the axial stress profile along the length of the fibers will be given by [7]:

$$\sigma_f(z,t) = T(t) [U(z)] - \frac{2\tau}{r} (z - \zeta(t)) [U(z - \zeta(t))] \quad 0 \leq z \leq l/2 \quad (3)$$

where t is time, z is the axial position along the length of the fiber, $T(t)$ is the time-dependent stress at the plane of the cracks, τ is the interfacial shear stress, r is the fiber's radius, $\zeta(t)$ is the time-dependent recession length of the fiber coating measured from the plane of the matrix crack, $[U(z - \zeta(t))]$ is Heaviside's unit function, and l_c is the matrix crack spacing.

Once the fibers are exposed to the environment, these will also oxidize, resulting in the formation of notches and rupture. When a fiber fails, the load being carried by that fiber will be transferred to the neighboring fibers. As the oxidation front moves from the surface of the specimen to the interior of the composite, more and more fibers will oxidize and fail, leading eventually to the failure of the composite. The changes in compliance associated with the rupture of the fibers can be best explained using a simple fiber bundle model. Let us consider a bundle of N_o linear-elastic fibers of uniform diameter d , and elastic modulus E . Let us assume that the strength of the fibers is described by a two-parameter Weibull distribution so that the probability of failure when the fibers are subjected to a stress T is

$$\Phi = 1 - \frac{N}{N_o} = 1 - \exp \left\{ - \frac{l}{l_o} \left(\frac{T}{\sigma_o} \right)^m \right\} \quad (4)$$

where l is the length of the fibers, σ_o is the Weibull characteristic strength for the reference gauge length l_o , m is the Weibull modulus, and N is the number of surviving fibers. Let us assume that we apply a load F to the entire bundle. Then the stress on each fiber is going to be

$$T = \frac{4F}{N_o \pi d^2 (1 - \Phi)} \quad (5)$$

while the elongation of the fiber bundle will be

$$\epsilon = \frac{T}{E} \quad (6)$$

Note that as the number of failed fibers increases as a result of oxidation, then Φ , T and ϵ will increase and because Equations 3 and 4 form an iterated function system (IFS), the failure of the entire fiber bundle will occur when the IFS becomes unstable [10]. The analogy to this process is that of a snow-ball effect. In this case, as fibers fail the load previously carried by those fibers will be transferred to their neighbors, increasing the probability of failure of these and resulting in the failure of more fibers. This process continues to occur until a critical number of fibers fail, leading to the failure of the entire fiber bundle.

Now let us consider the case of stress-relaxation. The initial elongation of the composite will result from both elastic and inelastic deformation upon the application of stress. Afterwards as the elongation of the composite is held constant, changes in compliance will result from the opening and growth of existing cracks in the matrix and

from the failure of the fibers. Once the cracks are open, the environment will ingress to the interior of the composite, resulting in the oxidation of the fiber coating and subsequently on the oxidation of the fibers. Subsequent changes in compliance will be associated with the reduction in the cross-sectional area of the carbon fibers as these oxidized. In principle, the rate of oxidation of the fibers could be determined from the time-dependent changes in the load being carried by the composite. Specifically at the plane of the matrix cracks the change in time of the load being carried by the composite will be given as follows

$$\frac{dF}{dt} = E \epsilon_o \frac{dA}{dt} \quad (7)$$

where E is the elastic modulus of the fibers, ϵ_o the applied strain and A is the total cross-sectional area of the unbroken fibers at the crack plane. Note that according to Equation 7 the rate of reduction in the load being carried by the composite is proportional to the applied strain, which is consistent with the results shown in Figure 10.

Summary

The time-dependent deformation of carbon fiber-reinforced melt-infiltrated silicon carbide was investigated in air at 1000°C under both constant stress and strain. It was found that in both cases, the material exhibits time-dependent changes in compliance, and that these changes result from the growth of cracks in the matrix, from the oxidation of the fiber coating that leads to decohesion between fibers and matrix, and from fiber oxidation.

A simple fiber bundle model was used to explain the accelerated rate of deformation that is observed prior to failure during stress-rupture testing. The possibility of determining the kinetics of fiber oxidation from the time-dependent changes in compliance during stress-rupture testing were identified.

During heating and prior to mechanical testing it was possible to determine the thermal expansion of the material and the linear coefficients of thermal expansion between room temperature and 1000°C.

Acknowledgments

This work was sponsored by the U.S. Department of Energy, Assistant Secretary for Energy Efficiency and Renewable Energy, Office of Industrial Technologies, Industrial Energy Efficiency Division and Continuous Fiber Ceramic Composites Program, under contract DE-AC05-00OR22725 with UT-Battelle, LLC.

References

- [1] Singh, M., "Melt infiltrated SiC ceramics and composites," in *Ceramic Innovations in the 20th Century*, Wachtman, J. B. Jr., Ed., The American Ceramic Society, Westerville, OH (1999) pp. 199-200.
- [2] Effinger, M. R., Tucker, D. S., and Barnett, T., B., "Tensile and Interlaminar Shear Evaluation of DuPont Lanxide CMCs," *Ceramic Engineering and Science Proceedings*, Vol. 17, No. 4 (1996) pp. 316-323.

- [3] Halbig, M. C., Brewer, D. N., Eckel, E. J., and Cawley, J. D., "Stressed Oxidation of C/SiC Composites," *Ceramic Engineering and Science Proceedings*, vol. 18, No. 3 (1997) pp. 547-554.
- [4] Lamouroux, F., Bourrat, X., Naslain, R., and Sevely, J., "Structure/Oxidation Behavior Relationship in the Carbonaceous Constituents of 2-D C/PyC/SiC Composites," *Carbon*, Vol. 31, No. 8, (1993) pp. 1273-1288.
- [5] Lamouroux F., and Camus, G., "Oxidation Effects on the Mechanical Properties of 2D Woven C/SiC Composites," *Journal of the European Ceramic Society*, Vol. 14 (1994) pp. 177-188
- [6] Lamouroux, F., Camus, G., and Thebault, J., "Kinetics and Mechanisms of Oxidation of 2D Woven C/SiC Composites: I, Experimental Approach," *Journal of the American Ceramic Society*, Vol. 77, No. 8 (1994) pp. 2049-2057.
- [7] Lebrun, G. A., Lamouroux, F., and Lamon, J., "Lifetime Predictions for C/SiC Composite at High Temperature," unpublished results (1999)
- [8] Lara-Curzio, E., "Stress-Rupture of Nicalon™/SiC Continuous Fiber Ceramic Composites in Air at 950°C," *Journal of the American Ceramic Society*, Vol. 80, No. 12, pp. 3268-3272 (1997).
- [9] Lara-Curzio, E., "Analysis of Oxidation-Assisted Stress-Rupture of Continuous Fiber-Reinforced Ceramic Matrix Composites at Intermediate Temperatures," *Composites Part A*, Vol. 30, No. 4 (1999) pp. 549-554.
- [10] Lara-Curzio, E., "Oxidation-Induced Stress-Rupture of Fiber Bundles," *Journal of Engineering Materials and Technology*, vol. 120 April 1998, pp. 105-109.

Charles A. Lewinsohn, Charles H. Henager Jr., Edward P. Simonen, Charles F. Windisch Jr., and Russell H. Jones¹

The Relationship between Interphase Oxidation and Time-Dependent Failure in SiC_f/SiC_m Composites

Reference: Lewinsohn, C. A., Henager, C. H., Jr., Simonen, E. P., Windisch, C. F., Jr., and Jones, R. H., "The Relationship between Interphase Oxidation and Time-Dependent Failure in SiC_f/SiC_m Composites," *Mechanical, Thermal and Environmental Testing and Performance of Ceramic Composites and Components, ASTM STP 1392*, M. G. Jenkins, E. Lara-Curzio, and S. T. Gonczy, Eds., American Society for Testing and Materials, West Conshohocken, PA, 2000.

Abstract: Flaw-tolerant ceramic matrix composites typically possess an interphase between the reinforcing fibers and the matrix that allows debonding for desirable mechanical properties. However, commonly used interphase materials, such as carbon and boron nitride, are susceptible to oxidation at elevated temperatures. In general, oxidation of interphase materials produces gases and voids between the fibers and the matrix leading to an increase in the compliance of bridging fibers and a subsequent decrease in the toughening increment due to fiber bridging. On the other hand, silicon carbide fibers and matrices oxidize to form solid reaction products (oxides), leading to increased bonding between fibers and the matrix. A competition between interphase oxidation and the formation of solid oxide phases determines the composite failure mechanism under a given set of environmental conditions. The mechanisms by which oxidation degrade the mechanical properties of SiC_f/SiC_m will be discussed. Techniques for identifying failure mechanisms and approaches to modeling component lifetimes will be presented.

Keywords: silicon carbide, crack growth, interface oxidation, environmental susceptibility

Introduction

The use of non-oxide, ceramic matrix composites (CMCs) could improve the efficiency of combustion processes. An increase in efficiency would reduce the amount of fuels required for an equivalent output power, hence leading to environmental and economic benefits. In inert environments, CMCs exhibit greater mechanical reliability than conventional monolithic ceramics [1] that suggests that they can be used safely in

¹Research Scientist, Senior Staff Scientist, Senior Research Scientist, Staff Scientist, Senior Staff Scientist and Technical Group Manager, respectively. Pacific Northwest National Laboratory, PO Box 999, Richland, WA., 99352, operated for the U.S. Department of Energy (DOE) by Battelle.

demanding environments, such as combustion. Non-oxide CMCs rely on a material located between the fibers and the matrix, referred to as the interphase, that causes debonding between fibers and the matrix during crack propagation and subsequent toughening due to fibers that apply bridging stresses in the crack wake [2,3]. Two common interphase materials are carbon and boron nitride, both of which oxidize and form gaseous species in the presence of oxygen. Interphase degradation can also allow degradation of the fiber and matrix. Therefore, it is important to understand the mechanisms of environmental degradation in non-oxide CMCs.

The effect of air on the mechanical properties of non-oxide CMCs has been extensively studied [e.g. 4-6] because application of these materials will most likely occur in this environment. To understand the physical mechanisms caused by environmental exposure, however, it is useful to study the effect of individual components of the environment. This study has focussed on the effects of oxygen concentration and temperature, the moisture content was not controlled. The aim of the study is to determine environmental and microstructural parameters that control the failure of non-oxide, continuous-fiber reinforced ceramic matrix composites and to build mathematical models to describe these mechanisms.

Experimental Method

Subcritical crack growth and residual toughness experiments were conducted to investigate environmentally induced failure mechanisms of a non-oxide CMC material. All experiments were performed by flexural loading of single-edge-notched beam specimens (SENB) in 1/4 four-point bending in a fully articulated silicon-carbide fixture contained within a vertically oriented mullite tube. The mullite tube was located between the base and crosshead of an electro-mechanical rigid test frame² and was enclosed in an electrically resistance-heated furnace³. The atmosphere inside the mullite tube was controllable. Various mixtures of oxygen and argon were obtained via a system of mass flow control valves⁴, a valve flow-controller⁴, and a mixing chamber. The concentration of oxygen in the mixed gases was measured with a zirconia cell oxygen meter⁵. Specimens were placed in the sealed mullite tube and the atmosphere was allowed to equilibrate prior to heating the furnace. A schematic of the experimental setup is shown in Figure 1.

When the specimens had equilibrated at the desired atmosphere and temperature, a flexural load was applied to the specimen. System equilibration typically occurred within fifteen minutes of reaching the setpoint temperature and was monitored via the displacement signal. The load was calculated using a standard fracture mechanics equation, such that it produced an initial effective stress intensity factor at the notch tip of 10 MPa-m^{1/2}. A constant load was maintained throughout each experiment. The deflection of the specimen midpoint was measured by an alumina pushrod, also containing a thermocouple, attached to a strain-gauge extensometer. The displacements were corrected for differences between the load-point and mid-point and for the

² Model 4400, Instron Corp., Canton, MA.

³ CM Furnaces, Bloomington, NJ.

⁴ Multi Gas Controller 147, MKS Instruments, Andover, MA.

⁵ Thermox TM-II-BT, Ametek, Pittsburgh, PA

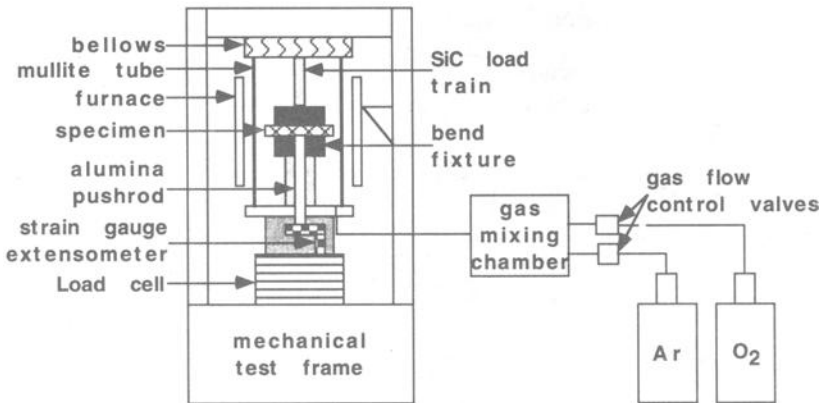


Figure 1 — Schematic of experimental apparatus

compliance of the test apparatus. Since, the subcritical crack growth rate was determined from an indirect measurement, which was based on calculating the instantaneous compliance of the specimen, it is also referred to as the effective crack velocity. Details of the testing methods can be found elsewhere [7].

The final crack length was measured for several specimens by sectioning the specimens, polishing with diamond pastes, and observing the crack with optical microscopes. Agreement between the crack lengths determined optically and via the compliance measurement was within 25%. The crack length calculated from the compliance measurement was consistently 20-25% longer than the optical measurements. Scanning electron microscopy (SEM) was used to investigate fracture surfaces.

In some cases, the residual toughness of specimens that had undergone subcritical crack growth was measured by loading the specimens to failure and applying the conventional fracture mechanics equation for SENB specimens in four-point loading [8]. To determine whether severe embrittlement due to oxidation required the presence of a load, some specimens were first subject to crack growth under identical conditions (1100°C, 2 000 ppm O₂) such that the calculated normalized crack length grew from 0.2 to 0.4. Then these specimens were placed in non-oxidizing or oxidizing environments, at various temperatures, and subsequently fractured (Table I).

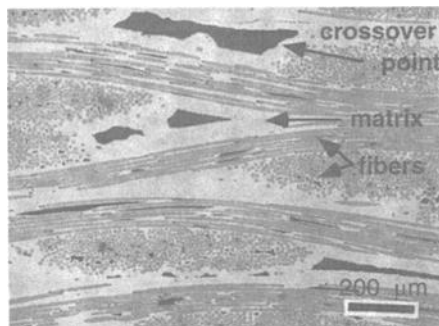


Figure 2 — Micrograph showing representative microstructure of material investigated

Table 1 — Matrix of Experimental Conditions for Residual Toughness Measurement

Pretreatment Temperature (°C)	Pretreatment Environment	Pretreatment Time (s)	Pretreatment Stress Intensity (MPa·m ^{1/2})	Test Temperature (°C)
1100	2 000 ppm O ₂	7 200	10	1100
1100	2 000 ppm O ₂	7 200	10	800
1100	1. 2 000 ppm O ₂ 2. 500 000 ppm O ₂	7 200 18 000	10 0	800
1100	3. 2 000 ppm O ₂ 4. 500 000 ppm O ₂	7 200 18 000	10 0	1100

The material was fabricated⁶ by chemical vapor deposition of silicon carbide on a fibrous preform (CVI). The fibrous preform consisted of approximately eight layers of two-dimensional plain weave (0/90°) ceramic-grade Nicalon[®] 7 fibers. Prior to deposition of the matrix, a thin layer of carbon was deposited on the fibers. According to the manufacturer, the thickness of this layer is 1.50×10^{-7} m. The resulting composites contained approximately 40 volume-percent fibers and a total of 10-15% porosity. Each specimen was approximately $50 \times 4.0 \times 3.0 \times 10^{-3}$ m (L x W x B). An approximately 1×10^{-4} m-thick coating of CVD-silicon carbide protected the edges of the specimen, however the tensile and compressive surfaces of the specimens were not coated because machining was performed following CVI processing. A representative micrograph of the composite material is shown in Figure 2.

Thermogravimetric analysis (TGA) was also used to investigate the oxidation behavior of the materials used in this study. Specimens were cut into blocks that were $4 \times 4 \times 8 \times 10^{-3}$ m large and all except one of the faces was coated with an oxidation resistant coating of silicon carbide. TGA analysis was performed at 1100°C. The gas flow rate in the specimen chamber was about 8×10^{-6} m³/s, at a total pressure of 1.013×10^5 Pa. The uncoated face was oriented perpendicularly to the direction of gas flow. The mass loss measured by the TGA analysis was assumed to be due to oxidation of only the carbon interphase, i.e., oxidation of the fiber and the matrix was neglected. For a typical TGA specimen, the exposed area of carbon was approximately 8.6×10^{-7} m², determined by image analysis of micrographs. This value includes only the interphase around fibers with their axis normal to the exposed surface. There is a slight error associated with interphase material around fibers with their axes parallel to the exposed surface and with contributions to the mass loss due to oxidation of the fibers and matrix.

⁶ DuPont Composites, Inc., Newark, DE. (currently AlliedSignal Composites).

⁷ Nippon Carbon Co., Tokyo, Japan.

Results

A comparison of the effective crack velocity as a function of time, for experiments conducted at different oxygen concentrations, at 800°C is shown in Figure 3. In addition to the presence of an inflection point in the crack velocity data for experiments conducted in oxygen, the position of the inflection point is dependent on the oxygen concentration. In comparison, the effective crack velocity for a specimen that was reinforced by Hi-Nicalon fibers, but otherwise had a similar microstructure to the materials reinforced with ceramic-grade fibers, that was tested at 1200 °C in gettered argon (< 20 ppm O₂) and a slightly higher initial effective stress intensity (to promote failure), did not show an inflection point prior to failure (Fig 4). This result indicates that the inflection point is not an artifact of the test technique. In addition, analysis of the temperature dependency of the effective crack velocity [9], before the inflection point, yielded apparent activation energies that were similar to those that were measured (via TGA) for oxidative weight loss [10].

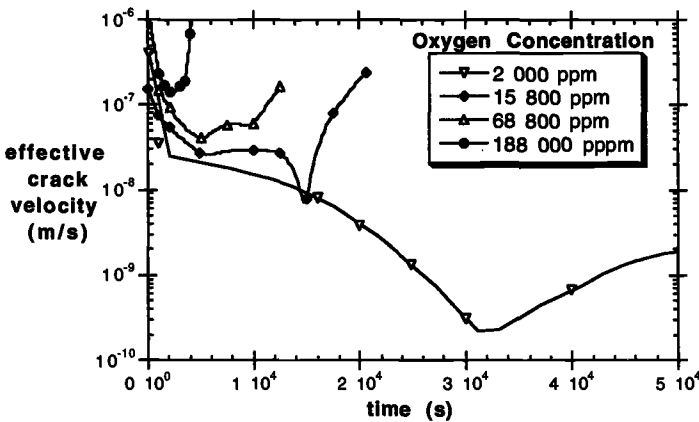


Figure 3 — The dependence of crack velocity on oxygen concentration

The effective fracture toughness of the composite material was measured at 25°C in the ambient environment, and at 800°C and 1100°C in gettered argon. The resultant value, $17.1 \text{ MPa}\cdot\text{m}^{1/2} + 0.5 \text{ MPa}\cdot\text{m}^{1/2}$, will be referred to as the intrinsic fracture toughness of the material. Although these materials do not obey linear elastic fracture mechanics, the effective fracture toughness was calculated from the peak load using a standard fracture mechanics equation [8]. Thus, the value of the intrinsic fracture toughness cannot be considered a material property, as the critical stress intensity factor is for true brittle materials, but can be used for a comparison between various treatments used in this study since the specimen geometry and testing procedure was constant throughout the study. The fracture toughness of specimens, measured at both 1100°C and 800°C, that had undergone crack growth at 1100°C in 2 000 ppm O₂ for 2 hours, was

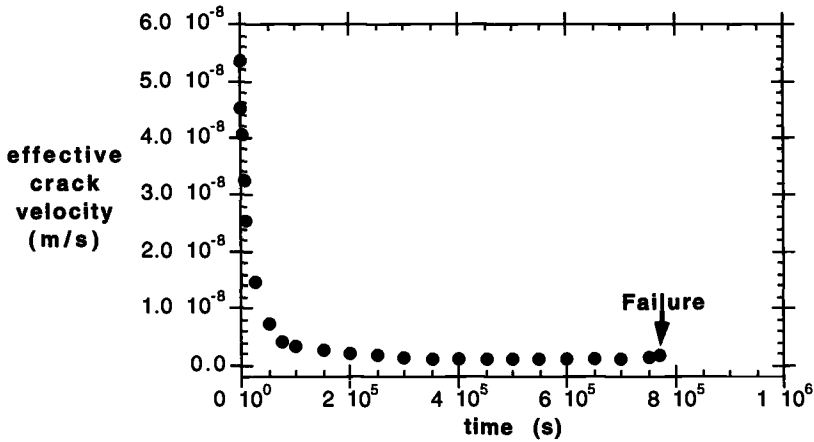


Figure 4 — Subcritical crack growth in gettered argon (<20 ppmO₂)

not significantly different from the intrinsic fracture toughness of the material. On the other hand, a specimen that underwent approximately the same amount of crack growth (1100°C, 2 000 ppm O₂, 2 h) that was then exposed to 500 000 ppm O₂ for 1 h, without an applied stress, had a lower effective fracture toughness and exhibited less load-bearing capacity after the peak load was obtained (Table 2).

Table 2 — Effective Fracture Toughness

Specimen	Test Conditions	Effective Fracture Toughness, MPa·m ^{1/2}
	25°C, ambient	
untreated	800°C and 1100°C, gettered argon	17.1 ± 0.5 MPa·m ^{1/2}
1100°C, 2000 ppm O ₂ , 2h	1100°C, 2 000 ppm O ₂	16.4 ± 0.5 MPa·m ^{1/2}
1100°C, 2000 ppm O ₂ , 2h	800°C, 2 000 ppm O ₂	17.5 ± 0.5 MPa·m ^{1/2}
1100°C, 2000 ppm O ₂ , 2h	800°C, 500 000 ppm O ₂	15.0 ± 0.5 MPa·m ^{1/2}

Finally, the time-to-failure (defined as the loss of ability to carry load) as a function of the oxygen concentration used during each experiment did not exhibit a unique dependence on oxygen concentration for all temperatures (Figure 5). At 800°C, the time-to-failure was linearly dependent on the oxygen concentration, with a slope of -0.9 s/ppm O₂. At 650°C, however, the regression coefficient for a least-squares fit of the data was 0.8 (Figure 5).

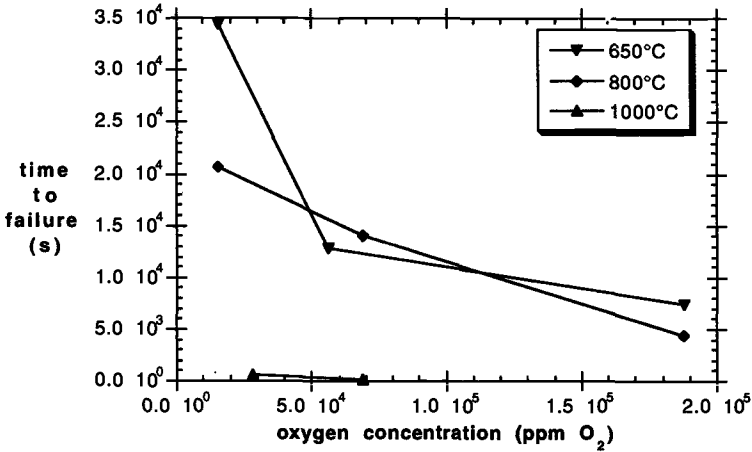


Figure 5 — Time-to-failure as a function of oxygen concentration

Discussion

It has been shown that stress relaxation, due to creep, in fibers that bridge matrix cracks leads to subcritical crack growth in environments that are inert with respect to $\text{SiC}_f/\text{SiC}_m$ [7]. Under these conditions, the temperature dependence of subcritical crack growth is nearly identical to that of fiber creep [9]. The temperature dependence calculated from the measured subcritical crack growth data in the presence of oxygen is 47 kJ/mol. The temperature dependence calculated from the measured weight loss data in TGA experiments is 50 kJ/mol. Subsequent to these weight loss experiments, analysis of the microstructure revealed that the carbon interphase between the fibers and matrix was progressively removed from surfaces or cracks that were exposed to oxygen. These results suggest that the observed subcritical crack growth in oxygen is controlled by interphase oxidation.

Although subcritical crack growth occurred in specimens tested at 1100°C in 2 000 ppm O_2 , the residual toughness was not affected by this type of crack growth. In addition, the residual toughness was not significantly different when measured at 800°C or 1100°C. On the other hand, the residual toughness measured after a severe exposure to 500 000 ppm O_2 at 800°C was significantly lower than the intrinsic toughness of the material. These results suggest that the fiber strength, which defines the peak load that the specimen can support, is not strongly affected by exposure to low oxygen concentrations, but it is degraded by exposure to high oxygen concentrations. Examination of the effective crack velocity, as a function of time, in oxygen containing environments (Figure 3) suggests that crack growth occurs in two stages: one with a decreasing crack velocity with increasing time, and the other with an increasing crack velocity with increasing time. Furthermore, consideration of the dependence of the time-to failure as a function of oxygen concentration also suggests that there is more than one

degradation mechanism caused by exposure of the material to oxygen containing environments.

Numerous authors have demonstrated that the growth of a solid oxide reaction product between the fiber and the matrix leading to an intensification of the stress on the fibers [11,12], or the growth of a solid oxide layer on the surface of the fibers that degrades their strength [13,14] causes severe embrittlement of non-oxide CMCs. This embrittlement has been shown to lead to rapid failure of these materials. Extensive testing [15] of these materials as a function of temperature and oxygen concentration has shown that low temperatures and low oxygen concentrations favor the first stage of failure. For example, Lara-Curzio [16] observed oxygen accelerated failure in non-oxide, continuous-fiber-reinforced, ceramic matrix composites at 450°C, in air, but did not find any evidence of oxide growth on the fibers or matrix of the specimens. In addition, during the first stage of failure the residual toughness of the material is not significantly lower than the “intrinsic” toughness. On the other hand, during the second stage of failure, the residual toughness is lower than the “intrinsic” toughness. These results can be rationalized by consideration of the competition between carbon interphase removal, which does not significantly affect the fiber strength, and the growth of a SiO₂ solid oxide reaction product by oxidation, which degrades the strength of the fibers or causes an increased stress on them due to mechanical bonding with the matrix. Carbon oxidation [17] has a lower thermal activation energy, but a higher reaction rate constant than the formation of SiO₂ from silicon carbide [18]. Hence, subcritical crack growth due to interphase removal is favored at low temperatures, and may be the mechanism controlling the first stage of failure; embrittlement is favored at higher temperatures, and maybe the second stage.

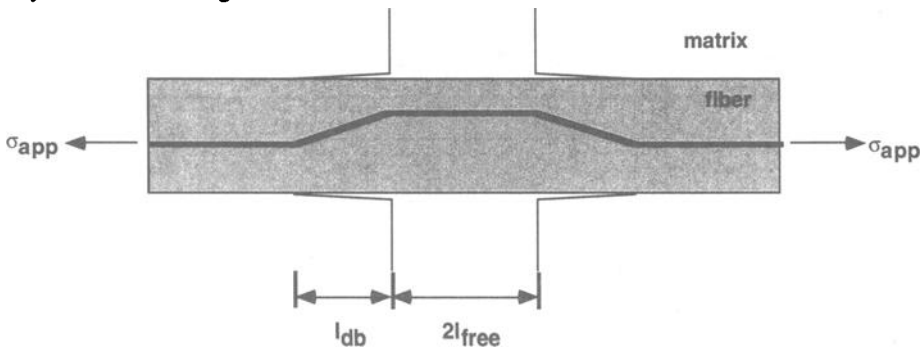


Figure 6 — A schematic diagram of the level of stress in a fiber bridging a matrix crack. The black line indicates the magnitude of tensile stress in the fiber

To verify the hypotheses stated above, numerical or analytical micromechanical models must be developed. The first step in the development of such models involves defining the effects of interphase oxidation on individual fibers bridging matrix cracks. Since several models exist that adequately describe oxidation embrittlement [e.g., 13,14], this paper will focus on the effects of interphase oxidation. A schematic illustration of the stresses on a bridging fiber is shown in Figure 6. It is generally accepted that, in a well-designed ceramic matrix composite, when a matrix crack intercepts a fiber the

interphase debonds between the fiber and the matrix. Stress is transferred along the debonded interface via shear forces limited by the frictional sliding resistance, τ . Under constant applied stress, a force balance is established such that the relationship between the debond length, l_{db} , and the stress on an individual fiber, σ_f , is given by

$$l_{db} = \frac{\sigma_f r_f}{2\tau} \quad (1)$$

where

r_f is the radius of the fiber.

Equating the stress in the fiber, due to shear loading along the debond length, with the stress in the fiber between the matrix crack faces, l_{free} , one obtains (assuming $l_{db} \gg l_{free}$)

$$\frac{2\tau l_{db}}{r_f} = \frac{l_{free} E_f}{l_{db}} \quad (2)$$

where

E_f is Young's modulus of the fiber.

Rearranging Equation 2 and substituting it into Equation 1, one can express the relationship between the length of fiber between the matrix crack faces, $2l_{free}$, and the stress on the fibers, σ_f

$$2l_{free} = \frac{\sigma_f^2 r_f}{\tau E_f} \quad (3)$$

In addition, it is useful to define a quadratic bridging compliance, Ψ_n

$$\Psi_n = \frac{r_f}{2\tau E_f} \quad (4)$$

The effect of interphase oxidation is to create an additional unbonded length, l_{ox} , between the fiber and the matrix (Figure 7). Assuming that there is no interfacial contact in the oxidized region, the frictional sliding resistance vanishes and the stress on an individual fiber can be expressed as (assuming $l_{ox} \gg l_{free}$)

$$\sigma_f = \frac{l_{free} E_f}{l_{ox}} \quad (5)$$

In this case, it is useful to define a linear bridging compliance, Ψ_l

$$\Psi_l = \frac{l_{ox}}{E_f} \quad (6)$$

In general, the relationship between the matrix crack opening displacement, $COD_m = 2l_{free}$, and the stress on the fibers can be expressed as

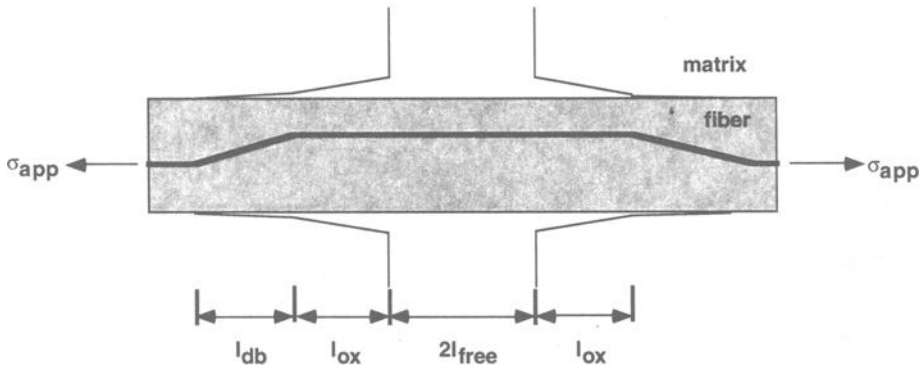


Figure 7 — A schematic diagram of the level of stress in a fiber bridging a matrix crack after interphase removal due to oxidation. The black line indicates the magnitude of tensile stress in the fiber

$$COD_m = 2[\Psi_n \sigma_f^2 + \Psi_f \sigma_f] \quad (7)$$

Equation 7 can be used to express the relationship between the crack closure stresses at a distance x from the crack mouth, $\sigma_f(X)$, and the matrix crack opening displacement, at that distance, that can then be used to calculate a composite stress intensity factor, K , that includes the effects of fiber bridging [3]

$$K = 2(c/\pi)^{1/2} \int_0^1 \frac{[\sigma_\infty - \sigma_f(X)]X}{\sqrt{1-X^2}} dX \quad (8)$$

where

c = crack radius (penny shaped, edge crack)

$X = x/c$.

This approach equates the crack opening displacement measured at a single fiber, Equation 7, with the global fracture mechanics conditions, Equation 8. The compliance terms used in Equation 7 are defined by measurable microstructural parameters. Furthermore, separate compliance terms can be included for the pertinent mechanical conditions.

Inspection of Equations 6, 7, and 8 indicates that as the interphase recession distance increases the bridging fibers become more compliant and the composite stress intensity increases. The increase in fiber compliance is linearly dependent on the increase in oxidation length. Previously, a discrete, micromechanics-based numerical model has been used to predict subcritical crack growth in inert environments due to fiber creep [7]. This model allows discrete bridging stresses to decay with time in accordance to published fiber creep laws. This is accomplished mathematically by defining a creep compliance for each bridging fiber. A weight-function approach is used to calculate self-consistent crack opening displacements and bridging stresses in an iterative manner.

Hence, the toughening increment and the crack tip stress intensity factor can be calculated. The crack tip stress intensity factor is compared to the critical stress intensity factor of the matrix and if it is larger the crack length is incremented a fixed distance. Results of this model are in good agreement with experimental measurements [7,10].

To include the effects of interphase oxidation on subcritical crack growth, the compliance functions defined in Equations 4 and 6 can be used. In addition, the interphase recession distance as a function of time must also be known. Experimental results show that interphase recession distance due to oxidation of 1 μm -thick carbon is linearly dependent on the exposure time [10,19]. In general, access of oxygen to unreacted interphase material may be limited by gas phase diffusion. Figure 8 illustrates the difference between the amount of interphase recession as a function of distance from the crack mouth of a matrix crack for the cases where transport of oxygen to unreacted interphase material or the interphase reaction-rate controls the rate of interphase recession. A rigorous model of subcritical crack growth due to interphase oxidation would consider the kinetics of interphase recession, residual stress effects, Poisson effects, and the effects of coating properties on the fiber bridging stresses. Furthermore, crack growth due to interphase recession would be expected to be limited by the time that it takes to grow a critical thickness of solid oxide reaction product that weakens the fibers or bonds the fiber and matrix together causing oxidation embrittlement.

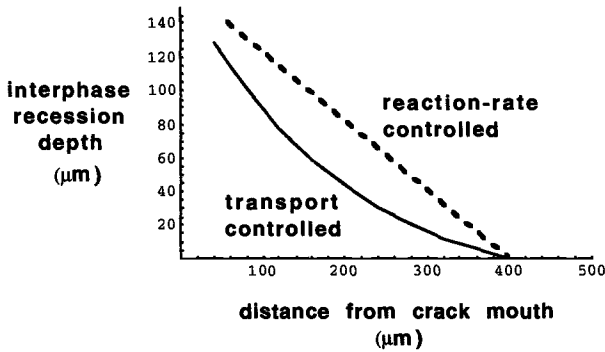


Figure 8 — oxygen concentration profile in a matrix crack limited by reaction-rate or gaseous phase diffusion.

Conclusions

Experimental observations suggest that interphase oxidation leads to subcritical crack growth in non-oxide, CMCs. Under a variety of conditions, oxidation causes interphase recession which increases the compliance of bridging fibers and decreases the resultant toughening increment due to fiber bridging. Efforts to model subcritical crack growth due to interphase recession must incorporate realistic oxygen concentration profiles within matrix cracks. These profiles may be limited by transport of gaseous products. Interphase recession can cause subcritical crack growth in non-oxide CMCs under

conditions that do not lead to embrittlement due to growth of solid oxide reaction products.

Acknowledgments

The authors would like to thank Professor Raj Bordia for useful discussions and Mr. J.P. Keaveney for diligently maintaining the experimental equipment. This work was supported, in part, by Basic Energy Sciences under U.S. DOE contract DE-AC06-76RLO 1830 with Pacific Northwest National Laboratory.

References

- [1] Marshall, D. B., and Ritter, J. E., "Reliability of Advanced Structural Ceramics and Ceramic Matrix Composites-A Review," *American Ceramic Society Bulletin*, vol. 66, No. 2, 1987, pp. 309-17.
- [2] Evans, A. G., and Zok, F. W., "The Physics and Mechanics of Fiber-Reinforced Brittle Matrix Composites," *Journal of Material Science*, vol. 29, No. 15, 1994, pp. 3857-96.
- [3] Marshall, D. B., and Cox, B. N., "The Mechanics of Matrix Cracking in Brittle-Matrix Fiber Composites," *Acta Metallurgica*, vol. 33, No. 11, 1985, pp. 2013-2021.
- [4] Heredia, F. E., McNulty, J. C., Zok, F. W., and Evans A. G., "Oxidation Embrittlement Probe for Ceramic Matrix Composites," *Journal of the American Ceramic Society*, vol. 78, No. 8, 1995, pp. 2097-2100.
- [5] Becher, P. F., Lin, H.-T., and More, K. L., "Lifetime-Applied Stress Response in Air of a SiC-Based Nicalon-Fiber-Reinforced Composite with a Carbon Interfacial Layer: Effects of Temperature (300-1150°C)," *Journal of the American Ceramic Society*, vol. 81, No. (7), 1998, pp. 1919-1925.
- [6] Lara-Curzio, E., "Stress-Rupture of Nicalon/SiC Continuous Fiber Ceramic Composites in Air at 950°C," *Journal of the American Ceramic Society*, vol. 80 No. 12, 1997, pp. 3268-3272.
- [7] Henager, C. H. Jr., and Jones, R. H., "Subcritical Crack Growth in CVD Silicon Carbide Reinforced with Nicalon Fibers: Experiment and Model," *Journal of the American Ceramic Society*, vol. 77, No. 9, 1994, pp. 2381-94.
- [8] Saxena, A., and Hudak, S. J. Jr., "Review and Extension of Compliance Information for Common Crack Growth Specimens," *International Journal of Fracture*, vol. 14, No. 5, 1978, pp. 453-468.
- [9] Lewinsohn, C. A., Henager, C. H. Jr., and Jones, R. H., Environmentally-Induced Failure Mechanism Mapping for Continuous-Fiber, Ceramic Composites, *Advances in Ceramic Composites IV, Ceramic Transactions*, vol. 96, J.P. Singh and N. Bansall, Eds., The American Ceramic Society, Westerville, Ohio 1999, pp. 351-359.
- [10] Jones, R. H., Henager, C. H. Jr., and Windisch, C. F. Jr., "High Temperature Corrosion and Crack Growth of SiC-SiC at Variable Oxygen Partial Pressures," *Materials Science and Engineering*, vol. A198, 1995, pp. 103-112.

- [11] Glime, W. H., and Cawley, J. D., "Stress Concentration due to Fiber-Matrix Fusion in Ceramic-Matrix Composites," *Journal of the American Ceramic Society*, vol. 81, No. 10, 1998, pp. 2597-2604.
- [12] Frety, N., Molins, R., and Boussuge, M., "Oxidizing Aging Effects on SiC-SiC Composites," *Journal of Materials Science*, vol. 27, 1992, pp. 5084-5090.
- [13] Evans, A. G., Zok, F. W., McMeeking, R. M., and Du, Z. Z., "Models of High-Temperature, Environmentally Assisted Embrittlement in Ceramic-Matrix Composites," *Journal of the American Ceramic Society*, vol. 79, No. 9, 1996, pp. 2345-2352.
- [14] Lara-Curzio, E., "Analysis of Oxidation-Assisted Stress-Rupture of Continuous Fiber-Reinforced Ceramic Matrix Composites at Intermediate Temperatures," *Composites: Part A*, vol. 30, 1999, pp. 549-554.
- [15] Jones, R. H., Henager, C. H. Jr., Lewinsohn, C. A., and Windisch, C. F. Jr., "Stress Corrosion Cracking of SiC/SiC Composites," *Journal of American Ceramic Society*, in press.
- [16] Lara-Curzio, E., and Ferber, M. K., "Stress-Rupture of Continuous Fibre Ceramic Composites at Intermediate Temperatures," *Journal of Materials Science Letters*, vol. 16, 1997, pp. 23-26.
- [17] Gulbrandsen, E. A., and Andrew, K. F., "Kinetics of Oxidation of Artificial Graphite at Temperatures of 425° to 575°C and Pressures of 0.15 to 9.8 cm of Mercury of Oxygen," *Industrial and Engineering Chemistry*, vol. 44, No. 5, 1952, pp. 1034-1047.
- [18] Ramberg, C. E., Cruciani, G., Spear, K. E., Tressler, R. E., and Ramberg, C. F. Jr., "Passive-Oxidation Kinetics of High-Purity Silicon Carbide from 800 ° to 1100°C," *Journal of the American Ceramic Society*, vol. 79, No. 11, 1996, pp. 2897-2911.
- [19] Lewinsohn, C. A., Eldridge, J. I., and Jones, R. H., "Techniques for Measuring Interfacial Recession in CFCCs and the Implications on Subcritical Crack Growth," *Ceramic Engineering & Science Proceedings*, vol. 19, No. 3, 1998, pp. 19-26.

Damage Accumulation and Material Development

Michael Verrilli,¹ Peter Kantzos,² and Jack Telesman¹

Characterization of Damage Accumulation in a Carbon Fiber-Reinforced Silicon Carbide Ceramic Matrix Composite (C/SiC) Subjected to Mechanical Loadings at Intermediate Temperature

Reference: Verrilli, M., Kantzos, P., and Telesman, J., “Characterization of Damage Accumulation in a Carbon Fiber-Reinforced Silicon Carbide Ceramic Matrix Composite (C/SiC) Subjected to Mechanical Loadings at Intermediate Temperature” *Mechanical, Thermal and Environmental Testing and Performance of Ceramic Composites and Components, ASTM STP 1392*, M. G. Jenkins, E. Lara-Curzio, and S. T. Gonczy, Eds., American Society for Testing and Materials, West Conshohocken, PA, 2000.

Abstract: Creep-rupture and fatigue tests were conducted to identify the failure modes and degradation mechanisms of a [0/90] carbon fiber reinforced silicon carbide (C/SiC) composite at 550 and 650°C. When compared on a maximum stress versus time to failure basis at a given temperature, fatigue testing yielded longer lives than creep-rupture testing. Tests conducted at 550°C had longer lives than 650°C tests. The rate of modulus degradation was similar for both temperatures and loading modes. Examination of tested specimens revealed that oxidation of the carbon fibers was the dominant damage mechanism for C/SiC at these temperatures and test conditions. The oxidation damage occurred globally within the surface of the specimen gage section, and locally in the interior of the composite, around pre-existing matrix cracks and pores. The results of this study indicate that, under the test conditions employed here, specimen life is governed by a combination of time at temperature and time-averaged stress and is not cycle dependent.

Keywords: C/SiC composites, fatigue testing, creep-rupture testing, oxidation, continuous fiber ceramic composite

Introduction

Advanced reusable launch vehicles (RLV) such as the X-33 will likely incorporate fiber-reinforced ceramic matrix composites (CMCs) in critical propulsion components. Use of CMCs is highly desirable to save weight, to improve reuse

¹ Materials research engineers, NASA Glenn Research Center, 21000 Brookpark Road, Cleveland, OH 44135.

² Research associate, Ohio Aerospace Institute, 22800 Cedar Point Road, Cleveland, OH 44142.

capability, and to increase performance. Potential applications for CMCs include turbopump rotors, housings, combustors, nozzle exit ramps, and throats. One of the candidate CMC materials for many of these components is carbon fiber reinforced silicon carbide, C/SiC.

In these applications, C/SiC components will be subjected to a service cycle that includes creep-fatigue loading under oxidizing environments. Evaluation of the high temperature capability of C/SiC has been reported in the literature [1-7]. To assess the applicability of CMCs as a thermal protection system for an advanced RLV, several C/SiC, SiC/SiC, and C/C composites systems were evaluated using thermomechanical fatigue cycles designed to approximate the anticipated service condition [1]. The lives of the SiC/SiC materials were longer than those obtained for the C/SiC materials when the TMF cycle included a low peak stress (77 MPa) and high partial pressures of oxygen (up to 27,000 ppm). Conversely, C/SiC composites performed better than SiC/SiC and C/C systems when the TMF cycle included lower partial pressures of oxygen (up to 7500 ppm) and high peak temperature (1455°C).

In another evaluation, studies of oxidation behavior of C/SiC were conducted. The results revealed three distinct composite degradation mechanisms, which correlated to three degradation modes of the carbon reinforcement [2,3]. Changes in oxidation rate and the presence of localized or global attack as a function of temperature and time were related to i) decreasing widths of microcracks with temperature and ii) the increasing reactivity of SiC and carbon with oxygen [3]. At low temperatures ($T < 800^{\circ}\text{C}$) the carbon reinforcement was uniformly degraded through oxidation throughout the samples. During oxidation exposures at intermediate temperatures ($800 < T < 1100^{\circ}\text{C}$), the degradation of the carbon fibers was observed to be nonuniform, and gradually changed from the surface of the samples to the bulk in regions adjacent to pre-existing microcracks. At high temperatures ($> 1100^{\circ}\text{C}$) the degradation was strictly localized at the outer surface of the test specimens.

The behavior of C/SiC under stressed oxidation (i.e. creep-rupture) conditions was investigated [5,6,7]. Test specimens exposed to stressed oxidation conditions over a temperature range of 350 to 1500°C had reduced residual strength [5]. Also, as test temperature and stresses increased, specimen life decreased. Oxidation of the pyrocarbon interface and carbon fibers was observed in all samples that failed [5].

A fundamental evaluation of the role of test temperature and loading mode (i.e., fatigue and stress-rupture) on damage mechanisms and life is needed to assess the applicability of C/SiC for a variety of RLV components. Also, characterization of composite damage progression is required to support development of a robust life prediction methodology. In the present study, mechanical testing at elevated temperatures and materials characterization were conducted to identify the degradation mechanisms, the progression of damage, and failure modes of C/SiC. Component lifetime requirements for RLV are expected to be less than 25 hours, so test stresses were selected to evaluate specimen lives of this duration. Test temperatures of 550 and 650°C were selected. In this intermediate temperature regime, previous work showed that oxidation damage of C/SiC occurs at a much slower rate at 550°C than at a higher temperature, such as 750°C [7].

Material and Test Specimen

The material examined in this investigation was a woven carbon fiber-reinforced SiC matrix composite manufactured by Allied Signal Composites³ using the chemical vapor infiltration (CVI) method. The SiC matrix is reinforced by [0/90] a two dimensional plain weave fabric of T-300⁴ carbon fibers. Fiber volume fraction was approximately 45%. The fiber coating was pyrolytic carbon, having a mean thickness of 0.5 micrometers. The composite density was 2.1 g/cm³ and the composite contained open porosity of about 10% [8].

The test specimen employed was 152 mm long, with a grip section width of 12.7 mm, a reduced gage section width of 10.2 mm, and a thickness of 3.0 mm. Test specimens were machined from composite plates using diamond grinding and then seal coated with CVI SiC. The seal coating thickness was 17.3±0.5 micrometers. To minimize variability of the test data, all test specimens were machined from C/SiC plates manufactured during the same CVI production run.

The microstructure of the as-manufactured composite specimens is shown in Figure 1. The composite contains microcracks within the matrix-rich regions and the [90] plies. This type of micro cracking in C/SiC has been well-documented [2,4,8,9]. In addition, the seal coating contains a regularly spaced array of microcracks created during cooling by the difference in the coefficient of thermal expansion (CTE) between the SiC matrix and the C fibers. These cracks are mostly confined to the coating itself.

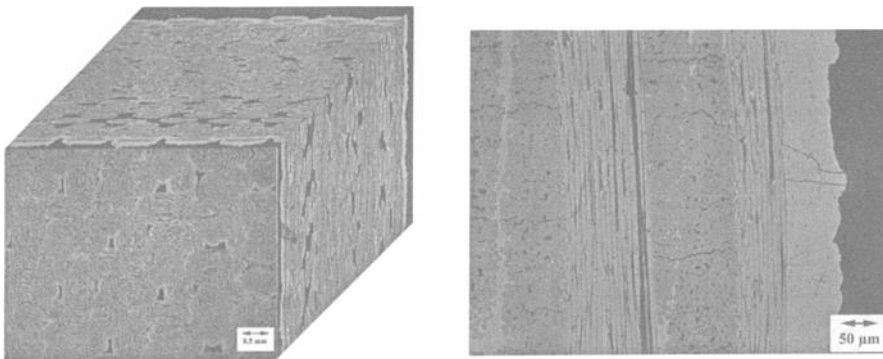


Figure 1 - Microstructure of as-manufactured Allied Signal Composites C/SiC.

³ Allied Signal Composites, Newark, DE.

⁴ Amoco, Danbury, CT.

Test Procedures

Axial creep-rupture and fatigue tests were performed. The bulk of the testing was conducted at 650°C, and limited testing was also performed at 550°C. A load control waveform, at a frequency of 0.033 Hz with an R-ratio (minimum load/maximum load) of 0.05, was used for the majority of the fatigue tests. Several tests were conducted using an R-ratio of 0.5. Also, a fatigue test was conducted at 100 Hz. The fatigue test matrix is given in Table 1. For the creep-rupture tests, a stress rate of 10 MPa/s was employed for loading to the creep load. Also, tensile tests were conducted at 550 and 650° to compare specimen damage to creep and fatigue induced specimen damage.

Table 1 – Fatigue Test Matrix and Results for C/SiC.

Specimen ID	Temperature [°C]	Maximum Stress, MPa	Load R ratio	Freq., Hz	Time to failure [hrs]	Cycles to failure
0184-02-001-1	650	105	0.05	0.033	4.28	504
0184-02-001-9	650	70	0.05	0.033	11.45	1328
0184-02-001-10	650	35	0.05	0.033	17.45	2041
0184-02-001-13	650	70	0.05	100	9.23	3327000
0184-02-001-27	650	70	0.5	0.033	6.283	745
0184-02-001-30	650	35	0.5	0.033	10.85	1297
0184-02-001-28	550	175	0.05	0.033	16.833	1980
0184-02-001-11	550	105	0.05	0.033	34.03	4015
0184-02-001-16	550	70	0.05	0.033	32.333	3924
0184-02-001-31	550	70	0.5	0.033	51.77	6001

In order to characterize the damage progression, several tests were interrupted prior to failure. Three creep-rupture specimens were tested at 650°C and stress of 70 MPa. These tests were interrupted prior to failure after 0.5, 1.25, and 2.5 hours, representing 8, 20, and 40% of the average life. These specimens were then sectioned for metallographic examination. For all the other tests, failure was defined as separation into two pieces. The creep-rupture test matrix is given in Table 2.

One test, conducted at 650°C using a stress of 70 MPa, was periodically interrupted to measure this specimen's resonant frequency as a function of life. A Non Destructive Evaluation (NDE) method was employed. A vibration technique was utilized in which the specimen was supported vertically from the upper node point of the first flexural vibration mode, and subjected to an impulse force near the lower end of the specimen [10]. An accelerometer placed at the top of the specimen was used to measure the response. Measurements of the applied load and response were used to compute the natural resonant frequency of the specimen [11].

Table 2 – Creep-Rupture Test Matrix and Results for C/SiC.

Specimen ID	Temperature, °C	Stress, MPa	Time to Failure, hrs.	Notes
0184-02-001-4	650	105	3.67	
0184-02-001-5	650	70	5	
0184-02-001-32	650	70	6.85	interrupted 7 times for NDE
0184-02-001-15	650	70	7.15	
0184-02-001-24	650	70	0.5*	interrupted prior to failure
0184-02-001-21	650	70	1.25*	interrupted prior to failure
0184-02-001-17	650	70	2.5*	interrupted prior to failure
0184-02-001-6	650	35	7.53	
0184-02-001-8	550	175	1.53	
0184-02-001-7	550	105	18.28	
0184-02-001-29	550	70	24.233	

* These tests were stopped prior to failure

Electromechanical test machines were employed for the tensile, creep-rupture, and the majority of the fatigue tests. A high frequency servohydraulic test machine was employed for the 100 Hz fatigue testing. Both types of machines used water-cooled wedge grips for specimen gripping. The environment was laboratory air. The creep-rupture tests were performed per the recommended procedures in ASTM Standard Test Method for Creep and Creep Rupture of Continuous Fiber-Reinforced Ceramic Composites under Tensile Loading at Elevated Temperatures (C 1337). The fatigue tests were conducted in accord with ASTM Standard Practice for Constant Amplitude, Axial, Tension-Tension Cyclic Fatigue of Continuous Fiber-Reinforced Advanced Ceramics at Ambient Temperatures (C 1360). Since C 1360 describes procedures for fatigue testing only at room temperature, specimen heating and temperature control were performed in accordance with C 1337.

Untested material was prepared in parallel with tested samples for microstructural examination. After holding the specimen sections under vacuum to enable pores and cavities to out gas, the metallurgical samples were covered with epoxy. The specimens were then placed in a pressure chamber and held with 10 MPa nitrogen to force epoxy in sample pores and damage locations. The metallurgical samples were then lapped and polished for examination. These specimen preparation procedures did not introduce any additional damage and did preserve testing-induced damage in other CMCs [12].

Results

Creep-Rupture and Fatigue Behavior

Creep-rupture lives of specimens tested at 550 and 650°C are given in Table 2 and shown in Figure 2. The 650°C data point represented by a filled circle is the test that was periodically interrupted for NDE inspection, and tested until failure. Lives of less than 20

hours were obtained, despite the fact that the creep stresses (35 to 175 MPa) were well below the composite tensile strength of 535 MPa for this temperature range [13]. Creep-rupture lives at 650°C were about 3.5 times shorter than at 550°C.

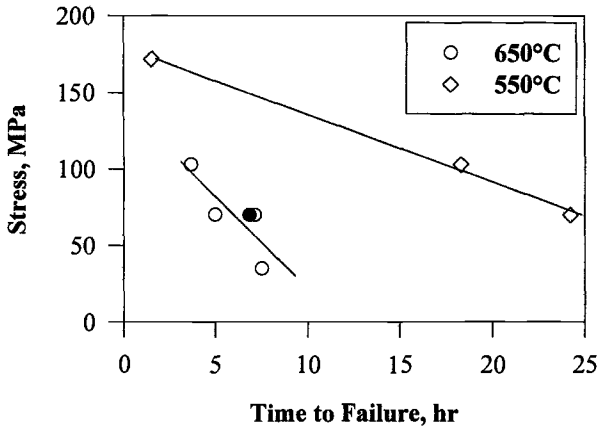


Figure 2 - Creep-rupture lives for C/SiC tested at 550 and 650°C. The filled symbol indicates the life for the specimen test that was periodically interrupted for NDE inspection.

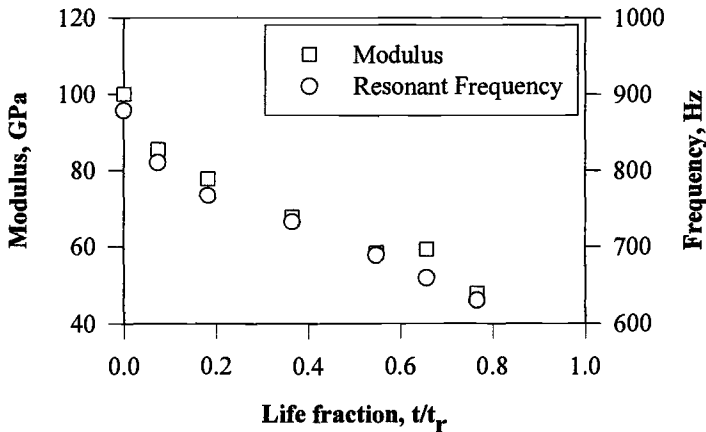


Figure 3 - Specimen modulus and resonant frequency results measured as a function of life fraction for a specimen creep-rupture tested at a stress of 70 MPa stress at 650°C.

Figure 3 shows the modulus as a function of life fraction for the periodically interrupted 650°C creep-rupture test. Modulus values shown are the initial tangent modulus measured during loading to the creep stress for the first creep exposure and upon reloading after the specimen was inspected via NDE. A continual decay in modulus as a function of test time can be seen.

The resonant frequency results for the same interrupted 650°C creep-rupture test are also shown in Figure 3. The frequency response shows the same continuous decrease with increasing life fraction as observed for the modulus. This agreement was expected, since the resonant frequency response is a measurement of test specimen stiffness. This behavior is believed to represent the ongoing progression of damage.

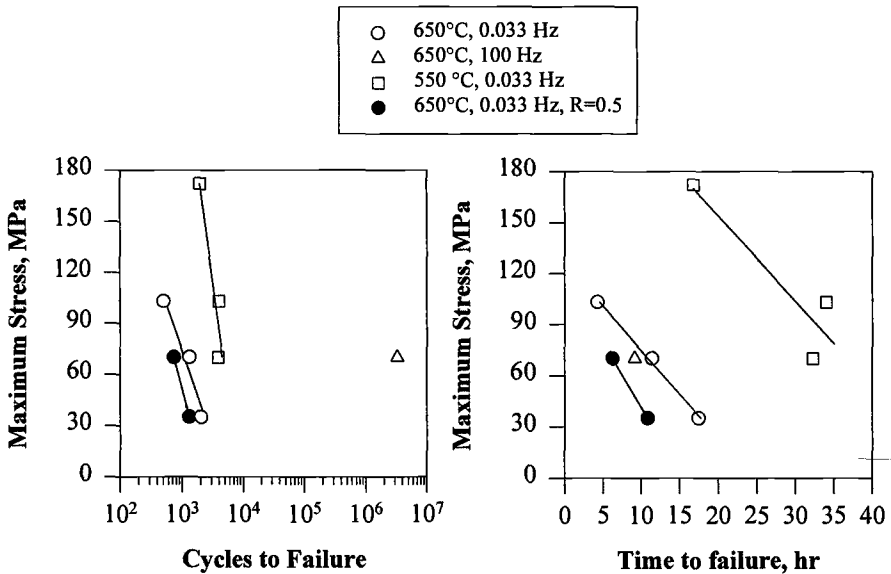


Figure 4 - Fatigue life data for C/SiC tested at 550 and 650°C, a) maximum stress versus cycles to failure, b) maximum stress versus time to failure.

The fatigue data for the C/SiC composite is shown as a function of cycles to failure in Figure 4a and as a function of time to failure in Figure 4b. As seen in both plots, the lives were lower at 650°C than at 550°C, a trend consistent with the creep-rupture behavior. Comparing the fatigue lives with respect to frequency, the high frequency (100 Hz) resulted in a significantly longer life (10⁵ cycles) than was obtained at the low frequency (0.033 Hz). However, the time to failure for both tests was the same.

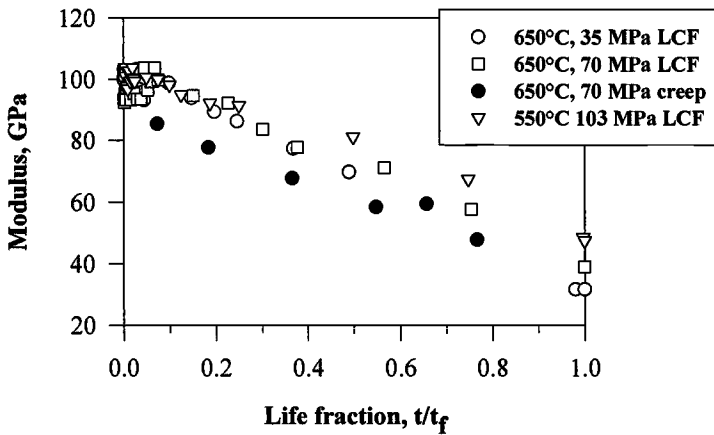


Figure 5 - Specimen modulus measured as a function of life fraction for specimens fatigue and creep-rupture tested at 550 and 650°C.

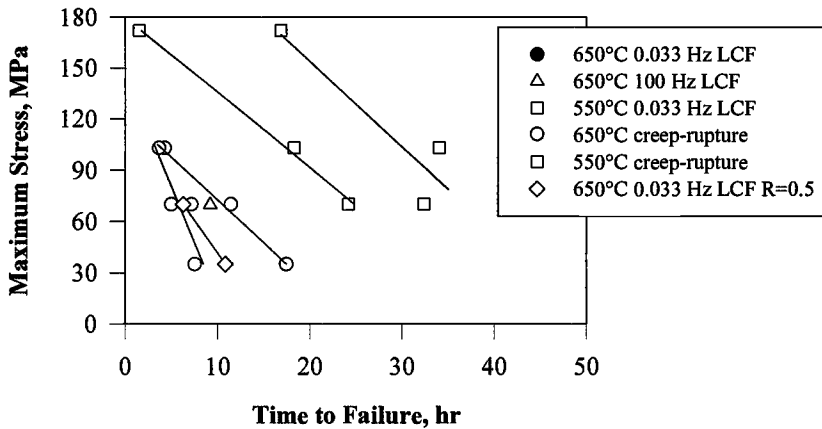


Figure 6 - Comparison of lives on a time to failure basis for creep-rupture and fatigue tests.

The modulus data as a function of life fraction for 550 and 650°C fatigue tests is shown in Figure 5 along with the data for the 650°C creep-rupture test. The initial moduli for both temperatures are about 100 GPa, similar to that reported elsewhere [13]. It is obvious that the observed degradation in modulus for creep-rupture loading also occurs during fatigue loading as well. Furthermore, the rate of degradation as a function

of life fraction is the same for both loading modes at these two temperatures. This implies that similar degradation mechanisms are present.

The creep-rupture and fatigue life data are summarized in Figure 6 on the basis of maximum stress versus time to failure. Tests conducted at 550°C had longer lives than the 650°C tests. In general, fatigue yielded longer lives than creep-rupture. However, the life trend lines for 650°C creep-rupture and fatigue tests converge at the highest stress (103 MPa). For the 650°C data, the time to failure for the fatigue tests conducted using an R-ratio of 0.5 fall in between the life lines for the creep-rupture tests and the 0.05 R-ratio fatigue tests.

Examination of Tested Specimens

A comparison of fracture surfaces of specimens tensile tested at 650°C and creep-rupture tested at 550 and 650°C is shown in Figure 7. The micrographs are of regions adjacent to the edge of the test specimens. The carbon fibers were severely oxidized during the creep-rupture tests and are largely absent from the fracture surface. Although not pictured here, the failed fatigue specimens also had similar fiber oxidation. The SiC matrix remaining near the specimen surface contains much cracking. In contrast, broken fibers were still present on the fracture surface of the tensile tested specimen. However, some fibers were beginning to show slight evidence of environmental attack.

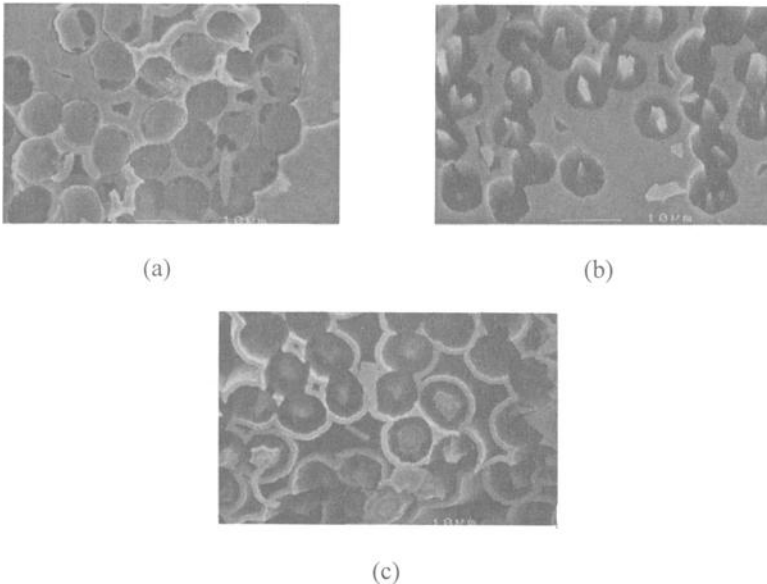


Figure 7 - Fracture surfaces of specimens tested under various conditions: a) 650°C tensile test, b) 650°C creep-rupture test, and c) 550°C creep-rupture test.

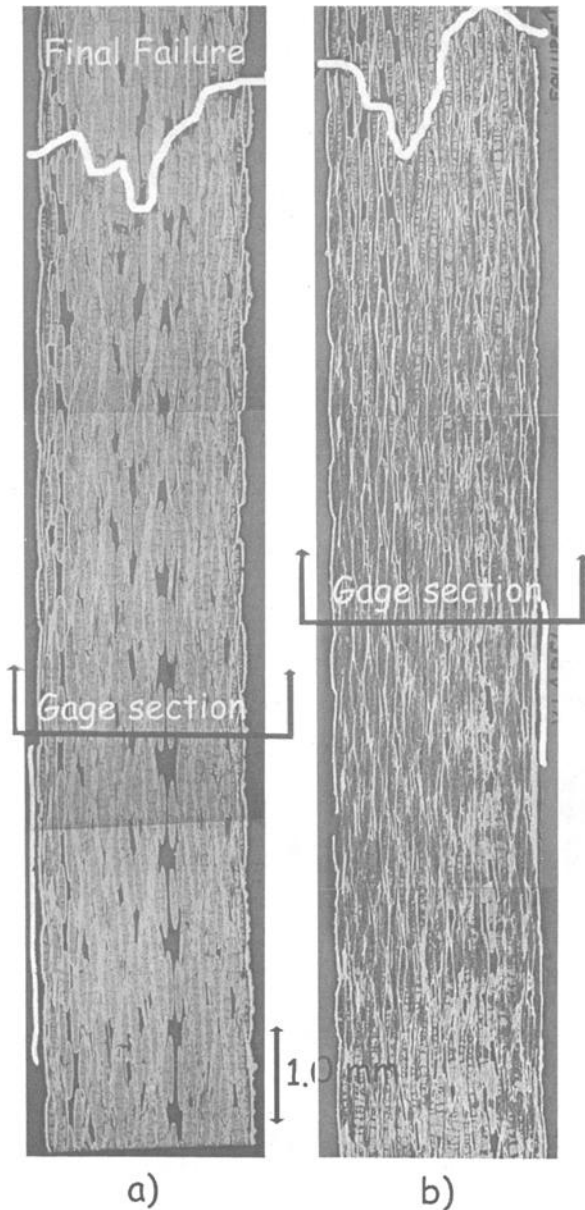
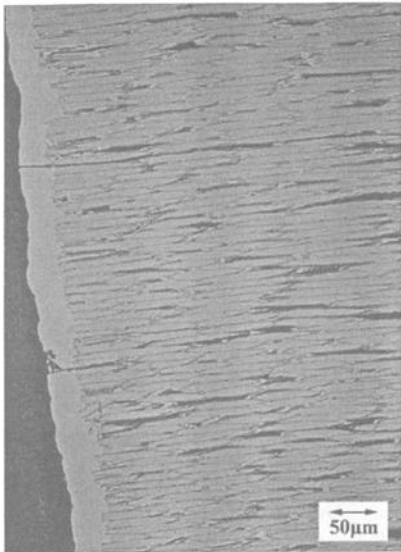
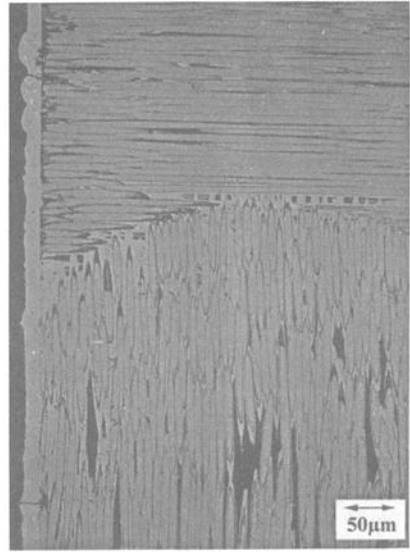


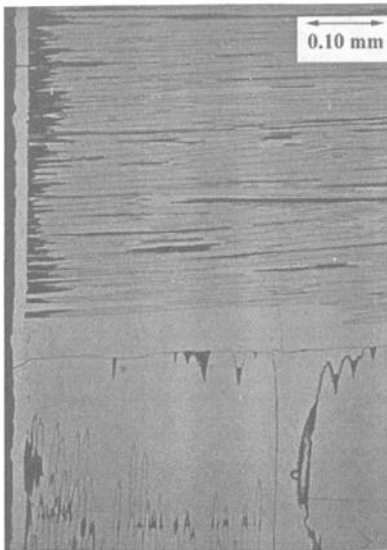
Figure 8 - Longitudinal polished sections of a specimen creep-rupture tested at 650°C; a) mid-thickness view of the specimen gage section, b) a view of the outer edge of the gage section.



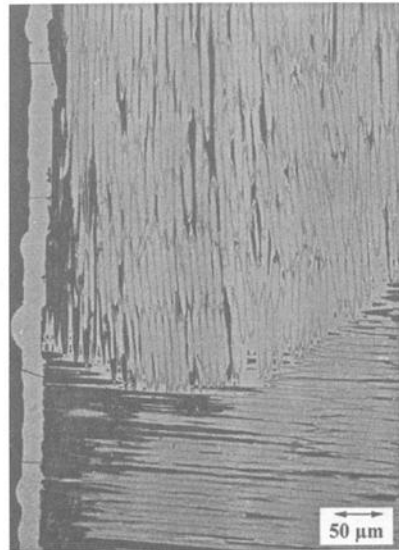
As Fabricated
0 min.



8% of life
30 min.



20% of life
75 min.



40% of life
150 min.

Figure 9 - Longitudinal polished sections of four test specimens showing the evolution of damage occurring at 650°C as a function of life fraction (and test duration).

The damage observed in longitudinal polished sections of a creep-rupture specimen tested at 650°C is shown in Figure 8. Shown are two sections, 1) a view of the center of the specimen obtained by a longitudinal slice of the gage section and 2) an edge-on view of the outer surface of the gage section. Extensive damage in the form of missing fibers can be seen on the specimen surface. Very little damage is present in the mid-thickness view, and it is localized around the pre-existing cracks. Also, the damage on the specimen surface occurs globally within the gage section, i.e., the location of the final fracture does not show any preferential attack. These observations imply that general oxidation is occurring.

The evolution of damage occurring at 650°C as a function of life fraction is shown in Figure 9. The figure contains micro graphs of polished sections of one untested specimen and of three specimens that were creep tested at 650°C and stress of 70 MPa and stopped prior to failure after 0.5, 1.25, and 2.5 hours (corresponding to 8, 20, and 40 % of the average life). Fiber oxidation can be seen in the three tested specimens, with the amount of oxidized fibers increasing with increasing test duration. This damage initially occurs at locations of pre-existing surface cracks. Also, as internal porosity is linked through the array of matrix cracks, oxygen can be more easily transported to the fibers throughout the composite thickness.

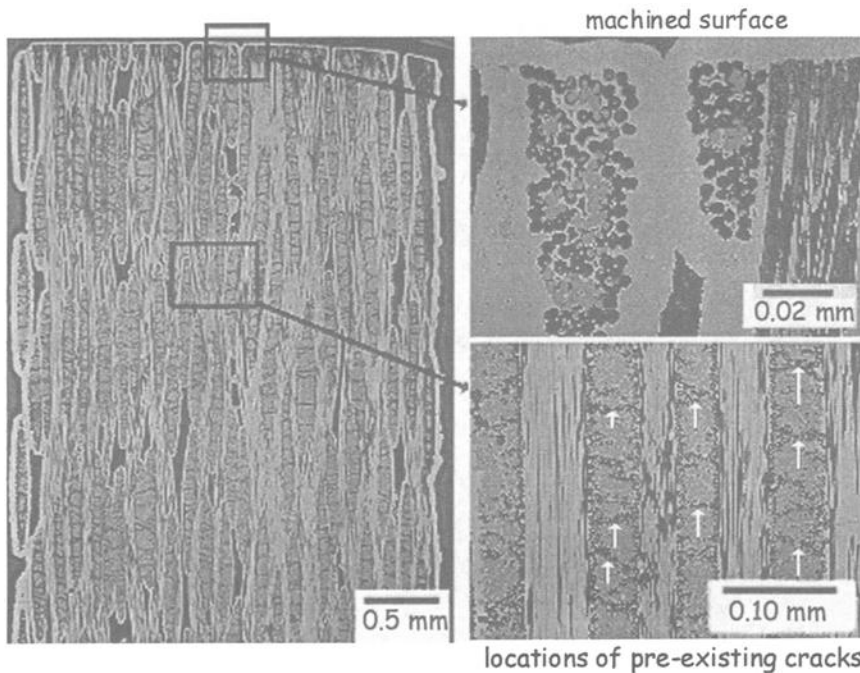


Figure 10 - Damage progression in C/SiC fatigue or creep-rupture tested at 650°C. The loading direction was perpendicular to the page.

The damage progression in C/SiC tested at 650°C is shown in Figure 10. The pre-existing array of matrix cracks enables fiber oxidation from the beginning of the tests. Initially, all the matrix cracks are bridged by fibers. Thus, the matrix plays very little role in the mechanical integrity of the composite. However, oxidation progressively degrades the fibers, overloading the remaining undamaged fibers, resulting in failure. Although not shown here, the same damage progression occurred in specimens creep and fatigue tested at 550°C.

Discussion

Both the fatigue and creep-rupture behavior of C/SiC at 550 and 650°C is dominated by the oxidation of the carbon fibers. Previous studies have shown that oxidation of carbon fibers with a pyrolytic carbon interface occurs at temperatures as low as 500°C [14]. At higher temperatures, around 700 °C, oxidation damage of the carbon fibers occurs very rapidly [3].

The extensive and pre-existing array of micro cracks in the seal coating and in the matrix provides a path for ingress of the environment, enabling the oxidation of the fibers [3,5]. Due to the presence of surface-connected matrix cracks, the environmental damage on the periphery of the specimens occurs globally throughout the heated gage section. On the specimen surface, whole fiber tows are missing and the damage is uniform (Figure 10). Oxidation of fibers in interior tows also occurs. However, this damage is generally localized around the pre-existing micro cracks, as also seen in Figure 10. The presence of porosity undoubtedly acts in conjunction with the micro cracks as a path for diffusion of oxygen and product species, especially into the specimen interior.

Fiber loss, due to oxidation, not only reduces the composite's load carrying ability but also breaks down the inherent crack bridging processes that strengthen the composite. The process by which crack bridging is formed and then progressively destroyed is shown in Figure 11. The pre-existing coating cracks allow for oxygen attack, and it is the damage of those fibers that extends the crack growth mechanism. The 0° tows act to bridge the cracks, allowing the composite to keep its integrity. However, as seen in the figure, they are also susceptible to the environmental attack. Once sufficient damage to the 0° tows takes place, the fibers carrying the tensile load begin to fail, leading to progressive deterioration of the composite. Progressive loss of fiber volume fraction due to oxidation eventually leads to composite failure through increased loading of the remaining intact fibers.

While this progressive deterioration of the integrity of the composite takes place, it is interesting to note that almost no further damage occurs on the surface of the seal coated specimens. Microscopic examination of the interrupted specimens did not show any increase in the seal coating cracks or other outward evidence of internal damage. Internal damage was observed in specimens that were sectioned and polished. This points to the need for further development of reliable nondestructive evaluation techniques, such as resonant frequency attenuation, to monitor the true degradation of the composite properties.

Residual strength degradation has also been observed in oxidized C/SiC specimens [2]. Oxidizing treatments performed at 700°C for 1.6 hours resulted in a 45% decrease in room temperature tensile strength relative to the as-manufactured C/SiC.

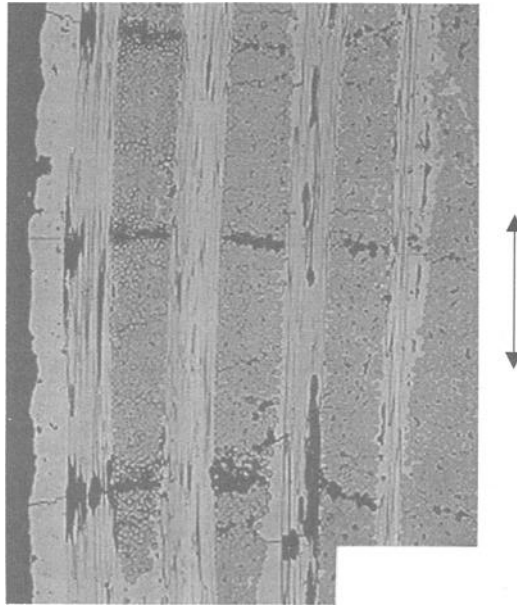


Figure 11 – *Degradation of crack bridging and oxidation of 90° fiber tows in C/SiC due to creep-rupture testing at 650°C. The arrow indicates the loading direction.*

In the present study, the fiber degradation mechanism is also substantiated by the observed progressive degradation in composite modulus. The composite stiffness decreases progressively as more of the load-carrying fibers are oxidized.

Shuler et. al. [9] also observed a progressive reduction in cyclic stress-strain modulus at peak stresses greater than 335 MPa for room-temperature fatigue of C/SiC at frequencies of 1, 10, and 50 Hz. Under these room temperature fatigue loading conditions, the composite stiffness measured at specimen failure was typically 85 to 90 % of the initial value. In contrast, the modulus at failure for specimens fatigue and creep-rupture tested at 550 and 650°C was 40 to 50% of the initial value. The degradation of C/SiC modulus is significantly greater in the presence of oxidation due to degradation of the fibers. On the other hand, the mechanisms of damage occurring during room temperature fatigue were matrix cracking, cyclic wear damage between fiber/matrix and fiber/fiber interfaces [9]. These damage mechanisms are not as detrimental to the integrity of the fiber as is oxidation.

Mechanical fatigue damage also does not appear to play a major role in composite failure for the temperatures, loading conditions, and test frequencies used in this study. As shown through fractography, metallography, and modulus measurements, it is obvious that the same mechanism is present during fatigue as well as creep-rupture. The lack of a synergistic interaction between fatigue damage and oxidation damage is evident when comparing the cyclic lives of specimens tested at different frequencies. Although the

specimen tested at 100 Hz lasted 10^5 more cycles, the time to failure was equivalent to the 0.033 Hz test. Further evidence that supports this notion is the fact that fatigue loading resulted in longer lives (on a time basis) than creep-rupture loading. Also, fatigue tests conducted at 650°C using an R-ratio of 0.5 resulted in lives between those obtained during R=0.05 fatigue and creep-rupture. These results suggest that a combination of temperature and integrated peak stress govern life. The integrated peak stress is the summation of stress versus time and is lower for a fatigue test conducted at the same peak stress as a creep-rupture test, so fatigue life is longer than creep-rupture life.

Since the dominant mechanism under these testing conditions is fiber oxidation, it is not surprising that the same trend in stiffness degradation as a function of life fraction was observed for both creep and fatigue. The good correlation observed between fatigue and creep modulus degradation is also supported by the resonant frequency results that showed the same trend in modulus as a function of time.

The use of specimen stiffness degradation as a method to quantify damage in CMCs has been proposed. For example, Hild et. al. [15] proposed a damage parameter based on composite stiffness degradation to model the effects of matrix cracking and debonding for a CMC subjected to repeated tensile loading at room temperature. In this study, modulus degradation is a manifestation of oxidization of fibers and correlates well with life fraction, thus making it promising as the basis for a life prediction model.

Summary and Conclusions

1. Oxidation of the fibers is the dominant damage mode at 550 and 650°C, for both stress-rupture and fatigue loading. Lives are longer at 550 than at 650°C because of the lower rate of oxidation of fibers at 550°C.
2. Damage occurs progressively during stress-rupture and fatigue. The pre-existing seal coating cracks allow the ingress of oxygen to attack the carbon fibers. The 90° fibers show preferential attack, with the 0° fiber tows acting to bridge the cracks. Once the 0° tows begin to fail, the composite integrity degrades. The damage manifests itself as modulus degradation with increasing time. Coupled with the observed carbon fiber oxidation, the modulus degradation implies that a loss of fiber volume fraction with increasing testing time.
3. LCF lives are longer than stress-rupture lives on a time basis. Under the conditions used for these tests, specimen life is governed by time at temperature and time-averaged stress and is not cycle dependent.

Acknowledgement

The authors would like to thank John D. Zima for his invaluable efforts in conducting the tests.

References

- [1] Weinberg, D. J., Myers, F. K., and Holmes, J. W., "Thermal-Mechanical Fatigue of Fiber-Reinforced Ceramics," Proceedings of the 21st Annual Conference on Composites, Advanced Ceramics, Materials, and Structures, Vol. 18, No. 3, 1997, pp. 555-569.
- [2] Lamouroux, F. and Camus, G., "Oxidation Effects on the Mechanical Properties of 2D Woven C/SiC Composites," Journal of the European Ceramic Society, Vol. 14, 1994, pp. 177-188.
- [3] Lamouroux, F. and Camus, G., "Kinetics and Mechanics of Oxidation of 2D Woven C/SiC Composites: I, Experimental Approach," Journal of the American Ceramic Society, Vol. 77, No. 8, 1994, pp. 2049-2057.
- [4] Lamouroux, F., Bourrat, X., and Nasalain, R., "Structure/Oxidation Behavior Relationship in the Carbonaceous Constituents of 2D-C/PyC/SiC Composites," Carbon, Vol. 31, No. 8, 1993, pp. 1273-1288.
- [5] Halbig, M. C., Brewer, D. N., Eckel, A. J., and Cawley, J. D., "Stressed Oxidation of C/SiC Composites", NASA Technical Memorandum 107457, 1997.
- [6] Effinger, M. R., Koenig, J. R., and Halbig, M. C., "C/SiC Mechanical and Thermal Design Data for a Turbopump Blisk," Proceedings of the 21st Annual Conference on Ceramic, Metal and Carbon Composites, Materials and Structures, 1997, pp.273-289.
- [7] Halbig, M. C, Brewer, D. N., and Eckel, A. J., "Degradation of Continuous Fiber Ceramic Matrix Composites under Constant-Load Conditions," *Environmental, Mechanical, and Thermal Properties and Performance of Continuous Fiber Ceramic Composite (CFCC) Materials and Components*, ASTM STP 1392, M. G. Jenkins, E. Lara-Curzio, and S. T. Gonczy, Eds., American Society for Testing and Materials, West Conshohocken, PA, 2000.
- [8] Geoghegan, P. J., "Chemical Vapor Infiltrated Composites," Flight-Vehicle Materials, Structures, and Dynamics – Assessment and Future Directions, Vol. 3, 1992, pp. 113-137, ASME.
- [9] Shuler, S. F., Holmes, J. W., and Wu, X., "Influence of Loading Frequency on the Room-Temperature Fatigue of a Carbon-Fiber/SiC Matrix Composite," Journal of the American Ceramic Society, Vol. 76, No. 9, 1993, pp. 2327-2336.
- [10] Pereira, J. M., Kautz, H. E., Roth, D. J., and Duke, J., "Measurement of Mechanical Damage in Ceramic Matrix Composites Using Vibration and Acousto-Ultrasonic NDE", Proceedings of the 7th HITEMP Review, NASA CP 10146, 1994, pp. 23-1 to 23-12.
- [11] Pereira, J. M., "Dynamic Response of Composite Plates with Interlaminar Damping Layers", *Vibro-Acoustic Characterization of Materials and Structures*, P. K. Raju, Ed., ASME NCA, Vol. 14, 1992.
- [12] Verrilli, M. J., Calomino, A.M., and Brewer, D.N., "Creep-Rupture Behavior of a Nicalon/SiC Composite," *Thermal and Mechanical Test Methods and Behavior of Continuous-Fiber Ceramic Composites*, ASTM STP 1309, M. G. Jenkins, S. T. Gonczy, E. Lara-Curzio, N. E. Ashbaugh, and L. P. Zawada, Eds., American Society for Testing and Materials, 1997, pp. 158-175.

- [13] Effinger, M. R., Tucker, D. S., and Barnett, T. R., "Tensile and Interlaminar Shear Evaluation of Dupont Lanxide CMCS," Proceedings of the 20th Annual Conference on Composites, Advanced Ceramics, Materials, and Structures, Vol. 17, No. 4, 1996, pp. 316-323.
- [14] Dacic, B. and Marinkovic, S., "Kinetics of Air Oxidation of Unidirectional Carbon Fibres/CVD Carbon Composites," *Carbon*, Vol. 25, No. 3, 1987, pp. 409-415.
- [15] Hild, F., Burr, A., and Leckie, F., "Matrix Cracking and Debonding of Ceramic-Matrix Composites," *International Journal of Solids and Structures*, Vol. 33, No. 8, 1996, pp. 1209-1220.

Özer Ünal¹

Effect of Loading Mode on High-Temperature Tensile Deformation of a SiC/SiC Composite

Reference: Ünal, Ö., “Effect of Loading Mode on High-Temperature Tensile Deformation of a SiC/SiC Composite,” *Mechanical, Thermal and Environmental Testing and Performance of Ceramic Composites and Components, ASTM STP 1392*, M. G. Jenkins, E. Lara-Curzio, and S. T. Gonczy, Eds., American Society for Testing and Materials, West Conshohocken, PA, 2000.

Abstract: Tensile deformation of a silicon carbide (SiC) matrix/Nicalon SiC fiber composite was studied under static and cyclic loads at 1300°C in nitrogen environment. Monotonic tensile tests were carried out to determine the stress levels to be applied during the ensuing tests. It was shown that under comparable stresses, higher strain accumulates under the static loads than the cyclic loads. Yet, the failure took place much more readily under the cyclic loads because of the damages induced on the load carrying 0°-fibers. When the applied cyclic loads were small, the total strain and the rate of strain accumulation were similar under both types of loading, indicating similar deformation mechanisms in this range. At higher loads, however, under the cyclic loading, the matrix and fiber cracking controlled the deformation; under the static loading, the fiber creep dominated the deformation.

Keywords: silicon carbide composite, tensile, creep, fatigue and high temperature

Introduction

The primary motivation behind the development efforts for the fiber-reinforced ceramic composites is the need to have damage-tolerant materials in high temperature structural applications. To achieve this goal, the critical studies of important service parameters such as, time, temperature, environments, loading mode, etc, on the material performance, must be carried out and the complex relationships between them should be established. Many of the potential applications are anticipated to involve both cyclic and creep loading. As a result, there has been added emphasis to learn more about the creep and fatigue behavior of ceramic composites [1-5]. However, most of these investigations focussed on either the creep or fatigue behavior of these materials. Moreover, because of the stability issues of Nicalon SiC fiber the majority of studies in this area focussed on temperatures below 1200°C. So, the goal of this investigation was to study the effect of loading mode (static and cyclic) on the high temperature tensile deformation behavior of a SiC/SiC at 1300°C.

¹ Associate Ceramist, Ames Laboratory, 207 Metals Development, Ames, IA 50011.

Experimental Procedure

The commercial SiC/SiC composite studied in this work (AlliedSignal Composites Inc., Newark, DE) contained Nicalon fibers (Nippon Carbon Co., Tokyo, Japan). The composites had two-dimensional plain-weave fiber mats stacked up in 0°/90° orientations. The mats were first coated with 0.5 μm pyrolytic carbon and then the chemical vapor infiltration (CVI) method was used to form the SiC matrix. The composite with 3.3 mm thickness had approximately 40% fiber volume and 10% porosity. The mechanical evaluation of the composites were made in tension using dog-bone shaped specimens having a 150 mm overall length and a 28 mm gauge length. The width of the test specimens was about 12 and 10 mm at the end and gauge sections, respectively. Testing equipment is a servo-hydraulic unit equipped with water-cooled hydraulic grips, a short furnace with graphite heating elements and a high-temperature contact extensometer with a 25 mm gauge length. As can be seen in Figure 1, the contact extensometer is positioned outside the hot-zone to avoid heat and is water-cooled. The strain information is collected directly from the test specimen by a pair of SiC contact rods which are attached to the extensometer. The testing apparatus is contained in an environmental chamber to carry out tests in controlled atmospheres. Since these composites are relatively brittle, and the strain-to-failure is small, the accuracy and stability of the strain measuring device and the alignment of load-train prior to tests are critical. The alignment of the load-train was checked using a dummy specimen containing strain gauges. At the end, a bending strain of less than 3% was obtained at 5 kN. This value decreased further at higher loads.

To achieve mechanical stability of the contact rods on the specimens, particularly under cyclic fatigue loads, a spring capable of exerting 600g force on a specimen through the extensometer rods was installed. Also, the thermal stability of the contact extensometer was maintained with a constant temperature circulator ($\pm 0.1^\circ\text{C}$). As a result, no slippage of the extensometer rods was observed, and thermal stability of the unit was very good. Before testing the specimens were allowed to equilibrate with the furnace for about one hour. Three types of tests were conducted and the load in all of them was applied in tension. Monotonic tension tests were conducted in strain control with a cross-head speed of 0.1 $\mu\text{m/s}$, corresponding to a strain rate of $4 \times 10^{-6} \text{ s}^{-1}$. Cyclic load tests were carried out in load control using a sinusoidal wave-form with a frequency of 0.5 Hz and a stress ratio ($R = \sigma_{\text{min}}/\sigma_{\text{max}}$) of 0.1 for 72,000 cycles (40 hrs). Static load tests were also conducted for 40 hrs in load control by applying a constant load throughout the test. All tests were carried out in a nitrogen atmosphere at 1300°C and under a small positive pressure.

Results and Discussion

Monotonic Tests

To determine the appropriate stress levels to be applied during the ensuing cyclic and static loading tests, a monotonic tensile test was first conducted at 1300°C. When conducted with very slow-strain rates, the uniaxial tensile stress-strain curve displayed distinct deformation regions due to the unique woven architecture of the composite and

the differences between matrix, interface and fiber properties [6]. The composite failure occurred by the creep of bridging fibers. As a result, fibers showed non-brittle fracture features (yielding) [6].

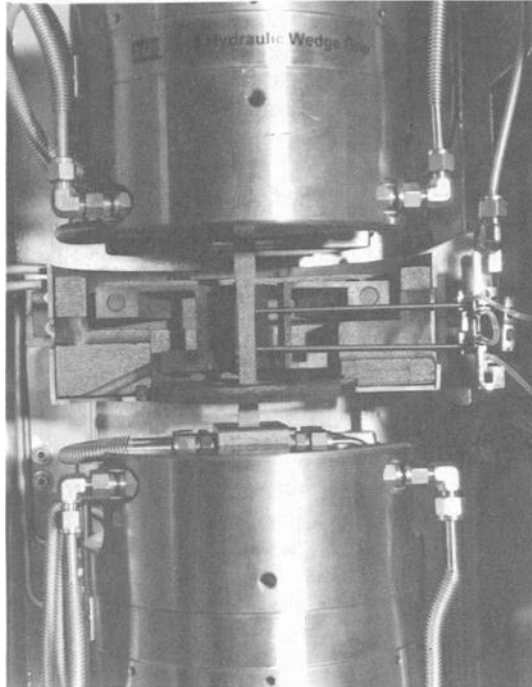


Figure 1. *High temperature mechanical testing unit used.*

Similar to most materials, temperature was seen to have a major effect on the deformation behavior of this composite. This effect can clearly be seen in Figure 2, where the stress/strain curves obtained at room temperature and 1300°C under the same experimental conditions were compared. It is clear that the largest impact of temperature was on the amount of deformation accumulated prior to failure. While the failure strain was ~0.45% at room temperature, it was about 1.5% at 1300°C, almost three times as large. Since elastic and inelastic components are expected to be similar at both temperatures, the difference could be attributed to the creep component of SiC fibers. The matrix failure, which took place at relatively low stress levels due to its low strain-to-failure value, was temperature independent, as can be seen from the similar values of proportional limits at both temperatures. The load carried by matrix was shed onto the fibers above the proportional limit. As a result, the strength of composite was mostly determined by the strength of load-carrying fibers, which appeared to be independent of

temperature in this non-oxidizing environment. However, in an oxidizing environment at 1300°C the strength of similar fibers decreased by about 45% [7]. The summary of results from the room temperature and 1300°C monotonic tests is tabulated in Table 1.

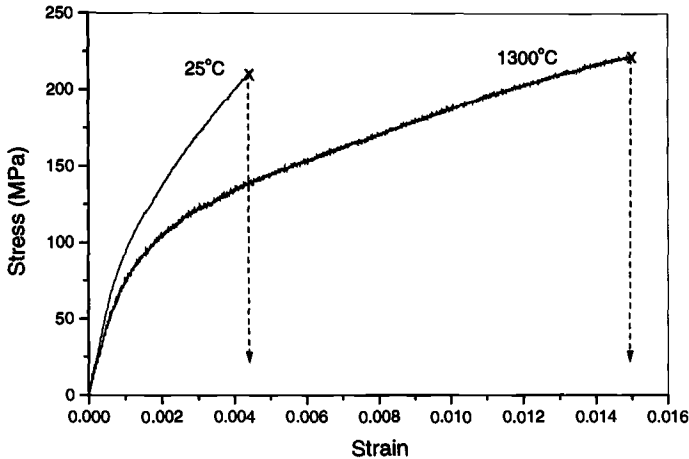


Figure 2. Comparison of stress/strain curves obtained at 25°C and 1300°C.

Table 1. Comparison of the tensile properties of SiC/SiC composite at 25°C and 1300°C.

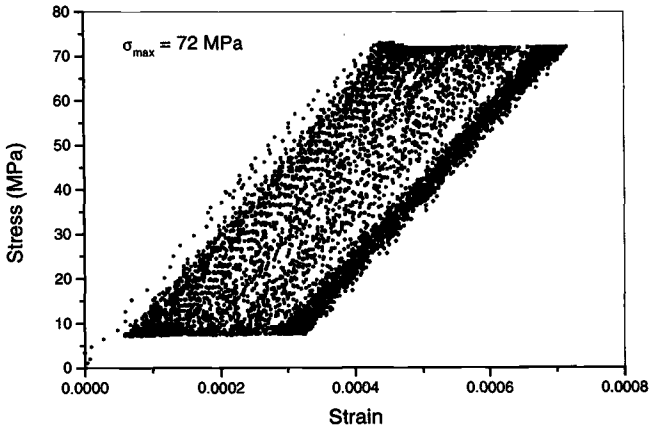
Temperature	Elastic Modulus (GPa)	Proportional Limit (MPa)	Strain to Failure (%)	Ultimate Strength (MPa)
25°C	118±10	62±16	0.45±0.1	210±13
1300°C	85	55	1.5	220

Cyclic Tests

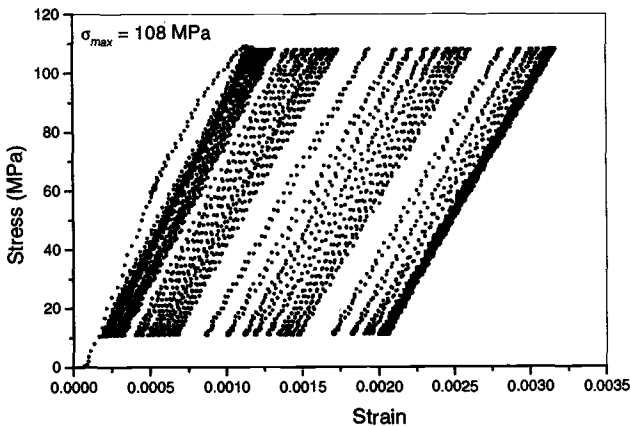
The stress levels applied to both fatigue and creep tests were determined based on the monotonic stress/strain curve at 1300°C in Figure 2. The maximum applied stress (σ_{max}) values in the cyclic tests were 72, 108, 145 and 188 MPa, which correspond to about 33, 49, 66, 85% of the failure stress. In all experiments, the loading started at zero value and continued until the end of test without any interruption. The loading/unloading cycles were controlled automatically by a computer and the data acquisition along the loading and unloading cycles was made in a logarithmic interval.

Figures 3a, 3b, 3c and 3d, respectively, show the entire cyclic data obtained during the tests with σ_{max} = 72, 108, 145 and 188 MPa. Since R=0.1, the corresponding

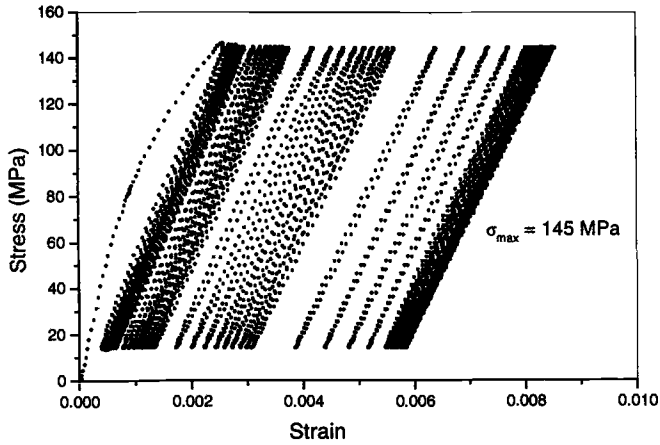
minimum stress values were $\sigma_{\min} = 7.2, 10.8, 14.5$ and 18.8 MPa. As will be discussed later in detail, the failure strains, strain-rates and failure times showed a strong dependence on stress amplitude. While the cyclic tests with $\sigma_{\max} = 72$ and 108 MPa survived the 72,000 cycle test period (40 hrs) the tests with higher stresses, $\sigma_{\max} = 145$ and 188 MPa, failed at about 7100 (~4 hrs) and 890 cycles (~0.5 hrs), respectively. Note that since these tests were conducted under constant stress amplitude, the inelastic deformation due to matrix and fiber fracture, and the plastic deformation due to fiber creep, increased continuously with the cycles, thus shifting the loading/unloading curves along the strain axis. Because the experimental parameters in all tests were the same, the magnitude of this shift (strain accumulation) showed the effect of stress amplitude in the cyclic tests.



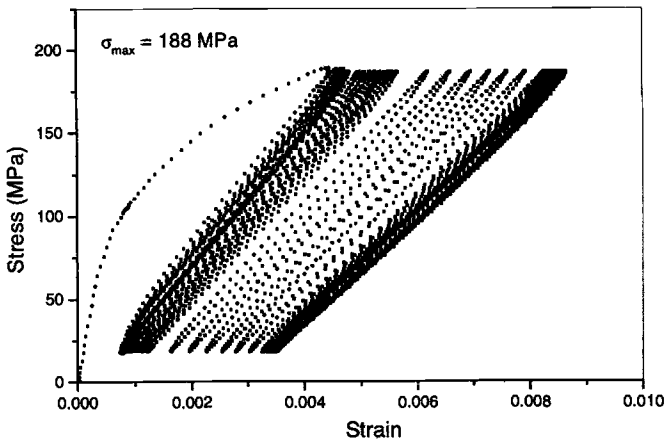
(a)



(b)



(c)



(d)

Figure 3. Cyclic tests conducted with a) $\sigma_{max}=72$, b) 108, c) 145 and d) 188 MPa.

Under cyclic loads the high temperature deformation was due to two important sources. First was the inelastic damage due to the sequential failure of matrix and fibers. This led to a change in specimen stiffness, as can be seen on the loading/unloading curves in Figure 3. This change depended strongly on the applied stress. At low stress levels, the density of cracks was relatively low and the cracking mostly occurred in the 90° -fiber bundles. Since these cracks closed easily during the unloading cycles and the fiber damage was not substantial, the change in stiffness was small (Figure 3a). However, with increasing stress, considerable fiber fracture occurred in addition to matrix cracks within the 0° -bundles, leading to a large decrease in stiffness (Figure 3d). Notice in Figure 3 that

most of such inelastic strain occurred at the initial stage of testing. In fact, the majority of damages in this particular composite were introduced during the first 100 cycles [6].

The second important source of strain at high temperature cyclic tests was the plastic deformation, which occurred mostly due to fiber creep. The strain accumulation due to creep was continuous during the cyclic tests, as can be seen from the shift of loading/unloading curves along the strain axis in Figure 3. In addition, because of the frictional events and energy dissipation during the repeated cycles, the high stresses also led to hysteresis loops. Figure 3d also showed an inflection point at the early states of the test, which was seen as an increase in stiffness at the bottom of the unloading curves. Such features in cyclic tests are generally attributed to crack closure effect in the presence of debris from matrix or/and fibers in the crack wake. Notice that with increasing cycle the inflection point was lost probably due to the grinding of debris under repeated cycles. Such loop formation in the fibrous composites was observed and studied in detail by others [5,8].

The strain accumulation during the cyclic tests was quantified by the strain-rate versus strain graph. This is because the strain-rate/strain plot in fatigue test appears to provide much more information than the corresponding strain/time plot. It not only shows whether or not a true steady state regime was reached during the cyclic loading, but also appears to have been sensitive to the fracture events during the test. The strain-rate/strain plots corresponding to tests in Figure 3 are shown in Figure 4. The strain-rate was determined from the average of several data points while the strain was taken at the maximum stress level. As a result, the starting point at each curve was approximately equal to the amount of elastic strain during the initial loading, which increased with the stress amplitude.

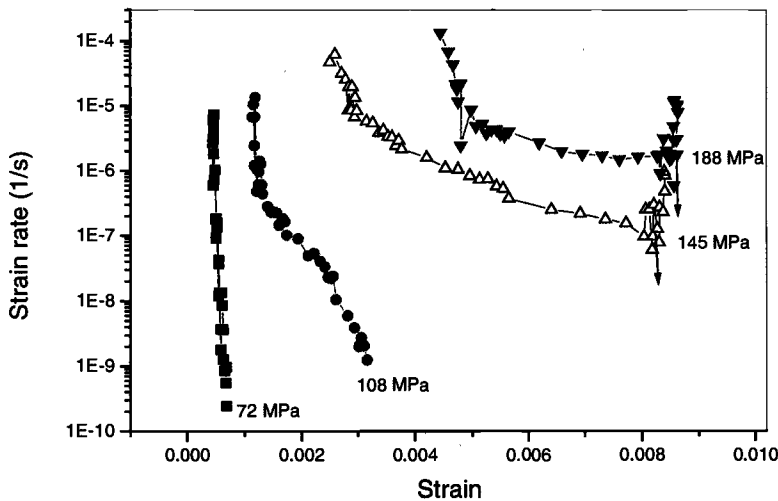


Figure 4. Strain-rate versus strain plots corresponding to cyclic tests in Figure 3.

Note that the curves, which correspond to the failed specimens, contain "jumps" in the strain-rate values prior to failure. This is believed to indicate the increased fiber fracture at the later stages of testing. Since the fiber failure increased the compliance, the net effect was an increase in the strain-rate values. As expected, the curves corresponding to low stress amplitudes did not exhibit such features since they survived the 40 hr. test. Figure 4 also shows that the strain-rate in all tests decreased with increasing strain. However, the curves did not show a "true" steady-state regime, although the strain-rate corresponding to $\sigma_{\max} = 145$ and 188 MPa appear to reach a lower level before failure. In tests with low stress values ($\sigma_{\max} = 72$ and 108 MPa), the strain-rate decreased continuously. This is believed to be due to the saturation of fatigue-induced damages (strains) at lower stresses. Thus, once this inelastic damage mechanism is not available, the strain accumulates only by the fiber and matrix creep.

Creep Tests

The creep tests were conducted at stress levels similar to those used in the cyclic tests. The constant stress creep experiments were carried out at the stress levels of 72, 92, 108 and 145 MPa for 40 hrs. As with the cyclic tests, the results of these tests were plotted as strain-rate versus strain graph in Figure 5. Similar to the observation made in cyclic tests, both the strain-rate and strain increased with applied stress. Among four tests conducted, only the test with 145 MPa failed and its failure time was 4.7 hrs. As compared to fatigue curves in Figure 4, the creep curves in Figure 5 appear to be relatively smooth. As in the case of fatigue tests in Figure 4, the strain-rate in the creep tests continued to decrease with strain, but again a steady-state creep regime was not reached. Due to the time dependence of the strain-rate, the creep behavior of this composite is described by the primary creep laws.

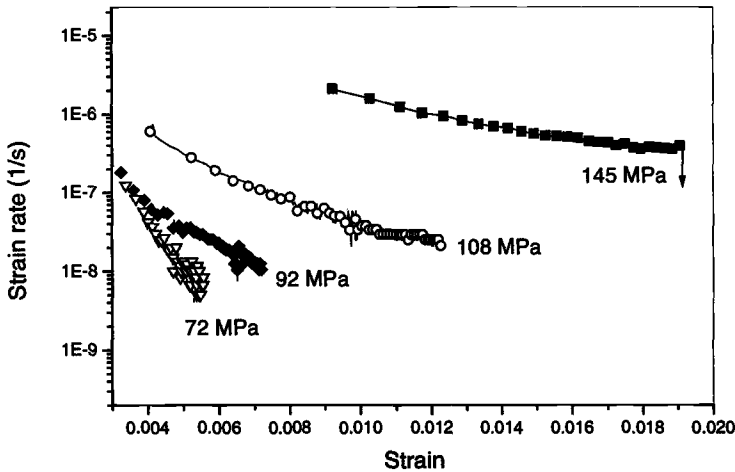


Figure 5. Strain-rate versus strain plots corresponding to static-load creep tests.

To understand the possible role of fiber in the deformation of composite Figure 5 could also be plotted as stress compensated strain-rate versus time plot (not shown here) using the constitutive creep equation of fiber in Eq (1) [9]

$$\dot{\epsilon} = B \sigma^{1.2} t^{-0.6} \quad (1)$$

where $\dot{\epsilon}$, B , σ and t are the strain-rate, constant, stress and time, respectively. Ideally, where the composite is completely cracked and deformation is controlled solely by fibers, data in the plot is expected to collapse into a single curve representing fiber. Present study, however, shows that curves come close to each other, but do not form a single curve. This should not be surprising since the matrix in this case was not completely lost and thus carried a portion of the applied load. Although the stress exponent of the composite was very different from that of the fiber, the average time exponent obtained in Figure 5 was remarkably similar to that of the single fiber, -0.62 . This observation may indicate the differing dependence of time and stress exponents on matrix in composites.

Comparison Cyclic and Static Load Tests

Since the cyclic load was applied as sinusoidal wave, its magnitude varied between σ_{\max} and σ_{\min} at a given time. Thus, to make a one-to-one comparison with the creep tests the cyclic stress values were expressed as mean stress, σ_{mean}

$$\sigma_{\text{mean}} = \frac{(\sigma_{\max} + \sigma_{\min})}{2} \quad (2)$$

The total strain in the specimens under the static and cyclic loads may be written as

$$\mathcal{E}_{\text{static}} = \mathcal{E}_{\text{elastic}} + \mathcal{E}_{\text{creep}} \quad (3a)$$

$$\mathcal{E}_{\text{cyclic}} = \mathcal{E}_{\text{elastic}} + \mathcal{E}_{\text{inelastic}} + \mathcal{E}_{\text{creep}} \quad (3b)$$

Because the interest is in deformation of specimens during the tests, the elastic component was removed from the total strain in each test. The strain-rate values were taken as the lowest value at the end of tests because none of these tests reached a steady-state value. The results from the cyclic and static tests were compared in graphs in terms of the strain (Figure 6a) and strain-rate (Figure 6b) as a function of applied stress. Each data point represents an individual test and the ones with arrows indicate those which failed during the experiments. Both the strain and strain-rate data in Figure 6 show that at low stresses, near and below the proportional limit, the cyclic and creep data follows nearly the same linear curve. Figure 6b, which was plotted in logarithmic scale, exhibits a stress exponent of 4.3 based on Norton's Law. This linear relationship suggests that deformation mechanisms under both types of loading are similar in low stress region. This observation should not be surprising since under low cyclic stress the density of matrix cracks would be minimal. Even if the matrix cracks form, the crack opening would

not be significant enough for typical cyclic inelastic deformation mechanisms to operate during the loading/unloading cycles.

For fatigue mechanisms to be active the matrix cracks must be present and open [10]. Therefore, as shown in Figure 6a, at low stress values, the irreversible strain under the cyclic loads is expected to be mostly due to the fiber and matrix creep, the same mechanism operative in the static tests. A study investigating the effect of cyclic σ_{\max} , in relation to proportional limits in the SiC fiber/Si₃N₄ composites, reported similar observation [4]. It was shown that while both the creep and fatigue mechanisms contributed to total strain above the proportional limit, only the creep deformation mechanisms were dominant below it.

Figure 6a also shows that at higher but comparable stress levels, more strain is accumulated in specimens under the static loads than the cyclic loads. However, Figure 6b shows that the rate at which the strain accumulated was higher under the cyclic loads. As a result, the failure took place much more readily in cyclic mode. The above statements may appear to be contradictory; however, they are not, as the failure times were also taken into account. Under cyclic loads the strain accumulated rapidly and led to failure in short times, even though the overall failure strain was lower in the cyclic tests.

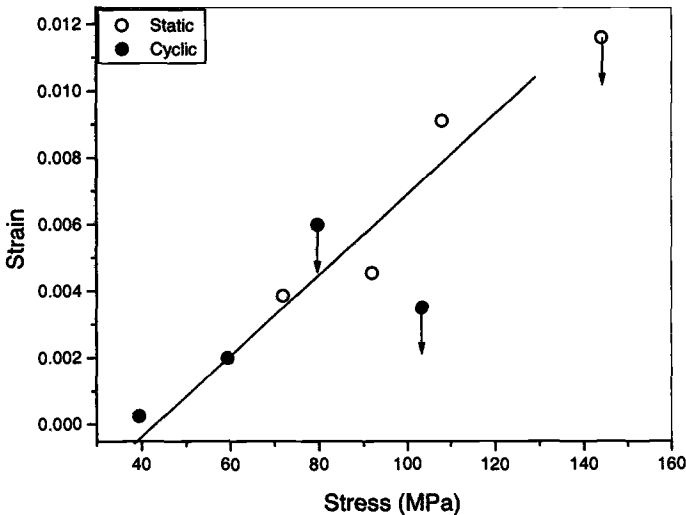


Figure 6a. Comparison of cyclic fatigue and static load creep results; Strain versus stress.

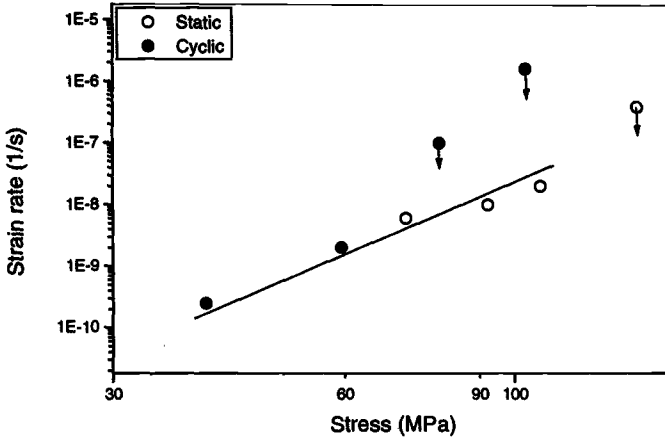


Figure 6b. Comparison of cyclic fatigue and static load creep results; Strain-rate versus stress.

The corresponding time versus stress results for these tests is shown in Figure 7. Again, the cyclic stress values were expressed as σ_{mean} , according to Eq (2). The arrows in this figure indicate the specimens, which did not fail.

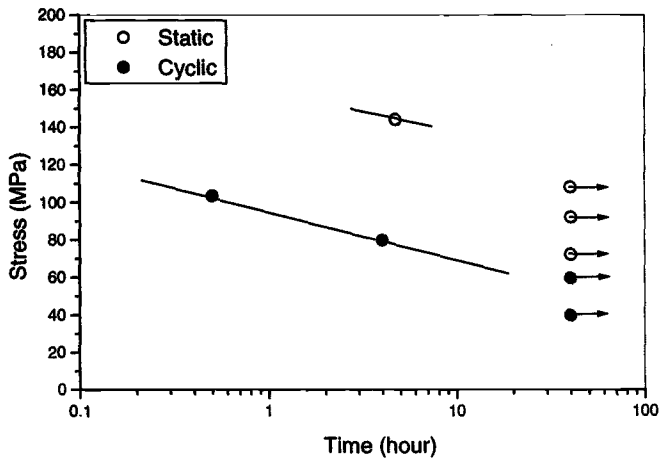


Figure 7. Comparison of stress versus time results for cyclic fatigue and static-load creep tests.

Although there are a limited number of data points, the information in Figure 7 is clear: which is, at comparable stress levels, the specimen fails much more readily under the cyclic loads than under the static loads. This is the case even though the less overall strain is accumulated under the cyclic loads. This implies that the overall strain is not the critical factor determining the life of the composite. Since the load is carried primarily by the fibers, the critical factor turns out to be the amount of damage on them during testing. The fiber damage could easily occur under cyclic loads as a result of frictional events in the presence of matrix debris during the load-reversal. No such mechanism is operative during static loading. Although it is not a factor in this study, the frictional internal heating was also shown to be an important factor in the cyclic life of the composites at high frequencies [4].

Figures 8a and 8b show the damage density in the composite test specimens tested under comparable cyclic and static loads, respectively. Note that both of these composites failed at similar times, the fatigued specimen in ~4 hrs and the crept specimen in ~4.7 hrs, although the applied stress for the fatigued specimen was smaller than that for the crept specimen, ~80 MPa (σ_{mean}), versus ~145 MPa, respectively. This comparison clearly indicates the dangerous nature of the cyclic loading as opposed to static loading. Moreover, at failure the strain in the cyclic specimen (Figure 8a) was less than half of that in the crept specimen (Figure 8b), 0.58% versus 1.15%, respectively. The comparison of microscopic crack density and the crack opening in Figure 8 clearly supports the experimental data shown previously.

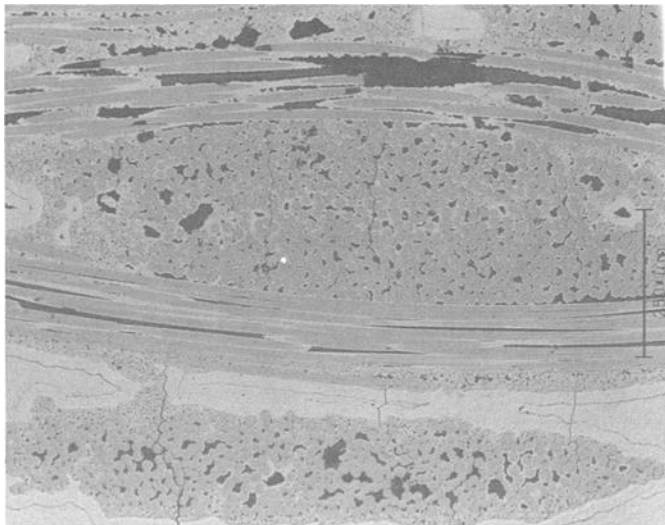


Figure 8a. Damage density in the specimen tested under cyclic load. The fatigue specimen had the failure time of 4 hrs and failure strain of 0.58% under the applied stress of $\sigma_{\text{mean}}=80$ MPa ($\sigma_{\text{max}}=145$ MPa).

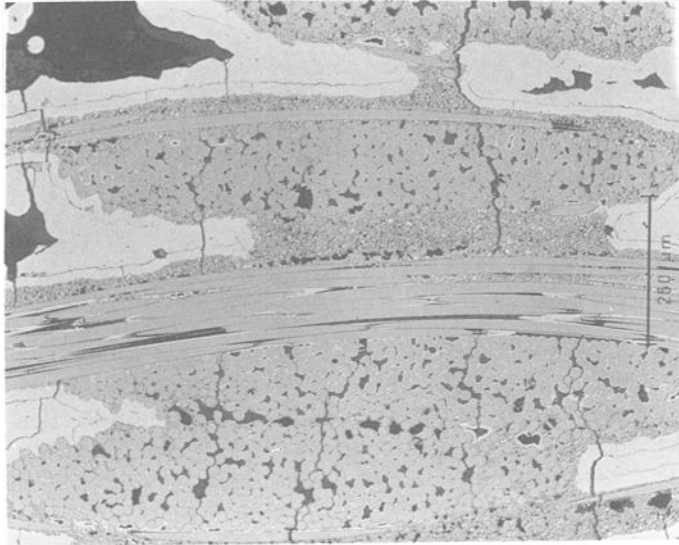


Figure 8b. *Damage density in the specimen tested under static load. The creep specimen had the failure time of 4.7 hrs and failure strain of 1.15% under the applied stress of 145 MPa.*

Conclusions

The irreversible strain accumulation in the SiC/SiC composite at 1300°C takes place under both the cyclic and static loads. Under cyclic loading, deformation occurs as a result of both the inelastic strain due to the matrix and fiber cracking, and the plastic strain due to fiber creep. Under static loading, deformation is dominated by the fiber creep. The magnitude and rate of strain accumulation under both types of loading depend on the applied stress. At comparable stress levels, the static loading leads to a larger strain while the cycle loading leads to a larger strain-rate. At low stress values, the dependence of strain and strain-rate on stress in both types of loading is similar, indicating that the fiber and matrix creep is dominant in this range. At higher stresses, however, the classical fatigue deformation mechanisms are operative. The failure takes much more readily under the cyclic loads than the static loads even though fatigue specimens accumulate smaller strain. This is because the load carrying fibers are likely to be damaged during the loading/unloading cycles in the presence of matrix and fiber debris within the cracks. The irreversible deformation rate decreases with increasing strain, but a steady-state regime is not reached in either types of testing.

Acknowledgment

Funding for this work was provided by Department of Energy, Office of Basic Energy Sciences under contract No. W-7405-ENG-82.

References

- [1] Shuler, S. F., Holmes, J. W., Wu, X., and Roach, D., "Influence of Loading Frequency on the Room-Temperature Fatigue of a Carbon-Fiber/SiC-Matrix Composite," *Journal of the American Ceramics Society*, Vol. 76, 1993, p. 2327.
- [2] Karandikar, P. G. and Chou, T. W., "Damage Development and Moduli Reduction in Nicalon/CAS Composites under Static and Cyclic Fatigue," *Journal of the American Ceramic Society*, Vol. 76, 1993, p. 1720.
- [3] Holmes, J. W., Wu, X., and Sorensen, B. F., "Frequency Dependence of Fatigue Life and Internal Heating of a Fiber-Reinforced/Ceramic Composite," *Journal of the American Ceramics Society*, Vol. 77, 1994, p. 3284.
- [4] Holmes, J. W., "Influence of Stress Ratio on the Elevated-Temperature Fatigue Behavior of a SiC fiber-reinforced Si₃N₄ composite," *Journal of the American Ceramics Society*, Vol. 74, 1991, p. 1639.
- [5] Steen, M., and Valles, J. L., "Unloading-Reloading Sequences and the Analysis of Mechanical Test Results for Continuous Fiber Ceramic Composites," *Thermal and Mechanical Test Methods and Behavior of Continuous Fiber Ceramic Composites*, ASTM STP 1309, M. G. Jenkins, S. T. Gonczy, E. Lara-Curzio, N. E. Ashbaugh, and L. P. Zawada, Eds., American Society for Testing and Materials, West Conshohocken, PA, 1997, p. 49.
- [6] Ünal, Ö., "Tensile and Fatigue Behavior of a Silicon Carbide/Silicon Carbide Composite at 1300°C," *Thermal and Mechanical Test Methods and Behavior of Continuous Fiber Ceramic Composites*, ASTM STP 1309, M. G. Jenkins, S. T. Gonczy, E. Lara-Curzio, N. E. Ashbaugh, and L. P. Zawada, Eds., American Society for Testing and Materials, West Conshohocken, PA, 1997, p. 113.
- [7] Bodet, R., Bourrat, X., Lamon, J., and Naslain, R., "Tensile Creep Behavior of a Silicon Carbide-Based Fibre with a Low Oxygen Content," *Journal of Materials Science*, Vol. 30, 1995, p. 661.
- [8] Domergue, J. M., Heredia, F. E., and Evans, A. G., "Hysteris Loops and the Inelastic Deformation of 0/90 Ceramic Matrix Composites," *Journal of the American Ceramics Society*, Vol. 79, 1996, p. 161.
- [9] DiCarlo, J. A., Yun, H. M., Morscher, G. N., and Goldsby, J. C., "Models for the Thermostructural Properties of SiC Fibers," *Ceramic Transactions*, Vol. 57, 1995, p. 343.
- [10] Evans, A. G., Zok, F. W. and McMeeking, R. M., "Fatigue of Ceramic Matrix Composites," *Acta Metallurgica*, Vol. 43, 1995, p. 859.

Monssef Drissi-Habti,¹ Nobuo Takeda,¹ Kikuo Nakano,² Yoshinori Kanno,³ and Toshihiro Ishikawa⁴

Effects of Temperature and Environment on the Mechanical Properties of Tyranno-Hex™ Composites

Reference: Drissi-Habti, M., Takeda, N., Nakano, K., Kanno, Y., and Ishikawa, T., “Effects of Temperature and Environment on the Mechanical Properties of Tyranno-Hex™ Composites,” *Mechanical, Thermal and Environmental Testing and Performance of Ceramic Composites and Components, ASTM STP 1392*, M. G. Jenkins, E. Lara-Curzio and S. T. Gonczy, Eds., American Society for Testing and Materials, West Conshohocken, PA, 2000.

Abstract: Tyranno-Hex™ is a newly-developed ceramic matrix composite (CMC) containing a high volume fraction (typically 90%) of fibers. The as-processed material exhibits strong bonding at the fiber-matrix interface; hence the composite behaves as a linear-elastic, brittle material at room temperature. However, at high temperatures (~1200° C), a composite “toughening” mechanism develops and a large non linear region is apparent on tensile stress-strain curves. This change in behavior is related primarily to the relaxation of the interfacial bonding following the crystallization of the silica matrix into cristobalite. The measured mechanical behavior is discussed based on the microstructural assessment using transmission electron microscopy (TEM). Preliminary studies on coating techniques (sol-gel and powder metallurgy derived) for oxidation protection of the composite are also presented.

Keywords: Tyranno-Hex™, ceramic matrix composite, bimaterial, toughening

Introduction and Background

In the past 25 years, a great deal of work has been devoted to the development of ceramic matrix composites (CMCs) [for example, 1]. CMCs are materials with promising applications in aerospace, gas turbines, nuclear reactors, etc. However, despite major strides, researchers are compelled to concede that the advances required for CMCs to achieve credibility for industrial-stage processing have not been achieved. Recently, a new concept has been proposed commercially for self-bonded-fiber ceramic

¹ Professor, Center for Collaborative Research, The University of Tokyo, 4-6-1 Komaba Meguro-ku, Tokyo 153, Japan

² Researcher, Japan Ultra-High Temperature Materials Institute, Higashi-machi, 507 Tajimi, Japan

³ Professor, Faculty of Engineering, Yamanashi University, Takeda 4-3-11, Kofu, Yamanashi, Japan

⁴ Researcher, Ube Research Laboratory, UBE Industries Ltd., 1978 Kogushi, Ube-city, Yamaguchi-ken 755-8633, Japan

matrix composites⁵ that are based on a high fiber volume fraction (V_f) of up to 90% (note that conventional CMCs contain V_f ranging between 30 and 60%).

The concept of Tyranno-Hex™ is of some interest for investigators of CMCs. Previous efforts to develop conventional composites have concentrated on CMCs with fiber volume fractions in the range of 30 to 60% because these volume fractions are predicted by composite theory as being necessary to achieve the best mechanical properties [for example, 2]. Given this premise, the justification of the Tyranno-Hex™ concept, or at least the presentation of some supporting arguments for the development of these materials, is necessary. These supporting arguments can be grouped as follows: 1) processing route, 2) theory of CMCs transverse matrix microcracking [3] and 3) management strategy. Note that arguments within these three groups are not separate but can be interactive.

Processing route - If we take a brief look at the processing route, it can be noted that the silica matrix, *in-situ* generated, is compatible with the fibers in terms of thermo-chemistry. This matrix originates simply from the migration of silicon from the bulk of the fibers to the surface during the preoxidation stage of the fibers. This is a positive point since in conventional composites the compatibility of the matrix and the fibers is not that easy to achieve. Many problems arise, such as residual stresses which require the addition of an interphase material at the fiber-matrix interface. Chemical reactions occur at high temperature in air as well. These problems should not occur in Tyranno-Hex™ materials because of the thermo-chemistry compatibility of the fibers and matrix.

Theory of CMCs - The theory (ACK) of transverse matrix microcracking of CMCs [3] provides some interesting insights. It is well known that under tensile loading at high temperatures in air, when the first transverse matrix crack develops, a pathway to the fibers is created for oxygen. Rapid degradation of fibers occurs leading to brittle fracture of the CMC. From a design point of view, it is therefore important to consider the strain, ϵ_m^R (or the stress, σ_m^R), corresponding to the first matrix cracking. When developing a new composite, ϵ_m^R can be thought of as a design parameter. Thus, from the ACK theory we note that ϵ_m^R is expressed as :

$$\epsilon_m^R = [(6\tau / E_C) * (\Gamma_m / E_m^2 V_m) * (E_f V_f^2 / R_f^2)] \tag{1}$$

where, E_C is the longitudinal elastic modulus of the composite, τ is the interfacial shear stress, Γ_m is the matrix fracture energy, E_m is the elastic modulus of the matrix, V_m is the volume fraction of the matrix, V_f is the volume fraction of the fibers, E_f is the elastic modulus of the fiber and R_f is the radius of the fiber. Generally, E_C , τ , and Γ_m are about the same in many composite systems (except for chemical vapor infiltrated (CVI)-derived SiC-SiC composites). Thus, these three parameters do not drastically influence ϵ_m^R . On the other hand, ϵ_m^R is a function of the ratio of the volume fraction of the fibers to their radius. In other words, ϵ_m^R can be increased to a certain level just by increasing the amount of fibers and/or by decreasing their radii. This is the special case of Tyranno-Hex™ where the fiber volume fraction is $V_f = 90\%$ and the mean diameter of the Tyranno™ Lox-M fibers is 8 μm (much smaller than the widely-used Nicalon™ fibers⁶ that have typical mean diameters of around 15 μm).

⁵ Tyranno-Hex™, UBE Industries Ltd., Ube-city, Yamaguchi-ken, Japan

⁶ Nicalon™, Nippon Carbon Ltd, Tokyo Japan

Table 1 - *Physical and mechanical properties of Tyranno™ fibers (Lox-M) [4]*

Diameter (μm)	Density (g/cm^3)	% Si wt	% C wt	% O wt	% Ti wt	C/Si wt	Elastic Modulus (GPa)	Ultimate Tensile Strength (MPa)	Strain at Fracture (%)
8.5	2.37	54	31.6	12.4	2.0	1.36	190	3.3	1.8

Management strategy - This third point, although not of direct scientific interest, should however be mentioned. It is linked to the management strategy of the composite supplier⁵. In fact, when increasing the fiber volume fraction, we also increase the total cost of the materials. However, one should keep in mind that these materials are commercialized by a worldwide fiber supplier⁵ and therefore the question of cost is not topical.

The objectives of this work were two fold: 1) to validate the concept of Tyranno-Hex™ and 2) to report some of the first results related to the mechanical behavior of Tyranno-Hex™ at room and high temperatures. In addition, the effects of environment on the evolution of the microstructure were carefully assessed. Finally, oxidation protection techniques suitable for these particular composites were investigated. Throughout the paper, emphasis is placed on processing as well as on thermomechanical properties.

Materials and Testing

Material

Baseline material - Tyranno-Hex™ composites are typically fabricated with continuous Si-Ti-C-O (Tyranno™ Lox-M) fibers. Some representative physical and mechanical properties of these fibers are shown in Table 1. The Tyranno-Hex™ materials for this study were processed in the following way. The as-processed Tyranno™ Lox-M fibers were heated (at 1100°C) in air for 40 h, to form an oxidized layer of about 500 nm surrounding the fibers. Prepregs, made of pre-oxidized fibers were laminated (eight harness satin weave) and hot-pressed at 1750°C, under moderate pressure (40 to 50 MPa) [5]. During hot-pressing, the interstices filled with an oxide material originating from the pre-oxidized surface layers of the fibers. The as-processed composite had a high fiber volume fraction ($V_f = 90\%$), but a small matrix volume fraction ($V_m = 10\%$) (Table 2). Note that this processing route leads to a strong fiber-matrix bond that has a pronounced influence on the mechanical behavior of as-processed test specimens at room temperature. Some selected mechanical properties of Tyranno-Hex™ from another study are shown in Table 3.

Table 2 - *Some physical properties of as-processed Tyranno-Hex™ composites*

Volume fraction of fibers, V_f (%)	Density (g/cm^3)	Open Porosity (%)
~90	2.45	<1

Table 3 - Mechanical properties of Tyranno-Hex™ composite [5]

Property	20°C	1300°C	1400°C	1500°C
Ultimate tensile strength (MPa)	180	180	-	195
Tensile strain at fracture(%)	0.2	0.25	-	0.95
Three-point-flexural strength (MPa)	350	-	-	-
Apparent fracture toughness (MPa√m)	13	13	13	13
Interlaminar shear strength (MPa)	75	-	-	-

Because thermally-activated changes in microstructure are known to affect the mechanical properties of Tyranno-Hex™, three flexural test specimens were exposed to ambient air at three temperatures (1300°C, 1400°C and 1500°C) for two h, followed by natural cooling. The mechanical properties of these thermally-treated test specimens were then evaluated and compared to as-processed materials.

Coatings for oxidation protection - Some materials for oxidation resistance coatings on Tyranno-Hex™ were evaluated to show proof of reliability mainly in aerospace industries. Among these materials was tetra-ethyl-ortho-silane (TEOS), which is commonly used as a source of external sealant for carbon/carbon (C/C) composites used in the nose cap and the leading edges of aerospace shuttles [6]. In addition to TEOS, we tested cordierite and lithium aluminosilicate materials.

The coating technique we propose is based on the encouraging possibilities of “soft chemistry” which can be quite relevant from a cost-effectiveness point of view. The technique (Fig. 1), consisted of immersing (“soak” time of ~10 min) large size non-notched flexural test specimens (50 x 10 x 3 mm) Tyranno-Hex™ test specimens into the prehydrolyzed sol-gel solution of the coating agent (that is, the most promising combination materials selected for their oxidation behavior [7]) at room temperature. The test specimens were then dried before heating in air for 30 min. Flexure tests were conducted at high temperature in air to evaluate the effectiveness of the coating.

Another method for oxidation protection consisted of coating Tyranno-Hex™ materials with oxides, such as aluminum oxide, silicon oxide, boron oxide and chromium oxide. This powder metallurgy (PM) derived coating procedure was as follows. As-processed Tyranno Hex™ test specimens were placed into a mullite tube. The tube was filled with the powder mixture of the coating agent and the top of the tube was blocked with a platinum lid. The whole assembly was then heated in air for several hours at a temperature in the range of 750° to 1000°C (Fig. 2). This procedure led to the formation of a thin and hard oxide film tightly bonded to the external surface of the substrate [7].

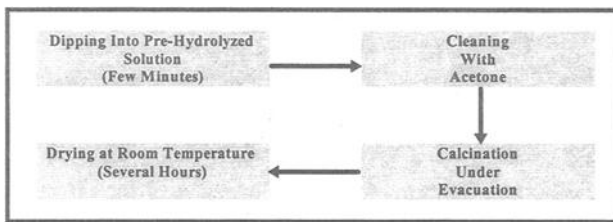


Figure 1 - Flow-chart explaining the stages necessary for producing sol-gel derived thin oxidation-protection coatings on Tyranno-Hex™ composites [7]

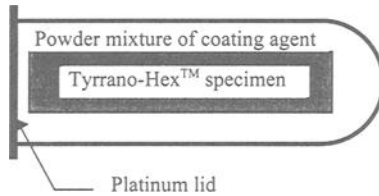


Figure 2 - Schematic illustration of the powder metallurgy (PM)-derived oxidation protection method for Tyranno-Hex™ materials

Flexural test specimens of Tyranno-Hex™ were coated using silicon dioxide, aluminum oxide, boron oxide, and chromium oxide. Flexure tests were conducted at high temperatures in air to evaluate the effectiveness of these coatings.

Testing

Mechanical tests were conducted on a commercial servo-hydraulic test machine⁷ equipped with hydraulic wedge grips for tension tests and special fixtures for flexure tests. For high temperature tests, this test machine was equipped with a furnace for tests in air (maximum temperature, $T_{\max}=1600^{\circ}\text{C}$) and in argon ($T_{\max}=2500^{\circ}\text{C}$). The same crosshead speed of 0.5 mm/min was used for both tension and flexure tests.

Tension - Mechanical tests at room temperature (RT) were carried out on dog-bone (length of 110 mm, gauge length of 40 mm and a nominal thickness of 4 mm) tensile test specimens. During tensile tests at RT, the deformation of the test specimens was recorded by means of strain gages adhered to several locations within the gauge length.

Flexure - Prismatic bar flexural test specimens (45 x 10 x 4 mm) were tested at both room and high temperatures. A four-point-flexure test configuration was adopted for the flexure test such that the distance between the inner and the outer spans of 20 and 40 mm, respectively. Notch sensitivity flexure tests were also performed on edge-wise notched (30% notch to depth ratio) and flatwise un-notched specimens.

At high temperature, only flexure tests were performed with the strain recorded by way of a conventional high-temperature extensometer. Flexural test specimens were positioned on the test fixture in the furnace and the temperature was increased ($50^{\circ}\text{C}/\text{min}$) up to the test temperature (1200°C , 1400°C , and 1500°C). The test specimens spent 10 min at the test temperature before the test was performed. For the oxidation coating study, the non-notched flexural test specimens were tested monotonically [5, 7] in four-point flexure at 1500°C , in air. It must be noted that in all subsequent calculations of flexural properties (for example, flexural stress and ultimate flexural strength) the questionable practice of applying simple beam bending relations to non linear behavior of CMCs was employed for simplicity.

Characterization - The evolution of the microstructure was checked using optical, scanning (SEM) and transmission (TEM) electron microscopes. Test specimens observed by TEM and x-ray diffraction (XRD) were slice cut perpendicular to the 0° fibers. The slices were then subjected to ion milling by means of an argon atomic beam (15kV , 1mA).

⁷ Model 808, MTS Test Systems, Minneapolis, MN

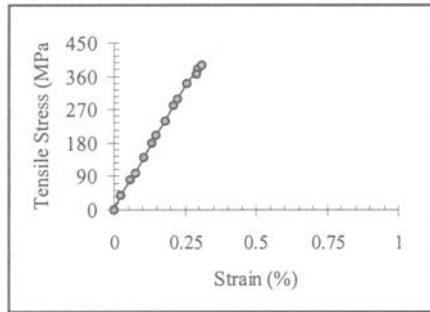


Figure 3 - Tensile stress-strain curve for an as-processed, non coated unidirectional Tyranno-Hex™ materials tested at room temperature in ambient air.

Results

Tests at Room Temperature

The mechanical behavior at room temperature for a unidirectionally (UD)-reinforced as-processed, non coated Tyranno-Hex™ is shown in the tensile stress-strain curve in Fig. 3. In the initial part of the stress-strain curve, the lack of variability in the linear elastic response is similar to the stress-strain curves of brittle ceramics. The stress increased continuously up to a maximum value of 390 MPa (corresponding to a maximum strain of 0.3%) at which point the test specimen failed. The measured longitudinal elastic modulus (E_L) was 134 GPa. Interestingly, the measured E_L is not equal to the elastic modulus for the composite, E_C , predicted by the rule of mixtures, ($E_C = 181$ GPa).

As previously noted, the mechanical behavior of Tyranno-Hex™ materials at room temperature is primarily linear-elastic. The behavior is due to the high shrinkage of the matrix onto the fibers in as-processed test specimens. At room temperature, the "toughening" effect of the composite is not strongly evident and the mechanical behavior is dominated by matrix flaws even though the matrix volume fraction is small (~10 %).

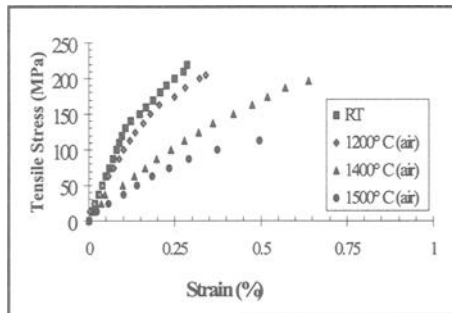


Figure 4 - Tensile stress-stain curves of two-dimensionally reinforced Tyranno-Hex™ test specimens tested in air at room temperature (RT), 1200°C, 1400°C and 1500°C.

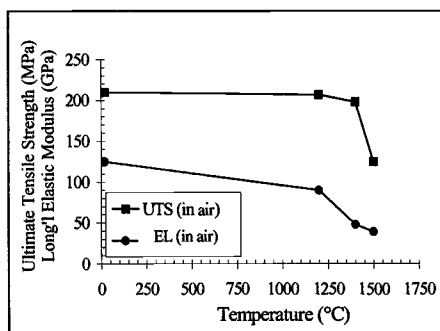
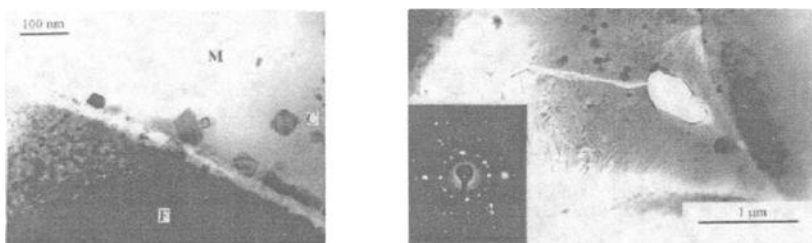


Figure 5 - Ultimate tensile strength (UTS) and longitudinal elastic modulus (E_L), both plotted as functions of test temperature (in air)

Mechanical Tests at High Temperature

The stress-strain curves from tensile tests of four tensile tests specimens of two-dimensionally reinforced (2D) Tyranno-Hex™ tested in air at RT ($\sim 20^\circ\text{C}$), 1200°C , 1400°C and 1500°C are shown in Fig. 4. Note the gradual change of the mechanical behavior from linear elastic (at RT) to greater variability and non linearity at high temperature (HT). At 1500°C , the ultimate strain at fracture ($\sim 1\%$) is similar to the ultimate strain at fracture of Tyranno™ Lox-M fibers ($\sim 1.5\%$).

In Fig. 5, the temperature-dependence of two mechanical properties, longitudinal elastic modulus (E_L) and the ultimate tensile strength (UTS) is presented. The UTS remains fairly constant up to 1200°C , but thereafter decreases continuously with increasing temperature. In the case of the E_L , a smooth decrease with increasing temperature is shown up to 1200°C , followed by a sharp decrease with increasing temperature. It appears that at 1200°C , the microstructure of these materials may undergo some important change that may be revealed through high magnification electron microscopy.



a) Fiber, matrix, and titanium crystals b) Matrix porosity and crystalline silica

Figure 6 - TEM micrograph of a Tyranno-Hex™ test specimens showing a) the fiber (F), the matrix (M) and some titanium containing crystals (C) and b) change in the matrix from amorphous silica to cristobalite after testing at 1300° in air.

Figure 6a shows an electron microscopy photograph of the Tyranno-Hex™ composite constituents: the fiber, the oxide matrix and the turbostratic interphase. The fiber was nanocrystalline structure of mainly SiC crystals, wrapped in a turbostratic carbon matrix (not well organized). For the test specimens examined using electron microscopy, including one tested at 1500°C, no change of the microstructure of the fiber was observed. This means that fibers did not degrade during primary processing of the composite. The composition of the matrix was based on silicon compounds, with no crystal organization (that is, mainly amorphous silica). Within the matrix, titanium-based crystals (e.g., TiC) were present (100 nm maximum size and volume fraction around 5%). The interphase was composed of a well organized turbostratic carbon (20 nm thickness), oriented parallel to the fiber axis, which may promote the interfacial sliding.

Test specimens tested at high temperature (1300° and 1500°C) showed two notable microstructural changes: 1) appearance of porosity inside the matrix and 2) the crystallization of the matrix into cristobalite (Fig. 6b). These two changes are strongly linked, since the change from silica (amorphous state) to cristobalite (crystallized state) is accompanied by a volume contraction. Therefore the porosity is the consequence of the ordering of the microstructure. Inside the matrix, the titanium containing crystals remain.

Mechanical Tests after Thermal Treatment

Load-displacement curves are shown in Fig. 7 for flexure tests at room temperature after unstressed exposure to air at high temperatures (1300°C, 1400°C and 1500°C) for 2 h. Note that there is an improvement of the mechanical properties in the case of the test specimen heat treated at 1500°C in terms of the maximum stress (gain of 12%), the longitudinal elastic modulus, E_L (gain is 40%). Interestingly, E_L after this heat treatment was equal to 180 GPa which is the value of E_c predicted by the rule of mixtures for the composite ($E_c = 181$ GPa). At the maximum stress, the fracture process is well controlled and contrasts with the mechanical behavior of as-processed test specimens.

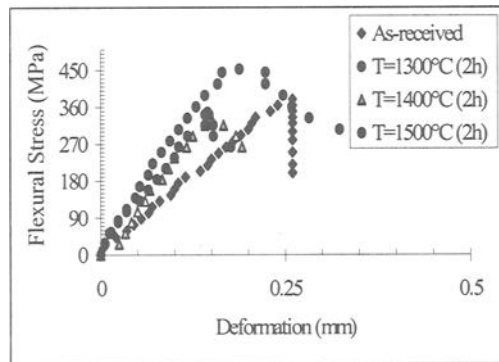


Figure 7 – Flexural stress-deformation curves in four-point flexure tests of as-processed material and three test specimens thermally treated at 1300°, 1400° and 1500°C, in air for 2 h (distance between inner and outer spans of 20 and 30 mm, respectively).

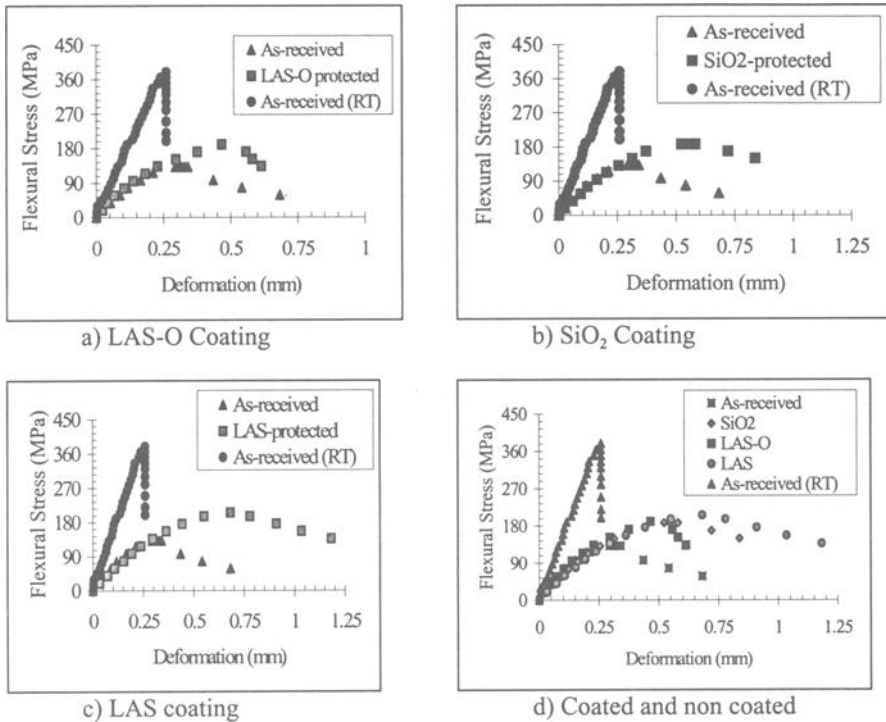


Figure 8 - Flexural stress-deformation curves for coated and uncoated and test specimens of Tyranno-Hex™: (a) LAS-O, (b) SiO₂, and (c) LAS); tested in four-point flexure configuration, at 1500°C, in air (d) comparison of flexural stress-deformation curves of coated and uncoated test specimens.

For the results of the mechanical tests of the coated test specimens, to provide ease of comparison, the monotonic flexural stress-deformation curves for non-coated and coated test specimens at 1500°C are plotted on the same graph (Figs. 8a to 8d) along with the flexural stress-deformation curve of a test specimen tested at RT. As shown, there is a significant gain of performance of Tyranno-Hex™ in terms of the maximum stress (up to 60%) and the deformation in all cases (126% for the LAS coating). However, there is no improvement of the stiffness of the materials, which implies that oxygen diffuses into the bulk of the test specimen. This has a detrimental effect on the E_L and the ultimate flexural strength (UFS). Note however that the thermal barrier efficiency of any coating material should be reflected by a gain of stiffness which is not obvious on the stress-deformation curves of coated materials.

For the test specimens coated using the PM-derived process and tested in four-point flexure at 1500°C, in air, the data are all plotted in Fig. 9 along with the flexural stress-deformation curve of the as-processed test specimen tested at room temperature. As shown, the test specimen coated with alumina [Al₂O₃, (2) in the Fig. 9] shows good thermomechanical behavior compared to other coated test specimens.

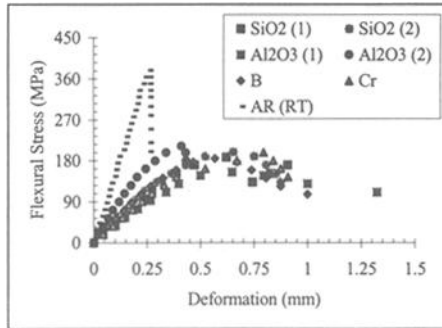


Figure 9 - Flexural stress-deformation curves of as-processed Tyranno-Hex™ tested in four-point-bending plotted along with PM-derived coated test specimens tested at 1500°C, in air.

Post-mortem examination of the surface of the Al₂O₃-coated test specimen showed that the coating was homogenous and tightly bonded to the substrate. Circumstantial evidence of this is: 1) the low deformation at the maximum load (0.4 mm) in comparison with LAS-coated flexural test specimen (0.7 mm, as shown in Fig. 10), which shows that the quality of the coating acted efficiently as an oxygen diffusion barrier; 2) the high retention (57%) of the maximum stress in flexure (213 MPa) in comparison with as-processed test specimen tested at RT (378 MPa).

Discussion

An important issue in this new class of composite is the pull-out mechanism, which has a different meaning compared to conventional CMCs, due to the high fiber volume fraction. We have shown that depending on whether the test specimen is as-processed or thermally-treated, the interfacial behavior is different.

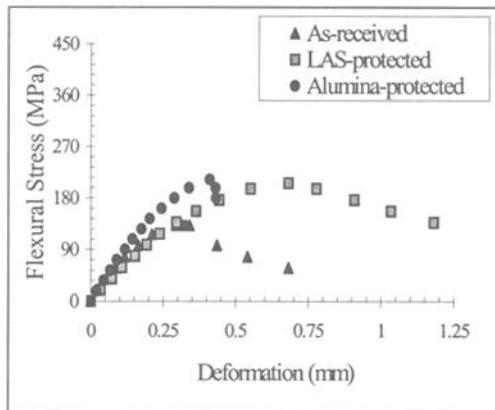


Figure 10 - Comparison between the flexural stress-deformation curves of as-processed, LAS-coated and Al₂O₃ (2) coated test specimens tested at 1500°C, in air.

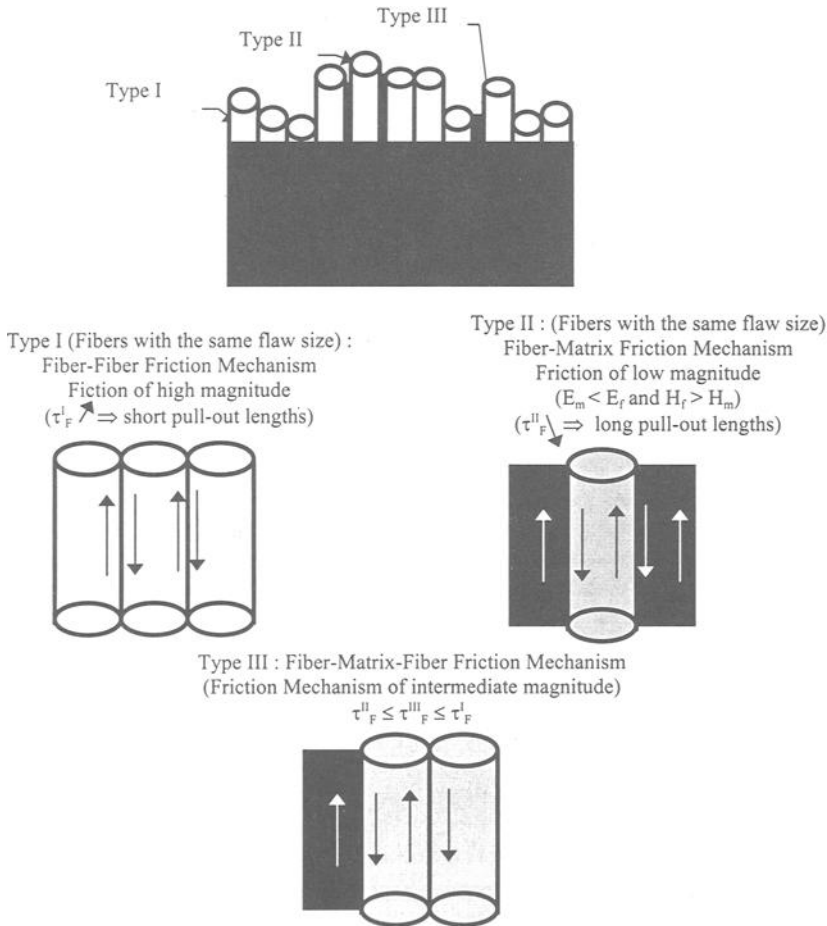


Figure 11 - Illustration of the three types of pull-out mechanism revealed by fracture surface of Tyranno-Hex™ test specimens.

In thermally-treated test specimens (which is the most interesting case from a technological point of view), at least three types of pull-out can be discriminated (Fig. 11). To better explain this, we can consider a test specimen that is cut so as to align the fibers longitudinally. The fibers are of the same radius and the flaw sizes are located in the same longitudinal plane (Fig. 11) :

- Type I : This corresponds to the case when a fiber is surrounded by two other fibers (no matrix exists at the interfaces). Knowing that the fibers have an E_f and a hardness greater than the matrix, it is clear that the fiber-fiber friction mechanism is of a greater magnitude than in the case of matrix-fiber friction and consequently the shortest pull-out lengths appear on the fracture surfaces

- Type II : This corresponds to the case when a fiber is surrounded by a block of matrix. This is the conventional pull-out mechanism, commonly shown in CMCs. Knowing that the matrix is of lower hardness and E_L than the fibers, leads theoretically to the longest pull-out lengths (that is, least magnitude friction mechanism)
- Type III : This corresponds to the case where a fiber is surrounded by a matrix from one side and by a fiber from the other side. Normally, this is the intermediate case and leads to intermediate pull-out lengths.

However, it is possible that because of the high fiber volume fraction, the most frequent case of pull-out encountered in Tyranno-Hex™ composites is type I. Such behavior may originate from the processing route that leads to a high shrinkage of the matrix onto the fibers [8]. Hence, the fibers cannot slide against the matrix and the mechanical behavior is brittle. It should also be noted that the UTS of 390 MPa is low in comparison with the ultimate strength of as-received Tyranno™ Lox-M fibers.

A brief comparison can be done starting from the assumption that there is no premature fiber failure up to the ultimate tensile strength. Then, by dividing UTS by the volume fraction of fibers ($V_f = 0.9$), the estimated tensile strength of Tyranno™ Lox-M fibers is 434 MPa. This value is roughly four times less than that reported for as-received Tyranno™ Lox-M fibers (1.5 GPa [9]). Even though this difference is high, it is not due, as it can be suggested, to the hot pressing stage of the composite, since the applied stress was rigorously maintained at 40 to 50 MPa (which are reasonable values). The difference may be due instead to two main factors:

- The first one is related to the bonding at the fiber-matrix interface. In these materials, the interface is very strong. As a matter of fact, any crack in the matrix will extend to the fiber without mode II deviation at the interface.
- The second one is that during the pre-oxidizing stage of the fibers, there is a massive migration of silicon from the bulk to the surface of fibers to form SiC [9] and then the oxide layer (SiO_2). This migration leads to the lowering of the concentration of silicon inside the fibers, thus leading to a decrease of the mechanical performance of the fibers. Therefore, in Tyranno-Hex™ composites, it is more appropriate to refer to the composite as based on quasi-Tyranno™ Lox-M fibers and silicon oxide matrix.

From the test results, the mechanical behavior of as-processed Tyranno-Hex™ composites seems to be limited to application temperatures less than 1200°C. Based upon the microstructural analysis, the variation of the mechanical behavior as a function of the temperature can be explained when referring to the process route. In fact, the pre-oxidization step of Tyranno™ Lox-M fibers leads to the formation of an amorphous silica layer that is strongly bonded to the external surface of fibers. Consequently, the interfacial sliding is restricted and "toughening" effect of the composite develops. Since the first damage initiates within the matrix, defects propagating from the matrix cross the fibers with no mode II deviation at the interfaces. This results in brittle failure. At higher temperature (typically ~1200°C), the crystallization of the matrix into cristobalite takes place. Hence, it is well known that the "ordering" of the microstructure following the change from amorphous to crystallized states is usually accompanied by a volume contraction which consequently relaxes the strong fiber-matrix interfacial bonding. This relaxation allows the sliding/friction of the fibers

against the matrix and therefore "toughening" effect of the composite develops. This is reflected by the extended non linear behavior shown on stress-strain (or stress-deformation) curves at temperatures greater than 1200°C (that is, the starting temperature of the microstructural change of the silica matrix).

One key point emerging from analyses of the processing route as well as the mechanical behavior of as-processed Tyranno-Hex™ at room temperature is the strong bonding at the fiber-matrix interface. We have shown that at high temperature, the silica matrix changes to cristobalite and this is seemingly the reason why the "toughening" effect of the composite appears. If this explanation is plausible, it was conjectured that with an appropriate thermal treatment (typically greater than 1200°C in air), followed by a natural cooling, the matrix would irreversibly change to cristobalite. As such, an improvement of the mechanical performance at RT was expected (and observed.)

The two schemes (sol-gel and powder metallurgy-derived techniques) to provide oxidation protection were employed. In both cases, the issues upstream are the development of a cost-effective technique able to bring together scientific and technological targets [8, 10]. Therefore, the preliminary results indicate the promising aspects of both techniques from both processing and performance perspectives.

Summary and Conclusions

The mechanical behavior of Tyranno-Hex™ composites was assessed at room and high temperatures. The observed behavior was closely related to the evolution of the microstructure. At room temperature, the mechanical behavior was primarily linear elastic and brittle with no apparent "toughening effect" because of the strong fiber-matrix interfacial bonding. Therefore, the mechanical behavior of the composite was governed by the quality of the matrix (that is, distribution of defects) because of the low ultimate strain at fracture of the matrix and the strong fiber-matrix interfacial bonding. At high temperatures (starting at 1200° C), extensive non-linearity occurred in the stress-strain (or stress-deformation) curves. This non-linearity came from the stress relaxation arising from shrinkage at the fiber-matrix interface (following the contraction of the matrix due to its crystallization). At 1500° C, the fibers had debonded from the matrix and the mechanical behavior of the composite was dominated by the fibers. With an appropriate thermal treatment (e.g., 1500° C in air), followed by natural cooling down to room temperature, the performance of Tyranno-Hex™ at room temperature was significantly improved.

Because of the limitations of the thermomechanical behavior of these composites starting from 1200°C, a variety of oxidation protection materials were applied with the goal of maintaining good thermomechanical properties up to 1500°C. Two methods were tried to develop thin coating materials, namely sol/gel- and powder metallurgy-derived techniques. The former (sol-gel LAS-coated Tyranno-Hex™) showed promising results, although it was shown that both its adherence to the substrate and its thermal barrier efficiency need improvement.

The latter technique (powder-derived alumina) showed a high efficiency when alumina [Al₂O₃ (2)] was applied as a protective material. The powder metallurgy derived technique showed some proof of reliability and seems promising for technological applications. Two main reasons for this are: 1) its low cost and its short processing time compared to some other techniques [for example, chemical vapor deposition (CVD)] and, as a key point, 2) its processing route can be adapted to complex shape structures, thus further justifying it as a cost-effective technique.

Acknowledgments:

This work was conducted within GERMA (Groupe d'Etudes et de Recherche sur les Matériaux Avancés). M. Drissi-Habti thanks the Science and Technology Agency of Japan for the financial support of this work.

References:

[1] Naslain R., "Fiber-Matrix Interphases and Interfaces in Ceramic Matrix Composites," *Composite Interfaces*, Vol. 1, No. 3, (1993) pp. 253-286.

[2] Aveston J. and Kelly A., "Theory of Multiple Fracture of Fibrous Composites," *Journal of Materials Science*, Vol. 8 (1973) pp. 352-362.

[3] Aveston J., Cooper G. A., and Kelly A., "Single and Multiple Fracture in the Properties of Fiber Composites," *Proceedings of the National Physical Laboratory*, IPC Sciences and Technology Press LTD., London, 1971, pp. 15-26.

[4] Reference to UBE Industries, LTD data for Tyrrano™ Lox-M fibers, 1999.

[5] Drissi-Habti, M., Després, J.F, Nakano, K., and Suzuki, K., "Preliminary Assessment and Thermomechanical Behavior of Tyrrano-Hex Composites in Relation with Microstructure," *Ceramic Engineering and Science Proceedings*, Vol. 21, No. 3 and 4, (2000) in press.

[6] Savage G., *Carbon-Carbon Composites*, First Edition, Chapman & Hall, London, 1992.

[7] Drissi-Habti M., Després J.F., Nakano K., and Hatta H., Ishikawa T., "Thermomechanical Behavior and Microstructure of Tyrrano-Hex," *The Third Conference on High Temperature Ceramic Matrix Composites (HT-CMC 3) Proceedings, Key Engineering Materials*, Vols. 164-165, Trans Tech. Pubs, Switzerland, 1999, pp. 189-192.

[8] Drissi-Habti M., Suzuki K., Nakano K., and Kanno Y., "Cost Effectiveness Concept Applied to the Development of Advanced Materials," *Advanced Composite Materials*, Vol. 8, No. 1 (1999) pp. 87-96.

[9] Ishikawa T., Kajii S., Matsunaga K., and Kohtoku Y., "Properties of Tyrrano Fibers Including Self Bonded Tyranno-Hex Composites, *Journal of Materials Science*, Vol. 30 (1995) pp. 6218-6222.

[10] Drissi-Habti M., Sakakibara S., Nakano K., Suzuki K., Yarii T., and Kanno Y., "On the Way to Cost-Effective Oxidation Protection Materials for Ceramic Matrix Composites," *The Third Conference on High Temperature Ceramic Matrix Composites (HT-CMC 3) Proceedings, Key Engineering Materials*, Vols. 164-165, Trans Tech. Pubs, Switzerland, 1999, pp. 291-294.

Michael C. Halbig,¹ David N. Brewer,¹ and Andrew J. Eckel²

Degradation of Continuous Fiber Ceramic Matrix Composites under Constant Load Conditions

Reference: Halbig, M. C., Brewer, D. N., and Eckel, A. J., “**Degradation of Continuous Fiber Ceramic Matrix Composites under Constant Load Conditions,**” *Mechanical, Thermal and Environmental Testing and Performance of Ceramic Composites and Components, ASTM STP 1392*, M. G. Jenkins, E. Lara-Curzio, and S. T. Gonczy, Eds., American Society for Testing and Materials, West Conshohocken, PA, 2000.

Abstract: Ten different ceramic matrix composite (CMC) materials were subjected to a constant load and temperature in an air environment. Tests conducted under these conditions are often referred to as stressed oxidation or creep rupture tests. The stressed oxidation tests were conducted at a temperature of 1454°C at stresses of 69 MPa, 172 MPa and 50% of each material's ultimate tensile strength. The ten materials included such CMCs as C/SiC, SiC/C, SiC/SiC, SiC/SiNC and C/C. The time to failure results of the stressed oxidation tests will be presented. Much of the discussion regarding material degradation under stressed oxidation conditions will focus on C/SiC composites. Thermogravimetric analysis of the oxidation of fully exposed carbon fiber (T300) and of C/SiC coupons will be presented as well as a model that predicts the oxidation patterns and kinetics of carbon fiber tows oxidizing in a nonreactive matrix.

Keywords: Ceramic Matrix Composites, Oxidation, Carbon Fiber.

Introduction

Ceramic matrix composites (CMCs), including carbon/carbon (C/C) composites, are promising materials for use in high temperature structural applications. This class of materials offers high strength to density ratios. Also, their higher temperature capability over conventional superalloys may allow for components that require little or no cooling. This benefit can lead to simpler component designs and weight savings. These materials can also contribute to increases in operating efficiency due to higher operating

¹Research Engineer, U.S. Army Research Laboratory, Vehicle Technology Directorate, 21000 Brookpark Rd, Cleveland, OH, 44135.

²Research Engineer, NASA Glenn Research Center, 21000 Brookpark Rd, Cleveland, OH, 4413.

temperatures being achieved. The wide range of applications for CMCs includes combustor liners, turbomachinery, aircraft brakes, nozzles, and thrusters [1-4].

When evaluating CMCs for potential use in high temperature structural applications, the basic characterization of the material obtained from mechanical and environmental testing is important in understanding the fundamental properties of the material. These types of tests however may not be able to provide enough information on how the material will perform at its application conditions. This is especially true when the many application conditions may include variables such as high temperature, mechanical and thermal stresses, flowing gases, reactive environments, high chamber pressure, and material reactivity/recession (oxidation). The ultimate performance test is to insert a CMC component into its true application (i.e., in an engine). This is often very expensive and impractical when dealing with developmental materials. Simpler, less expensive, and more practical test methods must be utilized. One type of performance test is stressed oxidation or creep rupture testing. This type of test allows materials to be screened at the stress, temperature and environmental conditions that it might see in a real application.

Stressed oxidation tests are proposed since stress may cause a material to behave very differently from when it is unstressed. Unstressed, high temperature, furnace exposure of a material in air may not give a true indication of how susceptible the material is to oxidation. Without sufficient thermal stresses, a mechanically unstressed material will have the same number (or absence) of cracks as it has in its as-received condition. In materials that are uncracked in their as-received condition, such as externally seal coated silicon carbide/silicon carbide (SiC/SiC), the interior will remain closed off from the outside oxidizing environment. The formation of a silica (silicon dioxide) scale on the surface will cover flaws and also protect the material from oxidation. Materials that have a high coefficient of thermal expansion mismatch between the reinforcing fibers and the matrix, such as carbon/silicon carbide (C/SiC), are thermally stressed upon cooling to room temperature from the processing temperature. These types of materials will be microcracked in their as-received condition. At exposure temperatures close to the processing temperature, thermal expansion and rapid silica formation can close the cracks and protect the carbon fibers and the pyro-carbon (pyro-C) interphase from oxidation. However, the material will still be prone to oxidation at lower temperatures where cracks remain open. When a constant load is added to the test conditions, the material may perform very differently. In materials, such as SiC/SiC, a stress above the first matrix cracking stress will induce cracks and make the material more prone to oxidation. In C/SiC materials, stresses will further open pre-existing cracks so that crack closing does not occur and the material is more prone to oxidation due to easier ingress of oxygen.

To obtain a better understanding of how a material might perform in certain application conditions, stressed oxidation (creep rupture) tests were conducted. In this paper, the results of stressed oxidation testing of ten different CMC materials are presented. Much of the analysis and discussion will then focus on the susceptibility of carbon fibers to oxidation and a finite difference model will be presented.

Experimental

In NASA Marshall Space Flight Center's CMC Material Robustness Program, stressed oxidation tests were conducted at NASA Glenn Research Center (GRC). Significant testing, which included tensile tests in air at 21, 1482, and 1648°C (70, 2700 and 3000°F), thermal expansion from -157 to 1649°C (-250 to 3000°F) and oxidative fatigue, was conducted at Southern Research Institute (SRI). Only the results of GRC's stressed oxidation testing and SRI's tensile testing will be presented. Further information about all testing conducted on the ten materials can be found in a proceedings paper [5].

The constituents and processing parameters of the ten CMC materials that were tested are shown in Table I. The materials included C/SiC, C/C, SiC/SiC, SiC/SiNC, and SiC/C ceramic matrix composites. The material vendors were DuPont-Lanxide Composites (DLC, now AlliedSignal Composites Incorporated, ACI), B.F. Goodrich, Carbon-Carbon Advanced Technologies (CCAT), Dow Corning Corporation, Carbon Composites Inc. (CCI), and Synterials. All materials had a two-dimensional plain weave fiber architecture with the exception of the Dow material, which had a 5-harness satin weave. All materials also had a pyro-C interphase except the Dow material, which utilized a proprietary interphase. The 15.2 cm. (6") length dog bone shaped coupons had cross-sectional areas in the gage region that were fairly consistent for a given material. However there was variation between the ten materials with the width ranging from 1.02-1.04 cm. (0.40"-0.41") and the thickness ranging from 0.25-0.43 cm. (0.10"-0.17").

	MATERIAL	MANUFACTURER	YARN	YARN HT	FIBER ARCH	YARN ENDS	INTERFACE COATING	MATRIX	DENSIFICATION	OXID. INHIB.	COATING
1	ENHANCED C-SiC	DUPONT LANXIDE	1KT-300	1700°C	2D PLAIN	19/IN	PyC ALPHA-3	SiC	ISOTHERMAL CM	YES	CV protect
2	STD C-SiC	DUPONT LANXIDE	1KT-300	NONE	2D PLAIN	19/IN	PyC ALPHA-3	SiC	ISOTHERMAL CM	NO	CV protect
3	C-SiC	BFG	1KT-300	1800°C	2D PLAIN	19/IN	PyC	SiC	ISOTHERMAL CM	YES	CVD SiC
4	CTD C-C	CCAT	1KT-300	1700°C	2D PLAIN	30/IN	PyC	C	PHEN. IMPREG	NO	PACK SiC
5	H NIC-SiC	DUPONT LANXIDE	1KH NICALON	NONE	5 HS	17/IN	PyC ALPHA-3	SiC	ISOTHERMAL	YES	NONE
6	H NIC-SiNC	DOW	0.5KH NICALON	NONE	2D PLAIN	16/IN	PROP. NON-C	SiNC	PIP	"YES"	NONE
7	H NIC-C	BFG	0.5KH NICALON	NONE	2D PLAIN	16/IN	PyC	C	ISOTHERMAL	NO	SiC
8	CTD C-C	CCAT / SYNTERIALS	1KT-300	1700°C	2D PLAIN	30/IN	PyC	C	PHEN. IMPREG	NO	Si ₃ N ₄
9	CTD C-C	CCI	1KT-300	NONE	2D PLAIN	19/IN	PyC	C	PULSED CM	NO	SiC
10	C-SiC w/cbs	DUPONT LANXIDE	1KT-300 1KT-300		2D PLAIN	19/IN	PyC	SiC	ISOTHERMAL CM	YES	CV protect

Table I-The material constituents and processing parameters of the 10 CMCs

Stressed oxidation tests of CMCs were conducted in an Instron 8500 Servo-Hydraulic load frame with hydraulic, water-cooled, wedge grips. Temperature was monitored through the use of thermocouples placed at the front face and rear face of the sample. Strain was monitored by extensometers with probes placed at both edges of the

coupon within the gage section. A SiC susceptor placed circumferentially around the sample's gage region was used to heat the gage section of the tensile bar. Heat up time was typically 20 minutes. Once the test temperature of 1454°C (2650°F) was reached, the load was applied. The software allowed the load to be applied at an even rate such that the load is reached in one minute regardless of the size of the final load. Three samples of each material were tested at stresses of 69 MPa (10 ksi) and 172 MPa (25 ksi). Seven of the materials were tested at 50% of their ultimate tensile strength (UTS). Tests were conducted in an air environment. Coupons remained under constant load at elevated temperature until they failed or until 25 hours had passed. The samples that survived 25 hours were fractured at room temperature to determine their residual strength.

Thermogravimetric analysis (TGA) was also conducted to compare and contrast the susceptibility of carbon fibers (T300) to oxidation when in a matrix and when fully exposed to the environment. The TGA testing of the T300 carbon fiber consisted of cutting approximately 0.4 g from a spool of T300 that was bundled in a 1K tow (bundle of 1000 fibers). The fiber material was then placed in an alumina basket and hung by a platinum wire in the TGA furnace. With the material in place, the furnace was brought to the desired temperature (ranging from 600°C to 1100°C). Tests were conducted in flowing oxygen at a rate of 100 cc/min. flowing from a 1" diameter tube. Weight loss and time were recorded. The tests were conducted until all carbon was consumed. TGA tests were also conducted on a C/SiC composite material, specifically DuPont-Lanxide Composites' plain woven standard C/SiC material. The material had a chemically vapor deposited pyro-carbon interphase on the fibers and a chemically vapor infiltrated SiC matrix. A final chemically vapor deposited external seal coating of SiC was applied to the outside of the machined test coupons. The test coupons had dimensions of about 2.54 cm. x 1.27 cm. x 0.32 cm. (1.00" x 0.50" x 0.12") and had weights of approximately 2.4 g. The amount of the carbon fiber within the composite was about 42 wt. %. At the desired temperature (ranging from 550°C to 1400°C), TGA tests were conducted in oxygen at the same flow rate as for the fully exposed T300 fiber. The TGA tests of the C/SiC coupons were conducted for a duration of 25 hours. The results of TGA tests will be presented in the discussion.

Stressed Oxidation Results

In order to interpret better the results of stressed oxidation testing, the ultimate tensile strength of the materials should be known. The results of tensile tests conducted by SRI at 21, 1482, and 1648°C (70, 2700 and 3000°F) are shown in Figure 1. As illustrated by the strengths at elevated temperatures, the C/SiC composites typically have higher strengths than the SiC/SiC composites. The specific C/C materials supplied by the vendors show some variation in strength.

The times to failure for the samples stressed oxidation tested at 69 MPa are shown in Figure 2. Three of the materials survived 25 hours of exposure. The three materials (DLC enhanced C/SiC, DLC C/SiC w/cbs, and Dow SiC/SiNC) all had oxidation protection enhancements which, seem to be a key in prolonging the life of both C/SiC and SiC/SiC composites. The DLC enhanced C/SiC material has a boron containing particulate in the composite that acts as an oxygen getter and forms borosilicate glasses

that seal cracks and protect the fibers from oxidation. The DLC C/SiC material with a cbs (carbon, boron, and silicon) coating uses a similar method of oxidation protection as the enhanced C/SiC material, however, a boron containing coating also provides an exterior form of protection. The Dow SiC/SiNC uses a proprietary, non-carbon, interphase on the SiC fibers. The three materials had relatively high residual strengths as determined from room temperature tensile tests. Two other materials, CCAT C/C and DLC SiC/SiC, did fail within 25 hr, but had relatively longer lives compared to the five other materials that failed at shorter times.

The times to failure for testing at a stress of 172 MPa are shown in Figure 3. All of the materials either failed on load-up or had much shorter lives than at 69 MPa with the exception of the DLC C/SiC material with the cbs coating. This material had lives over ten hours while the other materials either failed load-up or had lives of a few minutes or about half an hour. The cbs coating enhancement in the DLC material seems to be effective in sealing cracks and protecting the fibers even at stresses as high as 172 MPa. It should be noted that the DLC enhanced C/SiC and the DLC C/SiC w/cbs materials had failures in a thermal gradient region located in between the heated gage section and the water-cooled grips. This suggests that the enhancements in these materials are effective at our specific temperature of 1454°C, however the materials may be susceptible to degradation at intermediate temperatures.

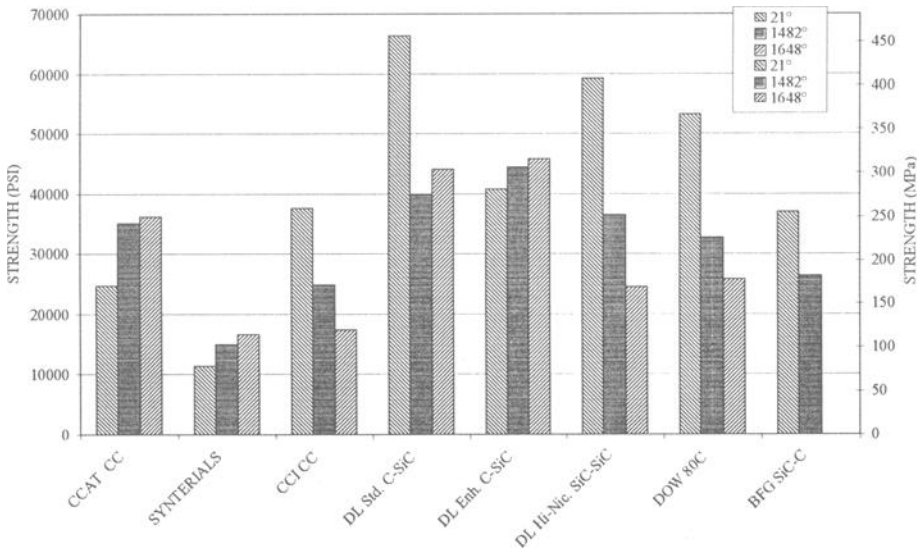


Figure 1-The tensile strength of eight of the program materials at temperatures of 21, 1482 and 1648 °C (70, 2700 and 3000°F). Tensile testing conducted by SRI.

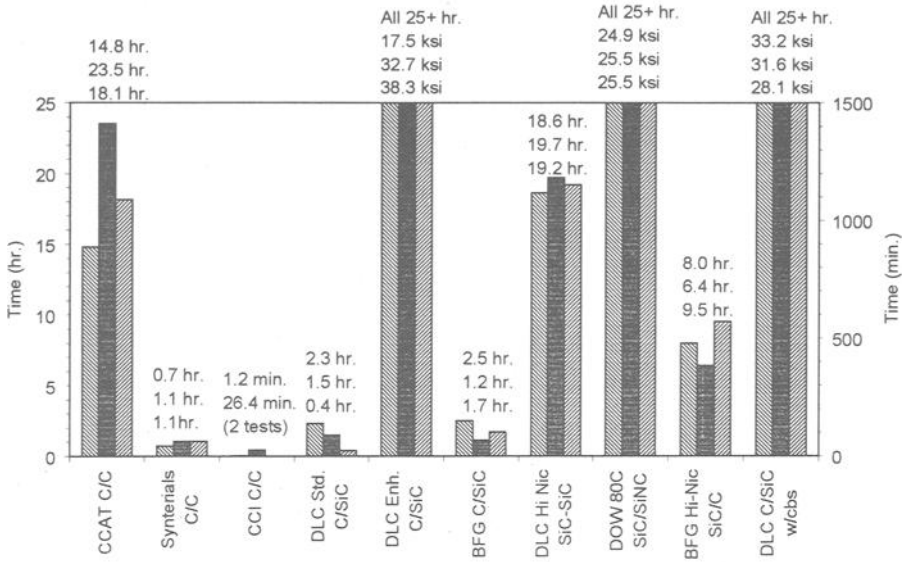


Figure 2-Times to failure for stressed oxidation tests at 1454°C 69 MPa.

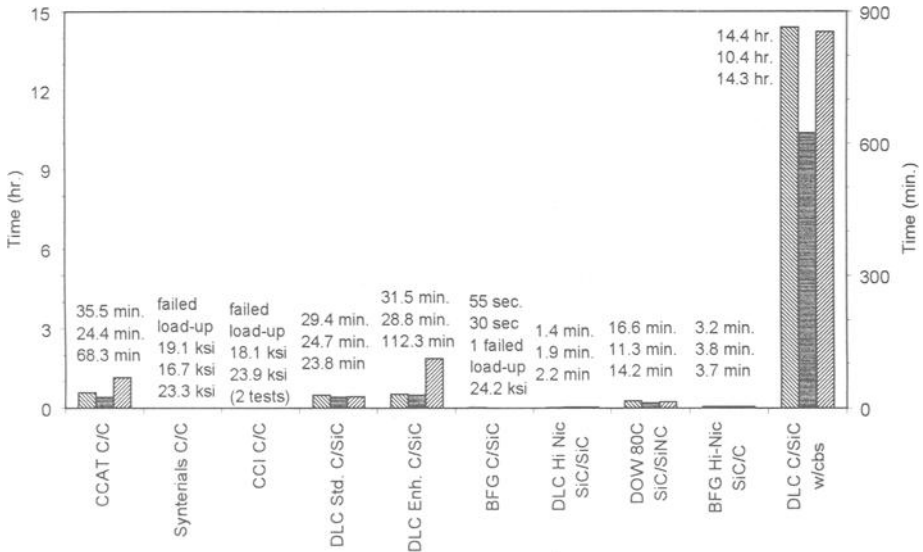


Figure 3-Times to failure for stressed oxidation tests at 1454°C 172 MPa.

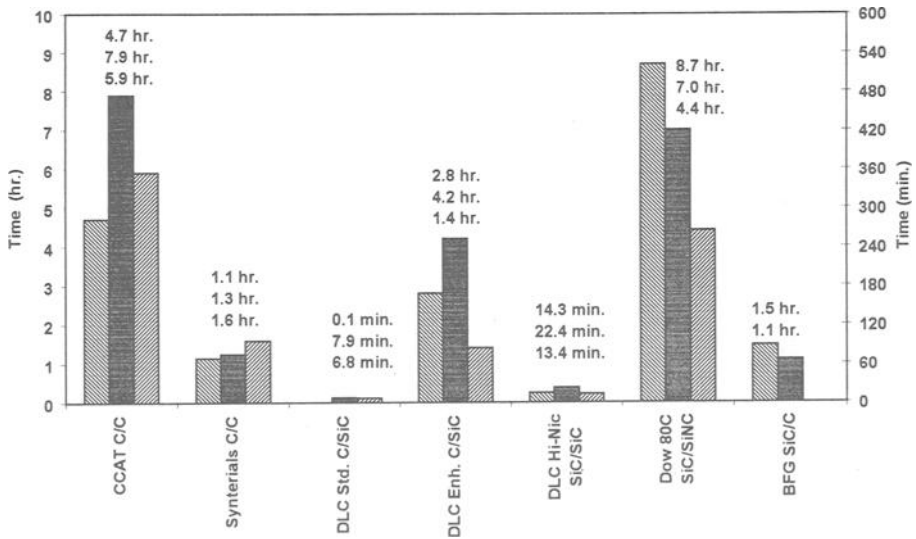


Figure 4-Times to failure for stressed oxidation tests at 1454°C/50% UTS.

Stressed oxidation was also conducted at stresses of 50% of the ultimate tensile strength of each material. The times to failure are shown in Figure 4. Testing at this stress was conducted so that all materials could be evaluated at a stress that seemed to be fairer for all materials regardless of the maturity of the material or the material type. However 50% of the UTS is likely above the first matrix cracking stress for the SiC/SiC and SiC/SiNC materials. Of the seven materials tested at this stress, two materials did better than the rest (CCAT C/C and Dow SiC/SiNC).

The conditions that the materials are exposed to under stressed oxidation tests are harsh enough that the susceptibility of the material to oxidation, creep, and mechanical damage can be determined. Post-test material characterization can help determine the extent and source of damage and which constituents within the CMC are more susceptible. Microstructural analysis of fracture surfaces using a scanning electron microscope and of polished cross-sections using an optical microscope is underway and will be reported in the near future. The remainder of this paper will focus on C/SiC composites and their behavior while under constant load conditions.

TGA Tests

Before the effect of a constant load on C/SiC composites is evaluated, it is beneficial to have an understanding of how the material and its fiber constituent behave in unstressed, high temperature, oxidizing conditions. The percent weigh loss of T300 carbon fiber versus time at temperatures ranging from 600-1100°C is shown in Figure 5. Slower reaction rates are seen for temperatures ranging from 600-750°C. Faster reaction rates and less of a temperature dependence are observed at temperatures above 800°C. At

all temperatures, the approximately 0.4 grams of carbon fiber had completely oxidized away within an hour. These same trends were observed in thermogravimetric analysis (TGA) experiments on T300 fiber conducted by Lamouroux et al [6].

The oxidation of the fully exposed T300 fiber is contrasted by the TGA results of externally-seal coated C/SiC test coupons as shown in Figure 6. At low temperatures, oxygen is able to diffuse into the pre-existing cracks within the composite and react with the carbon fibers. At 550°C, the start of a downward trend in weight loss is observed however the test had to be stopped early. At 750°C, oxidation occurs sooner and at a faster rate. Complete fiber burnout was observed to occur within 5 hours. However, at the higher temperatures, the trends in weight loss and complete fiber burnout did not continue as observed in the TGA tests conducted on the bare T300 fiber. As test temperatures were increased, weight loss rates greatly decreased so that low weight losses were observed even after 25 hours. It should be noted that two tests were conducted at 1000°C and both had different oxidation rates, which are believed to be due to the difference in pre-existing cracks in the external seal coating. Microstructural analysis of polished cross-sections revealed that one sample oxidized uniformly from the outer edges toward the interior while in the other sample significant oxidation occurred from one edge toward the interior but at the opposite edge little oxidation occurred.

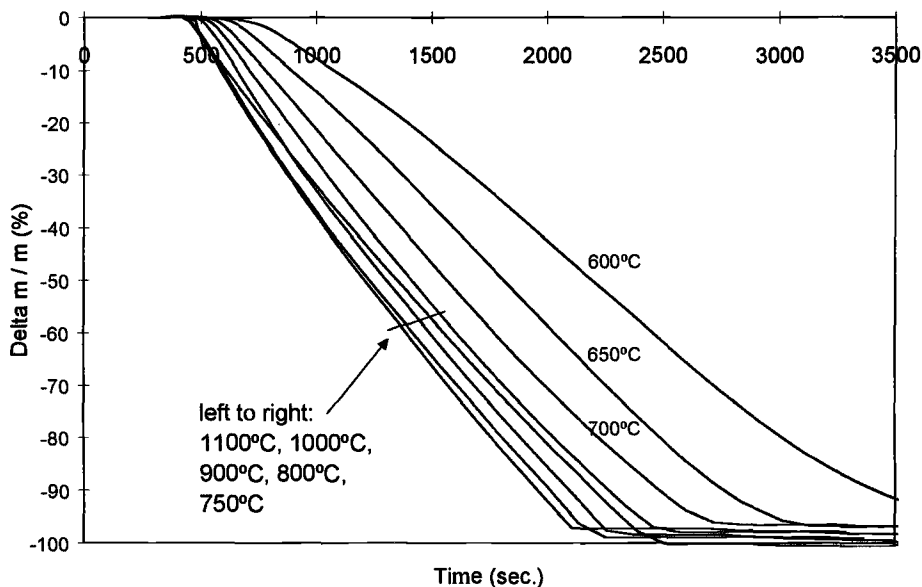


Figure 5-Weight loss versus time of T300 carbon fiber in flowing oxygen at temperatures ranging from 600-1100 °C.

The protection of interior fibers due to the formation of silica and crack closure has been observed by other researchers [7-9]. This effect is due to two factors, which aid in stopping or significantly decreasing the supply of oxygen into the interior of the composite. The first factor is due to crack edges coming very closely together at

temperatures at or near the processing temperature (typical CVI processing performed around 1100-1250°C). As the fiber and matrix expand to their original lengths at the processing temperature, residual thermal stresses are relieved and the pre-existing microcracks become narrower and pinch off the supply of oxygen to the fibers. The second factor is due to the formation of silica as oxygen reacts with silicon carbide. The oxide is in the form of a scale and can cover the surface of the composite and also fill in microcracks. The growth of the oxide scale can act as a sealant at high temperatures. In an unstressed condition, carbon fibers within a C/SiC CMC are therefore more susceptible to oxidation at lower temperatures than at the higher temperatures where thermal expansion, oxide scale growth, and enhancements are effective in closing cracks and cutting off the supply of oxygen to the fibers. However, some oxidation is still to be expected at high temperatures due to the slow growth of oxides compared to the rate at which carbon oxidizes. TGA experiments on chemically vapor deposited SiC at temperatures of 1200-1500°C and at one atmosphere in air were conducted by Ogbuji and Opila to study the oxidation kinetics of SiC. They determined the thickness of the oxide scale on SiC after oxidation at 1300°C for 75 hr to be 1.6 micrometers [10]. In addition to the slow rate at which silica scales grow, enhancements may also be slow in effectively sealing cracks.

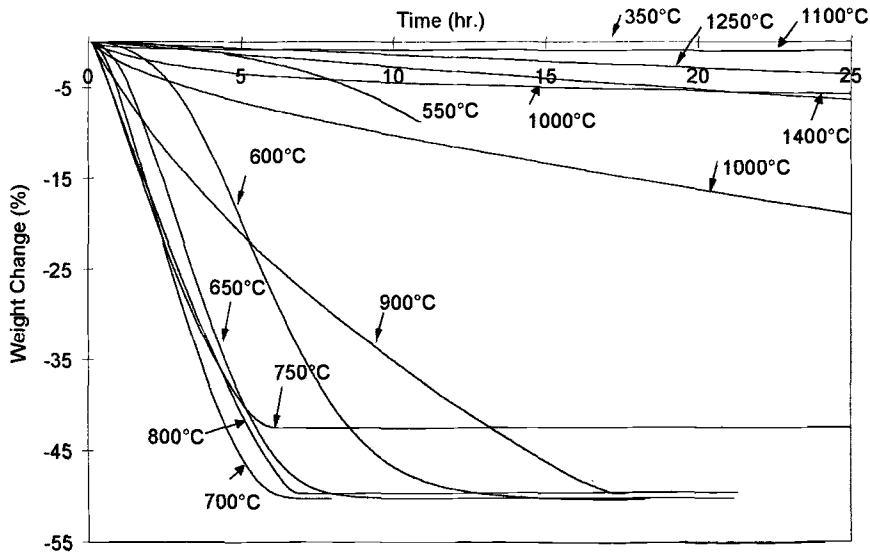


Figure 6-Weight loss versus time of standard C/SiC in flowing oxygen at temperatures ranging from 550-1400 °C.

Constant Load

When a constant load is applied to C/SiC at elevated oxidizing temperatures, the applied stress opens existing cracks and allows for easier ingress of oxygen to the fibers. At sufficiently high stresses, cracks may be open too wide for crack closure and sealing to

occur. The results of stressed oxidation of DLC's standard C/SiC material at stresses of 69 MPa and 172 MPa and at temperatures ranging from 750°C-1500°C are shown in Figure 7 [11]. This batch of material is two years older than the DLC standard C/SiC material tested under the NASA MSFC CMC Material Robustness Program.

In the strain versus time curves, the effect of stress can be seen. As expected, the samples tested at the higher stress had shorter lives. The samples tested at 172 MPa had curves that fall to the left side of the plot while the samples tested at 69 MPa had longer lives and were concentrated to the right side of the plot. Although the times to failure across the temperature range occurred within a fairly narrow range, times to failure increased from 750°C to 1250°C and then decreased at temperatures higher than 1250°C for both stresses. Another effect from temperature is the strain to failure. Samples tested in the higher temperature range showed a much more pronounced tertiary regime and higher strains to failure.

Carbon has been observed to oxidize at temperatures as low as 500-550°C [6, 12, 13]. Stressed oxidation of C/SiC at 550°C did show strength degradation due to oxidation. A sample tested at 172 MPa failed in 25 hours while a sample tested at 69 MPa survived 25 hours. The residual strength of the surviving sample was determined at room temperature to be only half that of the as-received material. The strength reduction and failure at 550°C was not attributed to mechanical damage from the sample being held at a constant load. This conclusion is based upon similar tests conducted in air at 350°C and in argon at 750°C. During 25 hours at load (69 and 172 MPa) and temperature, no significant change in strain due to creep was observed. After 25 hours of exposure, the tests were stopped. The residual strengths determined at room temperature were compatible with the tensile strength of the as-received material [11].

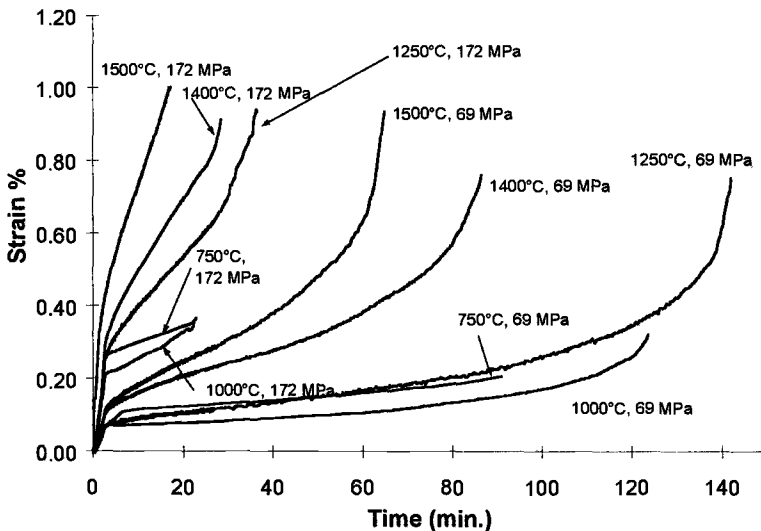


Figure 7-Strain versus time curves from stressed oxidation testing of C/SiC at stresses of 69 MPa (10 ksi) and 172 MPa (25 ksi) and temperatures from 750-1500 °C.

Modeling

Microstructural analysis of oxidation patterns in tested samples, times to failure of C/SiC in stressed oxidation testing, and reaction rates of T300 carbon fiber in TGA experiments suggests two types of kinetics, reaction controlled and diffusion controlled. In order to gain a better understanding of the oxidation of carbon within a CMC and the controlling kinetics, a finite difference model has been developed.

Only the results from the model and a comparison to experimental observations will be presented. Additional information about the model can be found in proceedings papers [14,15]. The model assumes the case of an 8 x 8 array of carbon fiber tows that bridge a cracked matrix. The 2-D model takes the case of pre-cracked as-received C/SiC and simplifies the many microcracks within the material by representing them as one continuous crack that spans the entire surface so that fibers bridge the open plane of the cracked matrix. The model is run at a given Sherwood number.

The Sherwood number is a dimensionless parameter that is equal to reaction rate constant (K [m/s]) times a distance (Δx [m]) divided by the diffusion coefficient (D [m^2/s]). The reaction rate constant and the diffusion coefficient both have a temperature dependence. Across the temperature range of 550-1500°C, theoretical calculations show that the diffusion coefficient will change by a factor of three while the reaction rate constant changes by three orders of magnitude. The calculations for the reaction rate are based on a carbon activation energy of 100 kJ/mol and use linear recession rate data from Eckel et al [16] to solve the Arrhenius reaction rate equation. The diffusion coefficients were calculated using Chapman-Enskog kinetic theory. Because of the temperature dependencies, the ratio of the value for the reaction rate constant to the diffusion coefficient will give high or low Sherwood values. At low temperatures, relatively low Sherwood numbers are obtained since the value of the reaction rate constant will be significantly lower and the value for the diffusion coefficient will only be slightly lower than their mean values in the temperature range of 550-1500°C. Therefore at low temperatures, the kinetics will be controlled by the lower or more limiting step of the rate of carbon-oxygen reactions, i.e. reaction controlled. At high temperatures, the reaction rate will be significantly higher and the diffusion coefficient will only be slightly higher than the mean values within the temperature range. This would give relatively high Sherwood numbers. In this case, the kinetics will be dependent on the rate at which oxygen is supplied to the carbon, i.e. diffusion controlled kinetics. For intermediate temperatures, mixed control kinetics may be observed as the kinetics are in transition from reaction control to diffusion control or vice versa.

In the model, a 170 x 170 grid pattern is laid out with an 8 x 8 fiber tow array in the middle of the matrix. The tows are ten grids in diameter and are spaced 10 grids apart. Therefore, the grids within the 170 x 170 grid pattern will either be open grids within the fiber bridged region where gas phase diffusion can occur or the grids will represent cross-sections of fibers that bridge the crack. The outer edge is maintained at a constant oxygen concentration due to atmospheric conditions. Oxygen is able to diffuse into the matrix until a quasi-steady-state is reached. The local oxygen concentration of each open grid is determined by sampling from its four neighboring grids over hundreds of iterations until steady state is reached. In a method used by Glime and Cawley [17] to study profiles of

oxidized carbon fiber tips, carbon is removed incrementally. The smallest time increment needed to oxidize away the carbon from a grid is determined across the whole array and oxidation is then allowed to occur for that amount of time. Then the whole process of oxygen diffusion until quasi-steady state is reached, determining the smallest time increment, and oxidation for that amount of time is repeated over several iterations until the desired amount of carbon has been reacted away.

The model was run at values (i.e. reaction rate constant, diffusion coefficient, and total oxygen concentration at the edge) correlating to conditions at 1400°C in air, and was compared to the microstructure of a tested coupon. Figure 8 shows the polished cross-section of a sample that had been stressed oxidation tested at 1400°C/69MPa. Severe carbon consumption is seen around the perimeter of the sample (darkened regions in the micrograph). In the close-up views, a reaction front can be seen as carbon is immediately oxidized as soon as oxygen is supplied so that the interior is starved in oxygen and no oxygen is present to react with carbon in the interior of the matrix. In the close-up view of the interior, a large void and cracks in the fiber tows are seen, however, no evidence of oxidation is observed. The oxidation patterns shown in Figure 8 suggest a steep gradient in oxygen concentration at the reaction front toward the interior of the sample. This is an oxidation pattern that would be expected from diffusion controlled kinetics. The results from running the model at conditions for 1400°C are shown in Figure 9. The oxidation pattern on a 2-dimensional surface within the fiber bridged region is shown at various stages in the top row of plots. A shrinking core effect is seen as fibers on the outer perimeter are consumed first and then the reaction front moves inward to the next perimeter of fibers. The interior fiber tows remain unreacted until the oxygen supply reaches them. The correlating oxygen concentration plots for one-quarter of the 2-dimensional section are shown in the bottom row. A steep gradient in oxygen concentration can be seen at the edge of the reaction front toward the interior of the sample. The interior is shown to be deprived of oxygen. These patterns agree well with experimental observations and suggest diffusion controlled kinetics at this relatively high temperature.

The model was also run at values correlating to conditions at 700°C, and were compared to the polished cross-section of a test coupon that had been stressed oxidation tested at 750°C. Figure 10 shows the polished cross-section of a sample stressed oxidation tested at 750°C/69 MPa. Minimal and uniform oxidation is seen along the edge of the sample as well as deep in the interior of the sample along the edges of fiber tows (bundles) and along the matrix cracks within the tows. This pattern suggests that the carbon/oxygen reactions are so slow that oxygen is able to bypass the carbon at the outer edge and saturate the interior at high concentrations so that oxygen is available throughout the matrix to supply the slow reaction process. This is the oxidation pattern that would be expected for reaction controlled kinetics. The results from running the model at conditions for 700°C are shown in Figure 11. The oxidation pattern of the bridging fiber tow array on the 2-dimensional surface is shown in various stages in the top row of plots. The correlating oxygen concentration plots for one-quarter of the

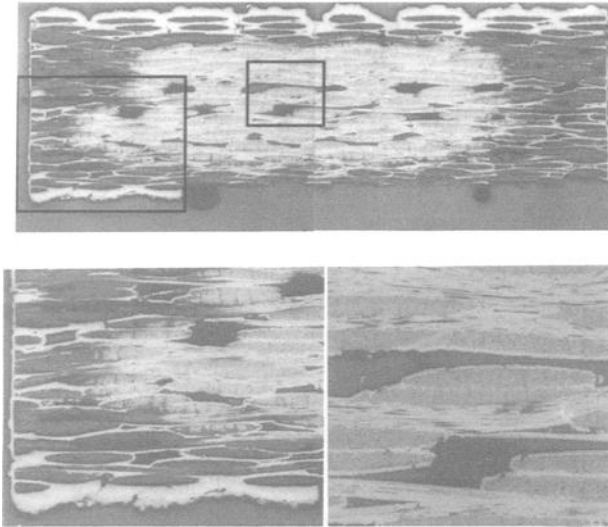


Figure 8-Diffusion controlled kinetics. Optical micrograph of a polished cross-section of a C/SiC sample stressed oxidation tested at 1400 °C/69 MPa. Time to failure was 86 minutes. Scale bar in top micrograph equals 0.5 mm.

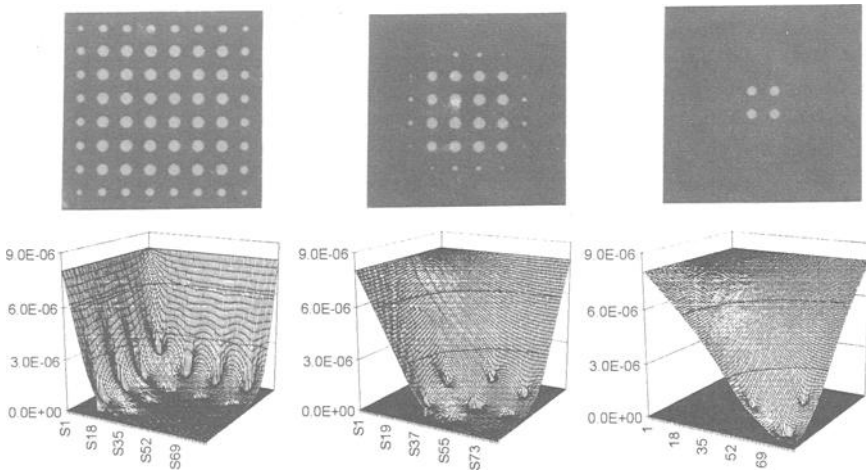


Figure 9-Diffusion controlled kinetics for $Sh = 1.07$ (relating to 1400 °C) at 25%, 75%, and 95% carbon consumption of the 8 x 8 fiber array. The top illustrations are of the remaining area of carbon on the 2-dimensional surface. The bottom plots are of the related oxygen concentrations (mol//cm3) for one quarter of the surface.

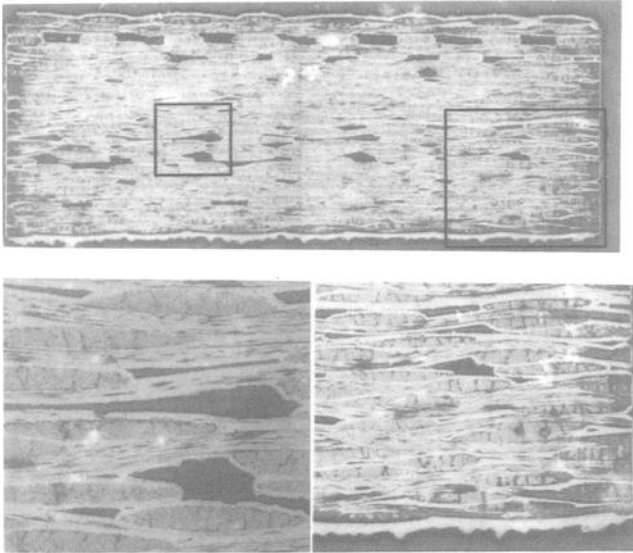


Figure 10-Reaction controlled kinetics. *Optical micrograph of a polished cross-section of a C/SiC sample stressed oxidation tested at 700 °C/69 MPa. Time to failure was 91 minutes. Scale bar in top micrograph equals 0.5 mm.*

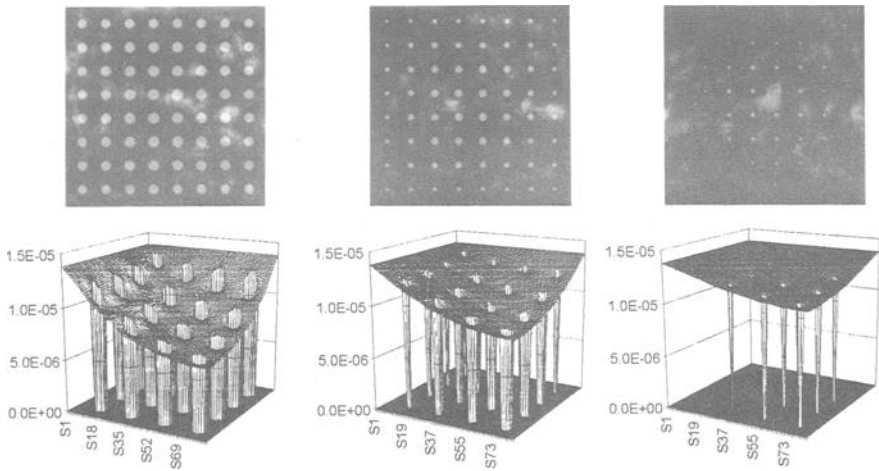


Figure 11-Reaction controlled kinetics for $Sh=1.57E-2$ (relating to 700 °C) at 25%, 75%, and 95% carbon consumption of the 6 x 6 fiber array. *The top illustrations are of the remaining area of carbon on the 2-dimensional surface. The bottom plots are of the related oxygen concentrations (mol/cm³) for one quarter of the surface.*

section are shown in the bottom row. Uniform carbon reactions and high oxygen concentration are seen throughout the 2-dimensional surface of the matrix. These patterns agree well with experimental observations and suggest reaction controlled kinetics at this relatively low temperature.

Conclusions

CMCs can behave very differently in stressed and unstressed conditions in air at elevated temperatures. Unstressed materials may oxidize considerably less than when a stress is applied. Cracks may not be present or may be closed when the materials are unstressed. However when stressed, materials can be greatly damaged due to mechanical stresses, oxidation, and creep. It was observed that the addition of oxidation inhibitors or enhancements can significantly increase the performance of a material. Stressed oxidation and microstructural analysis of C/SiC samples and TGA tests of T300 fiber show different trends in oxidation patterns, times to failure and fiber reactivity at temperatures above 800°C compared to the results obtained at temperatures below 800°C. These trends suggested reaction controlled kinetics at low temperatures and diffusion controlled kinetics at high temperatures. The finite difference model compared well with experimental tests and microstructural analysis in predicting oxidation patterns and kinetics.

References

1. Spriet, P. and Habarou, G. "Applications of CMCs to TurboJet Engines: Overview of the SEP Experience," *Key Engineering Materials*, Vols. 127-131, pp. 1267-1276, 1997.
2. Effinger, M. R., Koenig, J. R., and Halbig, M. C., "C/SiC Mechanical and Thermal Design Data for a Turbopump Blisk," Proceedings of the 21st Annual Conference on Composites, Materials, and Structures, Edited by Mark M. Opeka, Cocoa Beach, Florida, January 26-31, pp. 273-289, 1997.
3. Herbell, T. P. and Eckel, A. J., "Ceramic Matrix Composites for Rocket Engine Turbine Applications," *Transactions of the ASME*, Vol. 115, pp. 64-69, 1993.
4. Herbell, T. P. and Eckel, A. J., "Ceramic Composites Portend Long Turbopump Lives," published in the Proceedings of the 1993 SAE Aerospace Atlantic Conference and Exposition, Dayton, Ohio, April 20-23, 1993.
5. Koenig, J. R., Eckel, A. J., Halbig, M. C., Clinton, R. G., Effinger, M. R., "CMC Material Robustness Program," Proceedings of the 23rd Annual Conference on Composites, Materials and Structures, Cocoa Beach, Florida, January 25-28, 1999.
6. Lamouroux, F., Bourrat, X., and Naslain, R., "Structure/Oxidation Behavior Relationship in the Carbonaceous Constituents of 2D-C/PyC/SiC Composites", *Carbon*, Vol. 31, No 8, pp. 1273-1288, 1993.
7. Filipuzzi, L., Camus, G. and Naslain, R., "Oxidation Mechanisms and Kinetics of 1D-SiC/C/SiC Composite Materials: 1, An Experimental Approach," *J. Am. Ceram. Soc.*, 77 [2], pp. 459-466, 1994.

8. Vix -Guterl, C, Lahaye, J. and Ehrburger, P., "Reactivity of Silicon Carbide and Carbon with Oxygen in Thermostructural Composites," *Carbon*, Vol. 31, No. 4, pp. 629-635, 1993.
9. Lamouroux, F., Camas, G. and Thebault, J., "Kinetics and Mechanisms of Oxidation of 2D Woven C/SiC Composites: I, Experimental Approach," *J. Am. Ceram. Soc.*, 77 [8] 2049-57 (1994).
10. Ogbuji, L. U. J. T. and Opila, E. J., "A Comparison of the Oxidation Kinetics of SiC and Si₃N₄," *Journal of the Electrochemical Society*, Vol. 142, No. 3, pp. 925-930, 1995.
11. Halbig, M. C., Brewer, D. N., Eckel, A. J. and Cawley, J. D., "Stressed Oxidation of C/SiC Composites," *Ceramic Engineering & Science Proceedings*, Vol. 18, I. 3, pp. 547-554, 1997, Proceedings of the 21st Annual Conference on Composites, Advanced Ceramics, Materials and Structures-A, Cocoa Beach, Florida, January 12-16, 1997.
12. Shemet, V. Zh., Pomytkin, A. P. and Neshpor, V. S., "High Temperature Oxidation Behavior of Carbon Materials in Air," *Carbon*, Vol. 31, No. 1, pp. 1-6, 1993.
13. McKee, D. W. "Oxidation Behavior of Matrix-Inhibited Carbon/Carbon Composites," *Carbon*, Vol. 26, No. 5, pp. 659-665, 1998.
14. Halbig, M. C., Eckel, A. J. and Cawley, J. D., "Oxygen Diffusion and Reaction Kinetics in Continuous Fiber Ceramic Matrix Composites," *Ceramic Engineering & Science Proceedings*, Vol. 19, I. 4, pp. 143-150, 1998, Proceedings of the 22nd Annual Conference on Composites, Advanced Materials and Structures, Cocoa Beach, Florida, January 17-21, 1998.
15. Halbig, M. C. and Cawley, J. D., "Modeling the Oxidation Kinetics of Continuous Carbon Fibers in a Ceramic Matrix," to be published in the *Ceramic Engineering & Science Proceedings of the 23rd Annual Conference on Composites, Advanced, Materials and Structures*, Cocoa Beach, Florida, January 25-29, 1999.
16. Eckel, A. J., Cawley, J. D. and Parthasarathy, T. A., "Oxidation Kinetics of a Continuous Carbon Phase in a Nonreactive Matrix," *J. Amer. Ceram. Soc.*, 78, [4], pp. 972-980, 1995.
17. Glime, W. H. and Cawley, J. D., "Oxidation of Carbon Fibers and Films in Ceramic Matrix Composites: A Weak Link Process," *Carbon*, Vol. 33, No. 8, pp. 1053-1060, 1995.

Gregory N. Morscher,¹ John Z. Gyekenyesi,¹ and Ramakrishna T. Bhatt²

Damage Accumulation in 2-D Woven SiC/SiC Ceramic Matrix Composites

Reference: Morscher, G. N., Gyekenyesi, J. Z., and Bhatt, R. T., “**Damage Accumulation in 2-D Woven SiC/SiC Ceramic Matrix Composites,**” *Mechanical, Thermal and Environmental Testing and Performance of Ceramic Composites and Components, ASTM STP 1392*, M. G. Jenkins, E. Lara-Curzio, and S. T. Gonczy, Eds., American Society for Testing and Materials, West Conshohocken, PA, 2000.

Abstract: Ceramic matrix composites are envisioned for use at elevated temperatures (1000 to 1400°C) in oxidizing environments. For non-oxide composites, the time-dependent failure stress is dependent on the severity of reactions between the environment and the load-bearing fibers and interphase. One of the most severe pitfalls for these types of materials occurs at intermediate temperatures, 600 to 1000°C. Environmental access to load-bearing fibers occurs through matrix cracks that are bridged by load-bearing fibers. The rate at which these composites lose the ability to carry load is partially controlled by the extent of cracking in the matrix. In this study, the damage accumulation of woven SiC/SiC composites tested in tension was quantified using unload/reload hysteresis tests and modal acoustic emission. The behavior of composites reinforced with ceramic-grade Nicalon™, Hi-Nicalon™, and Sylramic® fibers, with carbon or boron nitride interphases and chemically vapor-infiltrated or melt-infiltrated SiC matrices was investigated. The most significant finding of this study is that the formation of matrix cracks that bridge the load-bearing fibers (0° cracks) occurs at approximately the same strain for all of the woven SiC/SiC composites tested. All of these systems have at least a CVI SiC matrix layer adjacent to the interphase. In addition, the onset stress-strain condition for 0° cracks corresponds to the tensile stress-strain condition above which intermediate temperature embrittlement occurs for BN interphase SiC/SiC composites. For carbon interphase SiC/SiC composites, the critical stress-strain condition for the onset of intermediate temperature embrittlement corresponds to the first cracks in the matrix which can occur at stresses half the 0° crack onset stress.

Keywords: SiC/SiC composite, damage accumulation, matrix cracking, intermediate temperature embrittlement

Introduction

The nature of stress-induced damage accumulation in woven SiC/SiC composites has been described in several studies [1-3] for the ceramic grade Nicalon (Nic) fiber

¹ Ohio Aerospace Institute, Senior Research Associates at NASA Glenn Research Center, MS 106-5, Cleveland, OH, 44135, gmorscher@arc.nasa.gov

² United States Army, at NASA Glenn Research Center, MS 106-1, Cleveland, OH 44135

(Nippon Carbon, Tokyo Japan), chemical vapor infiltrated (CVI) SiC matrix system. It was found that at low stresses initially non-fiber bridged microcracks emanate from macropores between different fiber plies and form in transverse (90°) bundles and dense matrix regions. With increasing stress (strain), these "tunnel" cracks [4] propagate into the 0° fiber bundles resulting in portions of the matrix crack bridged by load-bearing fibers. In addition, new cracks are formed in the matrix of the 0° bundles. Eventually, cracks would coalesce to form through-thickness cracks across the composite. The onset of 0° cracks occurred somewhere between 0.06 and 0.085% strain for the material in Reference 1. The result of such strain (stress)-dependent cracking is a tensile stress-strain curve characterized by a decreasing tangent modulus with increasing strain depending on whether cracks extend through the thickness of the composite, the number of cracks formed, the interfacial properties, and the elastic properties of the composite constituents. In addition, once 0° cracks are formed, unload-reload hysteresis "loops" would occur with shapes that depend on the same factors [5,6].

Matrix damage accumulation enables ceramic matrix composites to have the desirable properties of high "toughness" and high strength (if the load is shed properly to the fibers and the fibers are not damaged). Unfortunately, the onset of matrix cracking may also limit the use-stress for certain composite applications if reactions with the environment reduce the stress-life properties of a given composite. Such is the case for SiC/SiC composites at intermediate temperatures (600 to 1000°C) where reactions between the oxidizing environment and the carbon or boron nitride interphases have been shown to severely limit composite life in stress-rupture or low-cycle fatigue testing [7-15]. In order for intermediate temperature embrittlement effects to occur, the environment must have access to the load-bearing fibers through matrix cracks. For example, when stress-rupture conditions are applied below the matrix cracking stress for carbon-interphase systems, the composites do not fail [12, 13, 15].

For boron nitride (BN) interphase systems, the effect of embrittlement is not as severe as for C-interphase systems [16,17]. Figure 1 shows the rupture behavior of four different SiC/BN/SiC composites and a SiC/C/SiC system. The stress rupture data for composite with C-interphase are very similar to the stress-rupture data of all the other C-interphase composites listed in the literature [7-10, 12-15]. The time exponent, n , for rupture ($\sigma = t^n$ where σ is stress in MPa, t is time in hours) of C-interphase composites is approximately -0.25 [14]. For BN-interphase composites the time exponent for rupture ranges from -0.02 to -0.06 and rupture occurs at significantly higher stresses. It should be noted that the above data compares ceramic grade Nicalon (NIC) reinforced C-interphase composites and High Nicalon (HN) and Sylramic (SYL) reinforced BN-interphase composites. However, it has been shown for NIC/SiC tested in bending that BN-interphase composites are significantly better than C-interphase composites for rupture [18]. For HN-reinforced single-tow minicomposites, it was shown that BN-interphase minicomposite tensile rupture is superior to C-interphase minicomposite tensile rupture, similar to that in Figure 1 [19]. Therefore it can be concluded that BN-interphase composite rupture occurs at a slower rate and at higher stresses than C-interphase composite rupture.

The reason for this difference is the greater stability of BN in oxidizing environments and the fact that BN oxidation results in a condensed phase oxidation product with minimal recession of the interphase compared to the rapid recession of C-

interphases in oxygen-containing environments. Therefore, for air-breathing applications where long component lifetimes are desired, SiC/SiC composites with BN-interphases are preferred. However, even for BN-interphase SiC/SiC, intermediate temperature rupture-behaviors can vary for different fiber and matrix constituents (Figure 1). In another study, it was shown that the extent of matrix cracking affected the rate of rupture for the HN/BN/MI SiC system [17]. At lower stresses, the matrix was microcracked resulting in a slower rupture rate. At higher stresses, cracks in the matrix traversed through the composite specimen thickness resulting in a faster rupture rate [see HN-BN-MI(b) in Figure 1].

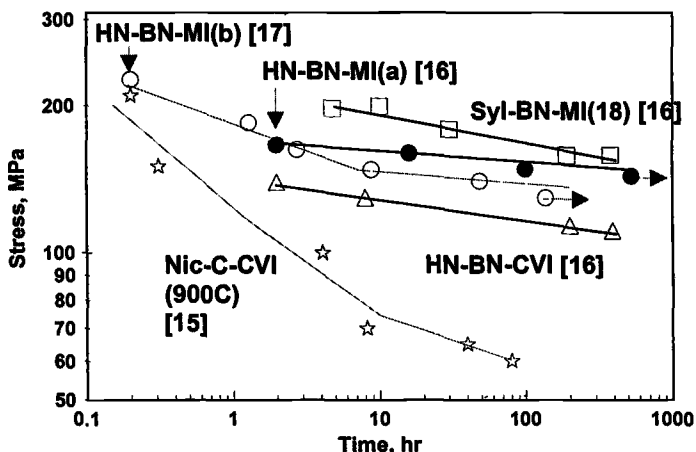


Figure 1 -- Tensile rupture behavior of several SiC/SiC systems at intermediate temperatures in air. All of the materials tested are BN-interphase SiC/SiC systems and were tested at 815°C with the exception of the NIC-C-CVI that was a C-interphase system and tested at 900°C.

The purpose of this study was to compare the extent of damage accumulation under tensile loading for these different systems and to determine how the damage accumulation affects the onset of intermediate temperature embrittlement. The approach was to perform room temperature tensile tests on different SiC/SiC composites in order to compare the onset of matrix cracking (tunnel cracks), the onset of 0°-transverse cracks, the extent of cracking, and the exhaustion of matrix cracking. Some of these experiments have been performed already in other studies [20, 21]; however, the analysis was extended in this study beyond that of the earlier studies. Modal acoustic emission (AE), i.e. use of digitized sound waves captured with high-fidelity sensors, was used to determine the onset of cracking [20, 21]. Traditional AE, i.e. parametric-based analysis with resonant frequency sensors, has been used to show the onset of matrix cracking in ceramic composites which occurs before any noticeable deviation from linearity in the stress-strain curve [22-24]. The significance of the modal AE technique over other parametric-based AE techniques is that exact location of source events can be determined from the speed of sound in the material, measured during the test, so that extraneous

noise from the machine and from the material outside of the gage section can be filtered out effectively. In addition, the amount of AE activity is related to the number of matrix cracks in the gage section. Unload, reload hysteresis loops [5,6] will be performed on some samples. The onset of 0° cracking will result in the formation of hysteresis loops and the width of the hysteresis loop will be related to the number of cracks and interfacial properties of the sliding interface between the fibers and the matrix. The stresses and strains for the onset of matrix cracking will then be related to the stresses and strains related to the onset of intermediate temperature embrittlement.

Experimental

Table 1 lists the SiC/SiC materials compared in this study. All of the specimens were flat with a contoured gage section (dog bone) of 10.2 mm width. The thickness ranged from 2.1 to 2.35 mm depending on the composite system. All of the specimen lengths were 152 mm with the exception of the HN-CVI that were 203 mm.

The composite systems differed in the fiber reinforcement, interphase, and/or matrix processing approach. All of the matrices first consist of a CVI SiC layer. For CVI matrices, the matrix was only CVI SiC. For melt-infiltrated (MI) matrices, the matrix first consisted of a thin 2 μm CVI SiC layer on top of the fiber/interphase preform followed by infiltration of SiC particle slurry and liquid silicon infiltration. The "CVI + Epoxy" matrix consisted of the same fiber/interphase/CVI SiC preform for MI composites except infiltrated with an epoxy.

Table 1 – Description of composite systems.

Fiber-Interphase-Matrix System	Weave	Average Interface Thickness, μm^a	0° Fiber Volume Fraction	Specimen length, mm
HN ^b - BN - CVI	8HS	0.4	0.15	203
HN - BN - MI(a)	5HS	0.4	0.17	152
HN - BN - MI(b)	5HS	0.6	0.17	152
HN - BN - CVI + Epoxy	8HS	0.5	0.15	152
SYL ^c - BN - MI(18)	5HS	0.9	0.15	152
SYL - BN - MI(22)	5HS	1.1	0.18	152
SYL - C - MI(22)	5HS	2.1	0.18	152

^a Based on interphase weight gain

^b Hi-Nicalon, Nippon Carbon, Tokyo Japan

^c Sylramic Fiber, Dow Corning Corp., Midland MI

Monotonic and unload-reload tensile tests were performed universal-testing machine (Instron Model 8562, Instron, Ltd., Canton, Mass.) with an electromechanical actuator. Glass fiber reinforced epoxy tabs (1.5 mm thick) were mounted on both sides of the specimen in the grip regions. The specimens were gripped with rigidly mounted hydraulically actuated wedge grips. A clip on strain gage, with a range of 2.5% strain and 25.4 mm gage length was used to measure deformation of the gage section.

Wide-band, 50 kHz to 2.0 MHz, high fidelity sensors (9.2 mm in diameter) were placed just outside the tapered region of the dog-bone specimen to record acoustic emission (AE) events. Vacuum grease was used as a couplant and electrical tape or mechanical clips were used to mount the sensors to the specimen. Acoustic emission waveforms were recorded and digitized using a 2-channel, Fracture Wave Detector (FWD) produced by Digital Wave Corporation (Englewood, CO). The FWD consisted of a personal computer with a 12-bit, 30 MHz analog to digital acquisition board. Each sensor was connected to a preamplifier and filter trigger module that was fed into the computer. The preamplifier was set at 20 dB, the filter signal was amplified 3 to 9 dB, and the filter trigger was amplified 21 dB. The load and strain were also recorded with the FWD computer. The post-test analysis was performed on Wave Detector™ software provided by the FWD manufacturer.

Results and Discussion

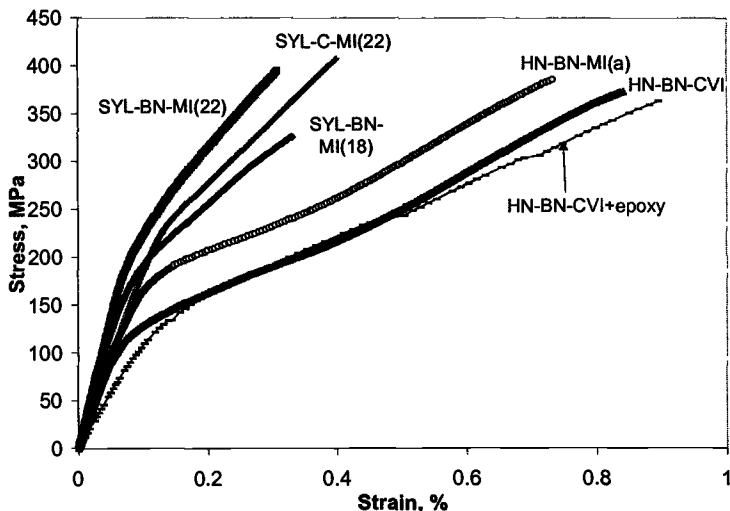


Figure 2 -- Stress-strain curves for several SiC/SiC systems.

Tensile stress-strain curves for all of the different systems tested in this study with the exception of HN-BN-MI(b) are shown in Figure 2. The mechanical properties in tabular form are listed in Table 2. Within a given SiC/SiC composite system there was little scatter in the elastic modulus (<10%), the shape of the stress-strain curves for monotonic and hysteresis loops (see [20,21]), and the ultimate strength and strain (< 5% for samples which failed in the gage section). On the other hand, the different SiC/SiC systems do differ significantly from one another in their respective stress-strain behavior. The elastic modulus, in general, is greater for SYL-containing composites than HN-containing composites since SYL has a higher modulus (380 GPa) than HN (270 GPa). The composite modulus is highest for MI matrix composites, followed by CVI matrix composites, followed by the epoxy infiltrated composites for the HN composite systems

as expected based on the amount of porosity in the matrix and the moduli of the matrix constituents. The only exception to these two trends was the SYL-C-MI(22) which had a very thick interphase. The large volume fraction of low modulus carbon caused the lower modulus for this system.

Table 2 – Tensile test results.

Fiber-Matrix System	Number Tested	E GPa	Ultimate σ (MPa)/ ϵ (%)	1 st Cracking Stress (MPa) AE/Non-lin	1 st Cracking Strain (%) AE/Non-lin
HN – CVI	2	200	370/0.84	51/73	0.025/0.044
HN – MI(a)	3	210	390/0.72	102/100	0.05/0.05
HN – MI(b)	1	214	NA	85/102	0.04/0.05
HN – CVI + Epoxy	2	110	365/0.9	45/60	0.04/0.052
SYL – MI(18)	3	260	326/0.34	90/101	0.035/0.039
SYL – MI(22)	3	280	400/0.33	100/100	0.04/0.04
SYL-C-MI	1	201	408/0.40	NA/73.5	NA/0.038

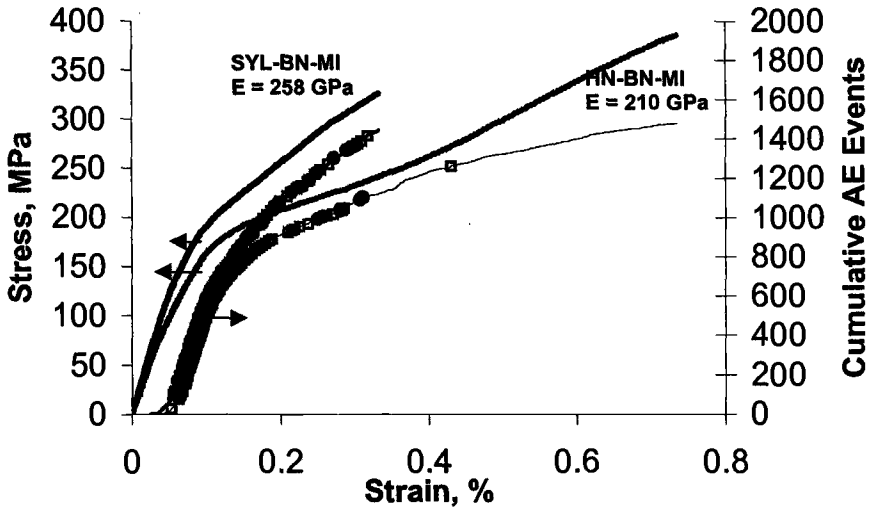


Figure 3 – Stress and AE events versus strain for two MI composites. The loudest (highest decade of energy events) and 2nd loudest (2nd highest decade of energy events) are plotted on the AE event curves as filled circles and open squares, respectively.

An example of the AE data is shown in Figure 3 for HN-BN-MI(a) and SYL-BN-MI composites. The AE data had to be sorted out in order to separate out the events that occurred in the gage section based on the difference in times of arrival at the two sensors

and the reduction in elastic modulus with increasing strain. The AE data was also sorted out according to the energy level of each event. Both of these methods of AE analysis are explained in detail in reference 21.

Cumulative AE events are plotted in Figure 3. The “loudest” (highest decade of energy events) and “2nd loudest” events (2nd highest decade of energy events) are delineated on the curves. For these systems, the onset of cracking occurs at nearly the same strain and the exhaustion of high-energy events occurs at approximately the same strain as well, $\sim 0.3\%$. It is evident that a greater number of high-energy events occurred for the SYL-BN-MI composite than for the HN-BN-MI composite, which is directly related to the larger number of matrix cracks occurring in the SYL-BN-MI composites. The first cracking stress-strain conditions as determined from the onset of AE activity and from the onset of non-linearity in the stress-strain curve are listed in Table 2. The stress-strain condition for the onset of AE activity was attributed to the fifth AE event because for two tests a few isolated events were detected at low stress-strain conditions. For all the tests, by the fifth event, the next AE event was recorded before a 0.001% increase in strain, i.e. AE activity was occurring at a very fast rate over the entire gage length. The stress-strain data up to 30 MPa was fit to a straight line (linear regression) and the stress above which the stress-strain deviated from linearity was deemed the first

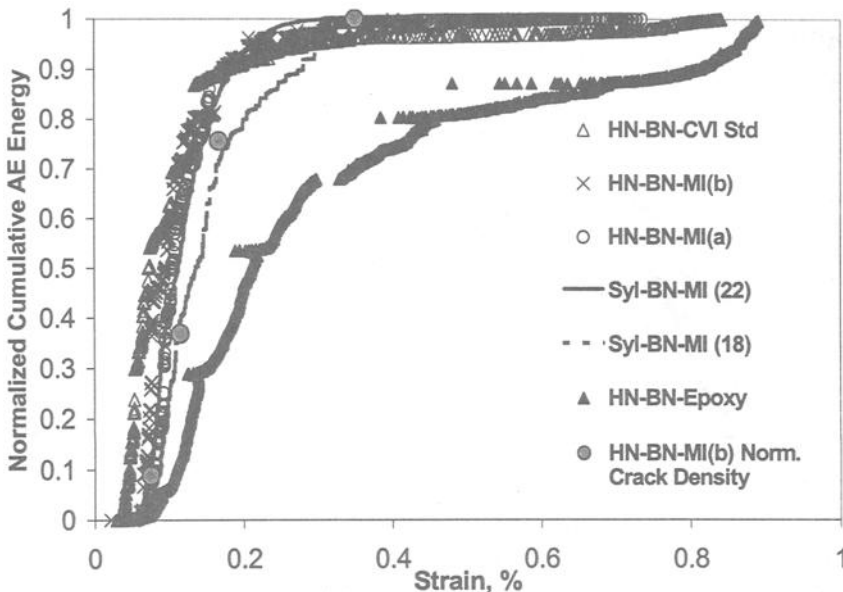


Figure 4 – Normalized cumulative AE energy versus strain for the SiC/SiC composite systems. The discontinuities in the AE energy curves, e.g. HN-BN-Epoxy, correspond to the AE activity occurring on unloading for a hysteresis loop tensile test. Also plotted is the normalized crack density as determined for HN-BN-MI(b) from [23].

cracking stress, based on non-linearity in the stress-strain curve. Usually, AE activity occurs at lower stresses (strains) than observable non-linearity in the stress-strain curve [22-24].

It has been shown in other work that matrix cracking can be related to the cumulative AE energy for these composites [25-26]. Figure 4 shows the normalized cumulative AE energy for the SiC/SiC systems tested in this study and the good correlation of this parameter with normalized linear crack density for the HN-BN-MI composites [26]. The shape of the AE energy plots are similar for all of the composite systems with most of the AE energy concentrated between ~ 0.05 and 0.3 % strain. The steep portions of the AE energy vs strain curves for all but the epoxy-containing matrix appear to increase at approximately the same rate with strain. However, they occur over slightly different strain ranges with the HN-BN-CVI composite occurring at the lowest strains and the SYL-BN-MI(18) occurring at the higher strains. The HN-BN-CVI+epoxy system shows a much broader strain range for AE activity and presumably matrix cracking. For all of these composite systems, the strain range corresponding to the steepest portion of the AE energy versus strain curve corresponds to just prior to and just after the "knee" in the stress-strain curve (Figure 2). It should be noted that for the HN-BN-CVI and HN-BN-CVI+epoxy systems, an increase in AE activity occurs at higher strains near the failure strain (Figure 4). This increase in AE activity is not associated with transverse matrix cracks but with fiber failure leading up to composite ultimate failure [21].

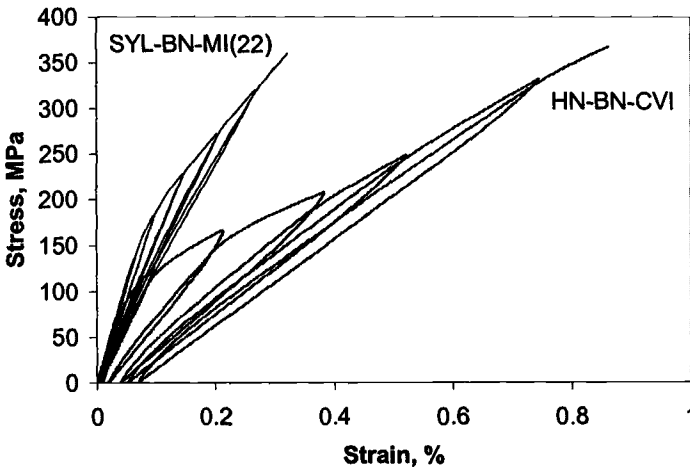


Figure 5 - Tensile unload-reload hysteresis stress-strain curves for two different SiC/SiC composites. The SYL-BN-MI(22) specimen did not fail in the gage section.

Representative hysteresis stress-strain curves from two different SiC/SiC composites are shown in Figure 5. The differences in loop width and permanent displacement can be quite dramatic. In addition, the shape of the loops differs for the

various composite systems. The HN fiber systems have unloading and reloading curves of the hysteresis loops that appear fairly parabolic. The SYL fiber systems have hysteresis loops with loading and unloading curves that have a steep modulus at low strains indicating crack closure when unloading occurs and the presence of a compressive stress in the matrix [6]. If the crack density is known, the interfacial shear strength, τ , can be estimated from the maximum width of the hysteresis loop based on the relationship,

$$\tau = (\sigma_p^2 / 2 \delta \epsilon_{max}) [b_2 (1 - a_1 v_f)^2 (R_f \rho_c) / \{4 v_f^2 E_m\}] \tag{1}$$

where σ_p is the peak stress of the hysteresis loop, $\delta \epsilon_{max}$ is the maximum hysteresis loop width, v_f is the volume fraction of fibers in the loading direction, R_f is the fiber diameter, ρ_c is the crack density, and b_2 and a_1 are constants based on the elastic constants of the composite constituents [27]. The crack density and interfacial shear stress values are listed in Table 3 for the different SiC/SiC composites for the systems that hysteresis experiments were performed for.

In order to determine the onset of 0° cracking, the maximum hysteresis loop width was plotted versus hysteresis loop peak stress (Figure 6) and hysteresis peak strain (Figure 7). Data from Domergue et al. [5] are also included in Figures 6 and 7 for a NIC-C-CVI system. The relative magnitude of the loop width data depends on the number of cracks, interfacial shear strength and the constituent properties. The 0° crack onset stress and strains were determined by extrapolating the data in Figures 6 and 7 to zero hysteresis loop width, respectively.

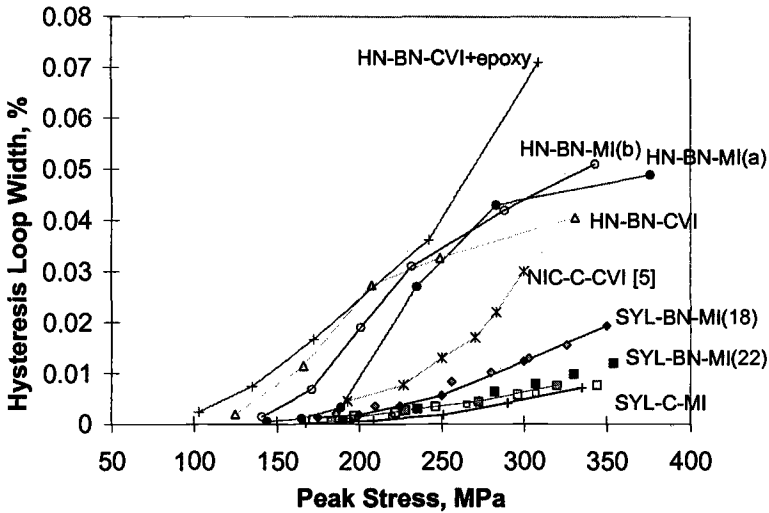


Figure 6 - Stress dependence of hysteresis loop width.

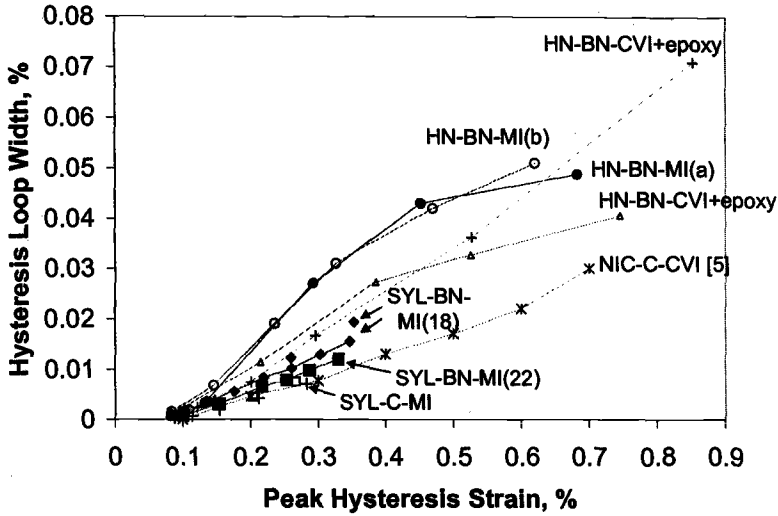


Figure 7 - Strain dependence of hysteresis loop width.

It is evident that the onset of 0° cracking occurs over a wide stress range for the different composite systems. The onset stress for 0° cracking appears to correlate with the elastic modulus of each system (Figure 8). However, there is significant variability in 0° crack onset stress with the different systems. There is a better relationship for the

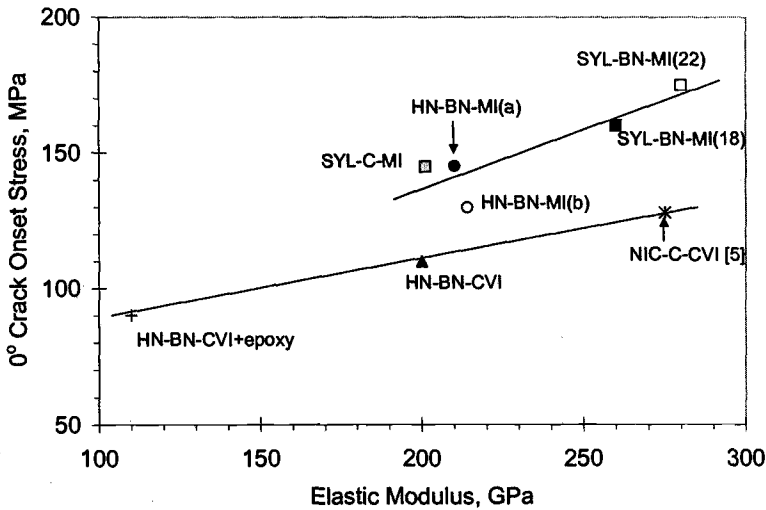


Figure 8 - Effect of elastic modulus on 0° crack onset stress for MI (top line) and CVI SiC (bottom line) matrix composites.

specific matrix systems where the 0° crack onset stress versus elastic modulus relationship appears more consistent (Figure 8). Based on these distinctions, MI composites, in general, have higher 0° crack onset stresses over CVI matrix composites. This is reasonable, since the CVI matrix composites have large pores with sharp corners where cracking initiates [20] (see also references 1 through 3) and probably intersects the 0° bundles more readily than the dense MI matrix composites that do not have macroporosity. Surprisingly the 0° crack onset strains are nearly the same for every SiC/SiC system tested in this study. Even though the hysteresis loop widths differ significantly and the 0° onset stresses vary, the onset strain for SiC/SiC composites with a portion of the CVI SiC matrix is $\sim 0.075\%$.

The 0° cracking onset stress-strain condition can then be compared to the onset of intermediate temperature embrittlement (defined here as the 500 hour run-out stress [16]). Table 3 shows the onset of intermediate temperature embrittlement for rupture of the BN interphase composites shown in Figure 1. There is excellent correlation between the 0° onset stress and the onset stress for intermediate temperature embrittlement. This provides a quantifiable "matrix cracking" stress (strain) condition above which time-dependent failure will occur for the SiC/BN/SiC system at intermediate temperatures when tested in air.

Table 3: Tensile hysteresis test results.

Fiber-Matrix System	Crack Density, #/mm	τ , MPa	0° Cracking Onset Strain (%)	0° Cracking Onset Stress (MPa)	Int. Temp. 500 hour Run-out Stress (MPa)
HN - CVI	2.9	36 ± 8	0.07	110	107
HN - MI(a)	1.1	11 ± 3	0.08	145	143
HN - MI(b)	1.7	25	0.07	130	133
HN - CVI + Epoxy	10	50 ± 10	0.08	90	--
SYL - MI(18)	6.1	~ 250	0.07	160	155
SYL - MI(22)	--	--	0.075	175	--
SYL-C-MI	--	--	0.08	145	--
NIC/C/CVI [5]	~ 75	~ 50	0.08	130	--

For C interphase Nic/CVI SiC composites, run-out conditions usually occur between 40 and 60 MPa [12,15]. This stress is considerably less than the 0° cracking onset stress estimated for Nic/C/CVI SiC from Domergue et al. [5] or compared to the HN/BN/CVI SiC tested in this study (Table 3). However, that stress range does correspond to the first cracking stress in CVI-SiC matrix composites (e.g. the HN/CVI SiC specimen in Table 2). These initial cracks would be transverse cracks that originate at the sharp pores or in the 90° plies and do not fully penetrate the 0° bundles. Since carbon is volatilized readily at these intermediate temperatures, presumably oxidation of the carbon interphase in the 0° bundles can occur through these initial transverse cracks. In addition, CVI SiC composites contain a network of interconnected porosity. As a

result, every single transverse crack whether on the interior of the composite or the exterior of the composite is most likely exposed to the environment. Therefore, the critical stress/strain condition for run-out of carbon interphase SiC/SiC is the first cracking stress (Table 2) and not the 0° cracking onset stress/strain. This is significant especially for the CVI SiC system where the first cracking stress and strain can be about half of the 0° cracking onset stress and strain, respectively. It should be noted that the matrices for the composite systems tested in references 12 and 15 were enhanced with B_4C which may have different first matrix cracking and 0° onset stress behavior than pure CVI SiC matrix composites. However, recent studies [28] with HN, BN or C interphase, enhanced CVI SiC matrix composites resulted in very similar first matrix cracking and 0° onset stress/strain behavior to that of the pure CVI SiC matrix material (Tables 2 and 3).

Conclusions:

The onset stress-strain conditions for matrix cracking have been characterized for several SiC fiber, SiC matrix systems which have CVI SiC as the initial portion of the matrix. The first detection of matrix cracks, from acoustic emission monitoring, always occurs at lower stress (strains) than the formation of matrix cracks which are bridged by load-bearing fibers (0° matrix cracks). The MI matrix systems usually had higher first matrix cracking stresses and 0° crack onset stresses than the CVI-only and CVI + epoxy matrix systems because the matrix was dense and did not contain the large sharp-edged pores of the CVI-only and CVI + epoxy matrices. However, for all of the composite systems tested in this study, the 0° crack onset strains were nearly identical (approximately 0.075% strain).

An understanding of the extent of matrix cracking is crucial for understanding the use stresses and strains of these composites when subjected to applied stress conditions under intermediate temperature environments. Comparing composite systems where stress-rupture data in air were available showed time-dependent life properties for carbon interphase systems occurs above the first matrix cracking stress; whereas time-dependent life properties for BN interphase systems occurs above the 0° cracking onset stress. The 0° cracking onset stress can be as large as a factor of two greater than the first cracking stress and therefore it would be expected that BN interphase composites can withstand twice the design stress expected for components with intermediate temperature applications or conditions. For the high-modulus fiber, MI SiC matrix composites tested in this study with BN interphases, the 0° cracking onset stresses were greater than 150 MPa.

Finally, it can be concluded from this study that the first cracking stress from the room temperature stress-strain curve or the 0° cracking onset stress from a room temperature unload-reload hysteresis tensile test can yield the lowest stress-strain condition for intermediate temperature embrittlement under stress-rupture conditions for carbon interphase or BN interphase SiC/SiC composites, respectively.

References:

- [1] Guillaumat, L. and Lamon, J., "Multi-fissuration de Composites SiC/SiC," in Revue des Composites et des Matériaux Avances, vol. 3, 1993, pp. 159-171.

- [2] Guillaumat, L. and Lamon, J., "Probabilistic-Statistical Simulation of the Non-Linear Mechanical Behavior of a Woven SiC/SiC Composite," *Composites Science and Technology*, Vol. 56, 1996, pp. 803-808.
- [3] Pluvinage, P., Parvizi-Majidi, A., and Chou, T.W., "Damage Characterization of Two-Dimensional woven and Three-Dimensional Braided SiC-SiC Composites," *Journal of Materials Science*, Vol. 31, 1996, 232-241.
- [4] Cox, B.N. and Marshall, D.B., "Crack Initiation in Fiber-Reinforced Brittle Laminates," *Journal of the American Ceramic Society*, Vol. 79, No. 5, 1996, pp. 1181-88.
- [5] Domergue, J.M., Heredia, F.E., and Evans, A.G., "Hysteresis Loops and the Inelastic Deformation of 0/90 Ceramic Matrix Composites," *Journal of the American Ceramic Society*, Vol. 79, No. 1, 1996, pp. 161-70.
- [6] Steen, M. and Valles, J.L., "Unloading-Reloading Sequences and the Analysis of Mechanical Test Results for Continuous Fiber Ceramic Composites," *ASTM STP 1309*, M. G. Jenkins et al., Ed., American Society for Testing and Materials, West Conshohocken, PA, 1997, pp. 49-65.
- [7] Heredia, F.E., McNulty, J.C., Zok, F.W., and Evans, A.G., "Oxidation Embrittlement Probe for Ceramic-Matrix Composites," *Journal of the American Ceramic Society*, Vol. 78, No. 8, 1995, pp. 2097-2100.
- [8] Lin, H.T. and Becher, P.F., "Stress-Temperature-Lifetime Working Envelope of Nicalon Fiber-Reinforced SiC Matrix Composites in Air," *Composites Part A*, Vol. 28A, 1997, pp. 935-942.
- [9] Lara-Curzio, E., Ferber, M.K., and Tortorelli, P.F., "Interface Oxidation and Stress-Rupture of NicalonTM/SiC CVCCs at Intermediate Temperatures," *Key Engineering Materials Vols. 127-131*, Trans Tech Publications, Switzerland, 1997, pp. 1069-1082.
- [10] Morscher, G.N., "Tensile Stress Rupture of SiCf/SiCm Minicomposites with Carbon and Boron Nitride Interphases at Elevated Temperatures in Air," *Journal of the American Ceramic Society*, Vol. 80, No. 8, 1997, pp. 2029-42.
- [11] Morscher, G.N., "The Effect of Static and Cyclic Tensile Stress and Temperature on Failure for Precracked Hi-Nicalon/BN/CVD SiC Minicomposites in Air," *Ceramic Engineering and Science Proceedings*, Vol. 18, No. 3, 1997, pp. 737-745.
- [12] Lipetzky, P., Stoloff, N.S., and Dvorak, G.J., "Atmospheric Effects on High-Temperature Lifetime of Ceramic Composites," *Ceramic Engineering Science Proceedings*, Vol. 18, No. 4, 1997, pp. 355-362.
- [13] Verrilli, M.J., Calomino, A.M., and Brewer, D.N., "Creep-rupture Behavior of a Nicalon/SiC Composite," *ASTM STP 1309*, M.G. Jenkins, S.T. Gonczy, E. Lara-Curzio, N.E. Ashbaugh, and L. Zawada, Eds., American Society for Testing and Materials, West Conshohocken, PA, 1997, pp. 158-175.
- [14] Lara-Curzio, E., "Stress-Rupture of Nicalon/SiC Continuous Fiber Ceramic Matrix Composites in Air at 950°C," *Journal of the American Ceramic Society*, Vol. 80, No. 12, 1997, pp. 3268-72.
- [15] Steyer, T.E. and Zok, F.W., "Stress Rupture of an Enhanced NicalonTM/SiC Composite at Intermediate Temperatures," *Journal of the American Ceramic Society*, Vol. 81, No. 8, 1998, pp. 2140-46.
- [16] Brewer, D., Calomino, A., and Verilli, M., unpublished research

- [17] Morscher, G.N., Hurst, J., and Brewer, D., "Intermediate Temperature Stress Rupture of a Woven Hi-Nicalon, BN-Interphase, SiC Matrix Composite in Air," *Journal of the American Ceramic Society* in print.
- [18] Lin, H.T. and Becher, P.F., "Effect of Coating on Lifetime of Nicalon Fiber-Silicon Carbide Composites in Air," *Materials Science and Engineering*, Vol. A231, 1997, pp. 143-150.
- [19] Martinez-Fernandez, J. and Morscher, G.N., unpublished research
- [20] Morscher, G.N. and Gyekenesi, J.Z., "Room Temperature Tensile Behavior and Damage Accumulation of Hi-Nicalon Reinforced SiC Matrix Composites," *Ceramic Engineering Science Proceedings*, Vol. 19, No. 3, 1998, pp. 241-249.
- [21] Morscher, G.N., "Modal Acoustic Emission of Damage Accumulation in a Woven SiC/SiC Composite," *Composites Science and Technology*, Vol. 59, No. 5, 1999, pp. 687-697.
- [22] Kim, R.Y. and Pagaon, N.J., "Crack Initiation in Unidirectional Brittle Matrix Composites," *Journal of the American Ceramic Society*, Vol. 74, No. 5, 1991, pp. 1082-1090.
- [23] Luo, Y-J, Chang, S-C, and Daniel, I.M., "Acoustic Emission Study of Failure Mechanisms in Ceramic Matrix Composites under Longitudinal Tensile Loading," *Journal of Composite Materials*, Vol. 29, 1995, pp. 1946-1961.
- [24] Jenkins, M.G., Piccola, J.P., and Lara-Curzio, E., "Onset of Cumulative damage and the Effects of Test Parameters on the Tensile Behavior of Continuous Fiber-Reinforced Ceramic Composites (CFCC)," in Fracture Mechanics of Ceramics, Vol. 12., Ed. R.C. Bradt, D.P.H. Hasselman, D. Munz, M. Sakai, and V.Y. Shevchenko, Plenum Publishing Corp., USA, 1996, pp. 267-282.
- [25] Morscher, G.N., "Modal Acoustic Emission of Damage Accumulation in Woven SiC/SiC at Elevated Temperatures," to be published in Review of Progress in Quantitative Nondestructive Evaluation, Vol. 18A, D.O. Thompson and D.E. Chimenti, Eds., Kluwer Academic/Plenum Publishers, NY, 1999, pp. 419-426.
- [26] Morscher, G.N., "Use of Modal Acoustic Emission for Source Identification in Woven SiC/SiC Composites," Review of Progress in Quantitative Nondestructive Evaluation, Vol. 19, , D.O. Thompson and D.E. Chimenti, Eds., Kluwer Academic/Plenum Publishers, 2000 in print.
- [27] Hutchinson, J.W. and Jensen, H., "Models of Fiber Debonding and Pull-Out in Brittle Composites with Friction," *Mechanics of Materials*, Vol. 9, 1990, pp. 139-63.
- [28] Morscher, G.N., Gyekenesi, A., and Kautz, H., unpublished research.

Summary

Since its establishment in 1991, ASTM Subcommittee C28.07 on Ceramic Matrix Composites has actively promoted both the development and the utilization of standards for continuous fiber ceramic composites (CFCCs) and the transfer of research results related to these materials. Indeed, a workshop organized by David C. Cranmer at the National Institute of Standards and Technology, Gaithersburg, Maryland in February 1990, resulted in the publication, "Workshop on Assessment of Testing Methodology for Glass, Glass-Ceramic, and Ceramic Matrix Composites," by D. C. Cranmer, *Journal of Research of the National Institute of Standards and Technology*, Vol. 96, No. 4, 1991 pp. 493–501 and helped set the stage for the establishment of ASTM Subcommittee C28.07. Following the establishment of ASTM Subcommittee, C28.07, a more informal workshop was organized by George D. Quinn in January 1992 at the ASTM Committee C28 meetings in Cocoa Beach, Florida. Finally, a formal workshop titled, "Thermal and Mechanical Test Methods and Behavior of Continuous Fiber Ceramic Composites (CFCCs)" and organized by Michael G. Jenkins, Stephen T. Gonczy, and Edgar Lara-Curzio was held in June 1994 at the ASTM C28 Committee meetings in Montreal, Quebec. The first formal symposium sponsored by ASTM Committee C28 and co-sponsored by ASTM Subcommittee C28.07, and E08.09, and the American Ceramic Society was held in Cocoa Beach, Florida in January 1996. This symposium, organized by Michael G. Jenkins, Edgar Lara-Curzio, Stephen T. Gonczy, Noel E. Ashbaugh, and L. P. Zawada resulted in the publication of ASTM STP 1309, *Thermal and Mechanical Test Methods and Behavior of Continuous Fiber Ceramic Composites* in 1997.

From 1991 to 1997, the impetus of these workshops and symposium was that anticipated engineering applications of CFCCs in industrial, aerospace, and propulsion systems require the exposure of materials to service cycles in aggressive environments which may include simultaneous temperature and load cycling or thermal/mechanical shock. Proper materials testing and characterization can elucidate aspects of the unique damage-tolerant (or intolerant) behavior of this class of advanced ceramics relevant to these aggressive environments. Such information can enable formulation of appropriate micro-mechanical and phenomenological models or component lifetime prediction and design, thus guiding further material development. These workshops and symposium have assisted in continuing the pre-market penetration standardization process required to ensure timely and rapid introduction of these emerging materials into national and international markets. Topics discussed by participant from industry, academia, and government included:

- development and application of novel test methods and equipment;
- application and experience with standardized test methods;
- environmental and thermal effects;
- tensile, compressive, or shear strength behavior;
- creep/creep rupture behavior;
- cyclic fatigue including frequency, waveform, and amplitude effects;
- thermomechanical fatigue;
- deformation behavior;
- multiaxial loading as applied to test specimen coupons or components (for example, tubes);
- effects of fiber architecture including laminate, fabric, or braided reinforcements;
- specimen design, including volume and geometrical effects;
- interfacial property measurement and effects of composite performance.

By 1999, ASTM Subcommittee C28.07 had succeeded in introducing nine full-consensus standards for CFCCs (with three more in advanced balloting). In addition, members of ASTM

Subcommittee C28.07 had acted as conveyors for one ISO standard for CFCC and were currently acting as conveyors for three more ISO standards.

This vigorous level of normalization activity was and is warranted because, while CFCCs are said to be an enabling technology for US industry, standards are viewed as an enabling *supporting* technology. Thus, without the common language and procedures of standards, CFCCs cannot be refined and improved to fill their premier role in advanced technology.

With these needs in mind, ASTM Subcommittee C28.07 organized a second symposium "Environmental, Mechanical, and Thermal Properties and Performance of Continuous Fiber Ceramic Composite (CFCC) Materials and Components" that was held in Seattle, Washington, 18 May 1999. The intent of this symposium was to formally report efforts to verify current full-consensus standards for CFCCs, introduce novel test methods for CFCCs, present some of the unique aspects of the thermal, mechanical, and environmental behavior of CFCCs, and address the application of existing standards to CFCCs and in advanced engineering designs. The presentations and the collection of papers in this special technical publication, ASTM STP 1392, are the results of recent and on-going research and development programs for CFCCs.

The papers in this special technical publication are a significant contribution to the development and understanding of the behavior of continuous fiber ceramic matrix composites. Each of the papers in the four sections is briefly summarized in the following paragraphs with some perspective on the significance of the work.

Plenary

"Relationships of Test Methods and Standards Development to Emerging and Retrofit CFCC Markets" by Barnett, Ojard, and Cairo—By way of an illustrative example of an industrial application (i.e. a gas turbine combustor), the authors provide evidence of the need for standardized methods for characterizing CMCs. In this case a test for determining hoop tensile strength of tubular components by internal pressurization was highlighted and results for a silicon carbide reinforced silicon carbide matrix CMC were presented.

Room-Temperature Test Results/Methods

"Multiple-Laboratory Round-Robin Study of the Flexural, Shear, and Tensile Behavior of a Two-Dimensionally Woven Nicalon™/Sylramic™ Ceramic Matrix Composite" by Jenkins, Lara-Curzio, Gonczy, and Zawada—ASTM Test Methods C 1275 (tension), C 1292 (shear), and C 1341 (flexure) were used as part of a multi-laboratory round robin program to determine the precision of the three test methods applied to a pre-commercial woven Nicalon™/Sylramic™ (polymer impregnated pyrolysis) CMC at room temperature. In addition, large, statistically significant data sets were created for design and processing purposes. For the first time, precision and bias statements for existing full-consensus standards for CFCCs are proposed.

"Test Procedures for Determining the Delamination Toughness of Ceramic Matrix Composites as a Function of Mode Ratio, Temperature, and Layup" by Polaha and Davidson—Improvements in current test procedures for Mode I, Mode II, and mixed mode delamination "toughness" are proposed by the authors. The procedures were applied to a Nicalon™/MAS-5 CMC at both room and elevated temperatures to verify the improvements.

"Detailed Study of the Tensile Behavior of a Two-Dimensionally Woven Nicalon™/ Sylramic™ Ceramic Matrix Composite" by Jenkins and Zawada—A pre-commercial woven Nicalon™/Sylramic™ (polymer impregnated pyrolysis) CMC was tested in tension at room temperature per ASTM Test Method C 1275. Ninety tests were conducted by nine laboratories giving interlaboratory coefficients of variations of 5.0%, 4.1%, 7.2%, and 9.2% for elastic modulus, proportional limit stress, ultimate tensile strength, and strain to failure, respectively.

“Testing Methodology for Measuring Transthickness Tensile Strength for Ceramic Matrix Composites” by Zawada and Goecke—An evolving test method for determining transthickness (normal to the plies) tensile strength is detailed. Currently the subject of ASTM balloting, the pre-standard test method was applied to a variety of materials including Nicalon™/MAS-5 and Nicalon™/Sylramic™ (polymer impregnated pyrolysis) CMCs. Details concerning adhesives, fixtures, testing conditions as well as the results of a mini round-robin are used to justify and verify the pre-standard.

“Flexural and Tensile Properties of a Two-Dimensional Nicalon™-Reinforced Sylramic™ S-200 Ceramic Matrix Composite” by Gonczy and Jenkins—Flexural and tensile results from a round-robin program using a pre-commercial Nicalon™/Sylramic™ (polymer impregnated pyrolysis) CMC are detailed. Differences between flexural and tensile results with implications for testing and design applications are discussed.

Test Results/Methods Related to Design Implications

“Stress-Rupture, Overstressing, and a New Methodology to Assess the High-Temperature Durability and Reliability of CFCCs” by Lara-Curzio—A unique testing methodology based on the application of random stress and temperature “spikes” to conventional stress rupture tests is proposed. The magnitude frequency of these “spikes” is representative of transients associated with a specific application. Experimental and non-conservative information obtained from this methodology includes the probability of fracture of the material as a function of overstressing incidents.

“Use of Unload/Reload Methodologies to Investigate the Thermal Degradation of an Alumina Fiber-Reinforced Ceramic Matrix Composite” by Campbell and Jenkins—Intermittent unloading/reloading cycles are shown to be a powerful tool to assist in interpreting the mechanical response of a Nextel™610/alumina (directed metal oxidation, DIMOX™) CMC. Correlations between fiber/matrix interphase changes and thermal exposure time/temperature are indicated.

“Fiber Test Development for Ceramic Composite Thermomechanical Properties” by DiCarlo and Yun—Test procedures for single fibers and single ply woven fabrics are presented and discussed. Creep rupture test results for Nextel™ 610 and 720, Nicalon™, Hi-Nicalon™, and Sylramic™ fibers are presented. Creep results are also presented for Nextel™ fibers. A method for predicting strengths of tows and single ply woven test pieces is presented.

“Effect of Fiber Waviness on the Tensile Response of 2D C(f)/SiC Ceramic Matrix Composites” by Steen—A “mastercurve” approach was used to analyze the response of satin weave and plain weave carbon fiber reinforced silicon carbide CMC. The “mastercurve” is developed by shifting hysteretic unload/reload monotonic stress-strain curves to account for residual stress and cumulative damage.

“Surface Finish and Notch Effect Model for Strength Predictions of Continuous Fiber Ceramic Composites (CFCCs)” by Ramulu, Jenkins, and Kunaporn—A mathematical model for effective stress concentration factor (k) that combines the effects of surface waviness and surface roughness was applied to tensile test results for a Nicalon™/alumina (directed metal oxidation, DIMOX™) CMC. Tensile test specimens had been fabricated by conventional diamond grit cutting/grinding and abrasive water jet (AWJ) cutting resulting in much rougher surface finishes for the AWJ cut surfaces. However, the similarity in tensile test results are attributed to similarity of effective k , which incorporates waviness and not just surface roughness.

“Notch-Sensitivity of a Woven Oxide/Oxide Ceramic Matrix Composite” by John, Buchanan, and Zawada—Semi-circular and narrow double edge notched tensile test specimens were used to evaluate the notch sensitivity of a woven Nextel™ 720/alumino-silicate CMC at elevated temperatures in monotonically loaded tensile tests and creep tests. No notch sensitivity is exhibited at temperatures less than 1000 °C, although greater notch sensitivity is exhibited under creep conditions at temperatures greater than 1000 °C.

Environmental Effects and Characterization

“The Effects of Microstructural Damage on the Thermal Diffusivity of Continuous Fiber-Reinforced Ceramic Matrix Composites” by Graham, McDowell, Lara-Curzio, Dinwiddie, and Wang—Thermal diffusivity was used to monitor the evolution of microstructural damage during monotonic and cyclic loading of a unidirectional Nicalon™/LAS II CMC. Thermal diffusivity is affected only in the direction parallel to the fibers. The important role of interfacial conductance on both longitudinal and transverse thermal diffusivity is demonstrated.

“Oxidation Behavior of Non-Oxide Ceramics in a High-Pressure, High-Temperature Steam Environment” by Ferber, Lin, and Keiser—Two recent studies are presented illustrating the roles of competing processes of scale formation and scale volatilization in monolithic and composite ceramic exposed to gas turbine combustion environments. Two materials: an α -silicon carbide monolith and a Nicalon™ reinforced/silicon carbide (chemical vapor infiltrated) CMC were subjected to such an environment in a new test facility. Recession and oxidation results quantify the roles of the various oxidation mechanisms.

“The Time-Dependent Deformation of Carbon Fiber-Reinforced Melt-Infiltrated Silicon Carbide Ceramic Matrix Composites: Stress-Rupture and Stress-Relaxation Behavior in Air at 1000 °C” by Lara-Curzio and Singh—Tensile test specimens of a carbon fiber/silicon carbide (melt infiltrated) CMC were subjected to constant loads and constant strains at elevated temperatures to determine creep strain and stress relaxation behaviors, respectively. The role of fiber failure in stress-rupture and stress-relaxation is described.

“The Relationship between Interphase Oxidation and Time-Dependent Failure in SiC/SiC_m Composites” by Lewinsohn, Henager, Simonen, Windisch, and Jones—Flexurally-loaded single edge notched beams of a woven Nicalon™/silicon carbide (chemical vapor infiltrated) CMC were tested at elevated temperatures in various atmospheres under constant loads. The role of oxygen, temperature, interphase recession and fiber creep on the velocity of crack growth were identified.

Damage Accumulation and Material Development

“Characterization of Damage Accumulation in a Carbon Fiber-Reinforced Silicon Carbide Ceramic Matrix Composite (C/SiC) Subjected to Mechanical Loadings at Intermediate Temperature” by Verrilli, Kantzos, and Telesman—Creep-rupture and cyclic fatigue tests at elevated temperatures were used to identify the failure modes and degradation mechanisms of a woven carbon fiber/silicon carbide (chemical vapor infiltration) CMC. The damage was quantified by monitoring the degradation of the elastic modulus of the composite. Oxidation of the carbon fibers is the dominant damage mechanism.

“Effect of Loading Mode on High-Temperature Tensile Deformation of a SiC/SiC Composite” by Únal—Statically- and cyclically-loaded tensile test specimens of a woven Nicalon™ fiber silicon carbide (chemical vapor deposition) CMC were evaluated. Cumulative damage was monitored via total strain and shows that the cyclic fatigue-induced strain accumulated more rapidly than the creep-induced strain, thus indicating the greater deleterious effect of cyclic loading.

“Effects of Temperature and Environment on the Mechanical Properties of Tyranno-Hex™ Composites” by Drissi-Habti, Takeda, Nakano, Kanno, and Ishikawa—Tensile and flexural strength tests were conducted in ambient air at elevated temperatures on a pre-commercial CMC (woven Tyranno™ in an oxidized matrix). Processing and test conditions were varied in an attempt to “optimize” the material. Thermal heat treatments were also performed to improve the high temperature performance of the composite.

“Degradation of Continuous Fiber Ceramic Matrix Composites under Constant Load Conditions” by Halbig, Brewer, and Eckel—Ten different CMCs were subjected to constant load

and constant temperature tensile tests in ambient air. Various failure mechanisms ranging from diffusion to reaction-controlled kinetics were observed and modeled.

“Damage Accumulation in 2-D Woven SiC/SiC Ceramic Matrix Composites” by Morscher, Gyekenyesi, and Bhatt—Five different CMCs were tested under tensile stress rupture conditions to quantify the rate at which the CMCs lose the ability to carry loads because of matrix cracks bridged by load-bearing fibers. A significant finding was that the strain at which matrix cracks bridged by load bearing fibers occurred was approximately the same for all the woven silicon carbide fiber-reinforced silicon carbides CMCs tested.

Michael G. Jenkins
Department of Mechanical Engineering
University of Washington
Seattle, WA 98195-2600
Symposium co-chair and co-editor

Edgar Lara-Curzio
Mechanical Characterization and Analysis
Group
Oak Ridge National Laboratory
Oak Ridge, TN 37831-67064
Symposium co-chair and co-editor

Stephen T. Gonczy
Gateway Materials Technology
Mt. Prospect, IL 60056
Symposium co-chair and co-editor

Author Index

- | B | J |
|--------------------------|---|
| Barnett, T. R., 3 | Jenkins, M. G., 15, 48, 86,
118, 160 |
| Bhatt, R. T., 306 | John, R., 172 |
| Brewer, D. N., 290 | Jones, R. H., 229 |
| Buchanan, D. J., 172 | |
| | K |
| C | Kanno, Y., 276 |
| Cairo, R. R., 3 | Kantzos, P., 245 |
| Campbell, C. X., 118 | Keiser, J., 201 |
| | Kunaporn, S., 160 |
| D | L |
| Davidson, B. D., 31 | Lara-Curzio, E., 15, 107, 185,
216 |
| DiCarlo, J. A., 134 | Lewinsohn, C. A., 229 |
| Dinwiddie, R. B., 185 | Lin, H. T., 201 |
| Drissi-Habti, M., 276 | |
| E | M |
| Eckel, A. J., 290 | McDowell, D. L., 185 |
| | Morscher, G. N., 306 |
| F | N |
| Ferber, M. K., 201 | Nakano, K., 276 |
| | O |
| G | Ojard, G. C., 3 |
| Goecke, K. E., 62 | P |
| Gonczy, S. T., 15, 86 | Polaha, J. J., 31 |
| Graham, S., 185 | |
| Gyekenyesi, J. Z., 306 | R |
| | Ramulu, M., 160 |
| H | S |
| Halbig, M. C., 290 | Simonen, E. P., 229 |
| Henager, C. H., Jr., 229 | Singh, M., 216 |
| | Steen, M., 148 |
| I | |
| Ishikawa, T., 276 | |

T

Takeda, N., 276
Telesman, J., 245

U

Ünal, Ö., 262

V

Verrilli, M., 245

W

Wang, H., 185
Windisch, C. F., Jr., 229

Y

Yun, H. M., 134

Z

Zawada, L. P., 15, 48, 62, 172

Subject Index

A

Adhesive, 62
 Aerospace applications
 high temperature, 172, 216
 Alumina, 118
 alumina-silica, 172
 ASTM standards
 C 1275, 15, 48, 86
 C 1292, 15
 C 1341, 15
 development, 3

B

Beam test, double cantilever, 31
 Boron nitride-containing
 interphase, 48, 86, 229,
 306

C

Calibration, compliance, 31
 Coating techniques, 276
 Combustor liner, high
 temperature, 3, 201
 Conductivity, thermal, 185
 Cracks and cracking, 245, 262
 growth, 229
 matrix, 134, 306
 stress, matrix, 148
 Creep, 172
 creep-rupture, 245, 290

D

Damage, 185
 accumulation, 306
 Debonding, 185
 Deformation, 134
 tensile, 262
 time-dependent, 216
 Degradation, 229, 290
 high temperature, 118
 modulus, 245
 Delamination toughness, 31

Density, bulk, 86
 Double cantilever beam, 31
 Double notch compression, 15
 Durability, high temperature,
 107

E

Elastic modulus, 86
 Embrittlement, temperature, 306
 End-notched flexure, 31
 Engine, turbine, 3, 62

F

Fatigue, 262
 testing, 245
 Fiber bridging, 229
 Fiber creep, 262
 Fiber waviness, effect on tensile
 response, 148
 Finite element calculations, 185
 Fixturing, 62
 Flexural properties
 C 1341, 15
 Flexural strength, 160
 Flexure test, 31, 86
 Fracture, 172
 Fracture properties, reinforcing
 fibers, 134
 Fracture stress, fiber, 148

G

Gas turbine, 201
 engine, 3
 Graphite/bismaleimide
 laminates, 160
 Gripping, 62

H

Hoop testing, 3
 Hysteresis, 118

I

Interfacial bonding, 276
 Interfacial conductance, 185
 Interfacial shear stress, 118
 Interphase, 306
 boron nitride, 48, 86, 229, 306
 carbon, 229, 306
 fiber/matrix, 118
 oxidation, 229

L

Laminate
 delamination, 15, 31
 graphite/bismaleimide, 160
 Larson-Miller, 134
 Loading, 107, 118, 216
 constant, 290
 mechanical, 185, 245
 mode, effect on tensile
 deformation, 262
 sustained, 172
 tensile, 148, 172

M

Mastercurve, 148
 Melt infiltration, 216
 Microstructure, 62
 analysis, 201
 assessment, 276
 damage, 185
 Mixed mode single leg bending
 test, 31
 Mode I double cantilever beam
 test, 31
 Mode II end-notched flexure
 test, 31
 Models and modeling, 3
 component lifetimes, 229
 micromechanics-based, 185
 notch effect, 160
 oxidation, 290
 oxidation/volatilization, 201
 rupture, 134
 Monkman-Grant, 134

N

Nextel720/AS, 172

Nicalon, 15, 86, 107, 262
 Hi-Nicalon, 306
 Nicalon-LAS II, 185
 Nicalon/MAS-5, 31
 Nicalon/Sylramic, 48
 Notch effect model, 160
 Notch strength, 172

O

Overstressing, 107
 Oxidation, 185, 290, 306
 damage, 245
 degradation, 229
 fiber coating, 216
 interphase, 229
 paralinear, 201
 protection, 276
 Oxide/oxide, 62, 172

P

Paralinear oxidation, 201
 Plain weave, 148
 Polysilazane, 15, 48

R

Ring burst, 3
 Rupture modeling, 134

S

Satin weave, 148
 Scale formation, 201
 Shear strength
 C 1292, 15
 Shear stress, 118
 Silicon carbide
 creep rupture, 245
 damage accumulation, 306
 degradation, 290
 durability, 107
 interface oxidation, 229
 loading mode effects, 262
 oxidation behavior, 201
 stress rupture, 216
 Silicon nitride, 210
 Silicon nitrocarbide, 48

Single leg bending, 31
 Steam environment, high
 pressure, high
 temperature, 201
 Strain accumulation, 262
 Strength predictions, 160
 Stress concentration, 160
 Stress-relaxation, 216
 Stress, residual, 118, 148
 Stress-rupture, 107, 216
 Stress-strain, 306
 curves, tensile, 276
 Stress, time-averaged, 245
 Surface roughness, 160
 Sylramic, 15, 48, 86, 306

T

Temperature effects on
 delamination toughness,
 31
 Temperature embrittlement, 306
 Tensile behavior, 148
 Tensile deformation, 262
 Tensile loading, 148, 172
 Tensile properties, 134
 Tensile strength testing
 C 1275, 15, 48, 86
 transthickness, 62

Tensile stress-strain, 306
 curves, 276
 Tensile testing, 262
 Tension testing, 86, 118
 Thermal conductivity, 185
 Thermal diffusivity, 185
 Thermal expansion, 216
 Thermal exposure, 118
 Thermogravimetric analysis, 290
 Thermomechanical properties,
 134
 Toughening mechanism, 276
 Toughness, delamination, 31
 Transmission electron
 microscopy, 276
 Transthickness tension, 62
 Turbine engines, 62
 Turbine, gas, 201
 Tyranno-Hex, 276

U

U.S. Air Force, 172

W

Waviness, fiber, effect on tensile
 response, 148

ISBN 0-8031-2872-X